Technical Report
TR-23-05
March 2023

Post-closure safety for SFR, the final repository for short-lived radioactive waste at Forsmark

Climate and climate-related issues, PSAR version

SVENSK KÄRNBRÄNSLEHANTERING AB

SWEDISH NUCLEAR FUEL
AND WASTE MANAGEMENT CO

Box 3091, SE-169 03 Solna
Phone +46 8 459 84 00
skb.se

ISSN 1404-0344
SKB TR-23-05
ID 1677520
March 2023

Post-closure safety for SFR, the final repository for short-lived radioactive waste at Forsmark

Climate and climate-related issues, PSAR version

Svensk Kärnbränslehantering AB

Keywords: Post-closure safety, SFR, Final repository, Low- and intermediate-level radioactive waste, Forsmark, Safety assessment, Climate, Global warming, Sea level, Temperate, Submerged, Periglacial, Permafrost, Glacial.

This report is published on www.skb.se

Summary

The final repository for short-lived radioactive waste (SFR) at Forsmark, Sweden is used for the final disposal of low- and intermediate-level operational waste from Swedish nuclear facilities. The PSAR assessment of post-closure safety is an important part of the construction license application for the extension of SFR. This report constitutes one of the main references supporting the **Post-closure safety report** and describes the current scientific knowledge on climate and climate-related issues that are relevant to the post-closure safety of SFR.

From a safety assessment point of view, it is not possible to predict a single climate evolution in a 100 000-year time perspective with enough confidence for a safety assessment. Instead, *a range* of future climate developments need be considered in the safety assessment in order to cover the uncertainties in future climate development that may influence post-closure safety for the repository.

In the present report, climate-related issues of importance for repository performance and safety are identified and described. These include i) development of permafrost and frozen ground, ii) isostatic and eustatic changes and resulting relative sea-level changes, iii) ice-sheet development and iv) surface denudation. Furthermore, the current knowledge on past, present and potential future evolution of climate and climate-related issues is documented. In support of the selection of climate developments for the post-closure safety assessment, a qualitative likelihood assessment of potential climate development over the coming 100 000 years is also conducted. Finally, five possible future developments of climate and climate-related issues in Forsmark over the next 100 000 years (here called “climate cases”) are selected and presented.

Three climate cases span the likely range of post-closure climate evolution. These are included in the *reference external conditions* evaluated in the safety assessment main scenario. The warm climate case assumes that similar-to-present levels of anthropogenic greenhouse gas emissions will continue for most of this century, resulting in the continuation of temperate climate conditions at Forsmark for the entire assessment period. The warm climate case also describes a prolonged period after repository closure during which the area above the repository remains submerged beneath the Baltic Sea. The cold climate case assumes that the anthropogenic greenhouse-gas emissions will decline within the next few decades, resulting in the development of periglacial (permafrost) conditions at Forsmark during the latter half of the assessment period. The warm and cold climate case are complemented with a simplified climate case where present-day climate conditions prevail during the entire assessment period.

The possibility of ice-sheet coverage over Forsmark within the assessment period is considered to be a less likely event, and is thus described in a climate case that is evaluated in a less probable scenario. Finally, permafrost development during the first 50 000 years after closure is considered to have very low likelyhood, and is thus included in a climate case that is evaluated in a residual scenario. The climate cases together cover the expected maximum range within which climate and climate-related issues of importance for post-closure safety may vary over the 100 000-year assessment time period.

Sammanfattning

Slutförvaret för kortlivat radioaktivt avfall (SFR) i Forsmark, Sverige används för slutförvaring av låg- och medelaktivt driftavfall från svenska kärntekniska anläggningar. Analysen av säkerhet efter förslutning i PSAR är en viktig del av ansökan om medgivande för utbyggnaden av SFR. Denna rapport utgör en av huvudreferenserna till **Huvudrapporten säkerhet efter förslutning.**

Klimat är inte förutsägbart på en 100 000-års tidsskala, vilket är den tidsrymd som analyseras i analysen av säkerhet efter förslutning. En mest sannolik framtida klimatutveckling kan därför inte förutsägas med tillräcklig tillförlitlighet och detaljeringsgrad för analysen av säkerhet efter förslutning. Istället behöver ett flertal tänkbara framtida klimatutvecklingar inkluderas i säkerhetsanalysen för att täcka osäkerheten i framtida klimatutveckling.

I denna rapport identifieras och beskrivs klimatrelaterade processer av betydelse för förvarets funktion och säkerheten efter förslutning. Dessa inkluderar i) utveckling av permafrost och frusen mark, ii) isostatiska och eustatiska förändringar vilka resulterar i förändringar av den relativa havsnivån, iii) utveckling av inlandsisar, och, iv) denudation vid markytan. Vidare dokumenteras dagens klimatförhållanden i Forsmark samt nuvarande kunskap om forntida och potentiella framtida utvecklingar av klimat och klimatrelaterade processer. Som stöd för valet av klimatutvecklingar för analysen av säkerhet efter förslutning görs även en kvalitativ sannolikhetsbedömning av potentiella klimatutvecklingar under de kommande 100 000 åren. Slutligen väljs och presenteras fem tänkbara framtida utvecklingar av klimat och klimatrelaterade processer i Forsmark, så kallade ”klimatfall”, för de kommande 100 000 åren.

Tre klimatfall representerar spännvidden av den förväntade klimatutvecklingen efter förslutning. Dessa ingår i de *externa referensförhållanden* som utvärderas i säkerhetsanalysens huvudscenario. Klimatfallet med varmt klimat förutsätter att mänskliga växthusgasutsläpp liknande dagens nivåer kommer att fortsätta under större delen av detta århundrade vilket resulterar i att tempererade klimatförhållanden råder under hela analysperioden i Forsmark. Fallet med varmt klimat beskriver också en förlängd period med havstäckta förhållanden ovanför förvaret. Fallet med kallt klimat antar att mänskliga utsläpp av växthusgaser kommer att minska inom de kommande årtiondena vilket ger upphov till framkomsten av periglaciala (permafrost) perioder i Forsmark under den senare delen av analysperioden. Utöver fallen med varmt och kallt klimat ingår i de externa referensförhållandena också ett förenklat klimatfall, i vilket dagens klimatförhållanden antas råda under hela analysperioden.

Inlandsisutveckling över Forsmark inom analysperioden bedöms ha låg sannolikhet och beskrivs därför i ett klimatfall som utvärderas i ett mindre sannolikt scenario. Förekomst av permafrost under de första 50 000 åren efter förslutning bedöms ha väldigt låg sannolikhet och beskrivs därför i ett klimatfall som utvärderas i ett restscenario. Klimatfallen täcker tillsammans det förväntade maximala intervallet inom vilket klimat- och klimatrelaterade processer av betydelse för säkerheten efter förslutning kommer att variera inom analysperioden.

Contents

1 Introduction

This document is one of the main references to the **Post-closure safety report** that contributes to the preliminary safety analysis report (PSAR) for SFR, the repository for short-lived radioactive waste at Forsmark in Östhammar municipality, Sweden (Figure 1-1).

This chapter gives the background and a short overview of the PSAR post-closure safety assessment undertaken as part of the construction license application for the extension of SFR. Moreover, the purpose and content of this report are described.

1.1 Background

SFR is operated by the Swedish Nuclear Fuel and Waste Management Company, SKB, and is part of the Swedish system for management of waste from nuclear power plants, other nuclear activities, industry, research and medical care. In addition to SFR, the Swedish nuclear waste system also includes the repository for spent nuclear fuel and the repository for long-lived radioactive waste (SFL).

SFR consists of the existing part, SFR1 (Figure 1-2, grey part), and the extension, SFR3 (Figure 1-2, blue part). SFR1 is designed for disposal of short-lived low- and intermediate-level waste produced during operation of the Swedish nuclear power reactors, as well as waste generated during the application of radioisotopes in medicine, industry, and research. This part became operational in 1988. SFR3 is designed primarily for disposal of short-lived low- and intermediate-level waste from decommissioning of nuclear facilities in Sweden. The extension is called SFR3 since the name SFR2 was used in a previous plan to build vaults adjacent to SFR1. The repository is currently estimated to be closed by year 2075.

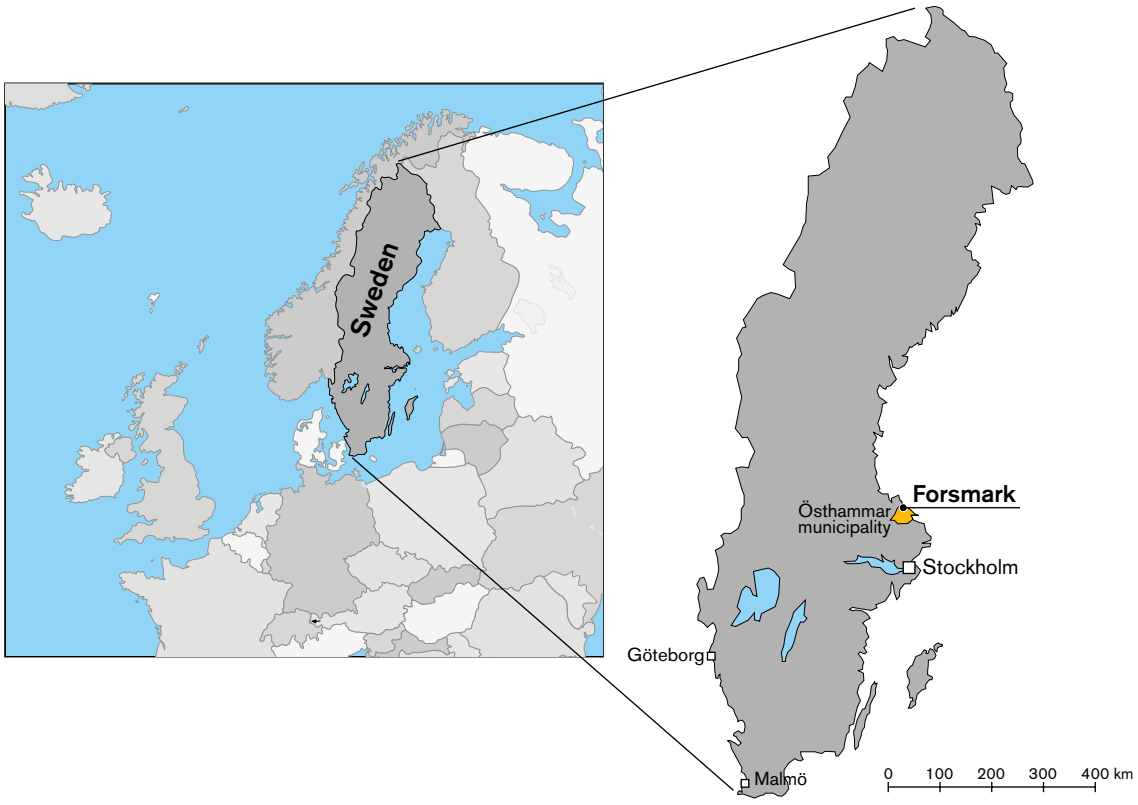

Figure 1-1. *Map showing the location of Forsmark. Forsmark is situated in Östhammar municipality, which belongs to County of Uppsala.*

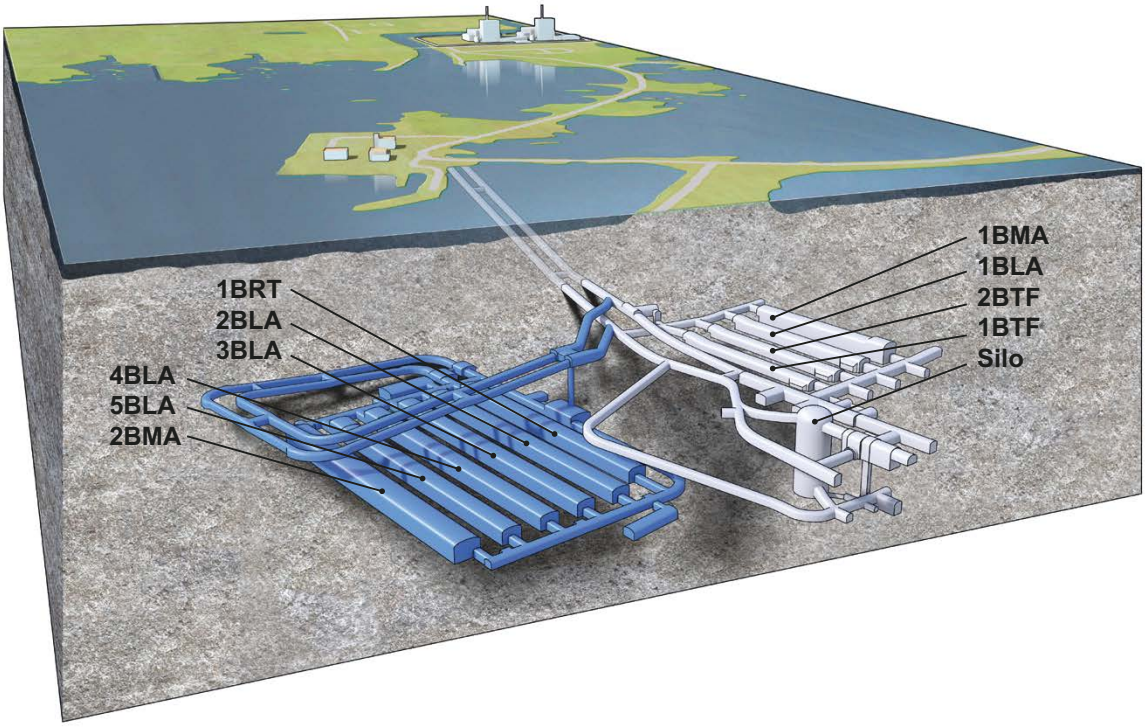

Figure 1-2. *Schematic illustration of SFR. The grey part is the existing repository (SFR1) and the blue part is the extension (SFR3). The waste vaults in the figure are the silo for intermediate-level waste, 1–2BMA vaults for intermediate-level waste, 1BRT vault for reactor pressure vessels, 1–2BTF vaults for concrete tanks and 1–5BLA vaults for low-level waste.*

The SFR waste vaults are located below the Baltic Sea and are connected to the ground surface via two access tunnels. SFR1 consists of one 70-metre-high waste vault (silo) and four 160-metre-long waste vaults (1BMA, 1–2BTF and 1BLA), covered by about 60 metres of bedrock. SFR3 consists of six waste vaults (2BMA, 1BRT and 2–5BLA), varying in length from 255 to 275 m, covered by about 120 metres of bedrock.

A prerequisite for the extension of SFR is the licensing of the extended facility. The licensing follows a stepwise procedure. In December 2014, SKB submitted two licence applications to extend and continue the operation of SFR, one to the Swedish Radiation Safety Authority (SSM) for permission under the Act on Nuclear Activities (SFS 1984:3) and one to the Land and Environment Court for permissibility under the Environmental Code (SFS 1998:808). In October 2019 SSM submitted their pronouncement to the Swedish Government and recommended approval of the permission sought by SKB. In November 2019 the Court submitted its statement to the Swedish Government and recommended approval of the licence application. The Swedish Government granted permit and permissibility in December 2021.

The current step in the licensing of the extended SFR is the processing of the construction license application, submitted by SKB to SSM for review under the Act on Nuclear Activities. The licence documentation consists of an application document and a set of supporting documents. A central supporting document is the preliminary safety analysis report (PSAR), with a general part consisting of ten chapters.[1] Chapter 9 of the general part of that report addresses post-closure safety. The **Post-closure safety report** is the main reference to Chapter 9, and this report is a main reference to the **Post-closure safety report**.

[1] SKB, 2022. PSAR SFR – Allmän del kapitel 1 – Introduktion. SKBdoc 1702853 ver 3.0, Svensk Kärnbränslehantering AB. (In Swedish.) (Internal document.)

1.2 Post-closure safety assessment

1.2.1 Overview

The main role of the post-closure safety assessment is to demonstrate that SFR is radiologically safe for humans and the environment after closure. This is done by evaluating compliance with respect to the Swedish Radiation Safety Authority's regulations concerning post-closure safety and the protection of human health and the environment. Furthermore, the post-closure safety assessment is being successively developed in the stepwise licensing process for the extended SFR, and thus the results from the PSAR assessment[2] provide input to the forthcoming updated assessment to be carried out before trial operation of the facility.

The overall aim in developing a geological repository for nuclear waste is to ensure that the amounts of radionuclides reaching the accessible biosphere are such that possible radiological consequences are acceptably low at all times. Important aspects of the regulations are that post-closure safety shall be maintained through a system of passive barriers. The barrier system of SFR comprises engineered and natural barriers and the function of each barrier is to, in one or several ways, contribute to the containment and prevention or retention of dispersion of radioactive substances, either directly or indirectly by protecting other barriers in the barrier system. To achieve post-closure safety, two safety principles have been defined. *Limitation of the activity of long-lived radionuclides* is achieved by only accepting waste for disposal that conforms with the waste acceptance criteria for SFR. *Retention of radionuclides* is achieved by the function of the engineered and natural barriers. The two safety principles are interlinked and applied in parallel. The engineered barrier system is designed for an inventory that contains a limited amount of long-lived radionuclides, given the conditions at the selected site and the natural barriers.

The basis for evaluating compliance is a safety assessment methodology that conforms to the regulatory requirements regarding methodology, and that supports the demonstration of regulatory compliance regarding post-closure safety and the protection of human health and the environment. The overall safety assessment methodology applied is described in the **Post-closure safety report**, Chapter 2. The methodology was developed in the SR-PSU (SKB TR-14-01[3]) based on SKB's previous safety assessment for SFR1 (SAR-08, SKB R-08-130). Further, it is consistent with the methodology used for the post-closure safety assessment for the final repository for spent nuclear fuel to the extent appropriate given the different nature of the two repositories.

1.2.2 Report hierarchy

The **Post-closure safety report** and main references for the post-closure safety assessment are listed and briefly described in Table 1-1, also including the abbreviated titles (in bold) by which they are identified in the text. Furthermore, there are numerous additional references that include documents compiled either by SKB or other organisations, or that are available in the scientific literature, as indicated in Figure 1-3.

[2] For brevity, the PSAR post-closure safety assessment for SFR is also referred to as "the PSAR assessment" or "the PSAR" in the present report.

[3] For SKB reports without named authors, the report number is used instead of publication year when referring to them in the text.

Table 1-1. Post-closure safety report and main references for the post-closure safety assessment. The reports are available at www.skb.se.

Abbreviated title by which the reports are identified in this report and in the main references Report number	**Content**
Post-closure safety report SKB TR-23-01	The main report of the PSAR post-closure safety assessment for SFR.
Initial state report SKB TR-23-02	Description of the expected conditions (state) of the repository at closure. The initial state is based on verified and documented properties of the repository and an assessment of its evolution during the period up to closure.
Waste process report SKB TR-23-03	Description of the current scientific understanding of the processes in the waste form and in the packaging that have been identified in the FEP processing as potentially relevant for the post-closure safety of the repository. Reasons are given as to why each process is handled in a particular way in the safety assessment.
Barrier process report SKB TR-23-04	Description of the current scientific understanding of the processes in the engineered barriers that have been identified in the FEP processing as potentially relevant for the post-closure safety of the repository. Reasons are given as to why each process is handled in a particular way in the safety assessment.
Geosphere process report SKB TR-14-05	Description of the current scientific understanding of the processes in the geosphere that have been identified in the FEP processing as potentially relevant for the post-closure safety of the repository. Reasons are given as to why each process is handled in a particular way in the safety assessment.
Climate report SKB TR-23-05 (this report)	Description of the current scientific understanding of climate and climate-related issues that have been identified in the FEP processing as potentially relevant for the post-closure safety of the repository. Description of the current scientific understanding of the future evolution of climate and climate-related issues.
Biosphere synthesis report SKB TR-23-06	Description of the present-day conditions of the surface systems at Forsmark, and natural and anthropogenic processes driving the future development of those systems. Description of the modelling performed for landscape development, radionuclide transport in the biosphere and potential exposure of humans and non-human biota.
FEP report SKB TR-14-07	Description of the establishment of a catalogue of features, events and processes (FEPs) that are potentially relevant for the post-closure safety of the repository.
FHA report SKB TR-23-08	Description of the handling of inadvertent future human actions (FHA) that are defined as actions potentially resulting in changes to the barrier system, affecting, directly or indirectly, the rate of release of radionuclides, and/or contributing to radioactive waste being brought to the surface. Description of radiological consequences of FHAs that are analysed separately from the main scenario.
Radionuclide transport report SKB TR-23-09	Description of the radionuclide transport and dose calculations carried out for the purpose of demonstrating compliance with the radiological risk criterion.
Data report SKB TR-23-10	Description of how essential data for the post-closure safety assessment are selected, justified and qualified through traceable standardised procedures.
Model tools report SKB TR-23-11	Description of the model tool codes used in the safety assessment.

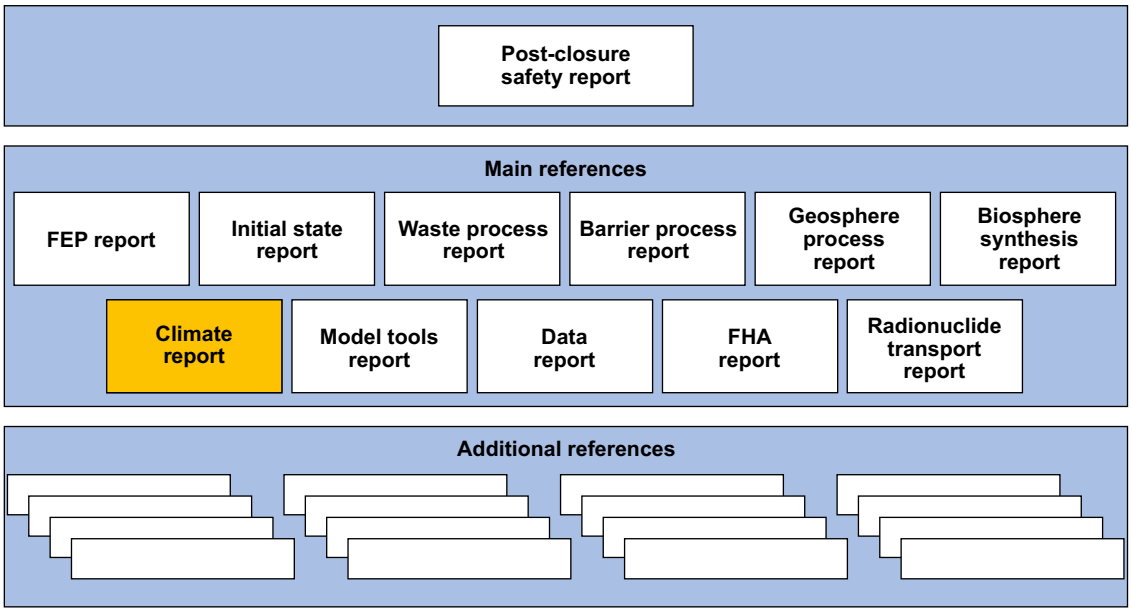

Figure 1-3. *The hierarchy of the Post-closure safety report, main references and additional references in the post-closure safety assessment.*

1.3 This report

1.3.1 The role of this report in the post-closure safety assessment

The ten steps in the methodology applied to assess post-closure safety (Figure 1-4) are carried out partly concurrently and partly consecutively. Information on climate and climate-related issues is essential for several steps of the methodology. Step 1 constitutes identification of all factors potentially important for the post-closure safety that hence need to be addressed in the assessment, as described in the **FEP-report**. The identified climate and climate-related issues are described in Chapters 2 and 3. Step 2 includes a description of the climate state at the time of repository closure. For the description of the repository environs, including the climate and climate-related issues, present-day conditions are assumed at repository closure.

Step 3 is the description of external conditions identified in Step 1, including selection and description of a few possible climate developments (*climate cases*). These climate cases are selected so that they together illustrate the most important and reasonably foreseeable sequences of future climate states and their impact on the protective capability of the repository and environmental consequences. A key point is the establishment of *reference external conditions*, defined as the probable climate evolution at Forsmark over the next 100 000 years. As the climate evolution over the next 100 000 years is associated with considerable uncertainty, for example with regards to future anthropogenic greenhouse-gas emissions and sea-level rise, it is not possible to assign a single climate development as probable. Therefore, the reference external conditions are represented by several climate developments that span the range of the probable climate evolution. The reference external conditions constitute the basis for the description of the reference evolution (step 7) and supports the selection (step 8) and analysis (step 9) of the safety assessment scenarios.

Based on the regulatory advice (SSMFS 2008:21, SSMFS 2008:37), three types of scenarios are considered in the safety assessment:

- The main scenario (**Post-closure safety report**, Chapter 7) takes into account the most probable changes within the repository and its environs based on the initial state, the probable evolution of the external conditions (climate) and the reference evolution. The main scenario constitutes a starting point for the analysis of the impact of uncertainties.

- Less probable scenarios (**Post-closure safety report**, Chapter 8) evaluate uncertainties related to alternative evolutions of the repository, or variations in the specified initial state or external conditions, that are not evaluated within the framework of the main scenario.
- Residual scenarios (**Post-closure safety report**, Chapter 9) are primarily designed to illustrate the significance of individual barriers and barrier functions and to evaluate radiological consequences of future human actions (FHA).

The calculation endpoints of the scenario analysis are annual effective dose to humans and annual dose-rates to non-human biota. The calculated annual doses from the main scenario and less probable scenarios are propagated to the assessment of radiological risk (step 9), where the estimated risk is compared with criteria stipulated in SSM's regulations (**Post-closure safety report**, Chapter 10). Annual dose calculations from residual scenarios are not propagated to the risk assessment.

Uncertainty management is an integral part of the post-closure assessment methodology (**Post-closure safety report**, Section 2.5), and thus also in the handling of external conditions. The uncertainty in climate evolution over the assessment period is primarily handled by considering several climate evolutions in the safety assessment, as is further described in Section 1.4.2.

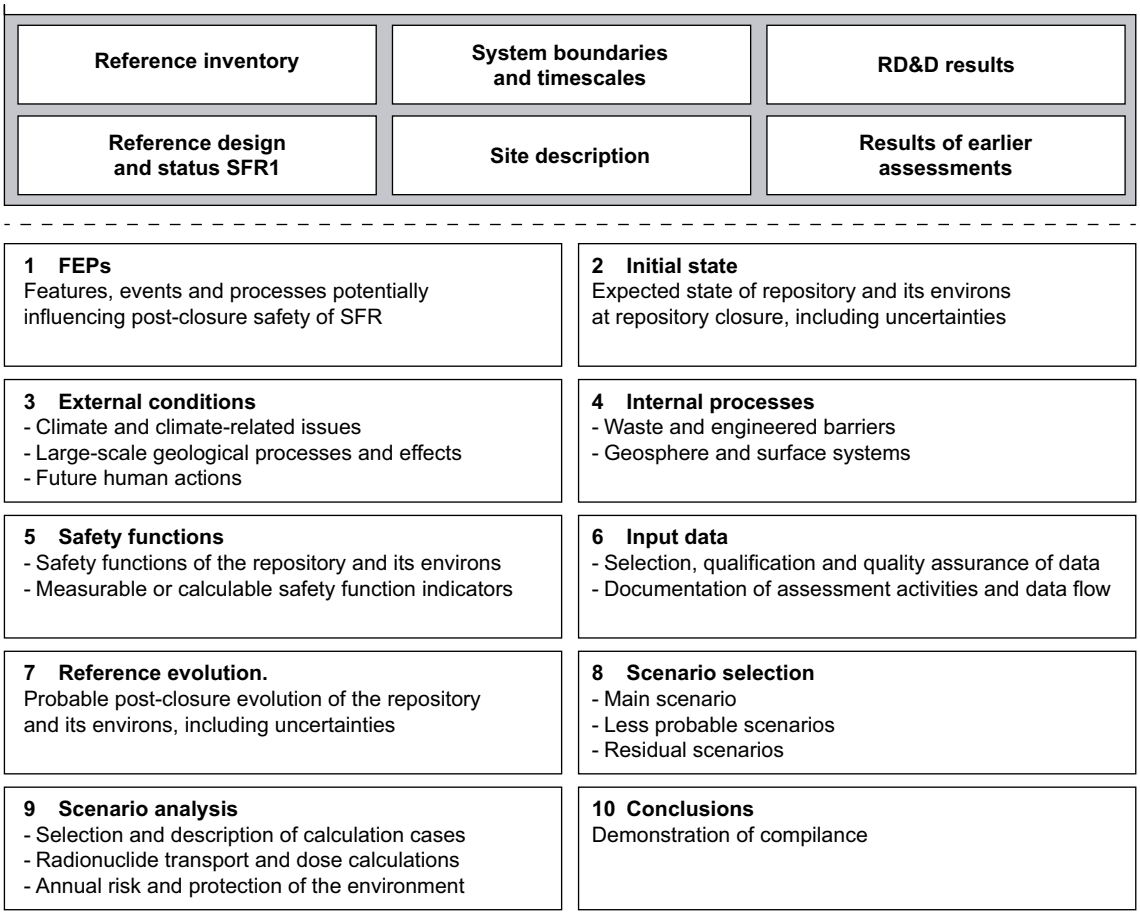

Figure 1-4. *An outline of the ten main steps of the present post-closure safety assessment. The boxes above the dashed line are prerequisites for the methodology and its implementation. This report contributes to step 3.*

1.3.2 Purpose

This report presents the current scientific knowledge on climate and climate-related issues, relevant to the long-term safety of a repository for low- and intermediate-level nuclear waste, to a level required for an adequate treatment in the PSAR. Based on this information, the report presents several possible future climate developments ("climate cases") for Forsmark in support of the analysis of the main scenario, less probable scenarios and residual scenarios. The present report is based on research published in the general scientific literature as well as research conducted and published by SKB.

1.3.3 Main developments since the SR-PSU

The previous post-closure safety assessment (SR-PSU) was reviewed by SSM (SSM 2019). The overall assessment on climate and climate-related issues from this review was that SKBs description of the future climate evolution and climate-related issues serves as an adequate starting point for the calculations in the safety assessment. The major feedbacks on climate and climate-related issues were the following:

- The calculation cases evaluating the effects of glaciation and extended global warming should be included in the radiological risk assessment and preferably handled as less probable scenarios.
- SKB should continue to monitor scientific developments concerning the historical and future climate evolution.

Based on this feedback, this report includes the following major improvements in the description of the climate and climate-related issues compared with the SR-PSU Climate report (SKB TR-13-05):

- An assessment on the relative likelihood of future climate evolution (Chapter 4). This assessment supports the selection of climate cases (Chapter 5) for the safety assessment scenarios.
- Updated descriptions of the historical climate of the last glacial cycle and the following interglacial (Section 3.2).
- Updated description of the present-day climate and relative sea level at Forsmark (Sections 3.3 and 3.5) as well as future climate and sea-level projections (Sections 3.4 and 3.5).
- Updated assessment on the future surface denudation in the Forsmark area (Section 2.4).

1.3.4 Structure of this report

This report comprises 5 chapters and 7 appendices. Following is a brief description of the contents:

Chapter 1 – **Introduction.** This chapter describes the background and the role of the report. Furthermore, an introduction to climate and climate-related issues as well as relevant definitions are given.

Chapter 2 – **Climate-related issues**. This chapter describes the climate-related issues of importance for post-closure safety of SFR.

Chapter 3 – Past, present and future evolution of climate and climate-related issues. This chapter describes the current knowledge on past and future climate evolution, both globally and regionally in Forsmark as well as the present climate at Forsmark.

Chapter 4 – Qualitative likelihood assessment. In this chapter, the likelihood of the future climate evolution is assessed.

Chapter 5 – Climate cases. In this chapter, the climate cases are selected and the associated climate and climate-related issues are described.

Appendix A – Terms and abbreviations. This appendix contains a list of terms and abbreviations.

Appendix B – Construction of surface air temperature and precipitation at Forsmark until 12 000 AD. This appendix presents an updated construction of the surface air temperature and precipitation changes at Forsmark for the next 10 000 years based on the scientific literature and climate modelling.

Appendix C – Estimating Forsmark surface air temperature and precipitation for the IPCC reference period 1986–2005 AD. This appendix presents an estimation of the average surface air temperature and precipitation at Forsmark between 1986 and 2005 AD.

Appendix D – Simplified methodology for estimating potential evapotranspiration in a warmer climate. This appendix presents an estimate of the potential evapotranspiration in a warmer climate using a simplified, temperature dependent, methodology.

Appendix E – Ice-sheet profiles. This appendix describes in detail the 2D ice-sheet profiles that are used for modelling of groundwater flow under glacial conditions (Vidstrand et al. 2010) and for THM studies (Lönnqvist and Hökmark 2010). The appendix has been adopted from SKB (TR-10-49).

Appendix F – Transitions between climate domains. This appendix presents an overview of typical transition durations between climate domains (defined in Section 1.4.3).

Appendix G – Construction of a Holocene relative sea-level curve for the Forsmark site. This appendix presents an updated relative sea-level curve for Forsmark ranging through the Holocene, based on data from Påsse and Daniels (2015) and Hedenström and Risberg (2003).

1.3.5 Contributing experts

Project leader for the PSAR safety assessment has been Jenny Brandefelt (SKB). Editor for this report has been Johan Liakka (SKB) and contributing authors have been Johan Liakka (SKB) and Jens-Ove Näslund (SKB). Parts of the report have been produced by adaptation of text and figures from the SR-PSU Climate report (SKB TR-13-05) and the supporting publications since the SR-PSU (Section 1.3.7).

This report has been significantly improved at different stages by adjustments in accordance with comments provided by factual reviewers. Factual reviewers have been; Mike Thorne (Mike Thorne and Associates Ltd.) and Andrey Ganopolski (Potsdam Institute for Climate Impact Research).

1.3.6 Structure for description of climate-related issues

In discussing each of the various climate-related issues in Chapter 2, the following standardised structure has been adopted.

Overview/general description

Under this heading, a general description of the current knowledge regarding the climate-related issue is given.

Controlling conditions and factors

Under this heading, the conditions and factors that control each issue are discussed. This includes conditions or factors that are both external and internal to the issue. External refers to systems that are not part of the described system/feature and that the described system/feature interacts with. For example, for “ice-sheet dynamics”, the atmosphere and the bed are external factors and relevant aspects of them are described. Internal refers to conditions and factors governing system/feature behaviour and that are generally included in models of the system/feature, e.g. for “ice-sheet dynamics” the creep process of ice.

A table summarising the influence of the climate-related issue on the geological barrier of the repository is presented. The table includes the geosphere variables influenced by the system/feature and the variables associated with the system/feature that are required to be known to quantify the interaction between the system/feature and the repository system, e.g. for “ice-sheet dynamics” basal temperature and melt-rate. In this context, the repository system includes both the geosphere and the engineered barriers.

Natural analogues/observations in nature

Under this heading observations in nature and, when applicable, present-day natural analogues regarding the process are summarised.

Model studies

In this section, model studies of the process are summarised. This documentation focuses on process understanding and, for instance, includes sensitivity analyses. The handling of external and internal controlling conditions and factors is described, e.g. if spatially and temporally varying internal conditions are considered.

Time perspective

The timescales on which the system/feature operates and changes are documented.

Handling in the safety assessment

The handling of the documented interactions with the repository is discussed. As a result of the information under this subheading, mappings of the climate-related issues to the method, or methods, of treatment and, in relevant cases, applicable models are produced. The mappings are characterised on various timescales.

Handling of uncertainties

Given the adopted handling in the PSAR as described above, the treatment of different types of uncertainties associated with the issue, within that general framework, is summarised under the following headings.

Uncertainties in mechanistic understanding: The uncertainties in the general understanding of the issue are discussed based on the available documentation and with the aim of answering the question: Are the basic scientific mechanisms governing the issue understood to a level necessary for the suggested handling? Alternative models may sometimes be used to illustrate this type of uncertainty.

Model simplification uncertainties: In most cases, the quantitative representation of a process contains simplifications, for instance in a numerical model. These may result in a significant source of uncertainty in the description of the system evolution. Alternative models or alternative approaches to simplification for a specific conceptual model may sometimes be used to illustrate this type of uncertainty.

Input data and data uncertainties: The input data necessary to quantify the process for the suggested handling are documented. The treatment of important input and output data and associated data uncertainties are described in detail in SKB (R-23-01), to which reference is made as appropriate.

Adequacy of references

Under this heading, the adequacy of references for supporting the handling in the PSAR are judged, i.e. whether the references are peer-reviewed papers or documents which have undergone factual review.

1.3.7 Publications supporting the PSAR Climate report

Within the SKB climate programme, the following supporting reports have been produced since the SR-PSU climate report (SKB TR-13-05).

- Schenk and Wohlfarth (2019) performed a study on climate evolution and variability in Scandinavia and Europe during the transition from a glacial into an interglacial climate state, combining a multi-proxy climate study with results from high-resolution climate modelling.
- Helmens (2019) conducted an extensive multi-proxy paleoclimate study on lacustrine and fluvial sediments spanning the last 130 000 years from northern Fennoscandia.

- To increase the knowledge on ice-sheet hydrological processes and their influence on both surface and subsurface environments, a comprehensive study on these subjects was made within the Greenland Analogue Project (GAP) (Claesson Liljedahl et al. 2016, Harper et al. 2016, and references therein), using the Greenland ice sheet as a natural analogue for future possible conditions in Sweden.
- Harper et al. (2019) conducted a follow-up study (ICE) to the GAP project in the same region of Greenland where GAP was performed with the aim of i) interpreting the physical framework of the ice-sheet bed, ii) quantifying the magnitude of and spatial gradients in basal water pressure, iii) investigating the presence of short duration water pressure transients in the ice-sheet basal drainage system, and iv) advancing the understanding of the distribution of water along the ice-sheet bed.
- Lord et al. (2019) used a combination of Earth system modelling techniques to simulate the possible evolution of future climate over the next one million years for a range of anthropogenic carbon dioxide emissions scenarios.
- Hall et al. (2019a) conducted a study with the aim to provide estimates of past and future depths and rates of denudation at Forsmark, using i) the Sub-Cambrian Peneplain as a reference surface against which to estimate Pleistocene glacial erosion, ii) mapping of the distribution, form and characteristics of glacial landforms and sediments on the shield surface to understand patterns and processes of glacial erosion, iii) studying fracturing related to past and future glacial erosion patterns, and iv) obtaining cosmogenic nuclide inventories from bedrock surfaces to denudation rates for the last glacial cycle and for the last 1 Ma. Based on the tentative information on the timing of the next future glaciation at Forsmark (Lord et al. (2019), tentative denudation rates for e.g. the coming 100 000 years were also calculated.
- Two complementary studies, investigating key conceptualisations of the basement surface, relevant for the glacial erosion study at Forsmark (Hall et al. 2019a) have also been performed (Goodfellow et al. 2019, Hall et al. 2019b).
- Pellikka et al. (2020) performed simulations of potential future sea-level rise (storm contribution and rise of mean relative sea level) with associated statistical measures, based on recent literature and simulations dedicated for the Forsmark site. The calculations were made for different carbon emission scenarios and for the time periods up to 2050, 2080 and 2100 AD.

Since the present report constitutes an updated version of the SR-PSU Climate report (SKB TR-13-05), it also contains considerable information from the SR-PSU supporting reports. Three reports were produced in support of the SR-PSU. A review of early Weichselian climate was performed by Wohlfarth (2013) to enhance knowledge on the last transition from interglacial to glacial climate conditions in Sweden, whereas Helmens (2013) re-examined the last interglacial–glacial cycle based on long proxy records from central and northern Europe. The aim of the two studies was to describe the complex course of events that took place when warm interstadial conditions, similar to those at present, turned into cold glacial conditions. Finally, Brandefelt et al. (2013) analysed the potential for cold climate conditions and permafrost in Forsmark in the next 60 000 years. The purpose was to provide information to the descriptions of the climate cases and to the analysis of freezing of SFR structures.

The present report also uses abundant information from reports and publications that were produced in support of the SR-Site Climate report (SKB TR-10-49). Many of the topics that were studied are, by necessity, linked to each other and in some cases therefore partly overlapping. Studies on climate, paleoclimate and Weichselian glacial history were conducted (Helmens 2009, Houmark-Nielsen 2009, Kjellström et al. 2009 (including erratum Feb 2010), Wohlfarth 2009). A special issue of Boreas (Wohlfarth and Näslund 2010), with papers on conditions in Scandinavia during a long period prior to the Last Glacial Maximum of the last glacial cycle, was published as a result of a workshop on this topic arranged by SKB in 2007 (Näslund et al. 2008). Permafrost development was studied by Hartikainen et al. (2010) whereas glacial hydrology was studied by Jansson and Näslund (2009). Surface denudation (i.e. weathering and erosion) was investigated by Olvmo (2010), while bedrock borehole temperatures, geothermal heat and paleoclimate were studied by Sundberg et al. (2009). Various aspects of glacial isostatic adjustment have been studied, such as isostatic adjustment and associated relative sea-level change (Whitehouse 2009) and crustal stresses under glacial conditions (Lund et al. 2009, Lund and Näslund 2009).

The studies performed within the SKB climate programme have resulted in more than 100 scientific publications in *peer-reviewed* journals or as PhD theses. In addition to the studies resulting from the SKB climate programme, a large number of papers from the general scientific literature have been used as input to this report.

1.4 Climate and climate-related issues

1.4.1 Importance for repository performance and safety

All features, events and processes (FEPs) of importance for the evolution and post-closure safety of the repository are compiled in the **FEP-report**. Seven FEPs related to climate and climate-related issues of importance for the post-closure safety have been identified. These are listed in Table 1-2 together with the section in this report where they are described.

Table 1-2. FEPs related to climate and climate-related issues, and references to corresponding descriptions in this report.

FEP name	Section in this report
Climate forcing	3.1, 3.3
Climate evolution	3.2, 3.3, 3.4
Development of permafrost	2.1
Ice-sheet dynamics and hydrology	2.3
Glacial isostatic adjustment	2.2
Shore-level changes	2.2, 3.5
Denudation	2.4

1.4.2 Strategy for handling climate and climate-related issues

The handling of climate and climate-related issues in safety assessments must be tailor-made for each repository concept and waste type to be analysed (Näslund et al. 2013). The climate is not predictable on a 100 000-year timescale at the level required for safety assessments. Therefore, a range of future climate developments must be considered in the safety assessment to cover the uncertainty in future climate evolution. This range is determined based on scientific knowledge on past, present and future climate evolution, as well as on knowledge of which processes are of importance for the functioning of the repository concept under consideration (Table 1-2). The latter has been obtained from the iterative process of having performed several safety assessments for a specific repository concept.

Based on this range, a few representative climate developments, so-called *climate cases,* are identified. These describe the most important and reasonably foreseeable sequences of future climate states of relevance for the protective capability of the repository. Collectively, the climate cases cover the expected maximum range within which climate and climate-related issues of importance for post-closure safety may vary over the 100 000-year assessment period. The actual evolution of the Forsmark climate over this time period is expected to fall within the range covered by the climate cases.

In the SR-PSU, four climate cases were described and used as a basis for the analysis of the future evolution of the repository and its environs and for the definition of scenarios, namely the global warming-, early periglacial-, extended global warming- and Weichselian glacial cycle climate cases. The global warming- and early periglacial climate cases were included as variants of external conditions in the analysis of the main scenario, whereas radiological consequences of the climate developments described by the extended global warming and Weichselian glacial cycle climate cases were illustrated in residual scenarios.

As described in Section 1.3.1, the description of the evolution in the main scenario is based on the reference external conditions, i.e. the range of probable climate evolution, whereas less probable scenarios account for uncertainties, including those related to the climate evolution, that are not handled in the framework of the main scenario. In the SR-PSU, no quantitative assessment was conducted to evaluate the relative likelihood of potential future climate evolutions in support of the

scenario selection. The assignment of climate cases to the main, less probable and residual scenario categories was therefore not straightforward (see Section 1.3.3). For example, the early periglacial climate case was included in the main scenario, although it was not explicitly assessed to be likely to occur. On the other hand, the potential effects of glaciation and post-glacial conditions included in the Weichselian glacial cycle climate case were analysed in a residual scenario, even though it was never shown that omitting such development from the risk assessment was justified.

In the PSAR, the selection of climate developments is therefore further developed from the SR-PSU to support the definition of scenarios. The main objective is to define climate cases in support of a main scenario, less probable scenarios and residual scenarios. For this purpose, a likelihood assessment of the future climate evolution is included in this report (Chapter 4).

As part of the iterative process of having performed several safety assessments for SFR, the strategy for handling climate and climate-related issues in the PSAR is also motivated by the results in the SR-PSU (SKB TR-14-01) including complementary studies (Näslund et al. 2017a, b). That is, the demonstrated importance of each climate and climate-related issue for the protective capability of the repository and dose to humans in the SR-PSU have also been considered when selecting the climate cases for the PSAR.

The resulting climate cases are presented in Chapter 5.

1.4.3 Definitions of climate change, climate domains and submerged conditions

There are various definitions of *climate change*. In the present report, climate change is defined according to the definition by the Intergovernmental Panel on Climate Change (IPCC), namely as "any change in climate over time whether due to natural variability or as a result of human activity" (IPCC 2001). This differs from the definition used by the United Nation's Framework Convention on Climate Change (UNFCCC) that defines climate change as "a change of climate that is attributed directly or indirectly to human activity that alters the composition of the global atmosphere, and that is in addition to natural climate variability over comparable time periods". Since climate may change due to both natural variability and to anthropogenic influences, and both types of change are relevant to the long-term safety of SFR, the definition of climate change in the PSAR follows that of IPCC. By the time of publication of this report, six assessment reports on the physical science basis have been published by the IPCC, of which the latest version (IPCC 2021) was published after most of the preparation of this report was finalised. Therefore, definitions, analyses and nomenclatures in this report almost exclusively follow that of the fifth IPCC assessment report (IPCC 2013a) rather than the latest, sixth, assessment report.

It is not possible to exactly predict the climate evolution over the next 100 000 years. However, based on knowledge of climate variations in the past and on inferred future climate changes, a range within which the climate of Sweden may vary can be estimated with reasonable confidence over this long timeframe. Within these limits, characteristic climate-related conditions of importance for repository safety can be identified. The conceivable climate-related conditions can be represented as *climate-driven process domains* (Boulton et al. 2001), where such a domain is defined as "a climatically determined environment in which a set of characteristic processes of importance for repository safety appear". In the following parts of this report these climate-driven process domains are referred to as *climate domains.* For Forsmark, a site on the Baltic Sea coast, a set of three climate domains was identified:

- The temperate climate domain.
- The periglacial climate domain.
- The glacial climate domain.

The purpose of identifying climate domains is to create a framework for the assessment of issues of importance for repository safety associated with specific climatically determined environments that may occur at the repository location in south-central Sweden. If a repository for low- and intermediate-level nuclear waste fulfils the safety requirements for plausible climate developments, including the transitions between climate domains, then the uncertainty regarding the precise extent in time and space of the climate domains is of less importance.

The temperate climate domain is defined as regions without permafrost or the presence of ice sheets. It is dominated by a temperate Baltic Sea coastal climate in a broad sense, with cold winters and either cold or warm summers. Precipitation may fall at any time of the year. The precipitation falls either as rain or snow. The temperate climate domain has the warmest climate of the three climate domains. Within the temperate climate domain, a site may also at times be submerged beneath the sea. Climates dominated by global warming due to enhanced atmospheric greenhouse gas concentrations are included in the temperate climate domain.

The term periglacial is used for a range of cold but non-glacial environments. In the periglacial environment, permafrost is a central, but not defining, element (French 2007). However, for the present work, the *periglacial climate domain* is defined strictly as regions that contain permafrost. Furthermore, the periglacial climate domain is a cold region but without the presence of an ice sheet. In this climate domain, permafrost occurs either in sporadic (less than 50 % spatial coverage), discontinuous (between 50 and 90 % coverage), or continuous (more than 90 % coverage) form. Although true for most of the time, regions belonging to the periglacial climate domain are not necessarily the same as regions with a climate that supports permafrost growth. For example, at the end of a period with periglacial climate domain, the climate may be relatively warm, not building or even supporting the presence of permafrost. Instead, permafrost may be diminishing. However, as long as permafrost is present, the region is defined as belonging to the periglacial climate domain, regardless of the prevailing temperature at the ground surface. This way of defining the climate domain is used because the presence of the permafrost is more important for the safety function of the repository than the actual temperature at the ground surface. In general, the periglacial climate domain has a climate colder than the temperate climate domain and warmer than the glacial climate domain. Precipitation may fall either as snow or rain. Within the periglacial climate domain, a site may also at times be submerged beneath the sea.

The glacial climate domain is defined as regions that are covered by glaciers or ice sheets. Within the glacial climate domain, the glacier or ice sheet may in some cases be underlain by sub-glacial permafrost. In line with how the periglacial climate domain is defined, areas belonging to the glacial climate domain may not necessarily at all times have a climate that supports the presence of ice sheets. However, in general, the glacial climate domain has the coldest climate of the three climate domains. Precipitation normally falls as snow in this climate domain.

In addition to the three climate domains, the surface above the SFR repository may be located above or below sea level. At present, SFR is covered by the Baltic Sea, with a maximum water depth of 7.2 m over SFR1 and 5.3 m over SFR3 (layout L3). Submerged conditions above the repository are defined to occur when the relative sea level is higher than −5.6 m (in the Swedish national reference height system RH2000, see SMHI 2020). This approximately corresponds to 5.8 m below the present mean sea level at the site. With the relative sea level located at this elevation, between 75 and 100 % of the surface above the repository has become terrestrial. Furthermore, when the relative sea level decreases to approximately this height, (i) the groundwater flow through the SFR disposal rooms begins to converge towards stationary values (Öhman and Odén 2018); (ii) the primary discharge area (biosphere object 157_2, see the **Biosphere synthesis report**, Chapter 5) begins to emerge above sea level (Brydsten and Strömgren 2013); and (iii) the area downstream of the repository where the groundwater associated with the highest concentrations of radionuclides is located 1 m above the sea level, allowing for extraction of water from a drilled well without the risk of salt-water intrusion (**Biosphere synthesis report**, Chapter 6).

Timescales

Climate studies covering long periods of time, several millennia, either use a calendar timescale (BC/AD) or a timescale related to the present (before present/after present or BP/AP). The present report covers processes acting on timescales shorter than 100 years as well as processes acting over glacial cycle timescales, i.e. 100 000 years (100 ka) and longer. Therefore, depending on the specific processes under discussion, the present report either use the BC/AD timescale (e.g. for analysis of relative sea-level changes on shorter timescales) or the BP/AP timescale for results related to the full glacial cycle time frame. The same dual approach is used in other studies covering similar topics (e.g. the future sea-level projection study by Clark et al. 2016). Having two timescales in the same report introduces a risk for mistakes. To minimise the risk of such mistakes, the present study reports both timescales in key figure captions and in tables.

2 Climate-related issues

2.1 Permafrost

2.1.1 Overview/general description

Permafrost is defined as ground that remains at or below 0 °C for at least two consecutive years (French 2007). This definition is based exclusively on temperature, and disregards the texture, degree of compaction, water content, and lithologic character of the material. As a result, the term *permafrost* does not always equate to *perennially frozen ground*, since, depending on the pressure and composition of groundwater and on the adsorptive and capillary properties of ground matter, water in the ground may freeze at temperatures below 0 °C. Therefore, permafrost encompasses the perennially frozen ground and a surrounding so-called *cryopeg*, i.e. a ground layer in which water remains unfrozen at sub-zero temperatures.

Permafrost and perennially frozen ground originate from the ground surface depending on a complex heat exchange process across the atmosphere-ground boundary layers and on an almost time-invariant geothermal heat flow from the Earth's interior. The heat exchange between the atmosphere and the Earth's surface is governed by shortwave and longwave radiative fluxes and sensible and latent heat fluxes.

Freezing of water is governed by thermal, hydraulic, mechanical, and chemical processes in the ground. In addition, freezing of water influences the thermal, hydraulic, mechanical, and chemical properties of the ground. Thermal properties change from those of unfrozen ground to those of frozen ground, affecting the heat transfer process. Ice formation in pores of the ground confines groundwater flow through the almost impermeable frozen ground, therefore altering the overall groundwater circulation pattern. Ice formation can also cause deformation of the ground and changes in the mechanical stress state. Frost weathering and degradation of the ground surface and patterned ground are additional consequences of cyclic freezing and thawing processes. Moreover, exclusion of salts in the freezing of saline groundwater can lead to increased salinity concentrations in adjacent unfrozen bedrock volumes.

Issues associated with permafrost development are comprehensively explained in Washburn (1979), Williams and Smith (1989), Yershov (1998), French (2007) and reviewed in e.g. Gascoyne (2000), Ahonen (2001) and Vidstrand (2003). Experimental investigations of thermal, hydro-chemical and mechanical impacts of freezing on bedrock properties have been reported by e.g. Mackay (1997) and Ruskeeniemi et al. (2002, 2004), whereas model studies of present and future permafrost development influenced by increasing atmospheric greenhouse-gas concentrations can be found in e.g. Lunardini (1995), Kukkonen and Šafanda (2001) and Slater and Lawrence (2013). Some model studies on thermo-hydro-mechanical impacts of freezing processes on bedrock properties with implications for interactions between glaciers and permafrost in a time frame of a glaciation cycle (~ 100 ka) have been conducted, e.g. Bauder et al. (2003), Hartikainen (2004, 2013), SKB (TR-06-23), Person et al. (2007), Lemieux et al. (2008a, b, c), Hartikainen et al. (2010), Hartikainen (2018). The effects of freezing of the geosphere on groundwater flow have been studied by e.g. Vidstrand et al. (2010, 2013).

2.1.2 Controlling conditions and factors

Climate and surface conditions

Heat exchange between the atmosphere and the Earth's surface is determined in the interplay of climate, topography, vegetation and snow cover, soil characteristics and water bodies. These factors can vary considerably with time and location. The main climatic parameters are incoming solar radiation (insolation), air temperature and humidity, wind, and precipitation. Absorption of incoming solar radiation by the Earth's surface governs the sensible and latent heat flux at the Earth's surface. Further, the longwave radiative flux is determined by the atmospheric and surface temperatures, respectively. Air temperature, which is commonly applied to map permafrost distribution, controls the longwave atmospheric radiation, the turbulent heat exchange, and evaporation and condensation. Wind, in turn, mainly influences the sensible heat exchange, but also latent heat exchange.

Precipitation together with evapotranspiration and condensation determine groundwater recharge, affecting the groundwater content and flow and hence the terrestrial heat flux.

Topography has a significant impact on climate conditions. Generally, air temperature decreases as altitude increases, being affected by radiation, convection and condensation. The average air temperature decrease is approximately 0.65 °C for every 100 metres increase in height (Danielson et al. 2003). In addition, inversions are common in hilly terrain causing low-slope low-lying areas to experience significantly lower temperatures than higher lying and steeper-slope areas. Furthermore, the slope angle and azimuth affect the flux of shortwave radiation, and where topographical differences are large a patchier distribution of permafrost is expected.

Vegetation and snow cover are sensitive to climatic conditions and topography. The characteristic parameters of the surface cover are surface albedo, emissivity, and roughness controlling the absorption of incoming shortwave radiation, the longwave terrestrial radiation and the turbulent heat exchange, respectively, as well as the thermal properties and the thickness of the surface cover affecting terrestrial heat transfer. In general, vegetation and snow cover moderate the ground temperature and thus the aggradation and degradation of permafrost. Vegetation is an insulating cover limiting cooling in winter and warming in summer, hence reducing the amplitude of the annual cycle of ground temperature. Vegetation is also important for the creation of snow cover, which protects the ground from heat loss in winter. However, the high albedo of snow can lead to a snow surface temperature almost 2 °C lower than the mean winter air temperature (Yershov 1998). As a rule, for most surface covers, permafrost can build from the ground surface if the annual mean air temperature is lower than a value ranging between –9 and –1 °C (Washburn 1979, Williams and Smith 1989, Yershov 1998, French 2007). An exception occurs with peat layers, which can insulate the ground from warming in summer more effectively than from cooling in winter, with the resulting effect that permafrost can exist where the mean annual air temperature is above 0 °C (Williams and Smith 1989).

Properties and thickness of the soil cover affect the terrestrial heat flow. Of importance are the porosity and water content of the soil, influencing the annual fluctuation of ground temperature and the thickness of the active layer, i.e. the seasonally thawing ground layer. The soil cover also acts as an insulating layer, since the thermal conductivity of the soil cover is lower than that of the underlying bedrock.

Water bodies, i.e. the sea, lakes, and watercourses, influence permafrost creation and distribution considerably since they have high values of specific heat. A talik, i.e. an unfrozen layer, can exist beneath water bodies that do not freeze to their bottom in winter. Depending on the characteristics of the climatic zone, the critical depth of a water body for it to remain unfrozen in winter is approximately 0.2 to 1.6 metres (Yershov 1998).

Sea water extensively reduces the development of costal permafrost. On the other hand, when the relative sea level of a highly saline sea is rising, submerged permafrost and perennially frozen deposits can survive for a long time beneath a cold seabed (Washburn 1979, Yershov 1998).

The hydrological conditions on the ground surface affect the freezing of groundwater. For instance, under glaciated conditions, a warm-based overlying ice sheet may increase the subglacial groundwater pressure, in which case the freezing point may decrease to such a degree that the subglacial ground is kept unfrozen. A similar, but minor, effect may occur when cold ground is submerged and submarine freezing is reduced by the pressure of the overlying sea water. Furthermore, groundwater flow, whether carrying fresh glacial meltwater or saline seawater, can influence the freezing process by altering the chemical groundwater composition.

Table 2-1 summarises how geosphere variables are influenced by permafrost development.

Geosphere and repository

The ground temperature that defines the presence of permafrost and primarily governs the freezing of water in the ground, is principally controlled by the ground thermal energy balance in terms of heat transfer, geothermal heat production, the specific heat content and the amount of heat generated by phase change processes of water. Heat transfer within the ground can occur through conduction, convection and radiation (Sundberg 1988). In general, only conduction is regarded as important to permafrost evolution, since radiation is of importance only in unsaturated high-porosity ground at high temperatures, and convection is of importance only when groundwater and gas fluxes are large.

Heat conduction depends on the ground temperature gradient, ambient temperature conditions, and the thermal properties of the ground matter. Thermal conductivity, describing the ability of material to transport thermal energy, and heat capacity characterising the capability of material to store heat, depend on several variables such as mineralogy, porosity and groundwater content. Having typically three to four times higher conductivity than other common rock-forming minerals, quartz is the most important mineral for determining thermal characteristics of rock materials.

When the porosity is less than 1 %, freezing of water has a minor effect on heat transfer in water-saturated ground. The degree of saturation has relevance to the thermal properties of the ground due to the very low thermal conductivity and heat capacity of air, e.g. the thermal conductivity of 1 %-porosity granite can decrease by over 10 % with decreasing saturation (Clauser and Huenges 1995). In rock, heat capacity is not very dependent on ambient temperature and pressure conditions, whereas thermal conductivity is a rather variable function of both temperature and pressure. The thermal conductivity of granite decreases with increasing temperature by approximately 5 to 20 % per 100 °C and increases with increasing pressure by about 1 to 2.5 % per 100 MPa (Seipold 1995). The pressure dependence of thermal conductivity is increased when rocks are unsaturated (Sundberg 1988, Clauser and Huenges 1995). Moreover, Allen et al. (1988) reported a strong correlation between lithology and permafrost depth, which could be directly explained by differences in thermal conductivity.

In addition to the thermal properties above, the hydrogeochemical and mechanical properties of the ground important for freezing of groundwater are permeability, porosity, adsorptive capacity of ground matter, chemical composition of groundwater and deformation properties of the ground.

Table 2-1. Influence of permafrost development on geosphere variables.

Geosphere variable	Climate issue variable	Summary of influence
Temperature	Permafrost depth	Permafrost is by definition a thermal condition hence having no influence on temperature.
Groundwater flow	Frozen/unfrozen fraction of groundwater	Freezing occurs at temperatures below the freezing point of bulk water (SKB TR-10-48). Groundwater transformed from liquid to solid phase can be regarded as immobile. Filling fractures and pores, ice also affects the groundwater flow through permeability, which decreases with a reduction in the unfrozen fraction of groundwater.
Groundwater pressure	Frozen/unfrozen fraction of groundwater	The volume increase in the phase change of water from liquid to solid state causes an increase in the pressure of water which remains liquid. Moreover, freezing of water in porous ground matter can lead to cryosuction and depression of groundwater pressure in the unfrozen ground.
Groundwater composition	Frozen/unfrozen fraction of groundwater	When saline water is transformed from liquid to solid phase, the solutes are typically not incorporated in the crystal lattice of ice but transferred in the liquid phase. Therefore, the salinity in the unfrozen fraction increases.
Rock stresses	Frozen fraction of groundwater	Deformations due to ice formation will lead to changes in rock stresses. The effect of the changes is strongest nearest to the surface where in situ stresses are lowest.
Fracture geometry	Frozen fraction of groundwater	Freezing can have some influence on the fracture geometry at shallow depths due to frost cracking. Close to the ground surface frost wedges can form down to depths of c. 10 m. Otherwise, there can be widening of fractures due to freezing but the effect may be reversible as thawing takes place.

2.1.3 Natural analogues / observations in nature

At present, approximately 25 % of the total continental land area of the Earth is occupied by permafrost. The permafrost distribution may be characterised into: i) continuous (more than 90 % spatial coverage), ii) discontinuous (between 90 and 50 % coverage), iii) sporadic (less than 50 % coverage), and iv) subglacial forms. About one fifth of this permafrost is estimated to be subglacial in Antarctica and Greenland. Permafrost is abundant in Alaska, the northern parts of Canada and Russia, and in parts of China (French 2007). Along the coast of southern and south-western Greenland both continuous and discontinuous permafrost can be found (Mai and Thomsen 1993). The Northern Hemisphere distribution of permafrost is illustrated in Figure 2-1.

The deepest known permafrost occurs in the central part of Siberia in Russia, where thicknesses of up to 1 500 m have been reported (Fotiev 1997). The extensive region of continuous permafrost in central Siberia corresponds to areas that are believed not to have been covered by Quaternary ice sheets and that experienced cold climate conditions during the last glacial cycle and before. In coastal areas, submarine permafrost may also exist, such as in northern Siberia where the permafrost formed during ice-free periods of the last glacial cycle in regions subsequently covered by the Arctic Ocean. Furthermore, permafrost is frequently observed in mountainous terrain. For example, in the area of Tarfala in the Kebnekaise massif in northern Sweden, discontinuous permafrost has been reported to be 100 to 350 m thick at an altitude above 1 500 m a.s.l. (King 1984, Isaksen et al. 2001).

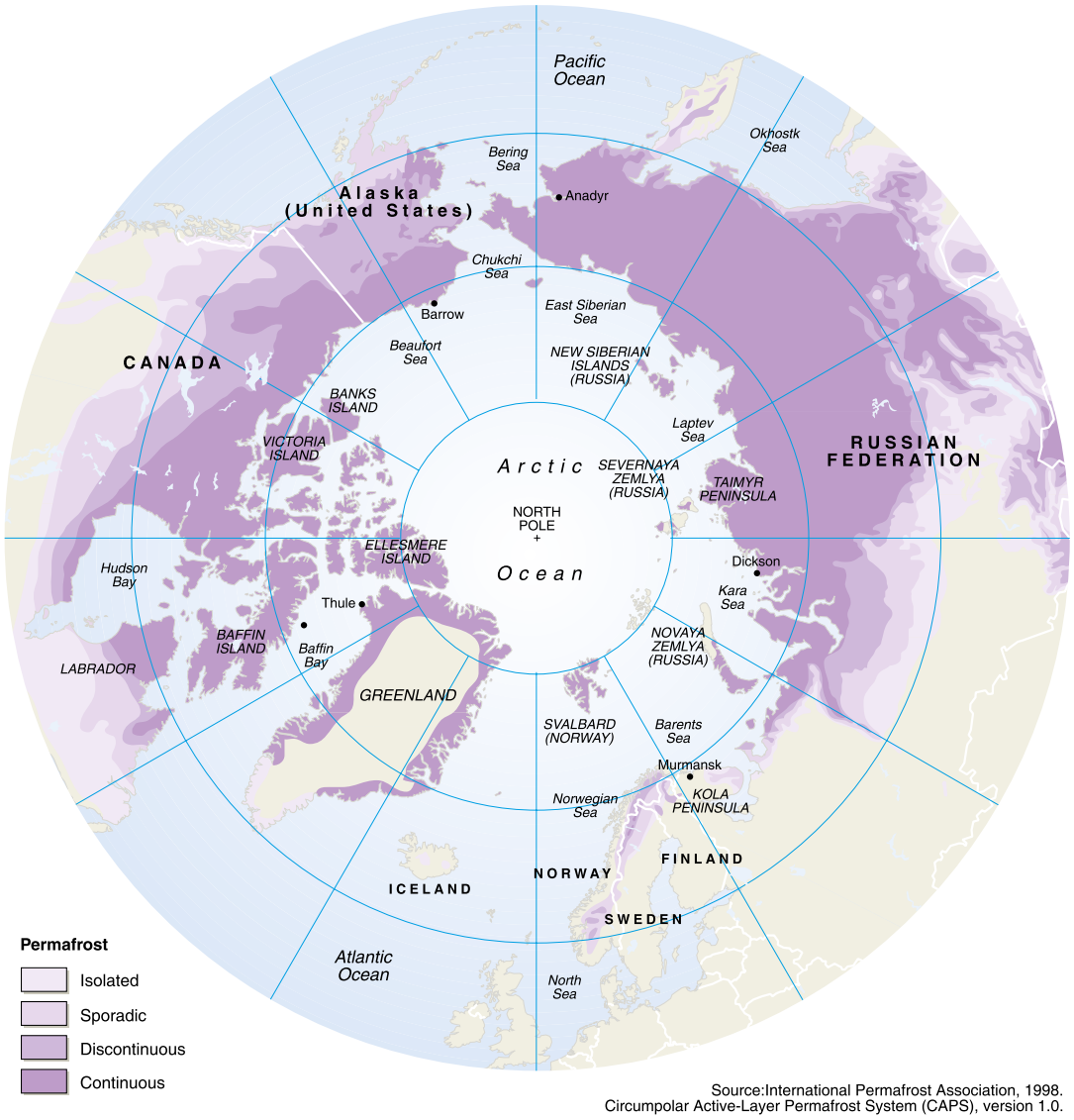

Figure 2-1. *Permafrost distribution in the Northern Hemisphere. From UNEP/GRID-Arendal (2005).*

SKB, together with co-funding parties from Finland (Geological Survey of Finland and Posiva), Great Britain (UK Nirex Ltd) and Canada (Ontario Power Generation and University of Waterloo), carried out a research project on permafrost at the Lupin gold mine in northern Canada (Ruskeeniemi et al. 2002, 2004). In this area, the depth of the permafrost extends to ~ 500−600 m. The main objective of the project was to provide data describing the subsurface conditions in a permafrost area with crystalline bedrock. Permafrost depth, temperatures, groundwater composition and hydraulic properties have been measured. The mean annual air temperature at this site is −11 °C and the annual mean precipitation is low; ~ 270 mm (Ruskeeniemi et al. 2002). Based on a seismic refraction survey, the depth of the active layer has been interpreted to be ~ 1.5 m, varying between 1.2 and 1.8 m. The present permafrost depth is believed to have been developed over the last 5 ka. In the Lupin area, all shallow lakes freeze down to the bottom during winter. Lakes deeper than 2–3 m are expected to have unfrozen bottoms all year. The latter lakes may have the potential to support closed taliks. The large Lake Contwoyto, located about 1 300 m from the mine at surface, provides the most significant talik structure that may extend through the deep permafrost. However, direct observations beneath this lake are lacking.

In order to investigate the distribution of permafrost and locate salinity differences in the deep groundwaters, electromagnetic soundings were conducted in the Lupin mine area. Furthermore, drillings were made from the deeper parts of the mine through the base of the permafrost, in order to sample groundwaters and to study the distribution of open fractures and hydraulic conditions. The main result of the electromagnetic sounding surveys was the identification of anomalies forming a subhorizontal layer at depths between 400 and 700 m. Paananen and Ruskeeniemi (2003) made the interpretation that this conducting layer represents saline or brackish water at the base of the permafrost. According to the temperature measurements made in the mine, the base of the permafrost occurs at a depth of 540 m. The drillings revealed the existence of a ~ 100 m thick unsaturated or dewatered zone below the permafrost. An alternative interpretation of the subhorizontal conductor at ~ 650 m depth could be that it represents the groundwater table (Ruskeeniemi et al. 2004). The dry zone below the permafrost could either be a natural result of very limited recharge through the permafrost or an effect of mine drainage. No pressurised water or gas flow was observed in the boreholes. The available data from water sampling do not provide any evidence of highly saline water below the permafrost (Ruskeeniemi et al. 2004).

Between 2009 and 2013, SKB, Posiva and NWMO conducted a comprehensive study on hydrology in western Greenland called the Greenland Analogue project (GAP) (Claesson Liljedahl et al. 2016, Harper et al. 2016). The main purpose of the project was to investigate the hydrological conditions at a site affected by the presence of the Greenland ice sheet, from the formation of meltwater at the ice-sheet surface and bed, through the groundwater flow in bedrock at KBS-3 depth (400–700 m), to the groundwater discharge through taliks into proglacial lakes. Detailed temperature measurements in a deep bedrock borehole drilled at an elevated area at the very ice-sheet margin showed that the proglacial permafrost at this site is ~ 400 m deep. Measurements of basal thermal properties in the lower and frontal-near part of the ice sheet showed warm-based conditions at all sites investigated, i.e. the basal ice temperature is at the pressure melting point and free water is available at the ice-sheet bed. This indicates that, at some distance in under the ice, the bedrock is fully thawed. However, a wedge of subglacial permafrost probably stretches in for some distance under the ice (Claesson Liljedahl et al. 2016, Ruskeeniemi et al. 2018).

Investigations made in the deep borehole at the ice margin show that groundwater flows beneath the frozen ground. Sampling of groundwater has been made at three different depths (511, 563 and 574 m) in the borehole. The water samples have been subject to geochemical and isotope analyses in order to study e.g. the presence of a glacial chemical signal at depth, and the characteristics of that signal.

Through taliks are common in the GAP study area. From field observations and modelling, all larger proglacial lakes in the area are assumed to support a talik (Claesson Liljedahl et al. 2016, SKB R-10-59). How they contribute to the hydrogeology depends on e.g. the properties of the lake-bottom sediments, underlying bedrock and surrounding hydraulic gradients. A bedrock borehole has been drilled at the shore of a nearby proglacial lake, through the permafrost and into the through-talik that is located under the lake. In this borehole, water samples have been taken at a depth of 140 m. The samples have been subject to geochemical and isotope analysis. The same lake, and its surrounding catchment, has also been subject to detailed water balance studies showing that, at

least for the hydrological year studied, the talik acts as a groundwater recharge area (Bosson et al. 2013, Johansson et al. 2015). Regional-scale groundwater flow modelling studies have also been performed in the GAP study area, see e.g. Jaquet et al. (2012).

For more detailed descriptions of GAP and the results obtained from the study, see Claesson Liljedahl et al. (2016), Harper et al. (2016), and references therein.

2.1.4 Model studies

The potential for permafrost in Forsmark in the next 60 ka was studied in Brandefelt et al. (2013). The purpose was to analyse the potential for climate conditions favourable for permafrost growth, and to analyse the resulting bedrock temperatures. Further, earlier studies have been conducted (SKB TR-06-23, Hartikainen et al. 2010) of the permafrost evolution reconstructed for the last glacial cycle in the Forsmark area. A broad range of sensitivity tests was made in these earlier studies, covering the range of uncertainties associated with various parameters of importance for permafrost development.

The simulations of permafrost for the reconstruction of the last glacial cycle were made with two types of models, a 1D permafrost model and a 2D permafrost model improved from the 1D model. The 1D modelling was performed for the SR-Can safety assessment (SKB TR-06-23), with some of the results used also for the SR-Site safety assessment (SKB TR-10-49, Engström et al. 2012). The 1D simulations were conducted specifically for the location of the planned spent nuclear fuel repository. The 2D modelling (Hartikainen et al. 2010) was conducted for the SR-Site safety assessment and covered a 15 km long and 10 km deep vertical cross-section crossing both the site for the planned spent nuclear fuel repository and the location of the SFR. Reconstructed air temperature for the Forsmark region for the past 120 ka, based on the ice-sheet modelling of this period (Section 2.3.4), was used as input to the 1D and 2D permafrost modelling for the reconstruction of the last glacial cycle. The methodology is described in SKB (TR-10-49, Appendix 1).

The 2D simulations of permafrost for the next 60 ka (Brandefelt et al. 2013) were conducted along the same 15 km profile as for the SR-Site simulations (Hartikainen et al. 2010), but with an improved version of the permafrost model. All the simulations (SKB TR-06-23, Brandefelt et al. 2013, Hartikainen et al. 2010) used site-specific input data from the Forsmark site investigation programme. Details on the input data used for the 1D and 2D permafrost simulations are given in SKB (TR-06-23, Section 3.4), Hartikainen et al. (2010) and Brandefelt et al. (2013, Section 2.4), respectively.

The purpose of the modelling studies was to analyse the main factors of importance for the development of permafrost and perennially frozen ground at Forsmark, and to exemplify how permafrost grows and degrades at this site. Further, in Brandefelt et al. (2013), the purpose was to analyse the potential for permafrost growth in Forsmark in the next 60 ka.

The permafrost models include mathematical expressions for freezing and thawing of saline groundwater-saturated bedrock. The bedrock is considered as an elastic porous medium and the groundwater as an ideal solution of water and ionic solvents. The models are based on the principles of continuum mechanics, macroscopic thermodynamics and the theory of mixtures; being capable of describing heat transfer, freezing of saline water, groundwater flow and deformations of bedrock. In the 2D version of the model, the freeze-out and transport of solutes is included (Hartikainen et al. 2010). The models are described further in Hartikainen (2004), SKB (TR-06-23), Hartikainen et al. (2010), Brandefelt et al. (2013) and Hartikainen (2018).

A 3D version of the model has also been used for simulating the development of permafrost and frozen ground at the Olkiluoto site in Finland (Hartikainen 2013).

To capture the most important factors and parameters affecting the development of permafrost, sensitivity analyses have been performed considering the following issues:

- Surface conditions.
- Subsurface conditions.
- Presence of heat from a KBS-3 repository.

Surface temperatures, together with the influence of surface covers such as snow, vegetation and water bodies, have been included as factors of importance in the surface conditions. The investigated bedrock conditions are thermal properties of the bedrock and the geothermal heat flow. The sensitivity simulations carried out with the 2D permafrost model (Hartikainen et al. 2010) are presented in SKB (TR-10-49). The heat generated by the spent nuclear fuel repository has been included in most simulations, and was also analysed in a dedicated 2D sensitivity simulation. In this context, it should be noted that the repository depth was changed between SR-Can (for which the 1D simulations were made) where it was 400 m and SR-Site (for which the 2D simulations were made) where it was 450 m. Despite this, the resulting permafrost and freezing depths are very similar between the two studies, as demonstrated later in the present report.

Main conclusion from the 1D and 2D permafrost modelling studies for the last glacial cycle

The conclusion drawn from the 1D permafrost investigations (SKB TR-06-23) was that the surface conditions are the driving force for the development of permafrost. This conclusion was strengthened by the 2D study (Hartikainen et al. 2010). In addition, the conclusion that the subsurface conditions and the heat from a spent nuclear fuel repository act as inhibiting factors for the development of permafrost and perennially frozen ground is also supported. The following main conclusions can be drawn from the 2D permafrost study performed for the SR-Site safety assessment for a spent nuclear fuel repository at 450 m depth in Forsmark:

- Given the temperatures reconstructed for the last glacial cycle, the study demonstrates how the site-specific spatial and temporal development of permafrost and perennially frozen ground takes place at the Forsmark site, developing from sporadic, to discontinuous to continuous coverage in various combinations and extents. The results show that through taliks may form at the site under certain conditions, and that groundwater may flow in these taliks.
- The study provides a full range of sensitivity analyses of uncertainties in sub-surface and surface conditions, including the reconstructed input air temperature for the last glacial cycle.
- For the reconstruction of last glacial cycle conditions, the simulated maximum permafrost (the 0 °C isotherm) depth over the KBS-3 repository is between 180 and 260 m depending on the surface conditions. The corresponding range for the entire 15 km profile is from 220 to 300 m.
- By making the very pessimistic combination of setting all known uncertainties (e.g. in air temperature, surface vegetation and snow conditions, bedrock thermal conductivity and heat capacity, and geothermal heat flow) as most favourable for permafrost growth, permafrost (i.e. the 0 °C isotherm) reaches 450 m depth after 45 ka in the reconstruction of the last glacial cycle. However, the perennially frozen ground does not reach KBS-3 repository depth. It should be noted that the combination of assumptions in this case is quite unrealistic.
- The prevailing surface conditions, such as temperature and surface moisture, are the main factors governing the spatial and temporal development of permafrost and perennially frozen ground at the Forsmark site.
- Subsurface conditions, such as bedrock thermal properties, geothermal heat flow and groundwater salinity, modify the spatial and temporal development of permafrost and perennially frozen ground, but are of secondary importance for modelled permafrost depths compared with surface conditions.
- The variation in thermal properties along the profile as well as 2D groundwater flow only have a slight influence on permafrost (the 0 °C isotherm) development. Therefore, the uncertainties introduced by excluding lateral variations in thermal properties, boundary conditions and convective heat transfer in the 1D model study (SKB TR-06-23) are considered insignificant.
- Under continuous permafrost conditions, the unfrozen groundwater content in the perennially frozen ground under lakes can exceed 10 % down to a ~ 50 m depth. This may indicate that taliks are able to form under lakes through perennially frozen ground, if favourable groundwater flow conditions with open flow paths prevail. When the unfrozen groundwater content decreases below 10 %, groundwater flow is reduced considerably, and taliks are no longer able to form or survive.

- Freezing can induce salt exclusion and salt transport when perennially frozen ground develops deeper than ~ 200 m. At shallower depths, the impacts of freezing are difficult to see since the salinity of groundwater has been diluted prior to the development of perennially frozen ground. When salt transport occurs more slowly than the freezing zone advances, the salinity concentration is increased within the perennially frozen ground.
- The uncertainty in dealing with groundwater flow with this permafrost model remains, since the 3D flow network is omitted in the 2D model. However, the topography of the Forsmark site is too flat to generate significant hydraulic gradients, compared with e.g. the gradients imposed by the ice sheet during glacial conditions, suggesting that the inclusion of 3D flow would only have a minor impact on the results for non-glacial conditions.
- The uncertainty regarding the neglect of salinity transport in the 1D model (SKB TR-06-23) seems to be insignificant, mainly due to the low rock porosity, although the present 2D model is not able to describe the groundwater flow realistically.

The potential for cold climate conditions and permafrost in Forsmark in the next 60 ka

Based on the two previous studies (SKB TR-06-23, Hartikainen et al. 2010), it can be concluded that permafrost growth can occur in Forsmark under cold climate conditions. It can also be concluded that the permafrost can penetrate deeper than the SFR repository structures, located at a depth of c. 140–60 m below the surface. Since the functionality of the concrete and bentonite barriers of SFR may be influenced by freezing temperatures, see the **Barriers process report**, the potential for permafrost and frozen ground at repository depth is of interest. Further, since the radionuclide inventory of SFR is dominated by relatively short-lived radionuclides, possible radiation doses to man or the environment are strongly dependent on the earliest timing of permafrost growth to repository depth.

In order to assess the potential for cold climate conditions and permafrost growth at the SFR repository location in the next 100 ka, a combined climate modelling – permafrost modelling study was performed by Brandefelt et al. (2013). Based on the known future insolation variations, with Northern Hemisphere summer minima at 17 ka and 54 ka AP, the study focused on the first 60 ka AP.

The latitudinal and seasonal distribution of incoming solar radiation (insolation) varies on millennial timescales due to variations in the Earth's orbit and axial tilt. These variations, together with variations in the atmospheric CO_2 concentration, are viewed as two main factors in determining the climate variation between interglacial (warmer) and glacial (colder) climates. Summer insolation at high northern latitudes is at a minimum 17 ka and 54 ka AP. These periods were therefore identified as potential future periods of cold climate conditions in high northern latitudes in general and in south-central Sweden in particular. Due to anthropogenic emissions of carbon to the atmosphere, the atmospheric CO_2 concentration is currently 409 ppmv (2018 AD), a substantial increase as compared to the range of atmospheric CO_2 concentrations of 180–295 ppmv found in ice cores for the last 400 ka. The future atmospheric CO_2 concentration is determined by i) future anthropogenic carbon emissions, ii) possible emissions due to feedbacks in the climate system, and iii) by the global carbon cycle.

Climate modelling for next 60 ka

To investigate the potential for cold climate conditions in south-central Sweden in the next 60 ka the future air temperature in Forsmark was estimated based on simulations with an Earth system model of intermediate complexity (EMIC), LOVECLIM version 1.2, and a state-of-the-art Atmosphere-Ocean General Circulation Model (AOGCM), Community Earth System Model version 1 (CESM1). To span the possible combinations of future orbital variations and possible future atmospheric CO_2 concentrations, three sets of simulations were performed. The first set consists of a suite of EMIC simulations performed for the future periods of minimum summer insolation at high northern latitudes (17 ka and 54 ka AP) with the atmospheric CO_2 concentration varying in the range 180–400 ppmv. These are equilibrium simulations with constant forcing conditions. The second set consists of two transient EMIC simulations with constant atmospheric CO_2 concentrations of 200 or 400 ppmv, respectively, and insolation variations for the full period from the present to 61 ka AP. The third set of simulations consists of two AOGCM equilibrium simulations with insolation for 17 ka and 54 ka

AP and atmospheric CO_2 concentration set to 200 ppmv and 180 ppmv respectively. This set was used, in combination with published results from climate model intercomparisons, to estimate the uncertainty in the EMIC results due to the simplified model formulation. When the atmospheric CO_2 concentration is varied from 180 ppmv to 400 ppmv the annual average air temperature at 2 m height (T_{2m}) at Forsmark varies from 1.6 °C to 5.7 °C in the EMIC simulations for orbital year 17 ka AP and from 0.96 °C to 5.3 °C in the simulation for orbital year 54 ka AP (Figure 2-2). The insolation difference between orbital years 17 ka AP and 54 ka AP results in a difference in the annual average Forsmark T_{2m} of c. 0.3 °C–1.2 °C, with a tendency towards larger differences for lower atmospheric CO_2 concentrations. These results indicate that the future atmospheric CO_2 concentration is more important than insolation variations for future cold climate conditions in Forsmark in the next 60 ka.

The AOGCM simulations reveal significant inter-model differences in the simulated climate, specifically in the regional climate, in line with earlier inter-comparison studies. Annual average Forsmark T_{2m} is 5.9 °C and 7.7 °C colder than the pre-industrial value in the AOGCM simulations for 17 ka AP and 54 ka AP, respectively. These values are 3.9 °C and 4.4 °C, respectively, lower than in the corresponding EMIC simulations.

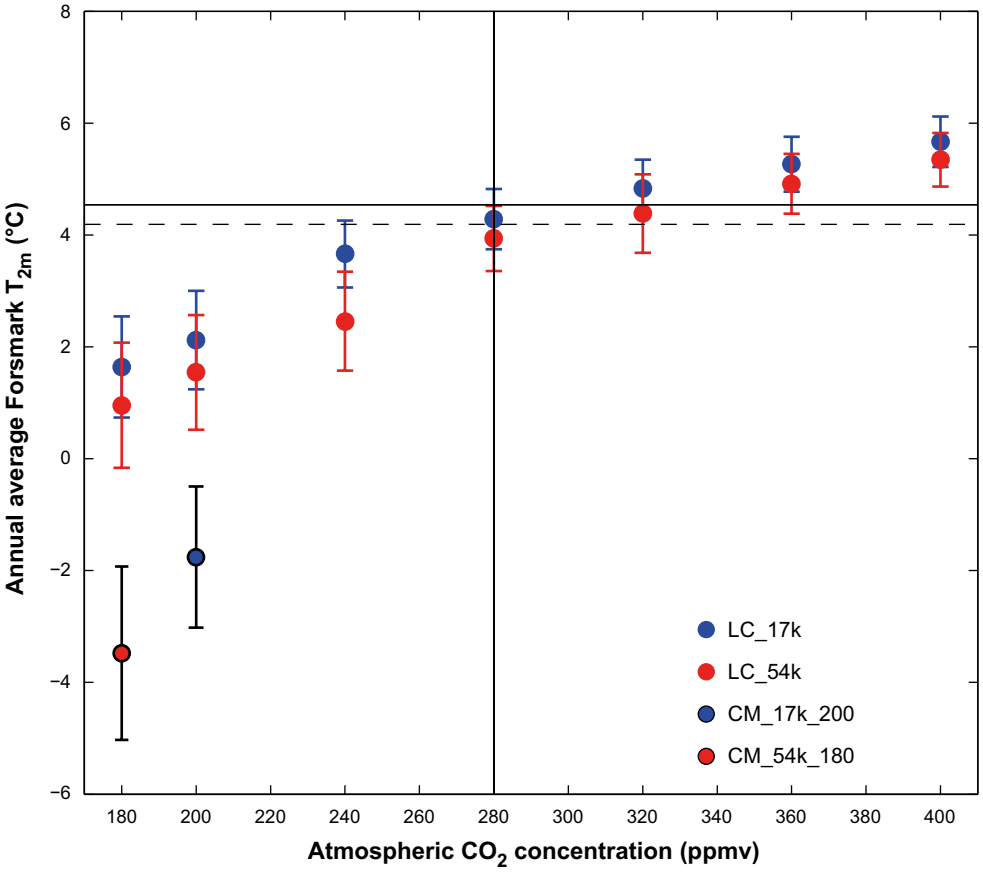

Figure 2-2. *Annual average near-surface air temperature (T_{2m}, °C) in Forsmark in the EMIC (LC_) and AOGCM (CM_) simulations with constant forcing and boundary conditions for orbital years 17 ka AP (blue circles) and 54 ka AP (red circles). T_{2m} is shown as a function of the atmospheric CO_2 concentration. The standard deviation of the annual average T_{2m} in Forsmark is indicated as error bars. The annual average T_{2m} in Forsmark in the EMIC simulation of pre-industrial (c 1850 AD) climate (+4.54 °C; horizontal black line) and in the AOGCM simulation of pre-industrial climate (+4.19 °C; horizontal black dashed line) is indicated. The pre-industrial atmospheric CO_2 concentration is indicated with a vertical line. The climate simulations are described in Brandefelt et al. (2013).*

The climate models used in Brandefelt et al. (2013) do not include glacier and ice-sheet dynamics, which gives rise to a potential warm bias in the simulated climate. Comparison of the results presented here with an earlier study of future climate evolution with EMICs that include ice-sheet dynamics (Pimenoff et al. 2011) indicate a potential bias of up to 5 °C in the results presented here. The uncertainties in the simulated Forsmark T_{2m} due to future glacier and ice-sheet growth, inter-model differences, internal variability and future greenhouse-gas concentrations are estimated. The collective uncertainty is taken to be larger for orbital year 54 ka AP, reflecting two factors. Firstly, inter-model differences generally increase when the difference between the simulated climate state and the present climate increases. Secondly, several earlier studies indicate that ice-sheet growth may occur at ~ 50 ka AP if the atmospheric CO_2 concentration reaches pre-industrial or lower values (see further Section 3.4.5).

The results of the climate modelling are summarised in Table 2-2. To assess the potential for permafrost in Forsmark in the coming 60 ka AP, the uncertainty in the climate model results must first be assessed. Models of the Earth's climate system are designed to simulate the dynamics of the system. The complexity of climate system dynamics is however partly unresolved, both in terms of incomplete knowledge of some processes and in terms of insufficient resources to numerically resolve small-scale processes in the models. Further uncertainty in the results of such models exists due to the nonlinear nature of the climate system. To assess the uncertainty in the T_{2m} in Forsmark used as input to the permafrost model, several sources of uncertainty have been identified. A comprehensive description is given in Section 3.4 of Brandefelt et al. (2013).

Table 2-2. The minimum annual average Forsmark T_{2m} when all uncertainties are taken into account. See Section 3.4 of Brandefelt et al. (2013) for a detailed description.

Atmospheric CO_2 concentration (ppmv)	180	200	240	280	320
Orbital year 17 ka AP	–7.4	–5.9	–2.3	0.3	0.8
Orbital year 54 ka AP	–11	–9.5	–6.5	–3.1	–2.6

2D permafrost modelling

To analyse the potential for permafrost development in the Forsmark region, the T_{2m} from the EMIC simulation with the coldest climate was used as input to a site-specific 2D permafrost model for Forsmark. This study provides a numerical estimation of the development of permafrost and perennially frozen ground along a profile covering a major portion of the Forsmark site and crossing the repository location, using site-specific surface and subsurface conditions. Special emphasis was put on the modelling of surface conditions, including climate (temperature and humidity), soil, vegetation, water bodies and topography, and on the representation of lateral variations in bedrock and surface physical properties. In addition, groundwater flow and salt transport processes were considered (in 2D).

The study made use of an improved version of the 2D thermo-hydro-chemical model of permafrost and perennially frozen ground that was used for the SR-Site safety assessment (Hartikainen et al. 2010). The 2D model domain was set up in the same way as in Hartikainen et al. (2010), and covers the same 15 km long and 10 km deep vertical cross-section of the Forsmark site (Figure 2-3). The profile crosses the SFR repository which is the main focus for the present study. The permafrost model includes mathematical expressions for freezing and thawing of saline groundwater-saturated bedrock. The bedrock is considered as an elastic porous medium and the groundwater as an ideal solution of water and ionic solvents. The model is based on the principles of continuum mechanics, macroscopic thermodynamics and the theory of mixtures, being capable of describing heat transfer, freezing of saline water, groundwater flow and deformations of bedrock. The freeze-out and transport of solutes is also included in the model.

A more detailed description of the 2D permafrost model used for the reconstruction of last glacial cycle permafrost conditions is found in Hartikainen et al. (2010). The improvement made to the model since the study by Hartikainen et al. (2010) is described below.

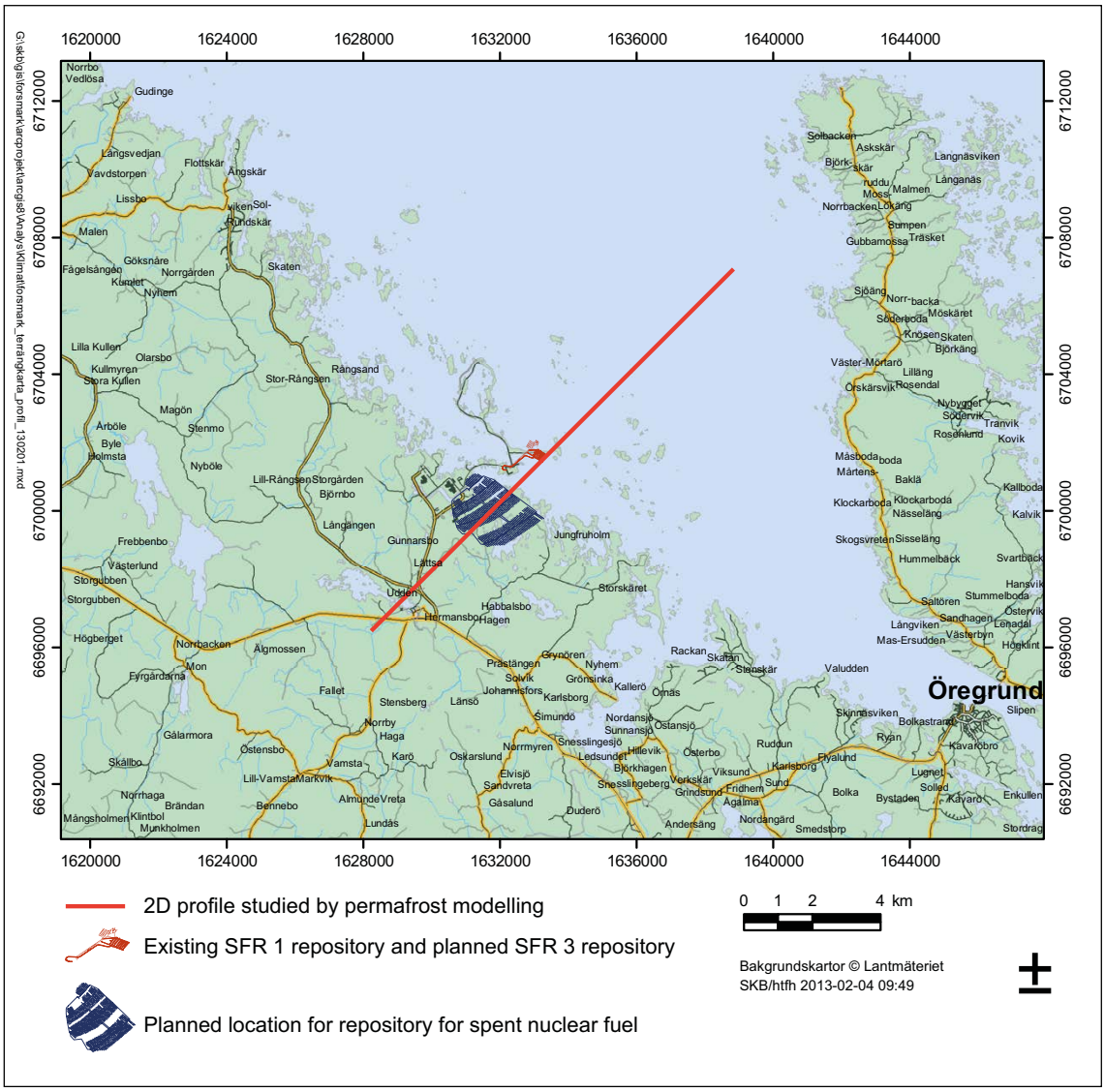

Figure 2-3. *The ~ 15 km long profile analysed in the 2D permafrost modelling study (Brandefelt et al. 2013; red line), SFR location (brown) and the planned location of the repository for spent nuclear fuel are also indicated.*

The improved version of the permafrost model includes seasonal freezing and thawing of the ground. Inter-annual variations in ground surface temperature are now expressed in terms of the monthly mean ground surface temperatures, T_s, which are determined by the monthly mean 2-m air temperatures, T_a, the freezing n-factor, n_{fr}, and thawing n-factor, n_{th}, as

$$T_s = \begin{cases} n_f T_a, T_a < 0 \\ n_{th} T_a, T_a \geq 0 \end{cases} \qquad \text{Equation 2-1}$$

The n-factors are statistical relations between the annual mean 2-m air temperature and annual mean ground surface temperature (Lunardini 1978). Values for the n-factors used in this study are given in Table 2-7 in Hartikainen et al. (2010).

The improvement allows for the thermal offset, i.e. a decrease, in the annual mean ground temperature profile due to seasonal freezing and thawing of the ground (Goodrich 1978). The offset can be several degrees depending on the amount of freezing water in the ground, and may in some cases, lead to development of perennially frozen ground in locations where the annual mean air temperature is above 0 °C.

Sub-surface properties and conditions

To capture the most important factors and parameters affecting the development of permafrost and frozen ground at the Forsmark site, detailed site-specific sensitivity analyses were previously performed considering surface and subsurface conditions (Hartikainen et al. 2010). Factors of importance, and analysed in the sensitivity studies, were air temperatures and the influence of surface covers such as snow, vegetation and water bodies.

The model domain encompasses an approximately 15 km long and 10 km deep vertical section consisting of six soil layers, 23 rock domains and 31 deformation zones as shown in Figure 2-3 and Figure 2-4. Figure 2-5 illustrates the thermally different rock mass domains, the deformation zones of the upper 2.1 km of the model domain, as well as the present-day level of the Baltic Sea. The soil layers are shown in Figure 2-6. The thermal and hydraulic properties of the soil domains are given in Hartikainen et al. (2010, Table 2-1), whereas Table 2-2 and Table 2-3 in the same publication give the thermal and hydraulic properties of the rock mass domains. Hydraulic properties of the deformation zones are presented in Hartikainen et al. (2010, Appendix D). The thermal properties of deformation zones are assumed identical to those of the corresponding rock mass domain. The bedrock below the depth of 2.1 km is assumed to have the same thermal and hydraulic properties as the rock domain in which the repository is located. The material properties of the bedrock are described in detail in Hartikainen et al. (2010, Appendices D and E). For the treatment of e.g. unfrozen groundwater content, see also Hartikainen et al. (2010). The numerical simulations were carried out using an unstructured finite element mesh of linear triangular elements. The mean grid spacing varied from less than 10 m close to the ground surface to about 300 m at the bottom of the model domain. The maximum time step for the adaptive time-integration scheme was limited to 100 years.

The geothermal heat flow is an important parameter for permafrost modelling. The geothermal heat flow, crustal radiogenic heat production and ground temperature to a depth of ~ 1 km are based on Sundberg et al. (2009), see also Hartikainen et al. (2010, Appendices B–F). For a description of how these parameters are modelled for depths from ~ 1 km to 10 km, see Hartikainen et al. (2010). Figure 2-7 shows the initial ground temperature calculated for mean thermal properties.

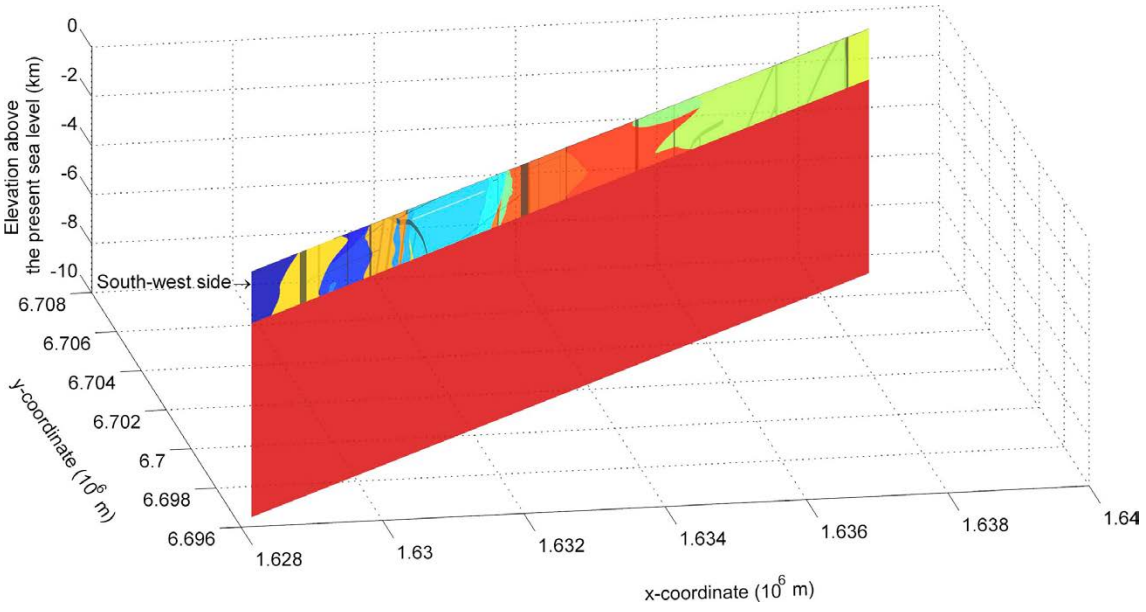

Figure 2-4. *The model domain used in the 2D permafrost simulations. Colours from blue to red signify the 23 rock domains considered and grey the 31 deformation zones. Physical and thermal characteristics for the rock domains and deformation zones were obtained from the site investigation programme at Forsmark, see Hartikainen et al. (2010). The six soil layers described in Hartikainen et al. (2010, Appendix B) and Figure 2-6, are too thin to be seen in this figure. The x-axis is directed eastward and y-axis northward. The RT-90 coordinates of the south-west corner are x = 1 628 228 m, y = 6 696 472 m.*

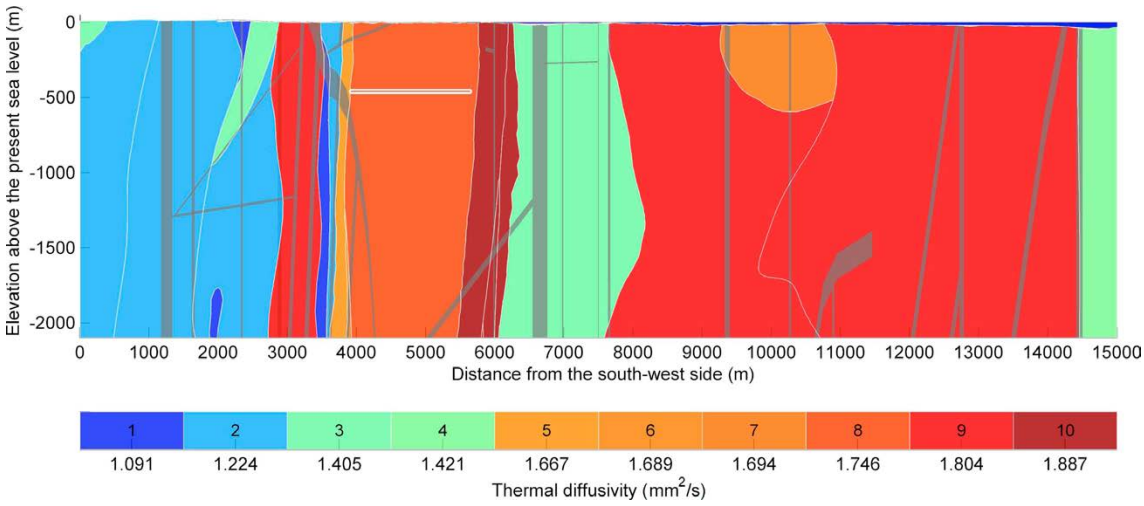

Figure 2-5. *The upper 2.1 km of the 2D model domain. Colours from blue to red signify rock domains with different thermal diffusivities. Numbers from 1 to 10 indicate the rock domains of Table 2-2 in Hartikainen et al. (2010). The location of deformation zones is illustrated in grey and the repository for spent nuclear fuel in white, at a depth of 450 m starting at about 4 000 m along the profile. The thin blue layer on the top surface represents the present-day level of the Baltic Sea. Further description and references for these data are found in Hartikainen et al. (2010, Appendix C).*

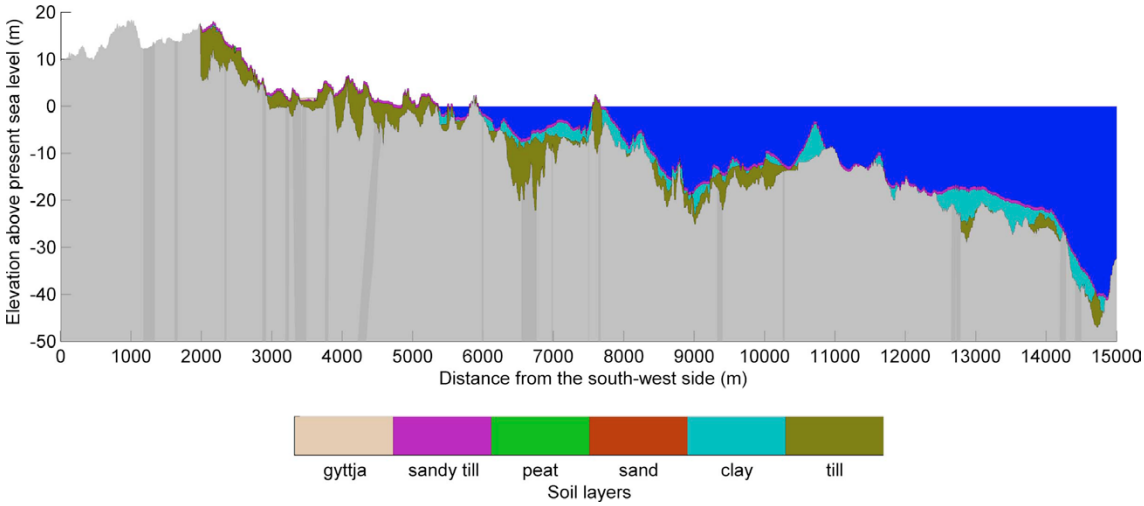

Figure 2-6. *The soil layers of the 2D model domain. Grey represents bedrock and blue the present-day Baltic Sea. The gyttja, peat and sand layers are too thin to be seen in this figure. In addition, because the first 2 000 m of the model domain is outside the area of detailed site investigations, no information about the soil cover is used there. Further description and references for these data are given in Hartikainen et al. (2010, Appendix B). Note that the vertical axis has a scale that gives a strong vertical exaggeration of topography.*

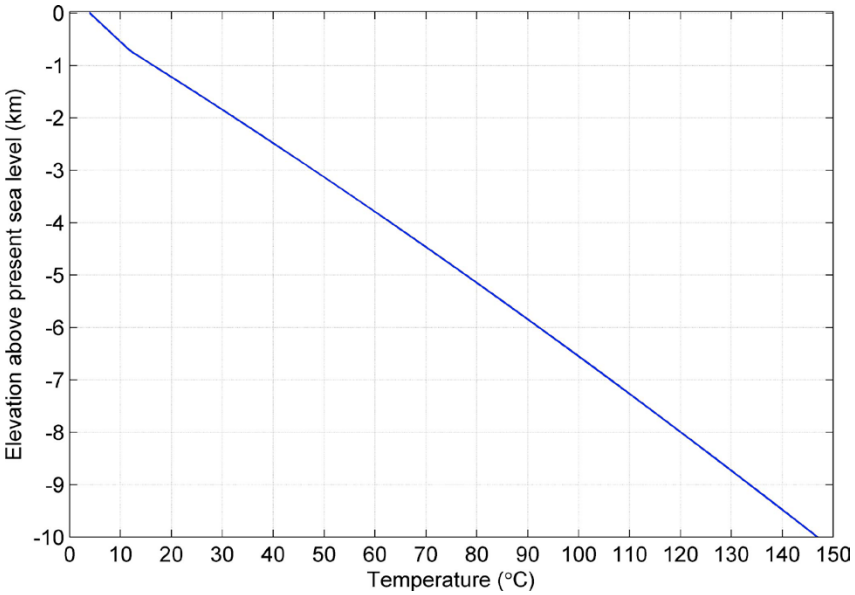

Figure 2-7. *Distribution of initial ground temperature for the mean thermal properties used in the 2D permafrost modelling. For a description of these properties, see Hartikainen et al. (2010, Table 2-2).*

The initial salinity concentration of groundwater for depths to ~ 1.5 km is described in Hartikainen et al. (2010 Appendix F), and for depths from ~ 1.5 km to 10 km it is obtained as a stationary solution using present concentration values on the surface and at the depth of 1.5 km.

Figure 2-8 shows the initial salinity distribution in the model domain.

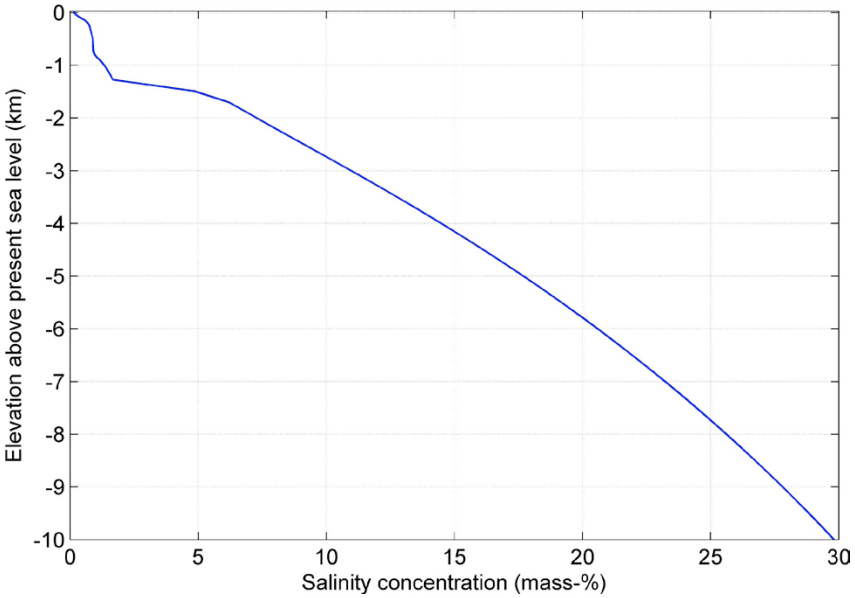

Figure 2-8. *Distribution of the initial salinity concentration of groundwater (Hartikainen et al. 2010).*

The present-day groundwater pressure is determined as hydrostatic pressure based on the initial conditions of ground temperature and groundwater salinity concentration as well as the hydrostatic pressure at the bed of the Baltic Sea. The results for initial groundwater pressure are shown in Figure 2-9.

In the present study, thermal conductivity and thermal diffusivity are set to the mean values given in Table 2-1 and Table 2-2 in Hartikainen et al. (2010). The uncertainty associated with these parameters is taken from Hartikainen et al. (2010). The geothermal heat flow is also set to the mean value given in Table 2-3 in Hartikainen et al. (2010). The uncertainty associated with this parameter is also taken from Hartikainen et al. (2010).

The planned SFR3 repository for short-lived low- and medium-level nuclear waste does not produce a significant amount of heat. In contrast to Hartikainen et al. (2010), the heat production from the planned nearby repository for spent nuclear fuel in Forsmark is *not* included in the current simulations. This is a pessimistic assumption in terms of permafrost development and freezing, since the exclusion of heat from a nuclear waste repository may result in somewhat lower bedrock temperatures (Hartikainen et al. 2010, Section 5.2).

Surface properties and conditions

The uncertainty in future precipitation and surface conditions is addressed by assuming conditions that in the previous studies were shown to be the most favourable for permafrost growth, i.e. a *dry climate* with *dry surface conditions* (Hartikainen et al. 2010). For more detailed definitions of these states see Hartikainen et al. (2010).

The impact of vegetation, snow cover and other climate factors on the ground surface temperature and permafrost development has been well investigated (Washburn 1979, Williams and Smith 1989, Yershov 1998, French 2007). In general, an annual mean air temperature ranging between –9 and –1 °C is required to build up permafrost for most surface covers, depending on other climatic conditions and topography. The surface conditions can be modelled by thermodynamic and hydrodynamic models using surface energy and water balance equations and information on climate conditions and topography, including radiation, precipitation, cloudiness and wind, and their annual and diurnal variations (Riseborough et al. 2008). However, these models are unsuitable for the long timespans associated with glacial cycles, because no climate data besides the air temperature can be adequately constructed. Therefore, an empirical approach based on *n*-factors (Lunardini 1978), i.e. statistical correlations between air and ground surface temperature, has been used to construct the ground surface temperature from the projected air temperature. For a detailed motivation for and description of the *n*-factors approach for treatment of surface conditions, see Hartikainen et al. (2010).

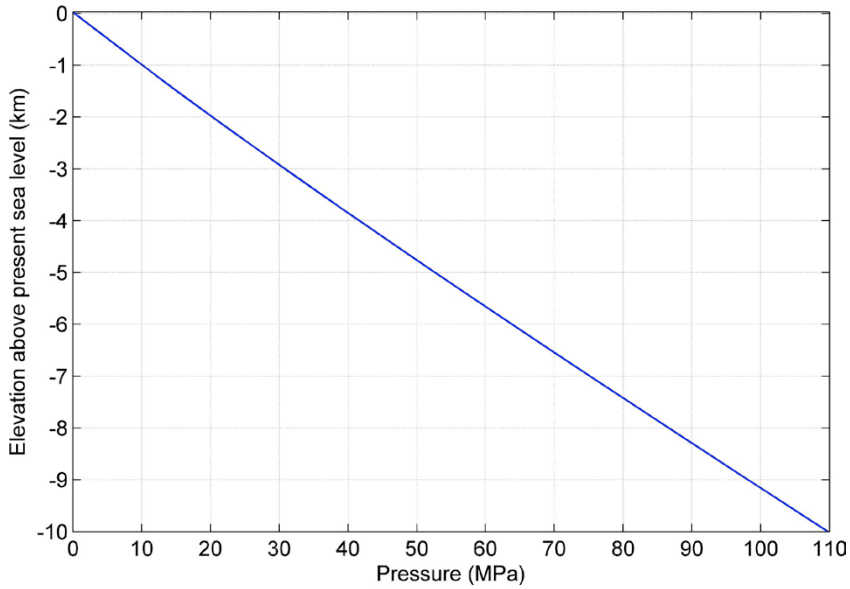

Figure 2-9. *Distribution of initial groundwater pressure associated with the temperature and salinity concentrations shown in Figure 2-7 and Figure 2-8.*

In accordance with the conclusions from the previous permafrost simulations for Forsmark (Hartikainen et al. 2010), the permafrost model was set up under the assumption of dry climate conditions and dry surface conditions to promote permafrost at the site. Several sensitivity simulations were performed to investigate the potential for frozen ground when the uncertainties in simulated Forsmark T_{2m} are taken into account.

In all permafrost simulations, the area above the repository is assumed to have become terrestrial, in accordance with predictions from Glacial Isostatic Adjustment (GIA) modelling (Section 2.2.4).

Near-surface air temperature

The monthly mean air temperature at 2 m height (T_{2m}) in Forsmark, derived from the EMIC simulation resulting in the coldest conditions in Forsmark, was used as input to the permafrost model. The sensitivity of the permafrost modelling to uncertainties in the climate model results was further analysed based on a suite of seven sensitivity simulations with the permafrost model. In these experiments, the annual average Forsmark T_{2m} was lowered by 2 to 8 °C as compared with the reference case. The amplitude and shape of the annual cycle of T_{2m} varies with the annual average T_{2m}. To account for this variation in the sensitivity experiments, a linear regression between the monthly average and annual average T_{2m} as determined for each month of the year using data from the EMIC simulation was adopted. The regression coefficients were thus used to determine the resulting annual cycle in Forsmark T_{2m} for each sensitivity experiment (Figure 2-10).

Sensitivity to model formulation improvement

The sensitivity of the results to the improvements made in the new version of the permafrost model was investigated. Thus, the results of the new version of the permafrost model were compared with experiments with identical forcing and boundary conditions performed with the old version of the model (described by Hartikainen et al. 2010). The new version, which includes an improved description of the influence of the annual temperature cycle on permafrost growth and thawing, simulates faster growth of permafrost and deeper equilibrium depths for the isotherms. The effect is larger for shallow depths than for deeper depths. For example, in the experiments with an annual average near-surface air temperature of –1 °C, the equilibrium depth of the 0 °C isotherm in the new model results is more than twice the depth in the old model version. In the experiment with –7 °C annual average near-surface air-temperature on the other hand, the 0 °C isotherm in the new model results is only c. 7 % deeper than in the old model version. Since the new version of the permafrost model describes the coupling between the air temperature and the bedrock in greater detail, it is reasonable to believe that this version gives more reliable results. Therefore, the results of this model version were used in the analysis.

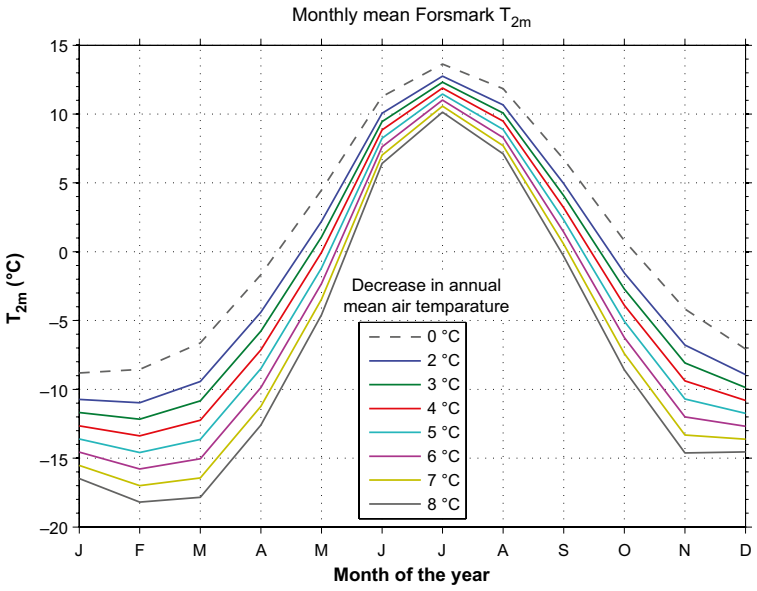

Figure 2-10. *Monthly mean Forsmark T_{2m} (°C) in the LC_54k_180 simulation (dashed line) and in the sensitivity experiments (solid lines) performed with the permafrost model.*

This choice further reduces the risk of using too shallow isotherm depths to analyse the potential for permafrost in Forsmark. The results are discussed in more detail in Section 3.4 of Brandefelt et al. (2013).

Potential for permafrost

The results of the permafrost modelling performed by Brandefelt et al. (2013) are summarised in Figure 2-11 which shows the maximum depth of the 0 °C, –1 °C, –2 °C, –3 °C, –4 °C and –5 °C isotherms at the SFR repository location after 10 ka of permafrost model integration as a function of the annual average Forsmark T_{2m} simulated for a cold climate period at 54 ka AP. The permafrost modelling results are given here as a function of the annual average T_{2m} in Forsmark.

In Brandefelt et al. (2013), it was concluded that an annual average T_{2m} of c. –1 °C and c. –2 °C is required for the 0 °C isotherm to reach the SFR1 and SFR3 repository depth, respectively (Figure 2-11). Based on a literature review of future atmospheric CO_2 concentrations (see Section 2.3.2 in Brandefelt et al. 2013), it was concluded that, although unlikely, an atmospheric CO_2 concentration of c. 230 ppmv at 17 ka AP cannot be excluded (see also discussion in Section 3.4.1), resulting in minimum annual average 2-m temperature at Forsmark of approximately –2 °C (Table 2-2). This leads to the conclusion that the 0 °C isotherm could, under pessimistic assumptions, reach the SFR1 and SFR3 repository depth at the insolation minimum occurring around 17 ka AP. It was also concluded that the –3 °C isotherm could not reach repository depth at this time.

For orbital year 54 ka AP, it was concluded that an annual average Forsmark T_{2m} below c. –1 °C or –2 °C cannot be excluded even for atmospheric CO_2 concentrations above 280 ppmv. The result of this is that both the 0 °C and –3 °C isotherms could, under pessimistic assumptions, reach the SFR1 and SFR3 repository depth at the insolation minimum occurring around 54 ka AP.

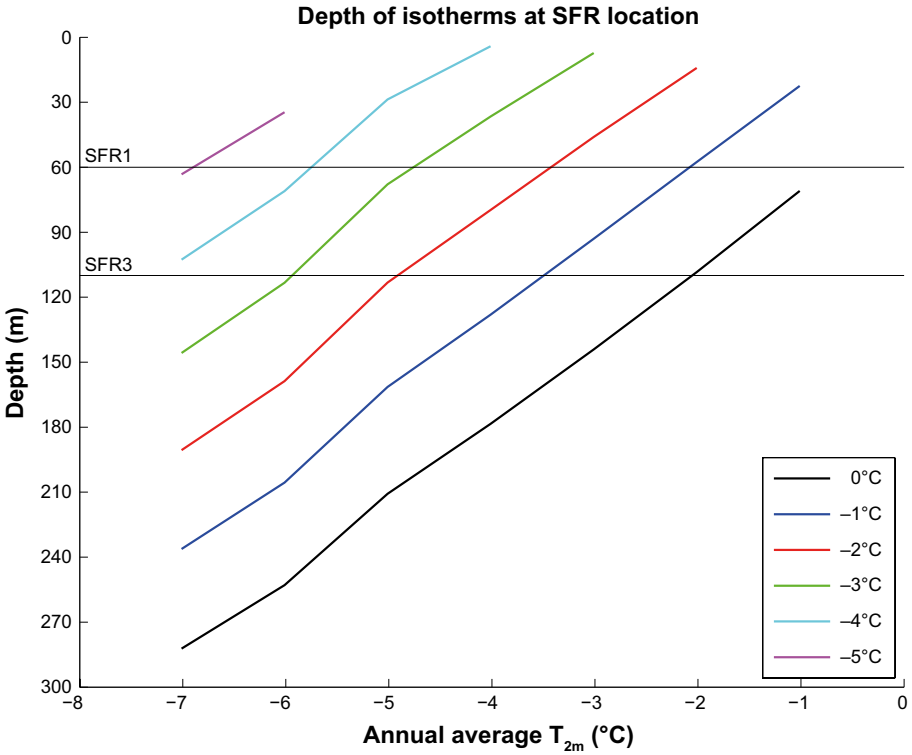

Figure 2-11. *Depth (m) of the 0, –1, –2, –3, –4° and –5 °C isotherms as a function of the annual average Forsmark T_{2m}. The depths of the existing SFR1 repository (c 60 m) and planned SFR3 repository (c 110 m) are indicated with black lines. The Forsmark annual average T_{2m} was c. +5.5 °C in the period 1961–1990 (Larsson-McCann et al. 2002) and +6.1 °C in the period 1986–2005 AD (Appendix C).*

As expected, the results from Brandefelt et al. (2013) demonstrate that lower temperatures at repository depth require even lower atmospheric temperatures and CO_2 concentrations. For example, Brandefelt et al. (2013) concluded that an annual average T_{2m} of c. –5 °C and c. –6 °C is required for the –3 °C isotherm to reach the SFR1 and SFR3 depths, respectively. Further, based on the results of the climate modelling summarised in Table 2-2, it is concluded that an atmospheric CO_2 concentration of c. 210 ppmv or less is required to get annual average Forsmark T_{2m} below c. –5 °C for orbital year 17 ka AP. Similarly, it is concluded that an atmospheric CO_2 concentration of c. 250 ppmv or less is required to get annual average Forsmark T_{2m} below c. –5 °C for orbital year 54 ka AP. Based on a literature review of future atmospheric CO_2 concentrations (see Section 2.3.2 in Brandefelt et al. 2013), it is concluded that an atmospheric CO_2 concentration of c. 250 ppmv or less at 54 ka AP cannot be excluded. Further, it is concluded that it is *not* likely that the atmospheric CO_2 concentration will be c. 210 ppmv or less at 17 ka AP (see also Section 3.4.1). In summary, a bedrock temperature of 0 °C cannot be excluded at c. 60 m and c. 110 m depth at 17 ka AP or at 54 ka AP (Brandefelt et al. 2013). Under the assumptions made in the study, it is further concluded that it is very unlikely to get a bedrock temperature of –3 °C or less at c. 60 m and c. 110 m depth at 17 ka AP, but that this possibility cannot be excluded at 54 ka AP. The main reason for the different conclusions for the two time periods is the projected decrease in atmospheric CO_2 concentrations between these times.

2.1.5 Time perspective

Changes in annual ground surface temperature can lead to development of permafrost and freezing of the ground. If the mean annual ground surface temperature at the SFR location is lowered to –7 °C, the 0 °C isotherm can reach 60 m depth in c. 460 years and 110 m depth in c. 820 years (Brandefelt et al. 2013, Tables 3-5 and 3-6). Similarly, the –3 °C isotherm can reach 60 m depth in c. 880 years and 110 m depth in c. 2 700 years, and the –5 °C isotherm can reach 60 m depth in c. 6 700 years (Brandefelt et al. 2013, Tables 3-5 and 3-6).

Under periglacial conditions, permafrost can aggregate from some centimetres to some decimetres a year. The depth of the 0 °C isotherm increases by up to c. 0.15 m a^{-1} in the first few centuries (Brandefelt et al. 2013, Figure 3-22).

Permafrost degradation can take place several times faster than aggregation (SKB TR-10-49, Figure 3-57), especially when the surface temperature is increased above 0 °C and permafrost decays simultaneously from the bottom upwards and from the top downwards. High degradation rates may also occur at the transition from cold-based to warm-based conditions during ice-sheet overriding.

2.1.6 Handling in the safety assessment

The potential for cold climate conditions and permafrost in Forsmark in the next 60 ka has been investigated by means of numerical modelling (Brandefelt et al. 2013). In this context, the main question for the safety assessment concerns the timing of potential periods of permafrost development and freezing of SFR concrete structures.

In the study of Brandefelt et al. (2013) it was concluded that the concrete structures of the repository will not freeze (bedrock temperatures of –3 °C or lower) during the next 50 ka, even taking all known uncertainties related to climate and permafrost development into account. However, under these pessimistic assumptions, they also showed that permafrost development at Forsmark (bedrock temperatures of 0 °C or lower), albeit highly unlikely (see also Section 4.3), cannot be excluded for the period of the next minimum in incoming solar radiation at high northern latitudes at 17 ka AP.

In the SR-PSU, it was demonstrated that periglacial conditions between 15.5 and 18.5 ka AP did not contribute to an increase of the maximum dose over the assessment period as compared to having temperate conditions during this time period (SKB TR-14-01 and Brandefelt et al. 2016). The hypothetical event of freezing of the repository concrete structures between 10 and 15 ka AP was evaluated in a subsequent complementary study (Näslund et al. 2017a, b). Whilst this assumption resulted in increased dose to humans during a period after the hypothetical permafrost, the maximum dose was not affected. Owing to its very low likelihood of occurrence and its demonstrated low impact on dose, it is not judged appropriate to handle an early period of periglacial conditions in the main scenario or

in a less probable scenario. The possibility of early permafrost, similar to that featured in the early periglacial climate case in the SR-PSU, is instead evaluated as a residual scenario in the *hypothetical early permafrost climate case* (Section 5.4.1).

Brandefelt et al. (2013) also found that permafrost is more likely to develop in response to the insolation minimum at 54 ka AP compared to that at 17 ka AP. Further, in contrast to 17 ka AP, it was found that freezing of the repository concrete structures cannot be excluded during this insolation minimum. The possibility of periglacial condition at Forsmark after 50 ka AP is supported by modelling studies on climate evolution over the next 100 ka and beyond. These studies collectively show that the onset of the next glacial inception will likely occur in conjunction with the insolation minimum at 54 ka AP if anthropogenic carbon emissions are strongly reduced within the next decades and/or they are removed by technological measures (Sections 3.4.5 and 4.3). As a result, the occurrence of permafrost after 50 ka AP are analysed in the *cold climate case* (Section 5.2.3), which is evaluated in the framework of the main scenario. Although freezing at repository depth cannot be excluded after 50 ka AP, the concrete barriers are also considered to degrade to such an extent within the first 50 ka that a potential freezing would no longer significantly influence the hydraulic properties of the concrete (**Post-closure safety report**, Section 7.4.2).

In the present safety assessment, glaciation at Forsmark is handled in the *glaciation climate case* (Section 5.3.1), which is considered in a less probable scenario. This climate case is specifically developed to study the radiological consequences from SFR of a glaciation in the Forsmark region. If the climate becomes sufficiently cold to enable ice-sheet development at Forsmark within the coming 100 ka, permafrost development is expected to occur prior to the ice-sheet development. Therefore, shorter periods of periglacial conditions are described prior to periods of glacial conditions in the *glaciation climate case* (see further Section 5.3.1).

2.1.7 Handling of uncertainties

Uncertainties in mechanistic understanding

There are no major uncertainties in understanding of mechanistic processes regarding permafrost development. Minor uncertainties in the 1D modelling experiments are associated with the fact that the exclusion of salts during the freezing of groundwater is not included. The process of freeze-out of salts is included in the 2D modelling.

Model simplification uncertainty

The major model simplification in the 1D permafrost modelling study was the exclusion of lateral variations in physical properties, boundary conditions and geometry. For example, full consideration of the anisotropy of thermal conductivity and heat capacity and the features of water bodies and topography, as well as the heat generation from the spent fuel, requires 3D modelling. However, this is to a large extent taken care of by the 2D modelling study reported here.

The 1D modelling approach could, in certain situations, result in somewhat higher temperatures than would be calculated using a 2D or full 3D approach. In the context of permafrost development, the effect of groundwater flow, cooling down the bedrock, is the most important factor here. However, compared with heat conduction, groundwater flow has only a minor role in permafrost development, as indicated by the 2D modelling results that included groundwater flow. Furthermore, the anisotropy of thermal properties is not a problem in 1D or 2D, since one can choose a combination of thermal properties that would give the lowest temperatures, or at least very close to the lowest temperatures. Therefore, it is unlikely that 3D simulations would yield notably lower temperatures than the range obtained in the full series of 1D and 2D sensitivity modelling cases that have been performed.

Input data and data uncertainty

Bedrock data

Some data uncertainty exists when it comes to thermal conductivity and heat capacity of rock at the Forsmark site. In the calculation of ground temperature and the rate of freezing, thermal conductivity is the most important input parameter in terms of thermal properties of the ground. Some uncertainty

also exists in determination of hydraulic and mechanical properties of bedrock and salinity concentrations of groundwater versus depth, see appendices in Hartikainen et al. (2010) and references therein.

A considerable uncertainty in the 1D permafrost study is associated with determination of the *in-situ* temperature and geothermal heat flow in the depth range of 1 000–10 000 m for the thermal boundary and initial conditions of the model. The *in-situ* ground temperature has been measured in boreholes to a depth between 500 and 1 400 m at the Forsmark site. The temperature at the same depth in different boreholes differs over a range of 2 °C (SKB R-05-18, SKB TR-06-19, SKB TR-06-23). These thermal data have been used for ground temperature modelling which provided new and better constrained values on geothermal heat flow as well as estimates on the difference between ground- and air temperature for the site (Sundberg et al. 2009). The results from the ground temperature modelling were applied in the setup of the 2D permafrost model, which considerably reduced the uncertainty associated with determination of the ground surface temperature from the air temperature and the estimation of the *in-situ* temperature and geothermal heat flow for the 1 000–10 000 m-depth for the thermal boundary and initial conditions.

In general, the uncertainty in thermal characteristics of the bedrock and geothermal heat flow has a significantly smaller impact on modelled permafrost and freezing depths than uncertainties related to ground conditions and climate.

Surface conditions

The impacts of the surface conditions on the spatial (along the profile) development of permafrost and perennially frozen ground were investigated by Hartikainen et al. (2010) using site-specific information on climate and landscape features including water bodies and topography. In the study of Brandefelt et al. (2013), the results of the previous investigations were used to choose surface conditions that promote permafrost development in Forsmark. Thus, dry surface conditions and dry climate conditions were used in these simulations.

Near-surface temperature

In Brandefelt et al. (2013), the annual cycle of near-surface air temperature in Forsmark was estimated based on climate model simulations and a literature review. All known uncertainties in the climate modelling results were addressed under the pessimistic assumption that they all would result in cooling in Forsmark. These uncertainties include inter-model differences and internal variability, atmospheric greenhouse gas and aerosol concentrations, and glacier and ice-sheet dynamics, see Section 3.4 of Brandefelt et al. (2013). Thus, the full range of uncertainty in near-surface air temperature was addressed in these simulations. The sum of all known uncertainties varies from 4 °C, for climates similar to the present, to 12 °C, for cold climates substantially different from the present climate.

Major uncertainties exist in the near-surface temperature used for the last-glacial-cycle permafrost modelling (SKB TR-06-23 and Hartikainen et al. 2010), including uncertainties as to its representativeness for the last glacial cycle climate. A detailed discussion and description of these uncertainties are found in SKB (TR-10-49, Appendix 1). To cover the estimated uncertainties in air temperature reconstructed for the last glacial cycle, a large range of sensitivity cases and alternative air temperature variations have been analysed. This was also motivated by the fact that the variation in surface conditions and climate has a larger impact on modelled permafrost and freezing depth than bedrock thermal conditions and geothermal heat flow.

Input data for the permafrost modelling are described in Hartikainen et al. (2010, Appendix H) and SKB (TR-10-49).

2.1.8 Adequacy of references

The SKB report produced for the handling of permafrost and freezing processes in the SR-PSU (Brandefelt et al. 2013) has undergone QA system handling, including a documented factual review procedure. Also, the SKB report produced for SR-Site (Hartikainen et al. 2010) and the SR-Can Climate report (SKB TR-06-23), from which some studies are used, have undergone QA system handling including a factual review process. Other references used for the handling of the permafrost

and freezing processes, in this report and in Brandefelt et al. (2013) are either peer-reviewed papers from the scientific literature or textbooks (e.g. Yershov 1998, French 2007).

2.2 Isostatic adjustment and relative sea-level changes

In addition to the descriptions in the present section, a detailed in-depth description of the physics of glacial isostatic adjustment (GIA), how it affects sea level, and the methods which are employed to study and understand these processes are presented in Whitehouse (2009).

The major part of Section 2.2.1 is adapted from SKB (TR-06-23, Section 3.4) written by P. Whitehouse, whereas some parts are adapted from Lund and Näslund (2009). Section 2.2.2 is adapted from SKB (TR-06-23). Section 2.2.3 is from Lund and Näslund (2009), and Section 2.2.4 is adapted from SKB (TR-06-23) and Whitehouse (2009).

2.2.1 Overview/general description

Shoreline displacement, sea level and relative sea level

The spatial location of the shoreline varies in time. Shoreline displacement is the result of eustatic changes relative to isostatic changes of the solid surface of the Earth. The shoreline location is determined by the height of the geoid surface, corresponding to the undisturbed ocean surface, relative to the solid surface of the Earth. The geoid is the equipotential surface of the Earth's gravitational field which best fits the undisturbed surface of the oceans. The shape of the geoid is governed by the gravitational field of the Earth and varies over time.

Sea level is defined to be zero on land and positive in the oceans, where it corresponds to the depth of the ocean. Relative sea level is the vertical height difference between the geoid at an arbitrary time and the present height of the geoid, where the height of the geoid is measured relative to the height of the solid surface. Relative sea level is defined to be zero at the present day. It is positive during *transgression*, when the intersection of the geoid with the solid surface is higher than at present and negative during *regression*, when the intersection of the geoid with the solid surface is lower than at present.

Relative sea level changes are a result of *isostasy* and *eustasy*. Isostasy is the response of the solid Earth to loading or unloading by ice or water, and/or unloading and loading due to denudation and sedimentation. Eustasy refers to changes in sea level arising from changes in ocean water volume, due to mass exchange between continental ice masses and the oceans and density changes associated with ocean temperature and salinity, and the spatial distribution of ocean water changes.

The solid Earth

The solid Earth consists of the crust, the upper and lower mantle, and the outer and inner core. The lithosphere comprises the crust and part of the upper mantle. The average thickness of the lithosphere is c. 100 km, although this value varies between less than 30 km for oceanic lithosphere and up to more than 200 km for continental lithosphere (Watts 2001). Lithospheric thicknesses in Fennoscandia range between ~ 60 km in the north-west and ~ 200 km in the south-east (Watts 2001). The lithosphere is less dense than the mantle below and responds approximately elastically to forces applied at the surface. The deformation of this layer is short-lived once the load is removed. The mantle responds viscoelastically to forces applied over a timescale of ~ 100 ka. The recovery of this layer to a state of isostatic equilibrium following loading takes several orders of magnitude longer than the recovery of the lithosphere. The rheological properties of the lithosphere and upper and lower mantle determine the precise magnitude and duration of solid Earth deformation, see further Sections 2.2.2 and 2.2.4.

Glacial isostatic adjustment

The redistribution of mass associated with the growth and decay of continental ice sheets gives rise to major glacial loading and unloading effects over timescales of several tens of thousands of years. For instance, during the decay of a major ice sheet, the unloading of mass results in a post-glacial

rebound of the crust that continues well after the disappearance of the ice. This process is well known from previously glaciated regions such as Canada and the United States, Fennoscandia, the British Isles and Siberia (e.g. Ekman 1991); areas where this process is still active today, some 10–15 ka after the last deglaciation. The response of Earth's crust, mantle and gravitational field is referred to as Glacial Isostatic Adjustment (GIA). The Earth's outer and inner cores are not affected by GIA processes. In previously glaciated terrain without strong tectonism, glacial isostatic adjustment is the most significant geodynamic process governing vertical deformation of the crust (e.g. Peltier 1994).

During the Last Glacial Maximum (LGM), around 20 ka ago, the Laurentide ice sheet of Canada and the United States, and the Fennoscandian ice sheet had maximum thicknesses of around 2.5–3 km, corresponding to a total of c. 120–135 m of global sea-level lowering at the LGM deduced from coral-reef data (Yokoyama et al. 2000). When these large ice masses slowly formed, their weight resulted in a slow downwarping of Earth's crust. One important factor that governed both this process and the following glacial unloading is the physical properties of Earth's crust and mantle. In the downwarping process, mantle material was displaced and flowed laterally in order to make room for the flexing crust. At times of ice-sheet decay, mantle flow is reversed and the crust rebounds. Since the mantle viscosity is high, the downwarping and subsequent rebound are slow processes. Furthermore, it has been shown that a deglaciation of large Northern Hemisphere ice sheets results in deformation of the Earth's entire surface, producing a series of upwarps and downwarps away from the areas of the former ice sheets (Figure 2-12). However, the deformation is largest in the regions that were glaciated.

The glacial isostatic adjustment process manifests itself not only in the slow rebound of regions of past ice sheets. Current melting of glaciers produces additional GIA effects. As an example, Iceland is currently undergoing rapid glacial rebound due to a mass loss of Vatnajökull and other smaller ice caps (e.g. Árnadóttir et al. 2009). Since the viscosity of the mantle is inferred to be three orders of magnitude lower beneath Iceland (Árnadóttir et al. 2009) than below, for example, Fennoscandia, uplift rates on Iceland are on the order of 20 mm a^{-1}, in spite of the much smaller volume of ice loss.

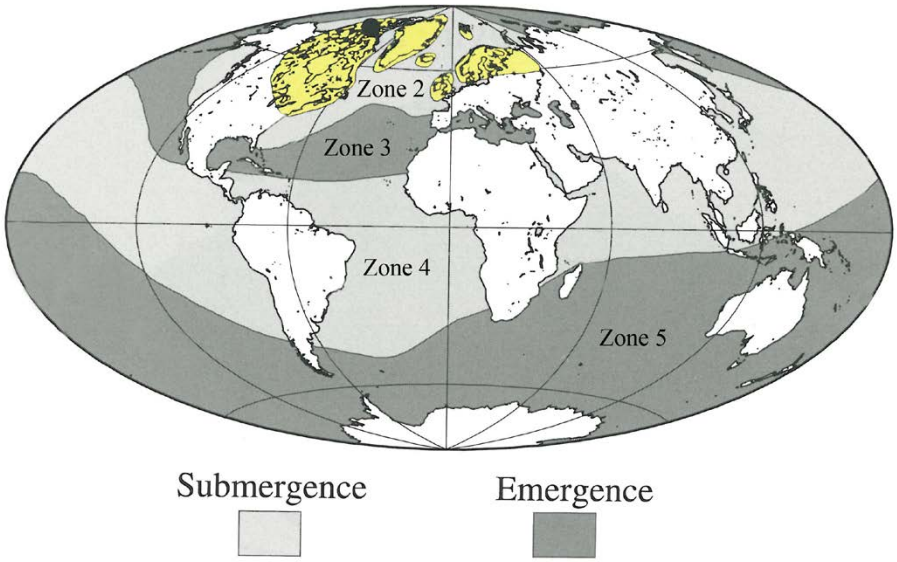

Figure 2-12. *Calculated deformation resulting from an instantaneous unloading of Northern Hemisphere last glacial cycle ice sheets at 16 ka BP. The results show five sea-level zones with similar sea-level histories within each zone. Sea-level zone 1 is marked in yellow. The entire Earth is affected by the unloading through a series of elevated and subsided regions away from the areas of the former ice sheets. Modified from Clark et al. (1978).*

Outside the ice-sheet margin, an uplifted forebulge, or peripheral bulge, is formed (e.g. Mörner 1977, Fjeldskaar 1994, Lambeck 1995). The forebulge is caused by flexure and a lateral displacement of mantle material extending outside the ice margin, and it may stretch for several hundreds of kilometres beyond a major ice sheet. The uplift of the forebulge is considerably smaller than the downwarping of the crust beneath the central parts of the ice sheet; on the order of tens of metres. During and after deglaciation, the area of the forebulge experiences land subsidence, exemplified by the ongoing lowering of the Netherlands, southern England and the east coast of the United States. It is worth noting that land subsidence in these regions is also a result of ongoing marine sediment loading. The location of maximum forebulge uplift migrates toward the formerly glaciated region as the ice sheet withdraws. In addition to the formation of the forebulge, the elasticity of the lithosphere may result in a downwarping of the crust, not only under the ice sheet, but also to some extent outside the ice margin. This produces a flexural depression between the ice margin and the forebulge, a depression where lakes may form from glacial meltwater.

At present, the crust beneath the Antarctic and Greenland ice sheets is depressed in a similar way as previously occurred under the North American, Fennoscandian and Siberian ice sheets. In Greenland and Antarctica, the crust would also be subject to significant glacial rebound if these areas were to be deglaciated in the future.

GIA-induced relative sea-level changes

GIA-induced sea-level changes arise as a result of the gravitationally-consistent redistribution of water between ice sheets and ocean basins, and thus the evolution of surface loading. Any redistribution of surface mass alters the shape of the geoid, which in turn defines the position of the surface of the oceans. Relative sea-level changes exhibit complex global spatial and temporal patterns and are strongly dependent upon the location relative to major ice sheets. Relative sea-level changes at locations far from ice sheets (hereafter referred to as far-field locations) are dominated by the eustatic signal; during deglaciation monotonic sea-level rise causes land inundation and the shift of shorelines inland. At locations close to ice sheets the isostatic signal dominates; rebound of the solid surface from the time of deglaciation onwards causes land emergence and the migration of shorelines oceanward. These are two end-member cases, and, in general, sea-level change, and hence shoreline displacement, is governed by a complex interplay of isostatic and eustatic processes, operating on different timescales.

GIA-induced sea-level changes depend on the following factors (Figure 2-13):

- The location and thickness of ice sheets.
- The depth and extent of the oceans.
- The structure and properties of the solid Earth and its response to surface loading.

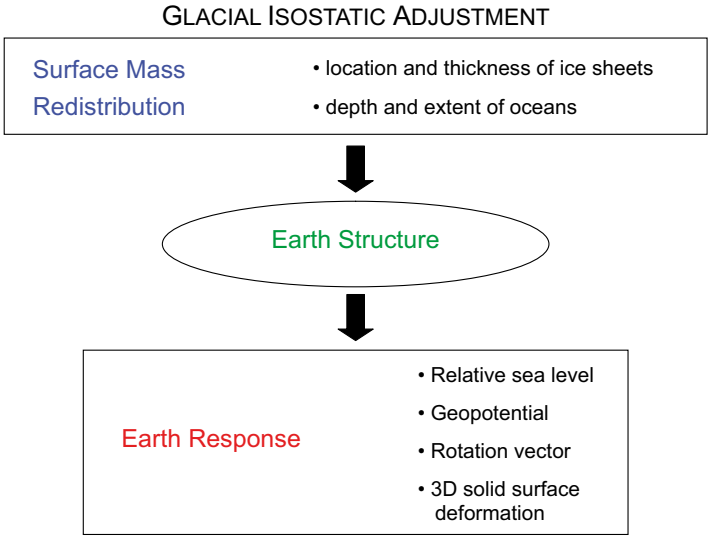

Figure 2-13. *The theory of Glacial Isostatic Adjustment (GIA): inputs and outputs of the system.*

Changes in surface loading arise due to the exchange of mass between ice sheets and ocean basins throughout a glacial cycle. The presence of ice-dammed lakes and the redistribution of sediments also contribute to changes in surface loading, although, in Fennoscandia, the short-lived nature of ice-dammed lakes, and their shallow depth, means that this perturbation to the pattern of surface loading probably has a negligible effect when considering the solid Earth response. The denudation of bedrock and redistribution of associated sediments persists over a much longer timescale, on the order of millions of years. On a regional scale, over a single glacial cycle, the effect of sediment redistribution upon solid Earth deformation is negligible in relation to the ice load, but over several glacial cycles, or locally, it may be of significance.

The height of the geoid, or mean ocean surface, is dependent upon *direct* and *indirect* geoid perturbations (Milne et al. 2002), as well as changes in ocean water volume and the capacity of ocean basins. *Direct* effects refer to the deflection of the geoid due to the direct attraction of surface mass loads, such as ice sheets. *Indirect* effects refer to geoid perturbations arising due to the surface load-induced deformation. The volume of the oceans will vary as water is transferred to and from the ice sheets. Also, changes in ocean capacity and bathymetry arise as a result of crustal and geoidal perturbations in response to ice and ocean loading. The ice-loading solid surface response includes the depression and rebound of the solid surface in the location of ice sheets, and the raising and lowering of glacial forebulges in areas surrounding the ice sheets. The ocean-loading response is similar to the ice-loading response. However, at continental margins ocean loading induces a levering of the continental lithosphere and a subsidence of offshore regions, this is referred to as *continental levering* (Clark et al. 1978) (see Figure 2-14). The combination of ice and ocean loading leads to a decrease in the volumetric capacity of the ocean basins during glaciation, and an increase during deglaciation due to the growth and decay of offshore peripheral bulges, resulting in a globally uniform rise or fall in sea level, respectively. The ongoing fall in sea level following the last deglaciation due to the migration of water from equatorial regions to subsiding peripheral bulge regions has been termed *equatorial ocean syphoning* (Mitrovica and Peltier 1991, Mitrovica and Milne 2002).

Changes in relative sea level result in shoreline displacement. A rise in relative sea level and the consequent inland migration of the shore may be due to solid Earth subsidence, an increase in the height of the geoid (ocean surface) as a result of ice-sheet melting, or a combination of these processes. Similarly, a fall in relative sea level and the consequent migration of the shore towards the ocean may be due to isostatic rebound, a fall in the height of the geoid due to ice-sheet build up, or a combination of these processes. In the vicinity of the Fennoscandian ice sheet, the effects of isostatic deformation and changes to the height of the geoid occur simultaneously and may have opposite effects on the position of the shoreline. Further, the surface of the Baltic Sea does not solely depend on the height of the geoid, but also on the elevation of its sills relative to the Atlantic sea level, and ice thicknesses at locations with potential connections to the sea; these may cause it to become isolated from the global ocean.

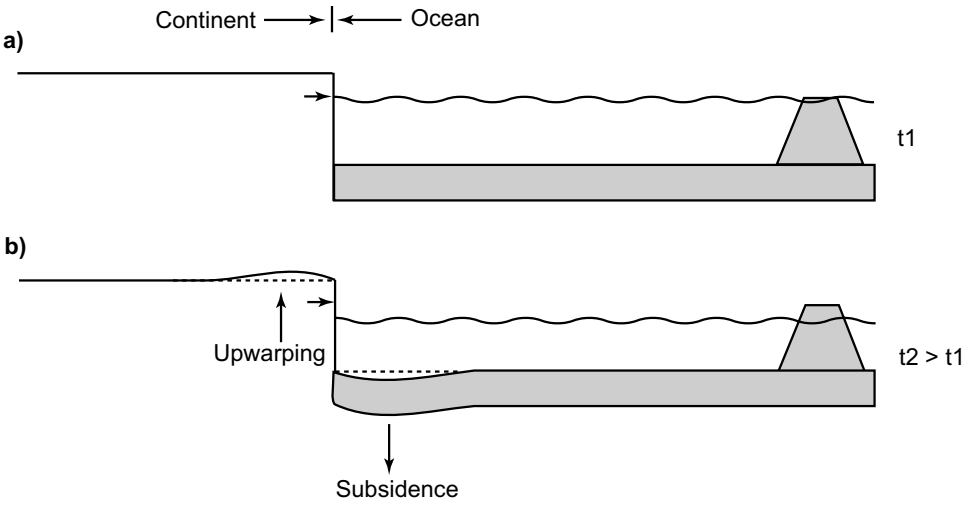

Figure 2-14. *Continental levering: the migration of water into offshore regions following deglaciation results in offshore subsidence and onshore upwarping. Ocean floor subsidence results in sea-level fall at far-field sites.*

Indirectly, groundwater flow and composition are influenced by shoreline displacement. If the site is not subject to permafrost, and it is not covered by an ice sheet, the sea, or a lake, then the groundwater surface follows a subdued version of the topography. Groundwater flow will be driven by topography, assuming precipitation exceeds evaporation. If the site is submerged the situation will be almost stagnant and groundwater flow will be driven by density variations only (SKB TR-10-48). Groundwater composition is affected, since relative sea level affects the salinity of the Baltic Sea. Relative sea level and the extent of the ice sheet determine whether there is a connection between the Baltic Sea and the ocean. This, together with the runoff to the Baltic basin, determines the salinity in the sea/lake water.

2.2.2 Controlling conditions and factors

Loading

The main factors governing the evolution of relative sea level during the last glacial cycle, and hence shoreline displacement, throughout Fennoscandia are the loading history – both in respect of ice and ocean water – and the rheological parameters governing the response of the solid Earth to such a load.

The relative sea level is very sensitive to variations in the evolution of the nearby ice sheet (Lambeck et al. 1998, Davis et al. 1999, Tamisiea et al. 2001, 2003, Milne et al. 2002, Kaufmann and Lambeck 2002). There remain uncertainties in the details of ice loading during the last glacial cycle, especially in respect of estimates of ice thickness within Fennoscandia.

The details of far-field ice sheets are irrelevant for the prediction of relative sea-level change in Fennoscandia (Peltier 1998, Mitrovica et al. 2001, Tamisiea et al. 2003, Bassett et al. 2005); mass changes in the far field mainly provide an influence on global average sea level. However, the overall characteristics of mass-changes in far-field ice sheets may also generate a long wavelength isostatic response in Fennoscandia. This response is likely to be dominated by the signal from a massive North American (Laurentide) ice-sheet complex. Due to the position of Fennoscandia on the Laurentide forebulge during the LGM (Mitrovica et al. 1994), the presence of the Laurentide ice sheet is estimated to have generated 25–30 m of solid Earth uplift in central Fennoscandia at this time (see Section 2.3.4). The magnitude of this signal does not vary greatly across Fennoscandia (unlike the relative sea-level signal due to local ice loading) and is not dependent upon the local geometry of the Laurentide ice sheet; only its volume.

During the last deglaciation, an ice-dammed lake prevailed within the Baltic depression when non-ice-covered sills were above sea level and all other potential connections between the Baltic Sea and the North Sea were dammed by the ice-sheet ice (e.g. Björck 1995, Lambeck 1999). The surface of the ice-dammed lake was constrained by the height of the ice sheet above sea level and the surrounding topography, i.e. the sill levels, and there is evidence to suggest that immediately prior to the draining of the so-called Baltic Ice Lake its surface was 25 m above the contemporary relative sea level (Björck 1995). Due to the relatively small volume of water released to the oceans as the ice lake drained the resulting perturbation of global sea levels was insignificant (Lambeck 1999). The shallow depth and the short duration of the ice lake mean that its impact on isostasy was negligible in comparison with the ice load.

Another process that may impact the loading is erosion and sediment transfer. Erosion and transport of sediment took place beneath warm-based parts of the ice sheet during previous glacial cycles, and this mass redistribution has affected isostatic loading and topography. However, the average total depth of glacial erosion over all Late Pleistocene glacial cycles in lowland Precambrian parts of Fennoscandia is on the order of a few tens of metres, see Section 2.4. Therefore, on the timescale of one glacial cycle, the average unloading/loading effect of this process may be neglected. However, any local reshaping of the land will affect the evolution of the shoreline, and this needs to be taken into account.

Rheological parameters and topography

In order to determine the Earth's response to surface loading, its internal rheological and density structure must be specified. The characteristic timescale for loading during a glacial cycle will excite both elastic and viscous responses; therefore, a viscoelastic (Maxwell) rheology is adopted. Such a system behaves elastically on a short timescale and viscously on a long timescale when placed under stress.

Parameters describing the rheological properties of the Earth's lithosphere and upper and lower mantle define its response to loading during a glacial cycle. The average density and elastic structure of the Earth can be taken from Dziewonski and Anderson (1981). The lithosphere is generally regarded as elastic for the purposes of GIA studies; this has been shown to be a good approximation throughout the development of the subject (McConnell 1968).

The upper mantle lies below the lithosphere, extending to a depth of 660 km, and then the lower mantle extends to 2 900 km below the Earth's surface. The viscosity of the upper and lower mantle has been constrained to lie in the ranges 1×10^{20}–2.6×10^{21} Pa s and 2×10^{21}–1×10^{23} Pa s, respectively, as determined from previous GIA studies (Davis and Mitrovica 1996, Mitrovica and Forte 1997, Simons and Hager 1997, Lambeck et al. 1998, Davis et al. 1999, Milne et al. 2001, 2002, 2004, Mitrovica and Forte 2004). Lateral variations in radial viscosity structure may be derived from seismic shear-velocity models by converting velocities to temperatures, and then using temperature to estimate viscosity.

Present-day topography is used to constrain paleotopography. When calculating paleotopography, see Section 2.4, we assume that all changes to the shape of the land arise from the differential GIA response across the region; however, topography is also affected by tectonic, erosional and depositional processes.

The isostatic adjustment and shoreline displacement described above may affect several geosphere variables of importance for a geological repository (Table 2-3).

Table 2-3. A summary of how geosphere variables are influenced by isostatic adjustment and shoreline displacement.

Geosphere variable	Climate issue variable	Summary of influence
Rock stresses	Isostatic depression/ rebound	The deformation of the Earth's crust will lead to altered rock stresses.
Groundwater pressure	Relative sea level	If the site is not covered by the sea or a lake the groundwater pressures will be determined by topography and groundwater recharge. If the site is submerged the groundwater pressure will be determined by the depth of the sea/lake.

2.2.3 Natural analogues/observations in nature

The GIA process may be observed by studying relative sea-level markers, both from the geological record and from tide gauge data, GPS observations of the 3D deformation of the solid surface, the time-variation of the gravity field as observed by satellites and land-based gravity surveys, and changes in the orientation of the Earth's rotation vector and length of day.

The geological data, including paleoshoreline positions, lake isolation and tilting information, cover a longer time period than the tide gauge data, but the tide gauge data are more accurate, both in terms of their vertical resolution and the dating of the information. In this context, shorelines or other geomorphological features that formed at the highest post-glacial sea level, in front of the retreating ice sheet margin, provide the oldest estimate of former relative sea-level positions. However, the total amount of post-glacial uplift at a site is typically larger than can be inferred from, for example, raised beaches. A significant portion of the uplift takes place as the ice sheet starts to decay, *prior to the actual deglaciation* of a typical site situated at some distance from the maximum ice margin. The total maximum amount of glacial rebound that has occurred due to the decay of the Fennoscandian ice sheet is around 800 m (e.g. Mörner 1979) (Figure 2-15). This may be compared with the largest value of rebound as inferred from the highest marine limit, which is situated at ~ 280 m a.s.l. in the Swedish coastal region of the Gulf of Bothnia. Another related method to study glacial rebound is to analyse the amount and direction of tilt of paleoshorelines of glacial lakes that formed beyond the retreating ice margin. A selection of geological relative sea-level data for Fennoscandia can be found in e.g. Lambeck et al. (1998), Påsse (2001), Eronen et al. (2001), Kaufmann and Lambeck (2002), Näslund (2011), Påsse and Daniels (2015), and references therein, but at present a complete compilation of such data does not exist.

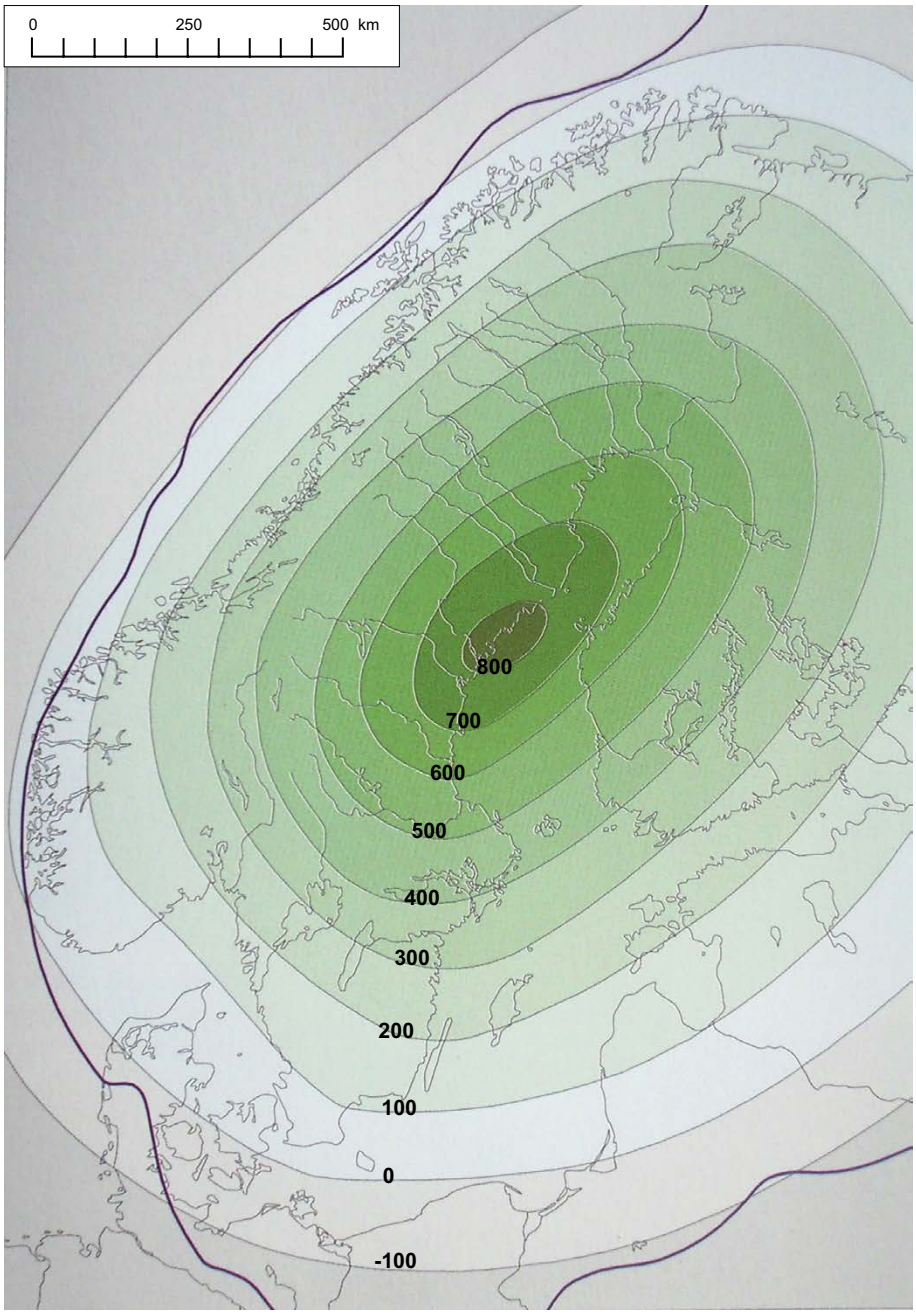

Figure 2-15. *Total amount of glacial rebound (metres) caused by the deglaciation of the Weichselian ice sheet. The bold line shows the approximate maximum extent of the Weichselian ice sheet. Note that the total amount of rebound is more than twice as large as the amount of rebound that may be inferred from raised beaches formed at the highest post-glacial sea level (see the text). After Fredén (2002).*

Care must be exercised when interpreting paleoshoreline data from the Baltic Sea; it is important to determine whether the data relate to sea level or a lake level. An overriding problem with geological data in Fennoscandia is the lack of relative sea-level data prior to the LGM. Most of the evidence of shorelines prior to that time has been destroyed by the ice sheet. This makes it difficult to test relative sea-level estimates for the period before 20 ka BP. Furthermore, the fact that shorelines can only form in ice-free locations provides an important temporal constraint on shorelines that would otherwise be undated.

One way of making direct observations of ongoing post-glacial crustal deformation is to use high quality data from networks of continuously operating permanent GPS receivers. GPS data provide satellite-measured observations of changes in baseline distances that yield present-day rates of

vertical and horizontal motion at a series of discrete positions. GPS data from the BIFROST project (Johansson et al. 2002) provide excellent spatial coverage of present-day solid Earth deformation throughout Fennoscandia to a high degree of accuracy. Typically, the GPS stations used in the BIFROST project were established within national land survey programmes with an initial aim of providing reference coordinates for other GPS measurements. The detailed analyses of data from such permanent GPS stations have provided new insight into the processes of post-glacial rebound or GIA in Fennoscandia and Canada (cf. Scherneck et al. 2001, Henton et al. 2006). The results provide information on both the rate of the vertical uplift component, as well as on the associated smaller horizontal component of crustal motion (e.g. Johansson et al. 2002) (Figure 2-16). The vertical component of GIA for the Forsmark site amounts to 6.7 ± 0.2[4] mm a^{-1} (Vestøl et al. 2019).

Uplift determined by these GPS observations shows the same concentric uplift pattern as that derived from sea-level and levelling measurements. The fastest rebound occurs approximately in the areas where the Laurentide and Fennoscandian ice sheets had their greatest thicknesses.

The maximum vertical uplift rate measured in this way in the area of the former Laurentide ice sheet is ~ 13 mm a^{-1} (Henton et al. 2006), whereas the corresponding value for Fennoscandia is ~ 10 mm a^{-1} (Figure 2-16). The largest horizontal displacements are generally found in the area of the ice margins of the maximum extent of the ice sheet. The difference between the maximum vertical uplift rates as observed from sea-level/levelling measurements and from the analysis of GPS data is to a large extent covered by the uncertainty errors of the measurements, mainly in the sea-level measurements.

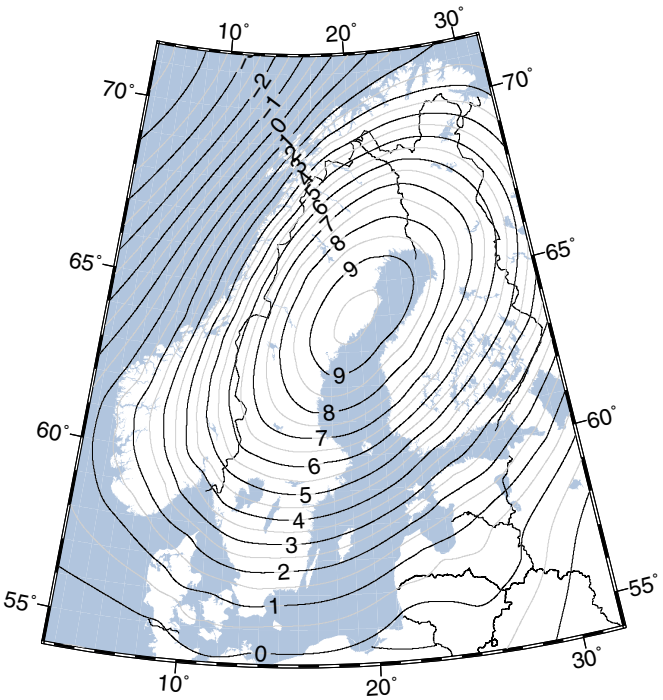

Figure 2-16. *Present-day crustal deformation rates over Fennoscandia as observed by continuous GPS measurements. The crustal rebound displays a concentric pattern with a maximum rebound rate of ~ 10 mm a^{-1} located approximately in the area of the former maximum ice-sheet thickness. The present-day isostatic uplift at the Forsmark site amounts to 6.7 ± 0.2 mm a^{-1}. Modified from Vestøl et al. (2019).*

[4] The uncertainty interval (1σ) constitutes a preliminary estimate by the Swedish National Land Survey

Since the GPS network yields an estimate for the full 3D deformation field, and the horizontal and vertical components of this field have different sensitivities to the ice history and Earth model, this gives the possibility of constraining model parameters more accurately when these data are combined with sea-level observations. Combining the GPS data with sea-level data is particularly important when one considers that the GPS data are limited by their relatively short time span and can only yield information about present-day deformation rates. The sea-level data are limited by their poor spatial coverage; a factor that is compensated for by the distribution of GPS observations throughout the interior of Fennoscandia.

Another, indirect, way of studying ongoing post-glacial rebound is by absolute gravity measurements (e.g. Lambert et al. 2001, Mäkinen et al. 2005), a method that may be used to estimate also the remaining uplift yet to be expressed in areas where the process is not complete.

2.2.4 Model studies

For a comprehensive and detailed review of GIA models, see Whitehouse (2009, Chapter 4). That chapter includes descriptions of different GIA approaches used by various research groups and the relative accuracy of these methods. Recent improvements of GIA theory are described, as well as current shortcomings of the models. The various data sets used to calibrate and verify the accuracy of the modelling are also briefly discussed. A shorter description of GIA models is given here, followed by the GIA simulations performed for the safety assessment.

Most GIA models solve the sea-level equation that was originally developed by Farrell and Clark (1976) and describe the gravitationally-consistent redistribution of water between ice-sheets and ocean basins, and thus the evolution of the distribution of water between oceans and land-based ice-sheets. Any redistribution of surface mass alters the shape of the geoid, which in turn defines the redistribution of water in the ocean basins; therefore, an iterative procedure is required to solve the sea-level equation.

The main results from the GIA modelling presented in this section are, together with future long-term projections of the global mean sea-level change from recent studies, used to estimate the future relative sea-level evolution at Forsmark up to 100 ka AP, described in Sections 3.5.3 and 3.5.4, respectively.

The GIA model

The GIA model used in this study was developed by Milne (1998), Milne and Mitrovica (1998), Milne et al. (1999). Three refinements to the original sea-level equation presented by Farrell and Clark (1976) have been developed by Mitrovica and Milne (2003). Firstly, time-dependent shoreline positions are represented when calculating the ocean-loading function. Shorelines can change position by several hundreds of kilometres in flat terrains, and this must be accounted for in applying the ocean load. Secondly, the water influx into regions vacated by retreating, marine-based ice is carefully accounted for in the distribution of the load (Milne et al. 1999). And thirdly, changes to the rotational state of the Earth because of both surface and internal mass redistributions are considered. The model used to generate predictions of relative sea-level change in this study is based on a new general theoretical foundation that includes all these advances. In this study, an Earth model with a laterally homogenous (1D) structure was used, since using a 3D model was out of scope at the time of the study. Subsequently, a comparison between the results obtained from the 1D model was made with results from a 3D model (with a laterally variable Earth structure), also described below.

The sea-level equation

The sea-level equation takes account of changes to the height of the geoid and the Earth's solid surface. Local factors, such as changes to the tidal regime, the consolidation of sediments, and tectonic processes, are neglected in this study.

$$\Delta\xi_{rsl}(\tau,\varphi) = \Delta\xi_{eus}(\tau)+\Delta\xi_{isos}(\tau,\varphi)+\Delta\xi_{local}(\tau,\varphi) \qquad \text{Equation 2-2}$$

In the above expression the left-hand side refers to changes in relative sea level at time τ and location φ. The first term on the right-hand side is the time-dependent eustatic signal, the second term varies in space and time, and relates to the isostatic effects of glacial rebound, including both ice and

water load contributions, and the third term refers to local factors, as described above. To solve Equation 2-2 in a gravitationally self-consistent manner, a pseudospectral algorithm (Mitrovica and Peltier 1991, Milne and Mitrovica 1998) is employed. Green's functions are constructed to determine the GIA-induced perturbations to the geopotential and solid surfaces due to loading. The resulting temporal convolutions are evaluated by describing the GIA loading history as a series of discrete Heaviside increments. The spatial convolutions are performed by transforming the problem to the spectral domain and employing the pseudospectral algorithm (Mitrovica and Peltier 1991, Milne and Mitrovica 1998).

The method by which relative sea level is calculated at a certain position, at a certain time, is displayed in Figure 2-17. At the start of the model run, loading is applied to an Earth model that is assumed to be in isostatic equilibrium. Once an ice load is applied at each time step the resulting deformation of the solid Earth and the perturbation to the geoid are calculated. The new shape of the geoid determines the redistribution of water in the oceans and the new extent of the oceans. However, this redistribution of water in turn affects the shape of the geoid and the deformation of the solid Earth in oceanic regions, therefore an iterative procedure is used to ensure the correct treatment of perturbations to the solid and geoid surfaces; recalculations of the perturbation to the geoid and the redistribution of water are carried out until there are no further changes, at which point loading for the next time step is applied. Loading is applied via forward time stepping.

The final output of the GIA model consists of a series of global relative sea-level predictions for all time steps used in the model. In the method used here, relative sea level is defined to be zero at the present day, and heights are given relative to this 'zero level' for all times in the past and future. Corrections are applied using present-day topography to determine the height of any point above or below sea level at any given time. Assuming that the underlying topography is unaltered by erosion and sedimentation the evolution of paleotopography is calculated via the following equation:

$$T(\varphi,\tau_p) = T(\varphi,\tau_0) - \xi_{rsl}(\varphi,\tau_p) \qquad \text{Equation 2-3}$$

where T is topography, defined to be the height of the solid surface above sea level at time τ, and ξ_{rsl} is relative sea level at time τ. τ_p refers to a time in the past, τ_0 refers to the present day, and φ is the location on the surface of the Earth. Shoreline positions at time τ_p are determined by the zero paleotopography contour at that time.

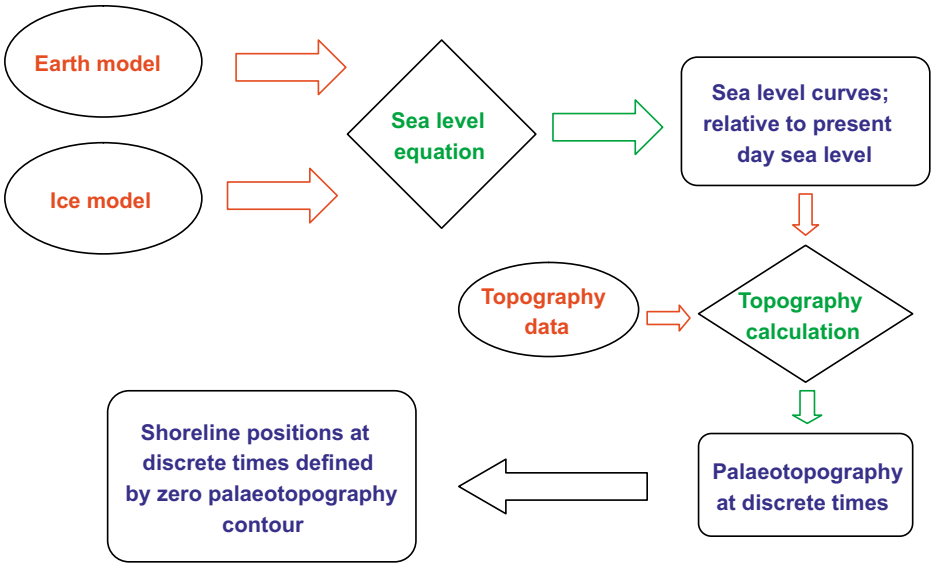

Figure 2-17. *Flow chart outlining the inputs (in red), calculations (in green) and outputs (in blue) required to calculate paleoshoreline positions due to GIA processes.*

Ice loading

The global ice loading model used in this study is modified from the ICE3G deglaciation history (Tushingham and Peltier 1991) and has been calibrated using far-field relative sea-level data (Radtke et al. 1988, Fairbanks 1989, Bard et al. 1990, 1996, Chappell and Polach 1991, Chappell et al. 1996, Hanebuth et al. 2000, Yokoyama et al. 2000). A eustatic curve has been used to tune the mass of ice contained within far-field ice sheets. The ice loading for Fennoscandia is described in Section 2.3.4 and has been derived using a thermodynamic ice-sheet model employing a proxy data palaeotemperatures curve. From this model, the extent and thickness of the Fennoscandian ice sheet at a series of discrete times from 116 ka BP to the present day has been derived and used.

Main results

In this section, only the experiments with different ice loading histories in Fennoscandia are presented, as the results from those experiments are ultimately used to construct the Forsmark relative sea-level curves used in the safety assessment (see Sections 2.2.6, 3.5.3 and 3.5.4). All other conducted GIA modelling experiments, e.g. sensitivity experiments with respect to Earth's rheology, isostatic memory and far-field ice sheets, are described in detail in SKB (TR-10-49, Section 3.3.4).

Ice-loading history within Fennoscandia is the principal factor governing relative sea-level change in Fennoscandia. The loading history presented in Section 2.3.4 was perturbed to investigate the sensitivity of sea-level change to differences in ice thickness, the timing of deglaciation, the pattern of ice build-up, and the timescale over which loading is considered (Table 2-4). The extent of ice at each time step since the LGM was not perturbed because the geometry of the ice sheets during this period is relatively well constrained by geological data. Details of the ice build-up prior to the LGM are less well constrained because geological evidence subsequently has been destroyed. However, for consistency, the ice extents for this period were also not altered. An Earth model consisting of a 96 km-thick elastic lithosphere, an upper mantle of viscosity 0.5×10^{21} Pa s, and a lower mantle of viscosity 1×10^{22} Pa s was used to investigate the response to the different loading models.

Table 2-4. Summary of ice-loading models used in this study. In all cases the ICE3G global ice model was used to constrain the distribution and thickness of ice outside Fennoscandia.

Model	Description of loading model	Model run time
1	Weichselian glacial cycle as described in Section 2.3.4	116 ka
2	Two Weichselian glacial cycles run after each other to give a double glacial cycle	232 ka
3	Weichselian glacial cycle, loading only applied from 40 ka BP	40 ka
4	Weichselian glacial cycle with 90 % ice thickness in Fennoscandia	116 ka
5	Weichselian glacial cycle with 80 % ice thickness in Fennoscandia	116 ka
6	Weichselian glacial cycle with the timing of deglaciation advanced by 500 years	116 ka
7	Weichselian glacial cycle modified with ice thickness allowed to increase linearly between 60 ka BP and 20 ka BP	116 ka

In Figure 2-18a, results using the same Fennoscandian surface loading are shown, but the model run was initiated at different times. Due to the assumption that the Earth is initially in isostatic equilibrium there will be some discrepancy between relative sea-level predictions at early times in a model started at 116 ka BP and one that has already been running for 100 ka, because the Earth's response is dependent upon loading history as well as the instantaneous load. Because the Earth has undergone a series of glacial cycles, a loading model that accounts for loading and unloading of the Earth during the previous cycle will give more realistic predictions for relative sea level during the cycle of interest. However, the negligible difference between relative sea-level predictions from the single cycle, double cycle and 40 ka models (models 1, 2, and 3 in Table 2-4), for times between 25 ka BP and the present day, imply that no long-term error is introduced when a model with a later start time is used. It is important that the shortest possible time steps are used to ensure that the full loading history is captured; failure to do so will miss short timescale fluctuations in ice distribution, leading to a decrease in the accuracy of the relative sea-level predictions.

The effect of altering the thickness of ice in the loading model is illustrated in Figure 2-18b. There is little difference in the shape and magnitude of predicted relative sea-level curves for the 80 %, 90 % and 100 % loading models during the minor glaciation between ~ 65 ka BP and ~ 50 ka BP (models 5, 4 and 1 in Table 2-4), but comparing results from the 80 % and 100 % models at the LGM yields differences of ~ 100 m at Forsmark. The larger the range of ice thicknesses used, the greater the range of relative sea-level predictions, as illustrated by the range of curves for Forsmark.

The timing of maximum relative sea level is the same for all loading models except where the timing of deglaciation is brought forwards by 500 years (model 6 in Table 2-4). In this case, maximum relative sea level also occurs 500 years earlier. Apart from this time shift, which decays to zero by the present day, there is otherwise no difference between predictions for this model, and the Weichselian glacial cycle. The magnitude of the maximum relative sea level is identical to that predicted by the single cycle, double cycle and 40 ka loading models (models 1, 2 and 3 in Table 2-4).

In model 7 (Table 2-4), ice thickness is allowed to increase linearly between 60 ka BP and 20 ka BP. This model has been developed to test the postulate that there was a continuous ice-sheet presence in Fennoscandia during this period (Lundqvist 1992), see also Section 3.2. The pattern of continuous, linear ice-sheet growth is purely an assumption of this model sensitivity test; the maximum ice thickness of the Weichselian glacial cycle is never exceeded, but the cumulative effect of loading the Earth for a longer period results in a greater amount of isostatic depression throughout Fennoscandia, and a greater relative sea-level maximum (Figure 2-18c). Therefore, the GIA signal is not only a function of the thickness and timing of ice loading at a given time, but also the evolution of the loading.

The rate of change of relative sea level throughout the glacial cycle is similar for all the loading models except the model where the pattern of ice-sheet growth has been markedly altered prior to the LGM (model 7 in Table 2-4, Figure 2-18c). However, predictions of present-day uplift rates for the various models do highlight small differences between the models (see Figure 2-19). Uplift rates for the single cycle, double cycle, 40 ka loading model and the model where the timing of deglaciation is shifted by a small amount are virtually identical. The best fit between the predictions from the GIA model and the present-day uplift rates is obtained when reducing the Weichselian ice-sheet thickness to 80 % (cf. Figure 2-16 and Figure 2-19e).

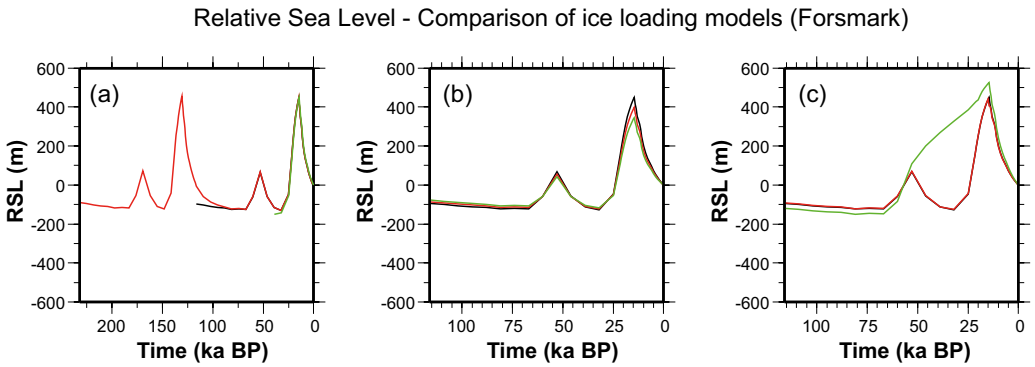

Figure 2-18. *Predicted relative sea-level curves for Forsmark. See Table 2-4 for details of the ice-loading models. An Earth model with a thin lithosphere and low upper mantle viscosity has been used in all cases. a) black: model 1, red: model 2, green: model 3. b) black: model 1, red: model 4, green: model 5. c) black: model 1, red: model 6, green: model 7.*

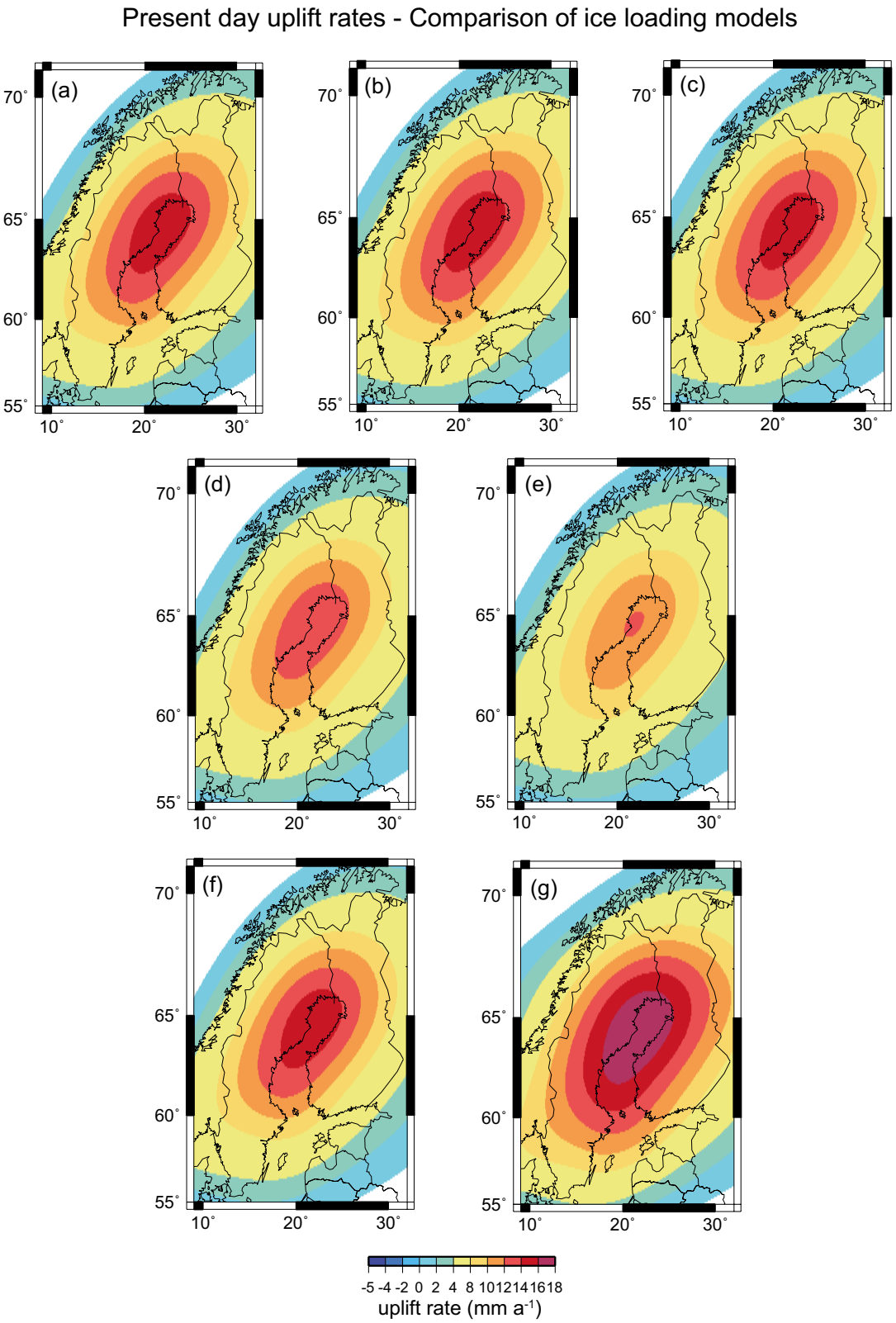

Figure 2-19. *Predicted present-day uplift rates throughout Fennoscandia for the various ice-loading models. See Table 2-4 for details of the loading models. An Earth model with a thin lithosphere and a low upper mantle viscosity has been used in all cases. a) Loading model 1. b) Loading model 2. c) Loading model 3. d) Loading model 4. e) Loading model 5. f) Loading model 6. g) Loading model 7.*

Comparisons between predictions from the GIA model, using the ice loading from the Weichselian glacial cycle as outlined in Section 2.3.4 (model 1 in Table 2-4), and observations of relative sea level and present-day uplift rates in Fennoscandia show that the modelling overpredicts the GIA response (see Figure 2-20 and Figure 2-21). There may be several reasons for this; either the ice load has been too large in the ice-load history, as tested above with load models 4 and 5 reducing the Weichselian glacial cycle ice-sheet thickness to 90 % and 80 % respectively, or the misfit could be a result of assuming a laterally homogeneous (1D) Earth structure, discussed in the section *A GIA case study with a Fennoscandian 3D Earth structure* below, or a combination of the two. Unlike the geological evidence relating to the spatial extent of the Weichselian ice-sheet, very few constraints upon the ice-sheet thickness exist, and one explanation for the misfit could be that ice thicknesses in the loading model are too large. As pointed out by Denton and Hughes (1981), early ice-sheet modelling studies of steady-state ice-sheets, including their own, produced ice thicknesses that were greater than one would expect from ice-sheets during a natural glacial cycle. This has since been confirmed by GIA modelling, showing that those thick ice-sheet profiles result in a poor fit to relative sea-level observations. Subsequent dynamical approaches to ice modelling outlined in Section 2.3, including the model used in the present study, produce considerably thinner ice-sheets, for example at the LGM. These models yield a closer fit to relative sea-level observations when used as an input to GIA models, but in the present study there is still a misfit to explain. Some of this difference may be explained by the fact that there are still gaps in our knowledge of basal processes related to, for example, sliding and sediment deformation under ice sheets. Another explanation could be that the assumption of a uniform Earth structure results in a too large GIA response, see below.

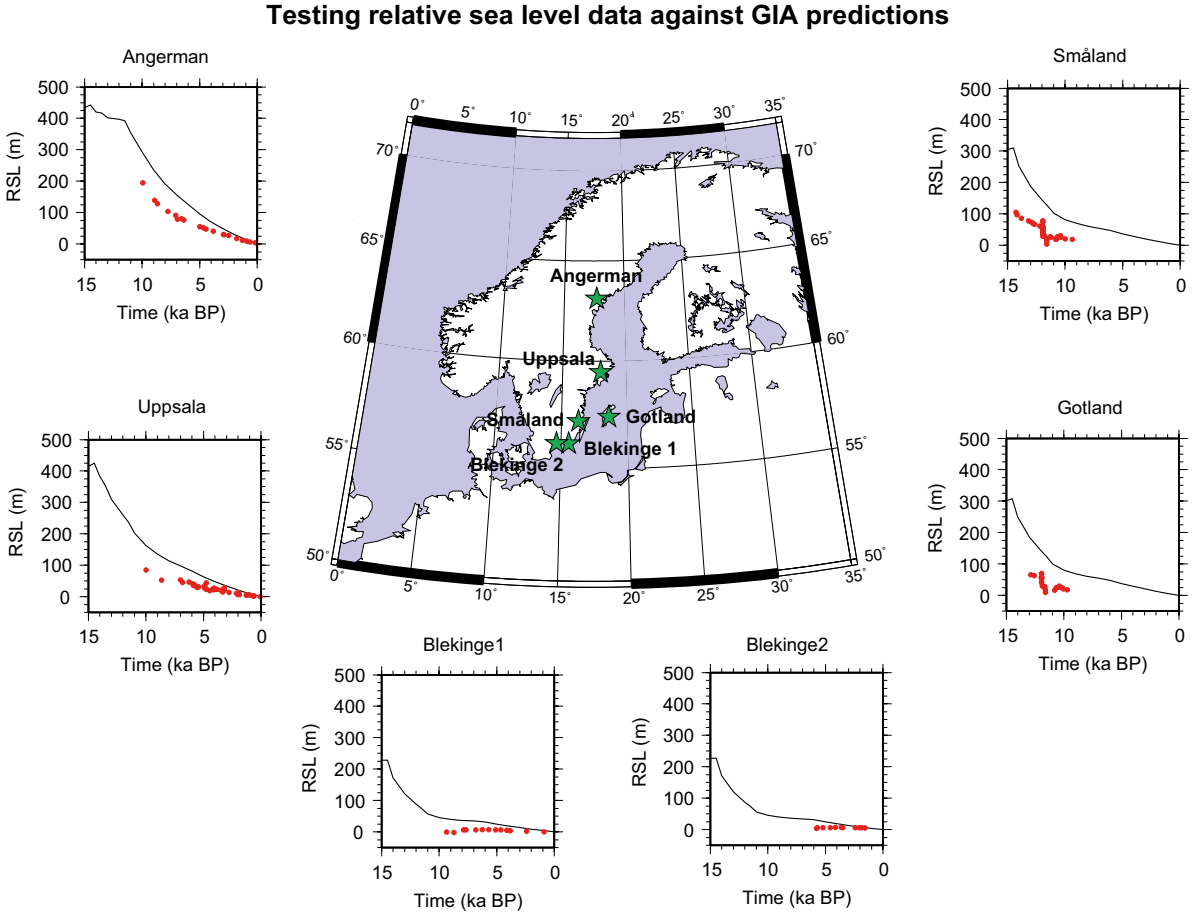

Figure 2-20. *Comparison between predicted relative sea level (black line) and observations from relative sea-level markers (red points) at six sites in Fennoscandia (green stars) for the last 15 ka. Data compiled from Lambeck et al. (1998).*

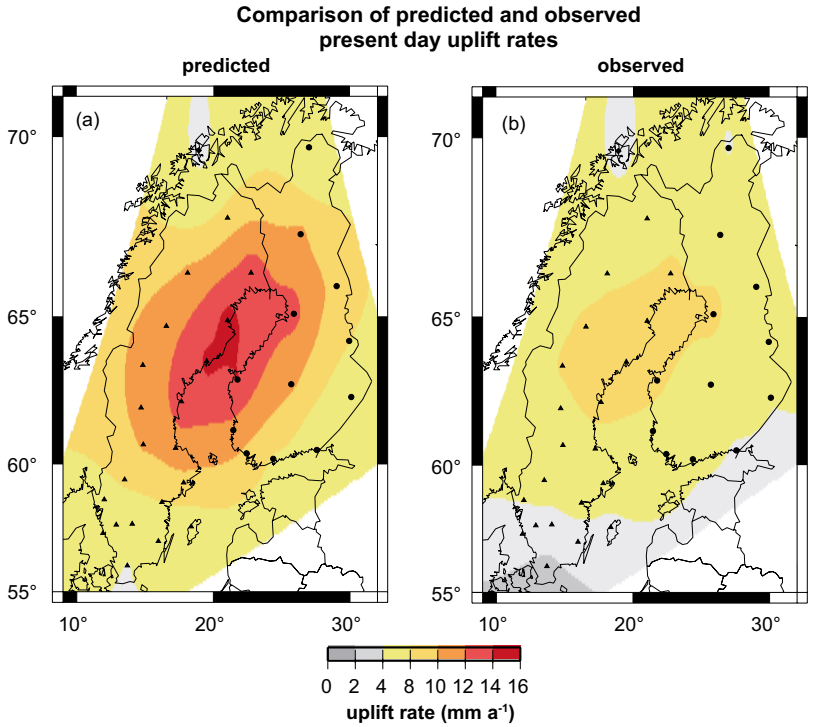

Figure 2-21. *Comparison of predicted and observed present-day uplift rates. a) Predicted present-day uplift rates interpolated at GPS sites (black dots and triangles). Data generated using the Weichselian glacial cycle loading model (model 1 in Table 2-4) and an Earth model consisting of a 96 km-thick elastic lithosphere, an upper mantle of viscosity 0.5 × 1021 Pa s, and a lower mantle of viscosity 1 × 1 022 Pa s. b) Observed present-day uplift rates interpolated at GPS sites. Data from the BIFROST project (Johansson et al. 2002).*

A GIA case study with a Fennoscandian 3D Earth structure

In this 3D Earth structure case study, adapted from Whitehouse (2009), the overall aim was to investigate the sensitivity of GIA predictions to lateral Earth structure. To this end, a comparison was made between dedicated 1D and 3D GIA simulations where the Earth structure has been specifically adjusted to give a relevant comparison between the two models. In turn, this means that the Earth structures have not been selected to give a best fit of e.g. uplift rates and relative sea-level changes against observed data. Also note that the 1D-3D comparison study described here uses a different ice-sheet load history from the Weichselian glacial cycle used in the 1D simulations described in previous parts of Section 2.2.4. The 3D model was adapted from Latychev et al. (2005). In the following, a brief overview of the most important results from this case study is provided. The study is adapted from Whitehouse (2009), but is also fully described in SKB (TR-10-49, Section 3.3.4).

The main result from Whitehouse (2009) is that the 3D Earth structure likely helps to improve the estimation of present-day uplift rates in the model. This is evident when comparing the predictability between the 1D and 3D models of the relative sea-level history for most of the Holocene (the last 10 ka) (Figure 2-22). Whereas the introduction of a 3D Earth structure appears to only have a limited influence on the Holocene sea level along the Norwegian west coast (upper left panel of Figure 2-22), it significantly helps to improve the simulation of relative sea level along the Swedish east coast (represented by Ångermanälven) with respect to observations (upper right panel of Figure 2-22). The improvement obtained with the 3D model is explained by a reduction of the predicted uplift rates in most areas covered by the Fennoscandian ice-sheet (bottom panel of Figure 2-22).

The difference in relative sea-level predictions for the 1D and 3D models is also plotted for Oskarshamn and Forsmark in Figure 2-23. To exemplify the magnitude of the error introduced by using a 1D Earth model instead of a 3D Earth model to predict relative sea level, as was done in the GIA studies, the difference at 10 ka BP is ~ 60 m at Forsmark (Figure 2-23).The difference between 1D and 3D GIA simulations presented in this case study means that ignoring lateral Earth structure and using a 1D Earth model in Fennoscandia leads to an overestimation of present-day uplift rates during deglaciation. This, in turn, conclusively shows that a significant part of the misfit between the 1D GIA model results and GPS observations (Figure 2-21) arises from the 1D Earth structure adopted.

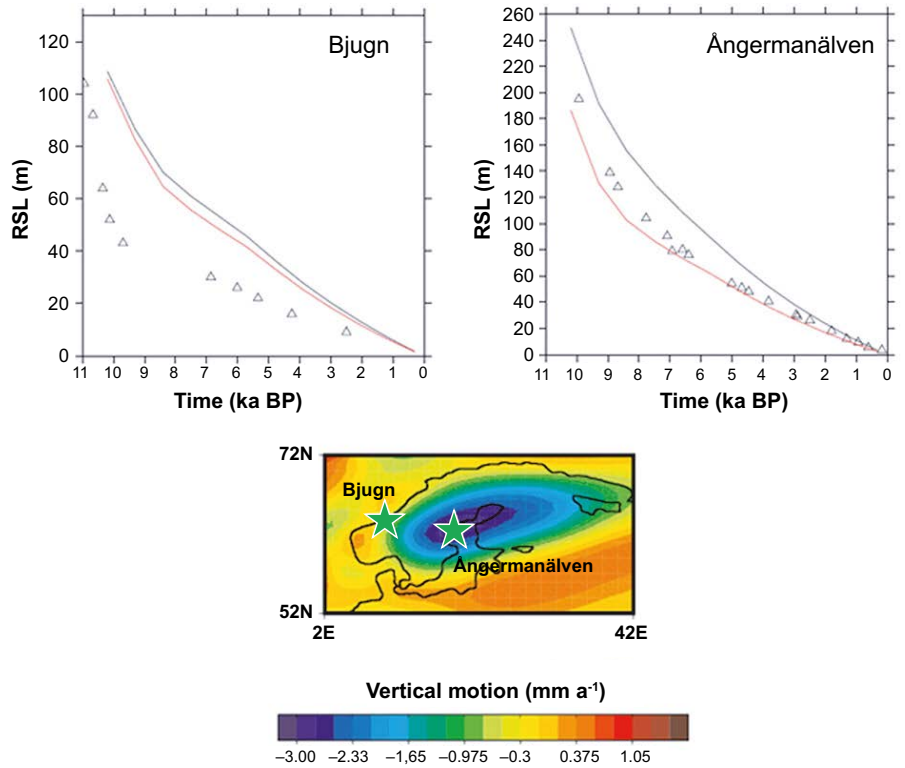

Figure 2-22. *Predicted relative sea-level history at Bjugn (top left) and Ångermanälven (top right) for the last 10 ka. Black line: 1D model. Red line: 3D model. Relative sea-level proxy data are shown as triangles; see Lambeck et al. (1998) for references. Bottom plot: Location map for Bjugn and Ångermanälven overlaid upon the difference in predicted present-day uplift rates between the 3D and 1D models.*

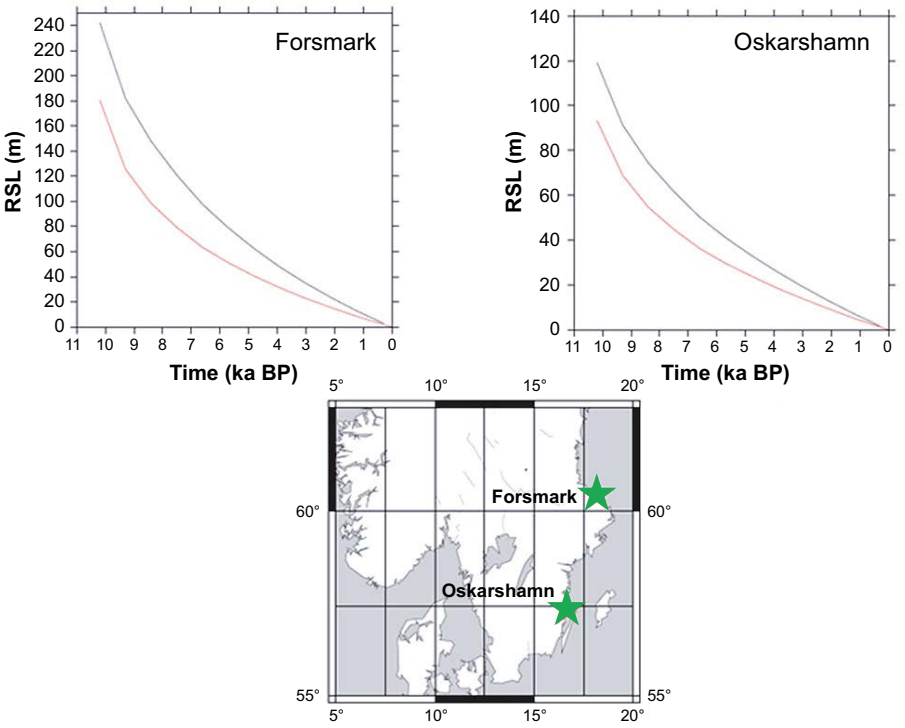

Figure 2-23. *Predicted relative sea-level curves for Forsmark and Oskarshamn calculated using 1D (black line) and 3D (red line) Earth models. Note that both the 1D and 3D GIA simulations used for this plot use a different ice-load history from that used in the 1D GIA simulations in the previous parts of Section 2.2.4. The results should only be used to exemplify the error introduced by using 1D instead of 3D GIA modelling. At Forsmark, the difference at 10 ka BP is ~ 60 m.*

GIA-modelling of future relative sea level

The isostatic development at Forsmark under a future warm climate has been analysed in dedicated GIA simulations. In that simulation, no ice loading was applied to the simulations for the first 50 ka, after which a full glacial cycle with 80 % ice thickness (loading model 5 in Table 2-4) was added. In addition, the GIA simulations also assumed that the Greenland ice sheet melts away at a linear rate within the first 1 ka. However, although the Greenland ice sheet contributes to the global sea-level rise by ~ 7 m, its effect on the Forsmark region is negligible (~ 0 mm a^{-1}) due to the counterbalancing gravitational effect associated with the removal of the mass of the Greenland ice sheet (Milne et al. 2009, Whitehouse 2009). Therefore, the future relative sea-level curve projected by the GIA modelling in the global warming case essentially only represents the isostatic signal at the Forsmark site until the first major ice-sheet advance near 100 ka AP.

Using 80 % ice thickness in the global warming simulation is motivated by the fact that this ice-loading experiment resulted in the best prediction of the present-day uplift rates in the Forsmark area (cf. Figure 2-16 and Figure 2-19). However, it is important to note that this choice only has a minor influence on the resulting isostatic change. Because of the assumption that the next glaciation in the global warming scenario is shifted 50 ka further into the future compared with the Weichselian glacial cycle, only the first, relatively modest, peak of the GIA-induced relative sea level (Figure 2-18) has an impact on the Forsmark area within the coming 100 ka. For this peak, however, the difference in the predicted isostatic change between the 100 %, 90 % and 80 % ice-loading experiments is very small (Figure 2-18b).

The simulated relative sea-level development at Forsmark under the global warming scenario is shown in Figure 2-24. For comparison, the relative sea-level evolution of the reconstructed last glacial cycle, projected into the future, is also shown in Figure 2-24. The figure demonstrates that isostasy continues to be a contributing factor in the Forsmark region for another ~ 30 ka, contributing to a lowering of the local relative sea level. Thereafter, the relative sea level remains virtually constant (i.e. isostasy is ~ 0 mm a^{-1}) until the next glaciation in the Forsmark region which is projected to occur by ~ 110 ka AP in the global warming scenario and by ~ 60 ka AP for the repetition of the last glacial cycle.

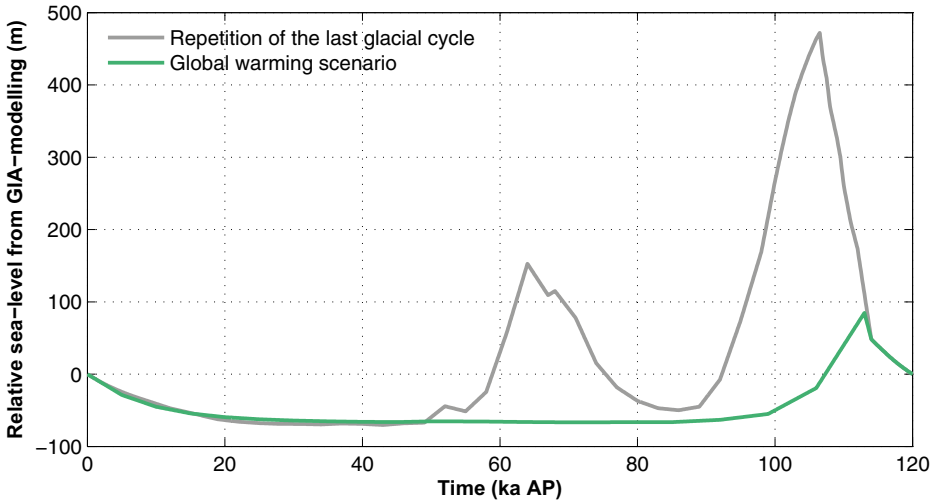

Figure 2-24. *Relative sea-level evolution at Forsmark as projected by GIA modelling for a future warm climate. For comparison, the relative sea-level evolution for the reconstructed last glacial cycle, projected into the future, is also shown. Negative numbers indicate that the area is situated above the contemporary sea level. The curves were constructed by GIA modelling combined with results from observations of historical uplift rates of the Holocene (Appendix G). Note that the relative sea-level curve projected by the GIA modelling in the global warming scenario essentially only represents the isostatic signal at the Forsmark site until the first ice-sheet advance at the end of the 120-ka period, see the text. Therefore, this curve is used together with long-term projections of the global mean sea-level change from contemporary studies to analyse the range of relative sea level change at Forsmark until 12 000 AD (Section 3.5.3) and until 100 ka AP (Section 3.5.4).*

2.2.5 Time perspective

Shoreline displacement is an ongoing process. It is strongly coupled to the global distribution of water between the oceans and land-based ice sheets, and the isostatic response of the Earth to loading during a glacial cycle. This isostatic deformation is a slow process in relation to the rate at which ice sheets grow and decay during such a cycle.

As ice sheets grow, water is removed from the oceans and global eustatic sea level falls. During the build-up to the last glaciation, eustatic sea level fell at a mean rate of ~ 1.3 mm a^{-1} between 120 ka BP and 20 ka BP (Fleming et al. 1998, Yokoyama et al. 2000, Clark and Mix 2002, Milne et al. 2002, Peltier 2002, Mitrovica 2003), although there were many departures from this rate during the build-up period, due to higher frequency climatic oscillations (Imbrie et al. 1984, Lambeck et al. 2002, Waelbroeck et al. 2002, Siddall et al. 2003). During deglaciation, the initial rate of eustatic sea-level rise between ~ 21 ka BP and 17 ka BP was only ~ 6 mm a^{-1}, followed by an average rate of ~ 10 mm a^{-1} for the next 10 ka (Fleming et al. 1998). Perturbations from this rate occurred during meltwater pulses at ~ 14.5 ka BP and ~ 11 ka BP. These are attributed to rapid melting events, during which rates of eustatic sea-level rise reached ~ 15 mm a^{-1} (Fairbanks 1989, Bard et al. 1990, 1996, Clark et al. 1996, Fleming et al. 1998, Lambeck and Chappell 2001, Lambeck et al. 2002, Peltier 2005, Bassett et al. 2005). Rates of eustatic sea-level change fell to negligible values following the end of deglaciation around 5 ka BP. However, meltwater is not distributed uniformly throughout the oceans due to the alteration to the shape of the geoid following the redistribution of surface masses. Sea level can actually fall at sites within ~ 20° of a melting ice sheet (Farrell and Clark 1976), therefore the rate of eustatic sea-level change is a poor indicator of local rates of sea-level change, especially for a local melt source.

The local rate of relative sea-level change incorporates both local changes in sea level and the isostatic deformation of the solid Earth. The balance between rates of isostatic deformation and local sea-level change determine whether a site has advancing or retreating shorelines.

During the final build-up of the Fennoscandian ice sheet from ~ 32 ka BP, isostatic rates of solid Earth subsidence due to surface loading by ice are estimated to have reached values of 40 mm a^{-1} (see Section 2.2.4). During future glacial cycles, modelling predictions imply that maximum rates will be attained immediately prior to the time of greatest ice thickness. In general, the time of maximum ice thickness is predicted to precede the time of maximum solid Earth deformation, with the latter being delayed by up to ~ 3 ka. During the period between maximum ice thickness and maximum deformation, the rate of solid Earth subsidence will decrease to zero.

There is usually a delay between the time of maximum deformation and the time at which a location becomes ice-free. Again, modelling predictions imply that as an ice sheet thins, rates of isostatic rebound will be low; < 20 mm a^{-1} for this reconstruction of the Weichselian. Maximum rebound rates occur immediately following the final removal of an ice sheet, with uplift rates reaching ~ 75 mm a^{-1} in this model at sites which had the greatest ice cover. The rate of rebound then decays exponentially with time; maximum rates at the centre of present-day uplift in Fennoscandia are ~ 10 mm a^{-1}, and these are expected to decay to negligible values within the next 30 ka (see Section 2.2.4).

During a glacial cycle, immediately following the removal of ice, local uplift rates are far greater than the rate of local sea-level changes, consequently a situation of regression dominates, and shorelines migrate oceanward. The rate of shoreline displacement depends upon the local gradient of topography. A typical Swedish Baltic Sea shoreline with a gradient of 2 m of elevation per 1 km would experience 35 m a^{-1} of oceanward shoreline displacement for an uplift rate of 70 mm a^{-1}, or 5 m a^{-1} of oceanward shoreline displacement for an uplift rate of 10 mm a^{-1} (the present maximum in the Baltic region), assuming negligible changes in local sea level.

A combination of decreasing rates of isostatic rebound and sea-level rise due to far-field melting slows the rate of regression with time, with a switch to transgression taking place if rates of local sea-level rise exceed the rate of local isostatic rebound. This situation is likely to arise during a global meltwater pulse at sites with low rebound rates but will not be maintained because melting takes place on a shorter timescale than isostatic rebound. Rebound will once again become the dominant factor governing shoreline displacement as sea level changes become negligible. During the current interglacial period decaying uplift rates persist. These, along with processes related to ocean syphoning (see Section 2.2.1), act to maintain a situation of gradual oceanward shoreline

displacement throughout the majority of the Baltic region for the first few 10 ka of an interglacial so long as the higher interglacial temperatures do not give rise to a longer-term melting event, such as the destabilisation, and subsequent melting, of the Greenland ice sheet.

2.2.6 Handling in the safety assessment

The relative sea-level change at Forsmark has been investigated by means of GIA modelling. In this context, the main question for the safety assessment is whether the Forsmark site is submerged or not. The salinity in the lake/sea covering the site is however also of interest.

As discussed in Section 2.2.4, the future relative sea-level development projected by GIA modelling of the global warming scenario (Figure 2-24) essentially only represents the isostatic change for the coming 100 ka. This development is therefore used together with projections of the global mean sea-level change from recent studies to analyse the range of relative sea-level change at Forsmark under different warming scenarios until 12 000 AD (Section 3.5.3) and until 100 ka AP (Section 3.5.4). The resulting relative sea-level changes are subsequently used to estimate periods of submerged conditions at the Forsmark site for the *warm climate case* (Section 5.2.2), which is evaluated in the main scenario in the safety assessment (**Post-closure safety report**, Chapter 7). For all other climate cases (Chapter 5), it is assumed that the effect of global warming on the relative sea level is negligible, thus resulting in a shorter period of submerged conditions at Forsmark than in the *warm climate case*.

As further described in Section 3.5.3, the uncertainty in future global sea-level rise on multi-millennial timescales is very large, ranging from only a couple of metres to more than 50 m depending on the amount of global warming and the sensitivity of ice-sheet melting to a certain amount of warming. This translates into a large uncertainty in the duration of the current period of submerged conditions above the repository, ranging from approximately 1 ka to almost 20 ka. To account for this uncertainty, the safety assessment also includes a supporting calculation for the main scenario where different durations of initial submerged conditions are analysed (**Post-closure safety report**, Section 7.7).

2.2.7 Handling of uncertainties

Uncertainties in mechanistic understanding

The processes involved in GIA, and their effect upon shoreline displacement, are well understood. There are no major uncertainties in our understanding of the mechanistic processes that cause shoreline displacement.

Model simplification uncertainty

Discussions of the uncertainty in the calculated shoreline are based on the sensitivity analysis and case study presented above. The assumption of a 1D Earth model is a simplification of the situation in Fennoscandia. A comparison between 1D and 3D GIA simulations (Whitehouse 2009) shows that the assumption of a laterally homogeneous (1D) Earth structure over Fennoscandia probably results in an over-prediction of the isostatic response to ice-sheet load and present-day uplift rates. As an example, the 1D–3D GIA model comparison shows that the 1D simulation potentially overestimates the relative sea-level change over the last 10 ka by up to 60 m at Forsmark.

The time discretisation of the basic loading model is fairly coarse (every 7 ka) between 116 ka BP and 21 ka BP, reflecting the lack of constraints upon ice history and sea level prior to the LGM. If long time steps are used, the loading function may be under- or over-estimated, leading to inaccuracies in relative sea level, and hence shoreline displacement, predictions for this period. A higher time resolution has been investigated, and discrepancies in relative sea-level predictions may be up to 50 m between a model that uses a time step of 7 ka and one that uses a time step of 1 ka, during periods of rapid change in ice-sheet geometry. However, using a coarse timescale during the early stages of a model run has a negligible effect upon predictions of relative sea-level change during the latter stages of a model run. A high-resolution timescale has been used for ice loading since the LGM, i.e. for the period when the ice history is known reasonably accurately.

At the beginning of a model run, the Earth is assumed to be in a state of isostatic equilibrium, with no deformation remaining from a previous glacial cycle or any other process that upsets the isostatic balance of the system. In reality, as the Earth enters each glacial cycle it will be pre-stressed, with deformation ongoing as a result of the previous loading event. GIA-induced deformation decays over a few tens of thousands of years, and after this period there will be a negligible difference between predictions from a model that started from equilibrium and one that was pre-stressed. However, in order to reproduce the relative sea-level evolution for the Weichselian as closely as possible the model was run twice in succession, with the second run taken to represent the Weichselian development. Nevertheless, a degree of inaccuracy remains at early times in the model since deformation will depend upon the details of the Saalian deglaciation, about which information is scarce.

Input data and data uncertainty

Uncertainties in the lithospheric thickness and mantle viscosity parameters are currently significant. However, in SR-Site (SKB TR-10-49), a great similarity of the shoreline prediction for a range of rheological parameters was demonstrated. The values of such parameters will be more tightly constrained following detailed analysis of the results of the GIA modelling in comparison with relative sea level and GPS data.

Another source of uncertainty is associated with the ice load. Sensitivity tests using the 1D GIA model revealed that a reduction in ice thickness to 80 % of the value in the *reference glacial cycle* yielded GIA results on present uplift rates that were in accordance with the observed present-day uplift. It is important to note, as discussed above, that this result is only valid for the 1D GIA model as the 3D model results in a better agreement with present-day uplift rates using the full (100 %) ice thickness (Figure 2-22 and Figure 2-23).

2.2.8 Adequacy of references

The SR-Site (SKB TR-10-49) and SR-Can (SKB TR-06-23) Climate reports, from which the studies are taken, have undergone QA system handling including a factual review process. Also, the SKB report produced for the handling of isostatic adjustment and relative sea-level changes (Whitehouse 2009) has undergone the SR-Site QA system handling, including a documented factual review procedure. Other references used for the handling of ice-sheet dynamical processes are peer-reviewed papers from the scientific literature.

2.3 Ice-sheet dynamics

2.3.1 Overview/general description

Glaciers and ice sheets may form in climate regions where, in places, the winter snow precipitation is not completely melted away during summer. A glacier is an ice mass that has been formed by successive local accumulation of snow, with ice movement due to ice deforming under its own weight. An *ice sheet* is defined as a glacier that spreads out in all directions from a central dome, i.e. a large glacier ($> 50\,000$ km^2 in area) that is not confined by the underlying topography. In reality, the flow pattern of ice sheets is not radial from a single dome. Instead, ice often flows out from a few elongated *ice divides*, with the ice divides constituting the highest parts of the ice sheet.

Generally, ice-flow velocities are moderate to slow within an ice sheet, with ice moving a few tens of metres per year. However, certain well-defined parts of ice sheets, so called *ice streams*, exhibit significantly faster ice flow. Ice streams are typically some tens of kilometres wide and several hundreds of kilometres long. Ice velocities within present-day ice streams are several hundred metres per year, in some cases exceeding 1 000 m a^{-1} (cf. Joughin et al. 2004). Since surrounding ice typically moves considerably slower, high velocity gradients across the ice stream margins produce distinct *shear zones* with heavy crevassing. Because of the high ice flux in ice streams, these features may drain large portions of ice sheets. Ice streams are often characterised by specific basal thermal and hydrological conditions, differing from those of the surrounding ice sheet.

The margin of an ice sheet may be either on land or in water. If the ice margin is positioned in the sea or in a lake, it is common that the outer part of the ice sheet is floating on the water, constituting an *ice shelf*. The boundary between the floating and grounded ice is the ice sheet *grounding-line*.

If the basal thermal and topographical conditions are favourable, sub-glacial melt water may accumulate in topographic lows beneath the ice, forming *sub-glacial lakes*. These are common features under the present Antarctic ice sheet, whereas none have so far been found beneath the Greenland ice sheet.

Mass balance

The growth and decay of ice sheets are determined by the *mass balance* of the ice mass. The mass balance constitutes the result of the mass gain, or *accumulation*, and the mass loss, or *ablation*, typically averaged over one year. The mass gain of an ice sheet is completely dominated by the process of snow accumulation. Most of the snow falls and accumulates during winter seasons, but snow may also accumulate during summer. For ice-sheet ablation on the other hand, several processes may be involved, the two most significant being surface melting of snow and ice (if the summer climate is warm enough) and calving of ice bergs from ice shelves (when the margin is at the sea). In addition, mass may also be lost from the ice sheet by melting of basal ice, and locally on the surface by sublimation of ice and snow. When a certain part of an ice sheet exhibits more accumulation than ablation over one year, that part is said to belong to the *accumulation area* of the ice sheet. This is in contrast to the *ablation area*, where there is a net loss of mass over one year. Central parts of ice sheets typically constitute accumulation areas, whereas the in case of surface melting, lower parts of ice sheets constitute ablation areas (Figure 2-25). The line between the accumulation and ablation areas is called the *equilibrium line*.

If the total ice-sheet accumulation is greater than the total ablation over one year, the mass balance is said to be positive, whereas the opposite case produces a negative mass balance. If accumulation and ablation are equal, the mass balance is zero.

A positive mass balance over several years makes an ice sheet grow, whereas a negative mass balance reduces its size. However, changes in the size of ice sheets are very slow occurring over hundreds and thousands of years. The *response time* of an ice sheet is the time it takes for a steady-state ice sheet to come to a new steady-state condition after a climate change. It is often defined to represent the time to reach a near-steady state representing e.g. 90 % of the change to equilibrium. Since climate is constantly changing, ice sheets are never in true steady state, but are constantly adjusting their size and shape to the prevailing climate.

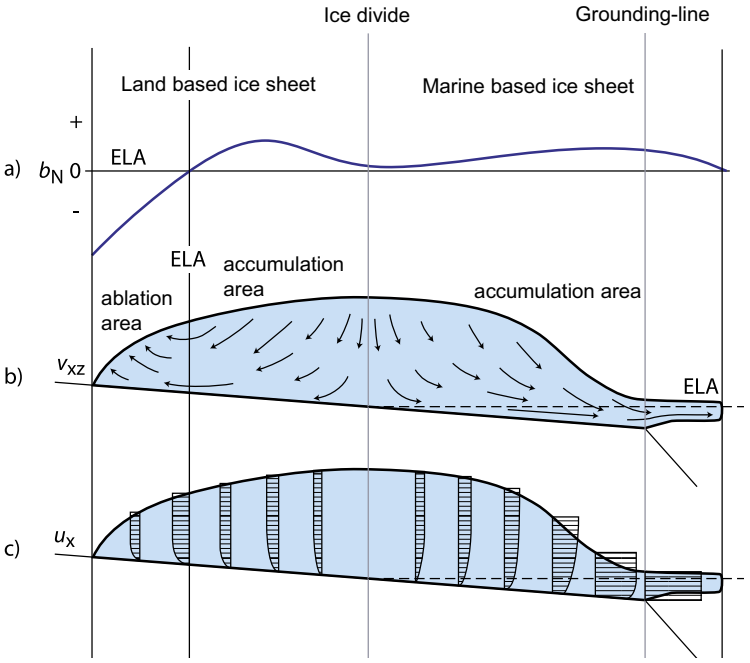

Figure 2-25. *Schematic ice sheet cross section. Panel a) shows the surface net balance distribution (bN), panel b) shows ice velocity trajectories (vxz) as well as distribution of accumulation- and ablation areas, and panel c) shows the horizontal velocity component (ux). ELA denotes equilibrium line altitude. Modified from Holmlund and Jansson (2003), after Denton and Hughes (1981).*

Ice temperature. The temperature of the ice is of fundamental importance for the behaviour and characteristics of glaciers and ice sheets. Among other things, it has a strong effect on the movement, dynamics and hydrology of the ice. Two types of glacier ice can be defined based on temperature; 1) *Temperate ice* (or *warm ice*) with the ice temperature at the pressure melting point, and 2) *Polar ice* (or *cold ice*) with the ice temperature below the pressure melting point. Cold ice is harder than temperate ice and impermeable to water unless crevasses are present.

Glaciers and ice sheets are often classified according to their thermal characteristics. A glacier where all ice has a temperature at the pressure melting point throughout the year is called a *temperate glacier* or *temperate ice sheet,* whereas a glacier in which all the ice is below the pressure melting point throughout the year is called a *polar glacier* or *polar ice sheet*. However, an ice sheet or glacier need not consist exclusively of temperate or polar ice. In many cases, it can contain both ice types, and in such a case it is called *polythermal*.

Of particular interest is the temperature of the ice at the ice-sheet bed, i.e. the basal thermal condition. An ice sheet can be *cold-based* or *warm-based*. A cold-based ice sheet has cold basal ice and it is frozen to its bed. There is no free water at the bed, and no sliding of basal ice over the substrate is taking place. A warm-based ice sheet is at the pressure melting point at the bed. Free water is, in this case, present at the ice-bed interface, and the ice may slide over the substrate. This has important consequences both for ice kinematics and landform development. A polar ice sheet may be either cold-based or warm-based. In the case of a warm-based polar ice sheet, it is typically only the lowermost part of the ice that is at the pressure melting point, whereas most of the ice sheet consists of polar ice. One part of a polar ice sheet may thus be cold-based at the same time as other parts are warm-based. This is the present case for the Greenland and Antarctic ice sheets. Warm-based and cold-based ice sheets are also called *wet-bed ice sheets* and *dry-bed ice sheets*.

Glaciers and ice sheets experience melting of basal ice where the basal ice temperature is at the pressure melting point. Heat for this melting can be added from geothermal heat flux and from frictional heating by internal deformation of basal ice. The thermodynamic situation at the base of an ice sheet is determined by the thermal properties of the ice. Energy can be transferred by diffusion along a temperature gradient in ice as in all materials. Also, the solidus of the ice-water vapour phase space has a negative slope, which means that the melting or freezing temperature is depressed with increasing pressure by 0.09 K Pa^{-1}. As a general statement, freezing of liquid water occurs when temperature and pressure satisfy the generalised Clapeyron equation (e.g. O'Neill and Miller 1985):

$$\frac{p_w}{\rho_w} - \frac{p_i}{\rho_i} = \frac{L}{273.15}T + \frac{P_0}{\rho_w} \qquad \text{Equation 2-4}$$

where p_w = water pressure, ρ_w = water density, p_i = ice pressure, ρ_i = ice density, L = ice density coefficient of the latent heat of fusion, T = temperature in degrees centigrade, and P_0 = osmotic pressure. Equation 2-4 couples the effect of temperature and pressure. It is a general thermodynamic relationship not specific for the case of ice sheets and glaciers. However, the phase change of the ice-water system is not only controlled by temperature and pressure. Two other factors may also be of importance; 1) the presence of solutes in water, and 2) surface tension arising from interface curvature. Just as in the case with an increasing pressure, an increase in solutes in liquid water also depresses the melting/freezing point. This effect is referred to as the osmotic pressure (e.g. Padilla and Villeneuve 1992), and it is included in Equation 2-5. If liquid water is present at the base of an ice sheet, and it contains solutes, this will, together with the pressure, modify the ice melting point. The second factor constitutes an ice/water interfacial effect. The finer the grains in a sediment, the higher the curvature of the ice-water interface becomes, which in turn lowers the melting point (Hohmann 1997). For example, in clays, liquid water has been observed at temperatures down to −10 °C (O'Neill and Miller 1985).

If the effect of phase curvature is taken into consideration the Clapeyron equation may be modified to (Raymond and Harrison 1975):

$$T = -\frac{273.15}{L}\left(\frac{1}{\rho_i} - \frac{1}{\rho_w}\right)p_w - \frac{273.15\sigma_{iw}}{L\rho_i r_p} - \frac{273.15}{\rho_w L}P_o \qquad \text{Equation 2-5}$$

where σ_{iw} = ice-water surface energy, and r_p = characteristic particle radius. Equation 2-5 is the fundamental equation for the ice-water phase transition given by Hooke (2004). In this equation, the first of the three terms describes the effect of pressure on the ice-water phase transition; the second term describes the effect of interfacial pressure; and the third term the effect of osmotic pressure. Equation 2-5 thus gives the complete treatment of the ice-water phase transition. Commonly only the first term is used for calculations of the pressure melting point beneath glaciers and ice sheets, often rewritten in glaciological literature to give a simplified expression for calculating the pressure melting point (cf. Remy and Minster 1993):

$$T = -\frac{h}{1503} \qquad \text{Equation 2-6}$$

where T = pressure melting point temperature (°C), and h = ice thickness (m). The effect of the lowering of the pressure melting point described above is, in the case of an ice sheet, that the melting point is lowered by c. 2 K beneath 3 km of ice. This is very important, since the basal conditions change drastically if the bed of an ice sheet becomes melted or frozen. This affects ice-sheet flow by turning on and off basal sliding; governs if glacial erosion can take place or not; and of course, has a profound impact on basal hydrology.

To demonstrate the effect of ice-sheet surface conditions on the temperature distribution within polar ice sheets, we start with a simplified case of a steady-state ice sheet with no ice flow, corresponding to an artificial situation at an ice divide (no horizontal flow) without any precipitation (no vertical flow). Figure 2-26a shows the vertical temperature profile through such an ice mass given a surface temperature of −20 °C and a specified geothermal heat flux at the base. The resulting temperature profile is a straight line from the surface temperature down towards the bed. In this case the vertical temperature profile reaches the pressure melting point temperature near the bed, resulting in a warm-based polar ice sheet.

Next, we consider the same case but with snow accumulation at the ice-sheet surface, which means we are introducing a vertically downward directed ice movement. Generally, this lowers the temperatures within the ice sheet as seen in Figure 2-26b. Due to the vertical velocity and cold surface climate, cold ice is advected downward, while the geothermal heat warms this descending ice. The upper part of the ice sheet develops an almost isothermal zone, whereas the ice warms quickly near the bed. In this example, the ice sheet below this accumulation area has become cold-based. Higher precipitation rates at the surface, i.e. higher vertical velocities, result in an increased thickness of the isothermal zone and decrease the basal temperature. Furthermore, lower air temperatures at the ice-sheet surface also decrease the ice-column temperatures, and vice versa.

If we instead consider an ablation area, with net mass loss at the surface, the vertical ice movement will be directed upwards. In this case, the upward vertical velocity produces a generally warmer ice column, in this example resulting in temperate conditions at the bed (Figure 2-26c).

The last case to consider is a more realistic situation when we also have horizontal ice movement. Figure 2-26d shows a typical situation within the accumulation area of an ice sheet, but not located directly on an ice divide. The horizontal velocity component is advecting cold ice into the site, ice that was formed in higher, colder parts of the ice sheet. Compared with the situation in Figure 2-26b, the minimum temperature is now found at some depth below the surface, since the ice at the surface, formed locally at the site, is warmer (Figure 2-26d). This positive temperature gradient near the surface has been observed in several deep drill holes, see for example the Mirny, Century 13, and Byrd 9 drill hole temperatures in Figure 2-27. Furthermore, due to the horizontal ice movement, ice in the lower part of the ice sheet is warmed by internal friction, as this is where most of the internal deformation of the ice is taking place. In this example, the ice sheet has again become warm-based.

Including these processes, the resulting englacial and subglacial temperatures along a flow line are as shown in Figure 2-28. Typical polar ice-sheet accumulation rates and air temperatures are assumed. The lowest englacial temperatures are found in the highest central parts of the ice sheet, and the highest ice temperatures are found near the margin. Basal melting may take place in the interior part of the ice sheet and close to the margin, with a zone of basal frozen conditions in between. A narrow zone of basal frozen conditions at the margin may also occur due to decreasing vertical velocity (not shown in Figure 2-28).

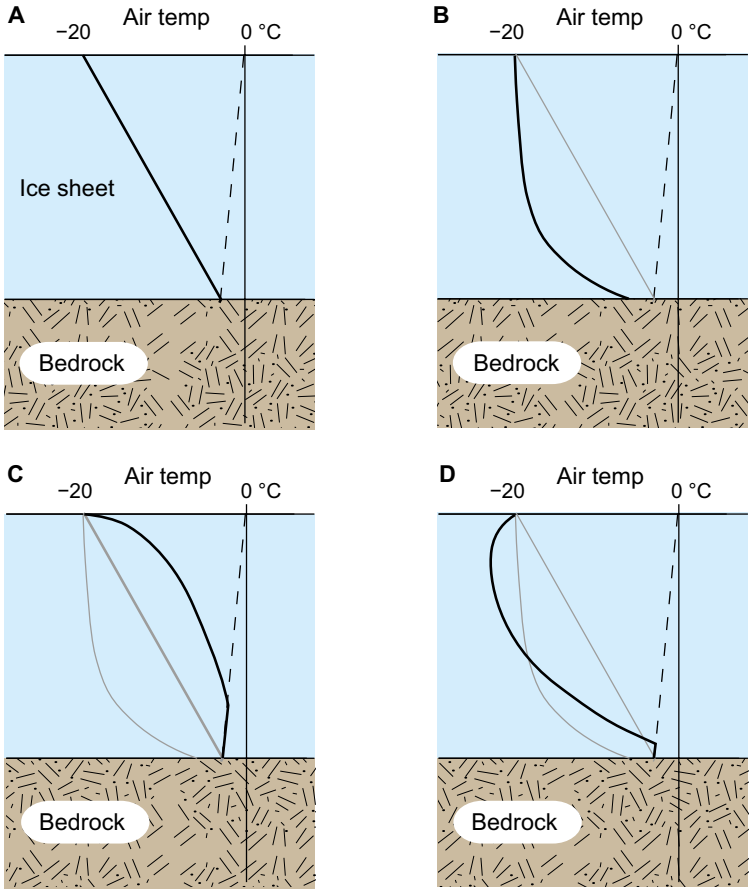

Figure 2-26. *Vertical temperature profiles through a 2 000 m thick theoretical polar ice sheet. The dashed line denotes the pressure melting point temperature. a) No ice flow (dead-ice body), b) Vertical ice flow only – accumulation area (reflecting only a surface accumulation rate), and c) Vertical ice flow only – ablation area, d) Horizontal and vertical ice flow – accumulation area. Grey lines show the cases from the previous plates. Modified from Holmlund and Jansson (2003), after Sharp (1960).*

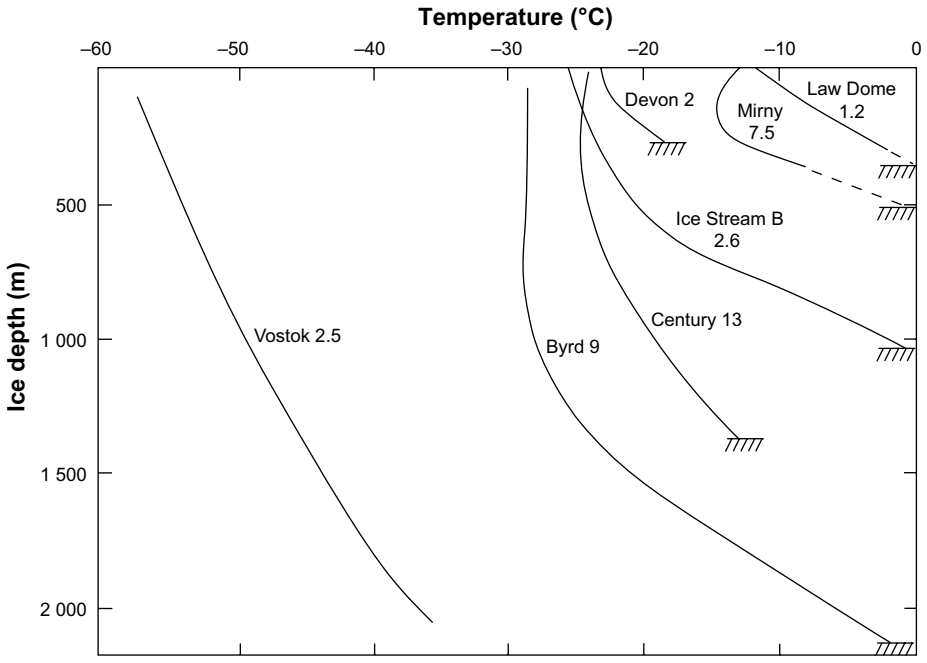

Figure 2-27. *Borehole temperature data from the Greenland and Antarctic ice sheets. Modified from Holmlund and Jansson (2003), after Paterson (1994).*

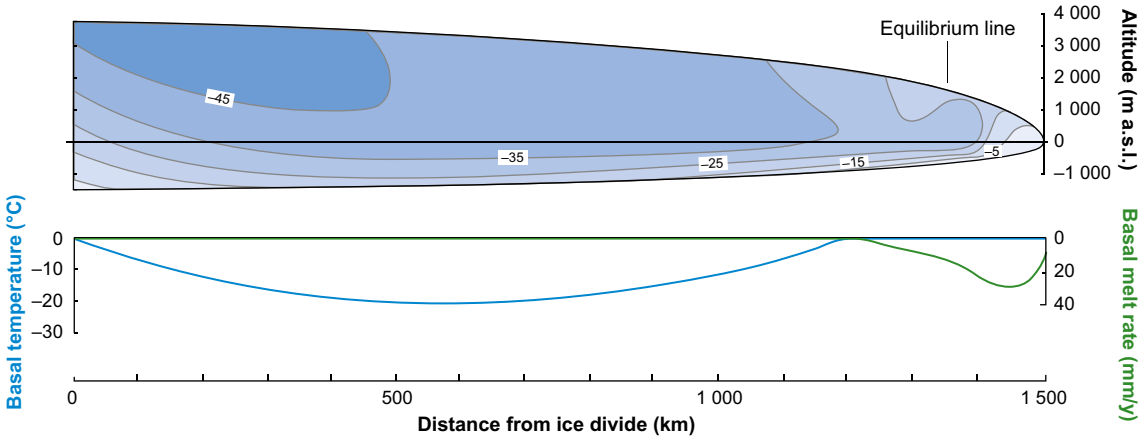

Figure 2-28. *Example of modelled ice-sheet temperature distribution along a flow line. Ice temperatures are in °C. Basal melt rates are high near the terminus because of the strain heating effect from rapid ice flow in the region around the equilibrium line. Modified from Hooke (1977).*

In nature, the topography of the landscape beneath the ice sheet is also of great importance for the basal temperature distribution. Topographic lows are more prone to experience basal melting conditions than topographic highs. This is both due to the pressure melting point being lowered more in depressions (due to the greater ice thickness and higher basal pressures) than over surrounding higher terrain, and due to the lower insulating capacity of thinner ice over topographic highs. The result is, for example, that the floor of a large valley in general is more likely to have experienced longer periods of basal melting than surrounding elevated areas (e.g. Näslund 1997).

An additional important process affecting ice temperature takes place if the air temperate allows surface melting during spring periods, for example at low elevations of an ice sheet in a warming deglaciation climate, or during times of early ice sheet formation. After the winter period with cold temperatures, the temperature in the upper snow/firn pack of the ice sheet is well below the freezing point. As surface melting starts, meltwater percolates down into the snowpack and re-freezes at some depth. During the re-freezing process, latent heat is released (334 kJ kg^{-1}), corresponding to the latent heat of fusion for ice) which warms the surrounding snow. As the process continues the entire snowpack can be transformed to temperate conditions during a few weeks. This is a very efficient process, and the result is that temperate ice instead of cold ice is formed at the location. This may have been an important process during build-up phases of Fennoscandian ice sheets, having an important effect on the thermal characteristics of early ice sheets (Näslund 1998).

Ice movement and thermodynamic feed-back. The stresses induced by the mass of overlying ice induce deformation or strain in the ice. The resulting ice movement, often referred to as *internal deformation*, is present in all glaciers (being one of the main criteria for the term *glacier*). The shear stress at the base of an ice sheet is calculated from:

$$\sigma = \rho\, g h \sin \alpha \qquad \text{Equation 2-7}$$

where σ is the shear stress, g is the acceleration of gravity, h is the ice thickness, and α is the ice sheet surface slope. The most common flow law of ice describing the strain rate of ice under pressure is Glen's flow law (Glen 1955):

$$\dot{\varepsilon} = \left(\frac{\sigma}{B}\right)^{n} \qquad \text{Equation 2-8}$$

where $\dot{\varepsilon}$ is the strain rate, σ is the shear stress, B is a viscosity parameter that increases as the ice gets more difficult to deform, a parameter depending on among other things ice temperature and crystal fabric, and n is an empirically determined constant (~ 3) that depends on the specific creep process that is operating. The main effect of Glen's flow law is that moderate increases in stress (ice thickness) result in a substantial increase in strain rate. For example, a doubling of the amount of stress results in a 2^3, that is 8, times higher deformation rate (Figure 2-29).

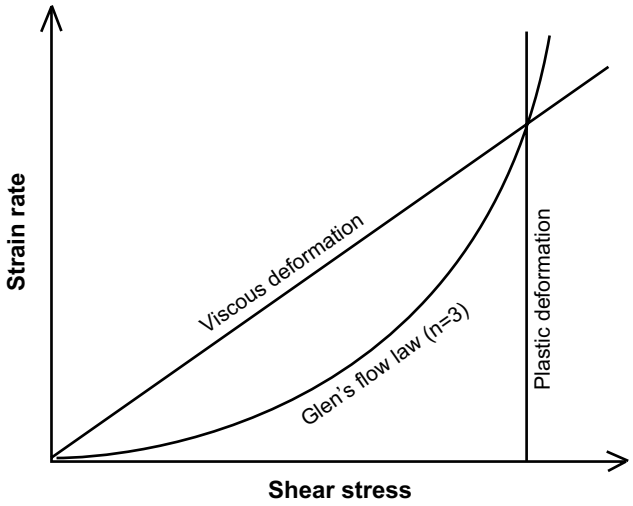

Figure 2-29. *Deformation rate versus shear stress for various flow laws, including Glen's flow law for ice. Modified from Holmlund and Jansson (2003).*

In ice sheets, the horizontal ice velocity increases from the ice divides, where it is zero, toward the margin. The steeper surface slope at the margin induces larger driving stresses which makes the ice deformation rate high. For an ice sheet with an ablation area, i.e. an ice sheet ending on land (Figure 2-25) the maximum horizontal velocity is at the equilibrium line, whereas in the case of a marine ice-sheet margin, the maximum velocity is at the ice sheet grounding-line (Figure 2-25).

The stress that acts on the uppermost layer of a glacier does not produce a plastic deformation. Instead the uppermost part of the ice, about 30–100 m thick depending on ice temperature, is brittle, often resulting in typical fractures, or *crevasses*. Most of the internal deformation takes place near the bed where stresses are highest. The overlying ice moves along more or less as a uniform block on top of the deforming ice. This is indicated as the internal deformation portion of the ice velocity in Figure 2-30.

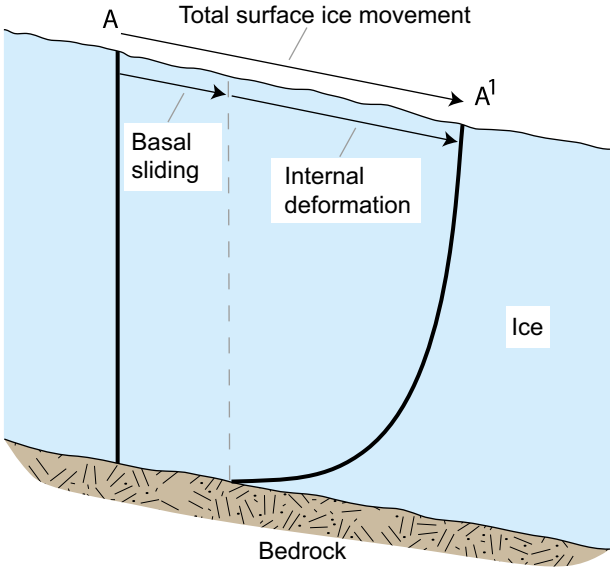

Figure 2-30. *Internal deformation and basal sliding demonstrated by the deforming of a steel rod from time A to A1. Modified from Holmlund and Jansson (2003), after Sharp (1960).*

There is also another process that may contribute to glacier movement. If the ice sheet is wet-based, the ice may slide over the substrate, and the substrate itself may deform, especially if the water pressure at the bed is high. The surface ice velocity is, in this case, the sum of the component from internal deformation and the component from basal sliding and deformation (Figure 2-30). For all practical purposes, one can assume that *basal sliding* does not occur if the bed is frozen. Therefore, not all glaciers, or all parts of an ice sheet, have the sliding ice-flow component. However, where it is present, it may be of great importance, for example in ice streams, which are typically warm-based. Here, the observed surface flow may be completely dominated by basal sliding (Engelhardt and Kamb 1998). High basal water pressures are favourable for intense basal sliding (Engelhardt et al. 1990), as well as smooth bed topographies and deformable, water-saturated tills (e.g. Kamb 2001, Iverson et al. 1995).

Within glaciers and ice sheets there are important thermodynamic feedback mechanisms, in the following exemplified by a discussion on ice streams. As seen above, the viscosity of the ice is affected by the ice temperature, with higher ice temperatures giving more easily deformable ice. At the same time, the internal deformation itself produces frictional heat, with higher velocities producing more heat. This gives a positive feedback mechanism; high internal deformation rates increase the temperature of the ice, which in turn makes the ice even easier to deform.

On the other hand, looking at the basal thermal conditions of ice streams, there may be additional thermodynamic processes acting. A fast-flowing warm-based ice stream may drain a lot of ice from the ice sheet. Over time this will reduce the thickness of the ice also over the ice stream itself. The thinner ice insulates less well from cold surface temperatures, which leads to less melting at the bed, and eventually also to a shift from warm-based to cold-based conditions. This reduces the velocity of the ice stream considerably and the ice flux deformational heating reduces accordingly. The ice stream now drains much less ice than before, which in time results in increased ice thicknesses (Payne 1995). The larger ice thickness warms the bed, which again may become wet-based and basal sliding may start again. This process suggests that ice streams may have an inherited built-in unstable behaviour. This has been suggested as one explanation for the cyclic Dansgaard–Oeschger events recorded in glacial marine sediments (cf. Andrews and Barber 2002).

In addition, the dynamics of an ice sheet and ice-sheet responses to changes in climate, are to a large degree governed by the subglacial hydrology. This field of knowledge is rapidly advancing, for instance through the contributions from the studies Greenland Analogue Project (GAP) (Claesson Liljedahl et al. 2016, Harper et al. 2016) and ICE (Harper et al. 2019), that provided observations and measurements from the western land-based sector of the Greenland ice sheet.

2.3.2 Controlling conditions and factors

The upper boundary of the ice-sheet system is the ice-sheet surface, whereas the lower boundary is the ice-sheet bed, i.e. the interface between basal ice and substrate. In accordance with ice-sheet fluctuations, the lateral extent of these boundaries as well as the vertical location of the upper boundary changes over time.

Upper boundary condition – Climate. The boundary condition at the ice-sheet surface is the prevailing climate, i.e. air temperature and precipitation, including its variation over time. The air temperature at the ice-sheet surface is determined mainly by the latitude, altitude and climate changes. The latitude at a site is fixed, but the altitude varies with the local thickness variations of the ice sheet and associated isostatic responses. The typical air temperature pattern over an ice sheet is with the lowest temperatures in the ice-sheet interior and higher surface temperatures closer to the margin. If temperatures are greater than 0 °C during summer, surface melting takes place on the lower parts of the ice-sheet surface. This melting typically amounts to several m of ice per year, with large variations according to the prevailing temperature regime. Surface melt rates are lower closer to the equilibrium line. In general, during cold stages of ice-sheet growth, the amount of surface melt water production is small compared with the amounts of water produced during deglaciation under warmer climate conditions.

Most precipitation that falls on ice sheets falls as snow. During relatively warm climates at low ice-sheet elevations, precipitation may occur as rain. Snow accumulation and surface ablation are not distributed evenly over the ice-sheet surface. The precipitation pattern reflects ice-surface elevation and degree of continentality, often giving a pattern of high accumulation rates close to the ice-sheet margin with diminishing values towards the interior. On mid-latitude ice sheets, like the former Fennoscandian ice sheet, the precipitation pattern is strongly affected by the prevailing west-wind belt and associated low-pressure tracks. This results in an orographic effect which gives most precipitation on the western side of large Fennoscandian ice sheets. Typical coastal accumulation rates of the Antarctic ice sheet are 0.3–0.6 m a^{-1} (water equivalents), whereas the interior parts get less than 0.1 m a^{-1} in precipitation (Giovinetto and Zwally 2000), i.e. here polar desert conditions prevail. On an ice-sheet surface, regional and local variations of great magnitude in the amount of snow accumulation often occur, mainly due to wind re-distribution of snow in regions close to the ice-sheet margin (Figure 2-31).

To initiate ice-sheet growth in a non-glaciated region, the local climate needs to change. That can either occur due to global climate change, towards lower local summer temperatures, or higher winter precipitation rates, or, over long timescales, by tectonic uplift, or a combination of climate and tectonics. Generally, ice-sheet formation in Fennoscandia involves small alpine glaciers in the Scandinavian mountain range that grow into a mountain-centred ice sheet, and then grow to a full-scale ice sheet (Andersen and Mangerud 1989, Lundqvist 1992, Kleman et al. 1997). Increasing evidence suggests very dynamic ice sheet and climate behaviour during the last glacial cycle, with ice-sheet growth phases interspersed by extended periods with restricted ice coverage, see also Section 3.2.

Lower boundary condition – Ice-sheet bed. The lower boundary condition of the ice sheet system is the ice-sheet bed. The substrate typically either consists of bedrock, in Fennoscandia normally crystalline rocks, or bedrock covered by till. There are two important parameters to consider here; 1) the topography of the landscape and 2) the amount of geothermal heat flow.

The topography of the bed is of importance for the basal boundary conditions of ice sheets, as discussed above. Above all, an ice-sheet bed with strong relief produces basal thermal conditions with stronger lateral temperature gradients than an ice-sheet bed with smooth topography. The first case also implies larger spatial variations in basal melt water production.

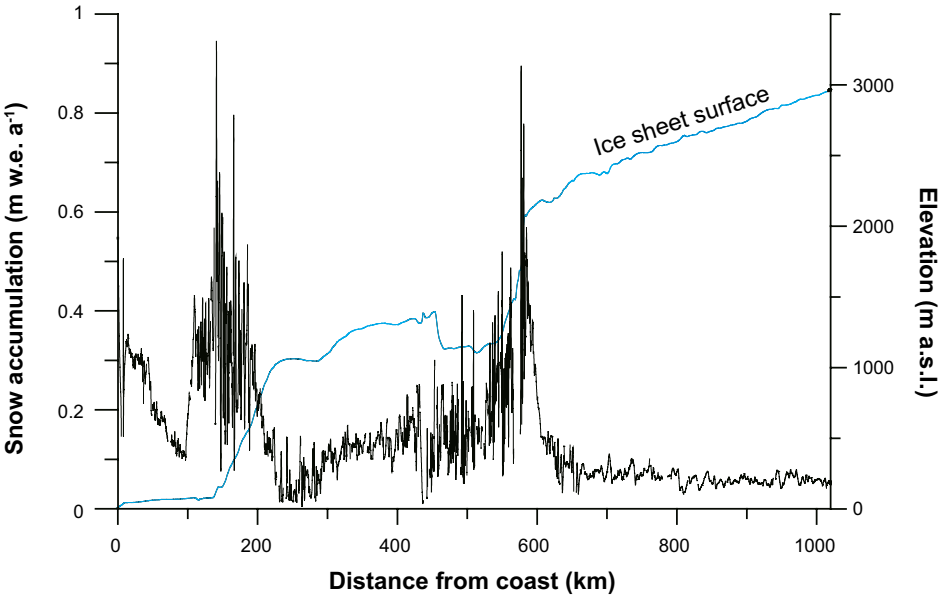

Figure 2-31. *Accumulation rates (in metres water equivalents per year) and ice surface elevations (in metres above sea level) along a profile in over the East Antarctic ice sheet. The accumulation is high in the coastal area and low in the interior. Due to wind redistribution of snow and increased topographically-induced precipitation, exceptionally high values of snow accumulation with strong variations are found in areas of nunataks and steep surface slope. From Richardson (2004).*

The geothermal heat flux is also of great importance for the basal condition of ice sheets (e.g. Waddington 1987), affecting basal ice temperatures, hydrology, ice dynamics, and the erosional capacity of the ice. Typically, for a 3 km thick ice sheet at steady-state, a 20 % error in geothermal heat flux generates a 6 K error in calculations of basal ice temperatures. This has direct implications on, for example, numerical ice-sheet modelling. If the geothermal heat flow is not realistic in the model setup, ice-sheet models will not produce useful data on basal melting and other characteristics. Numerical ice-sheet modelling studies have also shown that basal ice temperatures are sensitive to relatively small changes in geothermal heat flow (e.g. Greve and Hutter 1995, Siegert and Dowdeswell 1996).

For the modelling study presented in Section 2.3.4, Näslund et al. (2005) calculated a distributed, high-resolution geothermal heat flow data set for an approximate core area of the Fennoscandian ice sheet, and embedded this within lower-resolution data published for surrounding regions. In the following, a brief overview of the geothermal heat flux calculation is given.

The geothermal heat flow or surface heat flow density (HFD) in cratonic areas consists of two components: (1) heat produced within the mantle and core of the Earth and (2) heat produced within the crust. The contribution from the Earth's interior (so-called Moho- or reduced heat flow) arises from the cooling of the Earth and formation of a solid core, and from radiogenic heat production (e.g. Pollack et al. 1993). The crustal component consists of radiogenic heat production where heat is produced by the natural radioactive decay of primarily ^{238}U, ^{232}Th, and ^{40}K (Furlong and Chapman 1987). The Moho heat flow has a smooth spatial variation, possibly depending on mantle convection cell distribution (Beardsmore and Cull 2001), whereas the spatial variation in concentration of radioactively decaying nuclides in the lithosphere generates a heat flow with large spatial variations. The surface HFD can be estimated by a heat flow-heat production (Q-A) relationship of the form

$$Q = q_0 + DA_0 \qquad \text{Equation 2-9}$$

(Birch et al. 1968, Lachenbruch 1968, Beardsmore and Cull 2001) where Q is the surface heat flow density (or geothermal heat flow), q_0 is the Moho heat flow, D represents the vertical distribution of heat-producing radionuclides in the lithosphere and A_0 is the radiogenic heat production from near-surface rocks.

The regional HFD pattern does not correlate with gravity variations (Balling 1984), magnetic anomalies (Riddihough 1972), or crustal thickness (Čermák et al. 1993). However, within the Baltic shield, as well as in other areas with similar geological settings, there is a close correlation between HFD and regional geological units, with higher heat flow from acid (commonly granitic) areas and lower heat flow values from basic areas (e.g. Landström et al. 1979, Malmqvist et al. 1983).

The calculations of HFD values for Sweden and Finland were based on detailed data sets from numerous γ-emission measurements from bedrock and till. In Sweden, airborne surveys of γ-emissions have been carried out by the Geological Survey of Sweden (SGU), sampling data at 70 m intervals along flight lines with 17 km separation. To avoid shielding effects from vegetation and lakes, only data from exposed bedrock and till surfaces were used in the calculations. The Finnish data set is based on radiometric γ-emission measurements of 1 054 till samples providing full spatial coverage of the country (Kukkonen 1989).

The calculation of HFD is performed in several steps. First, the concentrations of ^{238}U, ^{232}Th, and ^{40}K are calculated from the γ-emission measurements, using information from detailed reference measurements over calibration plates with well-known isotopic concentrations. Near-surface heat production is then calculated from the concentrations of radionuclides. In addition, the Moho heat flow contribution needs to be considered. The distributed Moho heat flow data set by Artemieva and Mooney (2001) was added to the near-surface heat production data set. Finally, the HFD data set was re-sampled to a grid with 5 km resolution. To provide HFD coverage for the entire model domain, data for surrounding areas were added from the much coarser observed global HFD data set provided by Pollack et al. (1991). The resulting geothermal heat flow distribution is shown in Figure 2-32.

Within the LGM ice margin, the new data set shows that the geothermal heat flow varies by a factor of as much as 2.8 (geothermal heat flow values ranging between 30 and 83 mW m^{-2}, with an average of 49 mW m^{-2}). This average value is 17 % higher than 42 mW m^{-2}, which is the typical uniform value used in ice-sheet modelling studies of Fennoscandia. Using this new distributed data set on geothermal heat flow, instead of a traditional uniform value of 42 mW m^{-2}, yields a factor of 1.4 larger total basal

melt water production for the last glacial cycle (Näslund et al. 2005). Furthermore, using the new data set in high-resolution modelling, results in increased spatial thermal gradients at the bed. This enhances and introduces new local and regional effects on basal ice temperatures and melt rates. The results show that regional to local variations in geothermal heat flow need to be considered for proper identification and treatment of thermal and hydraulic bed conditions under the Fennoscandian and other similar ice sheets (Näslund et al. 2005).

Ice properties. The exponent n in Glen's flow law (Equation 2-10) is dependent on the active creep process. Numerous field experiments and laboratory tests of glacier ice suggest that n should be ~ 3. The typical creep process considered is a simple power-law creep, where the creep rate is proportional to the stress raised to some power greater than 1, for example:

$$\dot{\varepsilon} \propto \sigma^3 \qquad \text{Equation 2-10}$$

On the other hand, with certain temperature, stress, and grain-size combinations, diffusional creep instead of power-law creep could take place in ice sheets (Duval et al. 1983), which would lower the value of n to less than 3. Other recent studies suggest that n should be between 1 and 2 for deformation at low stresses, low temperatures, and low cumulative strains (Alley 1992, Montagnat and Duval 2000). However, some of these conditions are likely to be important only down to depths of a few hundred metres in the coldest parts of ice sheets.

The viscosity constant B in Glen's flow law is dependent on many parameters. Therefore, various modifications of Glen's flow law have been developed taking into account temperature, hydrostatic pressure, and crystal orientation. The last case is the most difficult, and it is done by introducing an anisotropy enhancement factor. The *c*-axes of the ice crystals are, to a large degree, uniformly distributed in the upper part of the ice sheet, i.e. the ice is basically isotropic. When the ice over time is affected by the weight of the accumulating overlying ice mass, it is vertically compressed and longitudinally stretched, which results in a conical distribution of c-axes orientations. Subsequently, when the ice is affected by the simple shear close to the ice-sheet bed, the *c*-axes are typically re-oriented to a preferred single orientation. Knowledge of the development of *c*-axis fabrics has been obtained by re-crystallisation and ice-grain rotation. Since it is known from ice-core studies that the crystal orientation in ice sheets is not isotropic at depth, a non-isotropic flow law of ice improves, for example, ice-sheet modelling (e.g. Placidi et al. 2010).

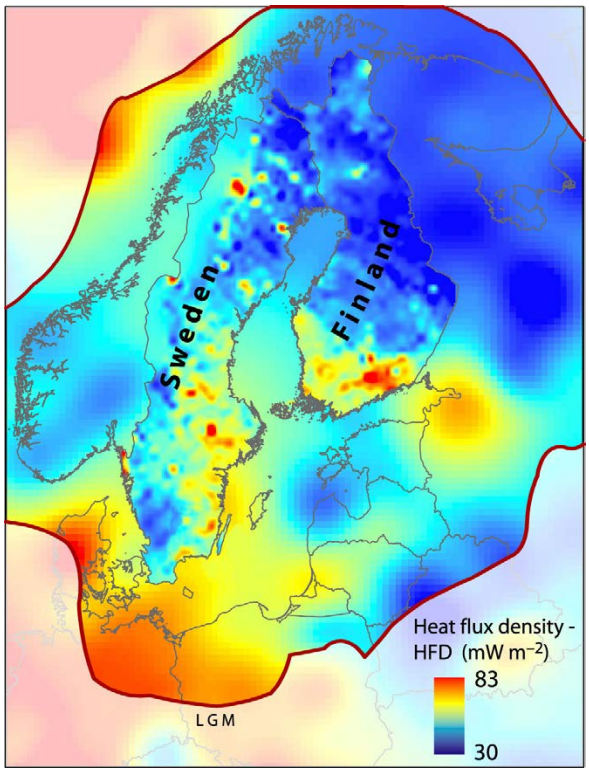

Figure 2-32. *Geothermal heat flow distribution over Fennoscandia. From Näslund et al. (2005).*

The ice sheet dynamics described above may affect several geosphere variables of importance for the SFR (Table 2-5).

2.3.3 Natural analogues/observations in nature

Paleo-ice sheets

The mid-latitudes of the Northern Hemisphere have experienced repeated continental-scale glaciations during the Late Cenozoic. As previously mentioned, these periods are referred to as *glaciations* and the warm periods between the glacials are called *interglacials*. The present interglacial is called the Holocene, and, in north-western Europe, the last glaciation is named the Weichselian.

Table 2-5. A summary of how geosphere variables are influenced by ice-sheet dynamics.

Geosphere variable	Climate issue variable	Summary of influence
Ground temperature	Basal ice temperature	During periods of cold-based ice coverage, low basal ice temperatures contribute to the formation of permafrost. During periods of warm-based ice coverage, basal ice temperatures at the pressure melting point contribute to permafrost degradation.
Groundwater flow	Basal thermal condition Basal melt rate Supply of surface melt water	If the ice sheet is cold-based no free water is available and there will be no groundwater recharge from basal melt water. If the ice sheet is warm-based, basal melting occurs at the ice/bed interface and groundwater recharge takes place. In addition, meltwater from the ice-sheet surface will, in both cases, be transported to the bed in frontal-near areas of the ice sheet. Groundwater recharge and flow will be determined by the presence of the ice sheet.
Groundwater pressure	Basal thermal condition Ice-sheet thickness Basal melt rate Supply of surface melt water	If the ice sheet is warm-based, the water pressure at the ice/bed interface may reach as much as the ice sheet overburden pressure, and in certain cases more. The groundwater pressure also depends on the melt water supply and the flow properties of the en- and sub-glacial hydrological systems. The groundwater pressure is also affected by the ice-load compression of the bedrock pores and fractures.
Rock stresses	Basal condition Englacial ice temperatures Ice-sheet thickness	Rock stresses will be influenced by the ice load and the hydrostatic pressure. Independently of basal conditions there will be an increase in vertical stresses corresponding to the ice thickness. The horizontal stresses will also increase. If the ice sheet is warm-based the prevailing water pressures at the ice/bed interface will also alter rock stresses. The alteration of rock stresses also depends on the duration of the ice load and the slope of the ice-sheet surface. The slope of the ice-sheet surface near the front is in turn highly dependent on englacial ice temperatures and basal thermal conditions.
Groundwater composition	Glacial melt water composition	The glacial melt water is oxygen rich. The combination of abundant melt water supply and high water pressures may cause injection of glacial melt water to larger depths than oxygen-rich waters would penetrate in non-glacial conditions. Also, the consumption of oxygen close to the surface may be limited due to the lack of organic matter and microbiological activity.

Paleo-ice sheets have left geological traces in previously glaciated terrain in Fennoscandia, North America and Siberia, as well as abundant glacio-marine traces in adjacent ocean basins. Studies of North Atlantic marine sediments have shown that the first traces of eroding glaciers in Greenland and Fennoscandia date back to between 12 and 6.6 Ma BP (Jansen and Sjøholm 1991, Fronval and Jansen 1996), with larger ice sheets present in Fennoscandia from around 2.75 Ma BP. Over the last ~ 800 ka, glacial–interglacial cycles of about 100 ka duration have dominated global climate variation (see Section 3.1). Before c. 800 ka BP, cycles of 41 ka dominated (e.g. Raymo et al. 1998, McIntyre et al. 2001).

Geological information on till stratigraphy, interstadial deposits, glacial landforms in loose sediments and in bedrock have for a long time been used for making reconstructions of the Weichselian glacial history. A summary of that work is provided in Lokrantz and Sohlenius (2006). Section 3.2 describes several recent studies that have been used for the reconstruction of the Weichselian glacial history and of climate conditions during this glacial cycle.

Various types of glacial landforms may also be used to infer information on basal thermal conditions of paleo-ice sheets (e.g. Lagerbäck 1988a, Kleman et al. 1997, Kleman and Hättestrand 1999, Kleman and Glasser 2007).

Present ice sheets

At present there are two ice sheets on Earth, the Antarctic (14 Mkm^2) and Greenland (1.7 Mkm^2) ice sheets. Large portions of these quasi-stable ice sheets are more than 3 km thick. In both cases, the ice-sheet load has depressed the bed so that large portions are situated below sea level. Offshore marine sediments show traces of waxing and waning Antarctic ice sheets of continental proportions back to 40–36 Ma BP (Haq et al. 1987, Hambrey et al. 1992), and Antarctic alpine glaciers may trace back to the Oligocene (Näslund 2001). The present configuration of the Antarctic ice sheet is thought to have been relatively stable for the last 15–11 Ma (cf. Shackleton and Kennett 1975, Marchant et al. 1993).

The spatial patterns of basal thermal characteristics of the Antarctic and Greenland ice sheets are complex due to ice-sheet dynamics, bed topography, and geothermal heat flux variability. For both ice sheets, parts of the bed are cold-based whereas other parts are warm-based, as seen from modelling studies (Figure 2-33), radar soundings and drill hole data. Ice-sheet modelling has also, together with geological field observations and remote sensing studies, showed that ice streams are prominent features of the Antarctic ice sheet, penetrating far into the ice-sheet interior (Figure 2-34). This has also been shown by remote sensing Interferometric Synthetic Aperture Radar (InSAR) studies (Joughin and Tulaczyk 2002). The outer coastal-near parts of these ice streams are typically wet-based, whereas their upstream parts, high in the catchment areas, often are cold-based.

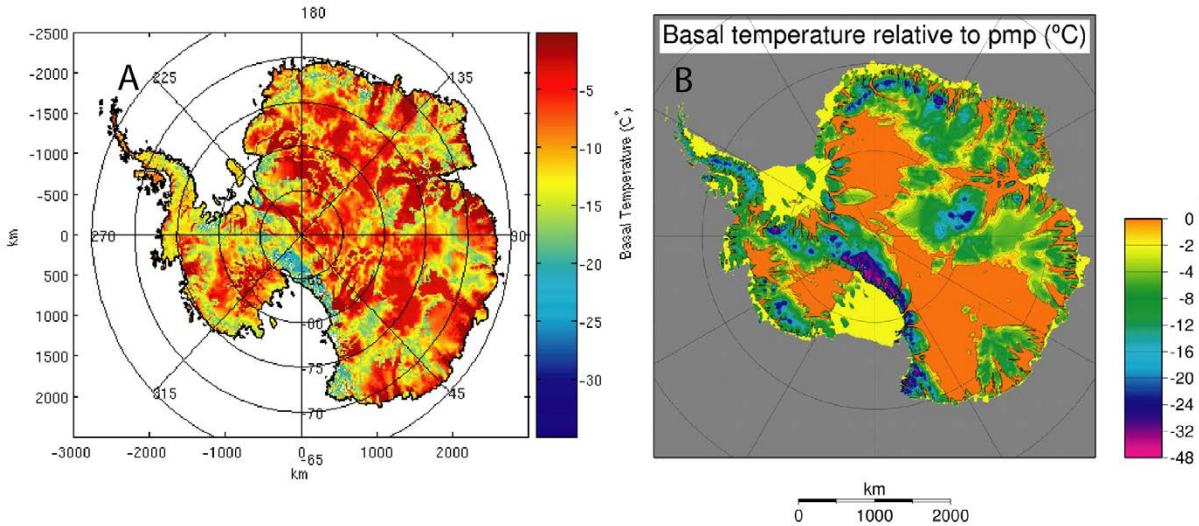

Figure 2-33. *Two examples of modelled present-day Antarctic ice sheet basal temperatures. Temperatures are expressed relative to the pressure melting point (pmp). Figure a) is from Johnson (2004) and b) from Huybrechts (2006).*

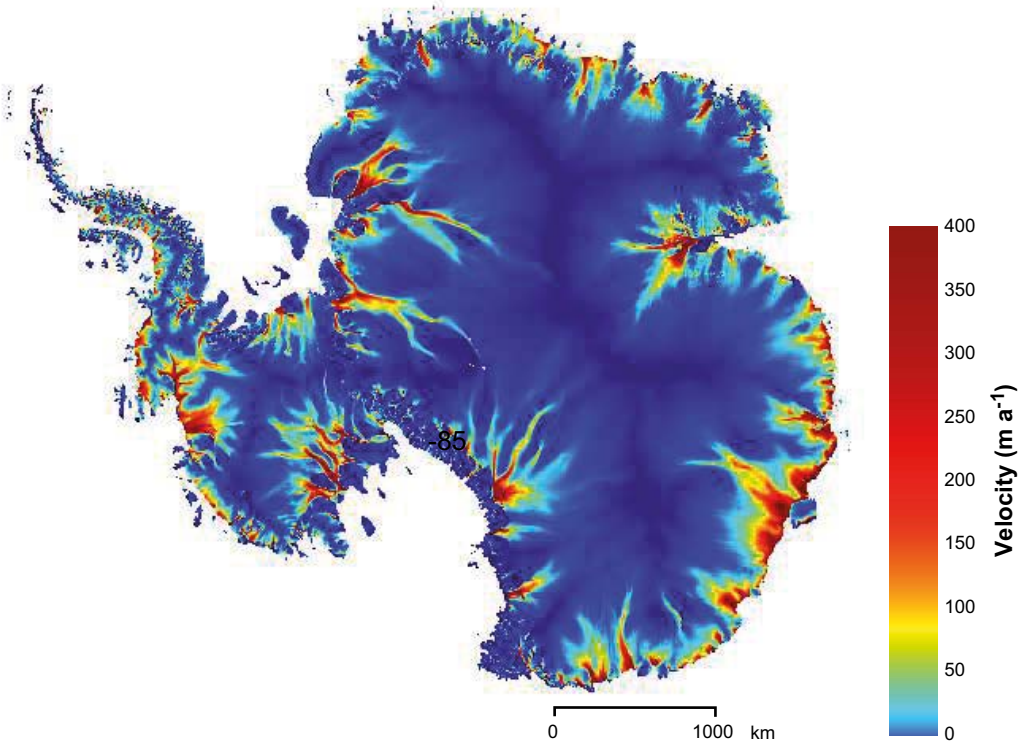

Figure 2-34. *Modelled Antarctic ice-surface velocities. Fast-flowing ice streams (red/yellow/green) reach far into the ice-sheet interior. From Johnson (2004) with numerical methods described in Staiger et al. (2005).*

During the main Pleistocene glacial periods, the Greenland and Antarctic ice sheets had a larger extent than at present. The major limiting factor on their maximum lateral extent is the bed topography; the Antarctic and Greenland ice-sheet margins are both today located close to the coastline. The continental crust does not extend out very far from the present-day coast lines, and, at the continental margin, the water depth quickly increases. When the ice sheets grow larger the grounding-line migrates outward, resulting in a larger area for the grounded part of the ice sheet. The grounding line cannot advance past the continental margin due to the larger water depths outside. The continental margin thus constitutes a definite constraint on the maximum spatial size of Antarctic and Greenland ice sheets during Late Cenozoic ice-sheet fluctuations. The situation was similar for part of the Fennoscandian ice sheet. From a bed topography point of view there were no constraints for ice-sheet growth from the Scandinavian mountain range towards the east (the Baltic depression is not deep enough to provide such a constraint), but Fennoscandian ice sheets, including the last Weichselian ice sheet, could not and did not extend farther west than the offshore continental margin (Svendsen and Mangerud 1987, Zweck and Huybrechts 2003).

Although the sizes of the Antarctic and Greenland ice sheets were greater during the Late Pleistocene glacials, the maximum thicknesses need not have been larger. On the contrary, because of atmospheric moisture starvation during the colder climates, the interior parts of the ice sheets probably were thinner during the coldest parts of the glacial cycles (e.g. Huybrechts 1990). In contrast, at the ice-sheet margins the ice-sheet thickness varies considerably during a glacial cycle. Areas where the ice thickness is zero during a warm interglacial period (i.e. at the exact margin) may experience an increase in ice thickness of several hundred metres, up to one kilometre, during a glacial maximum ice configuration (Näslund et al. 2000). In turn, this means that the temporal changes in basal conditions of the ice sheets, for example changes in basal ice temperatures from the present interglacial pattern, were highly complex. For example, due to the changed ice configuration affecting ice-sheet dynamics, some parts of the Antarctic ice sheet were warmer at the LGM ice configuration than at present, whereas, at the same time, other parts were colder (Figure 2-35) (cf. Näslund et al. 2000).

Recently, the coupling between the dynamic behaviour of the Greenland ice sheet and ice-sheet hydrological processes has been inferred from several studies, see e.g. SKB (R-10-59).

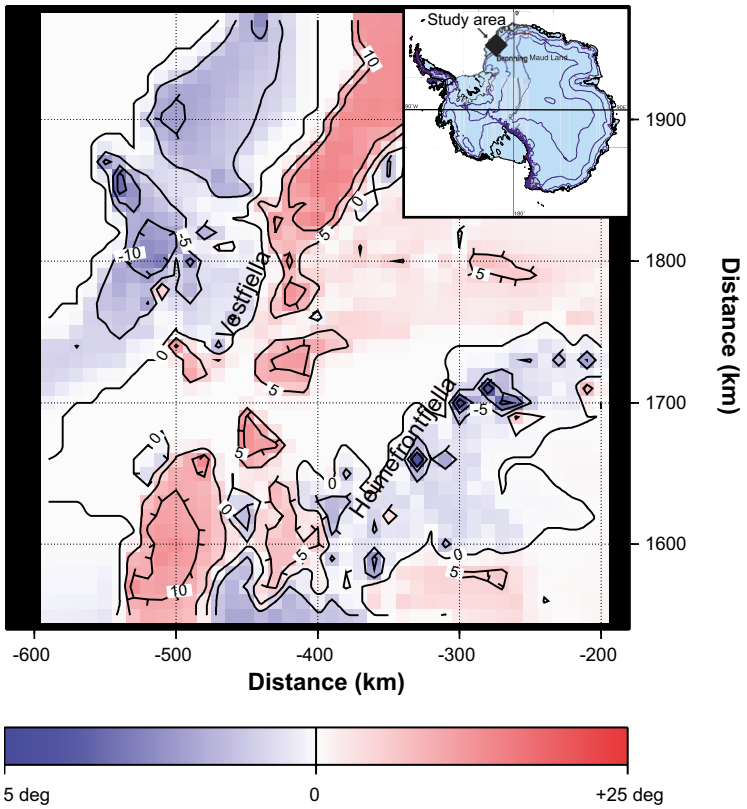

Figure 2-35. *Modelled difference in basal temperature between the present-day ice configuration and a maximum Pleistocene ice sheet configuration for part of the Antarctic ice sheet. For this single change in ice configuration, ice-sheet thermodynamics induce complex changes in basal thermal pattern; some parts of the ice sheet become warmer at the bed the same time as other parts become colder. From Näslund et al. (2000).*

2.3.4 Model studies

Ice-sheet modelling

Thermo-mechanical ice-sheet modelling is a well-established and useful tool for studying a large array of ice-sheet-specific and ice-sheet-related issues. Although ice-sheet models have their limitations, they can be used to study characteristics and behaviour of present ice sheets, paleo-ice sheets, and future ice sheets. As computer capacity has increased, more sophisticated models have been able to be run at higher spatial resolution, which, in turn, has made it meaningful to e.g. compare detailed model output with various types of geological information, both for model verification and testing of glacial-geological hypotheses (e.g. Pattyn et al. 1989, Van Tatenhove and Huybrechts 1996, Näslund et al. 2003, Staiger et al. 2005, Patton et al. 2016).

Reconstructions of paleo-ice sheet configurations, including ice thicknesses, may be done by two main groups of models. One group is thermo-mechanical ice-sheet models that are based on ice physics and thermo-mechanical interactions (e.g. Huybrechts 1986, Boulton and Clark 1990, Fastook 1994, Ritz et al. 1996, Payne and Dongelmans 1997, Marshall and Clarke 1997). The second group of models are isostatic rebound models that are used to invert observations of crustal rebound and shoreline locations to estimate paleo-ice thicknesses (e.g. Lambeck et al. 1998, Peltier 2004).

For the present study, UMISM (University of Maine Ice Sheet Model) (Fastook and Chapman 1989, Fastook 1990, 1994, Fastook and Prentice 1994, Johnson 1994) was selected for the simulation of last glacial cycle ice-sheet configurations. The UMISM code was selected because a large number of simulations of the last glacial cycle Fennoscandian ice sheet have been done with this model over the years (e.g. Fastook and Holmlund 1994, Holmlund and Fastook 1995, Näslund et al. 2003). The UMISM was part of the European Ice Sheet Modeling Initiative (EISMINT) model intercomparison experiment and yielded output in agreement with many other physically based ice-sheet models (Huybrechts et al. 1996, Payne et al. 2000), which further motivated the choice of this model.

The resulting reconstruction of last glacial cycle ice-sheet configurations for the Forsmark site, e.g. Figure 4-18 in SKB (TR-10-49), shows large similarities with corresponding data for a North American last glacial cycle scenario modelled using the Peltier model (Garisto et al. 2010). This indicates that the selection of the type of model is not critical for the general appearance of the ice sheets reconstructed for the last glacial cycle. In detail, however, the development of ice configurations over time in e.g. these two studies are expected to differ for several reasons, including that the studies deal with two different geographical areas and indeed two different ice sheets (the Weichselian ice sheet over Eurasia and the Laurentide ice sheet over North America). For instance, the last glacial cycle Laurentide ice sheet is known to have been considerably larger and thicker than the Weichselian ice sheet.

The ice-sheet system constitutes three main sub-systems: mass-balance, ice movement, and ice temperature. For these sub-systems the selected ice-sheet model solves differential equations describing conservation of mass, momentum, and energy respectively. In addition, the ice-sheet model is forced by the climate, represented by air temperature and precipitation. The spatial distribution of the precipitation was calculated based on several parameters; distance from the pole, saturation vapour pressure (function of altitude and lapse-rate), and surface slope. This was originally an empirical relationship developed from the Antarctic ice sheet (Fastook and Prentice 1994) but has successfully been applied also for simulations of Northern Hemisphere ice sheets (e.g. Fastook and Holmlund 1994, Holmlund and Fastook 1995, Näslund et al. 2003, Hooke and Fastook 2007, Kleman et al. 2013). Over a specified model domain, using a topography described by a Digital Elevation Model (DEM), this climate description gives a spatial representation of both air temperatures and precipitation at ground level.

The UMISM also includes a simplified isostatic description for the behaviour of deforming bedrock due to the weight of the modelled ice-sheet configuration. This is not a full self-gravitational spherical Earth model as used in the Glacial Isostatic Adjustment (GIA) modelling described in Section 2.2. Instead, it is a hydrostatically supported elastic plate model, considered adequate for the purpose of placing the ice-sheet surface at an appropriate altitude, and hence at an appropriate air temperature, for the mass balance calculations. Furthermore, the UMISM also includes a subglacial hydrology model (Johnson 1994) that can transport basal meltwater under the ice sheet according to prevailing pressure potentials governed by ice-sheet thickness and basal topography.

A paleo-temperature record was employed to run the ice sheet model (Figure 2-36). For the reconstruction of the Weichselian ice sheet, see below, the temperature proxy record for the last 120 ka from the Greenland GRIP ice core has been used (Dansgaard et al. 1993). The temperature file that was used contains 50-year averages of the original time series. For a comprehensive description of the construction of this Forsmark air temperature data set, including its use in the ice-sheet modelling and its estimated uncertainties, see SKB (TR-10-49, Appendix 1).

In the modelling process, variations in the proxy temperature are used to change the climate pattern (temperature and precipitation) over the model domain, initiating ice-sheet growth in Fennoscandia. Once glaciers/ice sheets are formed, the modelled thermo-dynamic ice-sheet system starts to evolve over time. In this way, the ice-sheet model simulates the behaviour of the ice sheet as it responds to the external forcing such as changing climate or sea level, as well as internal dynamics, such as ice-stream variations caused by internal temperature oscillations at the bed.

The following are input parameters to the ice-sheet model in the simulations of the Weichselian ice sheet:

1. The thermodynamic properties of the ice, including flow laws, sliding laws, feedback mechanisms etc.
2. Upper boundary conditions: A mass-balance parameterisation providing a climate description constituting fields of annual air temperature and precipitation over the model domain.
3. Lower boundary conditions:
   A. A DEM over Fennoscandia with a moderately high spatial resolution. For the reconstruction of the Weichselian ice sheet a grid size of 50 km was used. This resolution is sufficient to capture the general large-scale dynamics of the ice-sheet but would be too coarse in regions with large and highly variable topography. However, this is not the case for south-central Sweden which

is in general characterized by a relatively flat to very flat topography. DEM data were taken from the ETOPO2 data base[5], depicting both continental topography and bathymetry;

B. Geothermal heat flux at the bed.

4. Sea-level changes during the last 120 ka.
5. Proxy air temperature for the past 120 ka (GRIP data).

The modelling starts 120 ka BP, and the model was run at a five-year time step forward in time up to time zero (present). For each time step, output data were calculated for each grid cell and grid node. These data included:

1. Ice thickness.
2. Englacial and basal ice temperatures.
3. Ice velocity.
4. Direction of ice movement.
5. Isostatic depression of crust.
6. Amount of basal melting or freeze-on of water.

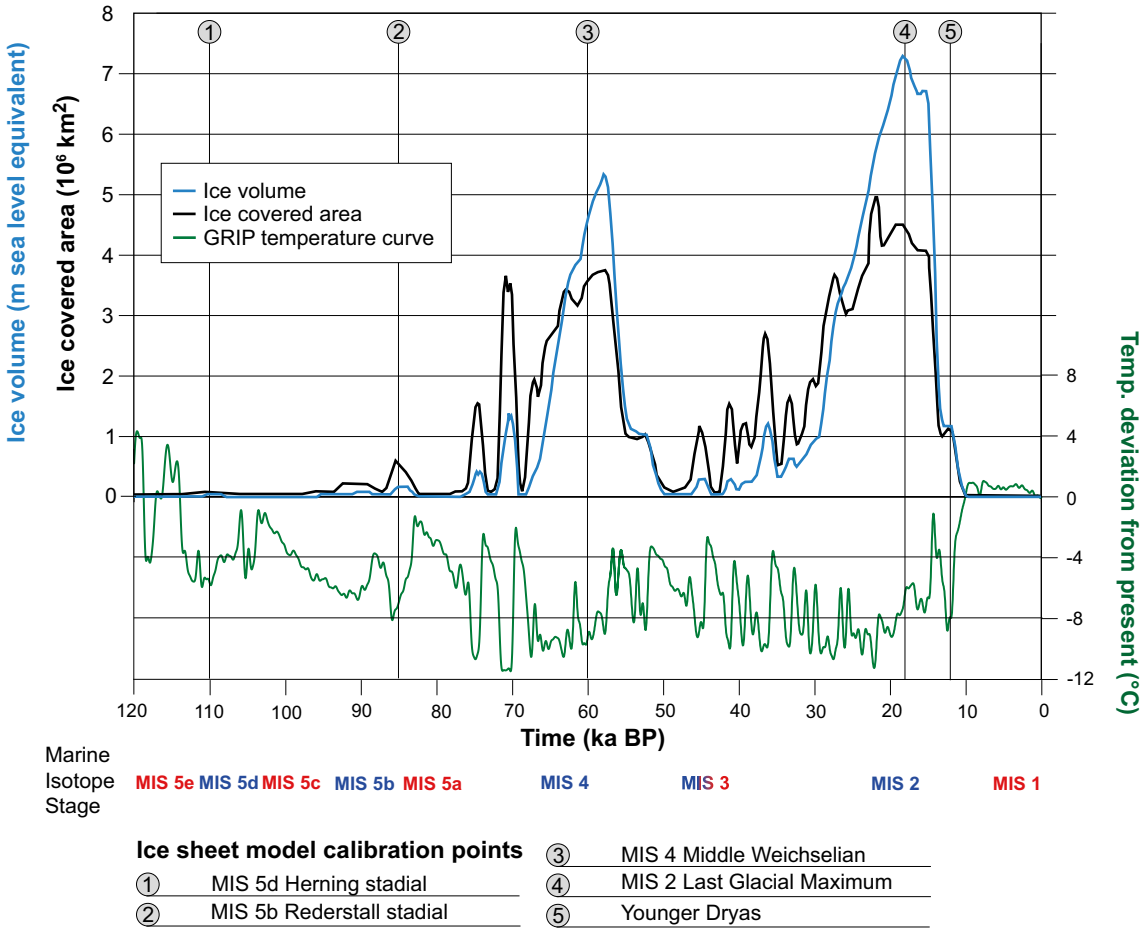

Figure 2-36. *GRIP proxy temperature and reconstructed ice-covered area and ice volume for the reconstruction of the Weichselian ice sheet. Times of model calibration are shown, as well as Marine Isotope Stages (MIS) (warm stages in red and cold stages in blue).*

[5] ETOPO2, 2001. Global Digital Elevation Model (ETOPO2) representing gridded (2 minute by 2 minute) elevation and bathymetry for the world. Data were derived from the National Geophysical Data Center (NGDC) ETOPO2 Global 2' Elevations data set from September 2001.

Model setup. A model domain was selected to cover the maximum extent of the Weichselian ice sheet over Fennoscandia, with a spatial DEM resolution of 50 km. The thermomechanical coupling between ice movement and ice temperature was enabled, as well as a function by which the amount of basal sliding is coupled to the amount of basal meltwater present at the ice-sheet bed. The *n* parameter in Glen's flow law (Section 2.3.2) was set to 3, whereas the value for the viscosity parameter *B* differed depending on ice temperature. Exemplified calculated values of *B* are seen in Figure 2-37. In the final model run, the model was run with a five-year time step and data were saved from the model simulation at a 100-year interval.

The traditional way of specifying the basal thermal boundary condition in ice-sheet modelling is to apply a single, uniform value of geothermal heat flow for the entire model domain. The magnitude of this geothermal heat flow value has often been set according to the general geological setting for the area to be studied. Thermodynamic modelling of Fennoscandian ice sheets has, for instance, used a single geothermal heat flow value typical for the Pre-Cambrian shield, the most common reported value being 42 mW m^{-2} (e.g. Boulton and Payne 1992, Huybrechts and T'Siobbel 1995, Payne and Baldwin 1999). Others have used higher values, around 50–55 mW m^{-2} (e.g. Hindmarsh et al. 1989, Forsström et al. 2003).

For the model reconstruction of the Weichselian ice sheet, the geothermal data set of Näslund et al. (2005) was used as the basal boundary condition. A so-called higher-order model, taking into account longitudinal push-and-pull effects within the ice sheet was used for specific studies of ice-flow behaviour in relation to geothermal heat-flow anomalies in Sweden, see Näslund et al. (2005).

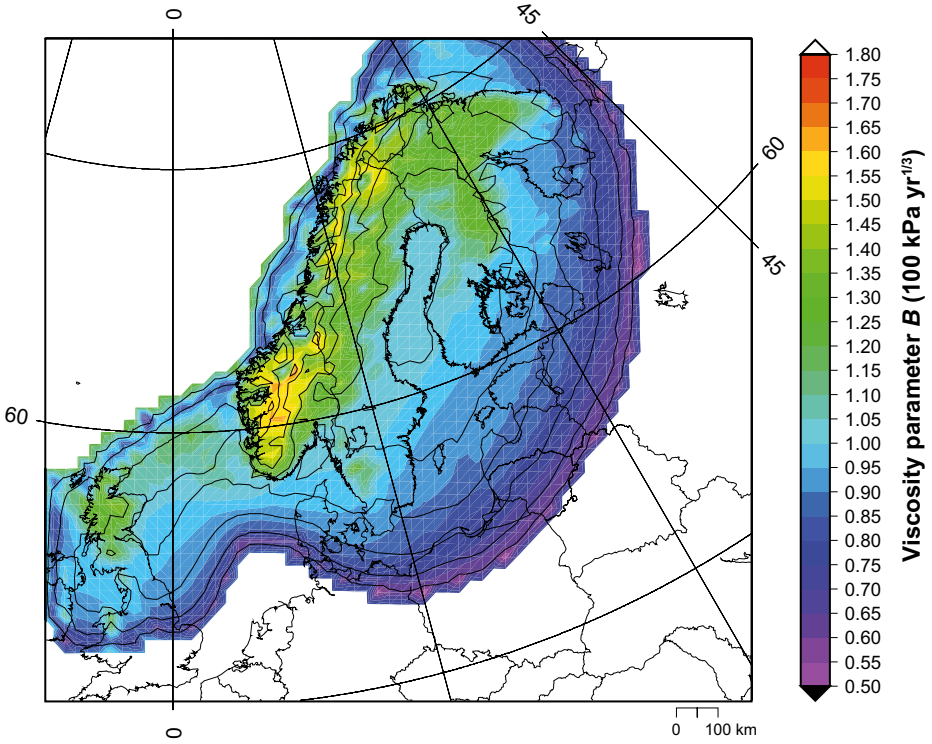

Figure 2-37. *Calculated flow-law viscosity parameter B at 18.5 ka BP (at around the Last Glacial Maximum), shown as vertically integrated values up the ice column. Colder and harder ice is seen in the central parts of the ice sheet and over the Scandinavian mountain range (larger B values), while warmer and softer ice is seen closer to the ice margin (smaller B values). The black lines show ice thickness contours with a 500 m interval.*

Model calibration. In studies in which ice-sheet modelling aims at simulating paleo-ice sheets, one needs to calibrate the behaviour of the model against known information on ice-sheet extents. The reason for this is that we do not have full knowledge on several the processes and boundary conditions involved, for example on climate, or ice-sheet basal processes. In the present reconstruction of the Weichselian ice sheet, the UMISM model was calibrated by adjusting the proxy air temperature (Figure 2-36). Over the years, many such simulations of the Fennoscandian ice sheet have been done with the UMISM model using this proxy air temperature, which has given extensive experience of how to perform the model calibration. As mentioned above, the forcing in temperature for the ice-sheet model is based on the GRIP ice core (Dansgaard et al. 1993), see also SKB (TR-10-49, Appendix 1). In the ice-sheet calibration process, the entire temperature time series was shifted and amplified (Figure 2-38) so as to obtain calibrated ice-sheet configurations that fitted as well as possible with geological observations on dated marginal positions. Model calibration was made for ice margins as described in Lokrantz and Sohlenius (2006) for MIS 5d (~ 110 ka BP), MIS 5b (~ 85 ka BP), MIS 4 (~ 60 ka BP), MIS 2 (~ 18 ka BP), and for the Younger Dryas (~ 12 ka BP) (Figure 2-38). Keeping all other input data constant in the calibration process, the modified temperature time series was obtained after model calibration results for Late and Middle Weichselian ice-sheet configurations in good agreement with dated ice-marginal positions and Early Weichselian configurations in reasonably good agreement with geological interpretations. The characteristics and applicability of the GRIP temperature time series for the present study is further described and discussed in SKB (TR-10-49, Appendix 1).

The resulting calibrated reconstruction of the Weichselian ice sheet is seen in Figure 2-36 and Figure 2-39. Ice extends over the model domain during the cold stadials during Marine Isotope Stages (MIS) 5d, 5b, 4, and 2. During warmer interstadials, such as MIS 3, the ice cover is more restricted. As expected, there is a clear trend of more and more pronounced ice coverage during the stadials through the glacial cycle, with the LGM peak occurring at around 18 ka BP.

Different types of output data have been extracted and post-processed from the reconstruction of the Weichselian ice sheet, for example 1) basal and surface melt rates for groundwater modelling (Jaquet and Siegel 2006), 2) basal and subaerial temperatures for permafrost modelling (Section 2.1 and SKB TR-10-49, Appendix 1 and 3), 3) ice-thickness variations for modelling of global isostatic adjustment (Section 2.2) and crustal stresses (Lund et al. 2009), and 4) 2D ice-sheet profiles for modelling of groundwater flow under glacial conditions (Vidstrand et al. 2010), see also Appendix E.

For more information on the ice-sheet model, see SKB (TR-10-51) and for further descriptions of model simplifications and uncertainties, see Section 2.3.7.

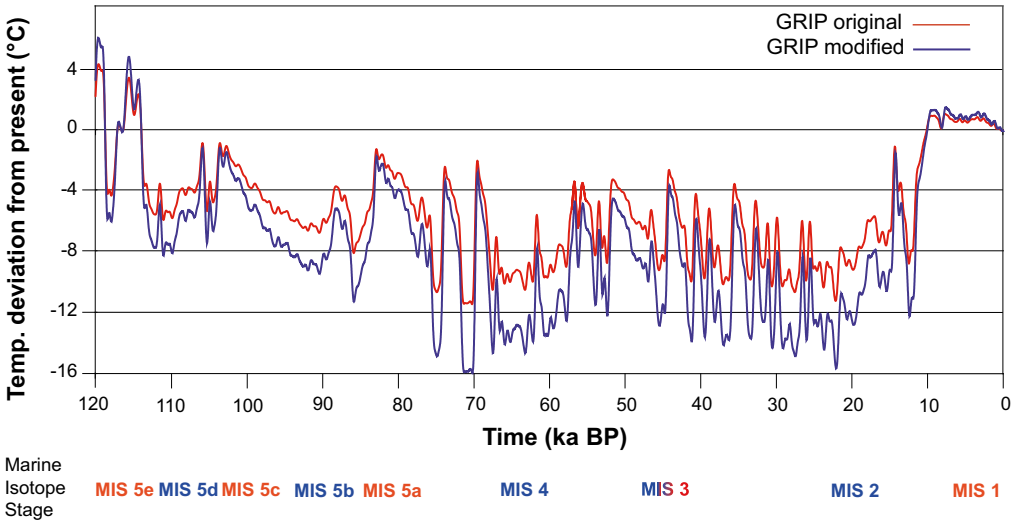

Figure 2-38. *Proxy paleo-air temperature from the calibration process of the UMISM ice sheet model. The final calibrated time series used in the ice sheet modelling (blue) has larger amplitude than the original data (red), i.e. cold periods were even colder in the calibrated time series. Modifications of the temperature data set were performed for the complete time series.*

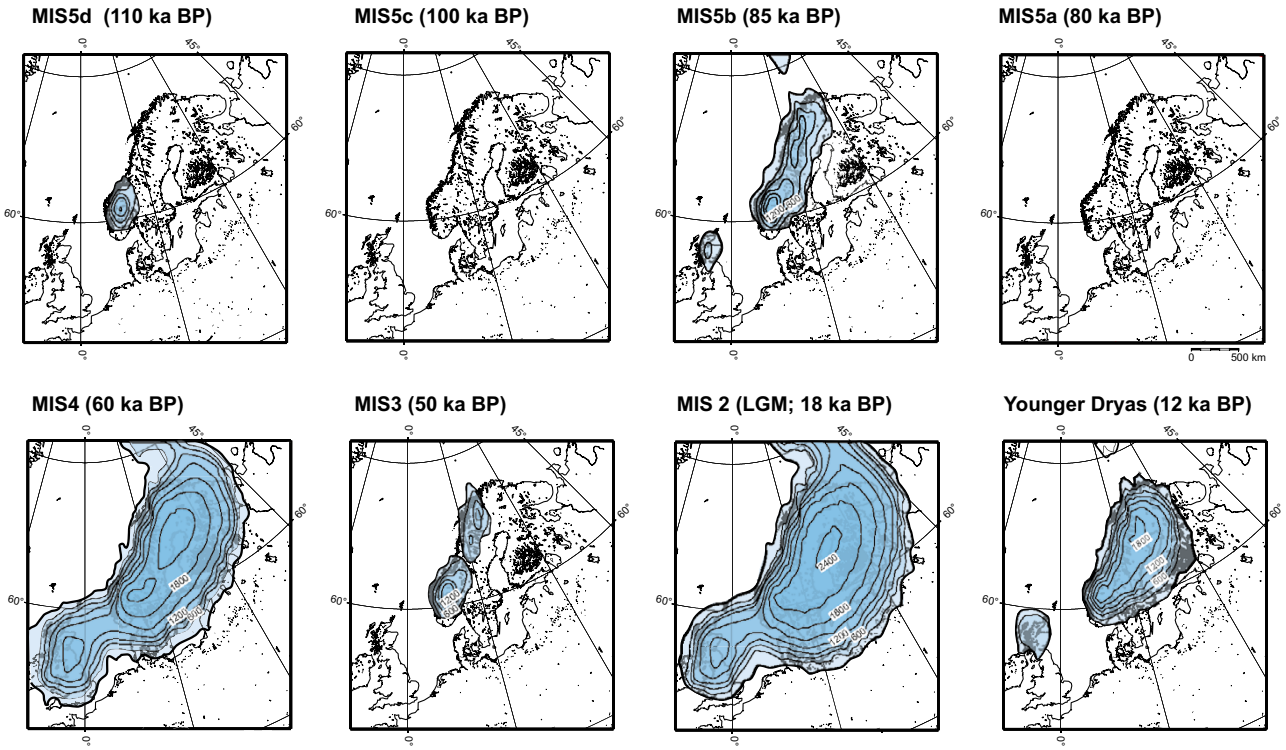

Figure 2-39. *Selected maps of ice-sheet surface topography for the reconstructed Weichselian ice sheet. The ice sheet grows to its full LGM configuration in progressive phases of increasing maximum extent, with intervening periods of more restricted ice coverage. Contour lines show ice-surface elevation with a 300 m contour interval. All maps show present-day shoreline position.*

2.3.5 Time perspective

It is generally agreed that ice sheets take longer to grow than to decay. However, our knowledge of the final deglaciation phase is much better than of inception phases, reflecting the fact that there are more geological traces from the last deglaciation than from earlier stages. Since ablation by surface melting is a more efficient process than snow accumulation, this suggests that the time for ice-sheet decay should be shorter than the growth time (Paterson 1994). In reality, this is accentuated due to efficient ice-shelf-calving processes for marine parts of ice sheets, for example calving of the Fennoscandian ice sheet in the Gulf of Bothnia. In line with the present modelling results of the Weichselian ice sheet (Figure 2-36 and Figure 2-39), it is generally concluded that ice sheets may build up in a series of glacial build-up periods, peaking in a glacial maximum close to the end of the glacial. The Fennoscandian ice sheet seems to have exhibited such dynamic behaviour during the last glacial cycle, see Section 3.2. This has also been inferred from studies of so-called Heinrich events (cf. Heinrich 1988) recorded in North Atlantic marine sediments, suggesting that even large ice-sheet systems are dynamic features, responding relatively quickly to rapid changes in climatic forcing.

During the last 800 ka, glacial cycles have typically lasted about 100 ka, with interglacials lasting around 10 to 20 ka (e.g. McIntyre et al. 2001, Tzedakis et al. 2009). As noted above and discussed in Section 3.2, the last glacial cycle was also characterised by a number of cold growth phases and intervening warmer periods with less ice, although from the geological record we still do not know how to date or correlate all observed interstadial localities (Lokrantz and Sohlenius 2006). A typical cold Weichselian stadial had a duration of some ka, see e.g. Figure 2-36 and Section 3.2. The deglaciation of the Weichselian ice sheet from the LGM ice margin to the last ice remnants in the Scandinavian mountain range took about 8 ka. During the deglaciation, several temporary halts, and in some cases also re-advances, took place, the most pronounced one occurring during the Younger Dryas (about 13–11.5 ka BP).

2.3.6 Handling in the safety assessment

The evolution of ice sheets is investigated by means of numerical modelling. In this context, the main question for the safety assessment concerns the timing of potential periods of ice-sheet development over the Forsmark site. Following an advance and retreat of an ice sheet over the site, the integrity of the engineered barriers cannot be expected to be retained. As a consequence, human settlements that emerge at the site subsequent to a glaciation may experience an enhanced risk of being exposed to radionuclides. Thus, the occurrence of temperate conditions *following* a succession of glaciated and submerged conditions at Forsmark is of particular interest in the safety assessment.

The ice-sheet model simulation of the Weichselian glaciation described in Section 2.3.4 is used to define periods of glacial conditions at Forsmark in the *glaciation climate case* (Section 5.3.1). These periods approximately coincide with the timing of anticipated future periods of ice-sheet growth in the Northern Hemisphere (Section 3.4.5). The succession of glacial, submerged and temperate conditions at Forsmark is unlikely to occur within the coming 100 ka (Section 4.4). Therefore, the effects of an ice sheet advancing over the Forsmark site, as described by the *glaciation climate case*, are analysed in a less probable scenario (**Post-closure safety report**, Section 8.3).

It should also be noted that glaciation at Forsmark may result in an increased denudation of the bedrock surface. This issue is discussed in detail in Section 2.4.

2.3.7 Handling of uncertainties

Uncertainties in mechanistic understanding

Model simplification uncertainty. The most important simplifications made in the ice-sheet modelling in the model reconstruction of the Weichselian ice sheet are the following.

The proxy temperature driving the model is the GRIP Greenland temperature time series. First, these data describe the climatic conditions for Greenland, but in the absence of similar paleoclimate data from Fennoscandia, or other closer areas, these are the best data available. With the applied modelling approach, the Greenland proxy data generate Fennoscandian ice sheets that are in fair agreement with geological information on LGM and Younger Dryas ice-margin positions, even *without* model calibration, which is a justification that this approach is valid. There are also uncertainties introduced by the conversion from oxygen isotope values in the ice core to Greenland paleo-air temperatures (Johnsen et al. 1995), see also SKB (TR-10-49, Appendix 1).

To improve the simulated Weichselian ice-sheet configurations, the model was calibrated against dated marginal positions as interpreted in studies of Quaternary geology and glacial history. One feasible way to make this calibration is to make use of the model input parameter estimated to have the largest uncertainty, in this case the last glacial cycle air temperature time series obtained from proxy data. In the present study, the air temperature was therefore selected for adjustment in the model calibration process. The full temperature time series was adjusted in a systematic way until a better fit was obtained between modelled and interpreted/observed ice-sheet configurations. For details, see Section 2.3.4. In the model, the amount of basal sliding is coupled to the thickness of the basal water layer of the ice sheet. This is a simplification but is a reasonable way of handling the difficult topic of basal sliding and the coupling between glacier hydrology and ice-sheet dynamics. One thing that is excluded in the model is the possible presence of subglacial deformable sediments, for example in the Baltic depression, which may enhance ice velocities, especially in ice streams. The exclusion of the effects of such sediments could, in some cases, lead to some overestimation of ice thickness.

The UMISM model used in the present study employs the so-called shallow ice approximation. This means that the horizontal velocity only depends on the local driving stress. Horizontal englacial stresses are neglected, i.e. there are no push-and-pull effects within the ice sheet, as in nature. This is a reasonable and appropriate assumption for the major part of the ice sheet, except for near-marginal locations and at ice divides. However, it is judged that the model has not been used in such detail that the results would be significantly different if a higher-order ice-sheet model (e.g. Pattyn 2003) had been used.

In the UMISM model, horizontal advection of heat was not included in the thermodynamic treatment of the ice. The result is that the model may overestimate basal ice temperatures to some extent. This is likely to be of importance only in fast-flowing situations like ice streams.

The hydrostatically supported elastic plate model included in the UMISM model is a simplification, but is adequate for adjusting bed- and ice-sheet surface elevations to obtain a reasonably good surface mass balance.

The UMISM model does not include an ice-shelf model. Instead, ice shelves are simulated by adjusting a marine calving rate directly at the dynamic grounding line.

The spatial resolution of model domain is approximately 50 × 50 km. This resolution may, in some cases, be too coarse to correctly depict smaller features in for example geothermal heat flow pattern.

Input data and data uncertainty

The proxy temperature. See section on Model simplification and uncertainty above, Section 2.3.4 and SKB (TR-10-49, Appendix 1).

Digital elevation data. The accuracy and spatial resolution of the ETOPO2 DEM is sufficient for the 50 × 50 km and 10 × 10 km resolution ice-sheet model simulations performed.

Geothermal heat flux. The high-resolution data set on spatially varying geothermal heat flux is of high quality in the context of ice-sheet modelling. In the new data set, high resolution geothermal data are available only for Sweden and Finland, not for the entire area covered by the Weichselian ice sheet. However, this does not affect modelled basal conditions in Sweden, since basically all parts of Sweden are located down-stream from areas with high-resolution data. There are assumptions made in the calculation of the data set that could be refined to improve the data set in the future, for example using a varying lithospheric thickness in the calculation of surface heat flow. Also, denser data on γ-emission measurements from bedrock are available for parts of Sweden, which may be used for future versions of the data set. All in all, this new type of ice-sheet model input has improved ice-sheet modelling significantly from all previous reconstructions of paleo-ice sheets by numerical modelling.

Sea level. The sea-level data used as input were derived from numerical ice-sheet modelling of all Northern Hemisphere ice sheets. The present volume of the Antarctic ice sheet was held constant. The maximum lowering of sea level in this data set is 100 m, somewhat less than the ~ 120–135 m of global sea-level lowering at the LGM deduced from coral-reef data (Yokoyama et al. 2000). However, this is of minor importance since the position of the grounding-line in the western Atlantic part of the ice sheet is determined by the bed topography (i.e. continental shelf location), and the eastern part is advancing and retreating over the Baltic Sea which does not have contact with the Atlantic during such low global sea levels.

2.3.8 Adequacy of references

The SR-Can and SR-Site Climate reports (SKB TR-06-23, SKB TR-10-49), which report some of the studies that have been used, have undergone QA system handling including a factual review process. Other references used for the handling of ice-sheet dynamical processes are either peer-reviewed papers from the scientific literature or from a textbook (Paterson 1994).

2.4 Surface denudation

2.4.1 Overview/general description

The downwearing of the Earth's surface by exogenic processes is accomplished by weathering, erosion, and transportation of material. The combined effect of all weathering and erosion processes is referred to as denudation, i.e. denudation is the sum of the processes that results in the wearing away or the progressive lowering of continental relief. The energy needed for the denudation processes is

gained from endogenic and exogenic sources. Glacial erosion is usually regarded as the dominant erosion process in Fennoscandia during the Quaternary. However, as large parts of Fennoscandia were not covered by ice during significant periods of the Quaternary (Porter 1989) including the last glacial cycle (Section 3.2), other denudation processes must also be considered in quantifications of erosional budgets (e.g. Lidmar-Bergström 1997).

Weathering

Weathering can be defined as mechanical and/or mineralogical break down of rock to form regolith through the cumulative effects of physical, chemical and biological processes operating at or near the surface (e.g. Reiche 1950, Selby 1993). The definition indicates that weathering occurs when minerals/rocks are exposed to temperatures, pressures and moisture conditions characteristic of the atmosphere and hydrosphere, i.e. in a near-surface environment that differs significantly from the conditions at depth in which most igneous and metamorphic rocks, as well as lithified sedimentary rocks, were formed. In this way, the alteration of rocks by weathering forms new materials (minerals) that are in near-equilibrium with conditions at, or near, the Earth's surface.

By definition, weathering occurs in situ and does not directly involve erosion. This means that it leads to the formation of a residual material that differs from the parent, unweathered rock with respect to its physical and chemical properties. Weathering normally lowers the strength of rock and increases the permeability of the surface material and thus makes it more prone to mass wasting and easy to erode by running water, glaciers, wind etc. In addition, it is also an important prerequisite for the widespread development of flora and fauna on land by releasing nutrients to soils that are taken up by plants and other organisms.

Weathering is generally divided into physical-, chemical- and biological components. Physical or mechanical weathering occurs when volumetric expansion or other stresses lead to failure and disintegration of the rock. For example, volume changes due to decreased overburden load can result in the creation of new fractures at various scales. Crystallisation and volumetric alteration of salt crystals, freezing of water and freeze-thaw effects, as well as thermal fatigue due to repeated (diurnal) heating and cooling, may also cause physical weathering.

Chemical weathering comprises reactions between water and rock minerals. Examples are solution of minerals, carbonation, hydrolysis, hydration, and oxidation and reduction. Common to chemical weathering processes is that they depend on water composition, for example pH, salinity, CO_2 and redox potential. The prevailing temperature is another important parameter determining the type and efficiency of chemical weathering.

Under present temperate climate conditions in Sweden, weathering occurs slowly where bedrock is exposed. Swantesson (1992) has estimated the postglacial weathering of bare bedrock surfaces in southern Sweden during the Holocene to be less than 0.02 m. Weathering rates beneath soils in tropical climates range between 2 and 48 m Ma^{-1} (Thomas 1994). Although the tropical weathering rates have a large span, due to differences in rock type, temperature and humidity conditions, they show that weathering is a slow process even under the most favourable tropical climatic conditions.

For a description of climatological-, hydrological- and geological factors affecting weathering, see e.g. Olvmo (2010, Section 3.3.3). Estimated denudation rates for the Forsmark region are presented and discussed below.

Erosion

Erosion can be defined as the removal and transport of bedrock and earth materials by a moving natural agent, such as air, water or ice. Erosion is often preceded by weathering and followed by transport and sedimentation. Air or water flowing over a bed of loose particles generates a shear stress that tends to initiate particle movement (Collinson 2005a). There is a critical boundary shear stress related to wind velocity and turbulence and water flow velocity above which particle movement occurs. With the exception of small grain sizes, the critical shear stress will increase as the grain size increases. For small grain sizes (less than 0.1 mm, silt and clay) increased cohesive strength and lower surface roughness means that higher velocities are required to initiate movement. In this section, a brief description is given of the main mechanisms of aeolian-, marine-, fluvial- and glacial erosion.

Aeolian erosion

Erosion of sediments by the wind, i.e. aeolian erosion, occurs in environments with sparse or non-existent vegetation, a supply of fine-grained sediments and strong winds, for example periglacial regions, semi-arid and or arid. Aeolian processes depend on weathering or other natural agents, e.g. rivers and waves, to supply sediments for transport. Particle movement is achieved due to wind shear stress and atmospheric turbulence. Particles begin to move when wind forces exceed the effect of weight and cohesion; the first particles to move dislodge or impact other grains and the number of particles in movement increase exponentially. However, the particles reduce the near-bed velocity of the wind and the transport reaches a dynamic equilibrium state in a few seconds. The mass flux of particles is related to the wind shear velocity, abrasion and the impact of particles moved by saltation and creep. The latter mobilise fine-grained material affected by cohesion but easily carried by the wind. Thus, the transport rate is limited both by wind shear velocity and the supply of particles.

Marine erosion

Marine erosion is largely limited to the reworking of sediment in the shore zone. In regions of rapid post-glacial emergence, such as in the Forsmark region, it is very low in solid rock because a shoreline at a given elevation is exposed to marine erosion for only a short period of time. Furthermore, the smooth, glaciated surfaces generally lack loose, fractured rock that can be exploited by wave action. Also, the wave energy in the Baltic Sea is relatively low, reducing the efficiency of marine erosion further.

Fluvial erosion

Less than 0.005 % of the global water is stored in rivers. Nevertheless, they are one of the most, if not the most, potent erosional forces operating on the Earth's surface. Rivers cut valleys, transport sediments and deposit their loads in a variety of depositional environments, such as flood plains and deltas. Vertical erosion by rivers is a striking feature of the world's mountainous areas where deep valleys dissect the landscape and form steep slopes, thereby creating the conditions for mass movement processes that are closely linked to fluvial vertical erosion.

Erosion and deposition of particles by water, i.e. fluvial erosion and deposition, is related to flow velocity. To generate water flow, a water supply and a flow gradient are required. Therefore, erosion by water generally requires a slope. Fluvial erosion occurs on slopes, in ditches, and in brooks and rivers. As with wind erosion, erosion by water depends on shear stress and turbulence, and particles begin to move when water fluid forces exceed the effects of weight and cohesion.

The material is transported in two distinct ways, it is either carried along with the fluid or it is in intermittent contact with the bed, described in e.g. Collinson (2005b). In the first case, fine-grained particles are supported by the upwards component of turbulence and carried away with the fluid in suspension. In the second case, generally referred to as bedload transport, coarser-grained material rolls (creep or erosion reptation) or bounces (saltation) on the bed. Particles carried in suspension will enhance the erosive capability of the fluid by abrasion and particles moved by saltation, creep or reptation will set other grains in motion.

Fluvial erosion at the base of slopes releases material that is transported to brooks and rivers, and into lakes and the sea. Erosion by water on a slope increases with increased intensity of rain or snowmelt, increased inclination and length of the slope and decreased resistance to erosion of the soil. As for wind erosion, the presence of vegetation may strongly reduce the erosion rate. For more information on fluvial erosion, see e.g. Olvmo (2010, Section 4.1) and references therein. When rivers reach the sea, the flow velocity falls, erosion ceases and the sediment load is deposited.

Glacial erosion

Glacial erosion has been the dominant process of erosion in and around the Baltic Sea Basin over at least the last 1 Ma (e.g. Hall and van Boeckel 2020). Glacial erosion is complex and depends on material properties of ice and rocks, ice thermodynamics, friction and lubrication at the ice/bed interface, chemical effects and subglacial hydrology. In addition, glacial erosion in bedrock is enhanced by pre-glacial sub-aerial weathering processes.

In recent years, interpretations of geomorphological features (e.g. Kleman et al. 1997, 2008), measurements of cosmogenic radionuclides (e.g. Stroeven et al. 2002a, Hall et al. 2019a) and ice-sheet modelling (e.g. Näslund et al. 2003) have identified the high variability of glacial erosion over Fennoscandia. In some areas, over time dominated by basal frozen conditions, glacial erosion has been limited, whereas in other areas, where basal melting and sliding have occurred (see Section 2.3), erosion has been considerable.

Glacial erosion is traditionally divided into two components; plucking and abrasion. Plucking is the process by which rock fragments of different size are loosened, entrained and transported away from the glacier bed. Plucking is responsible for the characteristic irregular and fractured surfaces of lee sides of bedrock bumps and small hills in formerly glaciated areas. Abrasion is the grinding of the substrate by rock fragments held in moving basal ice (cf. Sugden and John 1976, Benn and Evans 1998). Abrasion scours the bedrock by debris carried in the basal layers of the glacier (cf. Sugden and John 1976, Drewry 1986). The process leads to striation and polishing of bedrock surfaces (cf. Benn and Evans 1998) and is typical of the stoss side of rock bumps in formerly glaciated terrain. Yet another process of glacial erosion, called glacial ripping, have recently been suggested by Hall et al. (2020). This process invokes disruption of surficial bedrock by dilation of bedrock fractures under high hydrostatic pressures. Resistance to movement is reduced so that traction from the overriding ice sheet causes disintegration of rock surfaces and ripping apart into blocks.

Most glacial erosion exploits existing rock fractures, but subglacial processes can form new fractures at different scales. Pre-existing weakness, such as joints, cracks and foliation, and also pre-glacial weathering, exert strong control over rock mass strength (cf. Olvmo and Johansson 2002). Glacially induced cyclic water pressure variations may be important for new bedrock crack propagation (e.g. Hooke 1991, Iverson 1991), a process by which rock fragments may be formed and eroded from the bedrock. Many minor fracture features, such as chattermarks and crescentic gouges, observed on glacially affected rock surfaces, indicate that normal stress at the glacier bed, exerted by clasts travelling over the bed, may be sufficient to cause failure in some rocks. Loosening of rock fragments along fractures is caused by stresses set up by differential ice loads and high water pressures at the ice-bedrock interface (cf. Sugden and John 1976, Drewry 1986, Benn and Evans 1998). Melting of ice on the stoss side and refreezing of meltwater on the lee side of obstacles at the ice-sheet bed may occur under certain thermal and pressure conditions. This so-called regelation process may also contribute to glacial erosion and transportation of subglacial till (e.g. Iverson 1993, 2000).

The magnitude of glacial erosion by ice-sheets differs widely both in time and space. At a continental scale, the large-scale pattern of glacial erosion is controlled by ice-sheet thermal regime and topography of the subglacial landscape. Based on a simple glaciological model Sugden (1977, 1978) made a reconstruction of the thermal regime of the Laurentide ice-sheet. The reconstructed thermal pattern shows an inner wet-based area and an outer cold-bed area, which broadly corresponds to the pattern of glacial erosion indicated by the distribution of erosional landforms. The most intense erosion as indicated by areas with high lake density coincide with the transition zone between wet-based and cold-based ice in the model, which probably favours plucking and debris entrainment.

Näslund et al. (2003) used a numerical ice-sheet model to study regional ice flow directions and glacial erosion of the Weichselian ice-sheet in Fennoscandia. The quantity ‘basal sliding distance’ was introduced, describing the accumulated length of ice that has passed over the landscape by basal sliding. It was suggested that this entity could be used as a proxy for glacial erosion. The results indicate high basal sliding distance values in SW Sweden/SE Norway, in the Skagerrak, and along the Gulf of Bothnia, implying relatively large amounts of glacial erosion in these regions. On elevated parts of the Scandinavian mountain range and on adjacent plains in the east the basal sliding distance values are low, implying weaker glacial erosion, which is fairly in agreement with geological and geomorphological evidence (cf. Lagerbäck and Robertsson 1988, Riis 1996, Stroeven et al. 2002b, Olvmo et al. 2005). The method of estimating glacial erosion by simulated basal sliding distance (Näslund et al. 2003) was further developed by Staiger et al. (2005) who introduced a normalization of the sliding values by the duration of ice cover over a site. Staiger et al. (2005) also set up a relationship between normalized sliding distance and rate of glacial erosion. A basal sliding parameter is integral to recent ice sheet erosion models (e.g. Patton et al. 2016).

Another approach to the issue of glacial erosion is presented by Hallet et al. (1996) who made a comprehensive review of glacial erosion rates based on sediment yields. They found that rates of glacial erosion vary by many orders of magnitude from 0.01 mm yr^{-1} for polar glaciers and thin temperate plateau glaciers on crystalline bedrock, to 0.1 mm yr^{-1} for temperate valley glaciers also on resistant crystalline bedrock in Norway, to 1.0 mm yr^{-1} for small temperate glaciers on diverse bedrock in the Swiss Alps, and to 10–100 mm yr^{-1} for large and fast-moving temperate valley glaciers in the tectonically active ranges of southeast Alaska. These major differences highlight the importance of the glacial basal thermal regime, glacial dynamics and topographic relief on the rates of glacial erosion.

Yet another approach was presented by Påsse (2004). To estimate the average glacial erosion in the bedrock in non-mountainous regions he used seismic data and well-depth data on the thickness of the minerogenic Quaternary sediments in Sweden and Denmark. The average thickness of Quaternary sediments was estimated to be 16 m in the investigated area, which corresponds to 12 m of bedrock assuming that the whole volume is the result of glacial erosion of fresh bedrock. Since a part of the sediments likely consists of glacially redistributed Tertiary regolith, this number may be an overestimation of the glacial erosion depth in the bedrock. Considering this, Påsse concluded that the average glacial erosion during a full glacial period may be estimated to between 0.2 m and 4 m. This agrees with estimates of glacial erosion in the Precambrian basement based on geomorphological observations (Lidmar-Bergström 1997, Ebert 2009). Lidmar-Bergström distinguishes the estimates of glacial erosion of Tertiary saprolites (decomposed rock formed by weathering) from glacial erosion of fresh bedrock. The glacial erosion of saprolites is estimated between 10 and 50 m and glacial erosion of fresh bedrock is estimated at some tens of metres (Lidmar-Bergström 1997), although with great variations. Comparison of Pleistocene sediment volumes with geomorphological evidence for glacial erosion around the Baltic Sea Basin support depths of glacial erosion on basement in Sweden of 20 m over the last 1 Ma (Hall and van Boeckel 2020).

However, in Fennoscandia as a whole, large spatial differences in thicknesses of Quaternary deposits occur and distinct patterns of glacial scouring and deep linear erosion are observed in places. Kleman et al. (2008) point to the relative roles of mountain ice-sheets and full-sized Fennoscandian ice-sheets for this zonation and use spatio-temporal qualitative modelling of ice-sheet extent and migration of erosion and deposition zones through the entire Quaternary to suggest an explanatory model for the current spatial pattern of Quaternary deposits and erosion zones.

Also, on a more regional to local scale, the amount of glacial erosion of basement rock may vary considerably, as demonstrated for the Forsmark region by Hall et al. (2019a), see Section 2.4.4.

Glacial meltwater erosion may be an effective agent of erosion along meltwater routeways both in subglacial and proglacial environments. The sediment concentrations of glacial meltwater streams are often high, and the flow is often rapid and turbulent, which mean that flows transitional between debris flows and normal stream flow are common (Benn and Evans 1998). The erosivity of glacial streams is therefore often high both on bedrock and sediments. Apart from the high erosivity and the potential for high hydrostatic pressure in meltwater tunnels, the mechanisms of glacial meltwater erosion are the same as normal fluvial erosion including abrasion, cavitation, fluid stressing and particle entrainment from cohesionless beds as well as chemical erosion.

The relative efficacy of fluvial and glacial erosion, on a global basis, is presented in Koppes and Montgomery (2009). For a more detailed description of erosional and weathering processes relevant for Fennoscandian conditions and the Forsmark area in a 0.1 to 1 Ma time perspective, see Olvmo (2010). Estimated denudation rates for the Forsmark region are presented and discussed below.

2.4.2 Controlling conditions and factors

As mentioned above, weathering and erosion are complex processes affected by the prevailing environmental conditions. Given the characteristics of the rock, the degree of weathering depends on the availability of weathering agents such as salt, moisture, biota (e.g. microorganisms and lichens), and on the microclimatic conditions to which the rock is exposed. Weathering occurs in all climates, but high temperatures and humid conditions increase weathering rates. In areas where frost and/or permafrost occur, freezing and freeze-thaw effects are important geomorphic processes. However, weathering in periglacial environments is also affected by salt (in combination with freezing), wetting and drying, thermal fatigue and biological agents (French 2007).

During temperate climate conditions, the dominant erosion process is fluvial erosion. During periglacial climate conditions, when the climate can be expected to be drier and vegetation sparse, aeolian erosion may also be important. During spring when the snow melts, there may be significant erosion of sediments in the active layer in periglacial permafrost areas. Under glaciated conditions, ice-sheet erosion is paramount. It is mainly affected by the prevailing thermal and physical conditions at the ice-sheet/substrate interface. In areas where the ice is frozen to the bed, the ice acts to preserve its subsurface and practically no erosion occurs, whereas in areas of basal melting, erosion of bedrock and pre-existing sediment is likely to occur, with more erosion generally associated with faster ice flow. In sub-glacial tunnels, where melt water flows towards the ice-sheet margin, erosion of loose sediments and bedrock can be significant.

The topographic relief in Fennoscandia is generally low outside the Scandinavian mountains (e.g. Lidmar-Bergström and Näslund 2005). The resistance to denudation of the Precambrian rocks that dominate in Fennoscandia is rather uniform, as compared with, for example, the variation between the Caledonian bedrock types in the Scandinavian mountains. Although the relief locally may be steep at many places, the relatively homogeneous denudation resistance has contributed to the moderate to low relief of the Precambrian rock basement. Available relief is generally controlled by fracture patterns at different scales. The relative relief is exceptionally low (up to a few tens of metres) along significant portions of the Baltic Sea coastline of southern and south-central Sweden, due to the presence of the *sub-Cambrian peneplain*. This peneplain is interpreted as a denudation surface formed in crystalline rock down to sea level prior to the Cambrian period (cf. Rudberg 1954, Lidmar-Bergström 1995), with a typical relief of less than 20 m. A more recent study in southern Sweden by Hall et al. (2019b) follow the same overall interpretation of the sub-Cambrian peneplain but uses the term sub-Cambrian unconformity, emphasising the importance in the Uppland province of relief inheritance from this basement unconformity. An alternative explanation for the formation of specific parts of this flat denudation surface in southern Sweden, involving glacial erosion processes, have been presented by Goodfellow et al. (2019).

The low relief of this crystalline bedrock surface favours low subaerial erosion rates. The most important subaerial erosion process, fluvial erosion, increases with steeper topographical gradients.

Table 2-6 summarises how geosphere variables are influenced by surface denudation.

Table 2-6. Influence of surface denudation on geosphere variables.

Geosphere variable	Influence present (Y(N)	Summary of influence
Groundwater flow	Yes	The process refers to weathering and erosion at the surface. Even if there is no absolute boundary between surface- and groundwater this process only includes the action of surface water. Denudation could under certain circumstances affect permeability and thus the degree of infiltration, which would, marginally, change groundwater boundary conditions.
Groundwater composition	Yes	Surface weathering may to some degree change groundwater composition.
Rock stresses	Yes	The removal of bedrock by denudation changes the stress field.
Fracture geometry	Yes	Weathering may change fracture aperture in the upper metre of bedrock, for instance by widening of fractures due to freezing.

2.4.3 Natural analogues/observations in nature

The current landforms in Fennoscandia are a result of the interaction between tectonic processes, weathering, erosion and sedimentation and consequently the traces of these processes can be observed and interpreted in nature. In Fennoscandia, large-scale bedrock landforms outside the Scandinavian mountain range, such as denudation surfaces and landscapes of weathering and stripping of saprolites, are common, and reflect the varying phases of weathering, erosion, and sedimentation that have

occurred in association with tectonic events and climate change (e.g. Lidmar-Bergström 1997, Lidmar-Bergström and Näslund 2002).

Forsmark is situated inside the Svecokarelian orogen, active at 1.9–1.8 Ga, in the south-western part of the Fennoscandian Shield, a basement terrain which forms one of the ancient continental crustal fragments on Earth (Stephens 2010). Far-field tectonic events after 1.8 Ga included orogenic activity related to crustal build-up and crustal reworking at 1.7−1.6 Ga, at 1.6−1.5 Ga (Gothian), at 1.5−1.4 Ga (Hallandian) and at 1.1−0.9 Ga (Sveconorwegian), rifting during the Meso- and Neoproterozoic, and rifting and the development of a passive continental margin in the northern part of Europe during the latest part of the Neoproterozoic and the Cambrian (e.g. Stephens 2010). Deep denudation was largely complete by ~ 1.5 Ga when Jotnian sandstones were deposited on hilly to low relief basement surfaces on what is now the floor of the Bothnian Sea off Uppland (Hall et al. 2019a). These cover rocks, plus any additional sedimentary cover that once accumulated in the Sveconorwegian foreland basin, were removed from Uppland by the time of formation of the sub-Cambrian peneplain at ~ 541 Ma. The juxtaposition of the sub-Jotnian and sub-Cambrian unconformities at approximately the same erosional level indicates the exceptional stability of the craton over the last 1.5 Ga (Hall et al. 2019a). Although the craton has been buried repeatedly by thick foreland basin sediments (Larson et al. 1999), since eroded away, the ancient basement surface has experienced limited erosion.

During the Quaternary glacial cycles, ice-sheets have repeatedly covered parts or the whole of Fennoscandia, producing glacial erosional landforms in bedrock (e.g. Rudberg 1954) and moulding surficial deposits to form landforms such as drumlins (e.g. Kleman et al. 1997, 2008). Traditionally, it has been thought that a considerable part of the bedrock relief is a result of glacial erosion. However, as mentioned above, it has been shown that the amount of glacial erosion of Precambrian basement rock in low-land areas of Sweden in general is on the order of a few tens of metres (Lidmar-Bergström 1997, Hall et al. 2019a), with more erosion along valleys and depressions. Within the Scandinavian mountain range, valleys may have experienced several hundred metres of glacial erosion (Kleman and Stroeven 1997). Furthermore, during the last decades, our understanding of ice-sheet thermodynamics has developed a lot, showing that different parts of the ice sheet may have very different potential for glacial erosion, and that this changes in time and space during the course of a glacial cycle. Large portions of ice-sheets may be cold-based and thus have a negligible erosive effect. Over the same period, numerous glacial geological studies have shown that the occurrence of pre-glacial saprolite remnants is solid evidence that ice-sheets under certain circumstances cause very restricted glacial erosion, or even have a preserving effect on pre-glacial landforms (Lagerbäck 1988a, b, Kleman 1994), whereas under other conditions they may be highly erosive.

The long-term denudation history of southern Sweden is interesting for two reasons. Firstly, it may help to understand the denudation rate through time in the Forsmark area. Secondly, it is important because the different landforms and surfaces that have been recognised, such as the sub-Cambrian peneplain mentioned above, may be used as reference surfaces to understand the magnitude and patterns of denudation and glacial erosion since the surface formation, at least on a regional scale (cf. Hall et al. 2019a). Some examples from Sweden of calculated long-term denudation rates are available, most of them using ancient smooth bedrock denudation surfaces (unconformities) as reference surface. In eastern Småland and southern Östergötland, the maximum denudation of the tectonically uplifted sub-Cambrian peneplain is approximately 100 m. Once overlying sedimentary cover rocks had been removed, denudation and removal of the denudation products would have required a period of between 2 and 50 Ma (Lidmar-Bergström et al. 1997). On the Swedish west coast, a so-called *Sub-Cretaceous etch surface* has been incised into the sub-Cambrian peneplain by weathering. In some places, it has resulted in a maximum bedrock lowering of 135 m. The time required for this amount of denudation has been suggested to be between 3 and 68 Ma (Lidmar-Bergström et al. 1997), with the denudation occurring during the Jurassic-Early Cretaceous (around 200–100 Ma). Finally, saprolite thicknesses of 50 m in Skåne were interpreted to have been produced by weathering over a time interval of 1–25 Ma (Lidmar-Bergström et al. 1997).

Given the specific tectonic and climatic evolution, including phases of denudation, sedimentation, and stripping of saprolites, the above examples clearly show that the evolution of the sub-Cambrian peneplain in southern Sweden into a younger incised landscape has been a slow process, and that the total amount of material removed from the crystalline bedrock has not been large considering the very long time periods involved. The total maximum denudation of bedrock in areas of Precambrian crystalline basement in southern Sweden during the last 540 Ma is on the order of a few hundred

metres. A significant part of this denudation took place during Mesozoic (250–65 Ma) tropical climate conditions, considerably more favourable for chemical deep weathering than for instance a temperate climate. More detailed accounts of the long-term landform development and associated denudation in southern Sweden are given in Olvmo (2010) and Hall et al. (2019b).

2.4.4 Model studies

Quantification of denudation can be made by i) numerical models that *per se* describe the processes involved in the denudation, for instance the processes resulting in glacial erosion, ii) by estimates based on interpretation of landform development over time, or iii) cosmogenic nuclide exposure dating. A review of numerical modelling of glacial erosion can be found in Fisher (2009), whereas the second approach may be exemplified by Olvmo (2010). Hall et al. (2019a) used both geomorphological analysis and cosmogenic nuclide analysis in studies of glacial erosion and long-term denudation history of southern Sweden and Forsmark.

From a bedrock geomorphological point of view, the Forsmark region (Figure 2-40) can be divided into distinctive areas with different relief: i) a central area, hosting the Forsmark site, characterized by less than 20 m topographic relief of basement rock, ii) a coastal region SE of Forsmark with coast-parallel lineaments, iii) a southern part with more pronounced relief characterised by east-west trending fault scarps, and iv) an area with hilly relief in the northwest (Olvmo 2010). The low relief in the central area, including the Forsmark site, is characteristic of areas where the present bedrock surface has not been significantly lowered from that of the sub-Cambrian peneplain, in line with the interpretation by e.g. Lidmar-Bergström (1997). This central area of low relief has been dislocated by block faulting and tilting (Grigull et al. 2019). South of this low relief central area, an area with the peneplain broken into smaller blocks as compared to the area around Forsmark is found. Some of the blocks are elevated and partly dissected by weathering and erosion. South of the Forsmark area, the elevated rims of the uplifted blocks give rise to east-west trending horst ridges (Grigull et al. 2019), whereas in the Stockholm region the peneplain is highly dissected and gives rise to a so-called *joint valley landscape*, consisting of plateaux bounded by shallow straight, structurally controlled valleys (Figure 2-40). In the coastal low-lying areas between Forsmark and Uppsala, the relief is quite considerable along coast parallel tectonic lineaments. Here, the relative relief locally rises to 50 m along these fracture zones, often where Jotnian and Ordovician sedimentary rocks have been eroded from small half-grabens (Hall et al. 2019a). In this area, ~ 25 km southeast of Forsmark, the coastal landscape is more dissected. The area coincides with areas with a high frequency of rock outcrops which suggests that glacial erosion has been more effective in this region than at Forsmark, probably due to the closeness to the Baltic Sea depression (Olvmo 2010, Hall et al. 2019a). The Baltic depression may both have been formed by, and been influencing, Fennoscandian ice-sheet flow (e.g. Holmlund and Fastook 1993, Clason et al. 2014, Hall and van Boeckel 2020).

Even if the Forsmark site is situated within the area of the sub-Cambrian Peneplain, the present extension of overlying Lower Palaeozoic sedimentary cover rocks is not far away (10–20 km, see Figure 2-40). For a description of the erosion and burial history of basement rock in this region, see Chapter 2 in Hall et al. (2019a). In the Forsmark area, the most elevated parts of the bedrock surface are probably close to the original peneplain surface (Olvmo 2010, Hall et al. 2019a). The bedrock relief (Figure 2-40) is up to a few tens of metres only, see Figures 2-11 and 2-19 in Hall et al. (2019a). Glacial lineations in the Quaternary drift cover and other glacial landforms are, in general, also common features in the landscape (e.g. Figures 4-13, 4-19, and 4-27 in Hall et al. 2019a). As previously mentioned, the low-relief bedrock surface around Forsmark is dissected by block faulting (e.g. Grigull et al. 2019) probably of post-Ordovician age (after ~ 450 Ma) (Hall et al. 2019a). Over the past 1.8 Ma, this area has been subject to relatively stable large-scale tectonic conditions (Lidmar-Bergström and Näslund 2002, Olvmo 2010, Hall et al. 2019a).

A comprehensive study on past and future denudation has been performed in the Forsmark area and elsewhere in lowland southern/south-central Sweden (Hall et al. 2019a, b, Goodfellow et al. 2019). The aim of the study was to quantify the total historical denudation at the Forsmark site, including glacial erosion, as well as related questions such as bedrock surface stability, by employing a range of methodologies. To this end, Hall et al. (2019a) used a combination of cosmogenic nuclide analysis, geomorphological analysis of bedrock landforms and landforms in Quaternary deposits, bedrock fracture analysis, and shallow bedrock stress modelling, with the overall purpose to quantify the

amount of denudation over the past 100 ka and 1 Ma. Another purpose was to assess the potential amount of glacial erosion over the coming 1 Ma. In the following, the main results of the Hall et al. (2019a) study are presented.

Quantification of past denudation – cosmogenic nuclide analysis

Quartz in 32 surface bedrock samples and three boulder samples collected at the Forsmark site and in neighbouring areas of the Uppland province (Figure 2-41) was analysed for paired cosmogenic ^{10}Be and ^{26}Al nuclide concentrations. For a description of the cosmogenic nuclide exposure dating technique, see Hall et al. (2019a), where bedrock sampling procedures are described in Section 5.2.1, exposure age calculations in Section 5.2.2, and glacial erosion simulation methodology in Section 5.2.3 in that study.

Under the assumption that all glaciations that previously covered the Forsmark area and the Uppland province eroded the crystalline basement rock with similar mode and intensity, and using minimum and maximum values on non-glacial denudation of 0 and 5 mm ka^{-1} for ice free periods, the mid-range (25 % and 75 % percentiles) of the total denudation (i.e. including glacial erosion and all other non-glacial denudation processes) over the last 100 ka was estimated by Hall et al. (2019a) to 1.6–3.5 m Table 2-7). The full range (0 % and 100 % percentiles) of the total denudation for the last 100 ka varies between 0 and 8.6 m. The corresponding mid-range of the total denudation for the last 1 Ma is 13–27 m with the full range varying between 2 and 61 m (Table 2-7). Since the calculated denudation values do not show a correlation against elevation above sea level, bedrock relief, bedrock hardness (Schmidt hammer R-values), bedrock fracture spacing, latitude or (glacial) terrain type, see Hall et al. (2019a), the mid-range values probably are representative of the mean denudation rates in the area. However, in this context it is also worth noting that updated simulations have been performed on the Forsmark cosmogenic samples since the publication of Hall et al. (2019a). In the new simulations, a central best-fit value is calculated together with an asymmetric positive and negative uncertainty (J. Heyman, personal communication October 2020), whereas for the values in Hall et al. (2019a) shown in Table 2-8, a simple min-max span was been calculated. The newer improved simulations provide similar results, but also show that the lower denudation values are more realistic than the higher ones (cf. Table 2-8).

The above ranges in denudation of basement rock represent variations of simulated denudation from point samples and illustrate that, as expected, glacial erosion (the most efficient denudation process in this region) has a strong spatial variation over the investigated areas. To a smaller extent, the ranges also reflect uncertainties in assumptions adopted regarding different modes of glacial erosion in the calculations of erosion depths (see Hall et al. 2019a, Section 5.2.3). Nevertheless, given the large number of samples and their wide spatial distribution, the ranges of denudation are well-clustered and they indicate limited denudation, and hence also limited glacial erosion, in this low relief landscape (Hall et al. 2019a). For a summary of values on total denudation of basement rock from the cosmogenic nuclide analysis, see Table 2-8.

Quantification of past denudation – geomorphological analysis

In order to further estimate the total past denudation of crystalline basement rock at Forsmark and the Uppland province, an analysis of the difference between a reconstructed summit envelope surface (with the idea of closely representing the sub-Cambrian peneplain or unconformity) and the present land surface was made (Hall et al. 2019a). Since the values obtained by this GIS method are calculated from the reconstructed reference envelope surface, which is constructed by connecting present-day summit heights and assuming zero denudation of these summits (see Hall et al. 2019a, Section 4.3.5), any lowering of the summits needs to be added to the numbers calculated in the GIS. In Hall et al. (2019a), the summit lowering was preliminarily estimated to be 10 m.

If adopting the 10 m surface lowering value (Hall et al. 2019a, Figure 4-46), the results indicates that a mean of ~ 24 m of basement rock has been lost, in total, to denudation across the north-eastern Uppland region up until present-day, with increasing depths of erosion towards the south (Hall et al. 2019a). At the Forsmark site (Hall et al. 2019a, Figure 4-47), the equivalent mean denudation depth in basement rock is ~ 22 m (Table 2-8). The smallest total denudation is around 10 m, whereas the larger denudation depths, often around 30 m, come from rock trenches and basins. The overall highest

denudation depth at the Forsmark site from this analysis (50 m) is found in the trench along the West Gräsö Fault that lies 10 km east of Forsmark (Table 2-8 and Hall et al. 2019a, Figure 4-47). At this specific location, the erosion has exploited a pre-existing fault/fracture zone along the western base of the Gräsö fault block. Note that at this site, the additional 10 m of surface lowering has not been added to the GIS denudation value since this site is located at close proximity to the margin of overlying Ordovician strata to the west, see Hall et al. (2019a, Figure 2-21). This proximity indicates recent re-exposure of basement rock for this site and hence negligible basement summit lowering. Typical denudation depths at the Forsmark site, as well as the denudation depths at the repository location, are considerably shallower than the 50 m value along the West Gräsö Fault). For a summary of values on total denudation of basement rock from the geomorphological GIS analysis, see Table 2-8.

In this context, it is worth noting that the denudation depths obtained by the cosmogenic nuclide analysis over the past 1 Ma were larger than the 10 m surface height correction value used for the Forsmark site (see above). This could either mean that the summit lowering has been greater than 10 m, and/or that the larger 1 Ma denudation depths derived from cosmogenic nuclides also include removal of formerly overlying sedimentary cover rocks, see Hall et al. (2019a). In any case, if assuming a re-exposure of basement rock from below Early Palaeozoic cover rocks by glacial erosion within the last 1.1 Ma (Hall et al. 2019a, Hall and van Boeckel 2020), the results of the geomorphological analysis suggest that the total denudation of basement rock at the Forsmark site has been low. For more details on the geomorphological analysis, see Hall et al. (2019a).

The relief map in Figure 2-40 shows the present ground surface relief, i.e. it includes the relief of both bedrock and overlying Quaternary deposits. Within the Forsmark area, Quaternary deposits are thin, typically less than 5 m (Hall et al. 2019a Figure 2-27B), with an even lower mean thickness. Nevertheless, the geomorphological analysis of historical denudation of basement rock described above has been performed using the bedrock topography with surficial sediment cover removed.

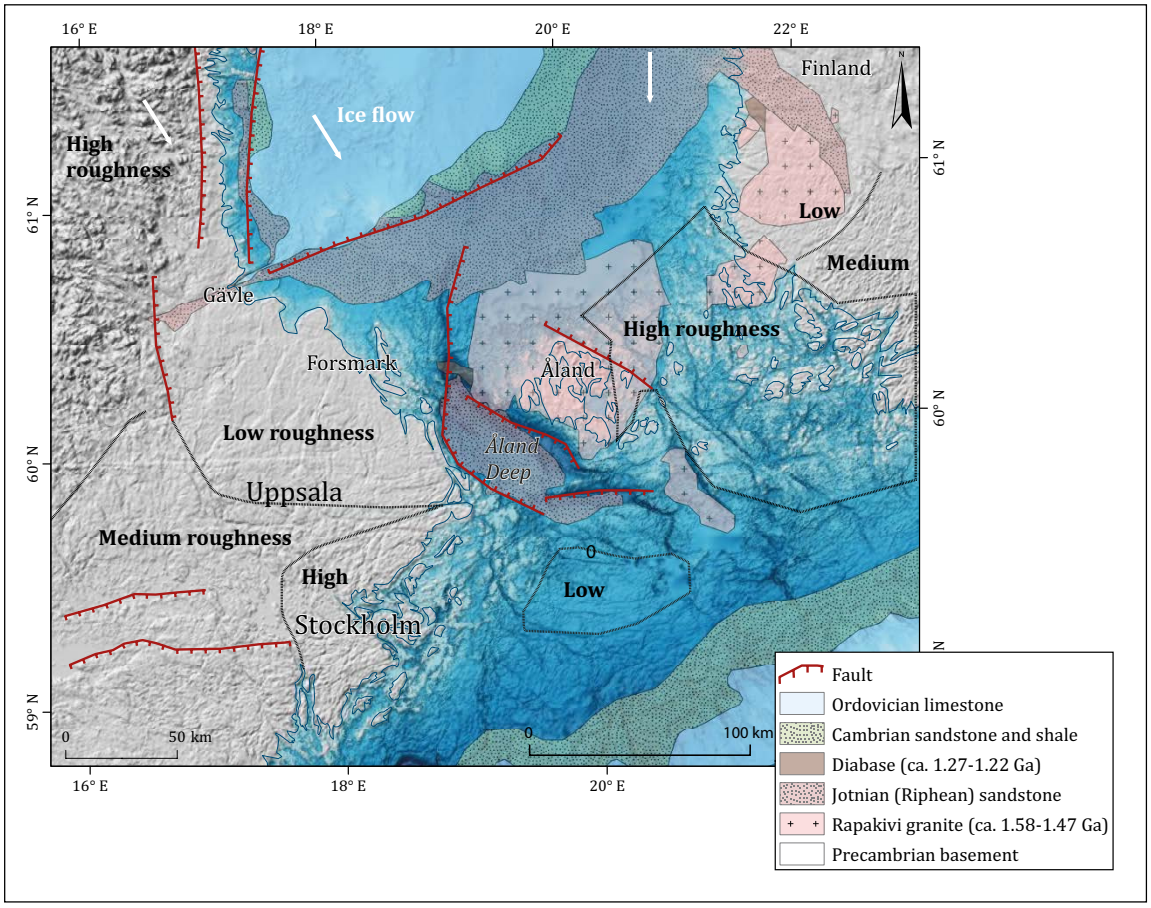

Figure 2-40. *Bedrock roughness (relief) at the landscape scale at Forsmark and surrounding areas. The map also shows the present distribution of remaining sedimentary cover rocks. From Hall et al. (2019a).*

Summary on past denudation

The results on total denudation of basement over the last 100 ka and 1 Ma from the cosmogenic nuclide analysis and geomorphological GIS analysis show similar results (Table 2-7 and Table 2-8).

Both the cosmogenic nuclide analysis and the geomorphological analysis suggest that typical total denudation of the crystalline rock at the Forsmark site over the past 1 Ma, including all Late Quaternary ice sheet erosion, have been restricted, from a few metres up to around 30 m (Table 2-7 and Table 2-8), depending on the exact location within the site. A few locations may have experienced a denudation up to 50–60 m. The typical denudation depths (25 % and 75 % percentiles) over the last 100 ka is 1.6–3.5 m for the Forsmark site (Table 2-7), whereas the full range (0 % and 100 % percentiles) is 0–8.6 m. Most of this denudation constitute glacial erosion.

The range in total denudation shows, as expected, that the amount of erosion has varied over the site, seemingly reflecting stochastic spatial variations in erosion depths and processes on topographic highs and fracture control on topographic lows. In an area further away from the Forsmark site, around 25 km towards southeast, glacial erosion have been more efficient and has produced a more pronounced relief along structurally aligned valleys.

The overall result of limited denudation and glacial erosion at Forsmark and adjacent areas of the Uppland province in the past (Hall et al. 2019a) is in line with the overall result obtained in the more restricted study by Olvmo (2010). The results are also in line with conclusions of Lidmar-Bergström (1997), whom estimated a total amount of glacial erosion by all Late Cenozoic ice-sheets in lowland terrain in Sweden to be ~ 10 m, as well as with the wider erosion budget for the Baltic Sea Basin and its surroundings (Hall and van Boeckel 2020).

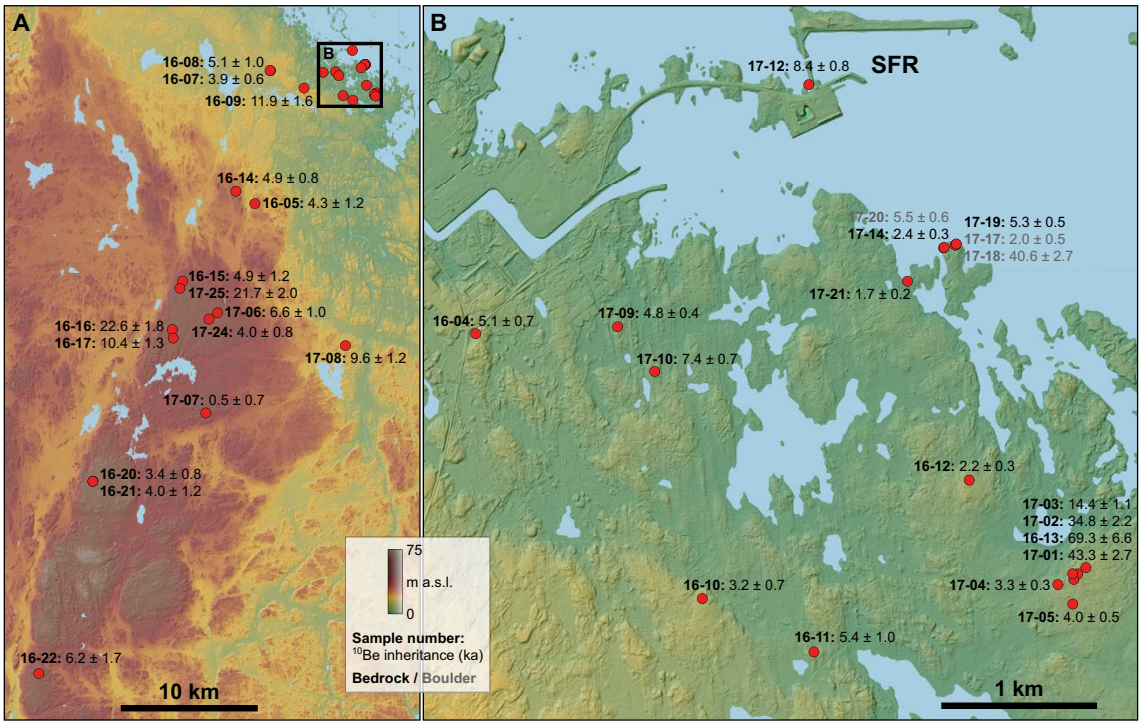

Figure 2-41. *Topographic maps showing locations of outcrops sampled for paired cosmogenic 10Be and 26Al nuclide concentrations at Forsmark and adjacent areas of the Uppland province (red dots). At the sample sites, sample numbers (bold characters) and calculated 10Be inheritance ages (regular characters) are given. A) Distribution of cosmogenic nuclide sample locations across the wider study area of Hall et al. (2019a) B) Location of SFR and cosmogenic nuclide sample locations close to this area. In addition, two depth profile samples were taken from a quartz vein exposed in a road cut adjacent to sample 16-04 (NRD-001 and NRD-003, not shown). The topographic maps are derived from a 2 m resolution LiDAR DEM, see Hall et al. (2019a). From Hall et al. (2019a).*

It is worth noting that the low denudation and glacial erosion rates at Forsmark in the past do not contradict the fact that there are glacially eroded bedrock landforms such as roche moutonnées in the area, since these landforms are relatively small. Similar results of low denudation have been found in other parts of Sweden, for example on the Swedish west coast, where cosmogenic exposure ages from around Hunnebostrand, an area with abundant roche moutonnées and large dislocated rock slabs, have shown that the Weichselian ice sheet only eroded up to a few metres of bedrock (Stroeven et al. 2016, J. Heyman personal communication). The results from the studies at Forsmark and Hunnebostrand show that estimates of past glacial erosion require methods such as cosmogenic nuclide analysis, and/or the use of a reference surface against which glacial erosion can be measured, in order to make quantitative statements on the total amount of past glacial erosion.

Quantification of future erosion at Forsmark

Lord et al. (2019) provided a first-order estimate of the timing and durations of ice-sheet coverage over Forsmark for the coming 1 Ma, based on e.g. IPCC greenhouse-gas emission scenarios. Hall et al. (2019a) concluded that if typical erosion depths for Forsmark over the past 1 Ma are assumed to be representative for erosion depths during the future high confidence ice covered periods modelled by Lord et al. (2019), then erosion rates over the coming 1 Ma will be restricted, just as concluded for the past. Adopting the higher-confidence future glacial periods of Lord et al. (2019) in the cosmogenic nuclide analysis, and using minimum and maximum values on non-glacial denudation of 0 and 5 mm ka^{-1} for the ice free periods, Hall et al. (2019a) estimated the total denudation depth of basement rock, including glacial erosion, over the coming 100 ka to be less than 1 m (95 % percentile) at the Forsmark site (Table 2-8) for the full range of RCP emission scenarios investigated in Lord et al. (2019).

Denudation rates for individual RCP emission scenarios and the ‘Natural’ scenario (without carbon emissions) for the higher-confidence future glacial periods of Lord et al. (2019), calculated by Hall et al. (2019a) for the coming 100 ka, are presented in Table 2-9. The table include the same results as in Figure 5-15 in Hall et al. (2019a). The results in Table 2-9 are valid under the assumption that typical erosion depths for Forsmark over the past 1 Ma are representative for future erosion depths during the high-confidence ice covered periods modelled by Lord et al. (2019). Table 2-9 also includes denudation calculations using two different modes of glacial erosion, ‘constant erosion rate’ and ‘erosion step’, as performed within the cosmogenic nuclide analysis. The ‘constant erosion rate’ simulations assume, as the name implies, a constant glacial erosion rate during the time of ice sheet coverage (in line with having warm-based erosive conditions at all times of ice coverage), whereas the ‘erosion step’ simulations assume no erosion up until the deglaciation, and at the time of deglaciation, a constant erosion depth is assumed. This is in line with a development of first having cold-based, non-erosive, conditions, followed by warm-based erosive conditions at the deglaciation. In effect, the two modes describe maximum (constant erosion rate) and a minimum (erosion step) models for glacial erosion. The combined ^{10}Be and ^{26}Al simulations, and the constant erosion rate mode, gives a 25–75 % percentile range of glacial erosion rate of 40–89 m ka^{-1}, whereas the 5–95 % percentile range is 16–144 mm ka^{-1} (Table 2-9). Correspondingly, the erosion step mode gives a 25–75 % percentile range of glacial erosion of 0.39–1.09 m per glacial overriding phase, whereas the 5–95 % percentile range is 0.14–1.66 m per glacial overriding phase (Table 2-9). For further information on the erosion rate and erosion step calculations, see Hall et al. (2019a).

In Table 2-9, note that none of the emission scenarios analysed in Lord et al. (2019) result in ice-sheet coverage at Forsmark over the coming 100 ka, and hence all denudation is a results of non-glacial processes (mainly fluvial erosion and chemical- and physical weathering). The one exception from this is the ‘Natural’ scenario which assumes no carbon emissions. In this scenario, a very short ice-covered period of a few thousands of years is present at the very end of the 100-ka period (Lord et al. 2019). The 0.48 m value for the ‘Natural’ scenario with glacial erosion step mode in Table 2-9 is slightly lower than the 0.5 m value for non-glacial conditions over the coming 100 ka. This is caused by the short ice-covered period at the end of the 100-ka period, for which cold-based non-erosive conditions are assumed. The deglaciation, with wet-based erosive conditions, of this glacial phase occurs after the 100-ka period.

The estimates of low future erosion at Forsmark is consistent with i) the long-term denudation of basement rock being low up until present, ii) the bedrock topography in the area having a very low relief that acts in favour of low glacial erosion (as compared to more commonly found higher relief settings), iii) the bedrock consisting of crystalline rock, which typically has a relatively high

resistance to erosion, and iv), the level of the Baltic sea constituting a base-level under which fluvial erosion cannot act. The present sea level would result in a maximum possible fluvial incision of a few m at the location of the planned spent nuclear fuel repository, whereas lower sea levels stands during future glacial periods would resulting in ~ 20 m of fluvial erosion as a maximum.

In the context of the low past and future glacial erosion rates for Forsmark obtained by e.g. Hall et al. (2019a), it is important to note that higher glacial erosion rates of smaller glaciers in e.g. steeper mountainous environments (see under the heading *Glacial erosion* in Section 2.4.1) are not applicable for an ice-sheet setting with a dramatically lower bedrock relief, such as in Forsmark. For instance, the sliding rates of basal ice, and hence the effectiveness of glacial erosion, may be very different between these two topographic settings. For examples of various glacial erosion rates from different climatological and topographic environments, see e.g. Olvmo (2010) and references therein.

The dissected coastal area ~ 25 km south-east of Forsmark, with a higher bedrock relief, may experience stronger glacial erosion during future glaciations than expected for the Forsmark site (see above). In this area, glacial erosion of more than 10 m in one glacial cycle may be expected locally in low topographic positions (Olvmo 2010). If considering a case where this area of higher glacial erosion south-east of Forsmark in the future would migrate towards the repository site through e.g. headward erosion, the distance over which this increased glacial erosion needs to occur is considerable. It is likely that this would require several glacial cycles, if it were to happen at all.

Summary and conclusions on future denudation at Forsmark

The quantification of the total amount of past and future denudation of crystalline bedrock from the cosmogenic nuclide analysis and geomorphological analysis of Hall et al. (2019a) are summarised in Table 2-7 and Table 2-8.

Table 2-7. Estimates of total denudation (i.e. including glacial erosion, non-glacial erosion, and weathering) from the cosmogenic nuclide analysis of basement rock at the Forsmark site by Hall et al. (2019a). Denudation has been calculated for the past 1 Ma and 100 ka and for the future 100 ka, based on paired cosmogenic ^{10}Be and ^{26}Al nuclide concentrations measured for 32 surface bedrock samples at the Forsmark site and adjacent parts of the Uppland province (see Figure 2-41). The estimates of future denudation are calculated by combining the information on past glacial erosion with future periods of ice sheet coverage at Forsmark as estimated by Lord et al. (2019), see the text. The values on total denudation are given for a mid- and a wide range scenario, see the text. The value marked by * has been corrected since Hall et al. (2019a), where it was erroneously given as 5.6 m. The values marked by ** include a very short period of ice-sheet coverage at the end of the 100-ka period emanating from the 'Natural' climate scenario adopted by Lord et al. (2019). If excluding the 'Natural' scenario and only using the results of the RCP scenarios from Lord et al. (2019), which do not have any ice sheet coverage over the coming 100 ka, the maximum denudation value is 0.5 m. This can be readily seen in Table 2-9, presenting denudation results for the individual RCP emission scenarios and for the 'Natural' scenario of Lord et al. (2019), as calculated by Hall et al. (2019a) for the coming 100 ka.

	Range	Total denudation last 100 ka (Weichselian glacial cycle) (m)	Total denudation Last 1 Ma (m)	Total denudation coming 100 ka (m) (using all emission scenarios of Lord et al. 2019)
All samples	Mid-range	1.6–3.5 (25 % and 75 % percentiles)	13–27 (25 % and 75 % percentiles)	< 1 (0–0.79** m, 25 % and 75 % percentiles)
	Full range	0–8.6 (0 % and 100 % percentiles	2–61 (0 % and 100 % percentiles	< 1 (0–0.99** m, 5 % and 95 % percentiles)
19 samples closest to and within footprint for the planned repository for spent nuclear fuel (5 km radius)	Mid-range (25 % and 75 % percentiles)	1.6–3.5	12–29	< 1
	Full range (0 % and 100 % percentiles)	0–8.6	2–61	< 1

Table 2-8. Estimates of past and future total denudation (i.e. including glacial erosion, non-glacial erosion, and weathering) of basement rock in the Uppland province and the Forsmark site from the geomorphological bedrock analysis in Hall et al. (2019a). In order to obtain the total denudation of basement rock, a summit lowering value (preliminary estimated to 10 m) have been added to the values from the GIS analysis (column four), see the text under the heading Quantification of past denudation – geomorphological analysis in the present section. *The additional 10 m of surface lowering has not been added to the GIS denudation value for the site with the largest denudation (50 m) since this site is located at close proximity to the margin of overlying sedimentary strata, see the text.

Analysed area	Value	Total historical denudation of basement rock up to present-day from GIS analysis	Total historical denudation of basement rock up to present-day from GIS analysis with added summit lowering	Estimated future denudation of basement rock
NE Uppland province excluding offshore area (see also Figure 4-46 in Hall et al. 2019a, showing results without summit lowering).	Mean	14 m	~ 24 m	-
Forsmark site, including offshore area (see also Figure 4-47 in Hall et al. 2019a, showing results without summit lowering).	Mean	12 m	~ 22 m	~ 2 m per glacial cycle. In basins and trenches, erosion rates may exceed 3 m per glacial cycle.
	Full range	0–50 m	10–50* m	

Table 2-9. Projected future total denudation of the Forsmark region over the coming 100 ka based on cosmogenic nuclide-derived simulations of glacial erosion (Hall et al. 2019a) and tentative 'high-confidence' periods of future ice coverage at Forsmark (Lord et al. 2019). The percentiles of denudation are based on combined cosmogenic ^{10}Be and ^{26}Al glacial erosion simulations. For ice-free periods, a non-glacial denudation rate of either 0 mm a^{-1} (for the 5 % and 25 % percentiles) or 5 mm a^{-1} (for the 75 % and 95 % percentiles) have been assumed, resulting in either 0 or 0.5 m of denudation over the coming 100 ka for all scenarios except the 'Natural' scenario, see the text. The results are visualised in Figure 5-15 in Hall et al. (2019a).

	Most likely 100 ka denudation range (m) (25 % and 75 % percentiles)		Wider range 100 ka denudation (m) (5 % and 95 % percentiles)	
Glaciation/emission scenario (Lord et al. 2019)	Mode of glacial erosion: glacial erosion rate (40–89 mm ka^{-1})	Mode of glacial erosion: glacial erosion step (0.39–1.09 m/glaciation)	Mode of glacial erosion: glacial erosion rate (16–144 mm ka^{-1})	Mode of glacial erosion: glacial erosion step (0.14–1.66 m/glaciation)
Natural (no emissions)	0.14–0.79	0–0.48	0.06–0.99	0–0.48
RCP 2.6 (low emissions)	0–0.5	0–0.5	0–0.5	0–0.5
RCP 4.5 (medium emissions)	0–0.5	0–0.5	0–0.5	0–0.5
RCP 8.5 (high emissions)	0–0.5	0–0.5	0–0.5	0–0.5

The main results of the analyses above are as follows:

- The Forsmark area has a very low topographic bedrock relief and the rock type is crystalline bedrock. Also, the repository is not situated in a major fracture zone or topographic depression. This results in a setting not prone to effective glacial erosion and denudation.
- The geomorphological analysis shows that the average total past denudation of basement rock over the Forsmark site, since (an estimated) re-exposure of basement 1.1 Ma ago, has been ~ 22 m.
- The corresponding past total range of denudation from the geomorphological analysis is 10–50 m for the Forsmark site.

- The typical denudation depths (25 % and 75 % percentiles) over the last 100 ka is 1.6–3.5 m for the Forsmark site (Table 2-7), whereas the full range (0 % and 100 % percentiles) is 0–8.6 m. Most of this denudation constitute glacial erosion.
- The expected denudation at the Forsmark site over the coming 100 ka, for all investigated emission scenarios, is less than 1 m. Most locations within the site is expected to have a denudation considerably smaller than this.

Note that the denudation over the coming 100 ka is estimated to be lower than the values for the last 100 ka. The reason for this is a shorter total period of ice sheet coverage, and therefore less glacial erosion, over the coming 100 ka (Lord et al. 2019, Figure 4-10) as compared to that of the Weichselian glacial cycle (Section 3.2.3). For a typical future (~ 100 ka glacial cycle, similar to that of the Weichselian, typical amounts of total denudation are estimated to be up to a few metres per glacial cycle (Table 2-7 and Table 2-8). In basins and trenches, erosion rates may exceed 3 m during a glacial cycle.

2.4.5 Time perspective

Weathering, erosion and sedimentation are active processes over most of the Earth's surface. In Sweden, rates of denudation can be expected to be limited in tectonically stable, lowland areas of low topographic relief. In the Uppland province, the Precambrian basement remained largely buried and protected from erosion for much of the last 540 Ma until it was re-exposed by glacial erosion in the Pleistocene (2.5 Ma BP to ~ 11 ka BP). For the region around Forsmark, the maximum glacial erosion over the last 1 Ma is estimated to be ~ 50 m (Section 2.4.4). The rates of weathering and erosion however have varied in time and space over this period. The typical denudation depths (25 % and 75 % percentiles) over the last 100 ka is 1.6–3.5 m for the Forsmark site (Table 2-7), whereas the full range (0 % and 100 % percentiles) is 0–8.6 m

2.4.6 Handling in the safety assessment

Present-day knowledge on denudation processes suggests that denudation of crystalline bedrock generally will be limited in lowland parts of Fennoscandia during the assessment period, just as it has been in the past (Hall et al. 2019a). In areas where the bedrock is highly fractured, denudation can be expected to be significantly more rapid than the numbers reported here. However, such circumstances do not apply for the SFR location at Forsmark. The impact of weathering and erosion on groundwater flow is considered to be insignificant over the 100-ka time period covered by the safety assessment.

The amount of denudation of basement rock over the coming 100 ka is estimated to be less than 1 m for expected climate developments (i.e. without ice-sheet coverage), see Section 2.4.4. Hence, the current knowledge on denudation at Forsmark and adjacent regions (e.g. Hall et al. 2019a and Olvmo 2010) supports a conclusion that the amount of future surface denudation will not affect repository safety in the time perspectives of 100 ka. Even in the case of having typical Late Quaternary ice-covered periods at Forsmark over the coming 100 ka, similar to that of the Weichselian, typical amounts of total denudation are estimated to be up to a few metres per glacial cycle (Table 2-7 and Table 2-8). In basins and trenches, erosion may, in this case, exceed 3 m (Section 2.4.4). Again, this limited amount of glacial erosion supports the conclusion that future surface denudation will not affect repository safety in the time perspective of 100 ka. Therefore, no account is taken of future surface denudation in the safety assessment scenarios.

2.4.7 Handling of uncertainties

Rates of weathering and erosion vary as environmental conditions change. The rates of weathering and erosion also depend on rock and sediment characteristics and topography. Despite the uncertainties in future environmental conditions, there is no reason to believe that denudation in the Forsmark region would diverge significantly from the values estimated above. The area consists of crystalline bedrock with a low surface relief and low topographic gradients, working in favour of limited fluvial and glacial erosion at the site.

Uncertainties in mechanistic understanding

There are uncertainties in the understanding of the detailed mechanisms of weathering and erosion. However, for the safety assessment, the approach of using also indirect estimates of the amount of erosion and weathering over long time-scales (i.e. the development of large-scale landforms), means that the total knowledge is sufficient for estimating the amount of weathering and erosion of fresh bedrock during the assessment period.

Model simplification uncertainties

Not relevant for this process.

Input data and data uncertainties

Not relevant for this process.

2.4.8 Adequacy of references

The SKB reports produced for the handling of surface denudation (Olvmo 2010, Hall et al. 2019a, b, Goodfellow et al. 2019) have undergone the SR-Site QA system handling, including a documented factual review procedure. Also, the SR-Can Geosphere process report (SKB TR-06-19), from which some of the studies are used, has undergone QA system handling including a factual review process. Other references used for the handling of surface denudation processes are either peer-reviewed papers from the scientific literature or from textbooks (Sugden and John 1976, Drewry 1986, Paterson 1994, Thomas 1994, Benn and Evans 1998, French 2007).

3 Past, present and future evolution of climate and climate-related issues

3.1 Introduction

The scientific basis for the selection and definition of the climate cases is given in this section. The current knowledge on past, present and future evolution of climate and climate-related issues is described, based both on reviews of international scientific literature and on studies performed for SKB to extend current knowledge in areas of major interest for the safety assessment.

Over the Quaternary period (past ~ 2.5 Ma), Scandinavia has experienced multiple cycles of glaciation (e.g. Ehlers and Gibbard 2004). Cold periods that include ice sheets gradually growing to maximum extents are known as *glacials*. These periods alternate with periods of warm climate called *interglacials*, with ice sheets of similar extent to those of the present day. A *glacial cycle* consists of a glacial and an interglacial. Within the glacial periods, warmer *interstadial* periods occur, as well as cool *stadial* periods. The shifting between glacials and interglacials is depicted for instance in the variation of the content of the heavy oxygen isotope, ^{18}O, in deep-sea sediments (e.g. Lisiecki and Raymo 2005), which reflects both the sea-water temperature and the volume of water that has been bound in land-based ice sheets and glaciers globally (Figure 3-1).

Figure 3-1 shows that over the last ~ 800 ka, glacial–interglacial cycles of about 100 ka duration have dominated global climate variation. To illustrate these variations in greater detail, the stacked $\delta^{18}O$ over this period is displayed in Figure 3-2 together with atmospheric CO_2 concentrations as measured in Antarctic ice cores and the variants in incoming solar radiation (insolation).

The latitudinal and seasonal distribution of insolation is the major external driver of the Earth's climate. This distribution changes over time due to variations in the Earth's orbit. These include variations in the eccentricity of the Earth's orbit, the obliquity (i.e. the tilt of the Earth's axis of rotation), and in the precession of the equinoxes, with dominant frequencies at about one cycle per 100 ka (eccentricity), 41 ka (obliquity) and 21–23 ka (precession). The ~ 100 ka timescale in the glacial/interglacial cycles of the last ~ 800 ka (Figure 3-1) is commonly attributed to control by these variations in the Earth's orbit. Milankovitch proposed that the Earth is in an interglacial state when its rotational axis both tilts to a high obliquity and precession to align the Northern Hemisphere summer with Earth's nearest approach to the Sun. June insolation at 60°N is displayed in Figure 3-2 for reference. Statistical analyses of long climate records supported this theory (Hays et al. 1976, Huybers 2011, Huybers and Wunsch 2005, Lisiecki and Raymo 2007), however many questions remain about how orbital cycles in insolation produce the observed climate response (Huybers 2011, Imbrie et al. 2011, Lisiecki 2010).

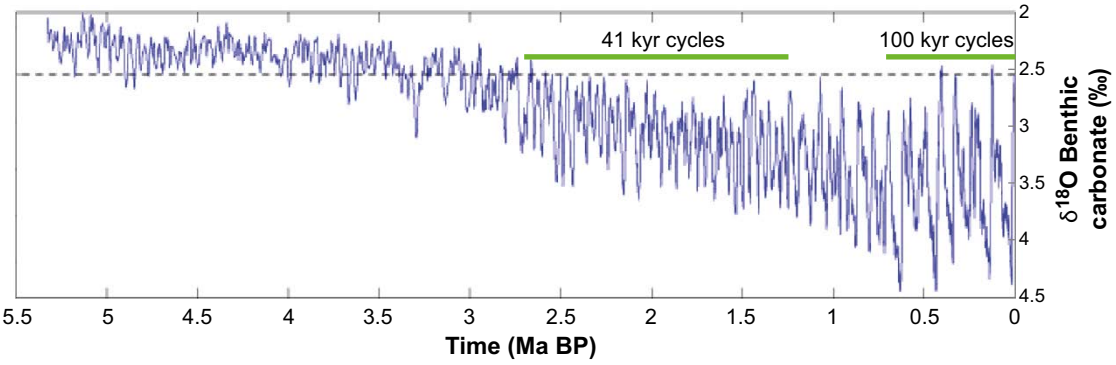

Figure 3-1. *Variations of δ18O in deep-sea sediments over the last 5.5 Ma (Lisiecki and Raymo 2005). High δ18O values indicate large global ice volume and low sea water temperature, i.e. colder climate conditions, whereas low δ18O values indicate the opposite. The last c. 800 ka have been dominated by 100 ka long glacial cycles. After Lisiecki and Raymo (2005).*

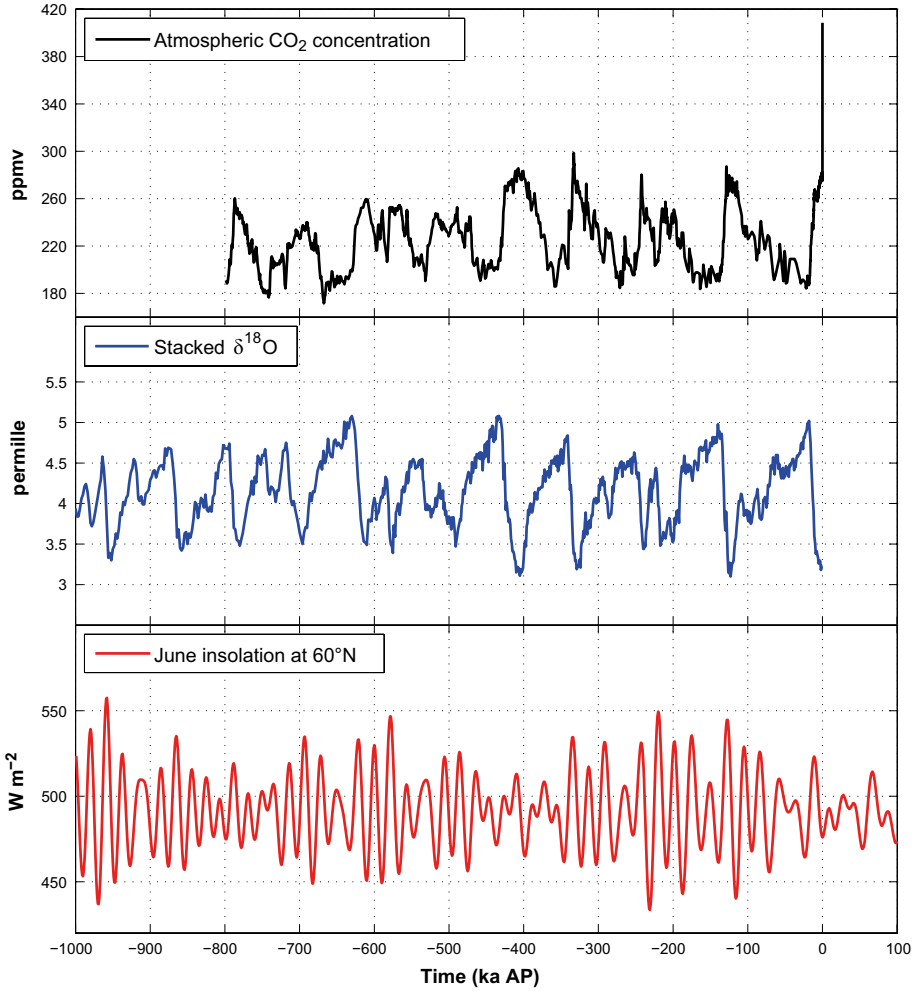

Figure 3-2. *CO_2 composite record (upper panel; Lüthi et al. 2008) complemented with the observed annual average atmospheric CO_2 concentration in 2018 AD (408.5 ppmv; www.esrl.noaa.gov). High values of CO_2 correspond to a warmer climate (interglacial state). A stack (middle panel; Lisiecki and Raymo 2005) of 57 benthic $\delta^{18}O$ records; the $\delta^{18}O$ is a proxy for the global ice volume. High values of $\delta^{18}O$ correspond to a colder climate (glacial state). June insolation at 60°N (lower panel; Berger 1978, Berger and Loutre 1991).*

The amplitude and the saw-tooth shape of the variations in the climatic records however imply that non-linearities and amplifications, e.g. through ice/snow albedo, atmosphere and ocean circulation and the carbon cycle, exist. Several modelling studies have been performed to enhance understanding of the physical mechanisms associated with deglaciation and glaciation (see e.g. Mysak 2008 for a review of modelling studies of glacial inception). For example, studies with so called Earth System Models of Intermediate Complexity (EMICs) that include simplified descriptions of the main components of the climate system, i.e. atmosphere, ocean, sea ice, ice sheets and sometimes vegetation, indicate that the combination of forcing by orbital insolation variations and prescribed glacial–interglacial atmospheric CO_2 variations give a reasonable agreement between simulated and reconstructed glacial cycles (e.g. Ganopolski et al. 2010, Loutre and Berger 2000).

The most contentious problem is why late Pleistocene climate records are dominated by 100-ka cyclicity. Insolation changes are dominated by 41-ka obliquity and 23-ka precession cycles, whereas the 100-ka eccentricity cycle produces negligible 100-ka power in seasonal or mean annual insolation. The study of Abe-Ouchi et al. (2013) used comprehensive climate and ice-sheet models to simulate the ice-sheet variation for the past 400 ka forced by the insolation and atmospheric CO_2 content. Their model realistically simulates the saw-tooth characteristic of glacial cycles (Figure 3-2), the timing of the terminations and the amplitude of the Northern Hemisphere ice-volume variations, as well as their geographical patterns at the LGM and the subsequent deglaciation (Abe-Ouchi et al. 2013).

They conclude that insolation and internal feedbacks between the climate, the ice sheets and the lithosphere–asthenosphere system explain the 100-ka periodicity.

To geologists of the future, the present Holocene interglacial, will look different from the previous major interglacial – the Eemian, which began around 130 ka BP (e.g. Solomon et al. 2011). During previous interglacials, the atmospheric CO_2 concentration reached a peak value of about 300 ppmv and thereafter began to fall; in the present interglacial, CO_2 will instead rise by an amount that will be determined by human activities. It is very likely that the anthropogenic release of CO_2 into the atmosphere, together with the future natural variation in insolation, will result in the present Holocene interglacial being considerably longer than previous interglacials, see also Section 3.4.5.

An up-to-date overview of scientific knowledge on past, present and future climate evolution was released by Working Group 1 of the Intergovernmental Panel on Climate Change (IPCC) Fifth Assessment Report (AR5; IPCC 2013a). IPCC (2013a) comes to the following conclusions.

- Warming of the climate system is unequivocal, and, since the 1950s, many of the observed changes are unprecedented over decades to millennia. The atmosphere and oceans have warmed, the amounts of snow and ice have diminished, sea level has risen, and the concentrations of greenhouse gases have increased.
- The atmospheric concentrations of CO_2, methane, and nitrous oxide have increased to levels unprecedented in at least the last 800 ka. CO_2 concentrations have increased by 40 % since pre-industrial times, primarily from fossil fuel emissions and secondarily from net land use change emissions.
- Continued emissions of greenhouse gases will cause further warming and changes in all components of the climate system. Limiting climate change will require substantial and sustained reductions of greenhouse-gas emissions.
- Global surface temperature change for the end of the 21st century is likely to exceed 1.5 °C relative to 1850 to 1900 for all emission scenarios.
- It is very likely that the rate of global mean sea-level rise during the 21st century will exceed the rate observed during 1971–2010.
- Most aspects of climate change will persist for many centuries even if emissions of CO_2 are stopped. This represents a substantial multi-century climate change commitment created by past, present and future emissions of CO_2.

Section 3.2 comprises up-to-date descriptions on the climate evolution during the penultimate interglacial, the Eemian, and the Weichselian glacial. The present-day climate at Forsmark is described in Section 3.3. Finally, the current knowledge on future climate and sea-level evolution on timescales from 100 years to 100 ka is summarised in Sections 3.4 and 3.5.

3.2 Glacial history, Weichselian climate and reconstructed last glacial cycle conditions at Forsmark

The Weichselian glacial cycle, and specifically the transition from the warm Eemian interglacial into the cold Weichselian glacial is of interest in assessments of long-term repository safety, since the present Holocene interglacial will eventually end and a transition to colder climates will occur. As further outlined in Section 3.4.5, the timing of this future event is uncertain. However, regardless of this timing, the present-day understanding and view of the most recent interglacial–glacial transition is of interest in this context. Much of the following is based on the main findings from Helmens (2013, 2019), Wohlfarth (2013) and Schenk and Wohlfarth (2019). In summary, these studies cover the following topics:

- The review by Wohlfarth (2013) addresses the transition from the last interglacial (the Eemian, MIS 5e) into the Weichselian glaciation in Europe, based on state-of-the-art paleoclimatic and paleoenvironmental information from selected terrestrial, marine and ice-core records.
- The transition to Weichselian glacial conditions was also studied in Helmens (2013) by comparing five Late Pleistocene terrestrial climate proxy records from central, temperate and northern, boreal Europe, using pollen, lithology and macrofossil- and insect-based temperature inferences.

- Helmens (2019) presented the results of a detailed study on sediments of MIS 5e age (i.e. the Eemian interglacial between ca. 130 and 115 ka ago), MIS 5d-c age (stadials and interstadials during the Early Weichselian ca. 115 to 90 ka ago) and the present Holocene interglacial (last 11 ka) recovered from the Sokli sedimentary basin in boreal north-eastern Finland. By applying multiple proxies and various quantitative climate reconstruction methods, a comprehensive reconstruction of environmental and climate conditions at Sokli during these time-intervals is made.
- Schenk and Wohlfarth (2019) performed a study on climate evolution and variability in Scandinavia and Europe during the transition from a glacial into an interglacial climate state, combining multi-proxy climate records with results from high-resolution climate modelling for the Bølling-Allerød (14.7–12.9 ka BP) and Younger Dryas periods (12.9–11.7 ka BP) of the last deglaciation.

In addition, ice-marginal fluctuations during the Weichselian glaciation in Fennoscandia were previously reviewed in Lokrantz and Sohlenius (2006). Section 3.2.1 gives a summary of the information from the studies listed above.

3.2.1 Weichselian glacial history and climate

The different warm and cold phases of e.g. the last glacial cycle are divided into numbered so-called Marine Isotope Stages (MIS). For a better understanding of the temporal aspect in the description of the last glacial cycle below, these stages are summarised and described in Table 3-1.

Table 3-1. Summary and description of Marine Isotope Stages, ages, stadials and interstadials of the Eemian, Weichselian and Holocene. Regional variations from the denoted warm/cold state occur and there is a wide range of regional names used for each of the stadials/interstadials, see e.g. Lokrantz and Sohlenius (2006), Helmens (2013, 2019) and Wohlfarth (2013).

Marine Isotope Stage	Age (ka BP)	Stadial/ Interstadial	Warm/Cold	Name (several other names are also used)	Weichselian phase
MIS 5e	...–115(110)	Interglacial	Warm	Eemian	–
MIS 5d	115(110)–105	Stadial	Cold	Herning (Melisey I)	Early Weichselian
MIS 5c	105–93	Interstadial	Warm	Brørup (St Germain 1c)	Early Weichselian
MIS 5b	93–85	Stadial	Cold	Rederstall (Melisey II)	Early Weichselian
MIS 5a	85–74	Interstadial	Warm	Odderade (St Germain II)	Early Weichselian
MIS 4	74–59	Stadial	Cold	Middle Weichselian stadial	Middle Weichselian
MIS 3	59–24	Interstadials/ Stadials	Warm/Cold	Middle Weichselian interstadials	Middle Weichselian
MIS 2	24–12	Stadial	Cold	Stadial including Last Glacial Maximum	Late Weichselian
MIS 1	12–0	Interglacial	Warm	Holocene	–

MIS 5, including the transition from the Eemian interglacial

The transition from the last interglacial (the Eemian, MIS 5e, Table 3-1) to the first phase of the Weichselian glacial (MIS 5d), as seen in NGRIP ice core records, is depicted in Figure 3-3 together with changes in the incoming solar radiation (insolation).

The end of the Eemian interglacial period and the transition into the subsequent glacial was initially triggered by a decrease in summer insolation at high northern latitudes (e.g. Wohlfarth 2013, Figure 3-3). The change in orbital configuration led to a series of time-transgressive changes (e.g. gradual vegetation replacement; changes in sea-surface temperature, salinity, strength of the North Atlantic Current). As Northern Hemisphere ice-sheets started to grow and expand these changes became progressively more pronounced (Wohlfarth 2013).

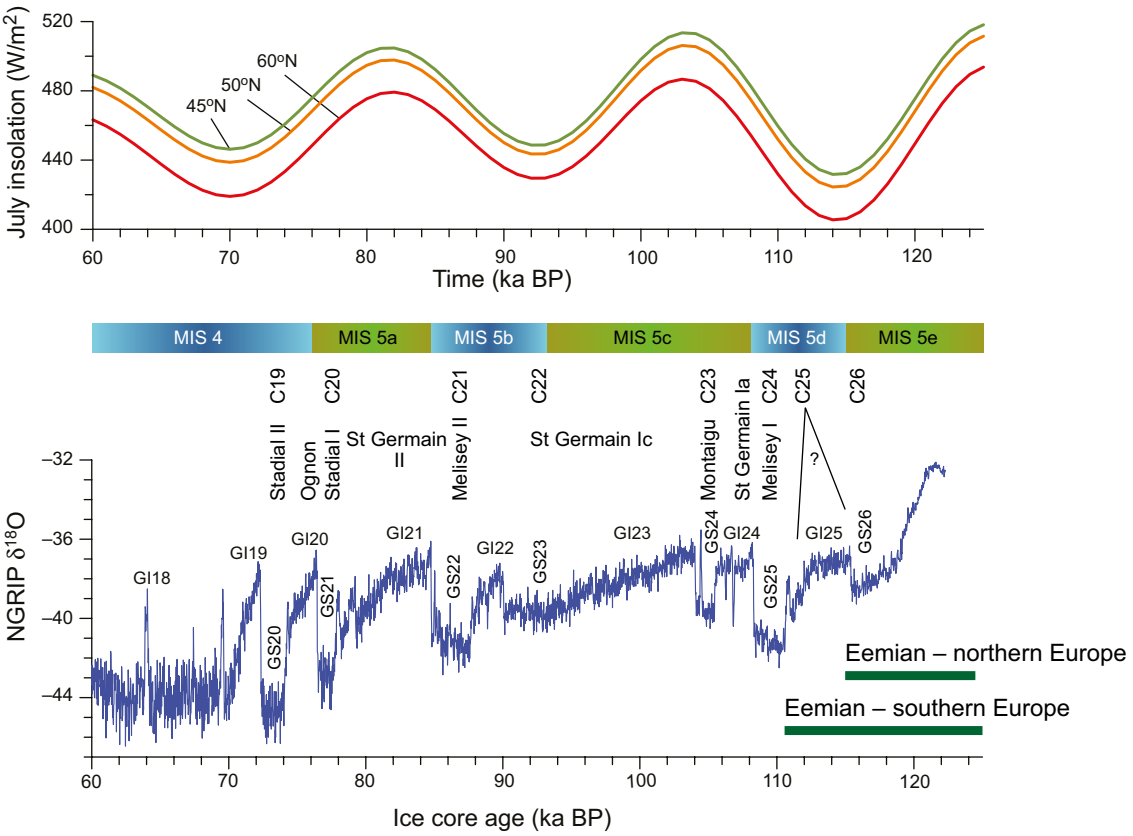

Figure 3-3. *Summer insolation at 60°, 50° and 45° N (Berger 1978) compared with the NGRIP $\delta^{18}O$ record (NorthGRIP community members 2004). The North Atlantic sea-surface cooling episodes (C26 to C19) and the terrestrial vegetation zones are according to Sánchez Goñi (2007). The correlation between marine and terrestrial events and the NGRIP record was inferred from Figure 13.1 in Sánchez Goñi (2007). The correlation between marine isotope stages (MIS 5e–4) and the NGRIP isotope record is tentative and partly follows Sánchez Goñi (2007) and partly Chapman and Shackleton (1999). The end of the terrestrial Eemian is according to Müller and Kukla (2004) and Sánchez Goñi (2007). GS = Greenland stadials; GI = Greenland interstadials. Note that the correlation of C25 and C26 to Greenland stadials is not entirely clear. C26 likely corresponds to GS26. From Wohlfarth (2013).*

The sequence of events leading from the Eemian into the last glacial has been described using climate models of different complexity and using various boundary conditions, paleodata series, and comparisons between model outputs and paleodata (see Wohlfarth 2013 for review). One possible scenario for the mechanisms involved relates to the development of summer sea ice in the northern North Atlantic already during the latter part of the Eemian interglacial, as a response to decreasing summer insolation. This would have accelerated a vegetation shift, which in turn would have led to a decrease in albedo. More extensive sea ice could, through brine formation, have increased the Atlantic Meridional Overturning Circulation (AMOC), which would have supplied more moisture to the cold high northern latitudes. This in turn would have favoured the growth of ice sheets.

The response of the vegetation in northern Europe to the decrease in summer insolation and to increased summer sea ice may be seen as early as 122–120 ka BP, but became most distinct around 115 ka BP, when North Atlantic sea-surface temperatures show signs of a first minor cooling (Wohlfarth 2013). This cold event (labelled sea surface cooling event C26, see Figure 3-3) defines the MIS 5e/5d transition in marine cores and seems to correlate with Greenland stadial GS26. This first distinct, but minor cooling event on Greenland is paralleled by cold temperatures in Antarctica, which implies synchronous cooling in both hemispheres. However, while Antarctica remained cold, Greenland started to warm just before 110 ka, suggesting the start of the so-called bipolar see-saw mechanism. The first marked cooling over Greenland at 110–108 ka BP (GS25, Figure 3-3) was accompanied by a distinct drop in North Atlantic sea-surface temperatures (C24 event), by an increase in ice-rafted debris and by marked vegetation changes in southern Europe. This shift in vegetation defines the end of the terrestrial Eemian in southern Europe, which in comparison to marine records, occurred during MIS 5d. Paleorecords

thus suggest that the response of the vegetation to North Atlantic cooling events was delayed in southern Europe by at least 5 ka as compared with northern Europe (Wohlfarth 2013).

The decrease in summer insolation at high northern latitudes thus led to a series of feedback mechanisms, which gradually became stronger as ice sheets grew larger. The initiation of the bipolar see-saw mechanism at around 110–112 ka BP seems to have triggered the series of abrupt and recurrent shifts between warmer interstadials and colder stadials that characterised the last glacial. While tundra and steppe-tundra vegetation seem to have developed in response to severe stadial conditions, the vegetation response to warmer interstadial temperatures was regionally different (Figure 3-4).

The overall conclusion from Wohlfarth (2013) is thus that the transition from the warm Eemian interglacial state (MIS 5e) to full glacial conditions during e.g. MIS 4 was complex, involving climate variability on different temporal and spatial scales. One aspect of this variability was manifested as the shifts between cold stadials and warm interstadials of multi-millennial duration during the Early Weichselian (MIS 5d–a) (Figure 3-3). Another aspect is associated with the millennial-scale climate variability superimposed on the longer-lasting climate fluctuations (Figure 3-3).

The high variability of the MIS 5 climate is also supported by the findings in Helmens (2013). More specifically, Helmens (2013) reported that the MIS 5 was characterised by three long mild forested interstadials (MIS 5e, 5c and 5a), both in temperate- and northern boreal Europe. These periods were interrupted by two cold and dry stadials (MIS 5d and 5b) with mountain-centred glaciation over Fennoscandia, shown in Figure 3-4. Also suggested in Figure 3-4 is that the Weichselian ice-sheet did not reach south-central Sweden and the Forsmark region during the Early Weichselian stadial periods.

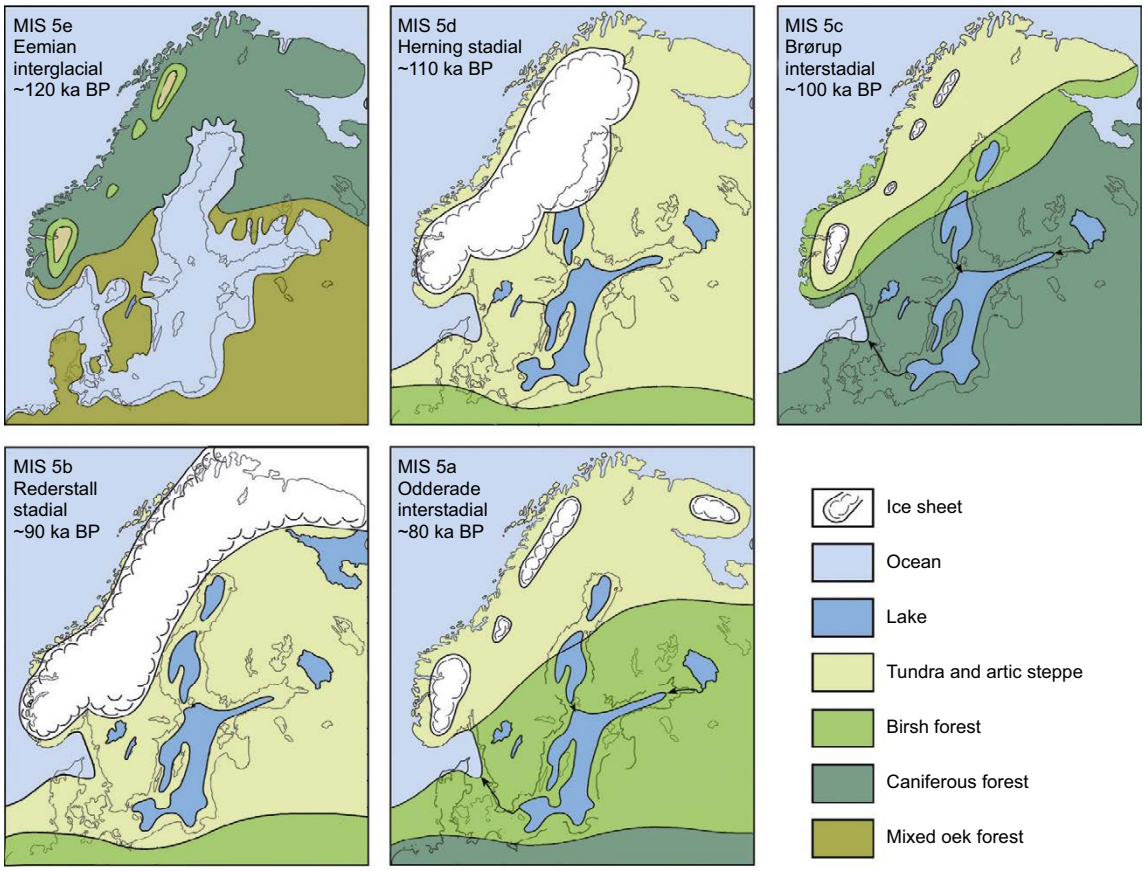

Figure 3-4. *Conceptual maps illustrating the development of the Weichselian ice sheet during the Eemian and Early Weichselian (MIS 5e–a). According to this reconstruction, the Weichselian ice sheet did not reach south-central Sweden and Forsmark during these periods of ice-sheet growth. Modified after Lundqvist (1992) and Mangerud et al. (2011). From Wohlfarth (2013).*

Helmens (2019) presents a detailed study on sediments of MIS 5e-c age (130–90 ka BP) recovered from the Sokli sedimentary basin in boreal north-eastern Finland. The study exploits the *in-situ* preservation of Late Quaternary sediments in the Sokli basin as well as the unusual large thickness and fossil-richness of the geological beds. The results from Sokli revise earlier paleo-environmental and paleo-climate reconstructions for the Early Weichselian in Fennoscandia. Earlier paleo-climate reconstructions were based on the long-distance correlation of poorly dated stratigraphic fragments with the marine oxygen-isotope record which was used as a proxy for global ice volumes. One of the main results from Helmens (2019) is that the summer temperature during the MIS 5d stadial remained relatively high in northern Fennoscandia, comparable to present-day values (Figure 3-5). This is in contrast to earlier studies that have suggested that the temperature in the region was several degrees lower during MIS 5d than at present (e.g. Engels et al. 2010).

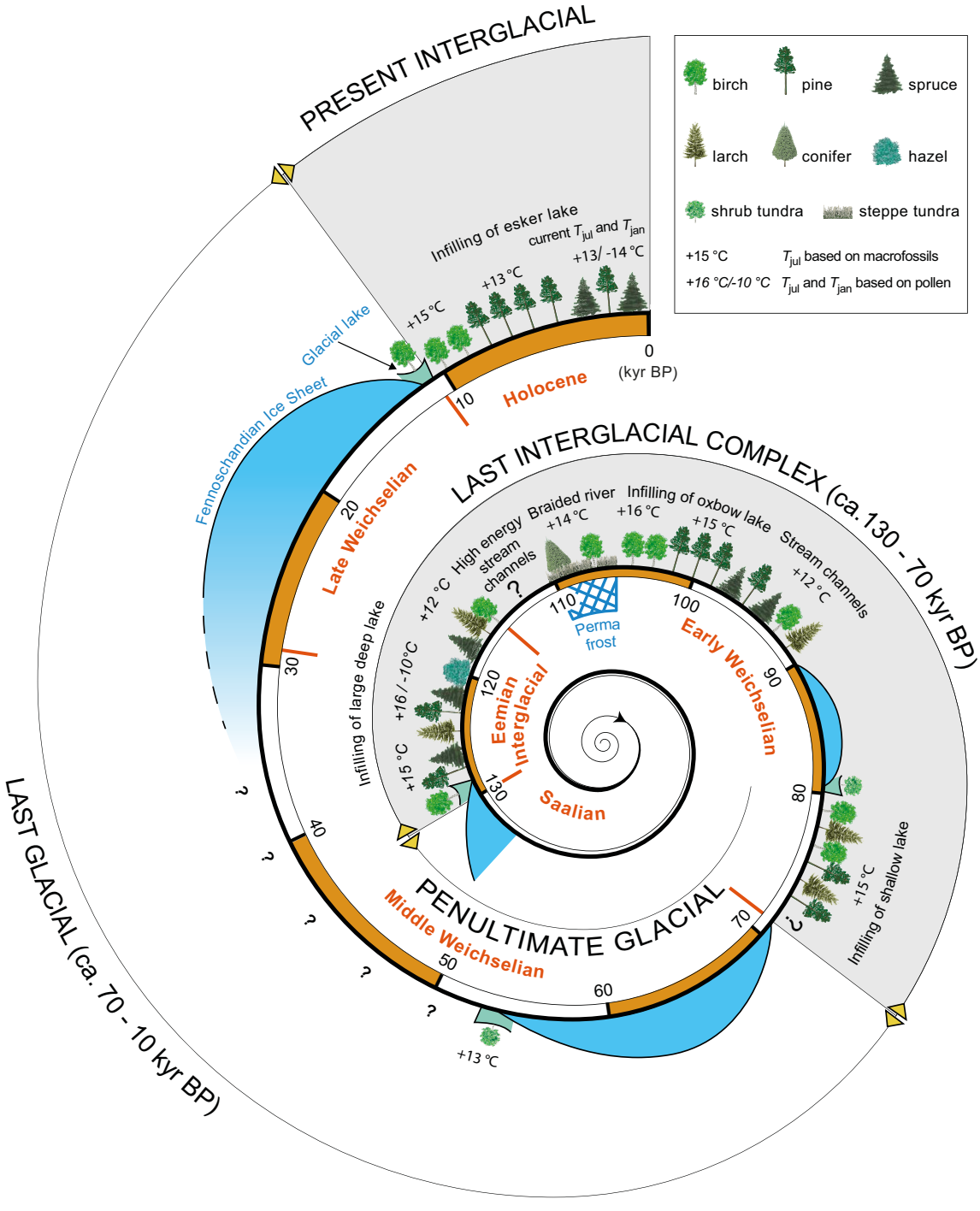

Figure 3-5. *Environmental and climate conditions at Sokli, northern Fennoscandia, during the last interglacial-glacial cycle (ca. 130 ka). From Helmens (2019).*

Helmens (2019) also provides a detailed description of the MIS 5 vegetation evolution in the Sokli area. During MIS 5d the presence of steppe-tundra vegetation and a braided river system demonstrate ice-free conditions with a severe continental climate. In contrast to MIS 5d, MIS 5c shows a more complex vegetation development of pioneer birch vegetation being replaced by pine-dominated forest and then mixed boreal forest. The exceptionally rich plant macrofossil assemblages associated with an overall fluvial depositional environment suggest that the summer temperature in the area was several degrees higher than today.

MIS 4 to MIS 2

Helmens (2013) compared five Late Pleistocene terrestrial climate proxy records from central, temperate and northern, boreal Europe. The records comprise the classic proxy records of La Grande Pile (NE France) and Oerel (N Germany) and more recently obtained records from Horoszki Duże (E Poland), Sokli (N Finland) and Lake Yamozero (NW Russia). The Sokli sedimentary sequence from the central area of Fennoscandian glaciation has escaped major glacial erosion in part due to non-typical bedrock conditions. Multi-proxy studies on the long Sokli sequence drastically change classic ideas of glaciation, vegetation and climate in northern Europe during the Late Pleistocene.

The comparison allows a re-examination of the environmental history and climate evolution of the last interglacial-glacial (MIS 5–2), and it shows that environmental and climate conditions during MIS 5 (c 130–70 ka BP) were different from those during MIS 4–2 (c 70–15 ka BP). As mentioned above, MIS 5 was characterised by three long warm intervals interrupted by two shorter cold and dry intervals. Subsequently, MIS 4–2 shows open vegetation both in central and northern Europe (Helmens 2013). It includes two glacial maxima (MIS 4 and 2) with sub-continental scale glaciation over northern Europe and dry conditions in strongly continental eastern European settings. During the cold MIS 4 and 2, south-central Sweden and the Forsmark region were ice covered (Figure 3-6). This contrasts with the MIS 3 period, during which climate oscillations of millennial scale (so-called Dansgaard–Oeschger events) dominated. Summer temperatures approaching present-day values are recorded for various warming events during MIS 3 (Helmens 2013), i.e. during the Middle Weichselian (Table 3-1). Mild climate conditions in early MIS 3 at around c. 50 ka BP were accompanied by large-scale deglaciation of the Weichselian ice sheet. Ice-free conditions with Betula-dominated vegetation (including tree birch) persisted over large parts of Fennoscandia, possibly interrupted by glaciation, into the middle part of MIS 3 to c. 35 ka BP.

Overall, MIS 5 was mostly mild with warmest or peak interglacial conditions at the very start during MIS 5e. MIS 4–2 was mostly cold with most extreme or peak glacial conditions in the closing phase during MIS 2. Additionally, the reviewed data (Helmens 2013) reveals restricted ice cover during MIS 3 and indicates that climate variability during parts of the last interglacial-glacial cycle was expressed mostly in terms of changes in degree of continentality possibly due to changes in sea-ice cover.

The MIS 3 period is also characterized by the presence of millennial scale climate oscillations (so-called Dansgaard–Oeschger events), yielding summer temperatures similar to present-day values for some of the warming events (Helmens 2013). There are still unsolved questions related to an ice-free interstadial period during parts of MIS 3, many of them concerning the datings of various interstadial and ice-advance phases. Nevertheless, it seems clear that the Weichselian ice sheet was considerably more dynamic during the MIS 3 period of the Middle Weichselian than previously thought, in line with the variable climate. One implication of such a revised MIS 3 glacial history is that the Forsmark site was free of ice for a considerable amount of time during the Middle Weichselian, prior to the LGM. If so, the climate at the end of MIS 3 at Forsmark was probably of a periglacial character, allowing permafrost conditions to develop and be maintained, see Sections 2.1.4 and 3.2.2.

After the MIS 3 period, during MIS 2, the Weichselian ice-sheet advanced to its Last Glacial Maximum (LGM) configuration. During the LGM, the entire area of Fennoscandia was covered by the ice-sheet, including south-central Sweden and the Forsmark region (lower panel of Figure 3-6). The ice volume was at its largest at ~ 20–21 ka BP, with the southern ice margin located in Germany and Poland. The ice reached its maximum LGM position at different times in different regions.

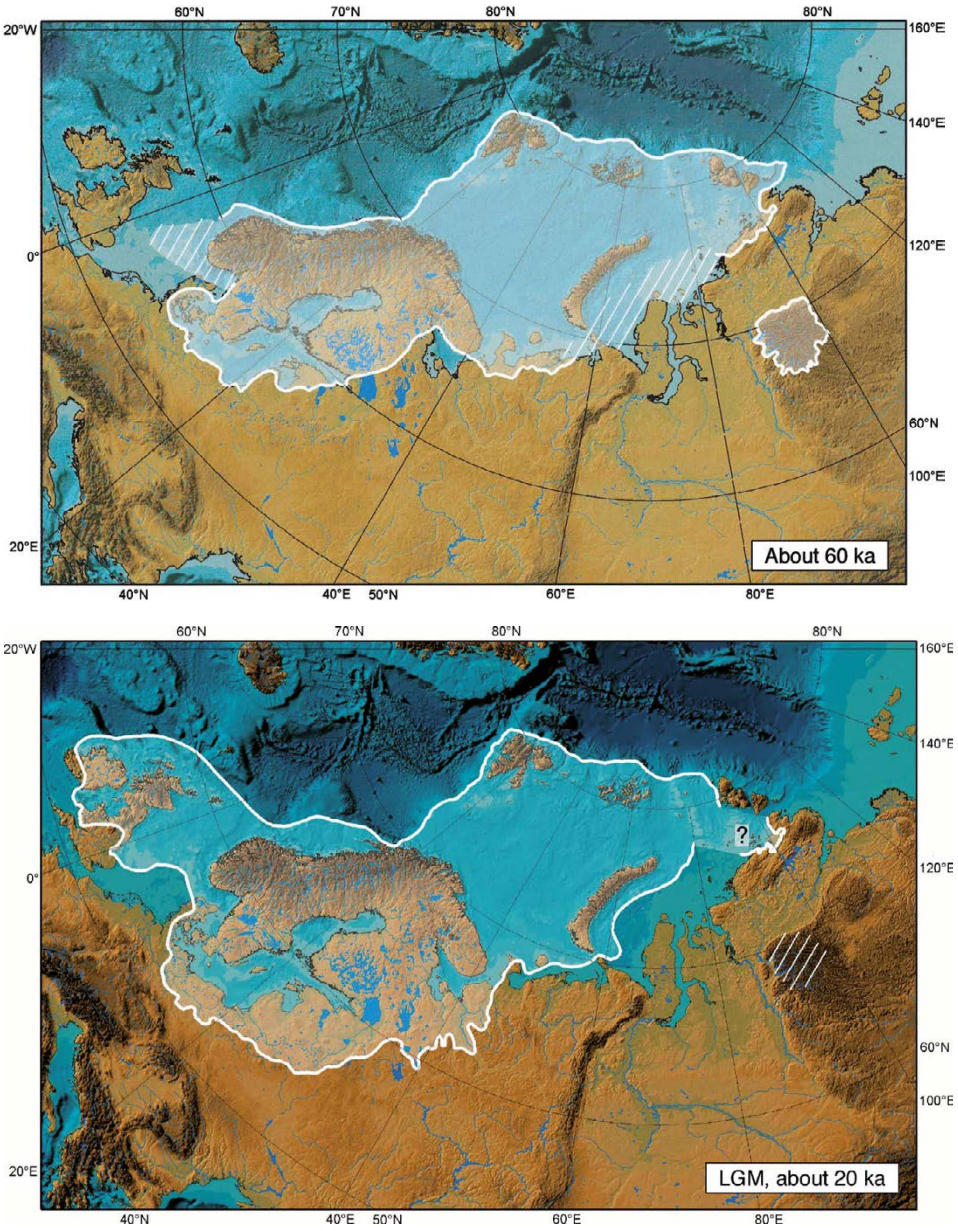

Figure 3-6. *Extent of the Eurasian ice-sheet during the glacial maximum stages of, the Middle Weichselian (60–50 ka BP, MIS 4) and the Late Weichselian (LGM, around 20 ka BP, MIS 2) as reconstructed from Quaternary geology. From Svendsen et al. (2004). Between these stages of maximum ice-sheet extent, the ice sheet had a more restricted configuration.*

Deglaciation from LGM to the Holocene (MIS 2 to MIS 1)

Following the LGM, the ice sheet started to retreat across e.g. northern Germany and Poland and subsequently over Fennoscandia, a sequence of events that is well-dated (e.g. Stroeven et al. 2016). Several re-advances took place during the deglaciation of the Danish and Norwegian coast. Furthermore, from Quaternary geological information it is known that temporary halts in the ice-sheet retreat took place several times in southern and south-central Sweden during the last deglaciation (e.g. Lundqvist and Wohlfarth 2000, Fredén 2002). For instance, the deglaciation was interrupted during the Younger Dryas stadial (12.9–11.7 ka BP), following the relatively warm Bølling-Allerød interstadial (14.7–12.9 ka BP). The ice-marginal deposits formed during the Younger Dryas can be identified all around Fennoscandia. A description of the characteristics of these stillstands during the last deglaciation in Fennoscandia is found in SKB (TR-10-49, Section 4.2.2).

In the combined proxy data-climate modelling study by Schenk and Wohlfarth (2019) and Schenk et al. (2018) it was found that the rapid climate shift between the Bølling-Allerød interstadial and the Younger Dryas stadial was primarily a result of changes in seasonality, rather than a reduction of the summer temperature.

Based on several lake records from southern Sweden, they found clear evidence from plant macrofossils that remarkably high summer temperatures of at least c. +16 °C prevailed throughout the deglaciation. Based on the oldest Swedish records, the high summer temperatures existed already directly after the ice-sheet retreated over southern Sweden during the pre-Bølling (15.5 ka BP) and remained high until the lakes became peatlands during the early Holocene (~ 10 ka BP).

In contrast to the warm summer air temperatures captured by plant macrofossils, lake water temperatures reconstructed from chironomids indicate distinct shifts between cold stadials and warm interstadials. These shifts co-vary with proxy-evidence from lipid biomarkers for dry conditions and a fresh moisture source during stadials and wetter conditions and a saltier moisture source during interstadials. The compilation and quantification of minimum mean July temperatures based on climate indicator plant species from over 120 European sites suggested that the warm summers seen in southern Swedish lake records were present also on a broader regional scale during the Bølling-Allerød and Younger Dryas.

In the high-resolution climate model simulations, Schenk and Wohlfarth (2019) and Schenk et al. (2018) found that summer temperatures during the Younger Dryas stadial remained at least as high as during the preceding Allerød, consistent with the proxy evidence from southern Sweden and the 120 European records. The persistence of high summer temperatures, seen in both proxy records and climate model simulations, results from atmospheric blocking of westerly winds over the Fennoscandian ice sheet during summer. The atmospheric blocking linked to the presence of the ice sheet was intensified by the cold North Atlantic sea-surface temperatures during the Younger Dryas stadial. The blocking is however only stable during a short summer period and severe cooling dominates during the Younger Dryas in spring, autumn and winter. The results of Schenk and Wohlfarth (2019) hence support previous studies that suggested that the abrupt climate shifts are dominated by a shift in seasonality with increased continentality during stadials.

In addition, the climate model simulation in Schenk and Wohlfarth (2019) and Schenk et al. (2018) supports the proxy evidence of drier stadial conditions which, according to the climate model, might have been extreme owing to much lower humidity in response to a very cold ocean state and southern sea-ice front. During summer, the intensified blocking further reduces the advection of precipitation from the North Atlantic. Based on the comprehensive multi-proxy study and climate modelling results, they found a high agreement between proxy data and climate simulations. They also found that the shifts between cold stadials and warm interstadials during the deglaciation were dominated by shifts in seasonality/continentality where cold ocean states during a weak AMOC leads to severe winter-spring cooling and aridity and warm ocean states during a strong AMOC lead to milder winters and increased precipitation.

After the Younger Dryas, the ice retreated towards the Fennoscandian mountain range more or less continuously. The retreat of the ice sheet, and associated increase of the summer temperature in northern Fennoscandia, is also seen in the Holocene lake sequence from the Loitsana Lake in the Sokli basin (Helmens 2019). Although the quantitative temperature reconstruction for the Holocene based on pollen of terrestrial plant taxa in the Loitsana sediments follows the classical trend of gradually increasing early Holocene mean July air temperatures in Fennoscandia, with a mid-Holocene maximum July warming between ca. 8 and 4 ka BP, plant macrofossils of telmatic vegetation, and chironomids, indicate an early onset of the maximum in July air temperatures in the early-Holocene prior to ca. 10 ka BP (Helmens 2019). The Holocene summer temperature evolution, recently reconstructed for aquatic/wetland taxa at several sites in northern Fennoscandia, follows the gradually decreasing orbitally-forced June insolation at 60°N since 11 ka BP. The chironomid-inferred continentality index suggests a more continental climate regime, with warm summers and cold winters, during the early Holocene than at present (Helmens 2019).

Hence, several independent studies, using different methodologies, suggest surprisingly warm summer conditions, up to present-day temperatures and above, and rich biotic communities during the last deglaciation (Schenk et al. 2018, Schenk and Wohlfarth 2019, Helmens et al. 2018, Helmens 2019), and also during previous last glacial cycle deglaciations (Helmens et al. 2018, Helmens 2019).

Note that the typical Quaternary ice-sheet configuration over Fennoscandia was considerably smaller than that of a full ice-sheet configuration, and also considerably smaller than during the Younger Dryas. For average Quaternary ice-sheet conditions, the ice sheet is centred over the Scandinavian mountain range (e.g. Porter 1989, Kleman et al. 2008), resulting in ice-free conditions in south-central Sweden including Forsmark.

For more detailed descriptions of the Weichselian glacial history, see Lokrantz and Sohlenius (2006), Lundqvist (2007), Wohlfarth (2010, 2013), Helmens and Engels (2010), Lambeck et al. (2010), Mangerud et al. (2011), Lundqvist et al. (2011, Figure III.3), Helmens (2013, 2019), and Schenk and Wohlfarth (2019).

3.2.2 Examples of Weichselian climates

During the Weichselian, climate shifted many times between warmer and colder periods, as reflected in the growth and decay phases of the Weichselian ice sheet, see Section 3.2.1. The variability and range within which the climate shifted during the last glacial cycle could be expected also during future glacial cycles. Therefore, quantitative descriptions of prevailing climate conditions for periods with fundamentally different climates during the Weichselian are given below for Sweden and the Forsmark region.

The aim of the following descriptions of Weichselian climates is not to give a full review of all that is known on climate and climate variability during the last glaciation. Instead, the intention is to provide examples of Weichselian climates by selecting climate reconstructions for both stadial and interstadial phases and to cover a broad time span of the glacial cycle.

Early Weichselian (MIS 5d-5a; 115–74 ka BP)

The Fennoscandian climate during the Early Weichselian (MIS 5d–5a, 115–74 ka BP, Table 3-1) varied significantly, as described in Section 3.2.1. Past environmental and climate conditions have been reconstructed for MIS 5d (the Herning stadial 115–105 ka BP, Table 3-1) by analyses of pollen from the Sokli sediment sequence (Helmens et al. 2012, Helmens 2019). The results show that, for the ice-free stadial conditions at the investigated site, the summer July air temperature was at least +12–14 °C (present summer mean temperature is 13 °C) accompanied by steppe-tundra vegetation with a local presence of birch trees and conifers for this period.

During MIS 5c (the Brørup interstadial, 105–93 ka BP), summer temperatures inferred from plant macrofossil remnants indicate surprisingly warm conditions for northern Fennoscandia (Väliranta et al. 2009, Engels et al. 2010). Minimum July temperatures were as high as +16 °C, which is 3 °C warmer than at present (Väliranta et al. 2009, Helmens 2019), probably driven by higher summer insolation. At that time, open birch woodland existed at the site within a subarctic climate. This result contrasts with other (lower-resolution) reconstructions from northern Fennoscandia which indicate MIS 5c temperatures 6–7 °C lower than present, see Engels et al. (2010). However, several central European sites indicate that there was a phase during the MIS 5d interstadial that was characterised by high summer temperatures, and a comparison between the high-resolution reconstructions from western Europe and the results presented in Engels et al. (2010) suggests that the north–south July air temperature gradient between the mid- and high-latitudes was much weaker during MIS 5c than at present.

Preliminary results from the multi-proxy data obtained for MIS 5a in Helmens (2019) suggest, following deglaciation of a MIS 5b ice-sheet cover of the Sokli site in northern Finland, the development of shrub tundra vegetation to sub-arctic birch forest and then pine-dominated forest with larch. The minimum July temperatures for this time are comparable to the present day (in the order of +12 to +15 °C, Figure 3-5). One suggested reason for the warm climate conditions during this interstadial is that the contemporary astronomical forcing resulted in a weaker north-south temperature gradient and a longer growing period, creating more favourable climate conditions than at present (Väliranta et al. 2009).

Middle Weichselian (MIS 4-MIS 3; 74–24 ka BP)

Examples of Fennoscandian climates during the MIS 3 interstadial (59–24 ka BP) have been studied by use of geological information (Helmens 2009, Wohlfarth 2009) and by climate modelling (Kjellström et al. 2009, including erratum Feb 2010). MIS 3 covers a long time period that includes both rapid millennial-scale climate shifts and longer trends in changing climate, see Wohlfarth (2009) and Helmens (2013). A few examples of climates occurring during MIS 3 are given below.

Early MIS 3 (at ~ 50 ka BP)

A comprehensive environmental reconstruction of early MIS 3 conditions, at around 50 ka BP, was made based on multi-proxy analysis on a two-metre-thick laminated, lacustrine clay-silt sequence obtained at the Sokli site in northern Finland (Helmens 2009). The analyses included lithological characteristics; organic content (loss-on-ignition, LOI); plant microfossils (pollen, spores, algal and fungal remains); macrofossils of plants (e.g. seeds, moss remains) and of aquatic animals (e.g. statoblasts of Bryozoa); head-capsules of chironomids (i.e. aquatic insects); and diatoms and other siliceous microfossils (e.g. phytoliths, chrysophyte stomatocysts). Additionally, geomorphic evidence and analyses of DEM data were employed in the environmental reconstruction. Mean July temperatures were reconstructed by applying transfer functions to the pollen, chironomid and diatom records.

The results have been surprising in various aspects, seriously challenging previous concepts on environmental conditions during early MIS 3 in the near-central area of the Weichselian glaciation. Traditionally, the area is thought to have been ice covered throughout MIS 4–2, i.e. from around 60 ka BP to the final deglaciation, see above. Helmens (2009) showed not only ice-free interstadial conditions but also climate warming to present-day temperatures. The laminated sediments seem to have been deposited in a sheltered embayment of a glacial lake impounded along the ice front of the Weichselian ice sheet. Throughout the deposition of the lacustrine sediments, the reconstructed terrestrial ecosystem on the deglaciated land is low-arctic shrub tundra very similar in composition to modern tundra in the continental sector of northern Fennoscandia. The distributional ranges of pine and tree birch were probably only a few hundred kilometres south or south-east of the Sokli site. This is concordant with the sparse evidence for the presence of boreal tree taxa during MIS 3 in the Baltic countries and further east in Europe but contradicts with the commonly inferred treeless tundra or grass-dominated steppe conditions in central Europe.

Mean July air temperatures similar to present-day values are reconstructed from the chironomid and diatom records as well as on the basis of fossils from aquatic plants and Bryzoa. Temperature inferences based on the terrestrial pollen are consistently lower than the temperatures reconstructed from the fossil aquatic assemblages. It is possible that the regional terrestrial and the local aquatic systems responded differently to the climatic and landscape features at around 50 ka BP. Warmest and moistest conditions are recorded in the lower part of the laminated lacustrine sequence. The chironomid-inferred mean July air temperatures are around 13 °C (i.e. the current temperature) ± 1.15 °C in the lower part of the lake sequence and around 12 ± 1.15 °C in the upper part. The mean July air temperatures inferred from the terrestrial pollen data lie within the range of around 12 ± 1.5 °C (lower part of sequence) and around 11 ± 1.5 °C (higher part of sequence). Hence, the records suggest, albeit with some uncertainty, that there is a gradual cooling during this time. This is consistent with the pattern of the Greenland millennium-scale Dansgaard–Oeschger interstadials in which abrupt warming is followed by a gradual cooling (Dansgaard et al. 1993). High summer temperatures are ascribed in part to enhanced July insolation compared with present at the high latitude of the site.

Comparison with recently published, well-dated sediment sequences in eastern and western Finland suggests ice-free and warm conditions in a major part of eastern Fennoscandia at ~ 50 ka BP. Open birch forest seems to be registered in eastern Finland during part of the warming event. Direct evidence is lacking to reconstruct the total time span with ice-free conditions at the studied sites. It is argued that the Sokli site was glaciated during the overall colder late MIS 3. The absence of well-dated geological data in northern Sweden hampers a reconstruction of the total ice-marginal retreat in the continental sector of the Fennoscandian Ice Sheet during the early MIS 3 climate warming event. For more details on this study, see Helmens et al. (2007, 2009), Engels et al. (2008, 2010), Bos et al. (2009), Helmens (2009) and Helmens and Engels (2010).

A warm climate during early MIS 3, such as reconstructed for northern Fennoscandia by e.g. Helmens (2009), is in line with, and probably necessary for, a deglaciation of the large ice sheet that existed during MIS 4.

Middle MIS 3 (at 44 ka BP)

A comprehensive climate modelling study was performed to investigate climate extremes within which the climate in Fennoscandia may vary on a 100-ka timescale (Kjellström et al. 2009, including erratum dated Feb 2010). Three different periods were simulated, a cold glacial climate (at LGM, ~ 21 ka BP), a periglacial climate (at MIS 3, 44 ka BP) and a warm future climate dominated by global warming (a few thousands of years after present). In the present section, results from the periglacial climate simulation are presented. Results from the LGM climate simulation are presented below in the present section, under the heading "Late Weichselian including LGM (24–12 ka BP)", whereas results from the global warming simulation are described in Section 3.4.6.

In order to give a detailed example of a modelled periglacial MIS 3 climate over northern Europe, climate modelling was performed using a global climate model (GCM) that produced boundary conditions for a regional climate model (RCM) (Kjellström et al. 2009). This model study was designed also to test whether a cold and dry climate favourable for permafrost growth would exist in the ice-free regions surrounding a Fennoscandian MIS 3 ice sheet with a restricted ice configuration. Based on forcing conditions for a selected period during MIS 3 (Greenland stadial 12 at 44 ka BP), a simulation of middle MIS 3 climate conditions was performed with the climate models. For the simulations performed and analysed within this study, atmospheric and land components of the CCSM3 GCM used a grid spacing of approximately 2.8° in latitude and longitude. The vertical resolution is 26 levels in the atmosphere and 40 levels extending to 5.5-km depth in the ocean. The regional climate model used a horizontal resolution of 50 km and a time resolution of 30 minutes. For details on the models, how they were employed, and a discussion on climate model uncertainties, see Kjellström et al. (2009).

The choice of period to simulate for MIS 3 followed from a workshop on MIS 3 organised by SKB in September 2007 (Näslund et al. 2008) with the specific purpose of supporting this selection. Only limited and in some cases controversial, paleo-information is available to reconstruct the extent of the Fennoscandian ice sheet during the different warm and cold intervals of MIS 3. It was here assumed, in line with several recent studies, see above, that the southern part of Fennoscandia was ice free during some of the MIS 3 stadials.

The modelling activities included the use of; i) a fully coupled Atmosphere-Ocean General Circulation Model (AOGCM; Community Climate System Model version 3, CCSM3), ii) a Regional Climate Model (RCM; Rossby Centre Regional Climate Model, RCA3), and iii) a dynamic vegetation model (DVM; the LPJ-GUESS model). The AOGCM was used to simulate the global climate in steady-state simulation for the selected time period. Even though AOGCMs are powerful models, they are relatively coarse in their resolution due to computational limitations. Therefore, the output from the AOGCM was used as input to an RCM that provides output at a relatively high horizontal resolution for Europe. Both global and regional climate models hold descriptions of the land surface, including vegetation. In the regional model, it is important to describe the vegetation cover with a high degree of regional detail. Such details are missing in available global fields and details of the vegetation cover have to be estimated, based on the global fields and consideration of, among other things, land/sea distribution. In order to improve the representation of the regional vegetation, a dynamic vegetation model was used to simulate the European vegetation resulting from the RCM-simulated climate. In a subsequent step, the new vegetation was used in a new RCM simulation that provided the final climate output. For the studied MIS 3 period, data on relevant climate parameters was extracted from the regional model for the Forsmark area.

The global model simulation of the periglacial MIS 3 climate used a CO_2 concentration in the atmosphere of 200 ppm (Kjellström et al. 2009). An ice sheet with a restricted configuration was assumed, and, in line with this, a simulated MIS 3 ice sheet configuration obtained from the Weichselian ice sheet reconstruction described in Section 2.3.4 was used (Kjellström et al. 2009). For a detailed description of the assumptions made in the modelling process, model forcing and initial conditions (such as astronomical and solar forcing, concentration of greenhouse gases and aerosols in the atmosphere, extents of ice sheets, distribution of land and sea, topography and vegetation), also see Kjellström et al. (2009).

In addition to the modelling activities, an effort was made to collect palaeoclimatic information by compiling various MIS 3 and LGM proxy data from different sources (Kjellström et al. 2009, Wohlfarth 2009). Part of this palaeoclimatic information was used to constrain the forcing conditions used in the climate models. Other proxy data were used for model evaluation purposes. Results from the global climate model were compared with proxy records of sea-surface temperatures and with terrestrial climate records. The regional climate model results have been compared with existing terrestrial palaeoclimate records from Europe.

Global climate

Figure 3-7 shows the simulated global climate from the middle MIS 3 simulation. Seasonal mean changes in temperature as compared with a simulation of the pre-industrial climate (with forcing conditions set at levels consistent with those preceding the 18th century) are also shown.

The annual mean surface cooling in the MIS 3 simulation as compared with pre-industrial conditions is most pronounced over the Laurentide and the Fennoscandian ice sheets and over the Greenland–Iceland–Norwegian Sea, with a maximum cooling of 25 °C (Figure 3-7). A large portion of the cooling over the Fennoscandian and Laurentide ice sheets is due to the increased elevation over the ice sheet. The cooling amounts to 5–10 °C north of 40°N in the Atlantic Ocean, the Arctic Ocean and over Antarctica and the Southern Ocean. The sea-ice extent is increased in the MIS 3 simulation in the North Atlantic and North Pacific as compared with the pre-industrial simulation (Figure 3-7).

Even though proxy data for the period around 44 ka BP are sparse, comparison with available sea surface temperature data shows that the globally modelled temperatures and proxy data are in reasonable agreement. For further results and discussion of the MIS 3 simulation from the global climate model, and for details about the comparison with MIS 3 climate proxy data, see Kjellström et al. (2009).

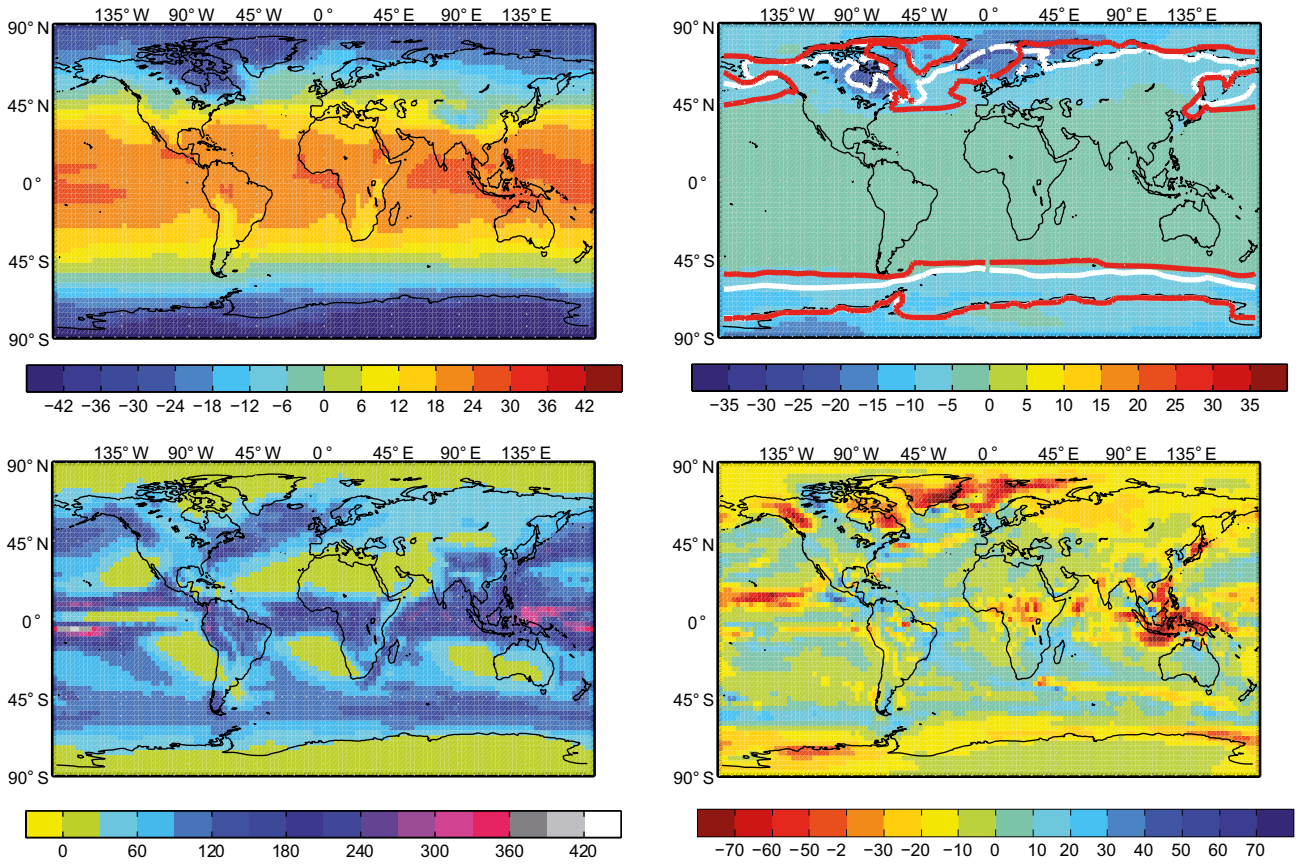

Figure 3-7. *Annual mean near-surface air temperature in the MIS 3 simulation (upper left) and the difference compared with a simulated pre-industrial climate (upper right). Units are °C. Also shown is the annual mean sea ice edge (defined at 10 % areal sea ice cover) for the pre-industrial simulation (white; upper right)) and the MIS 3 simulation (red; upper right). The lower panels show the simulated precipitation (lower left) and the difference compared with the simulated pre-industrial climate (lower right). Units are mm month^{-1}. From Kjellström et al. (2009).*

Climate in Europe and Sweden

The regional climate model was then used to downscale the model results of the global climate model in order to obtain a higher resolution data over Europe and Sweden. The resulting climate over Europe was used to produce a new vegetation distribution with the vegetation model. This vegetation was in turn, used as input to the regional climate model, to produce a climate in line with the new vegetation. An evaluation of the results from this iterative process is given in Kjellström et al. (2009). Figure 3-8 to Figure 3-11 presents selected results on temperature and precipitation from the regional modelling.

During this part of the middle Weichselian, the simulated temperature is dominated by a very strong seasonal cycle (Figure 3-9) and a pronounced north–south gradient in the winter (Figure 3-8, upper row, middle panel). In the north, the effect of the Weichselian ice sheet is clearly seen in the isolines of temperature showing low temperatures in parts of Fennoscandia. The isotherm showing 0 °C annual mean temperature goes south of Ireland, through England and the southern parts of Denmark, just south of Sweden and then eastwards (Figure 3-8, upper row, right panel). Compared with the present climate (1961–2000), the annual mean temperature in the MIS 3 simulation is ~ 5 °C colder around the Mediterranean, 5–10 °C colder in central Europe and more than 8 °C colder in the ice-free parts of Fennoscandia (Figure 3-8, lower row, right panel). The same values as for difference in annual temperature apply for winter temperature in southern and central Europe. The winter temperature of the British Isles is 10–15 °C colder and the southern tip of Fennoscandia around 15 °C colder in comparison with the present climate (Figure 3-8, lower row, middle panel). Over the ice sheet in northern Fennoscandia, temperatures are at least 30 °C colder than in the present climate (1961–2000) simulation. On Iceland and over the Norwegian Sea, the difference from the late 20th century is even larger. In summer, most of continental Europe is 0–5 °C colder than in the late 20th century, western Europe and the British Isles are 5–10 °C colder and northern Fennoscandia is 10–15 °C colder than in the simulated present climate (Figure 3-8, lower row, left panel).

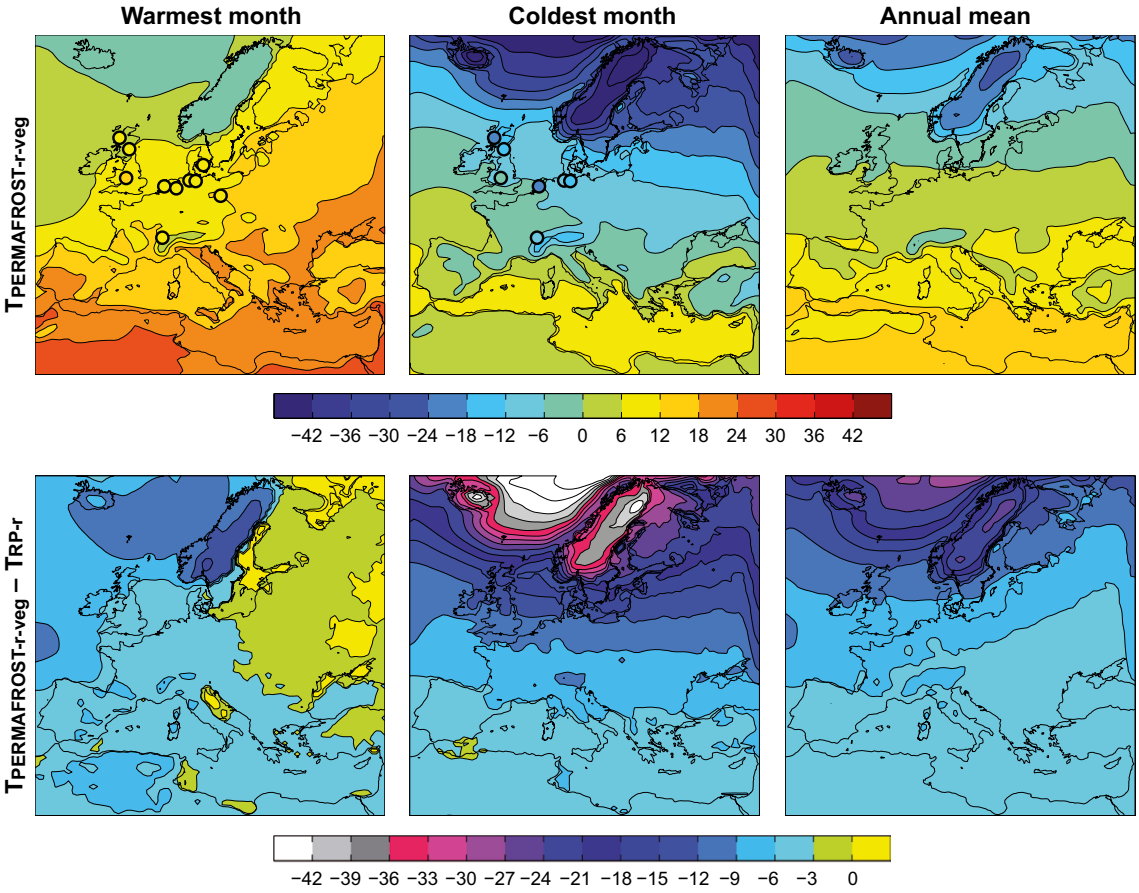

Figure 3-8. *Mean air temperatures of the warmest month, coldest month and annual mean in the MIS 3 simulation (top). Shown also are temperature estimates based on proxy data as described in Kjellström et al. (2009, Section 2.4) (coloured circles). The lower row shows the differences between the simulated MIS 3 climate and a recent-past climate simulated for the period 1961–2000. From Kjellström et al. (2009).*

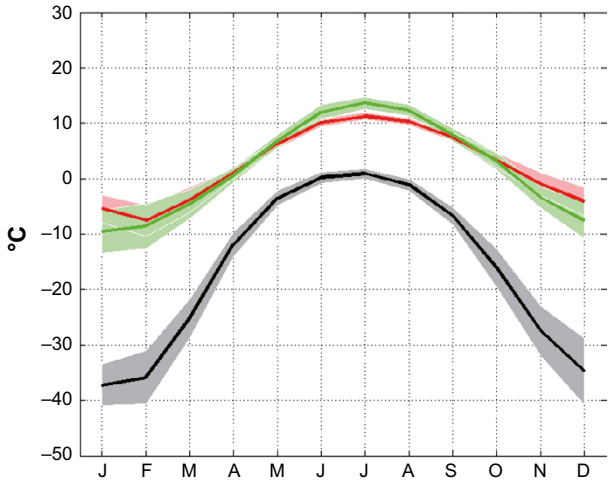

Figure 3-9. *Annual temperature range in Sweden for MIS 3 (black), simulated present climate (red) and according to the CRU (Climate Research Unit, East Anglia) observational data for the time period 1961–1990 (green). Shaded areas in corresponding colours indicate the ± 1 standard deviation range of individual monthly averages in the three data sets. From Kjellström et al. (2009).*

The annual mean precipitation in the MIS 3 simulation is characterised by considerably drier conditions than in the simulated present climate (1961–2000), by more than 360 mm a^{-1} in large parts of Fennoscandia and over the North Atlantic, and by an increase in precipitation of up to 360 mm a^{-1} in parts of the southwest (Figure 3-10, upper row right panel). In the rest of the model domain, differences are, with few exceptions, smaller.

The drier climate in northern Europe is reflected in the seasonal cycle of precipitation. For Sweden there is a reduction of more than a factor of two in winter and substantial reduction also during summer (Figure 3-11). Further south, the reduction is most evident in the winter half of the year, whereas in southernmost Europe the changes relative to the present climate are small for all months.

For further results, on the European scale, from the MIS 3 climate simulations, including results and discussion of the simulations of MIS 3 vegetation, comparisons with climate proxy data, and comparisons with other model simulations of MIS 3 climates, see Kjellström et al. (2009).

Do the results support a cold and dry climate favourable for permafrost growth? Heginbottom et al. (1995) examined the relation between ground temperature and permafrost continuity. An annual ground temperature of between –5 and –2 °C is defined as the boundary for discontinuous permafrost (50–90 % of landscape covered by permafrost) and –5 °C and colder as the boundary for continuous permafrost (90–100 %). However, it is also stated that a large fraction of areas with continuous permafrost has a ground temperature warmer than –5 °C. Since the ground temperature differs from the near-surface air temperature by a few degrees, the simulated annual mean ground temperatures over Europe for MIS 3 are presented in Figure 3-12.

In central and northern Fennoscandia, outside of the prescribed ice sheet, the modelled MIS 3 annual average ground temperature is colder than –5 °C (Figure 3-12), which suggests that the climate conditions are favourable for development of continuous permafrost. South of this, the modelled annual average ground temperature increases, reaching 0 °C in the southernmost parts of Fennoscandia. The higher ground temperatures in the southern areas including northernmost Denmark, southern Sweden, Estonia and part of what today is the Baltic Sea and Gulf of Finland do not fulfil the thermal requirements for extensive permafrost. However, it is cold enough for sporadic permafrost (less than 50 % of landscape covered), which may exist when the annual mean ground temperature is between 0 and –2 °C. Based on these results of Kjellström et al. (2009) it is concluded that conditions were favourable for permafrost growth in the inferred ice-free parts of Fennoscandia.

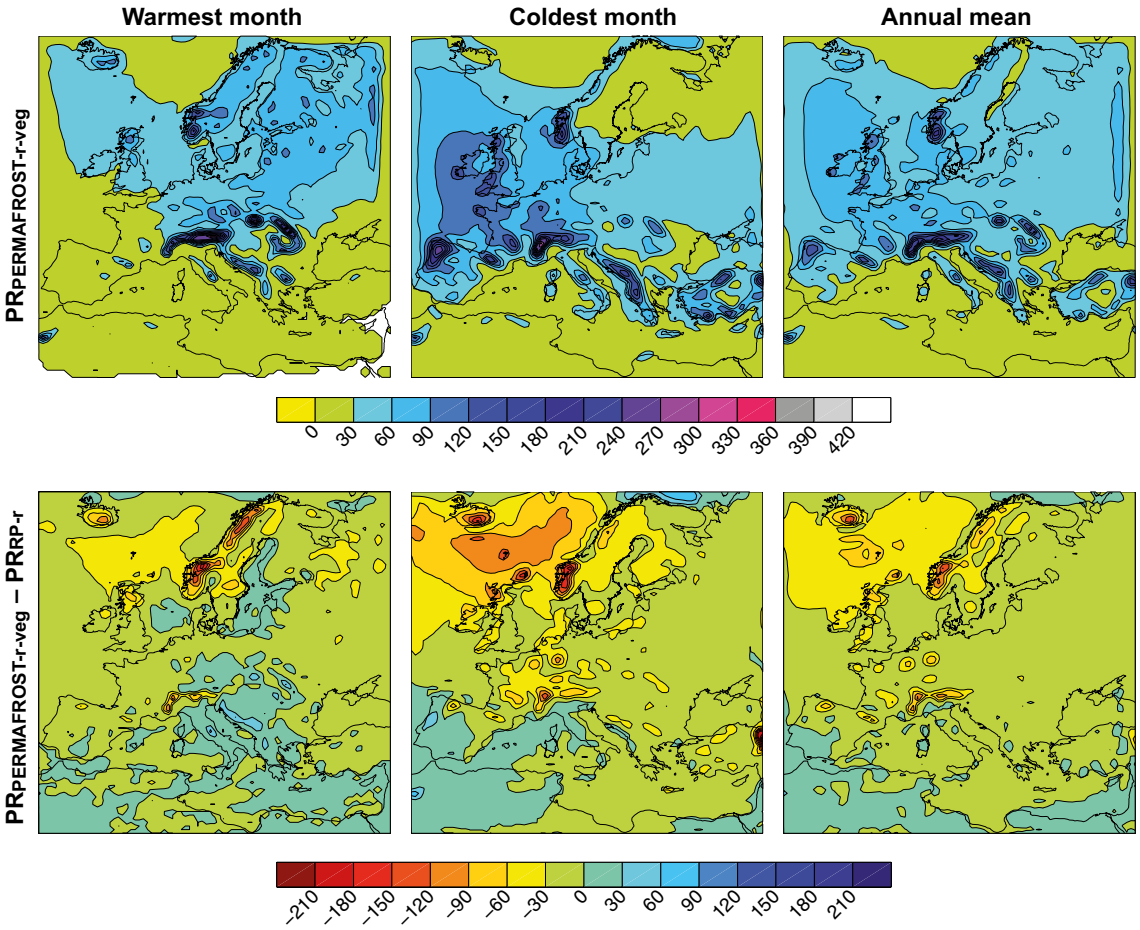

Figure 3-10. *Mean precipitation of the warmest month, coldest month and annual mean in the MIS 3 climate simulation (upper row). Also shown are differences between MIS 3 simulation and the simulation of the present (1961–2000) climate. Units are mm month^{-1}. From Kjellström et al. (2009).*

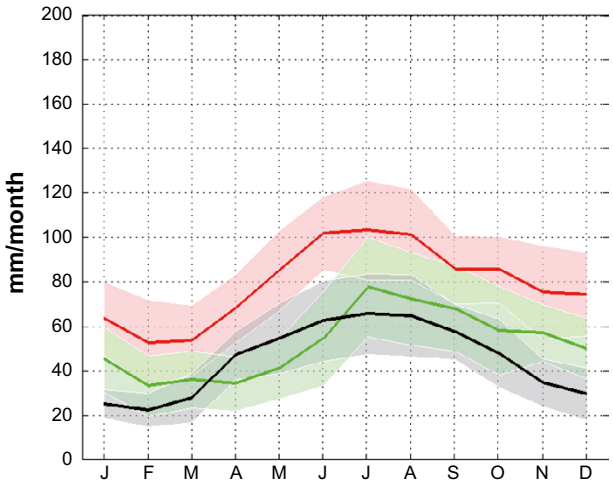

Figure 3-11. *Annual precipitation range in Sweden in the MIS 3 simulation (black), present climate simulation (1961–2000) (red) and according to the CRU observational data (green). Shaded areas in corresponding colours indicate the ± 1 standard deviation range of individual monthly averages in the three data sets. From Kjellström et al. (2009).*

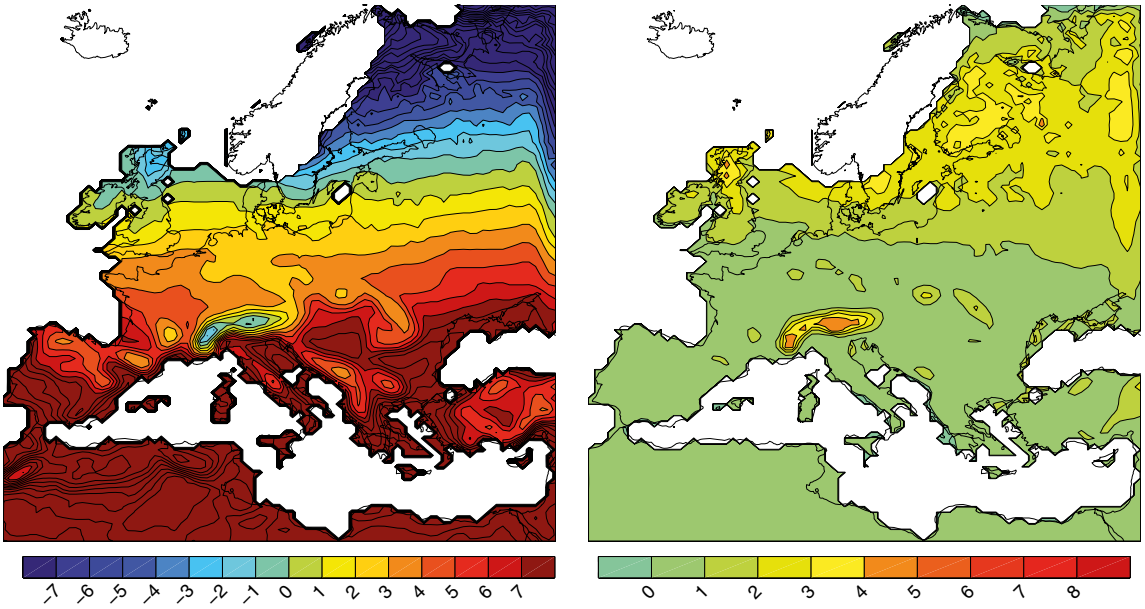

Figure 3-12. *Annual mean ground temperature (left) and difference between near-surface air temperature and the ground temperature (right) in the MIS 3 simulation. Units are °C. White areas in Fennoscandia are covered by the prescribed restricted MIS 3 ice sheet. From Kjellström et al. (2009).*

Do the results support a restricted MIS 3 Fennoscandian ice sheet? The global and regional climate models do not include dynamical modelling of ice sheets and thus an ice sheet cannot form in the models, even if the climate conditions are favourable for ice-sheet growth. The snowpack is, however, allowed to build up in the model. If the snow depth increases in time in a specific region, we can take this as an indication that an ice sheet would grow in this region if such processes were included in the model. However, the opposite situation, a lack of snow accumulation in front of, or at the margins of, a prescribed ice sheet, does not necessarily mean that the ice sheet would not grow (simply that the lowermost part of the ice sheet would have a net mass loss, which is typical for ice sheets ending on land). Growth of the ice sheet could still be possible if the precipitation over the ice sheet were large enough compared with its mass loss by melting, i.e. if conditions for the common pattern of ice-sheet growth were satisfied.

In the middle MIS 3 simulation, the snow depth in eastern Sweden, including the Forsmark region, does not increase in time. The annual minimum snow depth (occurring in September) is close to zero (varying from 0–0.02 m equivalent water depth). For the issue of whether the simulated climate is in line with the prescribed restricted middle MIS 3 ice sheet configuration, with ice-free conditions in e.g. the Forsmark region (Figure 3-12), one can therefore conclude that 1) an ice sheet would not grow locally from the local precipitation in front of the ice margin, 2) the modelled temperature and precipitation climate in front of the ice sheet is consistent with the assumed ice-free conditions and restricted ice-sheet coverage, but it does not exclude the possibility of a larger ice sheet.

Climate in the Forsmark region

Figure 3-13 and Figure 3-14 show average air temperature and precipitation for a 50-year period of the simulated MIS 3 climate, and a comparison with the climate simulated for present conditions. The results show that the climate is significantly colder and drier than at present, with arctic climate conditions prevailing in the Forsmark region.

The last step in the MIS 3 climate modelling study was to extract climatological data for the Forsmark region from these regional modelling results. Figure 3-15 show the grid boxes used for extraction of data. Information was extracted from the grid point located closest to the Forsmark site.

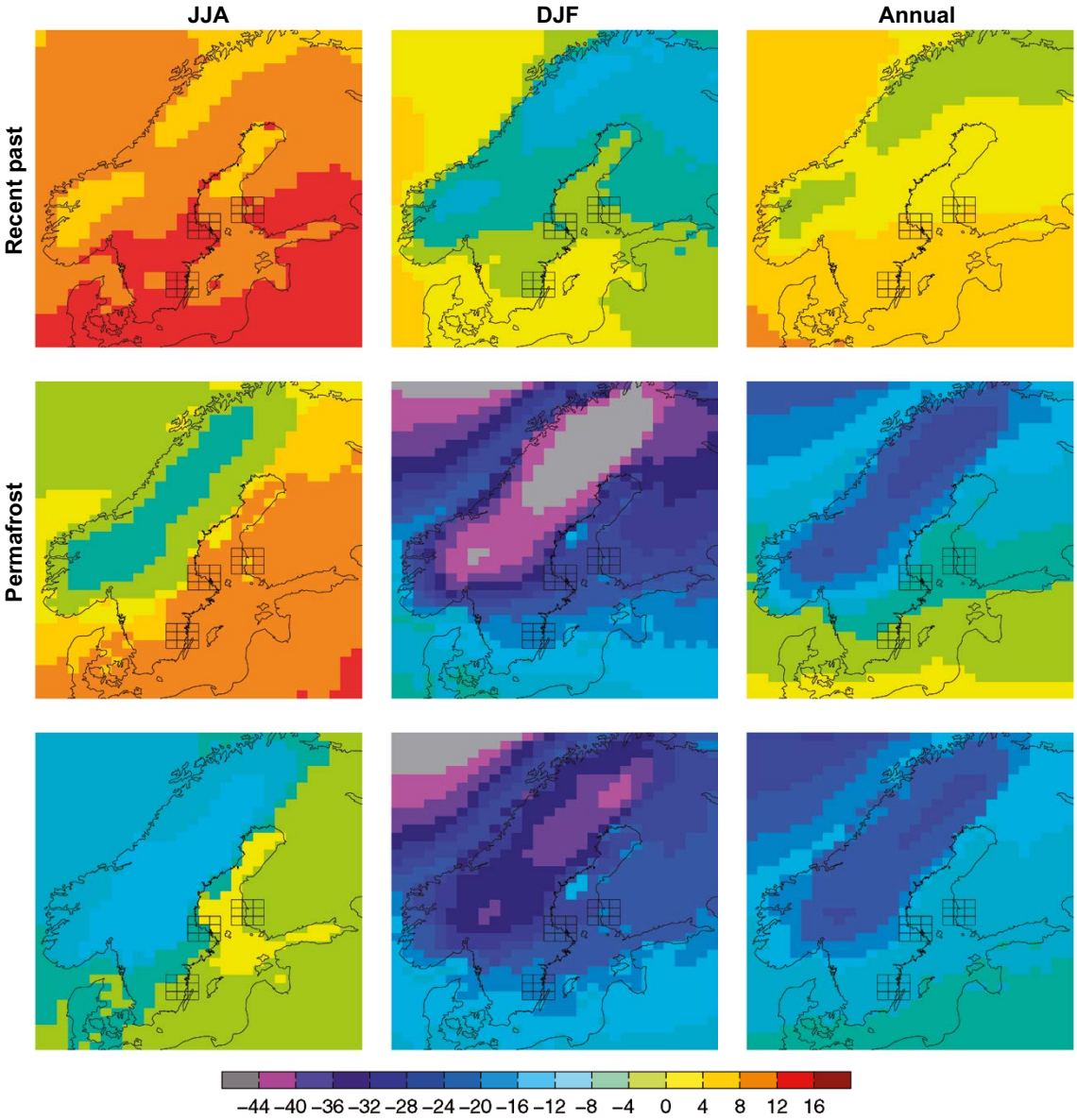

Figure 3-13. *Seasonal and annual mean temperature for the present (1961–2000) (upper row) and MIS 3 (middle row) climate simulations. The lower row shows the difference between the two. Units are °C. From Kjellström et al. (2009).*

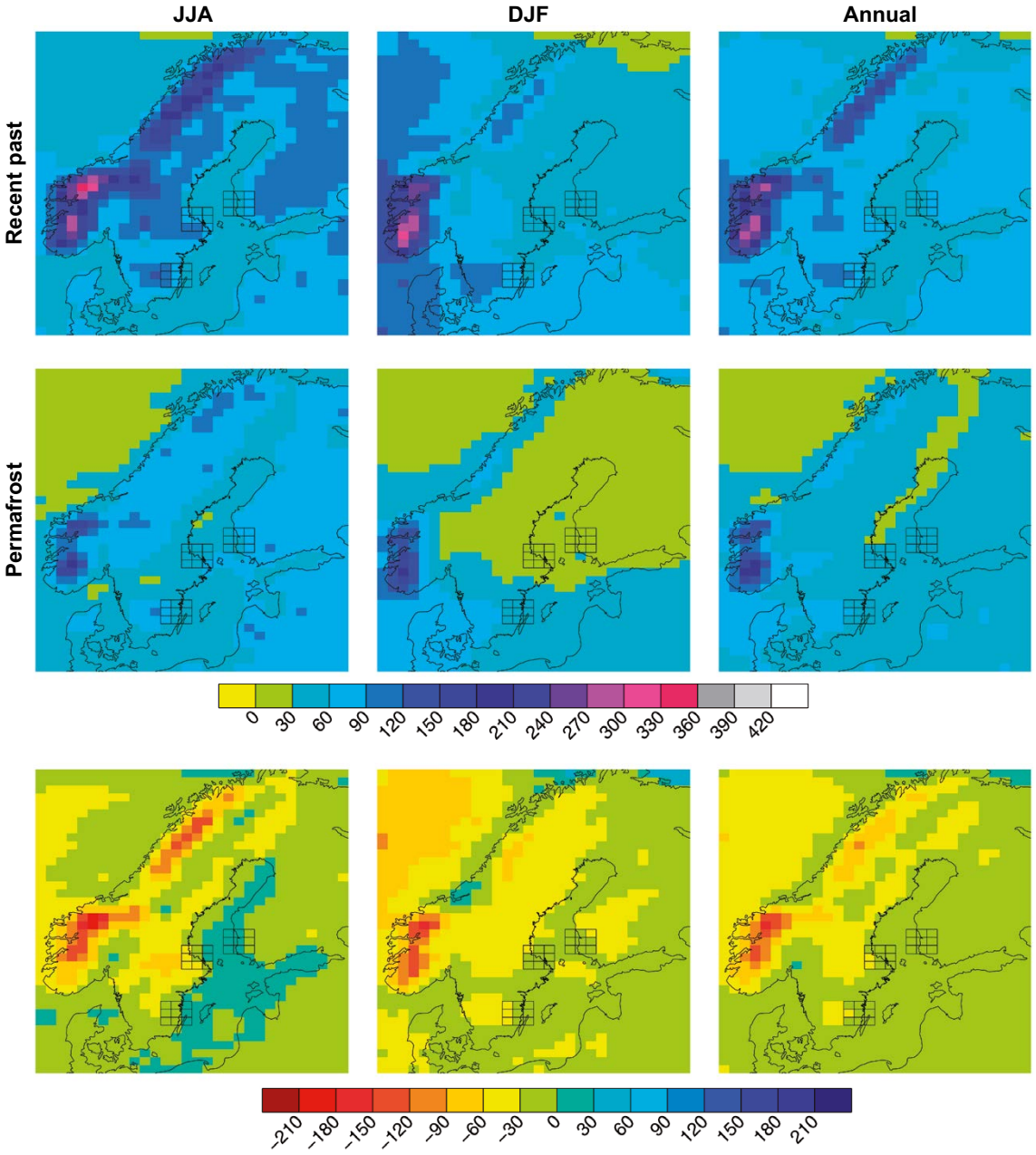

Figure 3-14. *Seasonal and annual mean precipitation in the present (1961–2000) (upper row) and MIS 3 (middle row) climate simulation. The lower row shows the difference between the two. Units are mm month^{-1}. From Kjellström et al. (2009).*

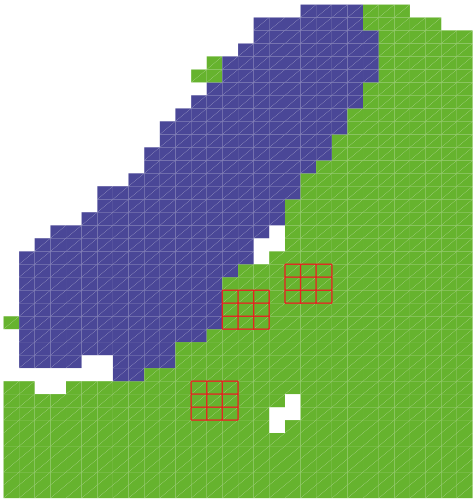

Figure 3-15. *Land (green), ice sheet (blue) and sea extent (white) in the Fennoscandian region used for the MIS 3 climate simulation. The 3 × 3-grids represent grid boxes covering the Forsmark (F), Oskarshamn (Os) and Olkiluoto Ol) sites (centre box) and the eight surrounding boxes. Grid boxes with a land fraction lower than 20 % are not filled. Results from Oskarshamn and Olkiluoto are presented in Kjellström et al. (2009). From Kjellström et al. (2009).*

50-year average values from the regional MIS 3 climate simulation show that the annual mean air temperature in the Forsmark region is –7.6 °C during the inferred ice-free stadial 44 ka ago. This is 12 degrees lower than in the simulated present climate (1961–2000). The largest difference compared with the simulated present climate in the seasonal cycle of temperature is seen in winter (Figure 3-16, upper row, second column).

The mean annual precipitation in the Forsmark region is 441 mm, which is 225 mm (or 30 %) less compared with the simulated present climate. In this periglacial climate, the precipitation is lower than in the present climate for most parts of the year, and there is a very strong seasonal cycle in snow cover as the temperatures during summer get well above 0 °C allowing complete snow melting Figure 3-16, upper and lower row, second column). The length of the completely snow-free season is three months and there is a more or less constant snow cover during at least 3 months.

The annual surface runoff is 139 mm in this exemplified periglacial climate, which is somewhat less (36 mm a^{-1}) than in the simulated present climate. In the MIS 3 climate, there is a clear spring peak in runoff connected with the snow melt which is more extensive than in the simulated present climate, since more snow is accumulated on the ground during the winter. During the remaining part of the year, the runoff is fairly small, due to the cold conditions during winter and the relatively small amounts of precipitation during summer. Given the uncertainties and assumptions used in the climate modelling, the model results thus show that the MIS 3 climate in the Forsmark region may be characterised as being a significantly colder and drier climate than at present and also that the surface runoff is reduced.

The annual mean ground temperature is about –4 °C in the Forsmark region (Figure 3-12). According to Heginbottom et al. (1995) this temperature indicates that climate conditions are favourable for discontinuous permafrost (covering 50–90 % of the landscape). The cold and dry climate with partially snow-free conditions implies that the climate is very favourable for permafrost growth.

In summary, the results from Kjellström et al. (2009, including erratum dated Feb 2010) show that i) the climate models produce a cold and dry arctic climate in the Forsmark region for a stadial during MIS 3, ii) the resulting climate is in agreement with ice-free conditions in south-central Fennoscandia and iii) that this climate is suitable for permafrost growth in the Forsmark region.

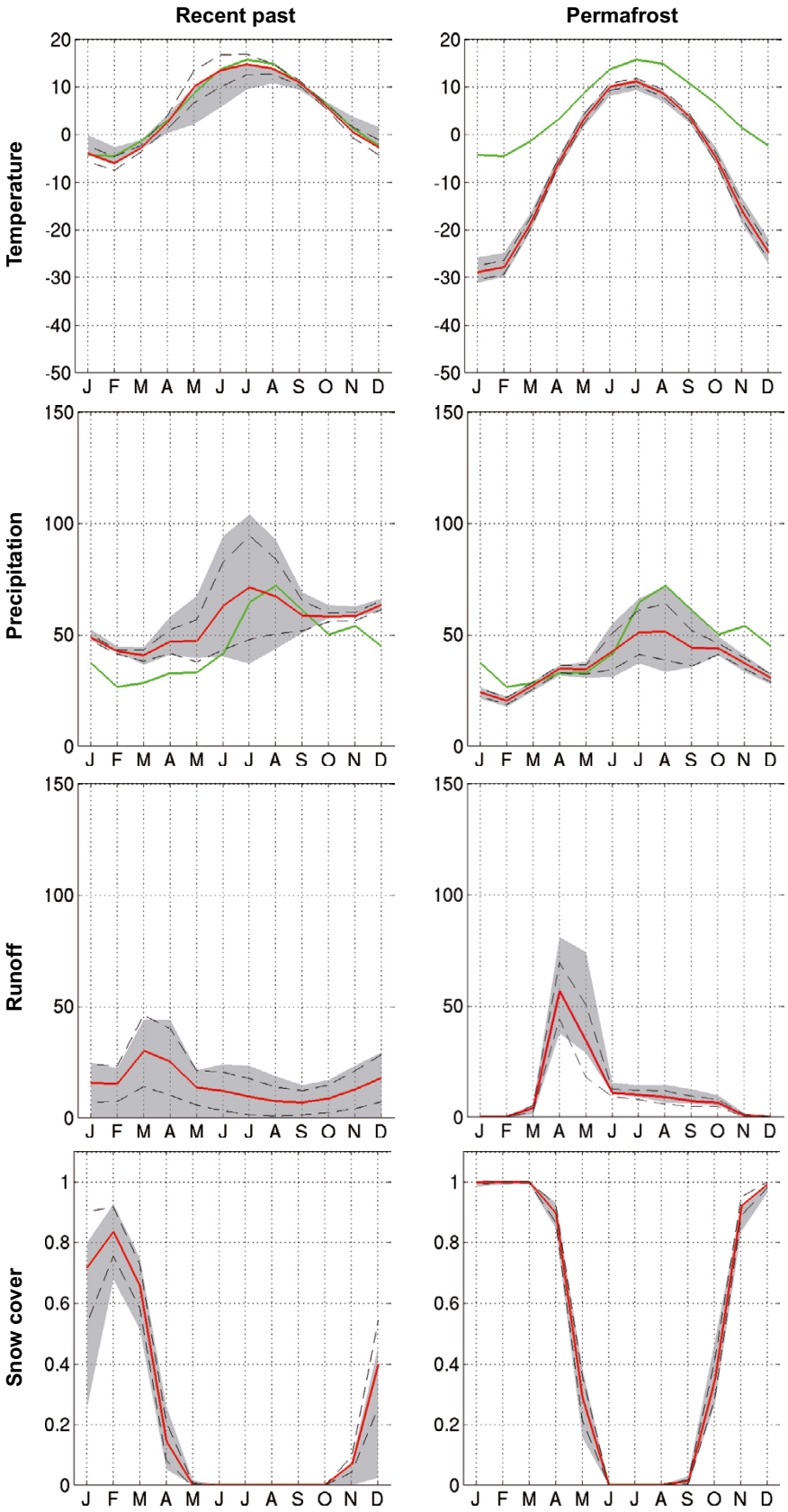

Figure 3-16. *Simulated seasonal cycles of temperature (°C), precipitation (mm month^{-1}), runoff (mm month^{-1}) and snow fraction (dimensionless ranging from 0 to 1) at the grid box closest to the Forsmark site (red line). The spatial variability in the 3 × 3-grids (Figure 3-15) is displayed with the dashed lines representing ± 1 standard deviation calculated from the 9 grid boxes, and the grey area representing the absolute maximum and minimum, of the 9 grid boxes. The green line for temperature and precipitation is the observed seasonal cycle from the CRU data set for the period 1961–1990, see Kjellström et al. (2009). From Kjellström et al. (2009).*

The major uncertainties in the climate simulation are related to uncertainties in forcing, model formulation and natural variability. These uncertainty aspects are discussed in detail in Kjellström et al. (2009). For further details on the setup, results, and discussion of the MIS 3 climate modelling results, see Kjellström et al. (2009 including erratum dated Feb 2010) and Brandefelt et al. (2011).

Following the very warm temperatures reconstructed for *early* MIS 3, described above, which are suggested to have resulted in ice-free conditions over large parts of Fennoscandia during MIS 3 (e.g. Helmens et al. 2009, Wohlfarth 2009, Wohlfarth and Näslund 2010), the low air temperatures simulated for Fennoscandia for the middle MIS 3 stadial (44 ka BP) are in line with the view that the Weichselian ice sheet needs to re-grow to attain the known large MIS 2 (LGM) ice configuration in a relatively short time.

Late Weichselian including LGM (24–12 ka BP)

As previously mentioned, all of Fennoscandia was covered by the Weichselian ice sheet during the Last Glacial Maximum, which occurred during the Late Weichselian. At that time, air temperatures were among the lowest of the last glacial cycle (Jouzel et al. 2007). To study the climate during the LGM in a consistent way with the simulation of a periglacial climate, the same models and modelling approach as for the periglacial climate modelling described above was used for LGM simulations. The LGM climate model simulations were set up to resemble conditions at the time of LGM in a way as similar as possible to what was done in the Palaeoclimate Modelling Intercomparison Project (Joussaume and Taylor 2000, Harrison et al. 2002). This choice facilitates comparisons with other GCM results. It also allowed the use of pre-existing long simulations with the general circulation model CCSM3 performed at the National Centre for Atmospheric Research (NCAR) in the USA (Otto-Bliesner et al. 2006), reducing the model spin-up time needed for this study. Further, as the LGM is part of the most recent Weichselian glacial period, there is a better possibility of finding climate proxy data than for earlier cold stadials during the Weichselian. The orbital year 21 ka BP and a CO_2 level of 185 ppm were used in the LGM simulation. Ice-sheet configurations were the same as in the PMIP-2 project (Harrison et al. 2002), which were based on the ICE-5G data (Peltier 2004). For a description of the set-up of all other forcing conditions see Kjellström et al. (2009).

Global climate

The global LGM simulation is a continuation of an LGM simulation performed at NCAR (Otto-Bliesner et al. 2006). The simulation was originally initiated from a simulation of pre-industrial climate, except for the ocean which was initiated by adding three-dimensional anomalies of ocean temperature and salinity derived from an LGM simulation with the Climate System Model version 1.4 (CSM1.4) (Shin et al. 2003) to the CCSM3 pre-industrial simulation. The simulation was first run for 400 years at NCAR and was then continued for another 856 years within the present study. The annual global mean surface temperature reaches quasi-equilibrium after 100–150 years, after which it continues to cool and reaches a new quasi-equilibrium after a total of 750–800 years. This second quasi-equilibrium extends until the simulation is ended at model year 1538 (Kjellström et al. 2009 erratum Feb 2010). The annual global mean surface temperature is 9.0 °C in the first quasi-equilibrium and 7.9 °C in the second LGM equilibrium, i.e. 4.5 °C and 5.6 °C colder than the corresponding simulated pre-industrial temperature (Kjellström et al. 2009, Brandefelt and Otto-Bliesner 2009). The second equilibrium also results in a 30 % reduction in the strength of the Atlantic Meridional Overturning Circulation (AMOC) compared with the first quasi steady-state (Brandefelt and Otto-Bliesner 2009).

The global climate model LGM simulation thus shows that the global mean air temperature during the LGM could have been more than one degree colder than previously thought, and also that the variability in global mean temperature was larger. The variability is attributed to coupled ocean–atmosphere–sea ice variations in the North Atlantic region. The difference between globally warm and cold years is focussed over oceans in the Northern Hemisphere outside the tropics. The largest difference between cold and warm years is found over Greenland and Northern Europe, with a maximum of 6.8 °C. The total amount of precipitation is up to 32 % higher over the North Atlantic and North Pacific region in warm years than in cold years at the LGM. Furthermore, the sinking branch of the AMOC is shifted further north in globally warm years as compared with cold years.

Further results, and discussions of their significance, are found in Kjellström et al. (2009, including erratum dated Feb 2010).

Significant effort was made to compile LGM climate proxy data for model validation. For the comparison between global LGM model results and marine and terrestrial LGM climate proxy data, see Kjellström et al. (2009).

Climate over Europe and Sweden

A very cold LGM climate, with annual mean temperatures below 0 °C in all of Europe north of about 50°N and also in high-altitude regions in southern Europe is clearly seen in the regional climate model results (Figure 3-17, upper row right). In winter, the situation is even more striking with the 0 °C line encompassing basically all of continental Europe and monthly mean temperatures below –40 °C over the northern parts of the ice sheet (Figure 3-17, upper row middle). During summer, the area with the lowest temperatures is more confined to the ice sheet, the extent of which is readily visible in Figure 3-17 (upper left). In winter when most parts of Europe are snow covered, the gradient is less pronounced as there is no abrupt shift from snow-covered to snow-free conditions. The annual mean temperature in the LGM simulation is 25–30 °C lower than the simulated present climate. Over the southern parts of the ice sheet (British Isles, southern Fennoscandia) the annual mean temperature is around 15 °C lower than today. At the edge of the ice sheet, there is a strong gradient towards smaller temperature differences. Central Europe is around 8 °C colder than today and southern Europe around 6 °C colder. In winter the temperature over the Fennoscandian ice sheet is around 40 °C colder than present Fennoscandian temperatures.

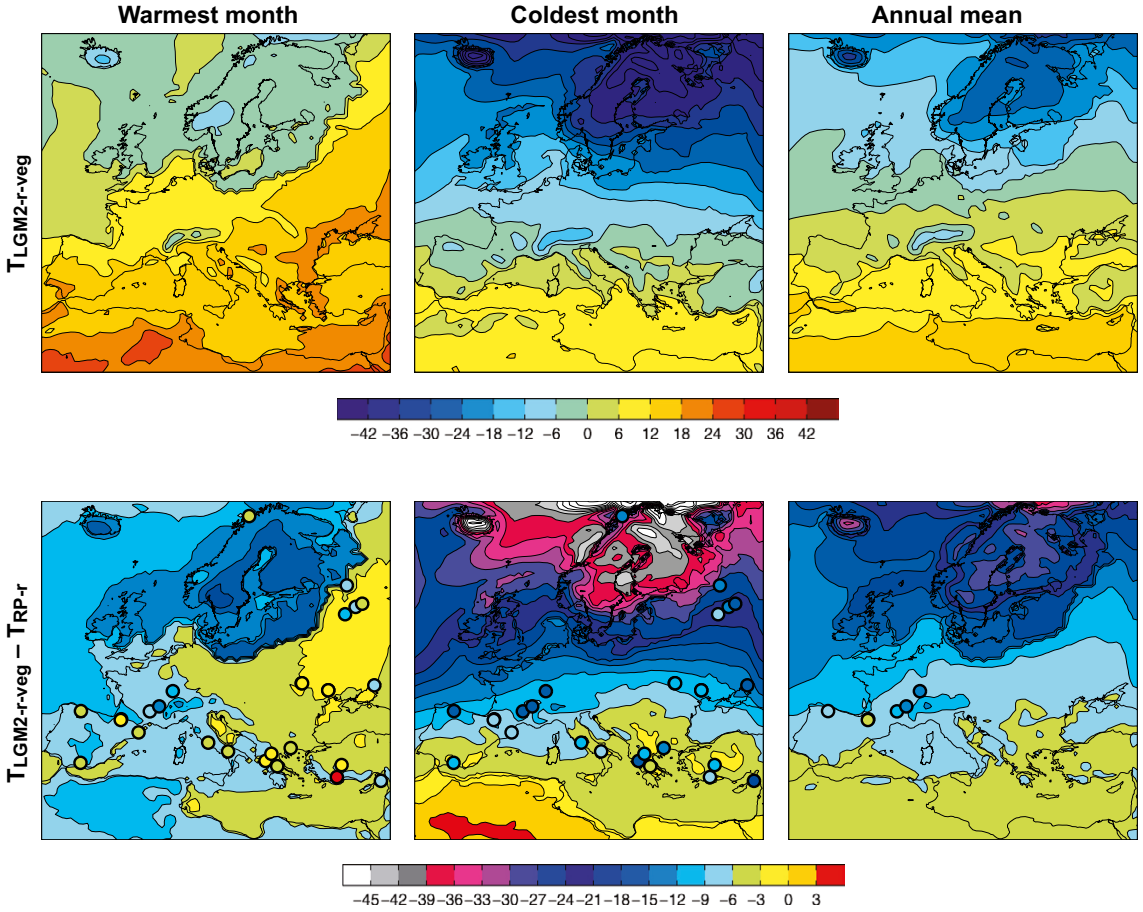

Figure 3-17. *Mean temperatures of the warmest and coldest month and annual mean for the LGM simulation (denoted LGM2-r-veg) (upper row). Also shown are differences between the LGM simulation and the simulation of the present climate (years 1961–2000 AD) (denoted RP-r) (lower row). Climate-proxy-based temperature reconstructions are denoted in the filled circles. Units are °C. From Kjellström et al. (2009).*

Annual mean precipitation has its maximum over the North Atlantic and over parts of Western Europe (Figure 3-18, upper right). Relatively small amounts of precipitation are simulated in the northern parts of Fennoscandia and over the Mediterranean Sea and North Africa. Compared with the simulated present climate (1961–2000), Fennoscandia, the British Isles and Iceland are drier (Figure 3-18, lower right). More precipitation than at present is seen in southernmost Europe (the Iberian Peninsula, Italy) and northwest Africa. Fennoscandia and Western Europe receive less precipitation than in the present climate. The steep coastlines of western Fennoscandia and Scotland which today are facing the ocean and therefore get a lot of precipitation were, during the LGM, parts of the ice sheet that extended further westward. Without the strong orographic effect, precipitation is considerably smaller in this region during the LGM. In summer, as in winter, precipitation is less than in the present climate in most parts of northern Europe. However, more precipitation in the LGM simulation is seen on the edge of the Weichselian ice sheet northwest of Fennoscandia and over the British Isles (Figure 3-18, upper and lower left panels). Another area with more precipitation than in the present climate is the area of what is today the Baltic Sea. During the LGM this area partly coincided with the most elevated parts of the ice sheet in which the regional climate model produces large amounts of precipitation during summer.

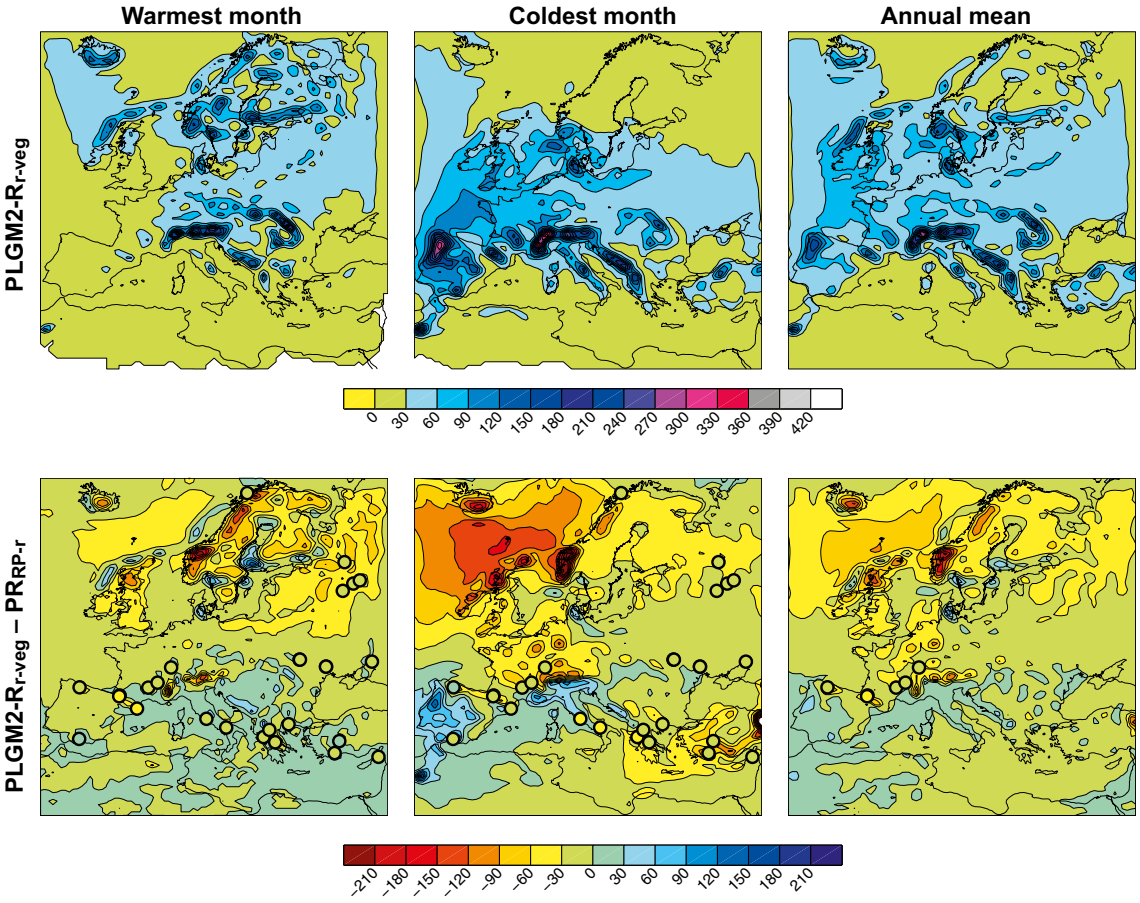

Figure 3-18. *Mean precipitation of the warmest month, coldest month and annual mean in the LGM simulation (denoted PLGM2-r-veg) (upper row). Also shown are differences between the LGM simulation and the simulation of the present climate (year 1961–2000) (denoted RP-r) (lower row). Units are mm month^{-1}. From Kjellström et al. (2009).*

Comparison with other model simulations

The simulated annual global mean temperature in the LGM simulation (i.e. the second quasi-equilibrium described in the beginning of this section) is 6.9 °C lower than in the present climate. This is a stronger response than in most of the PMIP1 (full range is 1.85–9.17 °C colder than in the present climate) and PMIP2 simulations (3.4–5.46 °C colder than the pre-industrial climate) presented by Kageyama et al. (2006). The results indicate that much of the strong cooling is associated with low Sea Surface Temperatures (SSTs) (up to 6 °C colder than some proxy data indicate) and extensive sea-ice cover in the North Atlantic and North Pacific.

These changes in sea-ice extent are a result of the changes in the temperature climate, but they also act to amplify the changes, as increased sea-ice extent leads to a colder climate through the feedback mechanisms involving increased surface albedo and reduced heat fluxes from the ocean to the atmosphere. This connection between low SSTs at high northern latitudes and the global mean temperature for the LGM simulation is in contrast with the PMIP simulations discussed by Kageyama et al. (2006). They find that winter and summer temperature changes over the North Atlantic, Europe and western Siberia do not relate closely to global temperature changes.

Regardless of possible biases in SSTs, the simulated changes in annual mean temperatures over Europe in the global model are similar to those obtained in the high-resolution atmosphere-only CCM3-simulations by Kim et al. (2008). In both our global and regional models, the coldest month of the year is warmer than proxy data indicate. This is a result also shown for the PMIP1 and PMIP2 simulations (Ramstein et al. 2007, Kageyama et al. 2006). However, even though the models are warmer than the proxy data indicates, Ramstein et al. (2007) conclude that they are within the confidence interval of the proxy-based reconstructions. Wu et al. (2007) suggest that LGM winter temperatures were ~ 10–17 °C lower than today outside the ice-sheet margin in Eurasia, with a more significant decrease in northern regions. This is in line with the results by Kjellström et al. (2009).

For a description of the results concerning using an improved representation of European vegetation for the regional LGM climate simulations, as well as for a detailed description of the comparison with climate proxy data, see Kjellström et al. (2009).

Just as for the simulation of a periglacial MIS 3 climate, results from the regional climate modelling were extracted for the Forsmark region also for the LGM simulation. However, for this situation, the results naturally show the climate conditions prevailing at the ice-sheet surface, high above the overridden Forsmark landscape. They are thus of less importance for the present report and are therefore not included here. The interested reader is referred to Kjellström et al. (2009).

Climate variability during the last glacial cycle

The difference between the present warm interglacial temperatures and the coldest temperatures during the last glacial cycle as recorded in the GRIP ice core is on the order of 12 °C (Figure 2-36). Using an alternative way of interpreting $\delta^{18}O$ values from the ice core in terms of air temperature, Lang et al. (1999) suggested that this cold event reflects a temperature change of 16 °C, which is several degrees more than proposed in Dansgaard et al. (1993). From the LGM climate modelling study described under the subsection *Late Weichselian including LGM (24–12 ka BP)* above, annual air temperatures in front of the southern sector of the ice-sheet are around 9–12 °C colder than at present (Figure 3-17, lower right) while further towards northeast, annual air temperatures are around 12–15 °C lower than at present. The largest difference compared to present occurs during the winter season (Figure 3-17, middle).

In a similar way, the air temperature simulated for the Forsmark region for a prescribed ice-free MIS 3 stadial at 44 ka BP, see subsection *Middle MIS 3 (at 44 ka BP)* above*,* are low, 12.5 degrees lower than at present. Also, for this situation, the largest change compared to present occurs during the winter season.

As exemplified by the climate development around the modelled cold stadial at 44 ka BP, such cold events were relatively short lived, around a few thousands of years long, and alternated with warmer interstadials. A striking climate variability was found also in the simulated LGM climate. These results, from geological archives and from climate modelling, illustrate a typical feature of the last glacial cycle, namely that the climate was highly variable on both long and short timescales.

This is also described in for instance the section on abrupt climate change in the description on palaeoclimate characteristics in IPCC (2013a). The last glacial cycle climate variability is also seen for example by looking at the full GRIP temperature proxy record (Figure 3-19). When severe cold conditions occur, these conditions do not persist for long periods of time. Such climate variability is observed also in frequency analyses of climate records (Moberg et al. 2005, Witt and Schumann 2005).

How low could temperatures have been in the Forsmark region during the last glacial cycle? The simulated temperatures for the MIS 3 stadial suggest that the annual mean air temperature in the Forsmark region was –7.6 °C, which is 12.5 °C lower than at present. If looking at the air temperature curve produced for the region (Figure 2-38), transferred from Greenland conditions to regional conditions in Sweden in a rather simplistic way (SKB TR-10-49, Appendix 1), the curve suggests that annual mean air temperatures during the ice-free stadials of the last glacial cycle may have been around −10 to −11 °C in the Forsmark region (Figure 2-38), that is c. 2–3 degrees colder than the temperature modelled for MIS 3 (Greenland Stadial 12) at 44 ka BP. However, considering the uncertainties in e.g. the transfer functions between $\delta^{18}O$ and temperature when constructing the temperature proxy curve (SKB TR-10-49, Appendix 1), temperatures could even have been lower.

The climate variability seen during the last glacial cycle, e.g. Figure 3-19, was caused by the combined effect of variations in Earth's orbital configuration and internal feedback mechanisms within and between the atmosphere, ocean, cryosphere and vegetation systems. These mechanisms will continue to operate also in the future. Therefore, it is reasonable to assume that a similar climate variability that was characteristic for the last glacial cycle would be characteristic also for future glacial cycles.

Descriptions of geological climate archives from various parts of the last glacial cycle found in Fennoscandia and Europe are presented in e.g. Hohl (2005), Kjellström et al. (2009), Wohlfarth (2009), Helmens (2009, 2019) and Schenk and Wohlfarth (2019).

Relevance and implications of the palaeoclimate studies made at the Sokli site, northern Finland

Prior to the palaeoclimate studies conducted at the Sokli site (e.g. Helmens 2009, 2013, 2019, Helmens et al. 2021), there were no terrestrial palaeoclimate record for Fennoscandia that covered the full last interglacial-glacial cycle (MIS 5-2; c. 130–10 ka BP) including the Holocene (last 12–11 ka) and the Eemian (ca. 130–115 ka BP) interglacials, and it was generally assumed that a steep latitudinal temperature gradient existed from northern to central Europe. The Sokli studies have provided such a palaeoclimate record, which gives important insight into the last interglacial-glacial cycle climate and environmental conditions. This is of relevance not only for northern Fennoscandia, but also for e.g. south-central Sweden including Forsmark, as described in the following. To date, no such palaeoclimate record is available for southern or central Sweden.

Given that the results from Sokli conclusively show non-glaciated conditions and summer temperatures reaching present-day levels for part of the Middle Weichselian MIS 3 period (ca. 50 ka BP) (Helmens 2009), the more southerly located Forsmark site also must have been deglaciated during part of MIS 3. This result is in line with the restricted MIS 3 ice sheet configuration obtained by ice sheet modelling for the reconstruction of Weichselian glacial conditions (that in turn form the basis for the safety assessment reference glacial cycle), see Section 3.2.3.

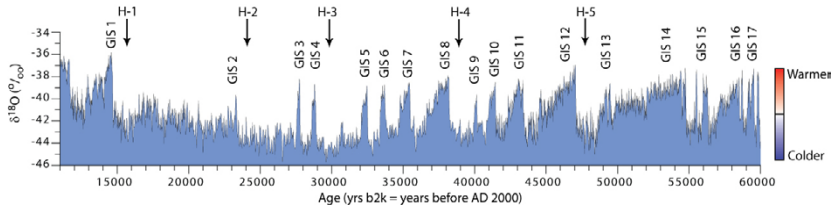

Figure 3-19. *The NorthGRIP oxygen isotope ($\delta^{18}O$) stratigraphy for MIS 2 and 3. Warmer Greenland interstadials were succeeded by colder stadial intervals. Heinrich (H) events 1–5, which have been described from North Atlantic marine sequences, occurred after a series of progressively colder interstadials and in the coldest phase of a stadial. From Wohlfarth (2009), modified after Krogh Andersen et al. (2006).*

The climate proxy studies conducted at Sokli have also revealed interglacial conditions with summers significantly warmer than today for the interstadials of the Early-Weichselian (MIS 5c and 5a at around c. 95 and 80 ka BP, respectively). Together with results from central Europe obtained in other studies, the results from the Sokli studies have demonstrated, in contrast to what was previously assumed, that there was only a weak temperature gradient from northernmost to central Europe during MIS 5c and 5a. Helmens (2013, 2019) and Helmens et al. (2021), suggest that these Early Weichselian climate reconstructions shorten the last glacial period by c. 50 ka, to MIS 4-2, as compared to the traditional view of the Weichselian glacial period being ca 100 ka long. In the PSAR, this new suggested re-definition of the Early Weichselian has not been employed, whereas the associated reconstructed paleoclimates of the Early Weichselian stages are included.

Since summer air temperatures as high, and even higher, than at present existed in the Sokli region north of Forsmark during the interstadial stages of MIS 5 and during the early part(s) of MIS 3 (Helmens 2009, 2019), similar to those in central Europe (e.g. Helmens 2013, Helmens et al. 2021), it is likely that south-central Sweden, including the Forsmark region, experienced similar warm summer climates during these interstadial periods. For these periods, the weak north-south temperature gradient can be used to estimate summer air temperatures for the Forsmark site, based on e.g. the temperatures at Sokli.

During the cold MIS 5d stadial of the Early Weichselian (at around 110 ka BP), the Sokli region, as well as central European sites, experienced a climate supporting a steppe-tundra type of vegetation (Helmens 2013), i.e. a cold climate characterized by a high degree of continentality. Given the similarity of these climates north and south of south-central Sweden, it is likely that the Forsmark region also experienced a cold climate supporting a steppe-tundra vegetation during MIS 5d. For this period, the temperature gradient from northernmost to central Europe was also weak.

In summary, the overall results obtained from the Sokli studies is of high relevance also for the Forsmark site. These include i) summer climates as warm, and warmer, than at present during the interstadial stages of the Early Weichselian, ii) ice free conditions and warm summers during part of the Middle Weichselian, and iii) a considerably more dynamic behaviour of the climate and ice sheet during the last interglacial-glacial cycle than traditionally assumed.

In general, the biota palaeoclimate proxies used in the Sokli studies have strong links to summer conditions but only weak links to winter conditions. Therefore, the Sokli palaeotemperature reconstructions have focused on reconstructing summer air temperatures, since this is what available palaeoclimate proxy methods at the latitude of Sokli are adequate for. Winter temperatures are important for e.g. reconstructions the degree of continentality for a site. Winter temperatures have been possible to quantitatively reconstruct for the warmest interval at Sokli, i.e. the Eemian interglacial (MIS 5e). In addition, relatively low winter temperatures can be inferred for MIS 5d at Sokli based on the occurrence of steppe-tundra vegetation.

The Sokli investigations also include climate proxy studies of the Holocene sequence. This is important since i) the Holocene is a period for which relatively abundant climate and environmental proxy information are available from other sites. It is very useful to compare the results from Sokli with other studies in order to verify that the results from the Sokli site does not contradict other results from this period, and ii) a lot of environmental information from the Holocene are preserved in the landscape today, and hence comparing this information with the one interpreted from the Holocene sediment sequence helps in interpreting the biota climate proxies in the sediment. The interpretations made from the older deposits that pre-date the Holocene hence also are improved. Therefore, a long paleo-record of climate and environment conditions, such as the one obtained from the Sokli site, needs also the most recent period to be studied in order to improve the interpretations of the proxies used and to demonstrate the applicability of the methodologies employed.

3.2.3 Reconstructed last glacial cycle conditions at Forsmark

In this section, results from Sections 2.1.4, 2.2.4 and 2.3.4 are summarised to present key parameters (development of permafrost, relative sea level and ice sheets) for the reconstruction of last glacial cycle conditions at Forsmark.

Permafrost evolution

In Section 2.1.4 reconstructions of permafrost and freezing depths for the last glacial cycle at Forsmark were made using two permafrost models (Figure 3-20 and Figure 3-21). The simulations were made by employing the air temperature curve reconstruction for the last glacial cycle (Section 2.1.4) together with site-specific data on e.g. bedrock, soil, groundwater, lakes and relative sea-level development, see Section 2.1.4 and Hartikainen et al. (2010).

The maximum simulated Weichselian permafrost depth at the location of the repository for spent nuclear fuel is ~ 250 m, which occurs around 70 ka BP prior to the MIS 4 ice-sheet advance over the region (Figure 3-20). The maximum permafrost depth in the surrounding region, here represented by a 15 km long profile, is ~ 300 m (Figure 3-21) and it occurs at the same time (Figure 3-21, lower part). At that time, the area is subject to continuous permafrost coverage (more than 90 % spatial coverage) (Figure 3-21, upper part). During periods of ice-sheet coverage, permafrost declines, especially during periods when the ice sheet is warm-based (Figure 3-24). At the time of ice-sheet retreat and deglaciation, there is no permafrost or frozen ground present.

The estimated last glacial cycle air temperatures at ground level (Section 2.1.4) are typically 2–4 °C lower than mean annual temperature in the uppermost part of the ground for the same climate, see Section 2.1.4 and Figure 3-12. As discussed in detail above, very low air temperatures during the last glacial cycle only prevailed during stadials that had a limited duration of some thousands of years. During cold ice-free periods, permafrost developed at the Forsmark site, but climate variability with alternating cold and warm periods, (e.g. Figures 3-53 and 3-65 in SKB TR-10-49), as well as the presence of the ice sheet (e.g. Figure 3-23), prevented permafrost from developing to great depths (Figure 3-20 and Figure 3-21) and Section 2.1.4.

It should be noted that the reconstruction of last glacial cycle permafrost development was performed specifically to define a future climate evolution based on a repetition of the last glacial cycle for the safety assessment SR-Site. Therefore, heat from the planned repository for spent nuclear fuel was included in the simulation. The difference between including and excluding heat from the repository was evaluated (see Figures 3-50, 3-87 of SKB TR-10-49 as well as SKB TR-06-23, Figure 3-59). However, the influence of this heat for the location of the SFR repository is negligible in terms of influence on permafrost growth. All uncertainties related to the permafrost simulations are examined in detail in Section 2.1.4 and in Hartikainen et al. (2010).

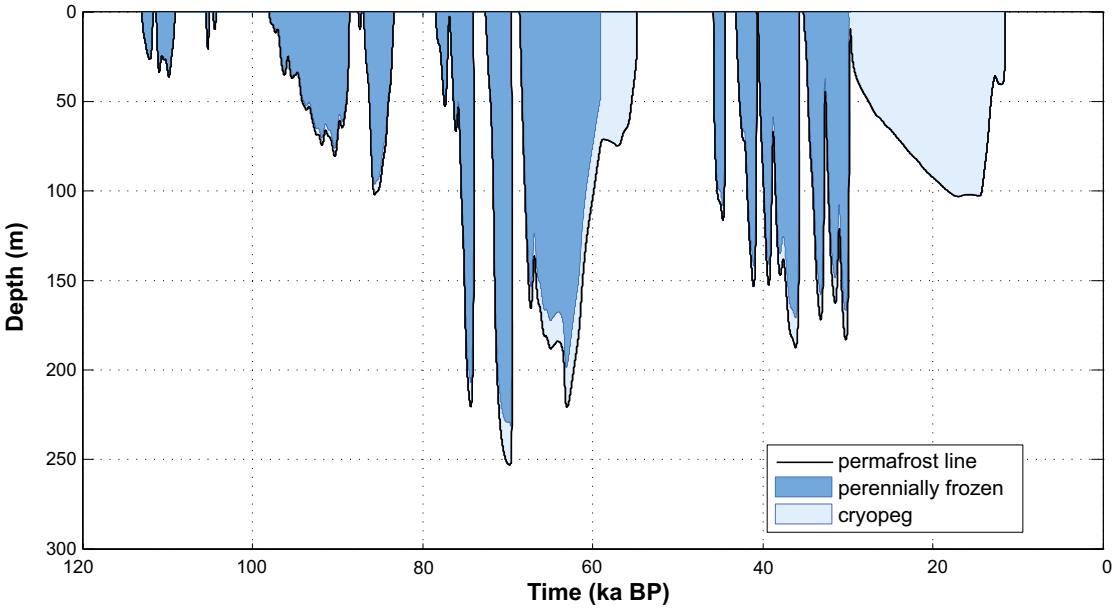

Figure 3-20. *Evolution of permafrost and perennially frozen ground depth for the reconstruction of last glacial cycle conditions in Forsmark (planned site for the spent nuclear fuel repository). The results were obtained using a 1D permafrost model (Section 2.1.4). Due to the high sub-glacial pressure, a thick unfrozen cryopeg exists within the permafrost (defined by the 0 °C isotherm) after 60 ka and after 30 ka BP (including the LGM). For the corresponding 2D modelling results see Figure 3-69 in SKB (TR-10-49).*

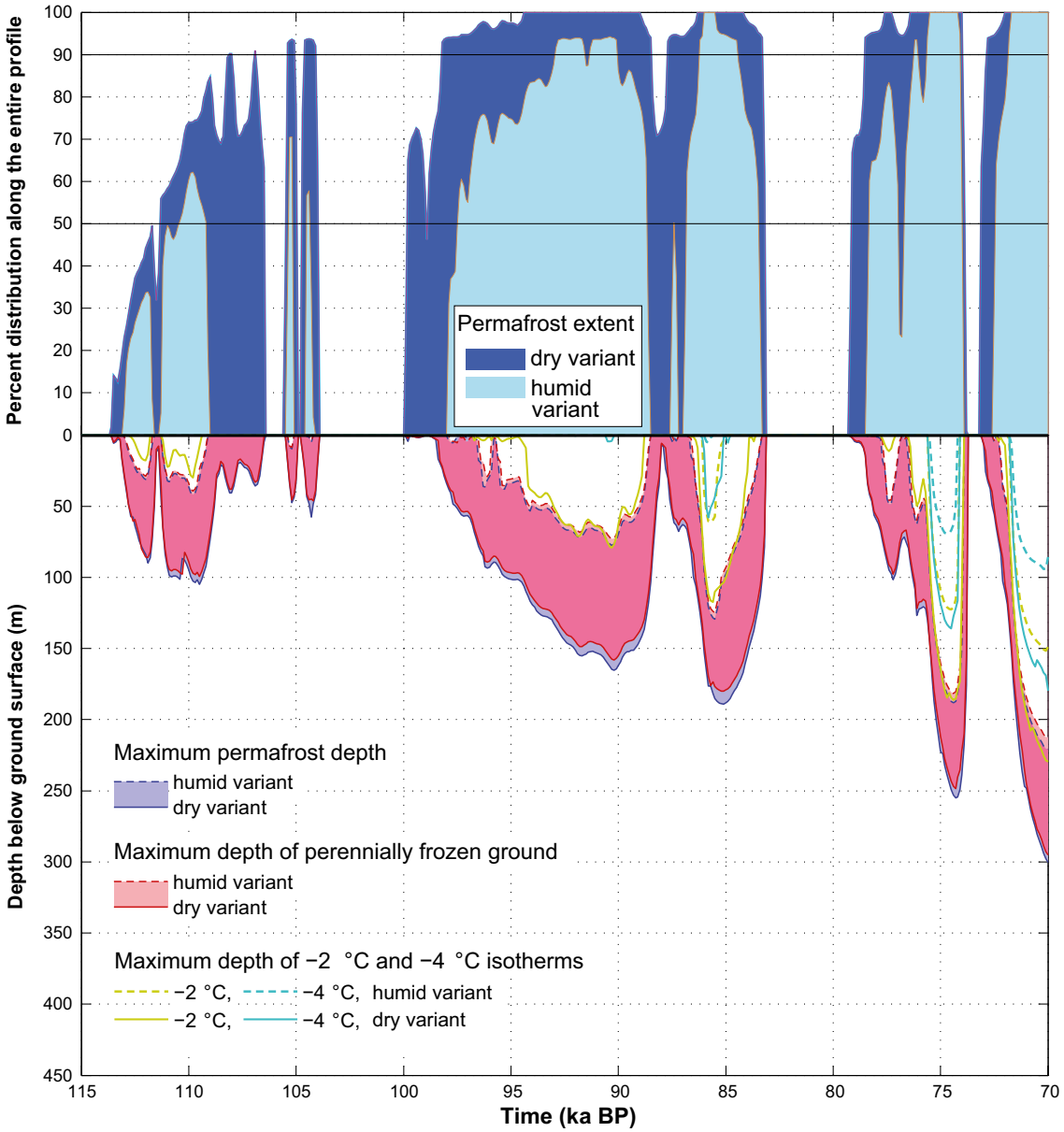

Figure 3-21. *Reconstructed evolution of maximum permafrost depth, maximum freezing depth and percent permafrost distribution over a 15 km long transect over the Forsmark area for the first 50 ka of the last glacial cycle, see Section 2.1.4. Upper panel: the transition from sporadic to discontinuous permafrost occurs at 50 % spatial coverage and from discontinuous to continuous permafrost at 90 % coverage. Lower panel: the shaded area in blue and red represents the range obtained when considering one dry and one humid variant. The lilac colour indicates that the results for permafrost and perennially frozen ground overlap.*

Relative sea-level evolution

At times of maximum isostatic depression, the Forsmark region was covered by the Weichselian ice sheet. In Section 2.2.4, a GIA model was used to reconstruct changes in relative sea level during the last glacial cycle, given input from various Earth models as well as the ice-load history from Section 2.3.4. Relative sea-level data were extracted for the Forsmark region (Figure 3-22) showing that the area was submerged after both reconstructed phases of ice-sheet coverage (Figure 3-23). The uncertainties in reconstructed levels are rather large (Section 2.2.4). Since the response to a specified ice load seems to be somewhat too large in the performed GIA simulations, this has resulted in the inferred water depth at Forsmark at the time of deglaciation (10 800 BP) in Figure 3-22 probably being too large. The results from the GIA modelling have for the following part of the Holocene been combined with results from other relative sea-level estimates (Appendix G) in order to decrease the uncertainty (Section 2.2.4). Uncertainties related to the GIA model simulation are discussed in Section 2.2.

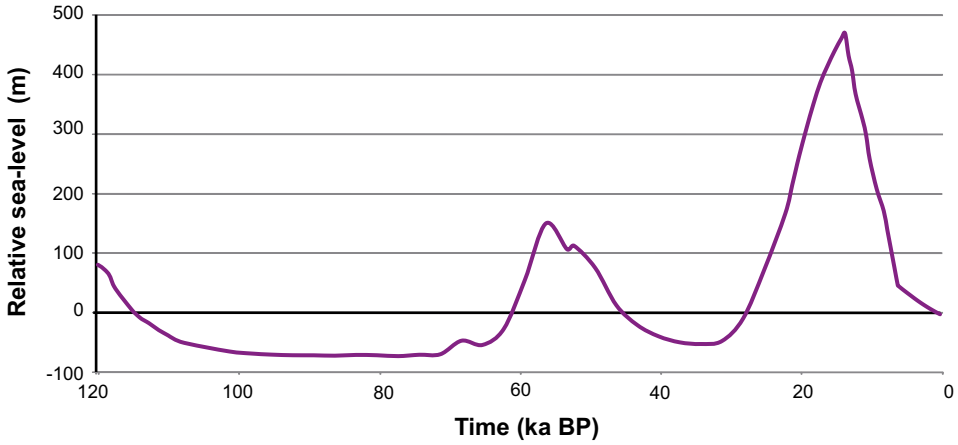

Figure 3-22. *Reconstructed relative sea-level change at Forsmark for the last glacial cycle using GIA modelling (Section 2.2.4) and Holocene data (Appendix G). Positive values mean that the area is submerged beneath the contemporary level of the Baltic Sea. Note that during periods of maximum isostatic depression, the area is situated under the ice sheet.*

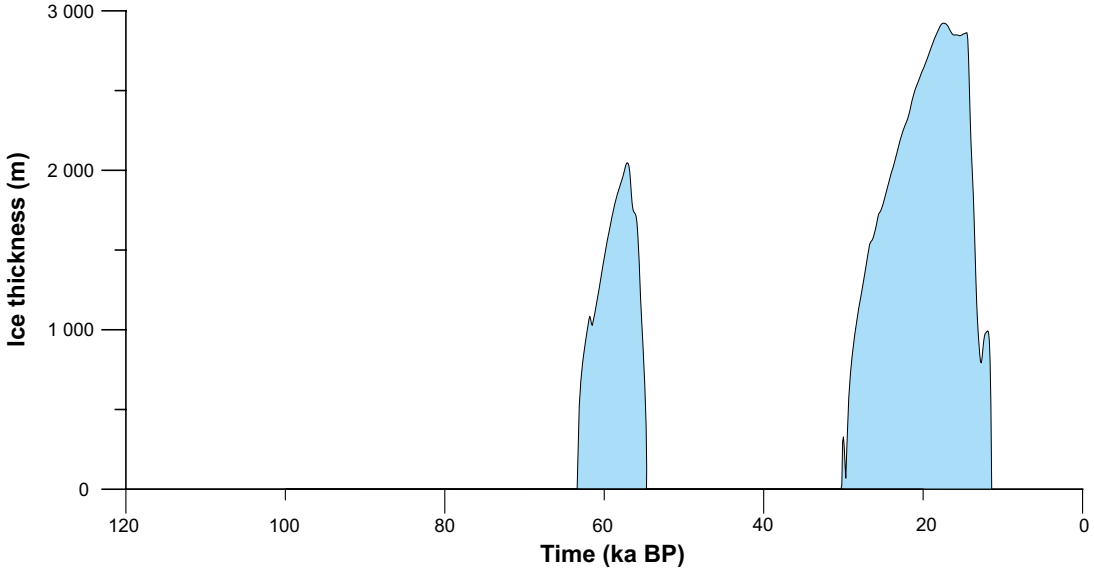

Figure 3-23. *Reconstructed ice-sheet thickness over Forsmark for the last glacial cycle (Section 2.3.4).*

Ice-sheet evolution

In Section 2.3.4, an ice-sheet model simulation of the Weichselian ice sheet was described, based on e.g. the temperature reconstruction of the last glacial cycle (Section 2.1.4). The modelled ice-sheet configurations during Weichselian stadials were calibrated against the known maximum ice margin positions for these periods. In the Weichselian ice-sheet reconstruction, the overall behaviour of the ice sheet can be characterised as being distinctly dynamic throughout the glacial cycle (Figure 2-39). For instance, during the MIS 3 period (which was *not* used for model calibration), large parts of Fennoscandia were modelled to be ice free (Figure 2-39), in line with several recent independent Quaternary geological studies (Section 3.2.1).

From the ice-sheet simulation, data on ice-sheet thickness were extracted for the Forsmark region (Figure 3-23). The Forsmark region was subject to two phases of ice-sheet coverage, during the cold stadials of MIS 4 and 2. During the last glacial maximum, the ice-sheet thickness reached ~ 2 900 m.

Combined reconstructed last glacial cycle parameters

Figure 3-24 shows the combined evolution of permafrost- and frozen ground depth, relative sea-level changes and ice sheet thickness at Forsmark as reconstructed in Sections 2.1.4, 2.2.4 and 2.3.4 and above.

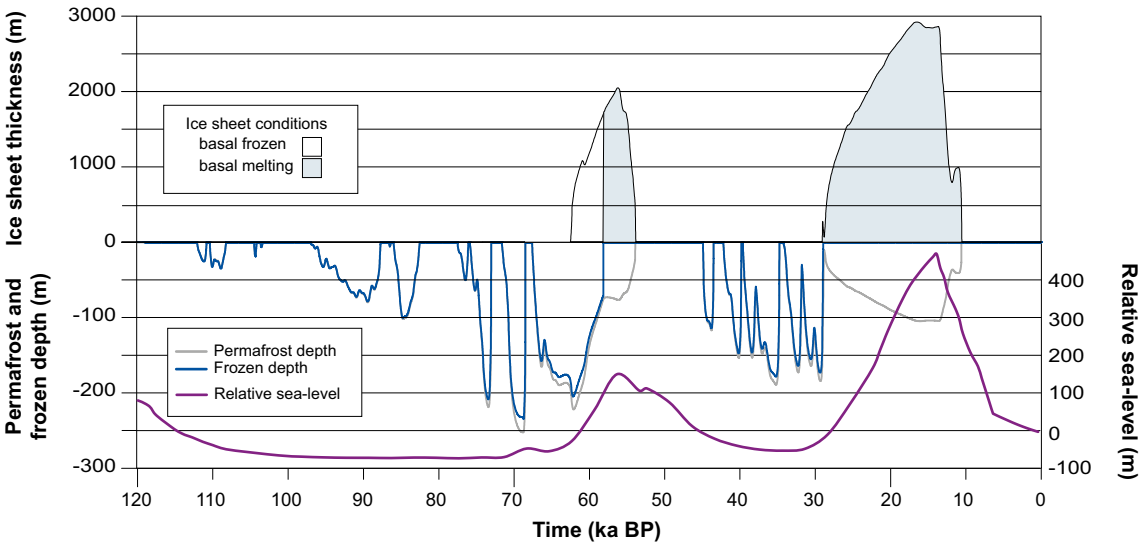

Figure 3-24. *Reconstructed Weichselian evolution of ice sheet, relative sea level, permafrost and frozen ground at Forsmark.*

3.3 Present climate at Forsmark

For the purpose of the post-closure safety assessment the present climate conditions at Forsmark are represented by locally measured meteorological data during the full year between October 2003 and September 2004, referred to as the *normal year*. During that year, the average SAT was 6.4 °C and the accumulated precipitation was 583 mm. The annual potential evapotranspiration of that year is estimated to have been 421 mm. These data were used for near-surface hydrological modelling in the SR-PSU (Werner et al. 2013), which is also used in the PSAR (**Post-closure safety report**, Section 6.3.3).

As weather patterns may deviate significantly from their average on seasonal to annual timescales, especially in the mid- and high-latitudes, using only one year of locally measured data to estimate the average climate conditions at a certain site is generally not considered to be sufficient. Instead, averages over several years, typically 20 or 30 years, are most often used when defining the average climate conditions. Thus, in this section, the validity of the normal-year data as a "proxy" for the average climate conditions at Forsmark is evaluated with respect to the average conditions computed over a longer time period. The comparison is made for annual-mean SAT and precipitation, but not for potential evapotranspiration as reliable data for this quantity over several tens of years is lacking.

The normal-year data are compared with several datasets. First, the present climate at Forsmark is described by the average conditions during the period 1986–2005 AD, i.e. the same as in the fifth IPCC assessment report (IPCC 2013a). This period is used as baseline in the projected future SAT and precipitation changes reported in Section 3.4, as well as most of the sea-level projections presented in Section 3.5. In addition, the 1986–2005 AD period covers the normal-year period between October 2003 and September 2004. The Forsmark SAT and precipitation for the 1986–2005 AD period are estimated using both local meteorological measurements from the site and data from nearby SMHI stations, see Appendix C for details. In addition to the IPCC baseline period, the comparison is also made with respect to the baseline period used in the SR-PSU (1961–1990 AD, SKB TR-13-05), the period when the site investigations were carried out (2004–2010 AD, Werner et al. 2014), including an extension of that dataset (2004–2014 AD, see Appendix C).

The present climate in the Forsmark region has typical values for south-central Sweden, with an annual average SAT of c. +6.1 °C using the 1986–2005 AD reference period (Appendix C, Section C2). This can be compared with an annual average SAT of c. +5.5 °C between 1961 and 1990 AD (SKB TR-13-05), +6.4 °C during the normal year, +6.7 °C between 2004 and 2010 AD (Werner et al. 2014) and +6.8 °C between 2004 and 2014 AD (Appendix C, Section C2). Thus, the annual average SAT during the normal year is consistent with the overall warming trend in the region.

Estimates of the 1986–2005 AD climatology suggest that annual precipitation at Forsmark was on average 607 mm during this period (Appendix C, Section C3). This can be compared with annual precipitation of 568 mm between 1961 and 1990 AD (SKB TR-13-05), 583 mm during the normal year, 589 mm between 2004 and 2010 AD (Werner et al. 2014) and 606 mm between 2004 and 2014 AD (Appendix C, Section C3). Thus, the annual precipitation during the normal year is similar to the average precipitation between the 1961–1990 AD and 1986–2005 AD reference periods.

In conclusion, the normal-year SAT and precipitation are well in line with the estimated conditions from longer time periods. Thus, the average normal-year conditions are considered to be an adequate representation of the present climate conditions at Forsmark for the purpose of the post-closure safety assessment.

3.4 Projected future climate evolution

Due to incomplete knowledge of the dynamics and interactions of the Earth's climate system (see e.g. Section 3.1), the future evolution of Earth's climate is difficult to predict on the timescales of interest for safety assessments of nuclear waste repositories. Nonetheless, abundant knowledge exists on past climates on these timescales and attempts have also been made to estimate future climate over the coming 1 Ma (Lord et al. 2019). Projections of future climate evolution based on knowledge on past climates provide valuable information and a range of possible future climate evolutions. The climate cases used in this safety assessment (Chapter 5) were designed to cover the uncertainty range related to the future climate development. In this section, the current knowledge on the Earth's future climate evolution over the coming ~ 100 ka is described in terms of global average evolution and large-scale patterns of climate change. Implications for future climate evolution in the Forsmark region are also discussed.

Atmospheric greenhouse gas concentrations and insolation variations due to variations in astronomical parameters are the major drivers of global climate variability. In the following, current knowledge on future greenhouse gas concentrations (Section 3.4.1) and insolation variations (Section 3.4.2) are described.

Projections of future climate evolution are obtained using models of varying complexity ranging from Earth System Models (ESMs; global climate models with integrated carbon cycle) through Atmosphere-Ocean General Circulation Models (AOGCMs), Earth System Models of Intermediate Complexity (EMICs) to Simple Climate Models (SCMs). In modelling studies of future climate evolution, assumptions regarding future variations in the forcing conditions, e.g. human carbon emissions, are made. In general terms, the range from ESMs to SCMs involves decreasing complexity of the model physics and dynamics of the different components of the climate system as compared with the real world, as well as decreasing spatial and temporal model resolution. The computational cost of state-of-the-art ESMs and AOGCMs prevents use of these models for modelling of more than a few centuries-millennia. To reflect both the complexity of the models and the spread in possible future climate evolutions, future climate projections, both globally and at Forsmark, are described for the current century (Section 3.4.3), for the next 10 ka (Section 3.4.4) and for the next 100 ka (Section 3.4.5).

3.4.1 Atmospheric greenhouse-gas concentrations

Global atmospheric concentrations of greenhouse gases have increased markedly as a result of human activities since 1750 and now far exceed pre-industrial values determined from ice cores spanning many thousands of years. Human greenhouse-gas emissions include both carbon dioxide (CO_2) and methane (CH_4), but CH_4 emitted to the atmosphere is converted to CO_2 after an average lifetime of only 12 years. Therefore, studies of future climate focus on CO_2. Studies with coupled climate-carbon cycle models have shown that the century-scale global mean temperature response to CO_2 emissions is independent of the emissions pathway (Eby et al. 2009, Zickfeld et al. 2009). Further, it has been demonstrated that global mean temperature remains approximately constant (e.g. Solomon et al. 2009, Gillet et al. 2011, Clark et al. 2016), or continues to increase (e.g. Eby et al. 2009, Frölicher et al. 2014), for several centuries after the CO_2 emissions have ceased. These results can be generalised to show that the global temperature response is proportional to cumulative

carbon emissions (Matthews et al. 2009, Collins et al. 2013, Herrington and Zickfeld 2014, Leduc et al. 2015, Zickfeld et al. 2016). This relationship also appears to be relatively constant over time (Collins et al. 2013).

Mankind has up to now released c. 400 petagrams of carbon (Pg C, 1 Pg = 10^{15} g) to the atmosphere resulting in ~ 1 °C warming above pre-industrial levels (IPCC 2018). The total cumulative emissions are projected to surpass 1 000 Pg C before the end of this century under business-as-usual scenarios (Archer et al. 2009). The remaining fossil fuel reserves that it might be reasonable to extract under present economic conditions totals c. 5 000 Pg C. Human emissions have so far increased the atmospheric CO_2 concentration from 280 ppmv in 1750 AD prior to industrialisation to 409 ppmv in 2018 AD (www.esrl.noaa.gov). A continued increase in the CO_2 concentration at the same rate as during the last decade (ca 2 ppmv per year) would result in an atmospheric CO_2 concentration of c. 570 ppmv in 2100 AD. This corresponds to approximately 10 Pg C emissions per year from fossil fuels and land-use changes, of which about half remains in the atmosphere (Le Quéré et al. 2018). From a geological perspective, the present anthropogenic carbon release rate is unprecedented during the past 66 million years (Zeebe et al. 2016).

Until 2300 AD

To produce climate projections for the next few centuries, coordinated experiments, in which many climate models run a set of scenarios, have become the standard (Knutti and Sedláček 2013). A wide variety of emission scenarios, or scenarios for atmospheric greenhouse gas concentrations, are used in these multi-model ensembles. The ensembles sample uncertainties in emission scenarios, model uncertainty and initial condition uncertainty, and provide a basis to estimate projection uncertainties. The Coupled Model Intercomparison Project Phase 6 (CMIP6; Eyring et al. 2016), coordinated by the World Climate Research Programme in support of the Intergovernmental Panel on Climate Change Sixth Assessment Report (IPCC AR6, expected to be finalized in 2021 AD) is the most recent of these activities. Currently (February 2019), climate modelling experiments are being submitted to CMIP6, but the key results from these experiments have not yet been published. The fifth IPCC assessment report, which was based on CMIP5 (Taylor et al. 2012), was published in 2013 (IPCC 2013a). This report was written and reviewed by the experts in the field and it provides an up-to-date description of current knowledge on the future evolution of climate and climate-related issues, such as sea level, in the next centuries to millennia. Since the sixth IPCC assessment report has not yet been finalized, the conclusions presented by IPCC (2013a), based on CMIP5, are used here.

In CMIP5, ESMs were used for the first time in CMIP. These are AOGCMs coupled to biogeochemical components and, in some cases, also include interactive prognostic aerosol, chemistry, and dynamical vegetation components. These models have the capability of using time-evolving emissions of constituents from which concentrations can be computed interactively. The CMIP5 projections of climate change are driven by concentration or emission scenarios consistent with the representative concentration pathways (RCPs; Meinshausen et al. 2011). In contrast to the SRES scenarios used in CMIP3, which do not include policy intervention, the RCPs are mitigation scenarios that assume policy actions will be taken to achieve certain emission targets. For CMIP5, four RCPs have been formulated that are based on a range of projections of future population growth, technological development, and societal responses: RCP2.6, RCP4.5, RCP6.0 and RCP8.5 (see Table 3-2) The number associated with the RCPs is a rough estimate of the radiative forcing (in W m^{-2}) in the year 2100 AD relative to pre-industrial times. Radiative forcing measures the combined effect of greenhouse-gas emissions and other features, e.g. atmospheric aerosols, on the climate warming. The radiative forcing in RCP8.5 increases throughout the twenty-first century before reaching a level of about 8.5 Wm^{-2} at the end of the century. This scenario assumes that no climate change mitigation policies are implemented until 2100 AD and beyond. In addition to this "high" scenario, there are two intermediate scenarios, RCP4.5 and RCP6.0, with relatively weak climate change mitigation resulting in stabilisation of emissions within this century. Finally, RCP2.6 is so-called peak-and-decay scenario, reflecting a future with strong climate change mitigation in which radiative forcing reaches a maximum near the middle of the twenty-first century before decreasing to an eventual nominal level of 2.6 Wm^{-2}. The RCP scenarios are summarised in Table 3-2. In addition, extensions to the RCP scenarios, so-called ECPs, also exist that project emissions to 2300 AD (Meinshausen et al. 2011).

Table 3-3 shows the atmospheric CO_2 concentration and cumulative fossil-fuel emissions by 2100 AD and 2300 AD for each RCP/ECP. Note that all RCP scenarios assume very low emissions beyond 2300 AD (Fyke and Matthews 2015) implying that the cumulative emissions will remain relatively constant for the subsequent centuries to millennia. However, even if all emissions of CO_2 and other greenhouse gases were to end 2300 AD, atmospheric CO_2 would remain high, well above pre-industrial levels, for several thousands or, in some scenarios, tens of thousands of years (see the following sections).

Table 3-2. IPCC emission scenarios used in CMIP5 (IPCC 2013a).

Emission scenario	RCP scenario used in CMIP5
Low	RCP2.6
Medium	RCP4.5 and RCP6.0
High	RCP8.5

Table 3-3. Atmospheric CO_2 concentrations, cumulative fossil-fuel emissions and projected range of global annual mean surface air temperature increases until 2100 AD and 2300 AD for the RCP2.6, RCP4.5, RCP6.0 and RCP8.5 emission scenarios used in IPCC AR5 (IPCC 2013a). The projected surface air temperature increase is shown as mean (outside square brackets) and 5 to 95 % percentiles (inside square brackets) across the CMIP5 multi-model ensemble. The atmospheric CO_2 concentration for each scenario is derived from Meinshausen et al. (2011), and the projected surface air temperature is obtained from Collins et al. (2013). The cumulative emissions are approximate estimates with respect to the pre-industrial era from Fyke and Matthews (2015). The global annual mean surface air temperature projections as well as the corresponding projections for Forsmark until 2100 AD are discussed in Section 3.4.3.

	RCP2.6	RCP4.5	RCP6.0	RCP8.5
Atmospheric CO_2 concentration (ppm)				
2100 AD	420	540	670	940
2300 AD	361	543	752	1962
Cumulative fossil-fuel emissions (Pg C)				
2100 AD	600	1100	1500	2200
2300 AD	400	1300	2200	5200
Global annual mean surface air temperature increase (°C)				
Relative to 1986–2005 AD				
2081–2100 AD	1.0 [0.3, 1.7]	1.8 [1.1, 2.6]	2.2 [1.4, 3.1]	3.7 [2.6, 4.8]
2281–2300 AD	0.6 [0.0, 1.2]	2.5 [1.5, 3.5]	4.2*	7.8 [3.0, 12.6]
Relative to 1850–1900 AD				
2081–2100 AD	1.6 [0.9, 2.3]	2.4 [1.7, 3.2]	2.8 [2.0, 3.7]	4.3 [3.2, 5.4]

* No temperature range is given for RCP6.0 until 2300 AD as data only exists from two climate models (Collins et al. 2013). The value 4.2 °C represents the average global-mean surface air temperature increase across those two models.

Until 12000 AD

The future atmospheric CO_2 evolution after human carbon emissions have stopped will depend on the cumulative emissions up to that point in time and on the processes that act to decrease the concentration (e.g. Zickfeld et al. 2012). Archer et al. (2009) performed a review and model inter-comparison of the atmospheric lifetime of fossil fuel CO_2 as predicted by nine different carbon cycle models and EMICs. The models were integrated for 10 ka starting from a pre-industrial CO_2 concentration of 280 ppmv and initial pulses of 1000 Pg and 5000 Pg C. Archer et al. (2009) concluded that 20–35 % of the CO_2 remains in the atmosphere after equilibration with the ocean (200–2000 years). Further, they concluded that neutralisation by calcium carbonate draws the airborne fraction down further on timescales of 3 to 7 ka. After 10 ka of integration following a 1000 Pg C initial pulse, 8–19 % of the emissions remained in the atmosphere. After 10 ka of integration following a 5000 Pg C initial pulse, 10–33 % of the emissions remained in the atmosphere. Archer et al. (2009) concluded that generally accepted modern understanding of the global carbon cycle indicates that climate effects of CO_2 releases to the atmosphere will persist for tens, if not hundreds, of thousands of years into the future.

Until 100 ka AP

Several modelling studies, described in Section 3.4.5, indicate that the atmospheric CO_2 concentration is of great importance for Earth's climate evolution in the next 100 ka. The future concentration is controlled by cumulative carbon emissions and the processes that act to reduce the atmospheric concentration, but also by the processes involved in the natural glacial–interglacial cycles in the last 800 ka (Lüthi et al. 2008; see also Figure 3-2). The results presented by Archer et al. (2009) strongly suggest that the atmospheric CO_2 concentration will remain above the pre-industrial 280 ppmv for the next 10 ka, and possibly even the next 100 ka, unless CO_2 is actively removed from the atmosphere by technological measures. However, past glacial–interglacial CO_2 cycles are not fully understood, and future human actions are uncertain.

An example of how the atmospheric CO_2 concentration might evolve under different emission scenarios over the coming 100 ka is provided by Lord et al. (2019). The objective of that study was to simulate the possible evolution of future climate over the next 1 million years for a range of anthropogenic CO_2 emission scenarios using a statistical climate emulator (Lord et al. 2017). The climate emulator was forced by variations in insolation (Berger and Loutre 1991; see also Figure 3-2), global ice-sheet volume changes and the future evolution of the atmospheric CO_2 concentration. The main results from the climate emulation in Lord et al. (2019) are summarised in Section 3.4.5. In this section, only their results related to the simulated atmospheric CO_2 are discussed.

In Lord et al. (2019), the future evolution of the atmospheric CO_2 concentration in response to anthropogenic CO_2 emissions was calculated using a carbon cycle impulse-response function (Lord et al. 2016). They adopted the RCP2.6, RCP4.5 and RCP8.5 anthropogenic emission scenarios (Table 3-2), as well as a "natural" scenario, which assumes no anthropogenic emissions (or in practice, that CO_2 will be actively removed from the atmosphere by technical measures). In order to account for the natural cycle of CO_2, i.e. variations of atmospheric CO_2 during glacial-interglacial cycles, atmospheric CO_2 concentration data for the last 800 ka (Petit et al. 1999) were regressed against reconstructed global temperature data for the same period (Jouzel et al. 1993), both of which were derived from paleoclimate proxy data.

In the 1 Ma emulation by Lord et al. (2019) the climate variables, and thus also the atmospheric CO_2 concentrations, were updated every 1 ka. Atmospheric CO_2 reaches a peak within the first 1 ka (i.e. immediately following the emission period) in the three anthropogenic emissions scenarios, with a maximum of 329 ppmv, 412 ppmv and 1 358 ppmv for the RCP2.6, RCP4.5 and RCP8.5 scenarios, respectively. In contrast, the average atmospheric CO_2 concentration in the "natural" scenario is 266 ppmv within the first 1 ka. It should be noted that the maximum atmospheric CO_2 concentrations projected by the response function for the different RCPs would be significantly higher if using an annual temporal resolution. However, due to the employed temporal resolution of 1 ka, those annual maxima occurring within the first 1 000 years are not captured in the emulation.

The resulting atmospheric CO_2 concentrations from Lord et al. (2019) over the coming 100 ka are shown in Table 3-4. The percentage values within brackets show how much atmospheric CO_2 is remaining relative to the first 1 000 years. In Table 3-4, the atmospheric CO_2 concentrations under the RCP4.5 and RCP8.5 scenarios remain elevated over the entire 100 ka period. At 100 ka AP, the CO_2 concentrations in the RCP4.5 and RCP8.5 scenarios are approximately 100 to 200 ppmv higher than in the "natural" scenario. This demonstrates the potential long-term consequences of present anthropogenic carbon emissions.

The results from Lord et al. (2019) suggest that the atmospheric CO_2 during the next boreal summer insolation minimum at 17 ka AP remains above 300 ppmv in all RCP scenarios (Table 3-4). In the "natural" scenario, the CO_2 is even *increasing* between 10 and 17 ka AP (Table 3-4), resulting in close to pre-industrial CO_2 concentrations at 17 ka AP. Hence, according to Lord et al. (2019), the CO_2 concentration (and also the resulting climate at Forsmark; see Section 3.4.5) would at the time of the first insolation minimum at 17 ka AP be similar to the pre-industrial era. If this were the case, there would be no major permafrost development in the Forsmark area at this time (cf. Section 2.1.4).

The study of Lord et al. (2019) provides an illustrative example on how the CO_2 concentration may evolve over the coming 10 to 100 ka. However, their results do not necessarily represent a bounding case of the future CO_2 evolution. To estimate such bounding case, represented by the fastest possible CO_2 decline by natural causes, information from geological data is used. First, it is assumed that the atmospheric CO_2 concentration at 10 ka AP is comparable with pre-industrial levels (~ 280 ppmv) as a result of a natural CO_2 decline (Archer et al. 2009) as well as removal of atmospheric CO_2 by technological measures. Second, the rapid decrease of the atmospheric CO_2 concentration found in ice-core data during the last glacial inception (Lüthi et al. 2008) is used. The record from Lüthi et al. (2008) reveals that the atmospheric CO_2 concentration decreased from interglacial levels of ~ 275 ppmv around 115.4 ka BP to ~ 228 ppmv around 108.0 ka BP, i.e. ~ 47 ppmv CO_2 in 7.4 ka. A similar rapid decrease from 10 ka AP and onwards would result in an atmospheric CO_2 concentration of c. 230 ppmv around 17 ka AP.

In summary, atmospheric CO_2 concentrations below pre-industrial levels cannot be excluded by 17 ka AP if (i) anthropogenic emissions of CO_2 were removed at a large scale from the atmosphere, and (ii) the insolation minimum at 17 ka AP were accompanied by a rapid natural CO_2 decline. This scenario can be regarded as a bounding case. Under more likely scenarios, the atmospheric CO_2 concentration would be at or above 280 ppmv at 17 ka AP as a result of future anthropogenic carbon emissions and a more modest CO_2 decline between 10 and 17 ka AP (Lord et al. 2019).

Table 3-4. Simulated atmospheric CO_2 concentrations from Lord et al. (2019) at some key time slices. The CO_2 concentrations in response to anthropogenic CO_2 emissions were calculated using a carbon cycle impulse-response function (Lord et al. 2016), and the interaction between the glacial-interglacial cycles and atmospheric CO_2 was calculated by regressing atmospheric CO_2 concentration data for the last 800 ka (Petit et al. 1999) against reconstructed global temperature data for the same period (Jouzel et al. 1993). The percentage-values within the brackets show how much atmospheric CO_2 is remaining relative to the first 1 ka of the simulation in each climate scenario.

Time slice (ka AP)	Natural (ppmv)	RCP2.6 (ppmv)	RCP4.5 (ppmv)	RCP8.5 (ppmv)
10	263 (98 %)	306 (93 %)	338 (82 %)	648 (48 %)
17	264 (99 %)	304 (92 %)	331 (80 %)	530 (39 %)
54	257 (96 %)	284 (86 %)	323 (78 %)	436 (32 %)
100	202 (76 %)	224 (68 %)	250 (61 %)	410 (30 %)

3.4.2 Insolation

As described in Section 3.1, glacial–interglacial cycles are believed to be driven by changes in insolation as a result of variations in the Earth's orbit around the Sun. Over the next 100 ka, the amplitude of insolation variations will be small, much smaller than during the Weichselian (Figure 3-2; Berger and Loutre 2002). For example, at 60°N in June, insolation will vary by less than 25 Wm^{-2} over the next 25 ka, compared with 110 Wm^{-2} between 125 ka and 115 ka BP (see Figure 3-2). Thus, from the stand-point of insolation, the Weichselian cannot be used as an analogue for the next millennia (Berger and Loutre 2002).

3.4.3 Climate change until 2100 AD

Atmospheric greenhouse-gas concentrations are expected to increase until 2300 AD at a rate mostly determined by human emissions (IPCC 2013a). This increase is expected to result in an increased global average surface temperature (Collins et al. 2013).

Based on the CMIP5 simulations, Collins et al. (2013) draws the following conclusions.

- The global annual mean surface air temperature anomalies (SAT) for 2081–2100 relative to the 1986–2005 AD reference period range from 0.3 °C–1.7 °C for the RCP2.6 scenario to 2.6 °C–4.8 °C for the RCP8.5 scenario (Table 3-3).

- In the next few centuries beyond 2100 AD, the global annual mean SAT is projected to start decreasing in the RCP2.6 scenario. In all other scenarios, however, global temperatures are expected to increase further (Table 3-3).
- Globally averaged SAT changes over land will exceed changes over the ocean at the end of the 21st century and the Arctic region is projected to warm most.
- Global precipitation will increase with increased global mean SAT.
- Changes in average precipitation will exhibit substantial spatial variation with an increase in the contrast of annual mean precipitation between dry and wet regions and between dry and wet seasons.

Climate at Forsmark until 2100 AD

The annual average temperature increase in the Forsmark region until 2100 AD is expected to exceed the global temperature increase due to stronger warming over land than over ocean and to stronger warming in the polar regions than in the tropics (typically referred to as "polar amplification") (IPCC 2013a). Multi-model CMIP5 ensemble mean changes for 2081–2100 AD in SAT relative to the 1986–2005 AD reference period are displayed in Figure 12.11 of Collins et al. (2013). The SAT anomaly for the Forsmark region ranges from 1.0–1.5 °C for the low emission RCP2.6 scenario, 2.0–3.0 °C for the intermediate emission RCP4.5 scenario, and 4–5 °C for the high emission RCP8.5 scenario (Table 3-5). Most of the temperature increase is projected to occur in the winter season. Note that the SAT ranges given here represent the shaded interval in Figure 12.11 of Collins et al. (2013) and hence give no indication of the uncertainty in the projected change.

Multi-model CMIP5 ensemble mean changes for 2081–2100 AD in annual precipitation relative to the 1986–2005 AD reference period are displayed in Figure 12.22 of Collins et al. (2013) for the high emission scenario RCP8.5. For the other RCPs, the median change (corresponding to the 50 % percentile) of the precipitation distribution from the CMIP ensemble is used for the 2081–2100 AD projection of annual precipitation (IPCC 2013b). The annual precipitation is projected to increase by 10–20 % for RCP8.5 (Table 3-5), of which most of the increase is expected to occur in the winter season (Collins et al. 2013). For the other scenarios the annual precipitation increase by 2100 AD is projected to be more modest as they all fall within the 0–10 % range (Table 3-5).

In addition to the CMIP5 simulations in Collins et al. (2013), regional climate projections for Sweden until 2100 AD have been carried out by the Swedish Meteorological and Hydrological Institute (SMHI). They used results from different CMIP5 models in Collins et al. (2013) as boundary conditions in 21st century regional climate model projections under the RCP2.6, RCP4.5 and RCP8.5 emission scenarios. The resulting projected 21st century changes in the climate for Uppsala County, where Forsmark is located, are presented in Sjökvist et al. (2015). The projected changes in annual mean temperature and precipitation for 2070–2099 AD relative to 1961–1990 AD from Sjökvist et al. (2015) are summarised in Table 3-5.

In general, the regional climate model projections of the end of 21st century SAT and precipitation changes in the Forsmark region by Sjökvist et al. (2015) agree well with the global climate model projections reported in Collins et al. (2013) and IPCC (2013b) (Table 3-5). A notable result from Sjökvist et al. (2015) is the large ensemble spread in the projected annual precipitation change under the RCP4.5 and RCP8.5 emissions scenarios. This illustrates that future projections of precipitation changes are typically associated with a lower confidence than the corresponding projections of temperature. The precipitation uncertainty is even greater if considering seasonal instead of annual changes. This is particularly true for the summer season, for which climate models suggest that Forsmark precipitation may either increase or decrease as a result of global warming, see Appendix B, Section B2 details.

In summary, the projected increase in annual mean SAT by 2100 AD at Forsmark is slightly higher than the global average (cf. Table 3-3 and Table 3-5). As mentioned above, the Forsmark climate is expected to be warm by more than the global average as a result of the polar amplification and the fact that land masses are projected to warm more than the oceans. However, the warming

at Forsmark is also mitigated by a projected weakening of the Atlantic Meridional Overturning Circulation (AMOC) until 2100 AD, resulting in a somewhat reduced warming in in the Forsmark region compared with e.g. comparable latitudes in central Russia. A more detailed assessment on the effects of polar amplification and AMOC changes on the Forsmark climate until 2100 AD is provided in Appendix B, Sections B1.3.1 and B1.3.2.

Table 3-5. Projected changes in annual mean surface air temperature and precipitation until 2100 AD in the Forsmark region under different scenarios of future greenhouse gas emissions (RCPs, see Section 3.4.1) from global (Collins et al. 2013, IPCC 2013b) and regional (Sjökvist et al. 2015) climate modelling. The projected changes are for the period 2081–2100 AD relative to the 1986–2005 AD reference period in Collins et al. (2013) and IPCC (2013b), and for 2071–2099 AD relative to 1961–1990 AD in Sjökvist et al. (2015).

Study	Surface air temperature change by 2100 AD (°C)				Precipitation change by 2100 AD (%)			
	RCP2.6	RCP4.5	RCP6.0	RCP8.5	RCP2.6	RCP4.5	RCP6.0	RCP8.5
Collins et al. (2013), IPCC (2013b)[1]	1.0–1.5	2.0–3.0	3.0–4.0	4.0–5.0	0–10[2]	0–10[2]	0–10[2]	10–20
Sjökvist et al. (2015)	1.8[3] [1.6–2.1]	2.9[4] [2.1–3.7]	-	4.6[4] [3.8–5.4]	6[3] [5–6]	15[4] [4–25]	-	23[4] [11–31]

[1] Data are from multi-model CMIP5 ensembles, and the ranges given in the table represent intervals from map figures in Collins et al. (2013) and IPCC (2013b) and therefore give no indication of the uncertainty in the projected change.

[2] Values represent the median change (50 % percentile) from the CMIP5 ensemble (instead of the mean change).

[3] Value represents the ensemble-mean regional climate model projection based on boundary condition data from three different global CMIP5 models. The values within square brackets represent the ensemble minimum and maximum of those three simulations.

[4] Value represents the ensemble-mean regional climate model projection based on boundary condition data from nine different global CMIP5 models. The values within square brackets represent the ensemble minimum and maximum of those nine simulations.

3.4.4 Climate evolution until 12 000 AD

A construction of the global annual mean SAT evolution over the coming 10 ka, based on recent ESM modelling studies of long-term climate change under different anthropogenic emissions scenarios, is provided in Appendix B. In this section, only a short summary of those results is given.

Some of the recent ESM simulations of long-term climate change are listed in Table 3-6, together with the results from Collins et al. (2013). Based on the results in Table 3-6, the following conclusions can be drawn (see Appendix B for details).

- For the higher emission scenarios, the peak annual global mean SAT response generally occurs several centuries after the emissions have ceased. This means that SAT may continue to increase even after the radiative forcing from anthropogenic greenhouse gases has started to decline.
- For lower emissions, the global annual mean SAT remains relatively constant for several centuries to millennia after the stoppage of emissions.
- Global annual mean SAT remains elevated over the entire 10 ka period; at least 50 % of the peak SAT anomaly persists after 12 000 AD in all emission scenarios.

The constructed global annual mean SAT increase until 12 000 AD under low, medium and high emissions (comparable to RCP2.6, RCP4.5 and RCP8.5, respectively), based on the studies in Table 3-6 and conceptual modelling of alternative emission scenarios (Appendix B), is shown in Figure 3-25.

An equivalent construction of the annual mean SAT change until 12 000 AD at Forsmark, provided in detail in Appendix B, Section B1.3, is summarised below.

Table 3-6. Summary of the projected global annual mean surface air temperature change (relative to present) until 12 000 AD as reported in the literature. The ranges in square brackets represent uncertainties associated with inter-model differences and/or internal variability. Only studies in which the models are integrated using historical emissions and realistic emission scenarios, comparable to RCP2.6, RCP4.5 and RCP8.5 (Section 3.4.1), are listed. In the following, cumulative emissions < 1 000 Pg C are comparable with RCP2.6, scenario B1 and cumulative emissions < 3 000 Pg C are comparable with RCP4.5, and scenario A2 and cumulative emissions > 5 000 Pg C are comparable with RCP8.5. Note that the modelling studies of Mikolajewicz et al. (2007), Eby et al. (2009) and Clark et al. (2016) include the global carbon cycle. This table is identical to Table B-1 in Appendix B.

Reference	Emission scenario/ Total carbon emissions	Max. ΔT (°C)	Timing of max. T increase (AD)	ΔT 2100 AD (°C)	ΔT 12000 AD (°C)
Mikolajewicz et al. (2007)[1]	B1[2]	2	2500	1	
	A2[2]	5	3000	2	
Eby et al. (2009)[3]	160 PgC[4]	0.3	2250	0.2	0.2
	640 PgC[4]	1.4	5500	1.1	0.8
	960 PgC[4]	2.0	4000	1.7	1.0
	1 280 PgC[5]	2.5	3800	0.8	1.5
	2 560 PgC[5]	4.7	3000	1.7	3.1
	5 120 PgC[5]	7.8	3200	3.0	5.9
Collins et al. (2013)	RCP2.6			1.0[6] [0.3–1.7]	
	RCP4.5			1.8[6] [1.1–2.6]	
	RCP8.5			3.7[6] [2.6–4.8]	
Clark et al. (2016)[7]	160 PgC[8]	0.4	2200	0.4	0.3
	640 PgC[8]	1.4	5500	1.2	0.7
	960 PgC[8]	1.9	3900	1.8	1.0
	1 280 PgC[9]	2.0 [0.8–3.2]	2300	1.3 [0.4–2.2]	1.3 [0.5–2.2]
	2 560 PgC[9]	4.1 [3.0–5.2]	2500	2.4 [1.2–3.6]	2.9 [2.4–3.5]
	5 120 PgC[9]	7.4 [7.0–7.7]	2600	3.9 [2.2–5.6]	6.2 [5.5–6.8]

[1] Earth system model simulations are integrated until 5000 AD. Temperature changes are shown relative to a control simulation with zero anthropogenic emissions.

[2] Emissions follow the SRES emission scenarios (used in the fourth assessment IPCC report, IPCC 2007) until 2100 AD, after which they are instantaneously reduced to zero.

[3] Temperature changes are relative to a 10 000-year control simulation with zero anthropogenic emissions. Incoming solar radiation was held fixed at its present-day value in all the simulations.

[4] Emissions follow observations until 2000 AD. At the beginning of 2001 AD, a pulse of CO_2 was applied over one year.

[5] Emissions follow the A2 SRES emission scenario until 2100 AD, after which they decline linearly to zero by 2300 AD. The scenarios were then created by scaling the A2 emissions such that the cumulative emissions reached the values reported in this table by 2300 AD.

[6] Same as in Table 3-3.

[7] Temperature changes are relative to the 1980–2004 AD reference period.

[8] Same Earth System Model and future emission pathways as in Eby et al. (2009) (see footnote 4), except for a varying future orbital forcing.

[9] Ensemble-mean surface air temperature response across eight versions of two different intermediate complexity Earth system models. Emissions increased linearly between 2000 and 2100 AD, after which they decline linearly back to zero by 2300 AD.

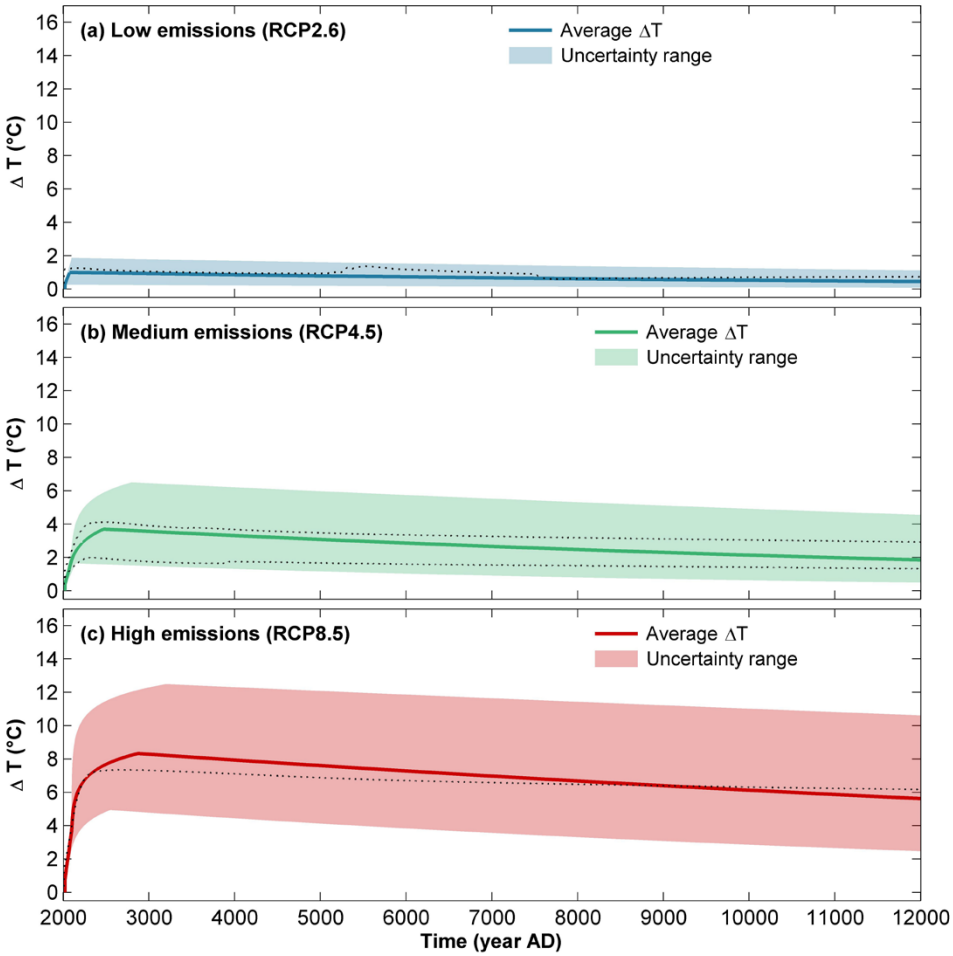

Figure 3-25. *Constructed global annual mean surface air temperature change until 12 000 AD (relative to present) for (a)low, (b)medium and (c) high carbon emissions (comparable to RCP2.6, RCP4.5 and RCP8.5, respectively). The uncertainty range has been constructed based on uncertainties among the studies in Table 3-6, and the average temperature change ("Average ΔT") has been calculated using average values of the parameters that were used construct the lower and upper uncertainty bounds (see Appendix B, Section B1 for details). To that end, average ΔT illustrates a typical mid-range temperature evolution for each emission scenario over the next 10 ka. The dotted lines in the figure shows the evolution of ensemble-mean temperature change from the Clark et al. (2016) projections with 640 Pg C cumulative emissions (comparable with RCP2.6; panel a), 1 280 and 2 560 Pg C cumulative emissions (comparable with RCP4.5; panel b), and 5 120 Pg C cumulative emissions (comparable with RCP8.5; panel c). Figure is identical to Figure B-3 in Appendix B.*

Climate at Forsmark until 12 000 AD

As discussed in Section 3.4.3, the temperature at Forsmark is expected to be higher than the global average by 2100 AD due to polar amplification and the fact that land warms faster than the oceans. Over multi-millennial timescales, the differences in heating between land and oceans are expected to be less significant because the oceans have had a longer time to equilibrate with the radiative forcing from the greenhouse gases. However, the polar amplification is expected to be fairly consistent also on longer timescales (Eby et al. 2009, Pimenoff et al. 2012), amounting to ~ 1.2–1.5 times the global average temperature change (see also Appendix B, Section B1.3.1).

For the centuries and millennia beyond 2100 AD, the fate of the AMOC is more uncertain. In an EMIC intercomparison study by Zickfeld et al. (2013), all models predicted an almost complete recovery of AMOC by 3000 AD under the low and intermediate RCPs. However, under the high emission scenario RCP8.5, the AMOC response was highly variable among the models; some models simulated an almost complete recovery, whereas others suggested a more persistent weakening. One of the 12 models even projected a collapse (defined here as a slowdown to an "off" state) of the AMOC

under this scenario. A collapsed AMOC beyond 2100 AD was also projected under the high emission scenario (SRES A2, approximately equivalent to RCP8.5) in Mikolajewicz et al. (2007) and Pimenoff et al. (2012), and for more moderate emissions levels in Liu et al. (2017). An equivalent AMOC collapse under low emissions, such as for RCP2.6, has not been reported and is therefore considered very unlikely.

Another important difference between global changes and the local changes in the Forsmark area is that the temporal evolution of the temperature increase in Forsmark is expected to have significantly higher variability on annual, decadal and centennial timescales. Regional climate is generally more variable than the global average. In addition, Forsmark is in the mid-latitude storm-track region, resulting in a more variable climate. One example of the temporal climate evolution in a specific region as simulated by one single model simulation by Pimenoff et al. (2012) is seen in Figure 3-26. In the high emission scenario, S1, the AMOC weakened and collapsed at ~ 2150–2250 AD, with dramatic effects for the Fennoscandian climate (Pimenoff et al. 2012). A temporary weakening of the AMOC was also simulated in the intermediate emission scenario, S3, around 2200–2300 AD (Pimenoff et al. 2012). In summary both Pimenoff et al. (2012) and Liu et al. (2017) reported that a collapse of the AMOC, in isolation, could serve to reduce SAT in the Forsmark area by approximately 3 °C (see Figure 3-26 and also Appendix B, Section B1.3.2).

The constructed SAT change at Forsmark until 12 000 AD, taking both polar amplification and uncertainties associated with the AMOC response into account, is shown in Figure 3-27. Note that as a result of polar amplification, the SAT increase at Forsmark is generally higher than the associated global average increase. However, the warming at Forsmark could also be largely mitigated by an AMOC collapse, which could even result in a net cooling for moderate emission levels.

As with the precipitation response until 2100 AD (Section 3.4.3), annual precipitation at Forsmark is expected to increase also on multi-millennial timescales as a result of elevated temperatures. However, the uncertainty in future precipitation response is large, especially if considering the seasonal response. For example, during the summer season precipitation may even decrease in a future warmer climate. The estimated seasonal and annual precipitation changes at Forsmark until 12 000 AD, along with corresponding estimated changes in SAT, are provided in Appendix B, Section B2. For a detailed example of how the climate in Forsmark may change a few thousand years into the future under a high emissions scenario, see Section 3.4.6.

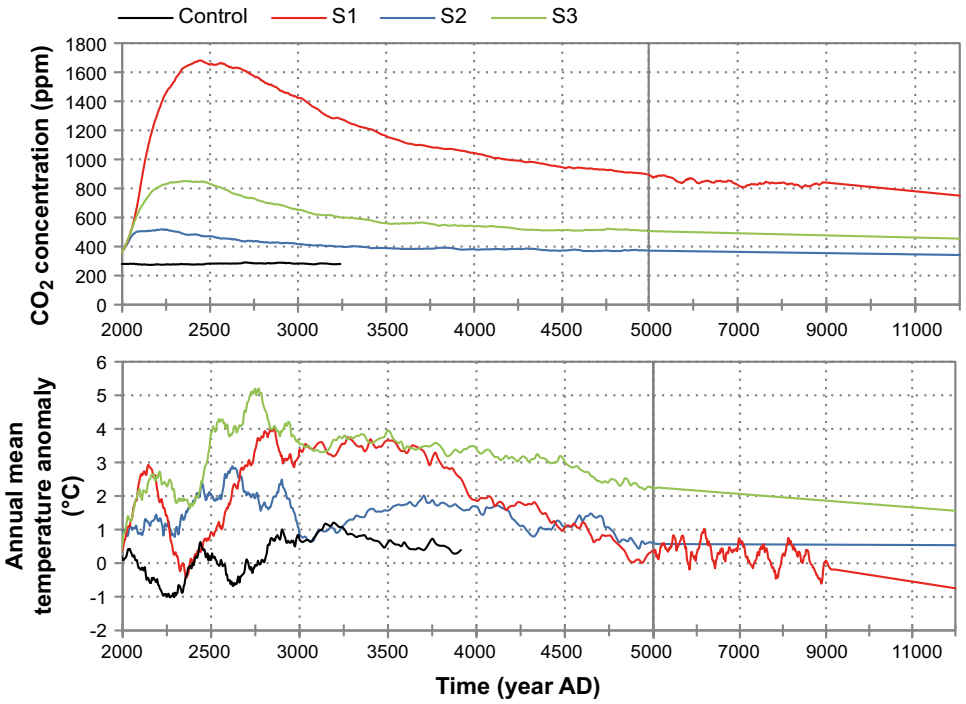

Figure 3-26. *Evolution of atmospheric CO_2 concentration (upper panel) and the annual mean temperature change relative to the period 1961–1990 (+4.8 °C at Rauma Kuuskajaskari) (lower panel). Note that the scale of the x-axis is not constant. Modified from Figure 15 of Pimenoff et al. (2012).*

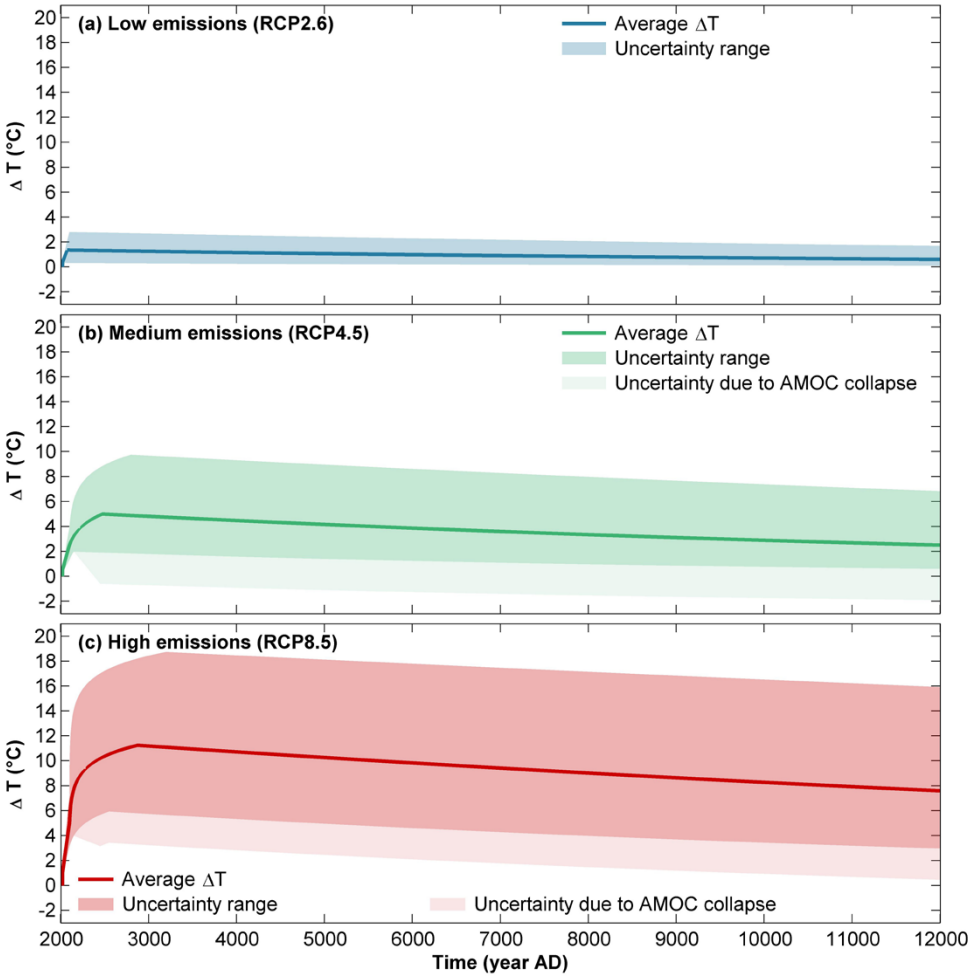

Figure 3-27. *Constructed annual mean surface air temperature change until 12 000 AD at Forsmark (relative to the present temperature for the period 1986–2005 AD) for (a) low, (b) medium and (c) high carbon emissions (comparable to RCP2.6, RCP4.5 and RCP8.5, respectively). The uncertainty range associated with a collapse of the AMOC in the medium and high emission scenarios is illustrated with another colour to highlight the lower confidence in this uncertainty range. Figure is identical to Figure B-4 in Appendix B.*

3.4.5 Climate evolution until 100 ka AP

State-of-the-art AOGCMs and ESMs have not been applied for studies of climate evolution beyond 12 000 AD, since these models are too computationally expensive. Several modelling studies of climate evolution in the next 100 ka AP have however been performed with simplified models (SCMs and EMICs). A question that has been extensively studied is the timing of the next glacial inception, i.e. initiation of ice-sheet build-up. For the purpose of the current safety assessment, this question, and the related question of when cold climate conditions may produce permafrost in the Forsmark region, is of importance.

For the next ~ 100 ka, climate models are forced with the known future variations in insolation due to variations in the Earth's orbital parameters (Berger and Loutre 1991) and different hypothesised atmospheric CO_2 concentrations. For all models, the event of glaciation is crucially dependent on the atmospheric level of CO_2. As described in Section 3.4.1, the current (2018 AD) atmospheric CO_2 concentration is c. 409 ppmv (www.esrl.noaa.gov). Unless CO_2 is actively removed from the atmosphere by technological measures, it is likely that CO_2 concentration would stay above pre-industrial levels for the next 10 ka and beyond (Section 3.4.1). A comprehensive review of the next potential glacial inception is provided in Liakka et al. (2021). In the following, published studies of Earth's climate in the coming 100 ka are briefly described, with a focus on the timing of glacial inception and maximum Northern Hemisphere ice volume. The results are summarised in Figure 3-28.

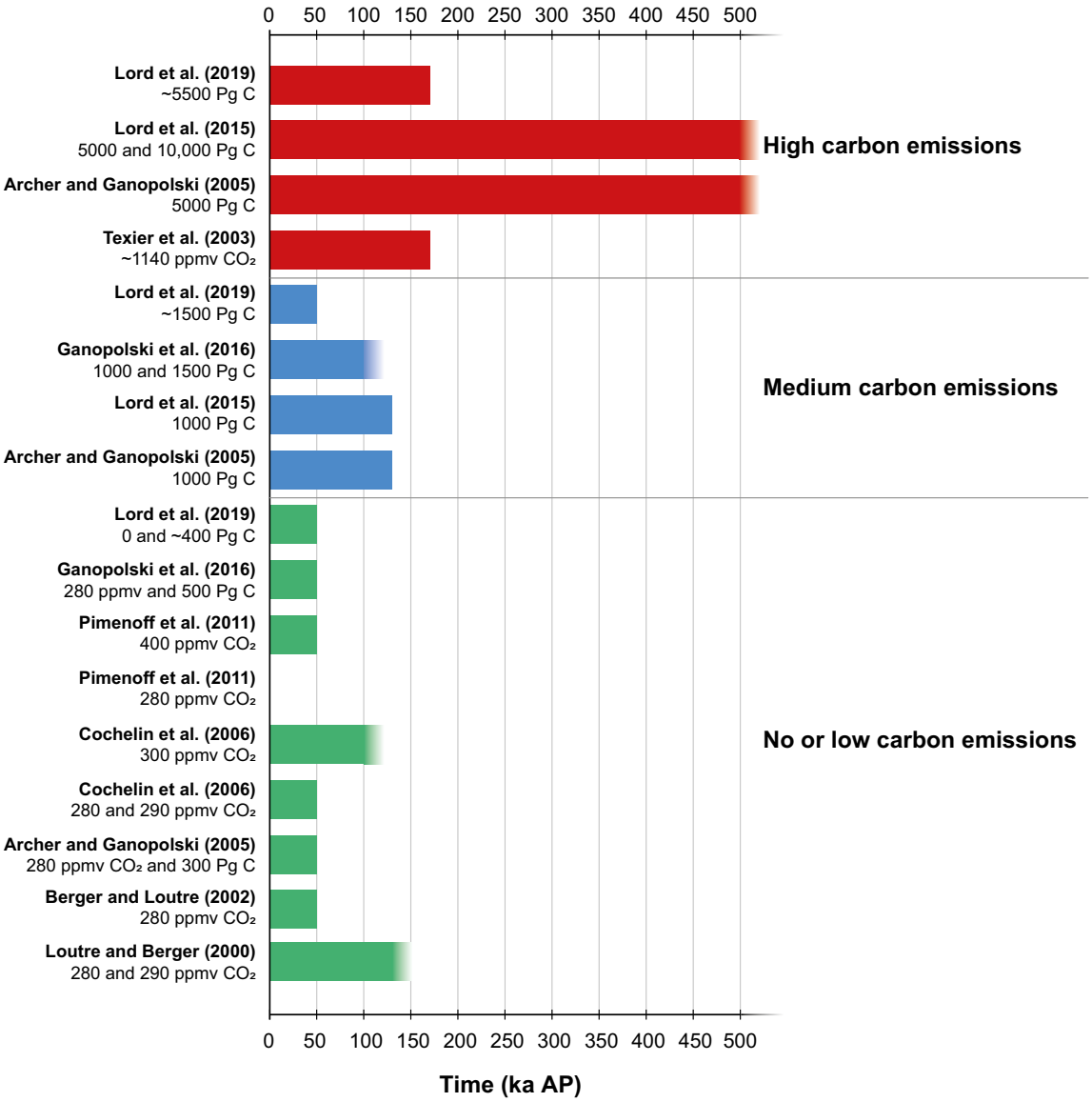

Figure 3-28. *Approximate timing of next glacial inception from different modelling studies. The bars ending with a colour-to-white gradient represent simulations that were not integrated sufficiently far into the future to project the next glacial inception. For those simulations, the bars thus show how long the simulations were integrated without glacial inception to occur. The study of Pimenoff et al. (2011) projects that glacial inception would be immediate for pre-industrial atmospheric CO_2 concentrations (280 ppmv). For Lord et al. (2019) only the timing of the next glacial inception as projected in the optimally tuned simulation is shown in the figure. The remaining 90 simulations in Lord et al. (2019) may however give other results (see Figure 3-30). For example, under medium emissions, most of the Lord et al. (2019) simulations suggest that glacial inception will occur after 100 ka AP whereas only a few of the simulations suggest a glacial inception around 50 ka AP as indicated in the figure. Cumulative CO_2 emissions are expressed in the unit "petagrams of carbon" (Pg C; 1 Pg = 10^{15} g). Modified from Liakka et al. (2021).*

Loutre and Berger (2000) simulated the coming 130 ka with the Louvain-la-Neuve two-dimensional Northern Hemisphere climate model (LLN 2-D NH) forced by future variations in orbital parameters and several different constant atmospheric CO_2 concentrations. They found that, in their model, glaciation occurs 50 ka into the future in simulations with CO_2 concentrations lower than 280 ppmv, whereas for CO_2 concentrations above this value glaciation is postponed beyond 50 ka into the future. For CO_2 concentrations lower than 220 ppmv glaciation inception was found to be already under way. It should also be noted that such low CO_2 concentrations likely requires the onset of full glacial conditions (see e.g. Figure 3-1).

Berger and Loutre (2002) simulated the period 200 ka BP to 130 ka AP with the LLN 2-D NH model forced by future variations in orbital parameters and three different scenarios for future atmospheric CO_2 concentration; constant concentration of 210 ppmv, constant concentration of 280 ppmv, and an anthropogenic scenario with the concentration reaching 750 ppmv in 200 years from now and decreasing to 280 ppmv in 1 000 years from now. In accordance with Loutre and Berger (2000), they found that glacial inception is imminent in the 210 ppmv scenario, whereas glacial inception occurs after ~ 50 ka in the 280 ppmv and the anthropogenic scenarios.

The BIOCLIM project (Texier et al. 2003) simulated the coming 200 ka with the LLN 2-D NH model, forced by variations in orbital parameters and prescribed time-varying atmospheric CO_2. For a fossil-fuel burning contribution resulting in peak atmospheric CO_2 concentration of ~ 1 100 ppmv in 2275 AD they projected nearly ice-free Northern Hemisphere conditions for the next 150 ka, and that the next glacial inception will occur in ~ 170 ka.

Archer and Ganopolski (2005) used the EMIC CLIMBER-2 to estimate a relationship between insolation and the critical level of atmospheric CO_2 that is required for glacial inception (see also discussion about Ganopolski et al. 2016 below). Based on this result, they used the conceptual model of global cycles from Paillard (1998) to predict the length of the current interglacial under different levels of cumulative emissions. They found that a carbon release from fossil fuels or methane hydrate deposits of 5 000 Pg C could prevent glaciation for the next 500 ka. For cumulative emissions of 300 Pg and 1 000 Pg C, on the other hand, they found that glacial inception occurs after ~ 50 ka and ~ 130 ka respectively. Archer and Ganopolski (2005) also pointed out that, for an atmospheric CO_2 concentration of 280 ppmv, a small change in the model parameters can easily tip the simulation to onset of glaciation now rather than in 50 ka.

Cochelin et al. (2006) simulated the coming 100 ka with the McGill Paleoclimate Model (MPM) forced by variations in orbital parameters and prescribed atmospheric CO_2. Their model produced three types of evolution for the ice volume: an imminent glacial inception (low CO_2 levels), a glacial inception in 50 ka (CO_2 levels of 280 or 290 ppmv), or no glacial inception during the next 100 ka (CO_2 levels of 300 ppmv and higher).

Pimenoff et al. (2011) employs the CLIMBER-2 model with the thermo-mechanical ice-sheet model SICOPOLIS to study the future evolution of climate in Olkiluoto, the site selected for the Finnish repository for spent nuclear fuel. They simulated the coming 120 ka with constant atmospheric CO_2 concentrations of 280 ppmv and 400 ppmv, respectively. The climate evolution differs substantially between these two experiments, with an immediate glaciation occurring in the 280 ppmv experiment as opposed to very restricted glaciation during the coming 120 ka in the 400 ppmv experiment. The insolation minimum at about 17 ka AP causes a large ice sheet over northern Fennoscandia in the 280 ppmv scenario as opposed to only some ice in the Scandinavian mountain range in the 400-ppmv scenario. The following insolation minimum at about 54 ka AP produces an extensive ice sheet in the 280 ppmv scenario as opposed to a small ice sheet from the Scandinavian mountain range to Finnish Lapland and parts of Northern Ostrobothnia in the 400 ppmv scenario. In the 400 ppmv scenario, the mean temperatures at Olkiluoto are warmer than at present for most of the time. An exception is the insolation minimum at about 54 ka AP, when the mean temperatures are about the same as at present.

Lord et al. (2015) developed an empirical response function that encapsulates the long-term removal of excess CO_2 from the atmosphere. Using this function, in conjunction with the known future variations of the Northern Hemisphere insolation and the model-predicted value of the insolation required for glacial inception from Archer and Ganopolski (2005), they projected potential periods of the next glacial inception for idealised pulse emissions of 1 000, 5 000 and 10 000 Pg C. They found that the addition of anthropogenic CO_2 to the atmosphere delays the next glacial inception until ~ 130 ka AP for the 1 000 Pg C scenario, and beyond 500 ka AP for the 5 000 and 10 000 Pg C scenarios. Ganopolski et al. (2016) proposed a critical relationship between boreal summer insolation and atmospheric CO_2 concentration, which explains the beginning of the past eight glacial cycles and might therefore also be used to predict future periods of glacial inception. Their analysis suggests that even in the absence of anthropogenic greenhouse gas emissions no substantial build-up of ice sheets would occur within the next several thousand years and that the current interglacial would probably last for another 50 ka. However, moderate anthropogenic cumulative CO_2 emissions of 1 000 to 1 500 Pg C, i.e. comparable to the RCP4.5 emission scenario (Table 3-3), would postpone the next glacial inception by at least 100 ka.

In Lord et al. (2019), future glacial-interglacial cycles were modelled using a conceptual global sea-level model (CGSLM), based on the insolation threshold model originally developed by Paillard (1998). Following Lord et al. (2015), the value of the critical insolation threshold that results in initiation of a glaciation was adopted from Archer and Ganopolski (2005). Similar to Archer and Ganopolski (2005), Lord et al. (2015) and Ganopolski et al. (2016), Lord et al. (2019) demonstrate that the critical insolation, and thus the timing of the next glacial inception, is largely controlled by the anthropogenic CO_2 emissions. They found that the next substantial build-up of ice sheets would occur in ~ 50 ka for future emissions comparable to RCP4.5 or less. However, for high emissions (RCP8.5), Lord et al. (2019) project that the next glacial inception will be delayed until approximately 170 ka AP.

In summary, most studies suggest that roughly pre-industrial atmospheric CO_2 concentrations would result in a substantial ice-sheet build-up around ~ 50 ka AP, whereas higher CO_2 levels would postpone the next glacial inception by an additional c. 50 to 200 ka. Furthermore, most studies agree that CO_2 concentrations well below pre-industrial levels are required to enable a substantial ice build-up prior to 50 ka AP. This is also illustrated in Figure 3-29, which shows the evolution of the high-latitude summer insolation (panel a) and the CO_2 threshold value for glacial inception adopted from Ganopolski et al. (2016) (panel b). The next glacial inception is estimated to occur once the actual CO_2 drops below the threshold value, shown in Figure 3-29b. The CO_2 threshold (p_{CO_2}) is computed from the following relationship which has been calibrated against the beginning of eight past glacial cycles (Ganopolski et al. 2016):

$$p_{CO_2} = 280 \times \exp\left(-(S-466)/77\right), \qquad \text{Equation 3-1}$$

where S is the maximum boreal summer insolation (here assumed to occur on June 21st), displayed in Figure 3-29a. Figure 3-29b illustrates that the CO_2 threshold for glaciation is well below the pre-industrial value (280 ppmv) for most of the coming 100 ka. The only times during which the CO_2 threshold approaches pre-industrial levels occur at 54 ka AP and, to a somewhat lesser extent, at 97 ka AP. Another interesting feature of Figure 3-29b is that Earth's orbital configuration during the next insolation minimum at 17 ka AP is actually *less* favourable for glacial inception than at present, manifested by ~ 8 ppmv lower CO_2 threshold at 17 ka AP compared to today.

There is also a large variability in the projections of the next glacial inception among the studies in Figure 3-28, in particular for medium and high emissions. This variability is partly a result of different models and modelling techniques being used. As already noted above, some of the models may be forced with constant or varying atmospheric CO_2 concentrations or with anthropogenic CO_2 emissions, or may include different components, processes and feedbacks of the climate and Earth system (e.g., vegetation, carbon cycle). These differences mean that the models respond differently to radiative forcing from insolation and atmospheric CO_2, which in turn results in different projections of the future climate.

Furthermore, simple climate models, such as those used to evaluate the timing of next glacial inception in Figure 3-28, have been shown to be highly sensitive to internal model parameters (e.g. Paillard 1998, Lord et al. 2019). Small changes in these parameters can therefore result in widely different projections of the future climate. This is, for instance, illustrated in Figure 3-30 which shows the projected future global sea-level evolution from 90 sensitivity simulations from Lord et al. (2019) with the CGSLM. All simulations under the same emissions scenario used identical representations of insolation and CO_2 forcing, but different combinations of poorly constrained model parameters. As illustrated in Figure 3-30, the simulations produce relatively similar results for the past global sea-level variations, in reasonable agreement with the data. However, despite this, the projected future global sea-level evolution for the next 100 ka varies substantially across the simulations, particularly "natural", RCP2.6 and RCP4.5 scenarios. For example, depending on the combination of model parameters, about 20 % of the sensitivity simulations under RCP4.5 suggest that the timing of the next glacial inception will occur in response to the insolation minimum at 54 ka AP, whereas the remaining 80 % of the simulations project the next glacial inception to occur after 100 ka AP. For RCP8.5 all projections suggest that the next glacial inception will occur after 100 ka AP. The sensitivity analysis in Figure 3-30, along with the differences in selected models between the studies that project timing of next glacial inception (Figure 3-28), highlight the large uncertainty involved with modelling the future climate for timescales of 100 ka. It is important to

stress that the timing of a future glacial inception, discussed here, does not mean that the ice-sheet covers e.g. the Forsmark site, since it may take considerable time before the ice sheet grows to cover such a large area. To this end, an important property of Figure 3-29 (Equation 3-1) is that it only shows when conditions are favourable for glacial inception, but not how extensive the resulting glaciation may be. According to Figure 3-29, conditions for glacial inception within the coming 100 ka are most favourable around the 54 ka AP insolation minimum. However, most of the studies that project glacial inception around this time also suggest that the Northern Hemisphere ice volume will be significantly higher towards the end of the 100-ka period, when insolation conditions are less favourable for glacial inception than around 54 ka AP (e.g. Loutre and Berger 2000, Berger and Loutre 2002, Archer and Ganopolski 2005, Cochelin et al. 2006, Lord et al. 2019). This pattern of progressive ice-sheet growth in response to insolation variations (of various amplitudes) is consistent with the observed pattern during the Late Quaternary, e.g. the Weichselian glacial cycle (Section 3.2).

The timing of first ice cover in the Forsmark area, exemplified by the study of Lord et al. (2019), is discussed below.

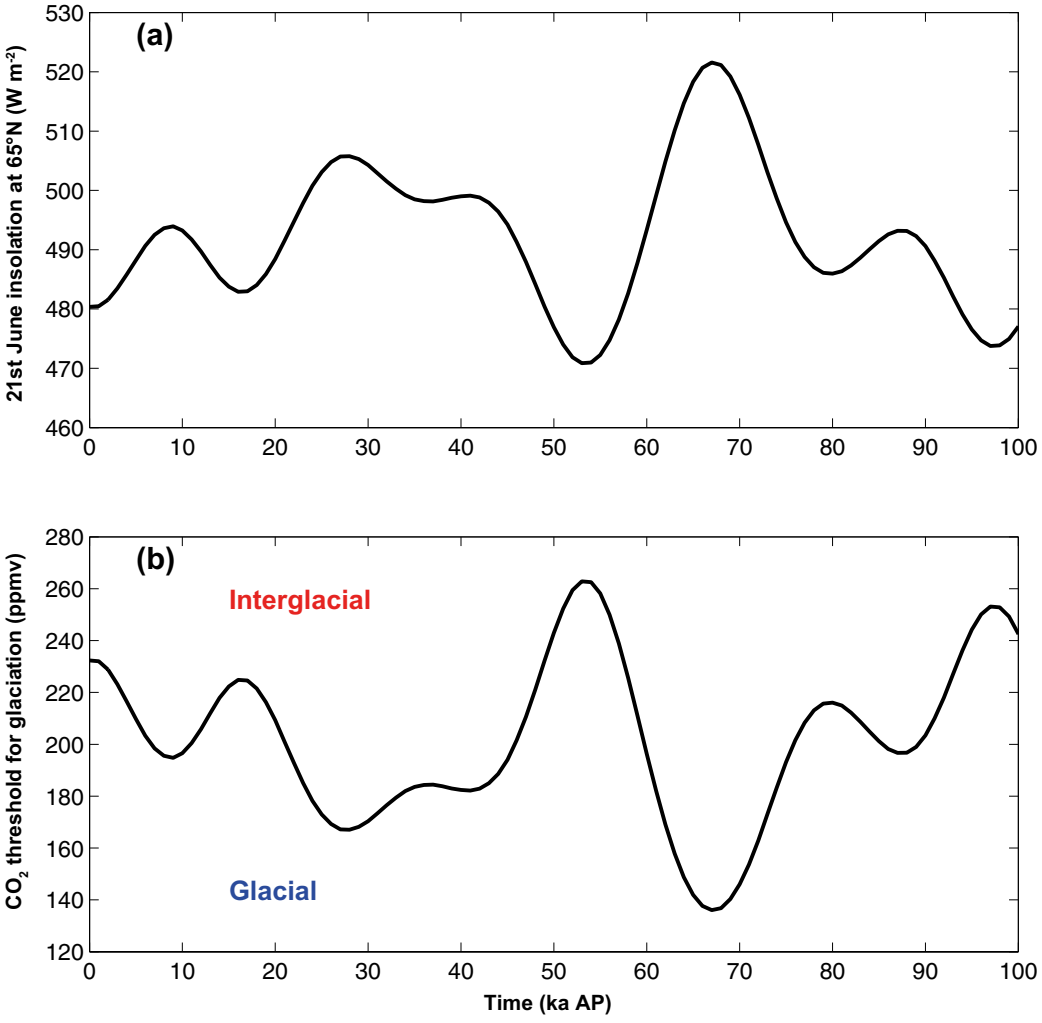

Figure 3-29. *(a) 21st June insolation at 65°N derived from the solution in Laskar et al. (2004). (b) Atmospheric CO_2 threshold for glacial inception during the next 100 ka, calculated from Equation 3-1, adopted from Ganopolski et al. (2016). The next glacial inception is projected to occur once the actual CO_2 drops below the CO_2 threshold. Most studies project that the next glacial inception will occur at ~ 50 ka AP in conjunction with the insolation minimum (i.e. CO_2 threshold maximum) at 54 ka AP, or after 100 ka AP. Note that an ice-sheet could reach the Forsmark area considerably later than the time of Northern Hemisphere glacial inception, see the text.*

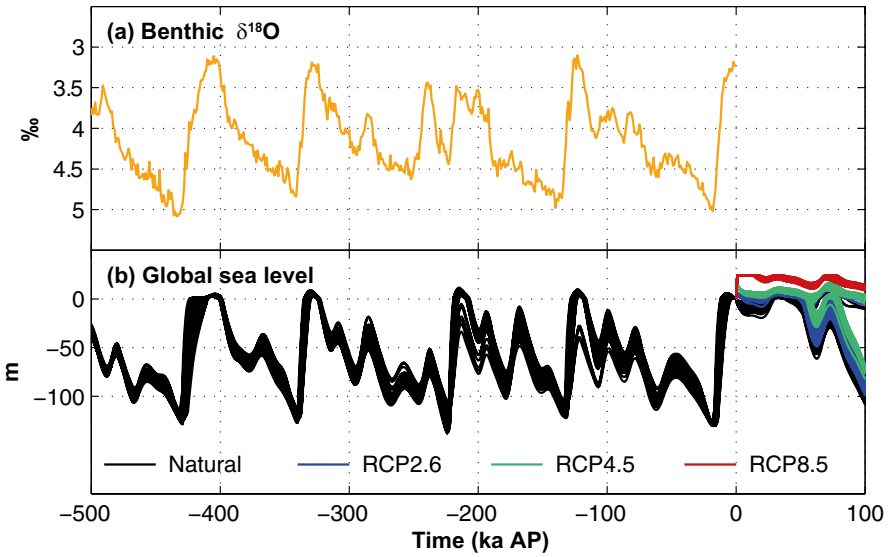

Figure 3-30. *(a) Proxy data for global ice volume from the stack of benthic $\delta^{18}O$ records of Lisiecki and Raymo (2005) from 500 ka BP until present day (a subset of the timeseries shown in Figure 3-1). (b) Simulated global sea level (m) from 500 ka BP until 100 ka AP for the "Natural" scenario (black lines), as well as from present-day to 100 ka AP for the RCP2.6 (blue lines), RCP4.5 (green lines) and RCP8.5 (red lines) emission scenarios (Lord et al. 2019). The global sea level was calculated in Lord et al. (2019) using the conceptual global sea-level model from Paillard (1998). A total of 90 simulations are shown for each emission scenario. The simulations were conducted with different model configurations, all of which however agree reasonably well with paleoclimate proxy data (cf. panel b). The optimally-tuned model configuration that best matched paleoclimate proxy data was used in Lord et al. (2019) as input to the climate emulator, which in turn was used to simulate the climate at Forsmark over the next 100 ka and beyond (see next subsection).*

Climate in Forsmark until 100 ka AP

Results from Lord et al. (2019) have been discussed in conjunction with the long-term evolution of the atmospheric CO_2 concentration (Section 3.4.1) and the timing of the next Northern Hemisphere glacial inception (this section; see above). However, the overall objective of Lord et al. (2019) was to project the temperature and precipitation evolution at Forsmark for the next 1 million years. The most important results from the first 100 ka of those simulations are presented here.

The climate at Formark in Lord et al. (2019) was simulated using a statistical climate emulator (Lord et al. 2017), which was calibrated using a large ensemble of AOGCM simulations with varying climate conditions representative for both glacial and interglacial states. The emulator was forced by the atmospheric CO_2 concentration, orbital variations and global ice-sheet volume changes. The future evolution of atmospheric CO_2 in response to anthropogenic CO_2 emissions was computed using a carbon cycle impulse response function (see Section 3.4.1), orbital variations were calculated using the solution of Laskar et al. (2004) (see Figure 3-29a), and global ice-sheet volume changes were estimated using the conceptual global sea-level model (CGSLM; see above).

Figure 3-31 shows the first 100 ka of the projected change (compared with pre-industrial) in annual-mean SAT and precipitation at Forsmark from Lord et al. (2019). In addition to the different levels of anthropogenic CO_2 emissions described by the RCP scenarios, Lord et al. (2019) also included a "natural" scenario which assumes no anthropogenic CO_2 emissions (Section 3.4.1). During the first 10 ka, the SAT response to anthropogenic emissions (Figure 3-31a) is structurally very similar to the SAT evolution discussed in Section 3.4.4 (see e.g. Figure 3-27): after an initial peak following the cessation of emissions, SAT starts to slowly decline towards pre-industrial values. The results from Lord et al. (2019) show that for RCP4.5 and RCP8.5 Forsmark SAT remains elevated for the entire period between 10 ka AP and 100 ka AP, suggesting anthropogenic CO_2 emissions may influence the Forsmark climate well beyond the first 10 ka.

For the "natural" and RCP2.6 scenarios, Forsmark SAT changes are relatively small between 10 ka AP and the first glacial inception at ~ 50 ka AP. At this time, the temperature starts to decline, culminating

in a maximum SAT decrease by ~ 60 ka AP of nearly 10 °C for the natural scenario and ~ 5 °C for RCP2.6. After the first occurrence of glacial conditions in the Northern Hemisphere, interglacial conditions prevail between approximately 70 and 80 ka AP resulting in an increase in SAT toward pre-industrial values. In conjunction with the second glaciation, starting at ~ 80 ka AP and extending beyond the 100 ka period, the SAT under the natural and RCP2.6 scenario decreases to even lower values than during the first glaciation at ~ 60 ka AP. Note that the large decrease in SAT during the two glaciated periods is *not* explained by glaciated conditions in the Forsmark area, as the SAT responses in Figure 3-31 have been simulated assuming no ice cover at Forsmark through the entire 100 ka period. Instead, the lowered temperatures are likely attributable to a combination of lower atmospheric CO_2 concentrations (Table 3-4), reduced boreal summer insolation (Figure 3-29a) and glaciated conditions elsewhere in the Northern Hemisphere.

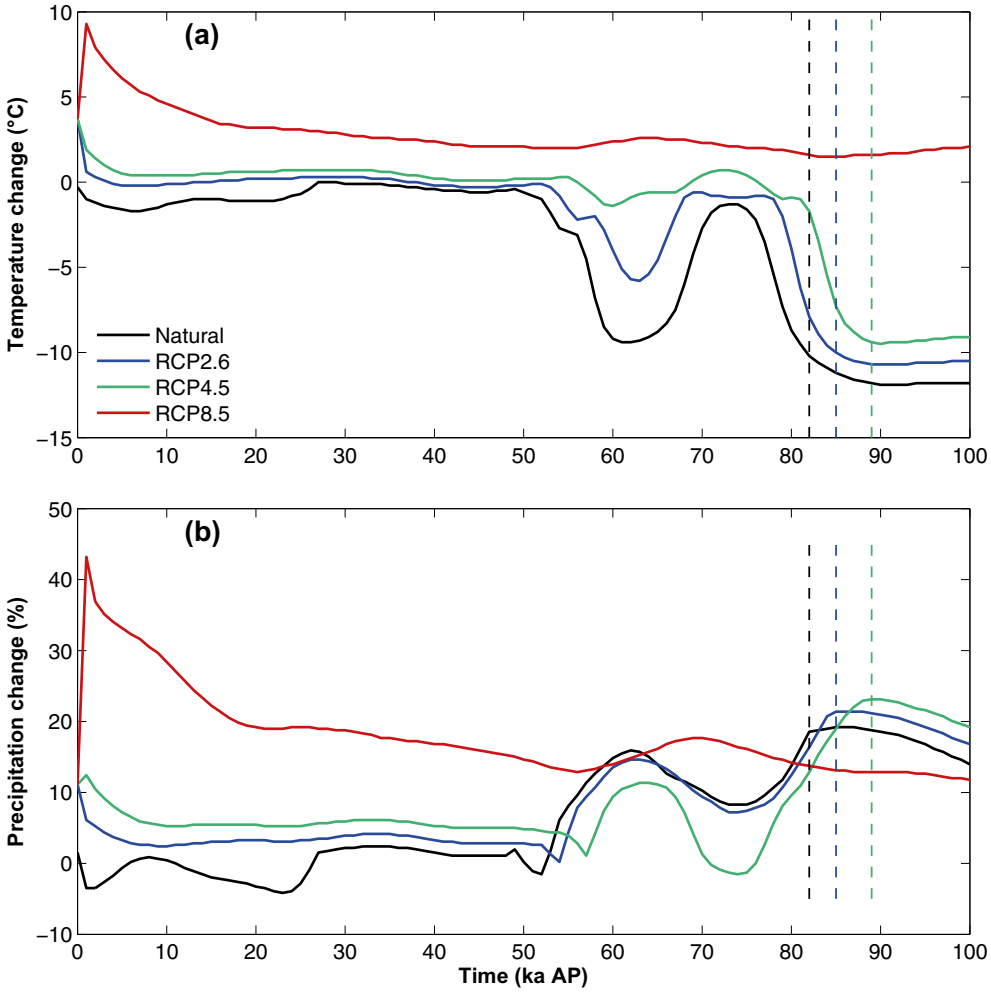

Figure 3-31. *Projected change (compared with pre-industrial) in annual-mean (a) surface air temperature (SAT) and (b) precipitation at Forsmark during the first 100 ka of the emulated climate in Lord et al. (2019). The projections were performed for low (comparable to RCP2.6; blue curve), medium (comparable to RCP4.5; green curve) and high (comparable to RCP8.5; red curve) future anthropogenic carbon emissions. For more information on the carbon cycle modelling in Lord et al. (2019), see Section 3.4.1. In addition, Lord et al. (2019) included a natural scenario (black line) which assumes no anthropogenic emissions. The dashed vertical black, blue and green lines, at 82, 85 and 89 ka AP, correspond to the earliest anticipated occurrence of glaciated conditions at Forsmark under the natural, RCP2.6 and RCP4.5 scenarios, respectively. For the RCP8.5 scenario the first periods of glaciated conditions are projected to occur after the 100-ka period and are therefore not indicated in the figure. The timings of glaciated conditions at Forsmark were estimated from global ice volume changes derived from the CGCLM (see also Figure 3-30 and associated text in this section); hence the geographical distribution of the future ice cover was not explicitly modelled. Therefore, the Lord et al. (2019) projection of future glaciated periods at Forsmark is uncertain. Note that the SAT and precipitation changes shown here have been modelled assuming no ice cover at the site over the 100-ka period.*

Lord et al. (2019) estimated that the first future occurrence of glaciated conditions in the Forsmark area (indicated by the vertical dashed lines in Figure 3-31) could take place at between 80 and 90 ka BP for the natural, RCP2.6 and RCP4.5 scenarios, and well beyond 100 ka AP for the RCP8.5 scenario. Note that the estimates of glaciated conditions at the site from Lord et al. (2019) are highly uncertain since they are only based on projected changes of global sea level with the CGSLM (see above), and not on temporal changes in the geographical distribution of the ice sheets. Furthermore, the projected changes in climate and ice cover at Forsmark were only analysed in one out of the 90 CGSLM sensitivity simulations. However, as seen in Figure 3-30, the global response in the 90 simulations is highly variable, even within the same emissions scenario, depending on the specific set of parameter values that were used. It is hence likely that these various global responses would also have a significant impact on the Forsmark climate evolution over the next 100 ka.

For the RCP8.5 scenario, the temporal evolution of the annual precipitation change in the Lord et al. (2019) study is structurally very similar to the projected SAT change (Figure 3-31). Hence, in that scenario, higher temperatures generally correspond to higher precipitation values and vice versa. This is the expected response of the annual-mean hydrological cycle at Forsmark to global warming on both shorter and longer timescales, see Sections 3.4.3 and 3.4.4. However, during periods of glaciation in the natural, RCP2.6 and RCP4.5 scenarios, there is a negative correlation between temperature and precipitation, characterised by a significant increase in precipitation as the temperature declines (Figure 3-31). This is likely explained by large-scale changes in the atmospheric and oceanic circulation. For example, several studies have reported that the vastly different environmental conditions during glacials compared with interglacials, in particular the existence of continental-scale ice sheets, may result in a large-scale reorganisation of the atmospheric planetary wave field (e.g. Liakka et al. 2016, Liakka and Lofverstrom 2018) and the latitudinal position of the mid-latitude storm track (e.g. Li and Battisti 2008, Löfverström et al. 2014).

3.4.6 Exemplified Forsmark climate under global warming conditions

In order to give a detailed example of the Forsmark climate under the influence of increased atmospheric greenhouse gas concentrations, a future temperate climate with increased greenhouse-gas concentrations in the atmosphere (750 ppm), a few thousands of years from now was simulated with global and regional climate models (Kjellström et al. 2009, including erratum Feb 2010).

The 750-ppmv atmospheric CO_2 concentration used by Kjellström et al. (2009) can be compared with Archer et al. (2009), described in Section 3.4.1, to show that this concentration represents a scenario with large human carbon emissions, but less than the entire carbon reserve.

In the climate model simulations, a complete loss of the Greenland ice sheet was assumed. Since such a deglaciation may take up to a couple of thousand years, if it were to occur, it is very uncertain what other climate-related conditions may be prevailing at that time. According to climate-change scenarios from simulations with GCMs, irreversible melting of the Greenland ice sheet may start at a time when the global mean temperature has increased by about 1.9–5.1 °C above today's conditions and the temperature over Greenland has increased by about 3–6.5 °C (Gregory et al. 2004, Gregory and Huybrechts 2006). Some recent studies indicate that the Greenland ice sheet might be more sensitive to increased concentrations of atmospheric greenhouse gases than previously thought (Robinson et al. 2012, Stone et al. 2010a, b), whereas other recent studies indicate the opposite (NEEM community members 2013).

Increases in temperature that may be large enough to make the Greenland ice sheet collapse are projected by GCMs within the 21st century for some emission scenarios (Meehl et al. 2007). If such high temperatures persist for a long enough time (several hundreds to a couple of thousand years depending on the degree of warming), the Greenland ice sheet may potentially collapse and disappear. In this time perspective, CO_2 levels will start to decrease again (when emissions cease). Nevertheless, at one thousand years from now, the atmospheric CO_2 concentrations will remain considerably higher than today (Archer et al. 2009). Further, if the Greenland ice sheet does collapse and disappear, a regrowth of the ice sheet is difficult to envisage as being initiated without substantial cooling. Here, the time period for the global warming simulation was chosen as a compromise between a high level of CO_2 (needed to simulate a warm climate that melts the Greenland ice sheet), and not too high a CO_2 level (since it needs to be that which remains in the atmosphere a long time after the

emissions have ceased). Thus, the simulations can be considered as representative of the climate a few thousand years into the future after a complete melting of the Greenland ice sheet and a partial recovery towards lower CO_2 concentrations.

For these simulations, a global GCM model (Community Climate System Model version 3, CCSM3), a regional climate model (Rossby Centre Regional Climate Model RCA 3) and a vegetation model (LPJ-GUESS) were used. For the simulations performed, atmospheric and land components of the CCSM3 used a grid spacing of approximately 2.8° in latitude and longitude. The vertical resolution is 26 levels in the atmosphere and 40 levels extending to 5.5-km depth in the ocean. The regional climate model used a horizontal resolution of 50 km and a time resolution of 30 minutes. For details on the models, how they were employed, and a discussion on model uncertainties, see Kjellström et al. (2009). As mentioned above, the simulation of the global warming climate used a CO_2 concentration in the atmosphere of 750 ppm. To also include the effect of other greenhouse gases in the RCA 3 model, a CO_2 equivalent value of 841 ppm was used (Kjellström et al. 2009). For a detailed description of the assumptions made in the modelling process, model forcing and initial conditions (such as astronomical and solar forcing, concentration of greenhouse gases and aerosols in the atmosphere, extents of ice sheets, distribution of land and sea, topography and vegetation), see Kjellström et al. (2009).

The simulated global warming climate should not be taken as a prediction or prognosis on how a future climate at Forsmark would manifest itself. Instead, it is *a detailed example* of how such a climate may be manifested. Given another forcing, for instance using a lower or higher CO_2 concentration, the resulting climate at this time would have been different. Further, given the same forcing conditions, differences between different climate model simulations exist (e.g. Kjellström et al. 2011). However, the model results are useful for exemplifying a climate affected by global warming as expressed at Forsmark. In this context, it is worth noting that the results of Kjellström et al. (2009) resemble those for many of the scenarios for the 21st century from the climate model inter-comparison project (CMIP3) (Meehl et al. 2007). For a detailed discussion and comparison with other climate model results, see Kjellström et al. (2009, Section 3.1.4).

Global climate

Figure 3-32 shows the simulated global warming climate from the GCM simulations. Seasonal mean changes in temperature in the global warming simulation as compared with a simulation of the present (1961–2000) climate are also shown in Figure 3-32. The removal of the Greenland ice sheet produces a strong heating of up to 17 °C over Greenland in both summer and winter, resulting in summer near-surface air temperatures of 0–12 °C in Greenland which prevent a regrowth of the Greenland ice sheet. This heating is primarily due to a combination of i) the lowering of the surface by up to 3 000 m and ii) the decrease in surface albedo and changes in heat fluxes between the atmosphere and the ground produced by the replacement of the glacier ice surface by tundra (Kjellström et al. 2009). As in all greenhouse warming scenarios presented in the IPCC AR4 report (Meehl et al. 2007), the Arctic region exhibits strong heating by up to 15 °C in winter (due to a substantial decrease in the Arctic sea-ice cover and a decrease in the snow cover). The seasonal mean temperature is up to 5 °C warmer in summer and up to 7.5 °C warmer in winter over Fennoscandia in the global warming simulation as compared with the simulation of the present climate. Seasonal mean summer temperatures in Sweden vary in the range 12–18 °C and winter temperatures vary in the range 0–6 °C. Sensitivity to changes in vegetation in these GCM simulations is discussed in Kjellström et al. (2009).

The change in precipitation in the global warming simulation as compared with the simulation of the present climate is also shown in Figure 3-32. The removal of the Greenland ice sheet leads to a 25 % decrease in precipitation, in particular over south-eastern Greenland in both summer and winter, indicating that much of the precipitation in that area in today's climate is triggered by the steep ice-sheet topography. As in all greenhouse-warming scenarios presented in the IPCC AR4 report (Meehl et al. 2007), precipitation is increased over mid-latitude Northern Hemisphere continents and the Arctic. For Fennoscandia there is an increase in precipitation, most notably in the north.

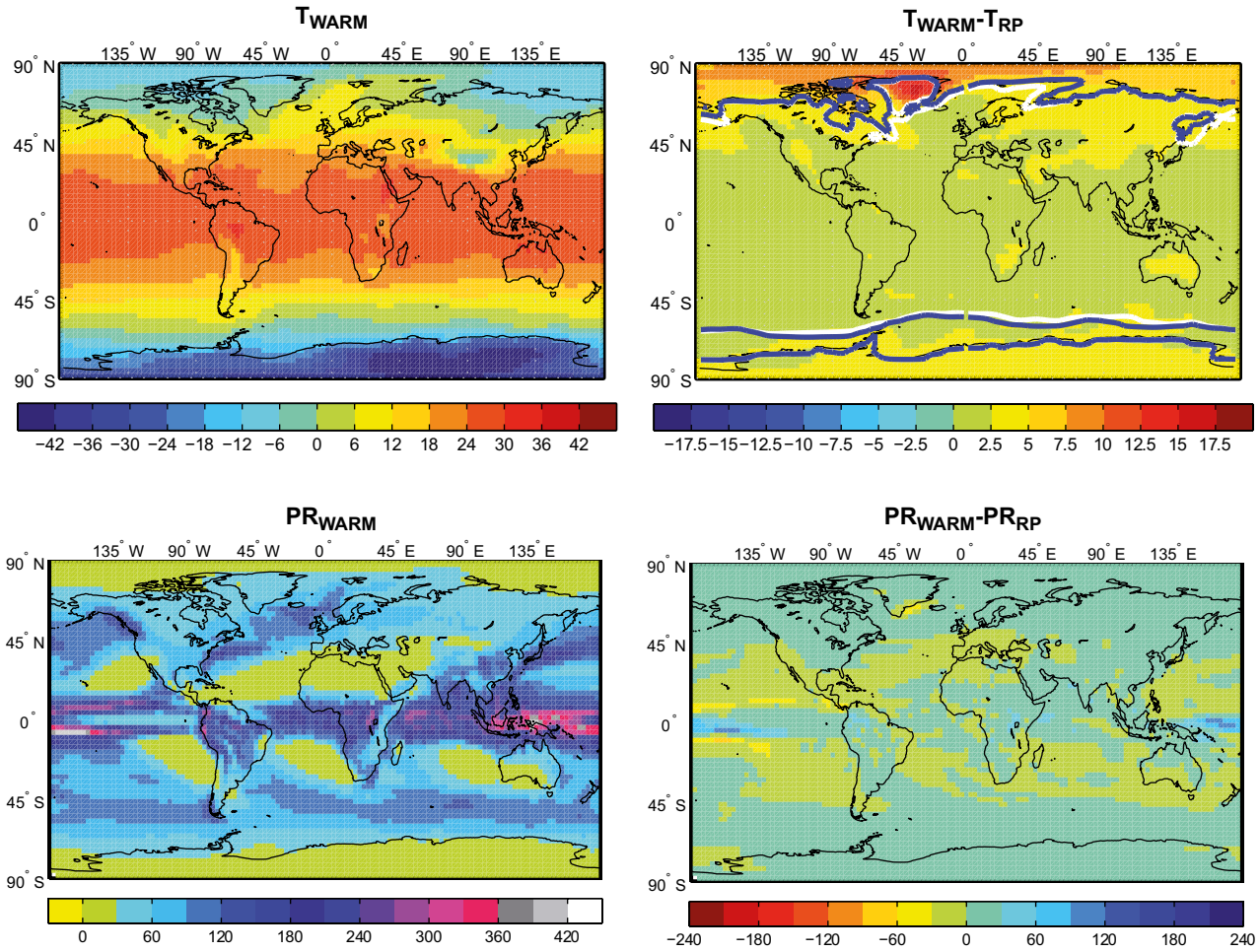

Figure 3-32. *Upper panels: Simulated near-surface air temperature in the global warming simulation (T_{WARM}) and the difference compared with the simulated present climate (T_{RP}) (1961–2000). Units are °C. Also shown by isolines in the rightmost panels is the extent of sea-ice in the simulation of the present climate (white) and in the global warming simulation (blue). Lower panels: Precipitation in the global warming simulation (PR_{WARM}) and the difference compared with the simulated present climate (PR_{RP}). Units are mm month^{-1}. From Kjellström et al. (2009).*

Climate in Europe and Sweden

The regional climate model was then used to downscale the results from the global climate model in order to obtain higher resolution data over Europe and Sweden. The resulting climate over Europe was used to produce a new vegetation distribution with the vegetation model. This vegetation was in turn, used as input to the regional climate model, to produce a climate in line with the new vegetation. An evaluation of the results from this iterative process is given in Kjellström et al. (2009). Figure 3-33, Figure 3-34 and Figure 3-35 present selected results on temperature and precipitation from the regional modelling.

In the regional global warming simulation, the warming compared with the simulated present climate (1961–2000) is strongest over northern Europe in winter. The simulated temperature increase for the coldest month is more than 5 °C in northern Fennoscandia (Figure 3-36, second row, middle panel). In southern Europe, the warming is stronger in summer, where the temperature of the warmest month increases by more than 4 °C over large areas (Figure 3-33, second row, left panel). The stronger warming in the areas of the Bothnian Bay, Bothnian Sea and in the Gulf of Finland in summer in this experiment is due to the land uplift converting sea to land in those areas. The same phenomenon is also responsible for the weaker warming in these areas in winter. Differences between the results of the global and regional model simulations are discussed in Kjellström et al. (2009).

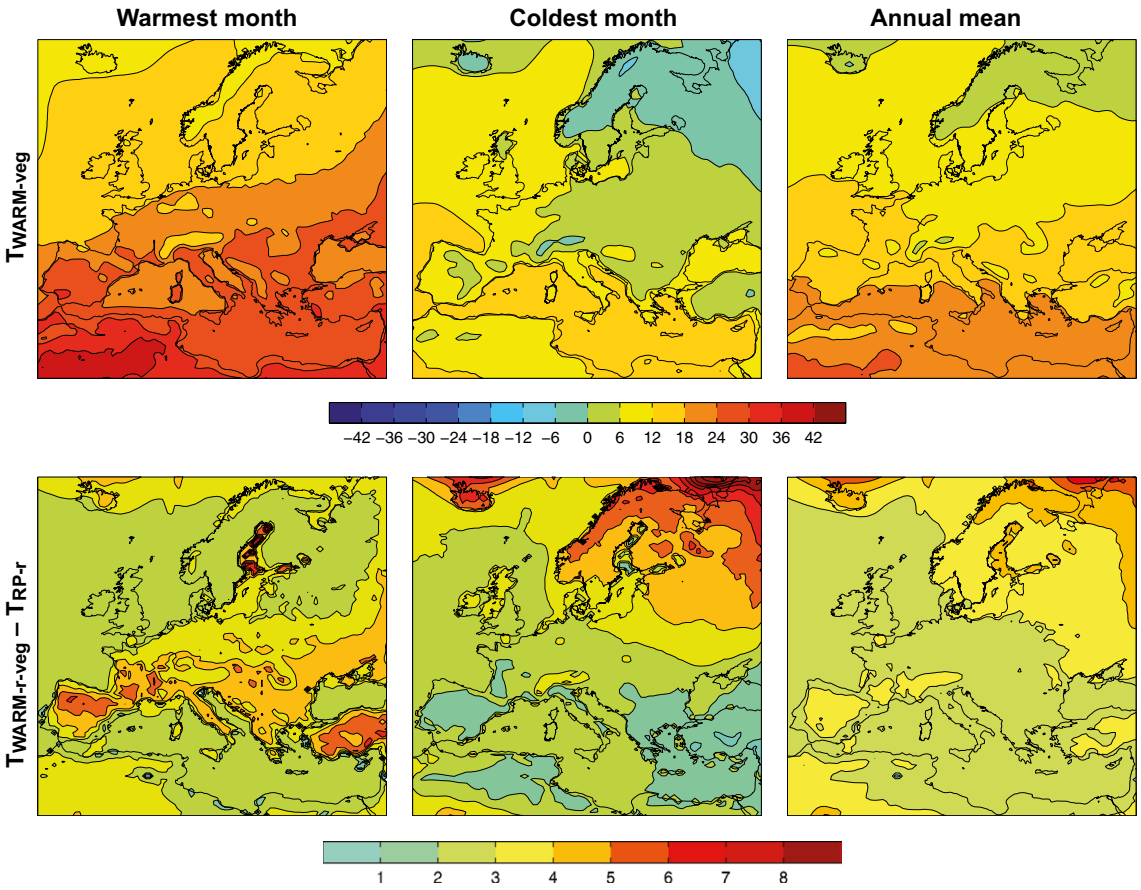

Figure 3-33. *Mean near-surface air temperatures of the warmest month, coldest month and annual mean in the global warming simulation with improved vegetation (upper row). Also shown are differences between the global warming simulation and the simulations of the present climate (RP-r) (1961–2000) (lower row). Units are °C. From Kjellström et al. (2009).*

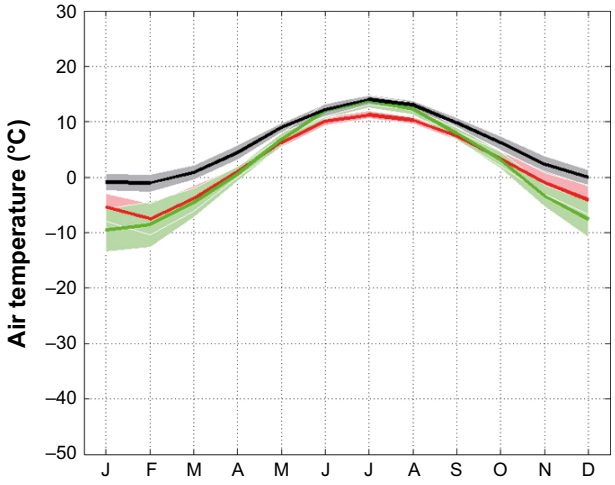

Figure 3-34. *Annual cycle of temperature for Sweden in the global warming case (black line) and for the simulated present climate (1961–2000) (red line). Also shown is the CRU observational data from 1961–1990 (green line). Shaded areas in corresponding colours indicate the ± 1 standard deviation calculated for the range of individual monthly averages in the three data sets. From Kjellström et al. (2009).*

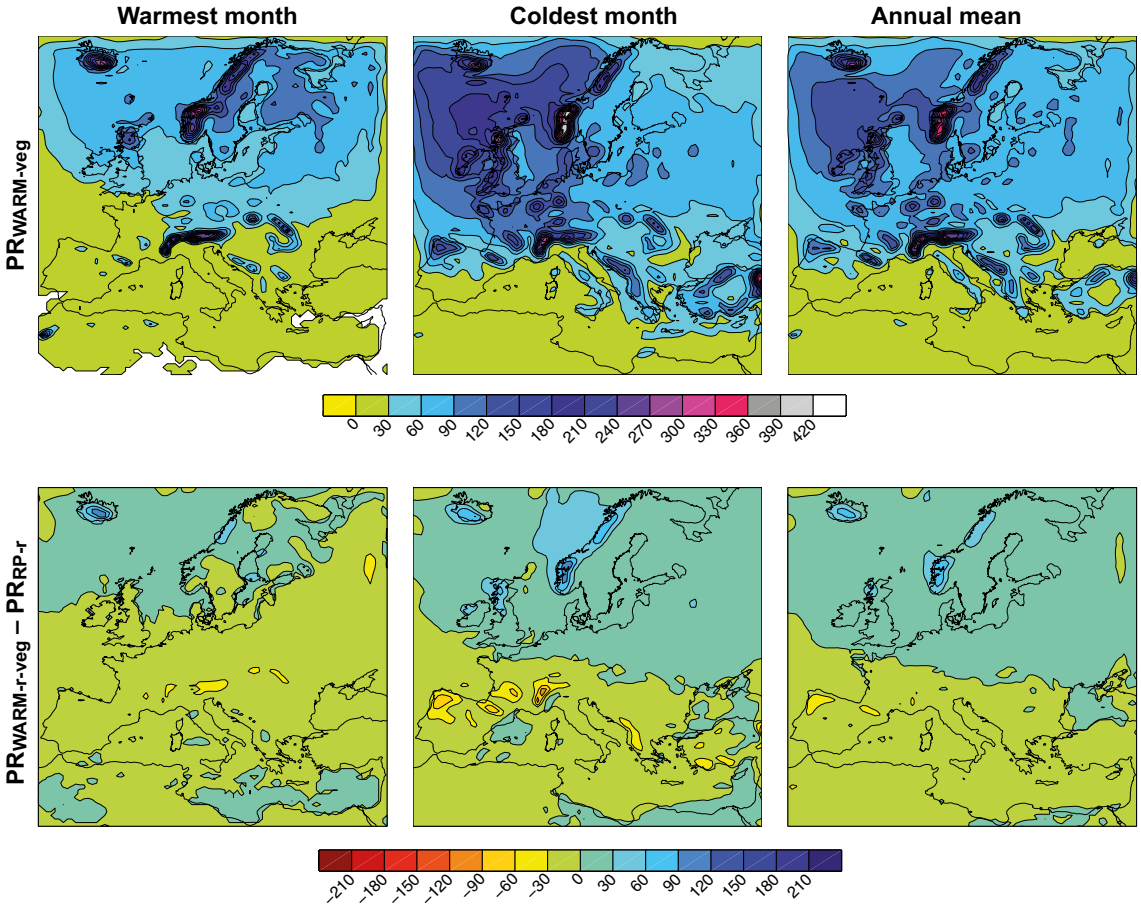

Figure 3-35. *Mean precipitation of the warmest month, coldest month and annual mean in the global warming simulation. Also shown are differences between the global warming simulation and the simulated present climate (RP-r) (1961–2000). Units are mm month^{-1}. From Kjellström et al. (2009).*

As expected, the simulated climate of the global warming case clearly resembles many of the scenarios for the 21st century from the climate model intercomparison project (CMIP3) as presented by IPCC (Meehl et al. 2007). Seasonal mean changes in precipitation and temperature from a large number of the CMIP3 scenarios have been analysed for Sweden by Lind and Kjellström (2008). Lind and Kjellström (2008) report an increase in temperature by 4–6 °C by the end of the 21st century in northern Sweden and about 3 °C in southern Sweden, relative to the 1961–1990 period. The corresponding increases in precipitation are about 25 % in the north and only a small average increase in the south, albeit with a large spread between the models. These changes are annual averages over a range of different emission scenarios. As noted in Kjellström et al. (2009), the uncertainties related to the future forcing in the global warming simulation are large and substantially lower or higher greenhouse-gas concentrations than the one used cannot be ruled out. Considering the large spread between the emission scenarios and the uncertainty related to the climate models one cannot rule out that a future warmer climate can be warmer than the one simulated in Kjellström et al. (2009).

Clearly, the results from the regional model give a climate change signal that is within the range defined by the global model results for southern Sweden compiled in Lind and Kjellström (2008), see Figure 3-15 in Kjellström et al. (2009). The climate-change signal for Sweden as a whole is +4 °C in winter and +3.5 °C in summer and the corresponding numbers for precipitation are +37 % in winter and no change (0 %) in summer. Further model results and discussion for all of Sweden from the global and regional climate modelling and from the vegetation modelling are presented in Kjellström et al. (2009).

The vegetation simulated by LPJ-GUESS for the global warming climate is reported in the context of the biosphere studies (Lindborg 2010).

Here it is also worth noting that the Greenland summer temperatures are well above 0 °C, clearly indicating that there is no chance of ice-sheet regeneration under these circumstances once the ice sheet has been removed. A similar result was obtained previously for the pre-industrial climate when the Greenland ice sheet was removed in the Hadley Centre HadCM3 coupled model (Toniazzo et al. 2004).

Climate in the Forsmark region

In the last step in the climate modelling study of the global warming climate, climatological data for the Forsmark region were extracted from the regional modelling. Figure 3-36 shows the grid boxes used for extraction of data. Information was extracted from the grid point located closest to the Forsmark site. As there is a high degree of spatial heterogeneity in land-sea distribution and topography, information from the surrounding eight grid boxes was also used to discuss uncertainties related to these inhomogeneities.

In addition to the results from the modelled case, data from the simulation of the present climate (1961–2000) (RP-r) and from the CRU observations representing conditions in the late 20th century are also shown for the Forsmark region (Figure 3-37). In addition to this, results from three other climate-change simulations with RCA3 for the 21st century as described in Persson et al. (2007) are also shown. These simulations follow the A2, A1B and B2 emission scenarios (Nakićenović and Swart 2000). The A1B emission scenario leads to greenhouse gas concentrations close to RCP4.5 by the end of the 21st century. The two other scenarios have more (A2) or less (B2) emissions than the A1B scenario.

The fairly small annual temperature range in the present climate is even smaller in the future global warming climate for the Forsmark region (Figure 3-37, upper row, first column). This reduction in the seasonal cycle of temperature is a consequence of the future warming being stronger in winter than in summer. The snow season is much shorter, or even totally absent, in the warm climate. The seasonality of the runoff is closely connected to the presence or absence of snow. In the warmer future climate, the spring peak in runoff is absent and there is a more widespread wintertime maximum related to the large amounts of precipitation for that season.

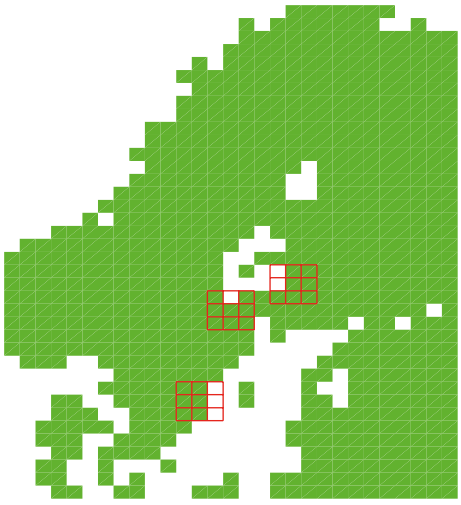

Figure 3-36. *Land (green) sea extent (white) in the regional climate model in the Fennoscandian region used for the global warming climate simulation. The 3 × 3-grids represent grid boxes covering the Forsmark, Oskarshamn and Olkiluoto sites (centre box) and the eight surrounding boxes. Grid boxes with a land fraction lower than 20 % are not filled. Results from Oskarshamn and Olkiluoto are presented in Kjellström et al. (2009).*

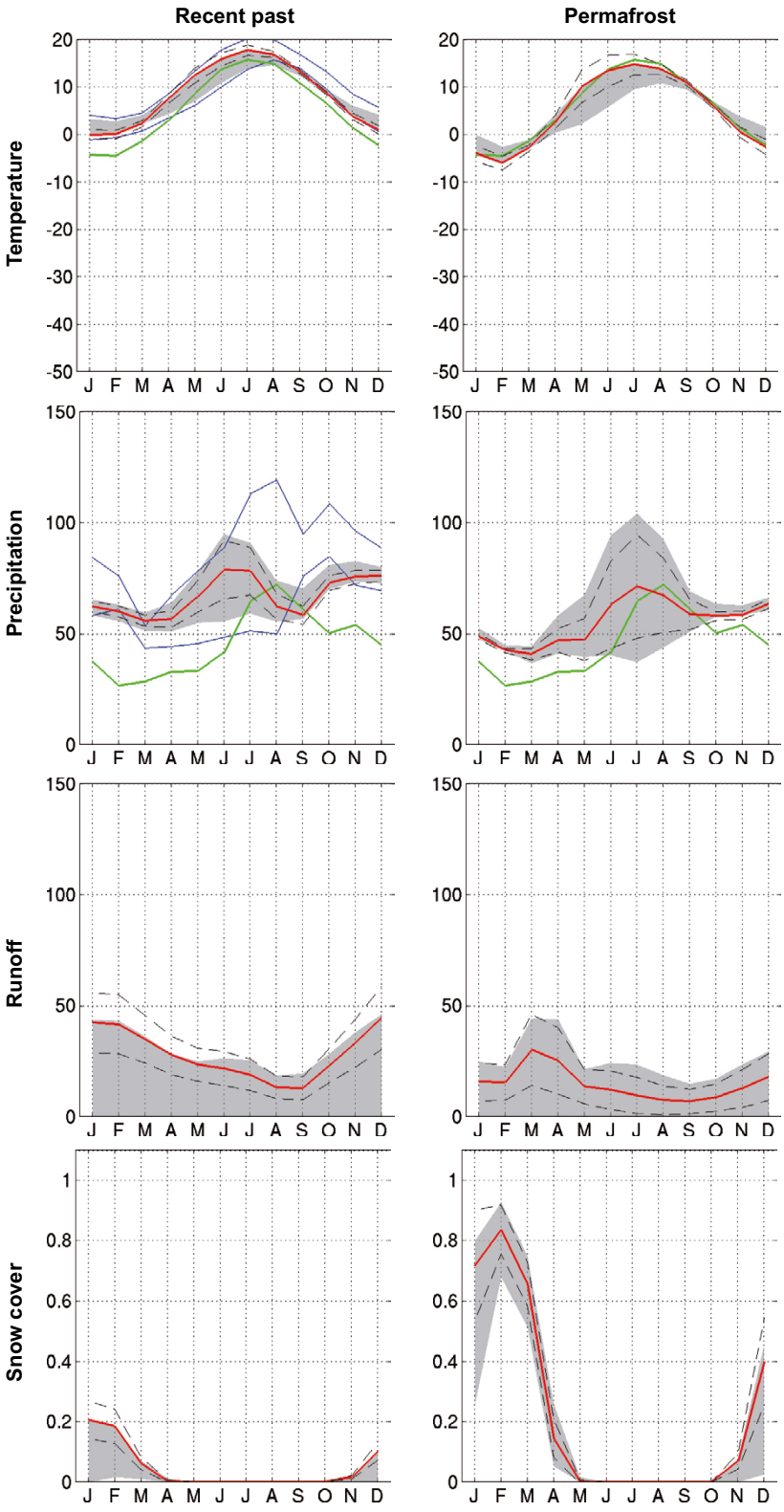

Figure 3-37. *Simulated seasonal cycles of temperature (°C), precipitation (mm month^{-1}), runoff (mm month^{-1}) and snow fraction (dimensionless ranging from 0 to 1) at the grid box closest to the Forsmark site (red line). The spatial variability in the 3 × 3-grid (Figure 3-36) is displayed with the dashed lines representing ± 1 standard deviation calculated from the 9 grid boxes, and the grey area representing the absolute maximum and minimum, of the 9 grid boxes. The green line for temperature and precipitation is the observed seasonal cycle from the CRU data set in the period 1961–1990. In the exemplified future warm climate (left column), an additional uncertainty range defined by ± 1 standard deviations of the data calculated from the 9 surrounding grid boxes from three additional simulations for the 21st century with RCA3 is shown with blue full lines. From Kjellström et al. (2009).*

In the global warming simulation, the spread in the presented variables due to differences in geographical location is reduced compared with that in the simulation of the present climate. This is partly a result of the land uplift turning two of the Baltic Sea grid boxes east of Forsmark into land. Thereby, the surrounding area becomes more homogeneous than in the present-day situation. When including also the uncertainty ranges based on results from the three other climate simulations for the 21st century, also simulated with RCA3 (Persson et al. 2007), it is seen that the weakening of the annual cycle is a robust trend when going to a warmer climate.

50-year averages values from the regional global warming climate simulation show that the annual mean air temperature in the Forsmark region is +8.3 °C. This is a temperature increase of 3.6 °C compared with the simulated present climate (1961–2000). The future warming is stronger in winter than in summer and there is an associated reduction in the seasonal cycle amplitude in temperature. The mean annual precipitation in the region is 804 mm, which is an increase of 138 mm (or 20 %) compared with the simulated present climate. Most of the precipitation increase occurs during the winter season (DJF). The snow season is much shorter than at present or even totally absent (Figure 3-37). Finally, the annual surface runoff is 337 mm in this exemplified global warming climate, which is an increase of 162 mm compared with the present climate. Given the uncertainties and assumptions used in the climate modelling, and the CO_2 level chosen, the model results thus show that the global warming climate in the Forsmark region, may be characterised by a clearly warmer and wetter climate than at present, and also that the surface runoff is significantly increased.

The major uncertainties in the climate simulation are related to uncertainties in forcing, model formulation and natural variability. These uncertainty aspects are discussed in detail in Kjellström et al. (2009). Another recent study that focussed on regional climate modelling is described in Kjellström et al. (2011). In that study, changes in seasonal mean temperature, precipitation and wind over Europe were studied in an ensemble of 16 regional climate model (RCM) simulations for 1961–2100. The RCM took boundary conditions from six different global climate models under four different emission scenarios. The study focused on the A1B emission scenario (Nakićenović and Swart 2000) in which the CO_2 equivalent in RCA3 reaches 902 ppm by year 2100, somewhat higher than the 841 ppmv used in calculations in Kjellström et al. (2011). Six-member ensemble means of winter season (DJF) conditions suggest an increase in temperature by c. 4 °C and precipitation by 20–30 % in south central Sweden, including the Forsmark region, by the period 2071–2100 as compared with the period 1961–1990. Corresponding model ensemble means for the summer season (JJA) indicate an air temperature increase of 2–3 °C and a precipitation increase of c. 10 %. The study also showed that the climate-change signal gets stronger the larger the forcing becomes, i.e. more greenhouse-gas emissions lead to a stronger warming and larger changes in precipitation. The results of the A1B-scenario-simulations are thus in line with the detailed results described above from Kjellström et al. (2009). Similar results were obtained also in the SWECLIM project (Rummukainen 2003, Tjernström et al. 2003). Other modelling results that give similar pictures of future global warming climates are reported in BIOCLIM (2003), Lind and Kjellström (2008), Meehl et al. (2007), Collins et al. (2013) and Sjökvist et al. (2015), of which results from the latter two are briefly discussed in Section 3.4.3.

3.5 Relative sea-level change at Forsmark

Changes in relative sea level are defined as the net effect of *eustatic* changes, i.e. absolute changes in sea level associated with e.g. changes in the volume and spatial distribution of ocean water, and vertical *isostatic* changes, i.e. vertical changes in the position of the Earth's crust, see also Section 2.2.1. The present-day rate of relative sea-level change at Forsmark as estimated from tide-gauge data is presented in Section 3.5.1. Section 3.5.2 contains an assessment of the relative sea-level change at Forsmark until 2100 AD, with particular focus on the high-end sea-level rise projections under the RCP8.5 scenario. Finally, Sections 3.5.3 and 3.5.4 provide assessments of the relative sea-level evolution over the coming 10 and 100 ka, respectively.

3.5.1 Present-day changes

The present-day rate of relative sea-level change at Forsmark can be estimated from tide-gauge data from the site, covering the period 1976–2017 AD (Holgate et al. 2013, PSMSL 2018). These data show an overall negative trend over the time period (Appendix G, Section G2.3 and Figure G-4), resulting in an average rate of change in the relative sea level by −4.1 mm a^{-1} (Table 3-7). This ongoing marine regression, i.e. lowering and off-shore migration of the shoreline, is a result of the active post-glacial isostatic uplift in the area that exceeds the present-day sea-level rise. This is, however, a situation that may change in the near-future, see next subsection.

Table 3-7. Present-day rates of isostasy, eustasy and relative sea level at Forsmark, and the estimated present-day global mean sea-level (GMSL) rise from WCRP Global Sea Level Budget Group (2018). The relative sea level is defined as the sum of the isostatic and eustatic contributions. For the Forsmark site, the relative sea-level change is obtained from tide-gauge data (Holgate et al. 2013, PSMSL 2018) covering the period 1976–2017 AD (Appendix G, Section G2.3), whereas the isostasy is estimated based on e.g. stationary GPS measurements (Vestøl et al. 2019). The eustatic contribution for Forsmark is indirectly estimated by calculating the difference between the relative sea-level measurements from tide gauges and the present-day isostatic uplift. Positive values are defined as a rise of sea relative to the land.

	Forsmark	Global average
Isostasy (vertical crustal movement)	−6.7 mm a^{-1}	-
Eustasy (sea-level change)	2.6 mm a^{-1}	3.1 ± 0.3 mm a^{-1}
Relative sea level (or shoreline displacement)	−4.1 mm a^{-1}	-

It is also possible to estimate the present-day eustatic component in Forsmark by taking the difference between the tide-gauge data, which represents the total relative sea-level change, and the local isostatic component which amounts to −6.7 mm a^{-1} (Vestøl et al. 2019, see Section 2.2.3). This calculation results in a present-day eustatic change at Forsmark of 2.6 mm a^{-1} (Table 3-7), which is comparable to the estimated global mean sea-level (GMSL) rise of 3.1 ± 0.3 mm a^{-1} between 1993 and 2017 AD (Table 3-7). The slightly lower value at Forsmark with respect to the global average may be explained by the longer time-period of the tide gauge record, hence covering older data with a lower eustatic component, than in the global mean estimate. However, also rotational effects and changes in the gravity field associated with the melting of ice sheets and water entering the ocean basins may contribute to explaining the difference in eustasy between Forsmark and the global average.

3.5.2 Relative sea-level change until 2100 AD

Changes in relative sea level until 2100 AD, i.e. during the construction and operational phases of the SFR repository, are of importance to planning and construction. Relative sea-level projections for 2100 AD at Forsmark are therefore assessed here, based on current scientific knowledge. Since the purpose of this analysis of short-term changes up to 2100 AD is mainly to provide input to e.g. construction planning of critical infrastructure, the present analysis does not focus on the most plausible projections of the 2100 AD sea-level rise. Instead, there is a focus on high-end estimates, based on the RCP8.5 emission scenario (found in the subsection *Strong global warming (RCP8.5)* below). In addition, a literature review of the global mean sea-level (GMSL) rise under the RCP2.6 and RCP4.5 emission scenarios is also provided in the subsections *Weak global warming (RCP2.6)* and *Moderate global warming (RCP4.5)* below. In addition to the RCP emission scenarios used in IPCC (2013a) (Section 3.4.1), so-called temperature stabilisation scenarios have received increased attention in recent years as a result of the 2015 Paris Agreement, which seeks to hold global annual surface air temperature (SAT) to '*well below 2 °C above pre-industrial levels and to pursue efforts to limit the temperature increase to 1.5 °C above pre-industrial levels*' (UNFCCC 2015). These scenarios have been used in several studies investigating the impact of increased temperatures on sea-level rise over the coming centuries. The results from those studies are summarised in the IPCC special report (SR15) on the impacts of global warming of 1.5 °C (Hoegh-Guldberg et al. 2018) and are also reported in this section. A global warming of 1.5 °C by the end of this century is equivalent to the projected global mean SAT corresponding to the upper end of RCP2.6 and lower end of RCP4.5, whereas a

global warming of 2 °C approximately corresponds to mid-range global mean SAT increase under the RCP4.5 scenario. In this report, the GMSL projections under the 1.5 °C scenario are presented in the subsection *Weak global warming (RCP2.6)* below, whereas the projections under the 2 °C scenario are presented in the subsection *Moderate global warming (RCP4.5)* below.

In the following, the GMSL rise projections from most of the published studies are shown as a median and percentile ranges of a statistical probability distribution. The most commonly used ranges are 17–83 % and 5–95 %, which are often referred to as the *likely* and *very likely* ranges, respectively (e.g. Horton et al. 2018)[6].The ranges can essentially be interpreted as probabilities. For example, if a study reports a certain GMSL rise interval in the 5–95 % range, it has been evaluated that the probability is 5 % that the "real" GMSL rise will exceed the 95 % percentile value. Because of this, in the case of strong global warming (RCP8.5), also studies showing more extreme percentile values are of interest and are reported upon. The higher percentile values have lower probabilities but often correspond to significantly higher GMSL rise values. As such, they constitute important components, in addition to sea-level rise contributions from storm surges, for assessing the maximum possible sea-level rise at Forsmark until 2100 AD. This assessment is provided in the subsection *Strong global warming (RCP8.5)* below.

Weak global warming (RCP2.6)

The compilation from Hoegh-Guldberg et al. (2018) shows the 17–83 % and 5–95 % percentile ranges (i.e. the *likely* and *very likely* ranges, respectively) of the projected 2100 AD GMSL rise under RCP2.6 and the 1.5 °C scenarios from different studies. However, in this section the median estimates of the GMSL rise, derived from the original literature sources, have also been included in the assessment (Table 3-8). In addition to the studies featured in Hoegh-Guldberg et al. (2018), Table 3-8 also includes the projected GMSL rise from the recent IPCC Special Report on the Ocean and Cryosphere in a Changing Climate (SROCC, IPCC 2019). In Table 3-8, the *likely* range of GMSL rise is 0.28–0.65 m under the RCP2.6 scenario, and slightly higher (0.29–0.77 m) under the 1.5 °C scenario. Similarly, the *very likely* range, which amounts to 0.24–0.96 m under the RCP2.6 scenario, increases to 0.20–0.99 m under the 1.5 °C scenario. Hence, Table 3-8 demonstrates a significant uncertainty associated with the GMSL rise until 2100 AD, even for a relatively weak global warming.

At Forsmark, the mean relative sea-level change by 2100 AD is projected to be significantly lower than the GMSL rise, primarily because the ongoing isostatic uplift in the Forsmark region (6.7 mm a^{-1}, Vestøl et al. 2019, see Table 3-8) compensates for a significant portion of the eustatic rise. As a result of the isostatic rebound, the study of Pellikka et al. (2020) projects that the relative sea level at Forsmark under RCP2.6 will *decrease* until 2100 AD, even for the high-end 95 % percentile, despite an increase of the GMSL (Table 3-9). This suggests that the current marine regression will continue until 2100 AD under a weak global warming.

In addition to the projections for 2100 AD, Pellikka et al. (2020) also reported relative sea-level changes by 2050 and 2080 AD (Table 3-9). Compared to 2100 AD, the median percentile (50 % probability) of the relative sea level is projected to be lower by 2050 and 2080 AD, suggesting that the most likely outcome under the RCP2.6 emission scenario is that the ongoing isostatic rebound will be greater than the eustatic rise for the entire period until 2100 AD.

A more detailed compilation of the maximum relative sea-level change at Forsmark until 2100 AD, including all regional effects, is provided in the subsection *Strong global warming (RCP4.5)* below. Equivalent compilations of GMSL rise under low carbon emissions for the period beyond 2100 AD are presented Sections 3.5.3 and 3.5.4, together with the ensuing relative sea-level change at Forsmark.

[6] Because it is more likely that the sea-level would end up in the broader 5–95 % interval than in the narrower 17–83 % interval, the former interval is often called the *very likely* range and the latter the *likely* range.

Table 3-8. Compilation of recent GMSL projections (in m) for 2100 AD under the RCP2.6 emission scenario and the 1.5 °C temperature stabilization scenario. For a description of those scenarios, see Church et al. (2013), Hoegh-Guldberg et al. (2018) and Section 3.4.1. Values are given as the median value and the 17 and 83 % percentile values (usually called the *likely* range) and the 5 and 95 % percentile values (usually called the *very likely* range). The projections are based on either process-based or probabilistic sea-level modelling, using either 2000 AD or the 1986–2005 AD reference period as baseline. Some studies present several GMSL projections under the same emission/climate scenario. From these studies, only the projection with the highest GMSL rise is included in this compilation.

RCP2.6			1.5 °C			Study
Median (50 %)	17–83 %	5–95 %	Median (50 %)	17–83 %	5–95 %	
0.44	0.28–0.61					IPCC (2013a)
0.75	0.59–0.94					Perrette et al. (2013)
0.50	0.37–0.65	0.29–0.82				Kopp et al. (2014)
0.38	0.28–0.51	0.24–0.61				Kopp et al. (2016)
	0.28–0.56					Mengel et al. (2016)
		0.40–0.71				Bakker et al. (2017)
0.57		0.45–0.72				Goodwin et al. (2017)
0.45	0.35–0.56					Nauels et al. (2017)
0.55		0.43–0.74				Wong et al. (2017)
0.43		0.29–0.59				IPCC (2019) (Special Report on the Ocean and Cryosphere in a Changing Climate)
0.75		0.52–0.96	0.77		0.54–0.99	Schaeffer et al. (2012)
			0.41	0.29–0.53		Schleussner et al. (2016)
			0.37		0.29–0.64	Bittermann et al. (2017)
					0.50–0.80	Sanderson et al. (2017)
			0.57	0.40–0.77	0.28–0.93	Jackson et al. (2018)
			0.39		0.24–0.54	Nicholls et al. (2018)
			0.48	0.35–0.64	0.28–0.82	Rasmussen et al. (2018)
			0.40	0.31–0.51	0.24–0.66	Goodwin et al. (2018)

Table 3-9. Projected Forsmark mean relative sea-level change (m, relative to 2000 AD) by 2050, 2080 and 2100 AD under the RCP2.6 emission scenario for the 50 % percentile (median), and the 17–83 % and 5–95 % confidence intervals. From Pellikka et al. (2020).

Percentile/confidence interval	2050 AD	2080 AD	2100 AD
50 %	−0.18	−0.29	−0.36
17–83 %	−0.21 to −0.13	−0.36 to −0.19	−0.48 to −0.22
5–95 %	−0.23 to −0.10	−0.40 to −0.10	−0.53 to −0.08

Moderate global warming (RCP4.5)

In the latest assessment report from IPCC (AR5), the maximum expected GMSL rise at 2100 AD for a high-emission scenario was estimated to +0.98 m IPCC (2013a). The corresponding value in the previous IPCC assessment was +0.59 m (IPCC 2007). The maximum 2100 AD sea-level estimates for the different RCP emission scenarios in AR5 was, however, based on a narrow selection of models. The selection excluded all non-process-based models of which many, at the time, suggested a considerably larger GMSL rise than the processed-based models finally selected by IPCC. Hence, following IPCC (2013a), many studies have pointed to a larger sea-level rise than suggested in AR5.

Table 3-10 presents a selection of recent GMSL projections for 2100 AD under the RCP4.5 emission scenario (see Church et al. 2013) and the 2 °C temperature stabilisation scenario (e.g. Hoegh-Guldberg et al. 2018). The studies are published between 2012 and mid-2018, except for the GMSL rise estimate from IPCC SROCC (IPCC 2019). In Table 3-10, the *likely* range of GMSL rise is 0.35–1.25 m under RCP4.5 and 0.35–0.93 m under the 2 °C scenario, whereas the *very likely* range is 0.22–1.58 m under RCP4.5 and 0.24–1.17 m under the 2 °C scenario. The studies in Table 3-10 hence clearly demonstrate the large uncertainty associated with the projection of future sea-level rise until 2100 AD under a moderate global warming.

At Forsmark, the mean relative sea-level change by 2100 AD is projected to be significantly lower than the GMSL rise, primarily because the ongoing isostatic uplift in the Forsmark region (6.7 mm a^{-1}, Vestøl et al. 2019, see Table 3-7) compensates for a significant portion of the eustatic rise. As a result of the isostatic rebound, the study of Pellikka et al. (2020) projects that the relative sea level at Forsmark under RCP4.5 will most likely *decrease* until 2100 AD, despite an increase of the GMSL (Table 3-11). However, similar to the GMSL projections, the uncertainty associated with the Forsmark relative sea-level change under RCP4.5 is large, demonstrated by a slight increase of the relative sea-level by 2100 AD for the upper 83 % and 95 % percentiles (Table 3-11).

In addition to the projections for 2100 AD, Pellikka et al. (2020) also reported relative sea-level changes by 2050 and 2080 AD (Table 3-11). Compared to 2100 AD, the median percentile (50 % probability) of the relative sea level is projected to be lower by 2050 and 2080 AD, suggesting that the most likely outcome under the RCP4.5 emission scenario is that the ongoing isostatic rebound will be greater than the eustatic rise for the entire period until 2100 AD. For the high-end percentiles (83 and 95 %) the situation is however reversed, with a higher Forsmark relative sea level by 2100 AD compared to 2050 and 2080 AD. For these higher, less likely, percentiles, the eustatic rise at Forsmark is thus projected to be larger than the isostatic compensation.

A corresponding compilation of GMSL rise under moderate carbon emissions, but for the period beyond 2100 AD and with projections of the resulting relative sea level at Forsmark, is presented in Section 3.5.3. The consequences in terms of relative sea-level rise at Forsmark for the high-end RCP8.5 emission scenario until 2100 AD, including the short-term sea-level variability due to storm surges, is described in the subsection *Strong global warming (RCP8.5)* below.

Table 3-10. Compilation of recent GMSL projections (in m) for 2100 AD under the RCP4.5 emission scenario and the 2 °C temperature stabilization scenario. For a description of those scenarios, see Church et al. (2013), Hoegh-Guldberg et al. (2018) and Section 3.4.1. Values are given as the median value and the 17 % and 83 % percentile values (usually called the *likely* range) and the 5 % and 95 % percentile values (usually called the *very likely* range). The projections are based on either process-based or probabilistic sea-level modelling, using either 2000 AD or the 1986–2005 AD reference period as baseline. The uncertainty range for DeConto and Pollard (2016) has been recalculated from 1σ standard error to the 5–95 % confidence interval. Some studies present several GMSL projections under the same emission/climate scenario. From these studies, only the projection with the highest GMSL rise is included in this compilation.

RCP4.5			2.0 °C			Study
Median (50 %)	17–83 %	5–95 %	Median (50 %)	17–83 %	5–95 %	
0.52		0.74–1.10				Jevrejeva et al. (2012)
0.53		0.36–0.71				IPCC (2013a)
0.86	0.66–1.11					Perrette et al. (2013)
0.59	0.45–0.77	0.36–0.93				Kopp et al. (2014)
0.54	0.35–0.73					Slangen et al. (2014)
0.58		0.12–1.05				DeConto and Pollard (2016)
0.54	0.36–0.72	0.22–0.85				Jackson and Jevrejeva (2016)
0.51	0.39–0.69	0.33–0.85				Kopp et al. (2016)
0.53		0.37–0.77				Mengel et al. (2016)
		0.54–0.97				Bakker et al. (2017)
0.69		0.55–0.84				Goodwin et al. (2017)
0.91	0.66–1.25	0.50–1.58				Kopp et al. (2017)
0.55	0.45–0.67					Nauels et al. (2017)
0.77		0.56–1.30				Wong et al. (2017)
0.55		0.39–0.72				IPCC (2019) (Special Report on the Ocean and Cryosphere in a Changing Climate)
0.90		0.64–1.21	0.80		0.56–1.05	Schaeffer et al. (2012)
			0.50	0.36–0.65		Schleussner et al. (2016)
			0.50		0.39–0.61	Bittermann et al. (2017)
					0.60–0.90	Sanderson et al. (2017)
			0.46	0.35–0.57	0.27–0.73	Goodwin et al. (2018)
			0.68	0.47–0.93	0.32–1.17	Jackson et al. (2018)
			0.49		0.31–0.65	Nicholls et al. (2018)
			0.56	0.39–0.76	0.28–0.96	Rasmussen et al. (2018)

Table 3-11. Projected Forsmark mean relative sea-level change (m, relative to 2000 AD) by 2050, 2080 and 2100 AD under the RCP4.5 emission scenario for the 50 % percentile (median), and the 17–83 % and 5–95 % confidence intervals. From Pellikka et al. (2020).

Percentile/confidence interval	2050 AD	2080 AD	2100 AD
50 %	−0.14	−0.19	−0.21
17–83 %	−0.19 to −0.07	−0.30 to −0.02	−0.37 to 0.05
5–95 %	−0.21 to 0.03	−0.35 to 0.21	−0.44 to 0.41

Strong global warming (RCP8.5)

As mentioned above, assessing high-end, pessimistic, projections under the RCP8.5 emission scenario is important for the planning, construction and operation of the SFR repository.

Pessimistic scenarios of large sea-level rise at Forsmark until 2100 AD need to consider contributions from both the rise of mean sea level through slow long-term processes, such as ocean thermal expansion and ice-sheet melting, and the contributions from fast short-term processes, i.e. storm surges. When considering construction at near-coastal sites, it may be useful to distinguish between the slow rise of mean sea level and temporary storm surge contributions with a typical duration of days to weeks. A key point here is that it is possible to monitor the mean sea-level rise due to slow long-term processes over the coming decades. This gives the important opportunity to take further necessary actions if and when mean sea-level rise proves to be larger than is foreseen at present.

The relative sea-level evolution at Forsmark and elsewhere is determined by the net effect of *eustatic* changes (i.e. the absolute changes in sea level associated with e.g. changes in the volume and spatial distribution of ocean water) and *isostatic* changes. At the Forsmark site, the latter is manifested through glacial isostatic rebound with an uplift rate of 6.7 mm a^{-1} (Vestøl et al. 2019). The present-day net effect of the two processes at the Forsmark site is a slow sea regression, i.e. a lowering and off-shore migration of the shoreline, at a rate of approximately 4.1 mm a^{-1} (Table 3-7).

An overview of the scientific knowledge on past, present and future sea-level evolution was given by IPCC (Church et al. 2013). The review presented by Church et al. included a wide range of processes contributing to eustatic changes, such as thermal expansion of ocean water, melting of glaciers and ice sheets, rapid dynamics of ice sheets, and land water storage. In the IPCC AR5, Church et al. (2013) stated that there is only low confidence in the projections made using semi-empirical models (e.g. Vermeer and Rahmstorf 2009), and also in kinematic constraints on ice-sheet melting (Pfeffer et al. 2008), and therefore excluded all available results from such models. Consequently, the final choice of AR5 sea-level projections for 2100 AD was based on a remarkably narrow selection of models/projections, which resulted in a narrow range of GMSL projections for 2100 AD presented by IPCC (0.52–0.98 m for RCP8.5).

Since the publication of AR5, many studies have reported the importance of including results not only from process-based models but also from semi-empirical and statistical models. Many of the more recent studies indicate that AR5 underestimated the GMSL rise to 2100 AD by the model selection made at the time, especially for the RCP8.5 scenario. IPCC recently updated their sea-level projections in the Special Report on the Ocean and Cryosphere in a Changing Climate (SROCC, IPCC 2019). Compared with AR5, GMSL rise projections in SROCC are about 0.1 m larger under RCP8.5, and the 5–95 % confidence interval extends beyond a 1 m rise due to a larger projected ice loss from the Antarctic ice sheet. A review of published information on future sea-level projections since 2012 for the RCP8.5 emission scenario is presented below.

Slow long-term processes

The slow long-term processes that contribute to changes in mean sea level include thermal expansion of warming ocean water, melting of the Greenland and Antarctic ice-sheets and of glaciers, rapid ice-sheet dynamics and changes in land water storage. Sea-level rise associated with these processes is distributed over the world oceans. However, the distribution is not uniform – some regions experience a smaller rise than the global-mean value whereas the situation is the opposite in other regions. These regional differences, which may be substantial, are caused by gravitational and rotational effects,

ocean dynamics, regional differences in water temperature and salinity, winds and air pressure, and air-sea heat and freshwater fluxes, see Church et al. (2013), IPCC (2019) and references therein. The present GMSL rise amounts to 3.1 ± 0.3 mm a^{-1} with an acceleration of 0.1 mm a^{-2} over the period 1993–2017 (WCRP Global Sea Level Budget Group 2018). Between 1993 and 2015, the relative contributions to GMSL rise from thermal expansion, glaciers, Greenland and Antarctica have been 49 %, 20 %, 17 % and 11 % respectively (IPCC 2019). This is in line with Nerem et al. (2018) who describes an ongoing acceleration in ice loss from the Antarctic and Greenland ice sheets. Studies showing that the GMSL rise is accelerating make the case for considering worst-case sea-level rise scenarios strong, an approach that is adopted in the present analysis.

For the present analysis of potential sea-level rise at Forsmark until 2100 AD, a starting point is to assess the spread in projections of GMSL rise in the scientific literature. Therefore, a review of published sea-level projections made since 2012 for the RCP8.5 emission scenario has been compiled (Table 3-12). The table includes most of the recent estimates of GMSL rise as well as associated local projections of relative sea level for Stockholm and Forsmark available in a few of the studies. Studies that only provide regional sea-level estimates from other regions have not been included. The compilation includes studies from 2012 to mid-2018, as well as one older study, previously used by SKB (Pfeffer et al. 2008), the recent IPCC SROCC (IPCC 2019) and relative sea-level projections under the RCP8.5 scenario from a recent dedicated study on extreme sea levels at Forsmark (Pellikka et al. 2020). In cases where values in review papers or reports differ from the corresponding values in the original papers, the values from the original publication have been used. Some compilations do not mention the reason for not using original paper values, whereas other do (Horton et al. 2018). The compilation of RCP8.5 GMSL for 2100 AD is illustrated in Figure 3-38.

As can be seen in that figure, most GMSL median values under the RCP8.5 emission scenario are lower than 1 m, whereas the upper end of the 17–83 % confidence range (i.e. the *likely* range) is typically around 1 m. The upper end of the 5–95 % percentile range (the *very likely* range) is typically around 1.5 m or between 1.5 and 2 m (light blue bars in Figure 3-38). Extreme GMSL values are typically around 2 m and in some case above 2.5 m, depending on the selected confidence interval (red colours in Figure 3-38). Estimated local relative sea-level values for Stockholm and Forsmark are clearly below the corresponding GMSL values. This is because the ongoing isostatic uplift in the region compensates for a significant portion of the eustatic rise, see below.

The compilation in Table 3-12 and Figure 3-38 clearly demonstrates the large spread in recent estimates of 21st century sea-level rise projections. The differences relate to e.g. different methodologies used in the studies (for instance the use of process-based models versus statistical models/semi-empirical models) and to how different processes related to ice-sheet melting have been handled. Overall, the large spread in the projections reflects the large prevailing uncertainty within this scientific field. This uncertainty mainly relates to the uncertainties in the response of the Greenland and Antarctic ice sheets to climate warming.

A pessimistic assessment of the maximum mean sea-level rise at Forsmark until 2100 AD under the RCP8.5 scenario can be based on the information compiled in Table 3-12. In terms of high maximum estimates, two studies stand out in the compilation – the *likely* and *very likely* ranges by Kopp et al. (2017) and Le Bars et al. (2017) (Figure 3-38 and Table 3-12). These two studies are the only ones that have accounted for potential sea-level rise as a result of the Antarctic marine ice cliff instability (MICI) hypothesis, first described by DeConto and Pollard (2016). While it has long been known that marine ice sheets are vulnerable to an adverse feedback loop once their retreat is triggered (the marine ice sheet instability or MISI hypothesis), the modelling study of DeConto and Pollard (2016) took into account new physical processes regarding the dynamics of vertical ice cliffs. The Antarctic coastline is fringed by large floating ice shelves that buttress the flow of ice and hence have a stabilizing effect on the grounded part of the ice sheet. The MICI hypothesis suggests that the vertical ice cliffs created by the disintegration of the ice shelves could collapse rapidly, causing a significant additional contribution to sea-level rise. At the time of writing, however, the hypothesis is controversial and under debate in the scientific community (e.g. Edwards et al. 2019). In addition, Edwards et al. (2019) argue that the interpretation made by Le Bars et al. (2017) about the shape of the probability distribution of the Antarctic contribution leads to an overestimation of the GMSL rise. Because of this, the assessment of the Forsmark sea-level rise until 2100 AD is not solely based on the maximum values of Kopp et al. (2017) and Le Bars et al. (2017).

Table 3-12. Compilation of recent sea-level projections for 2100 AD made for the RCP8.5 emission scenario since 2012. For a description of the emission scenario, see Church et al. (2013) and Section 3.4.1. All values represent GMSL rise, except for a few values for Stockholm and Forsmark. The local values represent relative sea levels for the sites, i.e. they are compensated for the ongoing isostatic uplift. Most values are characterised by the median value and a 17–83 % confidence interval (i.e. the *likely* range) and a 5–95 % confidence interval (i.e. the *very likely* range). Note that the studies use different reference periods. Whilst some of the studies (e.g. the IPCC) use the 1986–2005 AD period as a baseline, other studies (e.g. Pellikka et al. 2020) use the mean sea level in 2000 AD. The uncertainty range for DeConto and Pollard (2016) has been recalculated from 1σ standard error to the 5–95 % confidence interval. In addition to the median, 5–95 %, and 17–83 % percentiles, the table also includes extreme sea-level scenarios for RCP8.5 using e.g. the 99 % or 99.9 % percentiles. The study by Pfeffer et al. (2008) is included since it constituted the worst-case 2100 AD GMSL value in the SR-PSU (SKB TR-13-05). Some studies present several GMSL projections under the same emission/climate scenario. From these studies, only the projection with the highest GMSL rise is included in this compilation. Studies included in the ensemble of GMSL projections in Pellikka et al. (2020) are shown with an asterisk.

Sea-level rise 2100 AD (m) for RCP 8.5 Median values with percentile range within brackets	Percentiles used for ranges in column one Comments within brackets	Extreme scenarios Percentile within brackets	Reference
0.74 (0.52–0.98)	5–95 %	-	Church et al. (2013) (IPCC AR5)*
-	(Not RCP8.5)	2.0	Pfeffer et al. (2008)
1.10 (0.81–1.65)	5–95 %	-	Jevrejeva et al. (2012)*
1.02 (0.60–1.20)	5–95 %	-	Schaeffer et al. (2012)
-	-	2.25	Sriver et al. (2012)
0.77 (0.43–1.41)	(Not RCP8.5)	2.70	Miller et al. (2013)
(0.70–1.20)	17–83 %	-	Horton et al. (2014)
(0.50–1.50)	5–95 %		
0.80 (1.80)	95 %	-	Jevrejeva et al. (2014)
0.79 (0.52–1.21)	5–95 %	1.80 (99 %)	Kopp et al. (2014)*
0.79 (0.62–1.00)	17–83 %	2.50 (99.9 %)	
1.80	95 %	-	Rohling et al. (2013)
0.74 (0.45–1.04)	17–83 %	1.30	Slangen et al. (2014)
0.80 (0.58–1.20)	17–83 %	-	Grinsted et al. (2015)*
0.80 (0.45–1.83)	5–95 %		
0.75 (0.54–0.98)	17–83 %	0.84 (0.51–1.67) High end	Jackson and Jevrejeva (2016)
0.75 (0.37–1.18)	5–95 %	2.22 (99 %)	
0.76 (0.59–1.05)	17–83 %	-	Kopp et al. (2016)*
0.76 (0.52–1.31)	5–95 %		
0.85 (0.57–1.31)	5–95 %	-	Mengel et al. (2016)*
1.14 (0.55–1.73)	5–95 % (only Antarctic contribution)		DeConto and Pollard (2016)
0.90 (0.76–1.05)	5–95 %		Goodwin et al. (2017)*
1.46 (1.09–2.09)	17–83 %	-	Kopp et al. (2017)*
1.46 (0.93–2.43)	5–95 %		
1.84 (0.81–2.92)	5–95 %		Le Bars et al. (2017)*
0.79 (0.65–0.97)	17–83 %	-	Nauels et al. (2017)
0.79 (0.58–1.11)	5–95 %		
1.50 (1.03–1.90)	5–95 %	-	Wong et al. (2017)
0.84 (0.61–1.10)	5–95 %	-	IPCC (2019) (Special Report on the Ocean and Cryosphere in a Changing Climate)
0.37 (0.16–0.61)	5–95 %	-	SMHI (Nerheim et al. 2017) **Stockholm**
0.25 (0.04–0.49)	5–95 %	2.30 (95 % and including c. 1.8 m storm surge)	SMHI (Nerheim et al. 2017) **Forsmark**
0.17 (−0.17–0.52)	17–83 %	-	Kopp et al. (2014) **Stockholm**
0.17 (−0.41–0.80)	5–95 %		
0.25 (0.02–0.6)	17–83 %	1.80 (99 %)	Grinsted et al. (2015) **Stockholm**
0.25 (−0.13–1.17)	5–95 %		
0.1 (−0.13–0.45)	17–83 %	1.65 (99 %)	Grinsted et al. (2015) **Forsmark**
(−0.28–1.01)	5–95 %	2.07 (99.9 %)	
0.02 (−0.19–0.49)	17–83 %	1.66 (99 %)	Pellikka et al. (2020) **Forsmark**
0.02 (−0.29–1.11)	5–95 %	2.17 (99.9 %)	

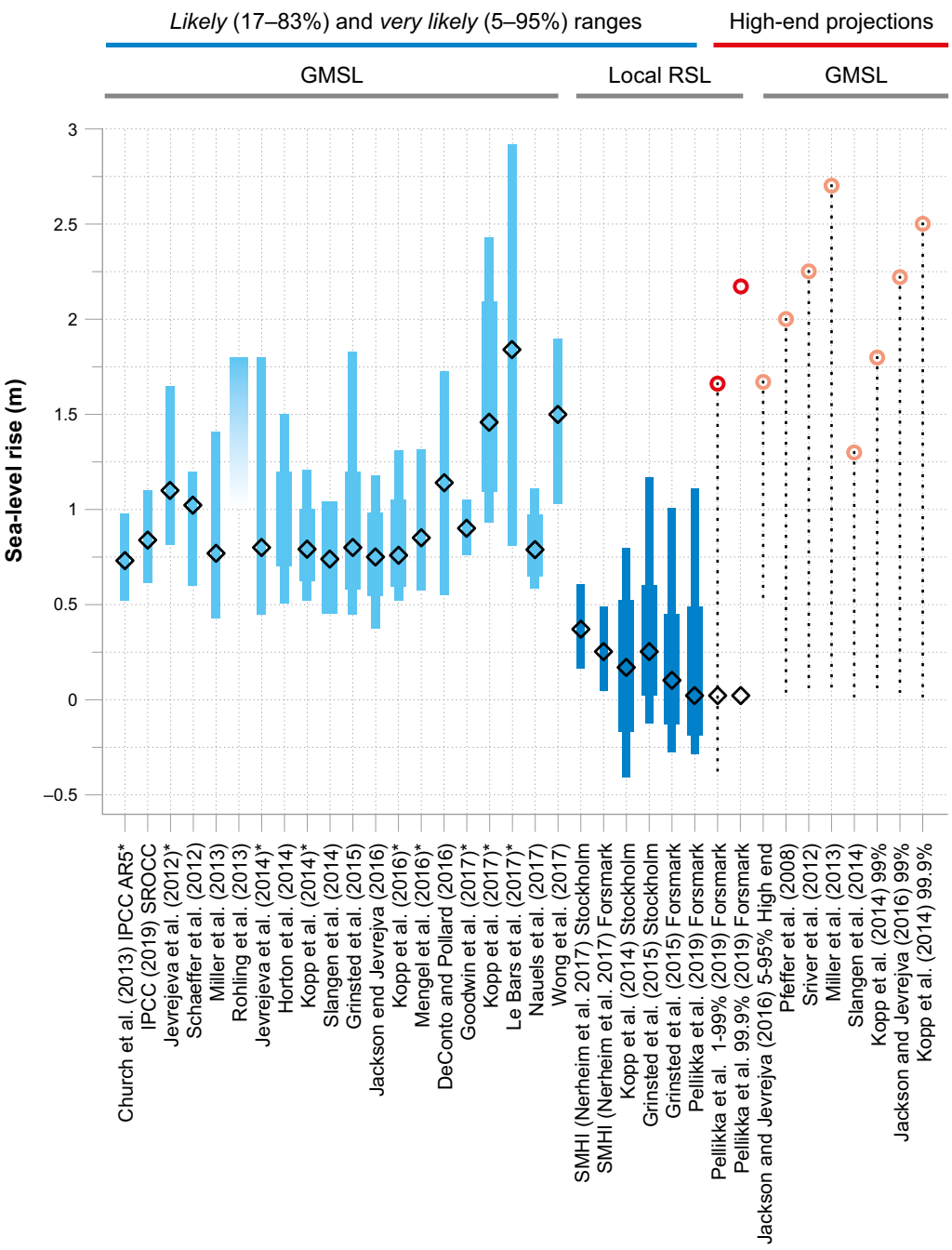

Figure 3-38. *Compilation of sea-level projections for 2100 AD under the IPCC RCP8.5 emission scenario and published between 2012 and 2018. The figure also includes the recent IPCC SROCC compilation (IPCC 2019) and relative sea-level projections for Forsmark from a recent study by Pellikka et al. (2020). Rhomb symbols show median values (the 50 % percentile). Blue colours show the "likely" range (17–83 % confidence interval) and "very likely" range (5–95 % confidence interval), displayed as broad and narrow bars respectively. Red circles show high-end RCP8.5 projections (99 % and 99.9 % percentiles). Values representing global mean sea level are shown in lighter blue and red colours, whereas local relative sea-level values (for Stockholm and Forsmark) are shown in darker blue and red colours. The local values are compensated for the isostatic uplift along the Baltic coast and therefore yield considerably lower maximum sea-level rise values (for corresponding percentiles) compared with GMSL values. The relatively small uncertainty interval given by SMHI (Nerheim et al. 2017), for example for Forsmark, compared with other recent estimates (e.g. Pellikka et al. 2020), is a result of SMHI using the IPCC AR5 (Church et al. 2013) estimates as a basis, which are known to include only a narrow selection of GMSL models/projections. Also note that the high-end projections by Pfeffer et al. (2008) and Miller et al. (2013) are not calculated based on RCP8.5 (Table 3-12). Studies included in the ensemble of GMSL projections used in Pellikka et al. (2020) are indicated with an asterisk.*

Instead, the assessment of the Forsmark mean sea-level rise until 2100 AD is based on a dedicated study of Pellikka et al. (2020). In Pellikka et al. (2020), the mean sea-level rise under RCP8.5 was analysed using a selected ensemble of GMSL projections from nine recent studies (highlighted by asterisks in Table 3-12). The ensemble intentionally includes both process-based and semi-empirical projections, including the high-end projections by Kopp et al. (2017) and Le Bars et al. (2017). It also includes low-end projections such as Church et al. (2013). To obtain a sea-level rise estimate for Forsmark, the nine global projections were first normalized to a common time interval (2000–2100 AD) by assuming a constant acceleration until 2100 AD and an initial rate of eustatic sea-level rise of 3.2 mm a^{-1}. The assumption of a constant acceleration between 2000 and 2100 AD stems from the fact that many studies have shown that the GMSL rise until 2100 AD is typically about 3–5 times greater than until 2050 AD (e.g. Jevrejeva et al. 2012, Mengel et al. 2016, Kopp et al. 2017). Subsequently, the normalised GMSL projections were regionalised to the Forsmark area by accounting for the regional-to-global ratio of the ocean thermal expansion as well as the uneven regional distribution of sea-level rise due to melting of the Greenland and Antarctic ice sheets and the world's glaciers. The resulting Forsmark sea-level rise from the regionalisation procedure in Pellikka et al. (2020) was found to be about 20 % lower than the GMSL rise. Finally, to combine all the included studies in the Pellikka et al. (2020) ensemble into a single estimate of the mean sea-level rise at Forsmark, the normalised and regionalised projections were summed into new probability distributions, assuming equal weight for all nine projections (i.e. all projections were assessed to be equally likely). The resulting probability distribution was then used to project the mean sea-level rise at Forsmark for the years 2050, 2080 and 2100 AD for different carbon emission scenarios.

Table 3-13 and Figure 3-39 present the Forsmark values on mean sea-level rise until 2050, 2080 and 2100 AD under the RCP 8.5 emission scenario from Pellikka et al. (2020).

Table 3-13. Contributions to extreme relative sea-level rise at Forsmark in 2050, 2080 and 2100 AD under the RCP8.5 emission scenario from Pellikka et al. (2020). The contributions are distinguished into mean relative sea-level rise (i.e. slow long-term eustatic change compensated for isostatic rebound) and storm surges (i.e. fast temporary processes). The sea-level rise is given both in relation to the present-day sea level at Forsmark, defined as the mean sea level in 2000 AD, and in the Swedish national reference height system RH2000. The difference in Forsmark mean sea level between RH2000 and 2000 AD is +0.17 m (SMHI 2020). The mean relative sea-level change is presented for the 95 %, 99 % and 99.9 % percentiles (corresponding to a 5 %, 1 % and 0.1 % probability of exceedance, respectively). Contributions from storm surges and the total relative sea-level rise are presented for exceedance probabilities of 10^{-3}, 10^{-4} and 10^{-5} events per year (discussed further below).

Type of contribution	Contribution to relative sea-level rise at Forsmark 2050 AD (m)	Contribution to relative sea-level rise at Forsmark 2080 AD (m)	Contribution to relative sea-level rise at Forsmark 2100 AD (m)
Mean relative sea-level rise (m)	**Relative to mean sea level in 2000 AD:** +0.20 (95 %) +0.34 (99 %) +0.48 (99.9 %) **RH2000:** +0.37 (95 %) +0.51 (99 %) +0.65 (99.9 %)	**Relative to mean sea level in 2000 AD:** +0.66 (95 %) +1.01 (99 %) +1.35 (99.9 %) **RH2000:** +0.83 (95 %) +1.18 (99 %) +1.52 (99.9 %)	**Relative to mean sea level in 2000 AD:** +1.11 (95 %) +1.66 (99 %) +2.17 (99.9 %) **RH2000:** +1.28 (95 %) +1.83 (99 %) +2.34 (99.9 %)
Storm surge level (m) with exceedance frequency (events per year)	**Relative to mean sea level in 2000 AD:** +1.64 (10^{-3}) +1.89 (10^{-4}) +2.15 (10^{-5}) **RH2000:** +1.81 (10^{-3}) +2.06 (10^{-4}) +2.32 (10^{-5})	**Relative to mean sea level in 2000 AD:** +1.64 (10^{-3}) +1.89 (10^{-4}) +2.15 (10^{-5}) **RH2000:** +1.81 (10^{-3}) +2.06 (10^{-4}) +2.32 (10^{-5})	**Relative to mean sea level in 2000 AD:** +1.64 (10^{-3}) +1.89 (10^{-4}) +2.15 (10^{-5}) **RH2000:** +1.81 (10^{-3}) +2.06 (10^{-4}) +2.32 (10^{-5})
Total combined relative sea-level rise during storm (m) with exceedance probability (events per year)	**Relative to mean sea level in 2000 AD:** +1.70 (10^{-3}) +1.96 (10^{-4}) +2.21 (10^{-5}) **RH2000:** +1.87 (10^{-3}) +2.13 (10^{-4}) +2.38 (10^{-5})	**Relative to mean sea level in 2000 AD:** +2.44 (10^{-3}) +2.70 (10^{-4}) +2.95 (10^{-5}) **RH2000:** +2.61 (10^{-3}) +2.87 (10^{-4}) +3.12 (10^{-5})	**Relative to mean sea level in 2000 AD:** +3.35 (10^{-3}) +3.62 (10^{-4}) +3.88 (10^{-5}) **RH2000:** +3.52 (10^{-3}) +3.79 (10^{-4}) +4.05 (10^{-5})

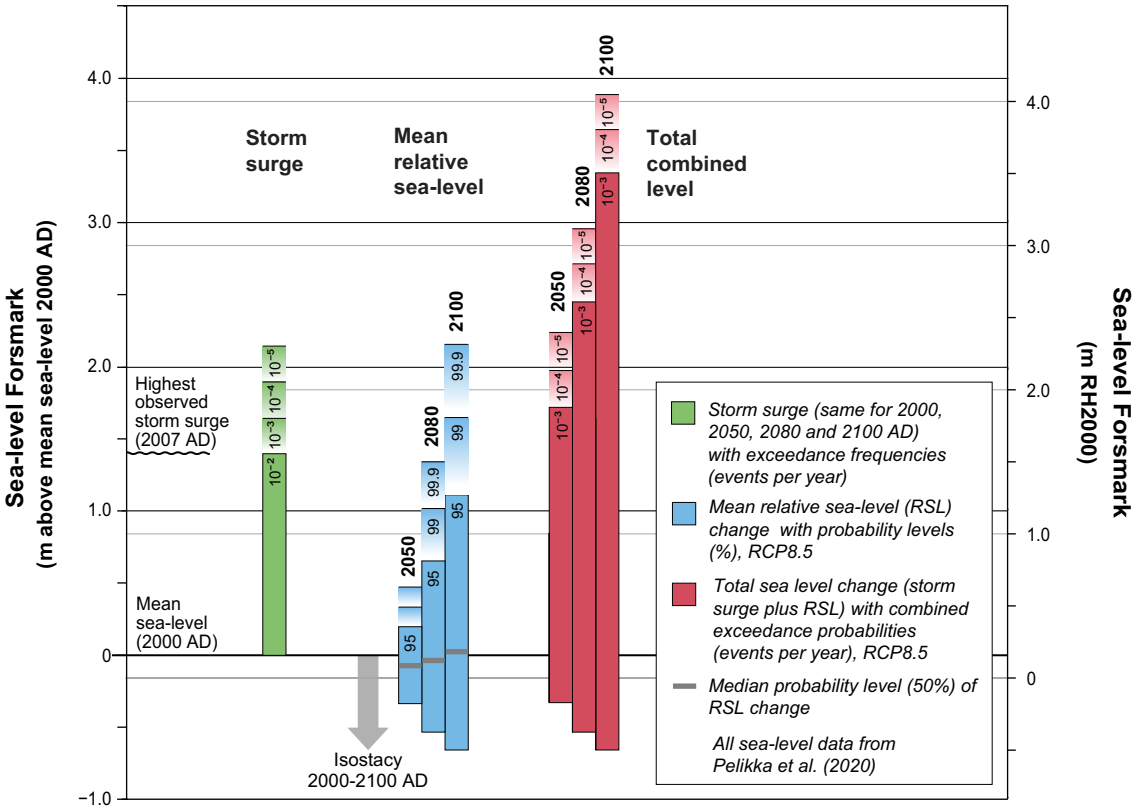

Figure 3-39. *Relative sea-level projections for 2050, 2080 and 2100 AD under the RCP8.5 emission scenario for Forsmark, based on data from Pellikka et al. (2020) (Table 3-13). The projected maximum total relative sea level is obtained by combining the contribution from the long-term mean relative sea-level rise and the maximum contribution from fast but temporary storm surges. The rise in Forsmark mean relative sea level is shown for the median probability level (grey horizontal lines within the blue bars) as well as for the 95 %, 99 % and 99.9 % percentiles, corresponding to 5 %, 1 % and 0.1 % probability, respectively. Because of the ongoing glacial isostatic rebound along the Swedish Baltic coast, a significant portion of the mean sea-level rise at Forsmark is compensated for by the isostatic uplift (amounting to 0.34 m, 0.54 m and 0.67 m until 2050, 2080 and 2100 AD, respectively). The storm surge levels are given for a range of exceedance probabilities between 10^{-2} and 10^{-5} events per year and are assumed to be constant-in-time for the entire period between 2000 and 2100 AD, see the text. The total combined relative sea level is shown for a range of combined exceedance probabilities between 10^{-3} and 10^{-5} events per year. The left axis shows the sea-level rise relative to the mean sea level in 2000 AD, and the right axis shows corresponding elevations in the RH2000 system. The difference in Forsmark mean sea level between RH2000 and 2000 AD is +0.17 m (SMHI 2020).*

Storm surges and wave height (fast temporary changes)

Sea level at coastal sites, such as Forsmark, varies on short time-scales due to variations in atmospheric pressure and winds associated with temporary weather systems. The resulting maximum present-day storm surge level at Forsmark, with an exceedance frequency of 10^{-2} events per year (i.e. a 100-year return period), was previously estimated to be +1.46 m (in RH2000, see SMHI 2020) based on observations for the period 1976–2000 AD (Engqvist A 2013, personal communication). The storm contribution to Forsmark sea-level rise for 2000 AD was also estimated by Pellikka et al. (2020) using an 850-year long simulation with a multi-component sea-level model. In their simulation, the storm surge level was found to be +1.56 m (in RH2000) for an exceedance frequency of 10^{-2} events per year. Similar values of the present-day storm surge levels at Forsmark have also been derived from SMHI (Nerheim et al. 2017). It should be noted that an exceedance frequency of 10^{-2} events per year means that there is a 63 % probability that a sea-level rise of this magnitude or higher occurs once in a 100-year period (Table 3-14). The sea level may thus occasionally rise above this value, as illustrated by the highest observed storm surge in Forsmark, +1.45 m above mean sea level for the year (corresponding to +1.58 m in RH2000), which occurred in 2007.

A 10^{-2} exceedance frequency is far too high to be used in the planning and construction of critical infrastructure such as the SFR repository. Therefore, in order to make a more useful assessment of the storm surge contribution to sea-level rise, it is necessary to account for lower probability events characterised by lower exceedance frequency than the 10^{-2} discussed above, such as 10^{-3}, 10^{-4} and even 10^{-5} events per year (Table 3-14). To estimate the 2000 AD sea-level rise for these low exceedance probabilities, Pellikka et al. (2020) extrapolated the probability distribution of daily sea-level maxima from the 850-year sea-level simulation towards lower frequencies. Their result suggests that the sea level increases by ~ 0.2–0.3 m for every order of magnitude reduction of the exceedance frequency. The results show that the present-day temporary storm surge level is +1.81 m, +2.06 m and +2.32 m (in RH2000) for an exceedance frequency of 10^{-3}, 10^{-4} and 10^{-5} events per year, respectively.

Table 3-14. Relationship between return time, exceedance frequency, and probability. The relationship is described by $P = 1-(1-1/T)^n$, where P is the probability, n is the length of the period over which the probability is computed (years), and T is the return time (years). The exemplified 60-year period in column three approximately corresponds to the remaining length of the operational period of SFR (up until 2080 AD).

Return time (T) [years]	Exceedance frequency [events per year]	Probability (P) n=60 years	Probability (P) n=100 years (e.g. 2000–2100 AD)
100	10^{-2}	45 %	63 %
1000	10^{-3}	6 %	10 %
10 000	10^{-4}	0.6 %	1 %
100 000	10^{-5}	0.06 %	0.1 %

The storm-surge contribution to the sea-level rise at Forsmark until 2100 AD is potentially also influenced by changes in the near-surface wind field in a warmer RCP8.5 climate. For example, the modelling study of Meier (2006) suggests that the changes in the weather patterns in a warmer climate may serve to increase the temporary high sea level in 2100 AD by approximately 0.3 m in the Forsmark region compared with the present day. The notion of higher storm surges in warmer climate is however somewhat refuted in Pellikka et al. (2020). Based on their own investigations and other studies, e.g. Ruosteenoja et al. (2019), they argue that there is no significant systematic change of the near-surface wind field in climate modelling projections until 2100 AD. Therefore, the storm-surge contributions in Pellikka et al. (2020), estimated for the year 2000 AD, are assumed to be identical for the entire period from 2000 to 2100 AD.

The storm surge contributions from Pellikka et al. (2020), used in the assessment of maximum sea-level rise at Forsmark, are summarised in Table 3-13 and Figure 3-39.

During storms, windy conditions typically contribute to an increase in the height of the waves entering the Forsmark shoreline. Wave height around the SFR repository, induced by a northerly storm of 25 m s^{-1}, was modelled in Brydsten et al. (2009) using the STWAVE model, which simulates wave refraction and shoaling, wave breaking, diffraction, wind-induced wave growth, wave-wave interactions and white capping (McKee Smith et al. 2001). The resulting wave height (defined as the distance between the wave crest and trough) is shown in Figure 3-40. The wave height in the northern part of Öregrundsgrepen amounts to more than 7 metres but declines rapidly down towards Forsmark. The pier built adjacent to SFR shelters the shores to the south, so the wave heights here are moderate (< 0.4 m). The southern shores of SFR are very well sheltered from northerly winds and thus have negligible wave heights (Figure 3-40). The largest wave height in the vicinity of SFR is just north of the repository with 1–2 m high waves. Since the wave height in STWAVE is defined as the distance between the wave crest and trough, the contribution from those waves on the temporary sea-level rise would be approximately 50 %, i.e. ~ 0.5–1 m. However, this simulation was not made in enough detail to resolve the detailed effects of these waves on the SFR shoreline. Also, the modelled wind speed was not pessimistically chosen for storm conditions. Therefore, these results are used only as a first-order indication of wave heights during storms, but not in the assessment of the maximum temporary sea-level rise at Forsmark by 2100 AD.

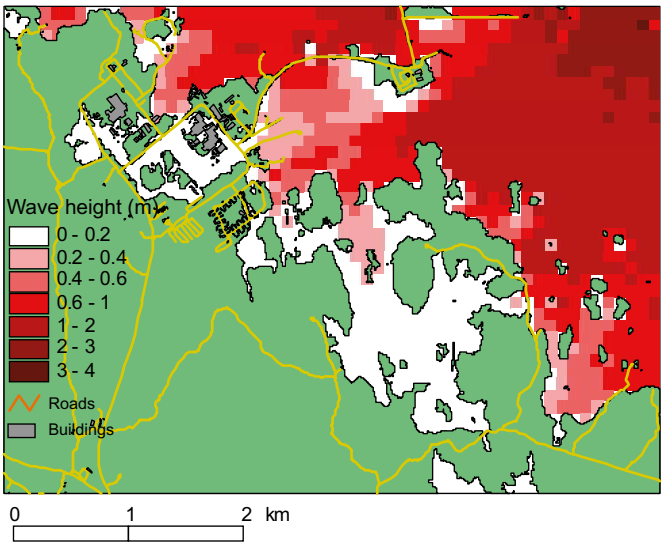

Figure 3-40. *Calculated storm-induced wave height by northerly winds of 25 m s^{-1} using the STWAVE model (Brydsten et al. 2009). Wave height is defined as the distance between the wave crest and trough. The contribution from wave height to the temporary sea-level rise would thus be approximately 50 % of the values shown in this figure. Near the SFR repository this means that the maximum wave height contribution is ~ 0.5–1 m.*

Resulting total relative sea-level rise at Forsmark until 2100 AD

As previously mentioned, for the operation, planning and construction of SFR, it is important to assess the risk that the total sea level, during storm, will exceed a certain height for the entire operational period. To that end, it is necessary to assess the probability of the *combined* maximum sea-level rise resulting from the long-term relative sea level change and short-term sea-level variability due to storm surges.

The combined probability of mean relative sea-level change and storm surges under RCP8.5 was analysed for Forsmark in Pellikka et al. (2020). In this study, the probability distributions for the mean relative sea-level change and the daily sea-level maxima were summed into a new distribution under the assumption that they are independent (convolution). The resulting combined probabilities were reported for the years 2050, 2080 and 2100 AD, and are summarised in Figure 3-39 and Table 3-13.

For the year 2100 AD, the total maximum sea level during severe storms is projected to be +3.52 m, +3.79 m and +4.05 m (in RH2000) for an exceedance probability of 10^{-3}, 10^{-4} and 10^{-5} events per year, respectively. For the years 2050 and 2080 AD, the total maximum sea level for each exceedance probability is consistently lower than for 2100 AD. For example, in 2080 AD the maximum sea level with an exceedance probability of 10^{-5} events per year is projected to be almost 1 metre lower than in 2100 AD, and in 2050 AD the corresponding sea level is approximately 0.7 m lower than in 2080 AD.

The consistently higher maximum sea levels in 2100 AD compared with 2050 and 2080 AD are attributed to an acceleration of the projected rise in mean sea level. As with the presently accelerating sea-level rise (see above and e.g. Nerem et al. 2018), also future sea-level rise is expected to accelerate with time. In Pellikka et al. (2020), the sea-level acceleration was assumed to be constant in time. Relative to 2000 AD, this translates to a 4 times higher mean sea-level rise by 2100 AD compared with 2050 AD. The assumption of a constant acceleration is in line with most recent studies, which show that the GMSL rise by 2100 AD is about three to five times the GMSL rise by 2050 AD (see above and e.g. Jevrejeva et al. 2012, Mengel et al. 2016 and Kopp et al. 2017).

To visualise the acceleration in mean sea-level rise in the projections by Pellikka et al. (2020), the temporal evolution of the projected mean relative sea level (i.e. excluding the storm surge contribution) at Forsmark is shown in Figure 3-41 for the different pessimistically chosen probability percentiles. As evident in Figure 3-41, the fastest mean relative sea-level rise is projected to occur between 2080 and 2100 AD, whereas the relative sea-level rise is considerably slower in the near future. For the percentiles considered here, the rise in mean relative sea level between 2080 and 2100 AD is projected to be greater than the equivalent rise between 2000 and 2050 AD. Importantly, the rise in mean relative sea level between 2050 and 2080 AD, corresponding to the latter part of the planned operational period, is also projected to be considerably larger than the rise between 2020 and 2050 AD. The latter part of the operational period is also, as expected, associated with greater uncertainties in the relative sea-level projections. This highlights the necessity of monitoring the mean sea-level rise over the entire operational period to assess the actual development of future sea-level rise. Another important feature of Figure 3-41 is that the maximum rise of mean relative sea level at Forsmark (excluding storm surge) is projected to increase by less 0.5 m until 2050 AD compared with the present day, even for the most extreme sea-level scenarios. The relatively slow increase of the sea level during this period enables a greater flexibility to adjust for changed circumstances in the future, e.g. if sea-level projections for the time of repository closure prove to be higher than foreseen at present.

Figure 3-42, Figure 3-43 and Figure 3-44 show areas at Forsmark that are permanently flooded and flooded during severe storms in 2080 AD, the planned closure time for SFR, for different levels of statistical probability. The maps show sea levels compensated for isostatic uplift, as described also in Table 3-13 and Figure 3-39.

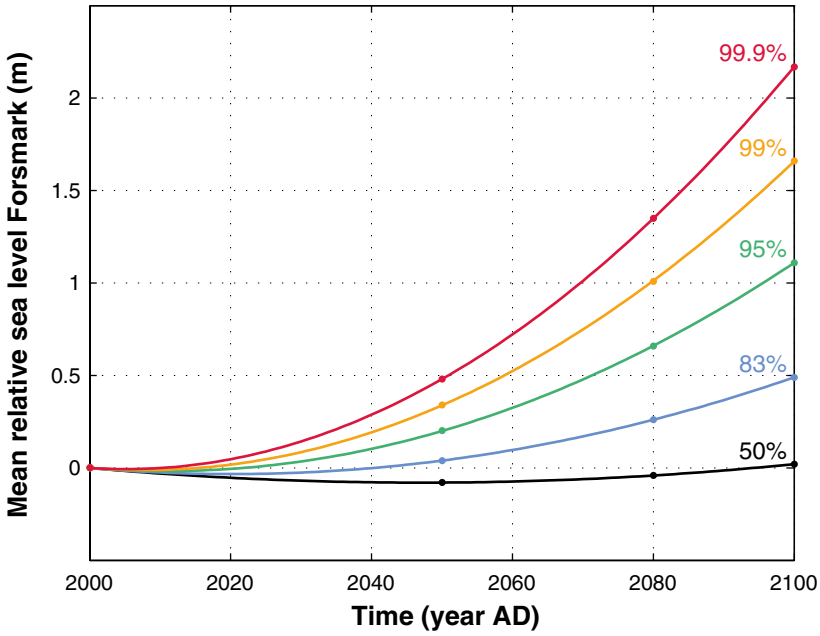

Figure 3-41. *Temporal evolution of the mean relative sea level (i.e. excluding the storm surge contribution) at Forsmark from 2000 to 2100 AD under the RCP8.5 emission scenario for different percentiles from Pellikka et al. (2020). The dots show the mean relative sea levels from Pellikka et al. (2020) in 2050, 2080 and 2100 AD (Table 3-12 and Table 3-13), whereas the lines represent fitted second-order polynomials for each percentile, following the approach in Pellikka et al. (2020). The choice of a second-order polynomial ensures a constant acceleration, as applied in Pellikka et al. (2020) which is in approximate agreement with most studies on future sea-level rise, see the text. Note that the probability of occurrence can be estimated by subtracting the percentile from 100 %, implying e.g. a 0.1 % and 1 % probability respectively for the 99.9 % and 99 % percentiles.*

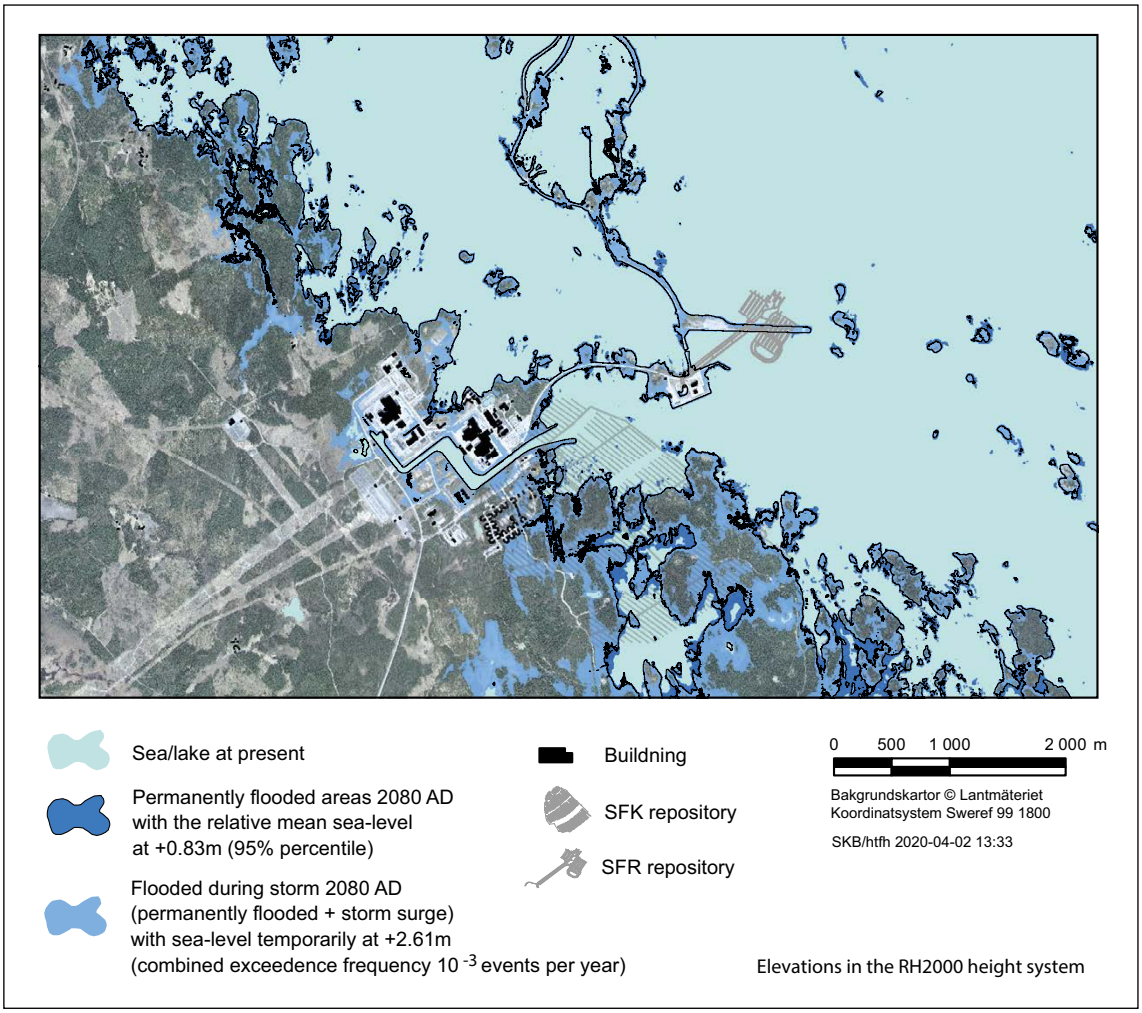

Figure 3-42. *Areas at Forsmark that are permanently flooded (dark blue colour) in 2080 AD (the planned closure time for SFR) as described by the 95 % percentile probability distribution under the RCP8.5 emission scenario (Pellikka et al. 2020). The relative mean sea-level rise at this time, i.e. sea-level rise compensated for isostatic uplift, amounts to +0.83 m. For an exceedance probability of 10^{-3} events per year, a total temporary sea-level rise of +2.61 m may occur during severe storms (light blue colour) (Pellikka et al. 2020. See also Table 3-13 and Figure 3-39). Figure 3-43 and Figure 3-44 show similar information, but for lower statistical probabilities. The present shoreline is based on the Lantmäteriet Property map (www.lantmateriet.se).*

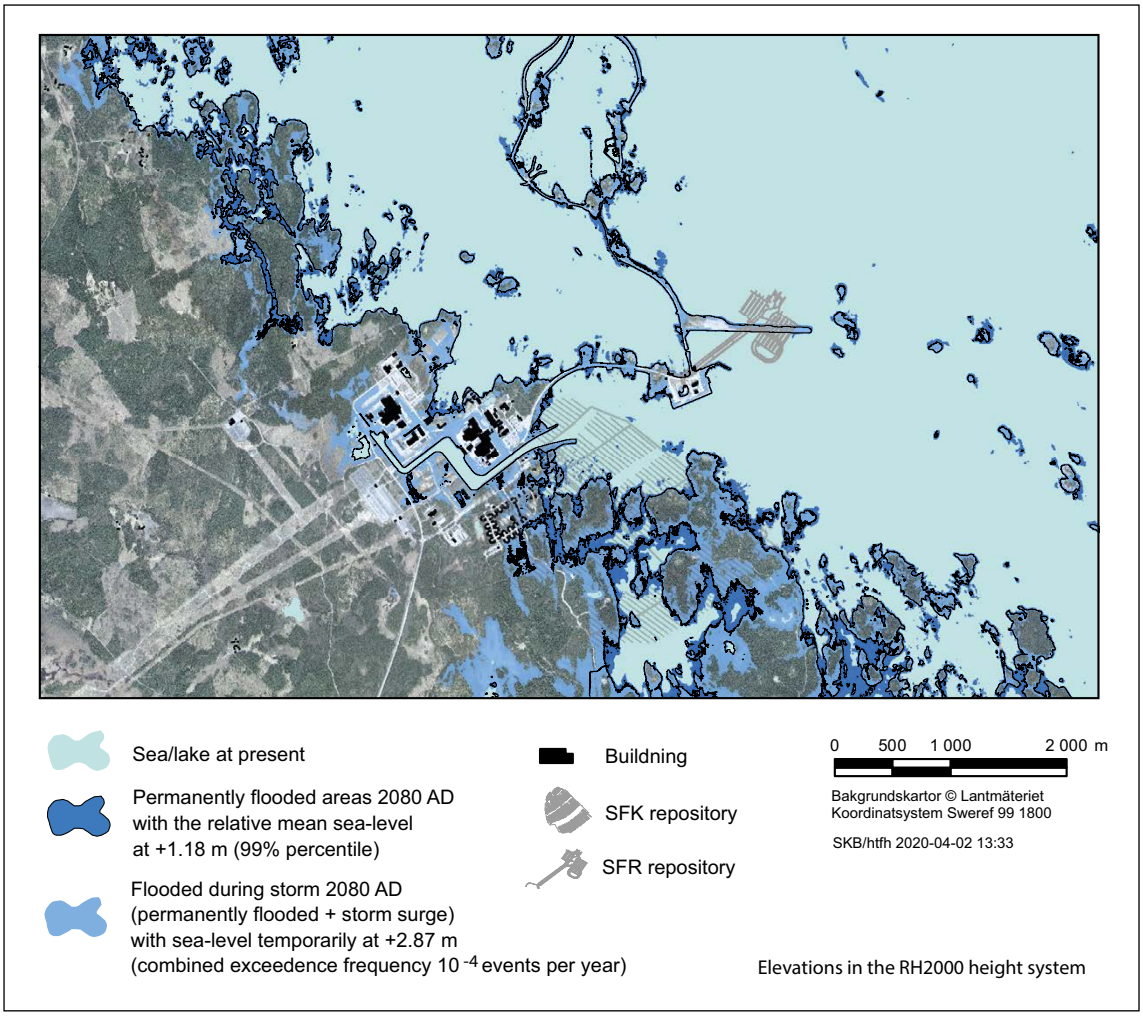

Figure 3-43. *Areas at Forsmark that are permanently flooded (dark blue colour) in 2080 AD (the planned closure time for SFR) as described by the 99 % percentile probability distribution under the RCP8.5 emission scenario (Pellikka et al. 2020). The relative mean sea-level rise at this time, i.e. sea-level rise compensated for isostatic uplift, amounts to +1.18 m. For an exceedance probability of 10^{-4} events per year, a total temporary sea-level rise of +2.87 m may occur during severe storms (light blue colour) (Pellikka et al. 2020. See also Table 3-13 and Figure 3-39). Figure 3-44 show similar information, but for lower statistical probabilities. The present shoreline is based on the Lantmäteriet Property map (www.lantmateriet.se).*

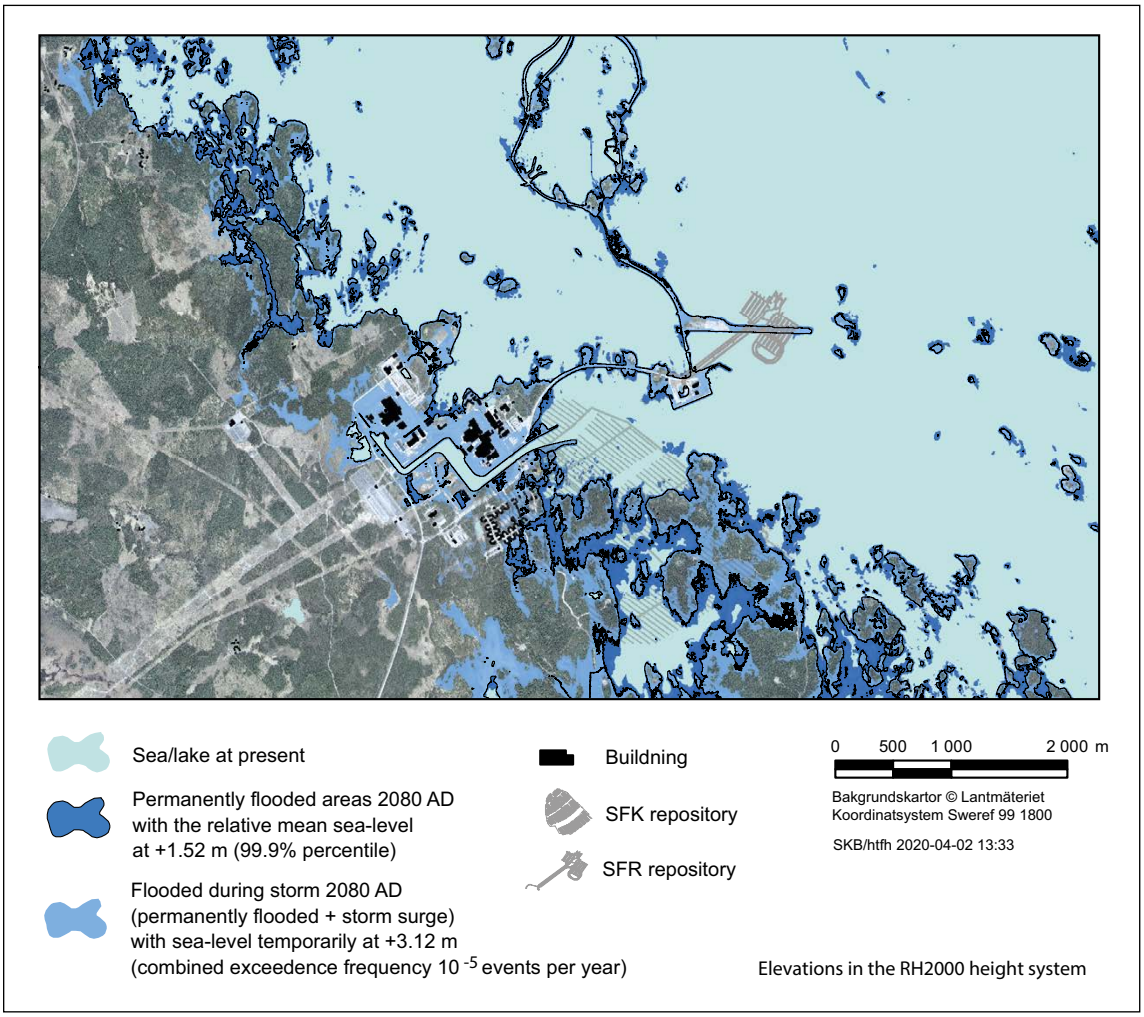

Figure 3-44. *Areas at Forsmark that are permanently flooded (dark blue colour) in 2080 AD (the planned closure time for SFR) as described by the 99.9 % percentile probability distribution under the RCP8.5 emission scenario (Pellikka et al. 2020). The relative mean sea-level rise at this time, i.e. sea-level rise compensated for isostatic uplift, amounts to +1.52 m. For an exceedance probability of 10^{-5} events per year, a total temporary sea-level rise of +3.12 m may occur during severe storms (light blue colour) (Pellikka et al. 2020. See also Table 3-13 and Figure 3-39). The present shoreline is based on the Lantmäteriet Property map (www.lantmateriet.se).*

3.5.3 Relative sea-level change beyond 2100 AD until 12 000 AD

As described in the section on relative sea-level rise until 2100 AD above, the uncertainty in future sea level response to global warming is large within the coming century. Sea-level change beyond 2100 AD is naturally associated with even larger uncertainties. As shown by the main conclusions related to sea-level change beyond 2100 AD presented in IPCC AR5 (Church et al. 2013), sea level will continue to rise after 2100 AD in a warming climate. Some of the main conclusions in this context stated by Church et al. (2013) are the following.

- It is virtually certain that GMSL rise will continue beyond 2100 AD, with sea-level rise due to thermal expansion continuing for many centuries. Longer term sea-level rise depends on future emissions.
- The available evidence indicates that global warming greater than a certain threshold would lead to the near-complete loss of the Greenland ice sheet over a millennium or more, causing a GMSL rise of about 7 m.
- Ocean heat uptake and thermal expansion take place not only while atmospheric greenhouse gas concentrations are rising but will continue for many centuries to millennia after stabilisation of radiative forcing, at a rate that declines on a centennial timescale.

As mentioned in Section 2.2.1, one crucial aspect of sea-level rise due to ice-sheet melting is that the effect of the rising sea level is not distributed evenly over the seas and along continental coasts. This is due to changes in the gravity field associated with the reduction of the ice sheets and water entering the ocean basins (e.g. Milne et al. 2009**,** Whitehouse 2009, Bamber and Riva 2010). For instance, a complete collapse of the Greenland ice sheet would result in gravitational changes that counteracts the sea-level rise in the near the collapsed ice sheet, resulting in a lower sea level, in the near field than when the ice sheet was present (Milne et al. 2009). This is one key aspect of the GIA modelling used for safety assessment purposes for the Forsmark site. Milne et al. (2009) studied this spatially variable change in sea level assuming a complete melting of the Greenland ice sheet and predicted a ~ 0 mm a^{-1} sea-level change in the region of Fennoscandia. The same effect in Forsmark was also seen in the GIA simulations performed for a future warmer climate described in Section 2.2.4.

Several studies have been published on the possible contribution to sea-level rise by the West Antarctic ice sheet (e.g. Mitrovica et al. 2009, Bamber et al. 2009, Ivins 2009, Rignot et al. 2008). Current knowledge suggests that the potential maximum rise in GMSL from the West Antarctic Ice Sheet is 3.3 m (Bamber et al. 2009). Other studies suggest that during the penultimate interglacial, the Eemian, the Greenland ice-sheet configuration was *not* drastically reduced although air temperatures over Greenland were 8 ± 4 degrees warmer that today (NEEM community members 2013). In order to close the global water budget, with 6–8 m higher global Eemian sea levels than today, this result suggests that the West Antarctic ice sheet needs to have contributed more to the Eemian sea-level rise, and in turn that the West Antarctic ice sheet might be more vulnerable to warming temperatures than previously thought (Schiermeier 2013). The effects of a collapse of the West Antarctic ice sheet were studied by Mitrovica et al. (2009) and Bamber et al. (2009). By using the traditional ice volume value for West Antarctica, corresponding to 5 m of GMSL rise, Mitrovica et al. (2009) estimated that a collapse of the West Antarctic ice sheet would result in a sea-level rise around Fennoscandia of 5 ± 1 m, when including the gravitational effects associated with the ice-sheet collapse. However, information on the ice- and bed-topography of the West Antarctic ice sheet suggest that it has about 3.3 m of equivalent global sea level grounded on areas with downward sloping bedrock (Bamber et al. 2009). Using this estimate Bamber et al. (2009) suggested that melting of the West Antarctic ice sheet would give a sea-level rise around Fennoscandia of around 3 m, with gravitational effects considered.

To assess the effects of uncertainties associated with sea-level change beyond 2100 AD, compilations of published estimates of GMSL rise beyond 2100 AD for a weak, moderate and strong global warming are reported in this Section. The published GMSL changes typically include the contributions from i) ocean thermal expansion, ii) melting of the Greenland and Antarctic ice-sheets, iii) melting of all glaciers and ice caps, and, in some cases, iv) changes in land water storage. Some of the studies only deal with the contribution from specific sources.

The compilations of the published GMSL rise estimates are thereafter used to estimate the uncertainty range of the relative sea-level change at Forsmark under each climate scenario. These uncertainty ranges are then used as basis for estimating (i) the long-term relative sea level until 100 ka AP (Section 3.5.4), and (ii) the duration of the initial submerged period over the repository for different climate cases (Chapter 5).

In contrast to the assessment of the sea-level change up until 2100 AD (Section 3.5.2), the usage of RCPs over timescales of 10 ka is not completely straightforward as these, even if including the extensions, are only defined until 2300 AD (Section 3.4.1). Therefore, studies investigating the GMSL rise over longer timescales typically use other metrics to define future scenarios, such as a maximum increase of the global mean SAT (e.g. Levermann et al. 2013) or simplified pathways based on total cumulative emissions (e.g. Clark et al. 2016). Here, the projected global mean SAT values from those studies are compared with typical estimated long-term SAT ranges for RCP2.6, RCP4.5 and RCP8.5 (Figure 3-25), in order to determine which of the GMSL rise experiments belong to the weak, moderate and strong global warming cases, respectively. However, this exercise is also not straight-forward since the temperature is expected to vary significantly over centennial to millennial timescales (Figure 3-25), and because the projected SAT ranges under the different RCPs have some overlap with one another (e.g. Table 3-3). Some GMSL projections may therefore be included in more than one compilation below. However, the typical 1.5 °C and 2 °C temperature stabilization scenarios over shorter timescales covered by the RCPs are, as in the case of sea-level rise until 2100 AD, sorted into the categories of weak and moderate global warming, respectively.

Furthermore, the large uncertainty related to the long-term sea-level change implies that differences in the projected GMSL rise between studies may reach several tens of metres. Hence, in contrast to reported sea-level projections until 2100 AD, it is not meaningful to report the published long-term projections in two separate height reference systems (as deviations from present-day and in RH2000), as the difference between those systems amounts to only ~ 0.2 m. Therefore, the reported sea levels in this section are only presented as differences to present-day, typically defined as year 2000 AD or the average between 1986 and 2005 AD.

Given that a major deglaciation of the Greenland and Antarctic ice-sheets under a warming climate would contribute with different sea-level rise fingerprints in Fennoscandia, as described above, it would have been useful if the projections had included the regional distribution of sea-level rise. This is however not the case for most of the studies, as they typically only report the GMSL rise. Nevertheless, for the long-term analysis beyond 2100 AD and up to 12 000 AD it is assumed that the GMSL value is representative also for the eustatic sea level in the Baltic Sea. If the GMSL projections were adapted to Baltic Sea conditions, the resulting 10 ka projections would likely be up to a few metres lower than the global mean. The reason for the lower sea-level rise in the Baltic Sea compared to the global mean is primarily explained by a smaller contribution from the Greenland ice sheet in this region (see e.g. Mitrovica et al. 2001 and Kopp et al. 2014).

Note that the compilations only include the change due to the *mean* sea-level rise. Short-term effects that do not add to the long-term rise of mean sea level (i.e. storm-surge events) are not included. During such events, the sea level could temporarily increase up to a few metres, which may be exemplified by the situation at 2100 AD (Section 3.5.2). It is also important to emphasise that the timing of the maximum contributions to sea-level rise differs for the different processes. In general, the processes are slow, especially the thermosteric sea-level rise which may reach its maximum value in several thousands of years.

Weak global warming (RCP2.6)

A compilation of selected GMSL projections from 2200 AD up to 12 000 AD, with a focus on projections based on low emission or temperature scenarios, representing a weak global warming, is presented in Table 3-15. Figure 3-45 displays the sea-level projections for the period 2200 AD to 12 000 AD from the data in Table 3-15, as well as the estimated isostatic uplift for the Forsmark site and the resulting local changes in relative sea level.

In Figure 3-45, the green curve shows the isostatic uplift at Forsmark as projected by the GIA modelling (Section 2.2.4). The only feature included in the GIA modelling that could potentially influence the future eustatic development is a complete collapse of the Greenland ice sheet. However, the results from the GIA modelling and results by e.g. Milne et al. (2009) constitute robust evidence that such an event would have negligible impact (~ 0 m) on the relative sea level in the Baltic Sea. Therefore, the future relative sea-level curve projected by the GIA modelling in the global warming scenario essentially only shows the isostatic signal at the Forsmark site. The difference between the eustatic and isostatic curves constitutes the estimated relative sea-level evolution at Forsmark, giving an estimate of potential periods of transgression and regression and hence also periods of submerged and terrestrial conditions at the site.

The highest long-term sea-level projection until 12 000 AD for a weak global warming, comparable to RCP2.6, is obtained in Clark et al. (2016) using the 960 Pg C total carbon emission scenario (Table 3-15). The global annual mean SAT increase for this scenario in Clark et al. (2016) is 1.8 °C by 2300 AD and 1.0 °C by 12 000 AD, hence broadly representative of the upper bound of RCP2.6 (Figure 3-25). The rate of GMSL rise in this projection is relatively fast over the initial thousands of years, but gradually slows down over the latter part of the 10 000-year period. At 12 000 AD, the global sea-level rise under the 960 Pg C scenario in Clark et al. (2016) reaches a level of 17.2 m (Table 3-15 and Figure 3-45). The lowest projection over the same period results in a sea-level rise of 2.5 m (Levermann et al. 2013). This projection is an estimate of the multi-millennial sea-level commitment of the ~ 1 °C global warming that has occurred until present, and hence represents a hypothetical situation where current emissions of greenhouse gases are suddenly stopped today.

Table 3-15. Compilation of recent (since 2012) GMSL projections beyond 2100 AD until 12 000 AD with a focus on projections based on the RCP2.6 emission scenario, or scenarios similar to RCP2.6. Values are given for the median value and a 17–83 % confidence interval (i.e. the likely range) and a 5–95 % confidence interval (i.e. the very likely range). It should be noted that the values are not directly comparable because they may be based on different climate/emission scenarios and use different methodological assumptions. The SAT response to the 960 Pg C total emissions scenario in Clark et al. (2016) approximately corresponds to the upper-end of the constructed long-term SAT evolution for RCP2.6, whereas the lower-end approximately corresponds to the present-day SAT (Figure 3-25).

Year (AD)	Sea-level rise for RCP2.6 or equivalent (m) Median values with confidence interval within brackets	Confidence interval used Comments within brackets	Reference
2200	1.0 (0.5–1.6) 1.0 (0.3–2.4)	17–83 % 5–95 %	Kopp et al. (2014)
	0.93 (0.43–1.61) 0.93 (0.20–2.41)	17–83 % 5–95 % (1.5 °C of warming)	Rasmussen et al. (2018)
2300	1.99 (1.18–3.09) 1.49 (0.87–2.36)	5–95 % (RCP2.6) 5–95 % (MERGE400[1])	Schaeffer et al. (2012)
	1.42 (0.32–2.88) 1.42 (−0.22–4.70)	17–83 % 5–95 %	Kopp et al. (2014) according to Horton et al. (2018)
	1.42 (0.83–2.30) 1.42 (0.50–3.0)	17–83 % 5–95 %	Kopp et al. (2017)
	1.02 (0.80–1.35)	17–83 %	Nauels et al. (2017)
	0.89 (0.53–1.27)	5–95 % (1.5 °C of warming)	Nicholls et al. (2018)
2500	0.53 (0.13–1.74)	5–95 %	Jevrejeva et al. (2012)
4000	2.3 (1.0–4.9)	1 °C of warming	Levermann et al. (2013)
12 000	2.5 (1.0–10.8)	1 °C of warming above pre-industrial levels	Levermann et al. (2013)
	3.7	320 Pg C total emissions	Clark et al. (2016)[2]
	12.7	640 Pg C total emissions	
	17.2	960 Pg C total emissions	

[1] The MERGE400 scenario aims at reaching a CO_2 equivalent concentration of 400 ppm by 2100 AD.

[2] No uncertainty ranges are reported in Clark et al. (2016) for sea-level projections under scenarios with < 1 000 Pg C total emissions.

The substantially lower GMSL projections in these studies compared with Clark et al. (2016) is primarily explained by a much lower contribution from the Antarctic ice sheets. For example, whilst the 960 Pg C scenario in Clark et al. (2016) projects that Antarctica will contribute with more than 15 m to the multi-millennial GMSL rise, the 1 °C warming projection in Levermann et al. (2013) suggests that the Antarctic contribution will be less than 2 m over the same time period. The widely different contributions from the Antarctica between the studies are likely attributed to different amounts of global warming (~ 2 °C in Clark et al. 2016 versus 1 °C in Levermann et al. 2013), but possibly also to a higher sensitivity to global warming of the ice-sheet melting in Clark et al. (2016) than in Levermann et al. (2013).

The GMSL rise according to the highest projection (Clark et al. 2016, upper dark blue line) together with the isostatic curve for the Forsmark site from GIA modelling (green line) results in the relative sea-level curve shown by the upper dark red line (Figure 3-45). This relative sea-level development shows a continued marine regression at Forsmark, albeit at a slower rate than at present.

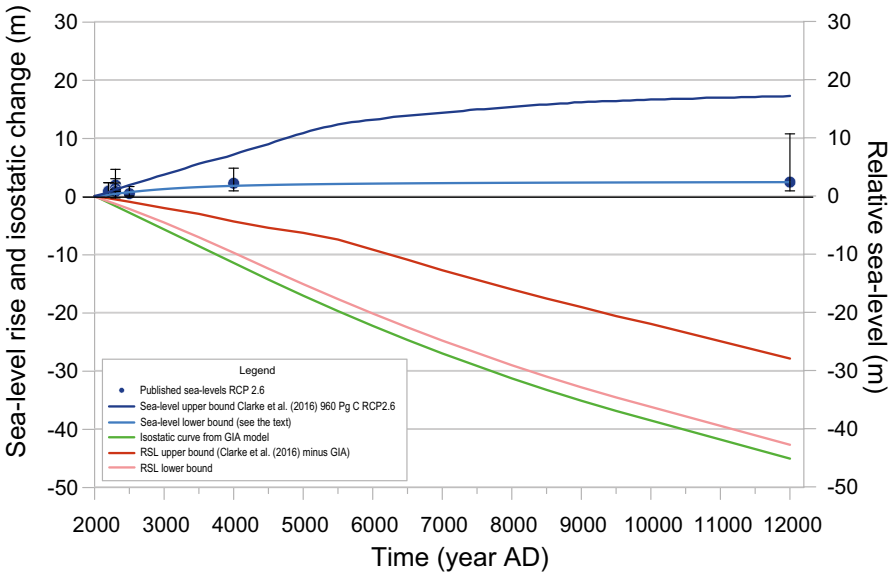

Figure 3-45. *Mean long-term sea-level rise projections (blue dots) for the period 2200 to 12 000 AD from the compilation in Table 3-15. The values constitute projections comparable with the RCP2.6 emission scenario, representing a weak global warming. Median values are shown by blue dots and the 5–95 % confidence intervals are shown by uncertainty bars. For the highest projected sea level at 12 000 AD (+17.2 m from Clark et al. 2016 for a 960 Pg C total emission scenario), the projected sea-level development leading up to the maximum level has also been plotted (dark blue curve), data from Clark et al. (2016, supplementary material). The 960 Pg C emission scenario by Clark et al. (2016) represents the highest long-term sea-level projection (dark blue line), whereas the 1 °C warming scenario from Levermann et al. (2013) represents the lowest long-term sea-level projection under a weak global warming (light blue line). The isostatic uplift rate for the Forsmark site as projected by GIA modelling (see the text and Section 2.2.4) is shown by the green curve. The evolution of highest relative sea-level estimate at Forsmark, constituting the net effect of the high-end eustatic change (dark blue curve) and the isostatic change (green curve) is shown in dark red. The evolution of lowest relative sea-level estimate at Forsmark, constituting the net effect of the low-end eustatic change (light blue curve) and the isostatic change (green curve) is shown in light red.*

In contrast to Clark et al. (2016), the lowest GMSL projections in Figure 3-45 do not provide much information on how the sea level changes with time. Therefore, a general time evolution of a low-end GMSL evolution (E_{low}), ranging from 2000 to 12 000 AD, is constructed using the following equation:

$$E_{low}(t) = a \arctan(bt), \qquad \text{Equation 3-2}$$

where t is the time (in ka) after 2000 AD, and a = 1.70 m and b = 0.97 ka^{-1}. The values of a and b were constrained under the following conditions: (i) E_{low} should be equal to +2.5 m at 12 000 AD, which is consistent with the lowest projection at this time under weak global warming (Levermann et al. 2013, see Table 3-15), and (ii) the initial relative sea-level change should be the same as the observed present-day rate at Forsmark, i.e. −4.1 mm a^{-1} (Table 3-7).

The constructed time series of the low-end GMSL evolution until 12 000 AD is shown by the lower light blue curve in Figure 3-45. If this curve is used together with the isostatic curve based on GIA modelling (green line), the resulting low-end relative sea-level change is shown by the lower light red line. This relative sea-level development shows a continued regression at the site, from the present and up to 12 000 AD and beyond.

All in all, the above analysis illustrates a large uncertainty range of long-term future relative sea-level evolution at Forsmark, amounting to ~ 15 m at around 12 000 AD even under a weak global warming. However, the isostatic rebound results in continued regression at the Forsmark site for this full uncertainty range; hence no period of sea transgression occurs over the coming 10 ka under this climate development.

Moderate global warming (RCP4.5)

A compilation of selected GMSL projections from 2200 AD up to 12 000 AD, with focus on projections based on the RCP4.5 emission scenario, or scenarios comparable to RCP4.5 (Section 3.4.1), is presented in Table 3-16. Figure 3-46 displays the sea-level projections for the period 2200 AD to 12 000 AD from the data in Table 3-16, as well as the estimated isostatic uplift for the Forsmark site, and the resulting local changes in relative sea level.

Table 3-16. Compilation of recent (since 2012) GMSL projections beyond 2100 AD up to 12 000 AD with focus on projections based on the RCP4.5 emission scenario, or scenarios comparable with RCP4.5 (Section 3.4.1). Values are given for the median value and a 17–83 % confidence interval (i.e. the likely range) and a 5–95 % confidence interval (i.e. the very likely range). It should be noted that the values are not directly comparable because they may be based on different climate/emission scenarios and use different methodological assumptions. The SAT response to the 2 560 Pg C total emissions scenario in Clark et al. (2016) approximately corresponds to the upper end of the constructed SAT range of the RCP4.5 scenario, whereas the 1 280 Pg C scenario in Clark et al. (2016) and 2 °C warming scenario by Levermann et al. (2013) approximately correspond to the lower end (Figure 3-25). The highest long-term sea-level projection under the RCP4.5 moderate emission scenario result from the 2 560 Pg C cumulative emissions in Clark et al. (2016), whereas the lowest projections are obtained in the 2 °C warming projection by Levermann et al. (2013). The uncertainty range for DeConto and Pollard (2016) and Clark et al. (2016) has been recalculated from 1σ standard error to the 5–95 % confidence interval.

Year (AD)	Sea-level rise for RCP 4.5 (m) or equivalent Median values with confidence interval within brackets	Confidence interval used. Comments within brackets	Reference
2200	1.30 (0.70–2.00) 1.30 (0.40–2.70)	17–83 % 5–95 %	Kopp et al. (2014)
	1.20 (0.57–1.97) 1.20 (0.20–2.81)	17–83 % 5–95 % (2 °C of warming)	Rasmussen et al. (2018)
2300	3.55 (2.12–5.27) 2.67 (1.56–4.01)	5–95 % (RCP4.5) 5–95 % (2 °C of warming)	Schaeffer et al. (2012)
	1.92 (0.7–3.49) 1.92 (0–5.31)	17–83 % 5–95 %	Kopp et al. (2014) according to Horton et al. (2018)
	4.21 (2.75–5.95) 4.21 (2.11–6.96)	17–83 % 5–95 %	Kopp et al. (2017)
	1.76 (1.29–2.30)	17–83 %	Nauels et al. (2017)
	1.17 (0.71–1.65)	5–95 % (2 °C of warming)	Nicholls et al. (2018)
2500	1.84 (0.72–4.30)	5–95 %	Jevrejeva et al. (2012)
	5.76 (4.12–7.40)	5–95 % (± 1σ (± 1.0 m)) Only Antarctic ice loss	DeConto and Pollard (2016)
4000	2.3 (1.0–4.9) 4.8 (2.6–7.5)	1 °C of warming 2 °C of warming	Levermann et al. (2013)
7000	4.72 4.48 8.47	Fast CO_2 drawdown Natural CO_2 drawdown No CO_2 drawdown Only Antarctic ice loss.	DeConto and Pollard (2016)
12 000	25.2 (19.3–31.1)	5–95 % (± 1σ (± 3.6 m)) 1 280 Pg C total emissions (~RCP4.5)	Clark et al. (2016)
	37.5 (33.7–41.2)	5–95 % (± 1σ (± 2.3 m)) 2 560 Pg C total emissions (~RCP4.5)	Clark et al. (2016)
	10.9 (3.1–13.4)	2 °C of warming above pre-industrial levels	Levermann et al. (2013)

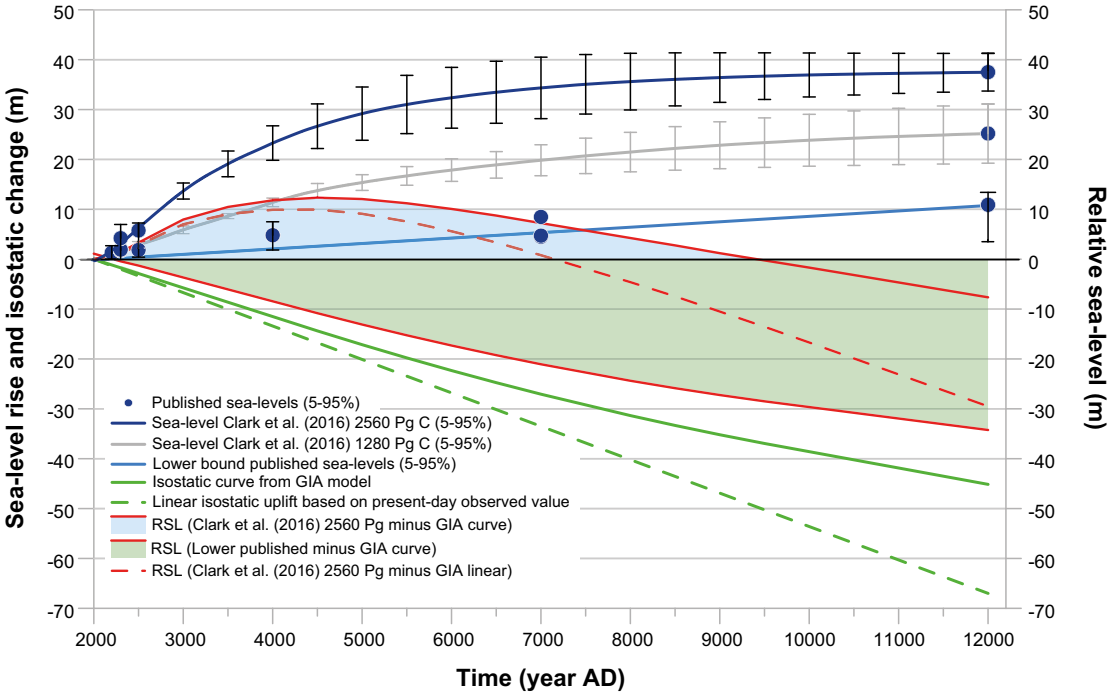

Figure 3-46. *Mean sea-level rise projections (blue dots) for the period 2200 to 12 000 AD from the compilation in Table 3-16. The values are based on projections comparable with the RCP4.5 emission scenario, representing a moderate global warming. Median values are shown by blue dots and the uncertainty bars show the total 5–95 % confidence interval based on all published sea-level projections at a given time slice. For the highest projected sea level at 12 000 AD (+37.5 ± 3.8 m from Clark et al. 2016 for a 2 560 Pg C total emission scenario), the projected sea-level development leading up to the maximum level has also been plotted together with the 5–95 % confidence interval (upper dark blue line with black bars), data from Clark et al. (2016, supplementary material). The 2 560 Pg C emission scenario by Clark et al. (2016) represents the highest long-term sea-level projection, whereas the 2 °C warming scenario from Levermann et al. (2013) represents the lowest long-term sea-level projection under the RCP4.5 moderate emission scenario (Table 3-16). Also, the 1 280 Pg C projection by Clark et al. (2016) (grey line) fits within the RCP4.5 scenario. Even though all sea-level projections are not directly comparable because of different methodologies etc, the substantial difference between the highest and lowest projections is striking, clearly demonstrating the large uncertainty within the field of future sea-level rise in a warming climate caused by moderate carbon emissions. The isostatic uplift rate for the Forsmark site as projected by GIA modelling (see the text and Section 2.2.4) is shown by the solid green line. The isostatic change at Forsmark, unrealistically assuming that the present-day uplift rate of 6.7 mm a^{-1} (Vestøl et al. 2019, see the text) would continue in the future, is shown by the hatched green line. The evolution of relative sea level at Forsmark, constituting the net effect of the eustatic changes (blue lines) and isostatic changes (green lines) are shown in red. For an interpretation of the relative sea-level development at the Forsmark site (i.e. periods with transgression and regression, and associated periods of submerged conditions), see the text.*

In Figure 3-46, the upper solid green curve shows the isostatic uplift at Forsmark as projected by the GIA modelling (Section 2.2.4), and the lower hatched green line (unrealistically) assumes that the present-day isostatic uplift rate (6.7 mm a^{-1}, see Table 3-7) will continue at the same rate in the future. The difference between the eustatic and isostatic curves constitutes the relative sea-level development at the Forsmark site, giving an estimate of potential periods of transgression and regression and hence also estimates of submerged and terrestrial periods at the site.

The highest long-term sea-level projection until 12 000 AD, comparable to RCP4.5, is obtained in Clark et al. (2016) by the 2 560 Pg C total carbon emission scenario. The global mean SAT increase for this scenario in Clark et al. (2016) is ~ 4 °C by 2300 AD and ~ 3 °C by 12 000 AD , hence broadly representative of the upper bound of RCP4.5 (Figure 3-25). The rate of sea-level rise in this projection is relatively fast over the initial thousands of years, whereas it slows down and is almost zero at the end of the 10 000-year period. At 12 000 AD, the relative sea-level rise has reached a level of 37.5 ± 3.8 m

(Table 3-16 and Figure 3-46). The lowest projection over the same period results in a sea-level rise of 10.9 m (Levermann et al. 2013). This projection is an estimate of the multi-millennial sea-level commitment of 2 °C warming above pre-industrial levels (corresponds to ~ 1 °C above present levels), hence representative of the lower SAT range under RCP4.5 (Figure 3-25).

The substantially lower GMSL projections in these studies compared with Clark et al. (2016) is primarily explained by a much lower contribution from the Antarctic ice sheets. For example, whilst the 2 560 Pg C scenario in Clark et al. (2016) projects that Antarctica will contribute with almost 30 m to the multi-millennial GMSL rise, the 2 °C warming projection in Levermann et al. (2013) suggests that the Antarctic contribution will only be of couple of metres over the same time period. The widely different contributions from Antarctica between the studies are likely attributed to different amounts of global warming (~ 4 °C in Clark et al. 2016 versus 2 °C in Levermann et al. 2013), but possibly also to a higher sensitivity to global warming of the ice-sheet melting in Clark et al. (2016) than in Levermann et al. (2013).

The sea-level rise according to the highest projection (Clark et al. 2016, upper dark blue line) together with the isostatic curve for the Forsmark site from GIA modelling (solid green line) results in the relative sea-level curve shown by the upper solid red line. This line shows an initial transgression at the Forsmark site, peaking at around 4500 AD at a level of +12.3 m. This is followed by a regression back to the present-day situation at around 9500 AD (Figure 3-46). The transgression thus results in a ~ 7 500-year long period with a higher relative sea level than at present for the highest sea-level projection. To estimate the shortest time that a raised relative sea level could prevail, with this eustatic projection, a comparison is given with the linear development of isostatic uplift (hatched green line). The resulting relative sea level is shown by the hatched red line, showing that the period of raised relative sea level caused by the transgression will not end before ~ 7500 AD (Figure 3-46) under the highest eustatic projection.

The areas that would be permanently flooded with a relative sea-level rise of +12.3 m are shown in Figure 3-47.

In contrast to Clark et al. (2016), the lowest GMSL projections in Figure 3-46 do not provide much information on how the sea level changes with time. Therefore, as in the case of weak global warming (see Section 3.5.3 *Weak global warming*) a general time evolution of a low-end GMSL evolution (E_{low}), ranging from 2000 to 12 000 AD, is constructed using Equation 3-2. Using the constraints that (i) E_{low} should be equal to +10.9 m at 12 000 AD, which is consistent with the lowest projection at this time under moderate global warming (Levermann et al. 2013, see Table 3-16), and that (ii) the initial relative rate of sea-level change should be the same as the observed present-day rate at Forsmark, i.e. −4.1 mm a^{-1} (Table 3-7), the parameters of Equation 3-2 were set to a = 11.1 m and b = 0.15 ka^{-1}.

The constructed time series of the low-end GMSL evolution until 12 000 AD is shown by the lower light blue curve in Figure 3-46. If this curve is used together with the isostatic curve based on GIA modelling (solid green line), the resulting relative sea-level change is shown by the lower solid red line. This relative sea-level development shows a continued regression at the site, from the present and up to 12 000 AD and beyond.

The multi-millennial warming described by medium emissions comparable to RCP4.5 (~ 2–4 °C globally, see Figure 3-25) is comparable to some reconstructions of the Pliocene Epoch (5.33 to 2.58 Ma BP). In particular the so-called mid-Piacenzian Warm Period (MPWP), which is an interval during the Late Pliocene (3.264 to 3.025 Ma BP) that has frequently been used as an analogue for future anthropogenic warming since the global mean temperature during this period is estimated to have been 2–3 °C higher than during the pre-industrial era (Haywood et al. 2013). Therefore, GMSL reconstructions of the MPWP may be used to constrain the uncertainty range of the long-term future GMSL rise under a moderate warming, such as those featured in Figure 3-46. However, these historical reconstructions are highly sensitive to the techniques used to estimate the GMSL. As a result, mid-Piacenzian GMSL estimates in the literature range from ~ 10 to over 50 m above present levels (Naish and Wilson 2009, Miller et al. 2012, Rohling et al. 2014, Dutton et al. 2015, Winnick and Caves 2015, Dumitru et al. 2019), thus covering the entire uncertainty range of the future GMSL projections in Figure 3-46. It is therefore judged that these historical data cannot be used to constrain

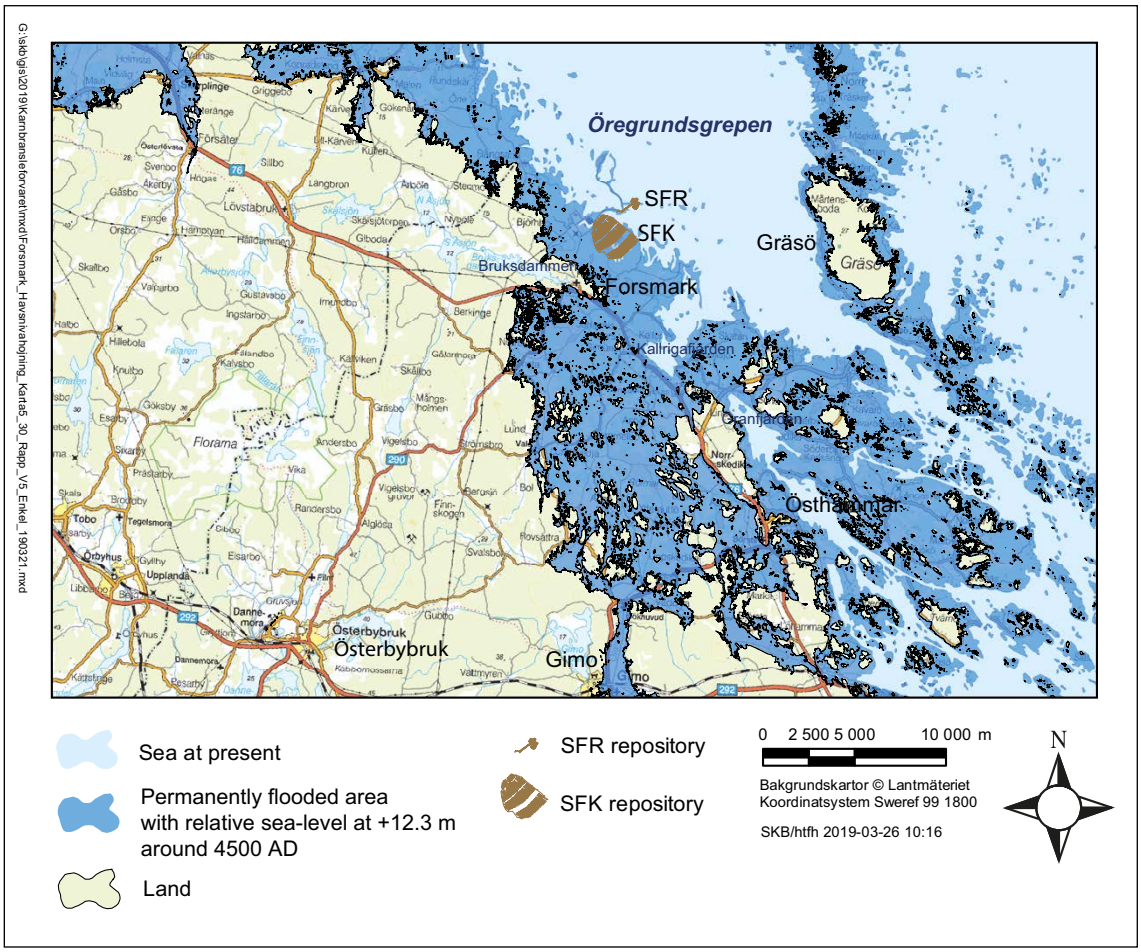

Figure 3-47. *Areas in the Forsmark region that will be permanently flooded with a relative sea level at 12.3 m (RH2000) at around 4500 AD. This transgression results from the intermediate emission long-term projection of GMSL rise of Clark et al. (2016) (Table 3-16 and Figure 3-46). In addition to this rise in mean sea level, the sea level may temporarily be higher than this by ~ 2 m during storm-surge events (c.f. info on the 2100 AD surge level, Table 3-13 and Figure 3-39). A raised relative sea level from this transgression would prevail until about 9500 AD, see the text. The present shoreline location is based on the Lantmäteriet Property map (www.lantmateriet.se).*

the uncertainty range of the multi-millennial sea-level rise under a moderate global warming.In summary, the above analysis shows that the very large spread in long-term projections of future sea-level rise (Table 3-16 and Figure 3-46) under a moderate global warming could result in either a transgression (more than + 12 m) at the Forsmark site, giving a higher-than-at-present relative sea level over the next 5 000–7 500 years (up until 7000–9500 AD), or, at the other end of the uncertainty spectrum, a situation with continued regression with no transgression at all at the site for the coming tens of thousands of years. As the uncertainty range cannot be constrained any further from GMSL data of past warm periods, both evolutions fit within the uncertainty range of long-term future sea-level rise under medium emissions.

Strong global warming (RCP8.5)

The compilation of selected GMSL projections from 2200 AD up to 12 000 AD, with a focus on projections based on high emissions, representing a strong global warming comparable to RCP8.5, is presented in Table 3-17. The published GMSL rise projections are illustrated in Figure 3-48 together with the estimated isostatic uplift for the Forsmark site, and the resulting local changes in relative sea level.

Table 3-17. Compilation of selected recent GMSL projections beyond 2100 AD until 12 000 AD with a focus on projections based on scenarios comparable with the RCP8.5 emission scenario. It should be noted that the values are not directly comparable because they may be based on different climate/emission scenarios and use different methodological assumptions. The 5 120 Pg C total emissions scenario by Clark et al. (2016) corresponds to a global annual mean SAT increase of up to ~ 7 °C (Figure 3-25), equivalent to the mid (for 2300 AD) to upper (2100 AD) bound of the RCP8.5 scenario, whereas Levermann et al. (2013) use a 4 °C warming scenario which approximately corresponds to the lower bound of RCP8.5 (Table 3-3). Hence the range in sea-level projections approximately represents the range in SAT increase for the RCP8.5 emission scenario. The 5 120 Pg C emission scenario by Clark et al. (2016) thus results in the highest long-term sea-level projection found in the literature, whereas Levermann et al. (2013) yields the lowest long-term projection under the RCP8.5 high emission scenario. The uncertainty range for DeConto and Pollard (2016) and Clark et al. (2016) has been recalculated from 1σ standard error to the 5–95 % confidence interval.

Year (AD)	Sea-level rise (m)	Notes	Reference
2200	2.7 5	83 % percentile 95 % percentile	Rohling et al. (2013)
	1.3–2.8 1.0–3.7	17–83 % percentile. RCP8.5 5–95 % percentile. RCP 8.5	Kopp et al. (2014)
	3 m per century	Worst case	Winkelmann et al. (2015)
	> 1 m		DeConto and Pollard (2016)
	1.0–3.7 9.7	RCP8.5 Extreme	Sweet et al. (2017b)
2300	0.92–3.59	RCP8.5	IPCC (2013a)
	2–3		Horton et al. (2014)
	0.6–3	Only Antarctic ice loss	Golledge et al. (2015)
	4.73 (3.41–6.82)	RCP8.5	Nauels et al. (2017)
	11.7 (9.1–15.6)	RCP8.5	Kopp et al. (2017)
2500	1.51–6.63		IPCC (2013a)
	15.65 (12.36–18.94)	5–95 % (± 1σ (± 2.0 m)) RCP8.5. Only Antarctic contribution	DeConto and Pollard (2016)
	5.48 (2.26–11.51)	5–95 %	Jevrejeva et al. (2012)
3000	1–2	Only Antarctic ice loss	Sutter et al. (2016)
3500	> 20	Only Antarctic ice loss	DeConto and Pollard (2016)
4000	9.0 (5.7–12.1)	4 °C of warming (lower end of RCP8.5)	Levermann et al. (2013)
5000	≤ 4	Only Antarctic ice loss	Sutter et al. (2016)
7000	9.55 15.41 35.99	Fast CO_2 drawdown Natural CO_2 drawdown No CO_2 drawdown RCP8.5. Only Antarctic ice loss	DeConto and Pollard (2016)
12 000	45.7 (42.2–49.2) 52 (47.9–56.1)	3 840 Pg C total emissions 5 120 Pg C total emissions (medium to upper end of RCP8.5)	Clark et al. (2016)
	25 ~ 38	For a 2.0 °C temp rise Specifically for RCP8.5	Clark et al. (2016) in Sweet et al. (2017a)
	13.9(11.8–15.9)	4 °C of warming (lower end of RCP8.5)	Levermann et al. (2013)

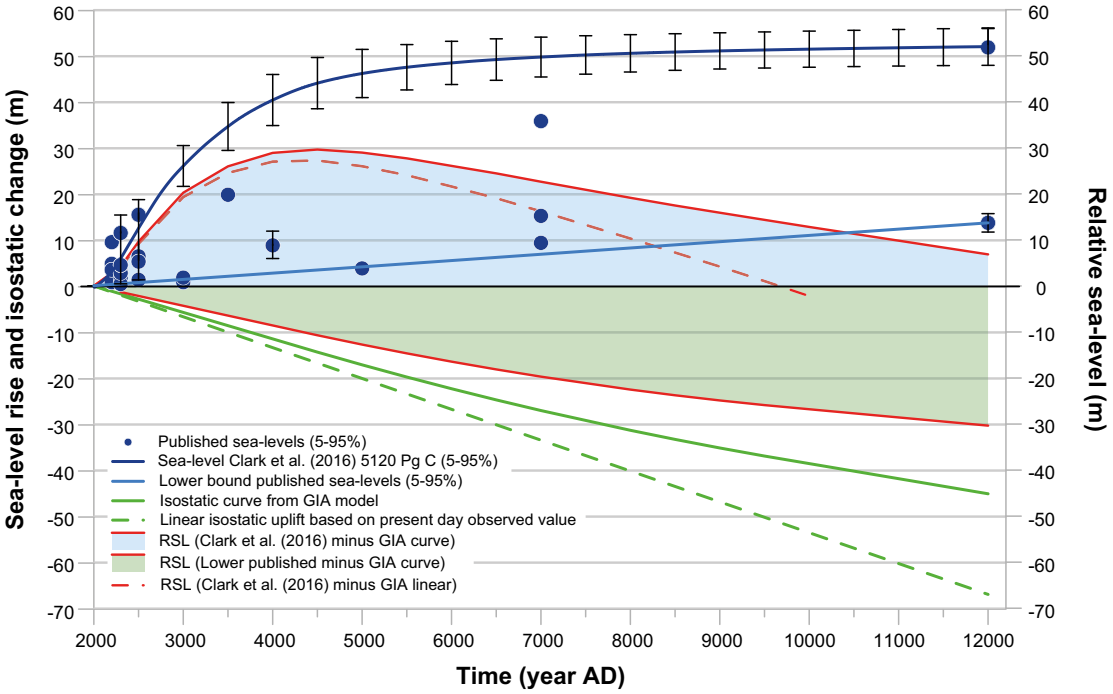

Figure 3-48. *Mean sea-level rise projections from 2200 to 12 000 AD from the compilation in Table 3-17. The values constitute sea-level projections under the RCP8.5 emission scenario or other high emission scenarios (Table 3-17) representing a strong global warming. Median values are shown by blue dots. When available, the uncertainty bars show the 5–95 % confidence interval based on all published sea-level projections at a given time slice. For the highest projected sea level at 12 000 AD (+52.5 ± 4.1 m from Clark et al. 2016 for a 5 120 Pg C total emission scenario), the projected sea-level development leading up to the maximum level has also been plotted together with the 5–95 % percentile error bars (upper dark blue line), data from Clark et al. (2016, supplementary material).The considerably slower sea-level rise according to the lowest projections in Table 3-17 is shown by the lower light blue line. In this way, the 5 120 Pg C emission scenario by Clark et al. (2016) represents the highest long-term sea-level projection, whereas Levermann et al. (2013) (Table 3-17) represents the lowest long-term projection. Even though all sea-level projections are not directly comparable because of different methodologies etc., the substantial difference between the highest and lowest projections is striking, clearly demonstrating the large uncertainty within the field of future sea-level rise in a warming climate caused by high-end carbon emissions. The isostatic uplift rate for the Forsmark site as projected by GIA modelling (Section 2.2.4) is shown by the solid green line. The isostatic change at Forsmark, assuming unrealistically that the present-day uplift rate of 6.7 mm a^{-1} (Vestøl et al. 2019, see the text) would continue in the future, is shown by the hatched green line. The evolution of relative sea level at Forsmark, constituting the sum of the eustatic changes (blue lines) and isostatic changes (green lines) are shown in red. For an interpretation of the resulting relative sea level at the Forsmark site (i.e. periods with transgression and regression) and the associated periods of submerged conditions, see the text.*

The highest 12 000 AD sea-level projection is the one given by Clark et al. (2016) (Table 3-17). This projection is based on a high emission scenario with a total release of 5 120 Pg C, corresponding to a global annual mean SAT increase of more than ~ 7 °C by 2300 AD (Figure 3-25), which corresponds to medium- to upper-end RCP8.5 temperatures (Figure 3-25, Table 3-3). The resulting GMSL rise is +52 ± 4.1 m by 12 000 AD (Figure 3-48, Table 3-17).

Figure 3-48 also includes the eustatic development leading up to this level, showing a rapid rise in GMSL over the coming 2–3 millennia, followed by a progressively slower increase up to 12 000 AD. For the 5 120 Pg C emission scenario, Clark et al. (2016) state that Greenland becomes ice free by ~ 4500 AD contributing with about 7 m of GMSL rise by that time, the Antarctic ice-sheets contribute with 45 m of GMSL rise by 12 000 AD, thermal expansion contributes with 2.8 m by the same time, whereas melting glaciers contribute with another 0.35 m GMSL rise within the coming few centuries. The sum of the above contributions is somewhat larger than the model ensemble mean sea-level rise of 52 m by 12 000 AD reported by Clark et al. (2016). The same study also suggests that the

470 Pg C already released by 2000 AD (IPCC 2013a) has committed Earth to a future GMSL rise of about 1.7 m (1.2 to 2.2 m). The minimum GMSL projections for the same 10 ka period include +1 m for 2200 AD (Kopp et al. 2014, Sweet et al. 2017b), 0.92 m for 2300 AD (for a RCP8.5 scenario in IPCC 2013a), 1–2 m at 3000 AD (for Antarctic ice-sheet loss only, in Sutter et al. 2016), 9 m at 4000 AD (for a 4 °C warming scenario in Levermann et al. 2013) and 14 m at 12 000 AD (for a 4 °C warming scenario in Levermann et al. 2013) (Table 3-17 and Figure 3-48).

The substantially lower GMSL projections in these studies compared with Clark et al. (2016) is primarily explained by a much lower contribution from the Antarctic ice sheets. For example, whilst the 5 120 Pg C scenario in Clark et al. (2016) projects that Antarctica will contribute with more than 40 m to the multi-millennial GMSL rise, the 4 °C warming projection in Levermann et al. (2013) suggests that the Antarctic contribution will only be approximately 5 m over the same time period. The widely different contributions from the Antarctica between the studies are likely attributed to different amounts of global warming (~ 7 °C in Clark et al. 2016 versus 4 °C in Levermann et al. 2013), but possibly also to a higher sensitivity to global warming of the ice-sheet melting in Clark et al. (2016) than in Levermann et al. (2013). Figure 3-48 also shows two curves of the isostatic uplift at the Forsmark site. The upper solid green curve shows the isostatic uplift at Forsmark as projected by the GIA modelling and the lower hatched green line, unrealistically, assumes that the present-day isostatic uplift rate (6.7 mm a^{-1}, see Table 3-7) would continue at the same rate over the next 10 millennia. The difference between the eustatic and isostatic curves constitutes the relative sea-level development at the Forsmark site, giving an estimate of periods of transgression and regression and hence also estimates on submerged and terrestrial periods at the site.

The highest sea-level projection (upper blue curve in Figure 3-48), in combination with the isostatic curve from GIA modelling (solid green curve) shows that the Forsmark site will be subject to a substantial initial transgression, since the isostatic uplift is far from being able to compensate for the strong eustatic rise over the coming millennia. The transgression peaks at around 4500 AD, with an RSL rise of ~ 30 m. If instead the linear isostatic curve is used (based on a constant present-day uplift rate, thus constituting the highest isostatic value that theoretically could prevail over this period of time), the resulting relative sea-level rise shows a similar peak at 4500 AD, and that this peak will be at least +27 m, given the high-end eustatic curve of Clark et al. (2016). The areas that would be flooded by a 30 rise in RSL are illustrated in Figure 3-49. Following the transgression, the results when using the isostatic curve from GIA simulations show a subsequent slow regression over many millennia, with the relative sea level reaching zero at around 15 700 AD (off the scale in Figure 3-48). This combination of highest projected eustatic rise and isostatic change according to the GIA simulations thus shows a higher-than-at-present relative sea level at the Forsmark site up to 15 700 AD.

This is in contrast to the result that follows from assumption of a constant isostatic rate for the next 10 ka (hatched green line in Figure 3-48), which most certainly overestimates the long-term isostatic development. However, the resulting relative sea-level curve (hatched red line) from using the linear isostasy and the highest sea-level projection, conclusively shows that the period with a raised relative sea level would not end sooner than ~ 10 000 AD. Hence, the two isostatic curves in Figure 3-48 can be regarded as representatives of two end members of possible isostatic developments at Forsmark. For the highest sea-level projections over the next 10 ka, this implies that Forsmark will be submerged at least up to ~ 10 000 AD but more probably up to 15 700 AD, when using the highest projection of sea-level rise (Clark et al. 2016, 5 120 Pg C emission case) (Figure 3-48, Table 3-17).

The results depicting a transgression up to around 15 700 AD (Figure 3-48) for the high emission eustatic projection by Clark et al. (2016), is in line with the results of potential future sea-level rise at Forsmark at 2100 AD under the RCP8.5 emission scenario (Section 3.5.2). In that analysis, the highest sea-level projections resulted in a clearly higher relative sea level at 2100 AD compared with at present (2000 AD) (Figure 3-39 and Table 3-13).

In contrast to Clark et al. (2016), the lowest GMSL projections in Figure 3-48 do not provide much information on how the sea level changes with time. Therefore, similar to the case of weak global warming (see Section 3.5.3 *Weak global warming*) a general time evolution of a low-end GMSL evolution (E_{low}), ranging from 2000 to 12 000 AD, is constructed using Equation 3-2. Using the constraints that (i) E_{low} should be equal to +13.9 m at 12 000 AD, which is consistent with ts-17), and that (ii) the initial rate of relative sea-level change should be the same as the observed present-day rate at Forsmark, i.e. −4.1 mm a^{-1} (Table 3-7), the parameters of Equation 3-2 were set to a = 20.6 m and b = 0.08 ka^{-1}.

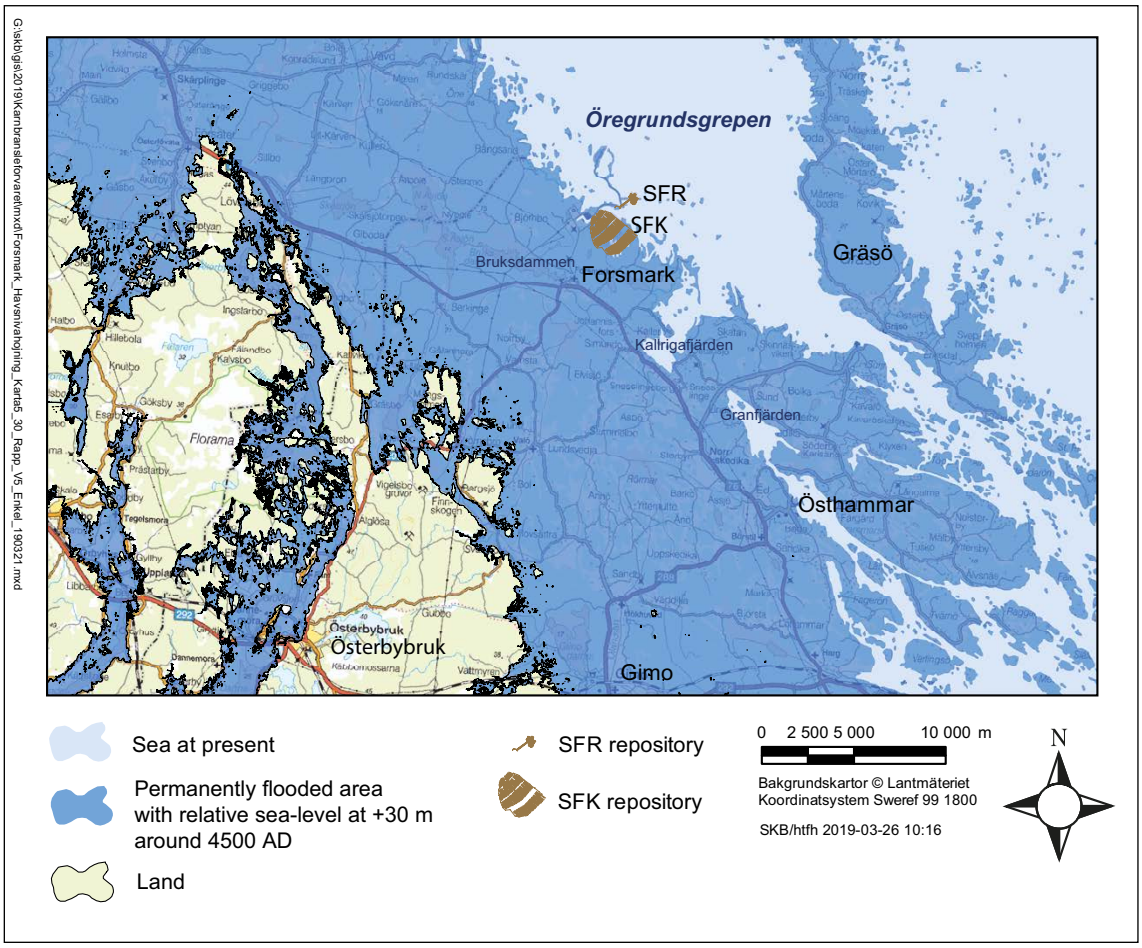

Figure 3-49. *Areas in the Forsmark region that will be permanently flooded with a relative sea level at +30 m (RH2000) at around 4500 AD. This transgression results from the high emission long-term projection of GMSL rise of Clark et al. (2016) (Table 3-17 and Figure 3-48). In addition to this rise in mean sea level, the sea level may temporarily be higher than this by ~ 2 m during storm-surge events (c.f. info on the 2100 AD surge level, Table 3-13 and Figure 3-39). A raised relative sea level from this transgression would prevail until at least ~ 10 000 AD but more likely up to 15 700 AD, see the text. The present shoreline location is based on the Lantmäteriet Property map (www.lantmateriet.se).*

The constructed time series of the low-end GMSL evolution until 12 000 AD is shown by lower light blue curve in Figure 3-48. If this curve is used together with the isostatic curve based on GIA modelling (solid green line), the resulting relative sea-level change shows that the Forsmark site will not be subject to a transgression at any time during the coming 10 ka. Instead, the present-day trend of a lowering of the relative sea level (a regression) would continue, despite the strong global warming comparable to RCP8.5. The same result, with no transgression, would be obtained by combining the lowest sea-level projections with the isostatic development based on a linear present-day uplift rate (green hatched line).

All in all, the above analysis shows that the very large spread in long-term projections of future sea-level rise (Table 3-17 and Figure 3-48) could result in either a very substantial transgression at the Forsmark site (up to +30 m in relative sea-level rise) with resulting conditions with a raised relative sea level prevailing for up to 12.5 millennia (up until 15 700 AD), or at the other end of the spectrum, a continued regression with no transgression at all at the site for the coming tens of thousands of years. Both evolutions fit within the uncertainty range of long-term future sea-level rise under high emissions.

Duration of initial submerged period above SFR

Table 3-18 summarises the possible durations of the submerged period at SFR for the amounts of global warming considered in this subsection. The values in the table have been calculated using the relative sea-level developments presented in Figure 3-45, Figure 3-46 and Figure 3-48 together with

the reference elevation for submerged conditions above SFR (−5.6 m in RH2000, see Section 1.4.3). As is evident in Table 3-18, the uncertainty in the duration of the submerged period is very large. The total uncertainty range is between 1 300 to 18 300 years depending on the amount of global warming and how the ice sheets and glaciers respond to the warming. The handling of this range in the overall safety assessment is described in the **Data report**, Chapter 12.

Table 3-18. Possible durations of the initial submerged period at SFR for different amounts of global warming.

Emissions scenario	Duration of submerged period
Weak global warming (RCP2.6)	1 300–2 700 years
Moderate global warming (RCP4.5)	1 400–9 400 years
Strong global warming (RCP8.5)	1 400–18 300 years

3.5.4 Relative sea-level change beyond 12 000 AD until 100 ka AP

Over timescales up to 100 ka, the uncertainties in the relative sea-level evolution at Forsmark are even greater than for the shorter timescales associated with the assessments of the relative sea-level change until 2100 AD (Section 3.5.2) and until 12 000 AD (Section 3.5.3). The large uncertainty is partially related to the long-term decline of atmospheric concentration of anthropogenic greenhouse gases, but also to the associated timing of the onset of the next glaciation (Section 3.4.5). Therefore, in contrast to the assessment of the relative sea-level change until 2100 AD and 12 000 AD, the analysis of the relative sea-level evolution until 100 ka AP also includes the possibility of extensive glaciations. This scenario is handled by assuming a repetition of the Weichselian glacial cycle for the next 120 ka. The constructed relative sea-level evolution in the Weichselian glacial cycle is primarily based on changes in isostasy, resulting from GIA modelling, and eustatic changes (Section 2.2.4). The resulting GIA development is shown by the grey curve in Figure 2-24 and discussed in Section 2.2.4 *Modelling of future isostatic adjustment*. The uncertainties associated with GIA modelling are discussed in Section 2.2.

In line with the approach used for the Weichselian glacial cycle, the GIA model in the global warming scenario was initiated by running one full glacial cycle to obtain realistic initial uplift rates. This was followed by a 50-ka long period of no change to the loading model, representative of a global warming climate without an ice-sheet forming in Fennoscandia. After that, the Weichselian glacial cycle with a 20 % reduction of the Fennoscandian ice-sheet thickness during the glaciated period was used for the remainder of the glacial cycle. The resulting isostatic adjustment is depicted by the green curve in Figure 2-24.

While the global warming scenario of the GIA modelling included a future collapse of the Greenland ice sheet, it did not account for any future changes of the Antarctic ice sheet (Section 2.2.4). However, as was also noted in Section 3.5.3, a collapse of the Greenland ice sheet would only have a negligible impact on sea level in the Baltic Sea and Forsmark area, implying that the GIA curve, in essence, only describes the isostatic change in the Forsmark area rather than being a realistic representation of the relative sea level. Because of this, the GIA curve can be used in combination with the estimated GMSL changes until 12 000 AD (Section 3.5.3) to estimate the range of possible relative sea-level changes at Forsmark for the next 100 ka under different levels of global warming.

The construction of the Forsmark relative sea level until 100 ka AP under a weak global warming (comparable to RCP2.6), moderate global warming (comparable to RCP4.5) and strong global warming (comparable to RCP8.5) is summarised in Figure 3-50. The methodology and assumptions leading up to the relative sea-level curves in that figure are described in the following.

- First, the high and low-end GMSL estimates until 12 000 AD (Section 3.5.3) were added to the first 10 ka of the isostatic curve from GIA modelling (green curve in Figure 2-24). Across all global warming scenarios considered here, the estimated GMSL change by 12 000 AD ranges from 2.5 m at the lowest end of a weak global warming (RCP2.6) to ~ 52 m at the high-end of a strong global warming (RCP8.5) (Section 3.5.3).

- For the period between 12 000 AD until 100 ka AP, it is assumed that the GMSL remains constant at its 12 000 AD value. Hence, during this period the relative sea level at Forsmark is completely determined by changes in the isostatic adjustment.
- The modelled isostatic adjustment, shown by the green curve in Figure 2-24, is used in the weak and moderate global warming cases. In those developments, it is assumed that Forsmark is glaciated by ~ 110 ka AP (Figure 2-24), resulting in a slight depression of the Earth's surface (i.e. an increase of the relative sea level) between ~ 85 and 100 ka AP (Figure 3-50a,b). In the case of a strong global warming, it is assumed that the onset of the next glaciation occurs (at least) several tens of thousands of years beyond 110 ka AP, implying that a local depression of the surface towards the end of the 100-ka period would not be physically justified. As a result, it is assumed that the local isostatic adjustment remains unchanged between 85 and 100 ka under a strong global warming.
- The resulting minimum in relative sea level occurs at ~ 70 ka AP for all cases, and ranges from –64 m for a low-end weak global warming to –15 m for a high-end strong global warming.

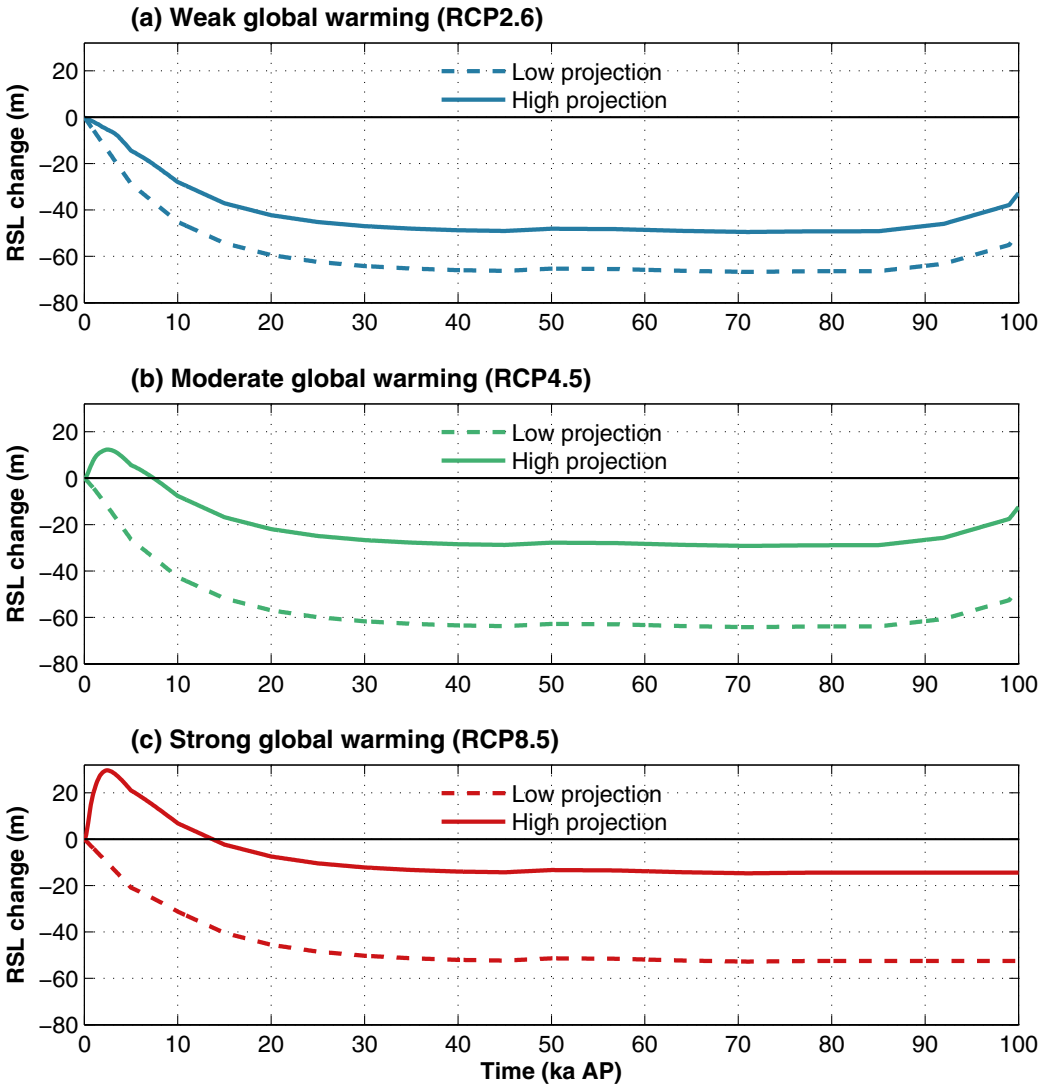

Figure 3-50. *Estimated relative sea-level evolution at Forsmark for the next 100 ka under (a) a weak global warming (comparable to RCP2.6), (b) a moderate global warming (comparable to RCP4.5), and (c) a strong global warming (comparable to RCP8.5). Solid curves represent high-end relative sea level estimates based on the highest GMSL projections until 12 000 AD, whereas dashed curves represent low-end relative sea-level estimates based on the lowest GMSL projections until 12 000 AD (Section 3.5.3). Zero sea-level change compared to present is highlighted by the black horizontal line.*

In addition to the uncertainties related to GIA modelling, discussed in Section 2.2, there are also other large uncertainties in the constructed relative sea-level curves presented in Figure 3-50 that need to be emphasised. First, the assumption of a constant GMSL between 10 and 100 ka AP is not realistic. During this period there will be significant variations of the Earth's orbit (Berger and Loutre 2002), yielding periods of both slightly colder and warmer temperatures than the ones simulated until 12 000 AD. Second, the climate during the next 100 ka will most likely be influenced by a continued decline of the atmospheric CO_2 concentration, resulting in a long-term cooling trend (Lord et al. 2019). These two effects combined, along with accompanying climate feedbacks, will influence e.g. the amount of water that is locked up in the ice sheets (and therefore the GMSL) both positively and negatively over this period. However, because the amplitude and timing of these changes are very uncertain, they have been omitted in the present analysis.

4 Qualitative likelihood assessment

4.1 Introduction

As described in Section 1.4.2, the handling of climate and climate-related issues aims to support the selection of the main scenario, less probable scenarios and residual scenarios. The selection of climate developments for the scenario categories is based on the combination of (i) likelihood of post-closure climate development and (ii) associated changes in the repository and its environs of relevance to post-closure safety.

To evaluate whether a specific climate development is probable (likely), unlikely or hypothetical (very unlikely), a qualitative likelihood assessment is conducted in this chapter. Specifically, the likelihoods of three aspects related to the future climate evolution are assessed, namely (i) the cumulative carbon emissions until 2100 AD (i.e. corresponding to the increase of the global mean SAT over the same time period, see further Section 4.2), (ii) the length of the current interglacial (i.e. corresponding to time up until the next occurrence of periglacial climate domain at Forsmark, see further Section 4.3) and (iii) time until the next glaciation at Forsmark (Section 4.4). The likelihoods related to the cumulative emissions are assessed for the RCP emission scenarios, whereas the likelihood of the next periglacial and glacial periods is assessed for different intervals within the 100-ka assessment period.

The likelihoods are measured qualitatively on a five-level scale based on current scientific understanding (Table 4-1), and support the selection of climate cases in Chapter 5.

Table 4-1. Qualitative likelihood scale used to identify relevant climate evolutions for the safety assessment scenarios.

Likelihood	Description
Very low	Highly unlikely to occur. Very little to no scientific evidence.
Low	Unlikely to occur. Not supported by most scientific evidence.
Moderate	Possible to occur. Scientific evidence is ambiguous. This category is also used when the likelihood assessment is highly uncertain.
High	Likely to occur. Supported by most scientific evidence.
Very high	Highly likely to occur. Scientific consensus.

4.2 Cumulative anthropogenic carbon emissions

As discussed in Section 3.4.1, the ratio of global SAT increase since the pre-industrial era to the cumulative carbon emissions is relatively constant over time and independent of emissions scenario (see also Collins et al. 2013 and references therein). This relationship arises as a consequence of the long lifetime of atmospheric CO_2 (Section 3.4.1), that the global-mean SAT anomaly is primarily controlled by the total amount of anthropogenic carbon emissions up to that point, including the historical emissions up until present.

Therefore, the likelihood assessment in this section focuses primarily on the cumulative amount of anthropogenic carbon emissions as described by the RCP scenarios. Further, the uncertainty in the SAT response to the amount of anthropogenic emissions is considered in the likelihood assessment.

The likelihood of the cumulative anthropogenic emissions and associated SAT response is assessed only until 2100 AD, though the SAT change on longer (multi-millennial) timescales is also of interest for the safety assessment (see Section 3.4.4). This choice is motivated by two reasons. First, the amount of reliable data that are needed to conduct a likelihood assessment is only available until 2100 AD. This includes abundant SAT projections, detailed descriptions of the underlying emissions scenarios, and simulations of the global carbon cycle. Second, most, if not all, emissions are projected to occur within this century, at least for the RCP2.6, RCP4.5 and RCP6.0 scenarios (e.g. Table 3-3). This means that the global SAT response, also over the next millennia and beyond, is expected to be largely determined by the course of events within this century. The same is however not necessarily

true for the RCP8.5 scenario, which is characterised by considerable emissions also during the next century. As RCP8.5 represents a high-end emissions scenario (see below), any departure from this scenario during the next century would likely result in lower emissions. However, if emissions were to be as high by 2100 AD as described by RCP8.5, it is reasonable to believe that similar emissions levels would continue also for at least a few decades into the next century. For simplicity, it is therefore assumed that the total cumulative emissions under RCP8.5 are an inevitable consequence of the high emissions until 2100 AD.

4.2.1 Background

Emission scenarios, such as the RCPs, which are used in future climate projections, are originally computed by so-called integrated assessment models (IAMs). In summary, these models describe how socioeconomic factors, such as population, economic growth, education, urbanisation and the rate of technological development may influence the natural world, including future greenhouse-gas emissions (e.g. IPCC 2014). The four RCPs used in the fifth IPCC assessment report (IPCC 2013a, hereafter referred to as IPCC AR5 in this section) were selected from a large ensemble of IAM simulations with the objective to cover a wide range of possible greenhouse-gas emission trajectories (e.g. van Vuuren et al. 2011). This range includes a high-end scenario without any specific climate mitigation target (RCP8.5), two intermediate scenarios with weak climate change mitigation (RCP4.5 and RCP6.0), and a strong mitigation scenario including the effect of net-negative emissions (RCP2.6). The total anthropogenic contribution is indicated by the number associated with each RCP (e.g. 4.5 and 8.5), which corresponds to the radiative forcing (in W m^{-2}) by 2100 AD relative to pre-industrial times (see also Section 3.4.1).[7]

Among the main advantages of the RCPs is that they provide standardised greenhouse-gas concentration inputs for climate models. This ensures that different models are driven by the same set of anthropogenic forcing, which in turn facilitates comparison between models without involving the large uncertainty associated with the global carbon cycle. One of the shortcomings of using RCPs, on the other hand, is that they lack any consistent set of socioeconomic descriptions, or "narratives", corresponding to each radiative forcing level (Moss et al. 2010). Therefore, in preparation for the sixth IPCC assessment report (IPCC AR6, IPCC 2021) a new set of scenarios was developed. In these new scenarios, entitled "Shared Socioeconomic Pathways" (SSPs), the radiative forcing targets from the RCPs have been accompanied with broad descriptions of different global socioeconomic trends. The SSPs describe different ways the world might develop in the absence of climate policy, and how different levels of climate change mitigation could be achieved when combined with different RCP targets. A total of five SSP narratives have been developed that describe a wide range of socioeconomic pathways, ranging from a world shifting towards renewable energy (SSP1) to a world dominated by an accelerated use of fossil fuels (SSP5), see Table 4-2. The radiative forcing targets from IPCC AR5 (2.6, 4.5, 6.0 and 8.5 W m^{-2}) are also included in the new SSP framework, together with some additional targets (1.9, 3.4, 7.0 W m^{-2}), see O'Neill et al. (2016). The naming of the new SSP scenarios generally follows the convention developed for the RCPs, with the exception that the corresponding number of the socioeconomic narrative is also included. As a result, for example, RCP8.5 corresponds to SSP5-8.5 in the new scenario framework.

Each SSP can be used with different levels of climate change mitigation (so-called mitigation scenarios), or in absence of climate mitigation policies (so-called baseline scenarios). Consequently, several 2100 AD radiative forcing targets can be achieved within the same SSP. For example, 6.0 W m^{-2}, which approximately corresponds to the 2100 AD baseline radiative forcing of SSP1 and SSP4 (Table 4-2), can also be reached under the other SSPs for different levels of climate change mitigation. Likewise, 4.5 W m^{-2} can also be achieved in every SSP. The same is however not true for 2.6 W m^{-2}, which was not possible to reach under SSP3 (Fujimori et al. 2017), and 8.5 W m^{-2}, which can only be achieved in SSP5 (see Table 4-2 and e.g. Riahi et al. 2017).

[7] Radiative forcing measures the combined effect of greenhouse-gas emissions and other factors, e.g. atmospheric aerosols, on climate warming.

Table 4-2. Summary of the Shared Socioeconomic Pathways (SSPs) used in the upcoming sixth IPCC assessment report (IPCC AR6, expected to be published in 2021). The baseline radiative forcing corresponds to the total anthropogenic forcing in the absence of climate policies. However, each SSP can also be combined with some level of climate mitigation to reach lower radiative forcing targets, see the text. For a complete description of the SSP narratives, see Riahi et al. (2017).

SSP	Short description	Approximate 2100 AD baseline radiative forcing (W m^{-2})
SSP1	Sustainability – Taking the Green Road	6.0
SSP2	Middle of the Road	7.0
SSP3	Regional Rivalry – A Rocky Road	7.0
SSP4	Inequality – A Road Divided	6.0
SSP5	Fossil-fueled Development – Taking the Highway	8.5

The fossil-fuel CO_2 emissions from the RCP and corresponding SSP scenarios are shown in Figure 4-1.[8] The grey shading of Figure 4-1 illustrates the no-policy baseline range from the SSP database (https://secure.iiasa.ac.at/web-apps/ene/SspDb, see Riahi et al. 2017). Figure 4-1 shows that the CO_2 emissions under RCP8.5 (and the new SSP5-8.5)[9] are close to the upper end of the baseline range, whereas emissions in the intermediate scenarios RCP4.5 (SSP2-4.5) and RCP6.0 (SSP4-6.0) stabilise close to the lower baseline range. As expected, the emissions under the strong mitigation scenario RCP2.6 (SSP1-2.6) are well below the baseline range. In summary, Figure 4-1 clearly illustrates the wide range of future emissions used by the IPCC to project different climate outcomes within this century, ranging from an emissions decline including net-negative emissions (RCP2.6 and SSP1-2.6) to a substantial emissions increase (RCP8.5 and SSP5-8.5).

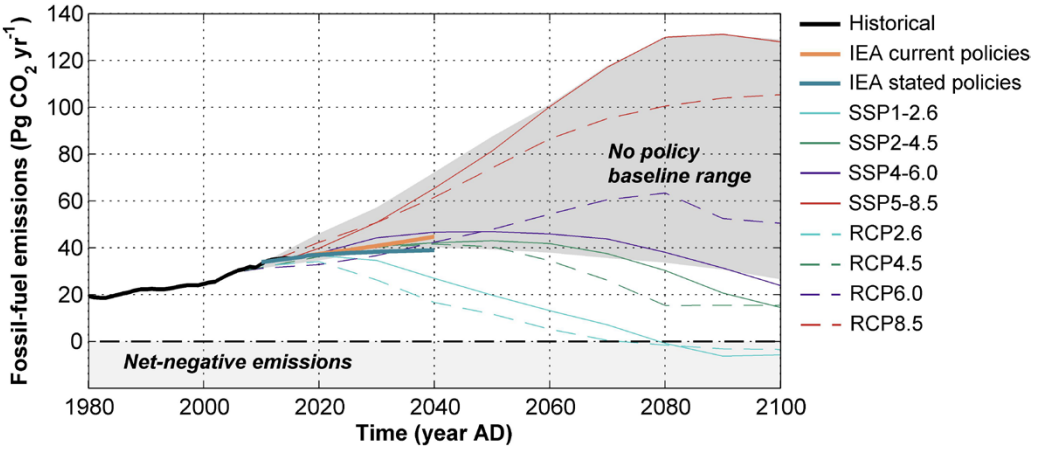

Figure 4-1. *Annual CO_2 emissions from fossil fuels (Pg CO_2 yr^{-1}) in all "Shared Socioeconomic Pathway" (SSP, Riahi et al. 2017) no-policy baseline scenarios (grey shading), RCP scenarios (dashed lines) and a subset of baseline and mitigation scenarios from the SSP database (thin solid lines). Also shown are the corresponding CO_2 emissions in the "current policies" (CPS) and "stated policies" (STEPS) scenarios from the International Energy Agency (IEA) World Energy Outlook (WEO) (IEA 2019), as well as historical emissions since 1980 AD from the Global Carbon Project (Le Quéré et al. 2018). RCP data were downloaded from https://tntcat.iiasa.ac.at/RcpDb (Moss et al. 2010), and SSP data were downloaded from https://secure.iiasa.ac.at/web-apps/ene/SspDb (Riahi et al. 2017).*

[8] Also other features, e.g. other greenhouse gases, aerosols and land use, contribute to the total 2100 AD radiative forcing described by the emission scenarios. However, as the fossil-fuel CO_2 emissions constitute the largest anthropogenic contribution to radiative forcing, it is shown here as illustration.

[9] The differences in CO_2 emissions between the RCPs and the SSPs, despite having similar total radiative forcings by 2100 AD, is explained by different contributions from atmospheric aerosols and other greenhouse gases. This means, for example, that the lower CO_2 emissions in RCP8.5 relative to SSP5-8.5 are compensated by greater emissions of other greenhouse gases, such that the total 2100 AD radiative forcing is approximately the same in both scenarios.

Whilst the IPCC emission scenarios reflect different potential climate outcomes, they have deliberately not been assigned any individual probabilities (Moss et al. 2010, Collins et al. 2013). As a result, they are typically treated with equal relative likelihoods in the climate literature. Contrary to the IPCC, however, other organisations have attempted to forecast the future development of anthropogenic emissions over the coming decades based on current policy plans, investment choices and trends in global energy supply and demand. An example of such work is provided in the recent UNEP Emissions Gap report, which predict that current policies would result in emissions from all greenhouse gases somewhere between RCP4.5 and RCP6.0 by 2030 AD (UNEP 2019).

A similar picture is revealed in the recent World Energy Outlook (WEO) by the International Energy Agency (IEA 2019). The WEO forecasts likely CO_2 emissions from fossil fuels until 2040 AD but does not include emissions from other greenhouse gases or CO_2 emissions from land-use change. They examine two scenarios based on current developments: (i) a current policies scenario (CPS) where no new climate policies are implemented, and (ii) a stated policies scenario (STEPS) where current climate policy commitments by countries are met. Both the IEA CPS and STEPS scenarios can thus be considered "business as usual" forecasts where either current or stated policies continue, but no additional climate policies are adopted after that point.

The fossil-fuel CO_2 emissions from IEA scenarios are also illustrated in Figure 4-1, together with the RCPs and SSPs. Both the IEA CPS and STEPS scenarios exhibit lower emissions until 2040 AD than most of the IPCC no-policy baseline scenarios. IEA CPS emissions are in the lower end of the SSP baseline emissions, comparable to RCP4.5 and RCP6.0, but well below RCP8.5. The STEPS scenario results in lower CO_2 emissions than any baseline scenario, with emissions slightly below RCP4.5. The fact that the IEA scenarios are below or in the lower end of the IPCC baseline range is not very surprising as several countries have already implemented, or committed to, various policies to mitigate climate change. This is also consistent with current trends in CO_2 emissions. Global emissions have indeed increased on average by approximately 1 % yr^{-1} over the last decade (Friedlingstein et al. 2019). At the same time, however, this increase would have been higher if it were not for the substantial emission reductions seen in several developed economies during this time (Le Quéré et al. 2019).

The IEA WEO forecasts are naturally associated with several uncertainties. First, they only cover the period up until 2040 AD and, therefore, give no insight on developments beyond that year. Second, there is also a large uncertainty associated with the future development of world's energy systems. For example, it has been demonstrated that the IEA forecasts consistently have underestimated the growth of renewable energy in past years (Creutzig et al. 2017). If this trend continues, the IEA might be overestimating future emissions even in the absence of new climate policies. Despite these uncertainties, it is here judged that the IEA forecasts are considerably more useful for estimating the likelihood of future emissions than the IPCC scenarios, where current trends in energy use and their consequences on future emissions are not specifically taken into account.

4.2.2 Assessed likelihoods

Table 4-3 shows the assessed likelihood of cumulative emissions based on different emissions scenarios. The likelihoods are motivated in the following subsections.

Table 4-3. Assessed likelihood of cumulative emissions based on the different emissions scenarios.

Emissions scenario	Likelihood of 2100 AD net cumulative anthropogenic carbon emissions
High emissions (RCP8.5)	Low
Medium emissions (RCP4.5 and RCP6.0)	high
Low emissions (RCP2.6 or lower)	moderate

High emissions (RCP8.5)

Under the RCP8.5 emission scenario, the global-mean SAT is projected to increase by ~ 4.5 °C by the end of the century relative to pre-industrial times (Table 3-3). RCP8.5 is comparable to scenarios with cumulative emissions of ~ 5 000 Pg C (Table 3-3). Different levels of high emissions have been considered when constructing the uncertainty range of the SAT evolution and relative sea-level change at Forsmark (Sections 3.4 and 3.5).

RCP8.5 was specifically designed to be a high-end no-policy scenario, located within the 90th and 98th percentile of the IAM scenarios developed in preparation for IPCC AR5 (van Vuuren et al. 2011). As discussed in Section 4.2.1, the radiative forcing target of RCP8.5 (8.5 W m^{-2} by 2100 AD) is also included in IPCC AR6 as part of the SSP scenario framework. However, as seen in Table 4-2, a forcing as high as 8.5 W m^{-2} can only be generated in one out of the five SSP baseline scenarios (see also Riahi et al. 2017). This suggests that RCP8.5 can only emerge under a narrow range of circumstances, and that any successful implementation of climate policies would lead to lower emissions and a radiative forcing below 8.5 W m^{-2} by 2100 AD.

To a certain degree, one could argue that the development towards lower emissions has already begun since the introduction of RCP8.5 about a decade ago. Since then, virtually all countries have signed the Paris Agreement, and several countries have implemented net-zero emission targets or other climate change mitigation policies. As a result, emissions have declined in several developed economies, mitigating the general increase of global emissions during this time (Le Quéré et al. 2019). Collectively, these developments mean that RCP8.5 has become, and continues becoming, increasingly unlikely each year. As a result, recent estimates of business-as-usual emissions suggest that they will more closely follow the path towards RCP4.5 or RCP6.0 rather than RCP8.5 (Figure 4-1).

A controversial feature of RCP8.5 is that the high emissions require a substantial increase in coal as a primary energy source, manifested by several-fold higher envisioned coal consumption at the end of century compared to present (Riahi et al. 2011, Kriegler et al. 2017, Ritchie and Dowlatabadi 2017). This development stems from a default assumption in most IAMs that abundant resources of coal and other fossil fuels are accessible at an affordable price (Capellán-Pérez et al. 2016). Two main arguments have however been put forward in recent years, from both a demand and supply side perspective, why such dramatic increase in coal use might not be very realistic.

First, the per-capita coal use has been relatively constant for the last 30 years and in general decline since 2014 AD (BP 2019). An unprecedented expansion of coal within this century, as featured in RCP8.5, is hard to envision even in the absence of new climate policies. This is particularly true when considering the rapid expansion and falling prices of renewable energy in recent years (e.g. Kåberger 2018, BP 2019). This development has for example resulted in renewable energy consumption in the USA recently surpassing coal for the first time in over 130 years (EIA 2020).

Second, although coal is typically seen as a vast abundant resource, there is a large uncertainty in the resource availability due to a lack of robust global estimates. Even if these uncertainties are taken into account, however, an emerging body of work in recent years propose that the amounts of coal required for RCP8.5 cannot be recovered economically and at a net energy profit (Mohr et al. 2015, Bauer et al. 2016, Capellán-Pérez et al. 2016, Ritchie and Dowlatabadi 2017). For instance, Capellán-Pérez et al. (2016) estimate that RCP8.5 only has 12 % probability of occurring based on the uncertainty in fossil-fuel resource availability.

In summary, the coal-dominated high emissions described in RCP8.5 are considered highly unlikely. This view is also shared among most energy experts, as illustrated in a recent subjective expert assessment which gives RCP8.5 only a 5 % change of occurring among all the possible no-policy baseline scenarios (Ho et al. 2019). Another aspect that points to the low likelihood of RCP8.5 is the possibility of so-called climate-economy feedbacks. In short, these feedbacks imply that damages from climate change reduce future economic growth, which would reduce emissions as a result (Woodard et al. 2019). The possibility of these feedbacks arguably contributes to reduce the low likelihood of RCP8.5 even further.

However, there are also other uncertainties that could potentially act in the opposite direction, i.e. they could result in a warming comparable to RCP8.5 even for relatively low emissions. One of the largest uncertainties is associated with the global carbon cycle and its response to global warming. As mentioned in Section 4.2.1, the introduction of the RCPs encouraged climate modelling groups to run their models with fixed concentrations of atmospheric greenhouse gases rather than the emissions underlying the RCPs. While this development facilitated comparison between models, it also meant that carbon cycle feedbacks were typically not included in the climate projections for IPCC AR5. It has been found that running the IPCC AR5 models using emissions underlying RCP8.5 leads to an average of 0.25 W m^{-2} higher 2100 AD radiative forcing across the models than when using a fixed set of concentrations (Friedlingstein et al. 2014). This suggests that when global warming is accounted for, simulated ocean and (possibly) land carbon uptakes are weaker than in the case when impact of climate change on global carbon cycle is not accounted for.

A similar conclusion was reached in a more recent study by Booth et al. (2017). Instead of comparing results from different models, as in Friedlingstein et al. (2014), they used a single climate model to explore a wide range of uncertain parameters for the land and ocean biogeochemical processes that influence carbon-cycle feedbacks. In their experiments, it was concluded that atmospheric CO_2 concentrations by 2100 AD may either decrease or increase compared with the standard RCP concentrations as a result of carbon-cycle feedbacks. However, they also found that the uncertainty range is greater towards higher concentrations rather than lower ones. As a result, for the RCP6.0 scenario, which is reasonably consistent with recent current-policy scenarios (see above), the CO_2 concentration across all carbon-cycle sensitivity experiments in Booth et al. (2017) was on average 8 % higher than in the standard RCP concentration. The highest estimate in Booth et al. (2017) exhibited a massive 40 % increase over the 2100 AD standard CO_2 concentration in RCP6.0. This means that under the highest carbon-cycle feedback estimates, emissions consistent with RCP6.0 could result in 2100 AD atmospheric CO_2 concentrations equal to those in the standard RCP8.5 scenario used in IPCC AR5. This is still considered an unlikely outcome, as only one of the 39 carbon-cycle feedback experiments in Booth et al. (2017) produced a result this high.

It is important to note that the range of carbon-cycle feedback estimates in Friedlingstein et al. (2014) and Booth et al. (2017) may still be relatively narrow, as many current carbon-cycle models lack a number of processes, including nitrogen cycle changes, dynamic vegetation and permafrost thaw.

The anthropogenic creation of reactive nitrogen is currently at least twice as large as the rate of the natural terrestrial creation (Ciais et al. 2013). This has resulted in significant nitrogen-cycle changes which have affected the climate in several ways, both directly and indirectly. Direct effects include increased atmospheric concentrations of nitrate aerosols and the greenhouse gas nitrous oxide (N_2O), which has increased from ~ 270 ppb during pre-industrial times to ~ 330 ppb at present (Myhre et al. 2013). Indirect effects include interactions with the global carbon cycle. According to IPCC AR5, "it is likely that reactive nitrogen deposition over land currently increases natural CO_2 sinks, in particular forests, but the magnitude of this effect varies between regions." (Ciais et al. 2013). This hence suggests that a stronger nitrogen cycle, on average, serves to mitigate the increase in atmospheric CO_2 concentration. Changes in vegetation cover may also have a large effect on the global carbon cycle in a warming climate. While the carbon storage in vegetation is projected to increase in high-latitude regions (e.g. Ciais et al. 2013), the situation in the tropics, where approximately half of the terrestrial carbon in vegetation is stored (e.g. Hubau et al. 2020), is much more uncertain. The projected increase in the amount of carbon stored in tropical land by 2100 AD ranges from ~ 0 to ~ 300 Pg C compared to present depending on the global carbon-cycle model (Cox et al. 2013). This large uncertainty can be partly explained by uncertainties in changes in tropical rainfall patterns (Jupp et al. 2010, Rammig et al. 2010), but also by different responses in different vegetation models (Galbraith et al. 2010).

Thawing of permafrost in high-latitude regions has the potential to release large amounts of buried carbon to the atmosphere. Current estimates suggest that carbon release from thawing permafrost soils range from 37 to 174 Pg C until 2100 AD under high-emission scenarios (IPCC 2019). Assuming, for simplicity, that all this carbon would end up as CO_2 in the atmosphere, this range corresponds to ~ 140–640 Pg CO_2 until 2100 AD. This can be compared with the difference in 2100 AD cumulative fossil-fuel emissions, which amounts to ~ 2 500 Pg CO_2 between RCP8.5 and RCP6.0, and ~ 4 300 Pg CO_2 between SSP5-8.5 and SSP4-6.0. Hence, high-end carbon-release estimates from permafrost

thawing account for ~ 25 % of the difference in fossil-fuel emissions between RCP8.5 and RCP6.0, and only ~ 15 % between the corresponding scenarios in the SSP framework. Moreover, recent studies have also found that most, if not all, of the potential CO_2 release from permafrost thawing may be offset by increased plant growth in high-latitude boreal regions, at least during this century (Kleinen and Brovkin 2018, McGuire et al. 2018). Hence, even if permafrost thawing will likely somewhat contribute to higher atmospheric CO_2 concentrations, current estimates suggest that its contribution is relatively small in comparison to the difference in anthropogenic emissions between RCP8.5 and RCP6.0.

Permafrost thawing may also release carbon as CH_4, which is a greenhouse gas with a stronger global warming potential than CO_2 (Myhre et al. 2013). However, while inducing a stronger global warming, CH_4 also has a much shorter lifetime in the atmosphere compared to CO_2, amounting to only a little more than a decade (Myhre et al. 2013). Hence, a sudden influx of CH_4 to the atmosphere may increase temperatures temporarily for a few decades, but it would have a relatively small impact on temperatures over the longer timescales considered here.

Another major uncertainty concerns the sensitivity of Earth's climate to increases in CO_2 and other greenhouse gases. Climate sensitivity is often measured by the equilibrium SAT increase in response to doubling of the atmospheric CO_2 concentration. In IPCC AR5, it was estimated that the climate sensitivity is likely between 1.5 and 4.5 °C per doubling of atmospheric CO_2. For the highest sensitivities, the SAT increase under RCP6.0 would be comparable to the projected median SAT increase under RCP8.5 (Collins et al. 2013). Although such high-end climate sensitivity cannot be excluded, it is not considered the most likely outcome. Most evidence from modelling, instrumental records and paleo data suggest that the sensitivity is in the range of 2 °C to 4 °C per doubling of CO_2 (IPCC 2013a). This sensitivity is also consistent with the average SAT increase under different RCP scenarios reported in IPCC AR5 (see Table 3-3).

There is also a possibility that fossil-fuel use will be prevalent for centuries after 2100 AD, even if a successful emissions-reduction is achieved within this century. To that end, cumulative emissions comparable to RCP8.5 may be reached in the long-term, well beyond 2100 AD. This also includes an uncertainty related to the potential exploration of unconventional fossil-fuel resources, i.e. coal, oil or natural gas that cannot be extracted by well-established methods. At the same time, over these longer timescales it is also conceivable that the technical development of efficient negative emission technologies has progressed sufficiently for it to be employed on a global scale. Such development would counteract possible increases of the cumulative emissions. All in all, it is virtually impossible to assess the likelihood of these socioeconomic and technological developments on these longer timescales, why this assessment focuses on the emissions up until 2100 AD.

In summary, accounting for the unlikely high anthropogenic emissions described by RCP8.5 as well as the uncertainties related to carbon-cycle feedbacks and climate sensitivity, the likelihood of the cumulative emissions and associated SAT increase described by RCP8.5 is assessed to be *low* (Table 4-3).

Medium emissions (RCP4.5 – RCP6.0)

Under the RCP4.5 and RCP6.0 emission scenarios, the end-of-century global-mean SAT is projected to increase by 2.4–2.8 °C relative to pre-industrial times (Table 3-3). Different levels of medium emissions have been considered when constructing the uncertainty range of the SAT evolution and relative sea-level change at Forsmark (Sections 3.4 and 3.5).

As discussed in Section 4.2.1, recent projections suggest that current and pledged climate policies will put global CO_2 emissions on a path within the range of RCP4.5 and RCP6.0 (IEA 2019, UNEP 2019, see Figure 4-1).

Given that these recent business-as-usual projections suggest that future anthropogenic emissions will be similar to RCP4.5 or RCP6.0, the likelihood of the cumulative emissions and associated initial SAT evolution described by these emission scenarios is assessed to be *high* (Table 4-3).

Low emissions (RCP2.6)

Under the RCP2.6 scenario, global warming is projected to stay below 2 °C relative to pre-industrial times (Table 3-3), i.e. compatible with the Paris Agreement (UNFCCC 2015). RCP2.6 is comparable with other low emission scenarios, e.g. emission pathways required for SAT stabilisation below 1.5 °C warming as explored in a recent IPCC special report (IPCC 2018), as well as to scenarios with cumulative emissions below ~ 1 000 Pg C (Table 3-3). This scenario also includes the possibility of "net-negative" emissions, i.e. net removal of CO_2 from the atmosphere by natural and technological measures. Different levels of low emissions have been considered when constructing the uncertainty range of the SAT evolution and relative sea-level change at Forsmark (Sections 3.4 and 3.5).

As discussed in Section 4.2.1, business-as-usual emissions are projected to be considerably higher than in RCP2.6 (Figure 4-1). Although renewable energy has been growing at an unprecedented rate in recent years (e.g. BP 2019), contributing to a significant drop in emissions in several countries (Le Quéré et al. 2019), a persistent reduction in current global greenhouse-gas emissions is yet to be seen (Friedlingstein et al. 2019). However, while global emissions on average have increased with ~ 1 % yr^{-1} over the last decade (Friedlingstein et al. 2019), they are expected to decline by ~ 4–7 % in 2020 as a result of the COVID-19 pandemic (Le Quéré et al. 2020). This is still slightly less than the 7.6 % drop in annual emissions required between 2020 and 2030 AD to limit global warming below 1.5 °C (UNEP 2019), but it is well in line with the necessary annual reductions to stay below 2 °C warming. It is however judged unlikely that such unprecedented rate of emissions reduction will continue also after the pandemic. Therefore, meeting the goals of the Paris Agreement solely by means of substantial emission reductions within the coming decades is also not considered a likely outcome in the present work. This assessment is however highly uncertain due to the potential development of future technologies that may be employed at a large scale to remove CO_2 from the atmosphere. Therefore, following the definition of handling highly uncertain assessments in Table 4-1, the likelihood of low net future carbon emissions and associated initial SAT evolution is assessed to be *moderate* (Table 4-3).

4.3 Timing of first transition to periglacial climate conditions (length of current interglacial)

In this section, the likelihood related to the timing of first transition to periglacial climate domain is assessed. This time also marks the end of the current temperate period at Forsmark.

4.3.1 Background

The present annual average SAT at Forsmark is about 6 °C based on the 1986–2005 AD reference period (Section 3.3). For permafrost to develop at the site, numerical modelling suggests the annual average SAT must be reduced to lower than 0 °C (Hartikainen et al. 2010, Brandefelt et al. 2013). A substantial cooling of that magnitude in the Forsmark area can only occur if embodied in a planetary-scale cooling trend, which would inevitably result in the initiation and growth of ice sheets elsewhere in the Northern Hemisphere. Therefore, it is judged that the first occurrence of periglacial conditions at Forsmark can only occur in conjunction with, or subsequent to, the next glacial inception in the Northern Hemisphere.

4.3.2 Assessed likelihoods

The assessed likelihoods of occurrence of the first transition to the periglacial climate domain during latter and first half of the 100-ka assessment period are shown in Table 4-4. The likelihoods are motivated in the following subsections.

Table 4-4. Assessed likelihoods of the timing of the first transition to the periglacial climate domain (length of current interglacial at Forsmark).

Timing of first transition to the periglacial climate domain (length of current interglacial)	Likelihood of occurrence
50–100 ka AP	Moderate
< 50 ka AP	Very low

50–100 ka AP

As discussed in Section 3.4.5, most studies project that the next glacial inception will occur following the insolation minimum at 54 ka AP for anthropogenic carbon emissions comparable to RCP2.6 or lower. In addition, a few sensitivity simulations of Lord et al. (2019) suggest that the next glacial inception may occur in the response to the 54 ka AP insolation minimum also under cumulative emissions comparable to business-as-usual (RCP4.5–RCP6.0). However, most of the simulations of Lord et al. (2019) as well as simulations from other studies (e.g. Archer and Ganopolski 2005, Ganopolski et al. 2016) collectively project that the next glacial inception will occur after 100 ka AP under business-as-usual emissions (Figure 3-28 and Figure 3-30). Since the business-as-usual emissions are considered to be the most likely development (Section 4.2.2), the first transition to periglacial climate domain will most likely occur after the end of the assessment period, and the current interglacial will thus most likely continue for more than 100 ka. However, the likelihood of strong mitigation of near-future climate change is assessed to be *moderate* (Section 4.2.2). Thus, the same likelihood is considered adequate for permafrost development within the latter half of the assessment period (Table 4-4).

< 50 ka AP

The period until 50 ka AP is mostly characterised by significantly higher summer insolation than at present (Figure 3-29a). Development of periglacial conditions at Forsmark during this period could realistically only occur in response to the summer insolation minimum at 17 ka AP. This insolation minimum is relatively weak, manifested by insolation values similar to those at the present day (Figure 3-29a). In the study of Brandefelt et al. (2013), it was concluded that permafrost can only develop in response to this weak insolation minimum for highly pessimistic assumptions about the ground surface conditions, and the future evolution of atmospheric CO_2 and climate (see also Section 2.1.4). However, no studies have illustrated the possibility of periglacial conditions at Forsmark caused by this insolation minimum, or any other period between present day and 50 ka AP, for *realistic* climate and surface conditions (Section 3.4.5). Glacial inception before 50 ka AP is only projected in one study in Section 3.4.5 (Pimenoff et al. 2011), which suggests that the next glacial inception is imminent for pre-industrial CO_2 levels (Figure 3-28). This result is however not considered realistic, in particular when accounting for the present elevated levels of atmospheric greenhouse gases. Therefore, the likelihood of periglacial conditions at Forsmark before 50 ka AP is assessed to be *very low* (Table 4-4).

4.4 Timing of first transition to glacial climate conditions

In this section, the likelihood related to the timing of first future glacial climate conditions is assessed.

4.4.1 Background

As described in Section 4.3.1, it is judged that the first occurrence of periglacial conditions at Forsmark can only occur in conjunction with, or subsequent to, the next glacial inception in the Northern Hemisphere. Glacial inception typically occurs in high-latitude mountainous areas. In Fennoscandia this would be expected to be in the Scandinavian Mountains. It would then take thousands or even tens of thousands of years for the Fennoscandian ice sheet to reach Forsmark. Therefore, the overall likelihood of glacial conditions at Forsmark within the assessment period is lower than that of periglacial conditions.

4.4.2 Assessed likelihoods

The assessed likelihood of occurrence of the first transition to the glacial climate domain during latter and first half of the 100-ka assessment period is shown in Table 4-5. The likelihoods are motivated in the following subsections.

Table 4-5. Assessed likelihoods of the timing of the first transitions to the glacial climate domain at Forsmark.

Timing of first transition to the glacial climate domain	Likelihood of occurrence
50–100 ka AP	Low
< 50 ka AP	-

50–100 ka AP

As shown in Figure 3-29, the climate system is particularly susceptible to glacial inception during two insolation minima within the latter half of the assessment period: at 54 ka AP and at 97 ka AP. Potential radiological consequences of a glaciation are only of interest after the deglaciation of the Forsmark area, and humans are again available for exposure. Thus, any potential ice-sheet development at Forsmark in response to the 97 ka AP is of minor relevance for this safety assessment. Therefore, only the likelihood of glaciation at Forsmark resulting from the insolation minimum at 54 ka AP is assessed in this section.

As discussed in Section 3.4.5 and 4.3.2, glacial inception in the Northern Hemisphere in conjunction with the insolation minimum at 54 ka AP is likely if anthropogenic carbon emissions are comparable to RCP2.6 or lower. However, even if glacial inception were to occur in response to this insolation minimum, it is far from certain that an ice sheet would reach the Forsmark site.

Over the course of a glacial cycle, ice sheets tend to grow slowly and progressively, with ice-sheet advances during relatively cold phases (stadials) and reduced ice growth, or even ice-sheet retreat, during warmer phases (interstadials), see Sections 3.1 and 3.2. This pattern of ice-sheet growth is seen in data of the last 800 ka and explains the general saw-tooth shape of the global ice volume evolution during this time (e.g. Figure 3-2). During the Weichselian glacial cycle, the slow and progressive pattern of ice-sheet growth meant that it took ~ 50 ka for the ice sheet to reach the Forsmark site after the initial glaciation in the Scandinavian mountain range (see e.g. Figure 2-39 and Figure 3-23). The time of Forsmark glaciation approximately corresponds to the third minimum in summer insolation since the start of the Weichselian glacial cycle (Figure 3-30), during the Marine Isotope Stage 4 stadial. A faster ice-sheet expansion than seen during the Weichselian glacial cycle would likely require more humid atmospheric conditions as this could induce higher precipitation rates along the ice-sheet slopes, and therefore, a faster propagation speed of the ice sheet (Sanberg and Oerlemans 1983, Liakka and Nilsson 2010).

The Weichselian glacial cycle was primarily dominated by ice growth in North America, characterised by a several-fold higher ice-sheet volume than in Eurasia (e.g. Kleman et al. 2013). Therefore, the timing of the first glaciation at Forsmark during the Weichselian glacial cycle may have been somewhat delayed as compared with other glacial cycles. If the next glacial cycle were to be characterised by a larger relative ice growth in Eurasia, similar to e.g. the penultimate Saalian glacial cycle (e.g. Svendsen et al. 2004), it is possible that glaciation at Forsmark would occur at an earlier stage than suggested by the Weichselian glacial cycle. There are, however, no reliable data of the early stages of the Saalian glacial cycle that could either confirm or reject this hypothesis (e.g. Colleoni and Liakka 2020).

The slow and progressive development towards colder conditions is generally also seen in model simulations of the future climate (e.g. Berger and Loutre 2002, Archer and Ganopolski 2005, Lord et al. 2019). These models typically do not yield information about the geographical distribution of future ice sheets, but they are useful for comparing global characteristics of anticipated future glacial inception events with past ones. In Lord et al. (2019), for example, most of the 90 ensemble

simulations under the "natural" scenario[10] project that the increase in global ice volume during the next glacial inception around 60 ka AP will be similar to the one during the last glacial inception around 110 ka BP, but lower than that during the time of Forsmark glaciation around ~ 60 ka BP (Figure 3-30). Based on this result, Lord et al. (2019) argue that the next glaciation of Forsmark will occur towards the end of the assessment period and prevail beyond 100 ka AP.

Although associated with significant uncertainties, most available scientific information, both from modelling and paleoclimate proxy data, suggests that a potential ice-sheet expansion following the insolation minimum at 54 ka AP would not reach the Forsmark site. Therefore, the likelihood of glacial conditions at Forsmark following this insolation minimum is assessed to be *low*, even if glacial inception were to occur elsewhere in the Northern Hemisphere at this time (Table 4-5).

< 50 ka AP

The possibility of ice-sheet development over Forsmark prior to 50 ka AP is judged as exceptionally low, and therefore not assigned a likelihood according to the five levels in Table 4-1. According to the long-term climate projections (Section 3.4.5), the only situation that could possibly result in a glaciation at Forsmark before 50 ka AP is an imminent glacial inception. Given the current elevated concentrations of greenhouse gases in the atmosphere, such situation is however considered unrealistic, despite a relatively low summer insolation at this time (Figure 3-29).

[10] The "natural" scenario in Lord et al. (2019) assumes no anthropogenic influence on the climate (see Section 3.4.5).

5 Climate cases

5.1 Introduction

This chapter presents the climate cases used in the PSAR safety assessment. The climate cases illustrate the most important and reasonably foreseeable sequences of future climate states of relevance for the protective capability of the repository. Thus, a climate case represents a possible future development of climate and climate-related issues in Forsmark over the next 100 ka. The definition of the climate cases is based on the climate-related issues relevant for post-closure safety (Chapter 2) and the scientific knowledge on the past, present and future climate evolution (Chapter 3). To account for the uncertainty in future climate evolution as well as different climate-related issues, several climate cases are defined.

The climate-related issues permafrost (Section 2.1), isostatic adjustment and relative sea-level change (Section 2.2) and ice-sheet dynamics (Section 2.3) are included in the description of the climate cases. Surface denudation above the repository is expected to be small such that post-closure safety is not affected (Section 2.4). Therefore, this issue is not included in the description of the climate cases.

As described in Section 1.4.2, the handling of climate and climate-related issues aims to support the selection of the main scenario, less probable scenarios and residual scenarios. The main scenario takes into account the most probable changes in the repository and its environs. To this end, the main scenario is based on a range of probable climate evolutions, as described by the reference external conditions (Section 1.3.1). Less probable scenarios consider uncertainties that are not accounted for in the framework of the main scenario. Thus, climate evolutions that are reasonably foreseeable, yet unlikely to occur within the assessment period, are analysed in less probable scenarios. Finally, highly unlikely or even hypothetical developments of the climate that would have a more severe influence on individual barriers and barrier function are identified in support of the analysis of residual scenarios. No process relevant for the integrity of the repository has been identified that could be impacted by the high temperatures projected for the high emissions scenario (RCP8.5). This *low* likelihood climate evolution is therefore not included in a climate case in the PSAR. The effects of a warmer climate of importance for post-closure safety, e.g. relative sea level, surface hydrology and irrigation demand, are considered in the main scenario (**Post-closure safety report**, Section 7.5). In addition, the potential importance of future sea-level rise for post-closure safety is further analysed in a dedicated supporting calculation of the main scenario (**Post-closure safety report**, Section 7.7).

The temporal development of the climate cases is described in terms of transitions between climate domains (Section 1.4.3). In the description of the climate cases, these transitions are assumed to occur instantaneously. In reality, however, the transitions may be relatively complex and occur over periods of several hundreds to thousands of years depending on the climate domains that are being considered. Typical transition durations between climate domains are presented in Appendix F.

5.2 Reference external conditions

In this section, the climate cases included in the reference external conditions are described. These describe the range of probable climate evolution over the next 100 ka. To this end, two climate cases are defined from the likelihood assessment in Chapter 4, namely (i) the *warm climate case*, representing a *high*-likelihood evolution based on business-as-usual anthropogenic greenhouse-gas emissions (comparable to RCP4.5/RCP6.0), and (ii) the *cold climate case*, representing a *moderate*-likelihood evolution by which climate change is strongly mitigated within this century (comparable to RCP2.6), see Section 4.2.

In addition to these two cases, the *present-day climate case*, is included in the reference external conditions. It describes a simplified development, characterised by continuation of present-day climate conditions at Forsmark for the entire assessment period. This climate case is identified by the overall safety assessment rather than from the anticipated future climate evolution. The *present-day climate case* is further described below (Section 5.2.1), followed by a description of the *warm climate case* (Section 5.2.2) and *cold climate case* (Section 5.2.3).

5.2.1 Present-day climate case

General description

The *present-day climate case* is chosen as a simplified development where present-day climate conditions prevail for complete assessment period, and the initial shoreline displacement is dominated by the isostatic rebound following the last glaciation. Although the assumption of present-day climate conditions over the next 100 ka is not realistic, per se, the *present-day climate case* is considered to give a reasonable basis for evaluation of developments in the repository and its environs that occur under constant climate conditions. Also, the overall development is in agreement with the assessment that the Forsmark climate will likely remain temperate for the next 100 ka if current, or higher, levels of anthropogenic greenhouse-gas emissions continue over coming decades (Section 4.3). Further, this climate case supports the regulatory requirement that the description should include a case where the biosphere conditions prevailing at the time for the application will not change (SSMFS 2008:37).

Air temperature, precipitation and potential evapotranspiration

The *present-day climate case* assumes that the present-day air temperature, precipitation and potential evapotranspiration at Forsmark, as documented in Section 3.3, will prevail for the entire assessment period of 100 ka.

Relative sea level

The *present-day climate case* assumes that the contribution of future sea-level rise is negligible, such that the relative sea-level evolution at Forsmark is dominated by the post-glacial isostatic rebound. Thus, the relative sea-level development indicated by the green curve in Figure 3-45 is assumed (associated data are given in Appendix A of Brydsten and Strömgren 2013). The same development was used in the global warming- and early periglacial climate cases in the SR-PSU (SKB TR-13-05, Chapter 4). This development results in 1 000 years of initial submerged conditions above the repository, using the definition outlined in Section 1.4.3.

Evolution of climate domains

Assuming present-day climate conditions for the entire assessment, consequently, also results in a continuation of temperate conditions at Forsmark during this period (Figure 5-1). Submerged conditions are considered for the first 1 000 years.

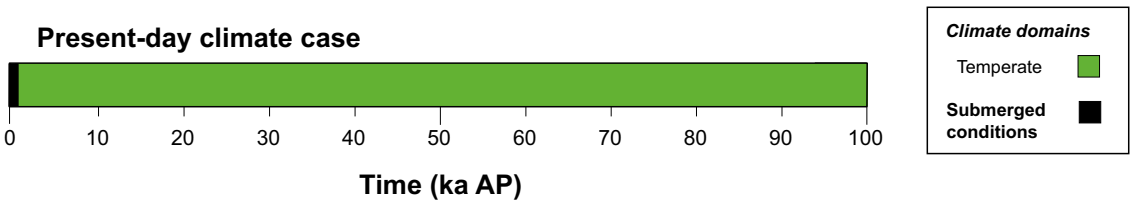

Figure 5-1. *Succession of climate domains, including periods of submerged conditions, in the present-day climate case.*

5.2.2 Warm climate case

General description

The *warm climate case* assumes that anthropogenic greenhouse-gas emissions comparable to present levels will continue for the next few decades, after which they gradually decline towards net-zero emissions by the beginning of the 22nd century. To this end, this climate case represents a likely development in line with the IPCC medium emissions scenarios RCP4.5 and RCP6.0 as well as recent projections of business-as-usual anthropogenic greenhouse-gas emissions (Section 4.2). This climate case also describes higher sea levels as a result of the warming, resulting in a prolonged period of submerged conditions in the area above SFR.

Air temperature, precipitation and potential evapotranspiration

In the *warm climate case*, the elevated concentrations of CO_2 and other atmospheric greenhouse gases result in a considerably warmer climate than in the *present-day climate case*. The annual average SAT is assumed to follow the average projection under RCP4.5 (Figure 3-27); thus, it increases by up to 5 °C above the present air temperature within the current millennium, after which it will slowly decline over the following tens of thousands of years.

Annual precipitation at Forsmark is projected to increase with higher temperatures (Section 3.4.4), with a maximum increase of 10–20 % relative to present-day for the maximum warming (5 °C) under RCP4.5 (green lines in Figure B-8, panel b). The range represents an uncertainty in the precipitation response during the summer months (June to August) where the lower value of the range corresponds to a decrease in the summer precipitation compared to present, whereas the higher value corresponds to increased summer precipitation (Appendix B, Section B2).

Due to increased air temperatures, the annual potential evapotranspiration is also expected to increase. In the *warm climate case*, the change in potential evapotranspiration with air temperature is calculated using the methodology introduced in Pereira and Pruitt (2004) and presented in Appendix D. Using this methodology, the maximum increase in annual potential evapotranspiration, resulting from a 5 °C warming, is estimated to be ~ 34 %.

Relative sea level

In the *warm climate case*, the initial submerged period is prolonged as a result of the climate warming. The uncertainty in Forsmark relative sea level under business-as-usual anthropogenic greenhouse-gas emissions (RCP4.5) is described by two alternative developments, corresponding to either a marine transgression or a continued marine regression over the next millennia (Figure 3-46 and Figure 5-2). As discussed in Section 3.5.3, it is not possible to deduce a most likely relative sea-level change from this range. Therefore, the mean of the uncertainty range is chosen for the *warm climate case*. The resulting initial period of submerged conditions above SFR is 4 500 years for this development (Figure 5-2).

The *warm climate case* is comparable to the extended global warming climate case in the SR-PSU, which also featured a prolonged initial period of submerged conditions above SFR (SKB TR-13-05, Chapter 4). The duration of this period in the SR-PSU climate case was only 2 200 years, thus considerably shorter than the 4 500 years included in the *warm climate case*. This difference reflects a general tendency in the scientific literature since the SR-PSU towards more high-end projections of future sea-level rise (Section 3.5).

Evolution of climate domains

Most modelling studies of the long-term future climate evolution project that the current interglacial will be prolonged for at least 100 ka under these levels of emissions (Section 4.3). As a result, similarly to the *present-day climate case*, the *warm climate case* is characterised by temperate climate conditions at Forsmark for the entire assessment period (Figure 5-3). The initial submerged period is set to 4 500 years, i.e. 3 500 years longer than in the *present-day climate case*.

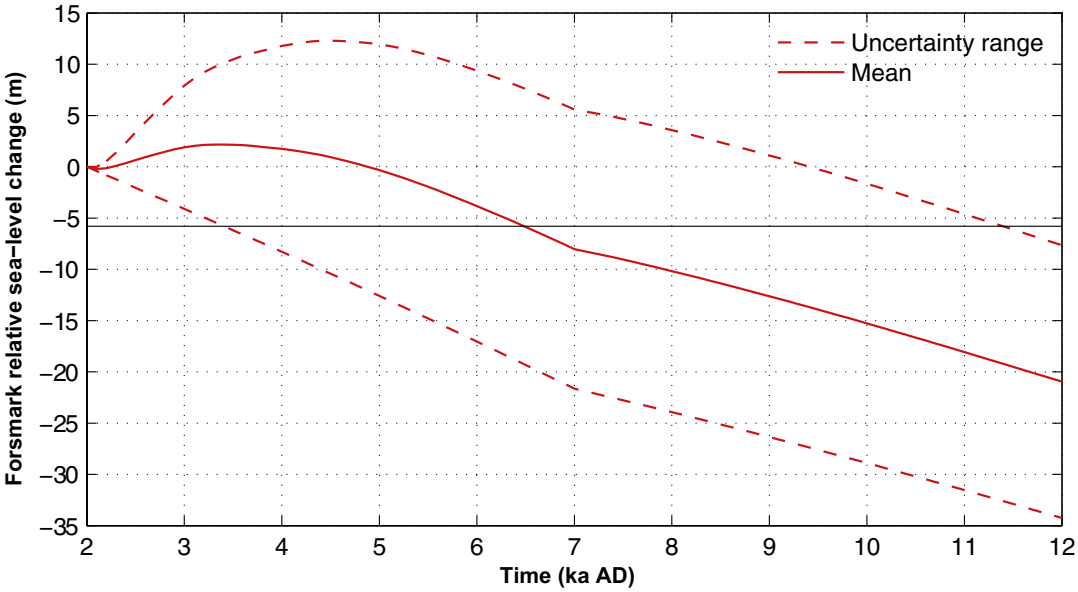

Figure 5-2. *Projected future relative sea-level change at Forsmark until 12 000 AD under the RCP4.5 emission scenario, which is in line with business-as-usual estimates of anthropogenic greenhouse-gas emissions. The uncertainty range (red dashed lines) represents the highest and lowest projected relative sea-level change at Forsmark under these emissions (same as the solid red lines in Figure 3-46). For details on how the uncertainty range has been compiled, see Section 3.5.3. The relative sea level evolution described in the warm climate case is taken as the mean of this uncertainty range (red solid line). The threshold at which point the area above SFR is defined to become terrestrial (see text) is shown by the grey horizontal line (Section 1.4.3). The relative sea level in the warm climate case meets this threshold after 6500 AD, thus resulting in 4 500 years of submerged conditions after the closure of the repository.*

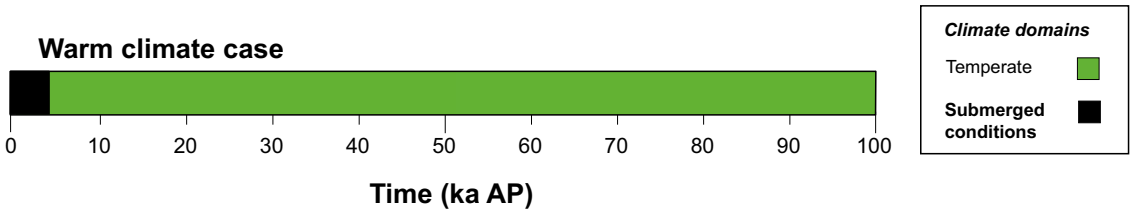

Figure 5-3. *Succession of climate domains, including periods of submerged conditions, in the warm climate case.*

5.2.3 Cold climate case

General description

The *cold climate case* represents a future development characterised by substantial reductions in anthropogenic greenhouse-gas emissions and/or removal of atmospheric CO_2 by technological measures. The development assumed in this climate case is thus comparable with the RCP2.6 emissions scenario. Under these developments, atmospheric CO_2 is projected to have returned to pre-industrial levels within the first 50 ka AP (Sections 3.4.1 and 4.3), resulting in growth of Northern Hemisphere ice sheets in response to the next substantial minimum in summer insolation around 54 ka AP (Section 3.4.5).

As described in Section 4.4, glacial inception in the Northern Hemisphere does *not* necessarily mean that the Forsmark site will be glaciated. Initial ice accumulation typically occurs in Arctic or subarctic high-altitude regions, such as the Scandinavian Mountain Range. Following this initial phase, it may take up to several tens of thousands of years for an ice sheet to grow sufficiently large to reach south-central Sweden and the Forsmark area (Sections 3.2 and 4.4). Thus, although it cannot be excluded, it is considered unlikely that an ice sheet will reach the Forsmark site following the insolation minimum at 54 ka AP (Section 4.4). Instead, build-up of ice sheets elsewhere in the Northern Hemisphere will likely induce further cooling of the climate at Forsmark too, resulting in periglacial conditions and

permafrost development in the region (Section 3.4.5). As a result, the *cold climate case* includes the occurrence of periglacial conditions and permafrost development at Forsmark during the latter half of the assessment period.

The main difference between the *cold climate case* and the *present-day climate case,* of relevance for the safety assessment, is the occurrence of periglacial conditions in the *cold climate case*. Therefore, the following descriptions mostly focus on the periglacial periods.

Air temperature, precipitation and potential evapotranspiration

For permafrost and frozen conditions to develop in the bedrock, modelling studies suggest that the annual average air temperature needs to drop at least below freezing (Hartikainen et al. 2010, Brandefelt et al. 2013). The colder climate during periglacial conditions emerges from the combination of relatively low atmospheric CO_2 concentration and reduced insolation during the boreal summer season, resulting in the growth of ice sheets elsewhere in the Northern Hemisphere. These global-scale changes naturally are associated with considerable uncertainties, resulting in a wide range of possible air temperatures that could influence the development of permafrost and frozen conditions at Forsmark. Brandefelt et al. (2013), for example, estimated that permafrost development in response to the insolation minimum at 54 ka BP could be accompanied by air temperatures at Forsmark ranging from approximately −11 °C to –1 °C, depending on e.g. atmospheric greenhouse-gas concentrations and Northern Hemisphere ice cover. The entire air temperature range is considered in the *cold climate case* during periglacial conditions.

Annual precipitation is expected to decrease during periods of periglacial conditions (e.g. Section 3.2.2). However, also the annual potential evapotranspiration is expected to decrease due to the colder conditions. Taken together, the simulations by Kjellström et al. (2009) suggest that potential evapotranspiration will decrease more than the precipitation, thus resulting in an increase of the net precipitation (i.e. the difference between precipitation and potential evapotranspiration). Based on the results from Kjellström et al. (2009), the *cold climate case* assumes that the net precipitation increases by ~ 25 % compared with the *present-day climate case* (see also Werner et al. 2013, Section 5.8.3).

During temperate conditions, the air temperature, precipitation and potential evapotranspiration are expected to be slightly higher than in the *present-day climate case*, especially during an initial period when the atmospheric CO_2 concentrations might be elevated compared to present day. However, as warmer-than-present air temperatures are already accounted for in the *warm climate case*, the same air temperature, precipitation and potential evapotranspiration as in the *present-day climate case* are assumed during temperate conditions in the *cold climate case*.

Relative sea level

The relative sea-level development at Forsmark in the *cold climate case* is assumed to be identical to that of the *present-day climate case*, i.e. it includes a negligible contribution of future sea-level rise (Section 5.2.1). This is a reasonable assumption as a development towards colder climate conditions in the latter half of the 100-ka assessment period likely requires that the ongoing climate warming is strongly mitigated within the next few decades (Section 4.3). Even if the consequences of the warming, such as global sea-level rise, may continue for centuries after the emissions have been reduced, isostatic effects mean that the current shoreline regression will likely continue if the emissions are strongly reduced (Section 3.5.3).

Periglacial conditions

The evolution of climate domains in the *cold climate case* is structurally similar to the global warming climate case in the SR-PSU (SKB TR-13-05, Chapter 4). As in the *cold climate case*, the SR-PSU global warming climate case also described temperate conditions for the first 50 ka, followed by colder climate conditions with recurring periods of periglacial conditions during the last 50 ka of assessment period. The timing and duration of each period with periglacial conditions in the SR-PSU were primarily inferred from reconstructed conditions of the Weichselian glacial cycle (Section 3.2.3). However, whilst these data yield information on the climate evolution of the last 120 ka, they are not representative for the next 100 ka when insolation changes will be very different compared to the past 120 ka (Section 3.4.5).

Therefore, the methodology for estimating the timing and duration of future periglacial periods has been updated since the SR-PSU. In the present safety assessment, these periods are derived from the modelling study of Lord et al. (2019). They used a combination of climate modelling techniques to analyse the impact of future changes in insolation, global ice volume and CO_2 on the Forsmark climate (Sections 3.4.1 and 3.4.5). To estimate future periods of periglacial conditions, it is assumed that permafrost prevails at Forsmark when the projected surface air temperature in their "natural" scenario (assuming no future CO_2 emissions) decreases by more than 7 °C below present. This approximately corresponds to an annual average air temperature at Forsmark of –1 °C, which is equivalent to the temperature threshold required for permafrost development when assuming relatively dry atmospheric conditions with limited snow and vegetation cover on the ground surface (Hartikainen et al. 2010, Brandefelt et al. 2013). In the projection by Lord et al. (2019), assuming no anthropogenic CO_2 emissions, the Forsmark air temperature drops below –1 °C during two periods within the coming 100 ka: between 59 and 67 ka AP, and between 79 and 100 ka AP (Figure 5-4). Although the exact timing of the periglacial periods is arguably sensitive to specific model parameters used in Lord et al. (2019), the broad trend in the long-term climate evolution obtained in that study, manifested by two phases of colder conditions after 50 ka, is consistent with most other modelling studies on long-term climate change (Section 3.4.5). Therefore, the timing of the periglacial periods, as derived from the simulations in Lord et al. (2019), is used to define the periods of periglacial conditions in the *cold climate case*.

Evolution of climate domains

The evolution of climate domains in the *cold climate case* is identical to the *present-day climate case*, with the exception of two periods of periglacial conditions: between 59 and 67 ka AP and between 79 and 100 ka AP (Figure 5-5).

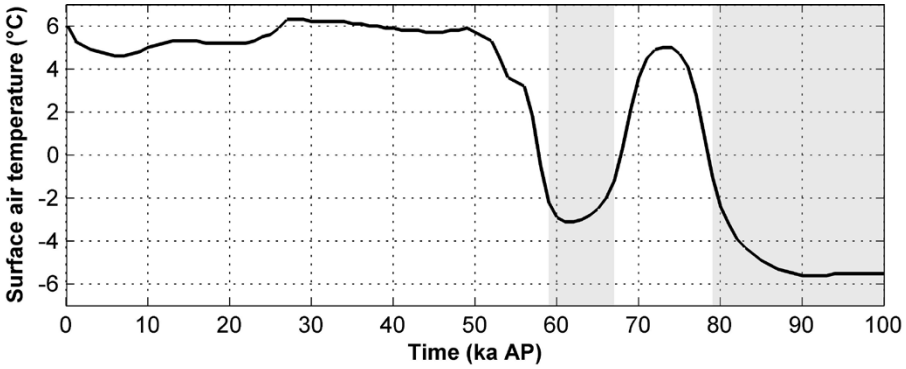

Figure 5-4. *Evolution of the surface air temperature change at Forsmark for the next 100 ka, as projected by the "natural" scenario (i.e. no anthropogenic greenhouse-gas emissions) in Lord et al. (2019) (black line). The grey shadings indicate periods when the Forsmark surface air temperature is projected to drop below –1 °C. This temperature threshold is used to define periods of periglacial conditions in the cold climate case (see the text).*

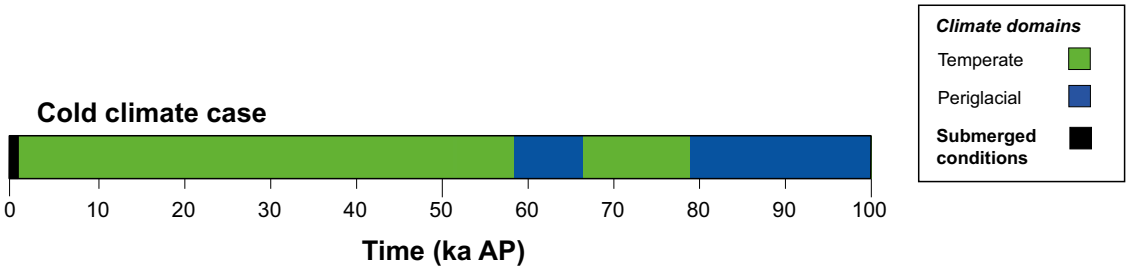

Figure 5-5. *Succession of climate domains, including periods of submerged conditions, in the cold climate case.*

5.3 Climate cases evaluated in less probable scenarios

Climate cases evaluated in less probable scenarios represent developments of potential importance for post-closure safety that are identified with *low* likelihood in Chapter 4. One climate case, the *glaciation climate case*, was identified based on these criteria.

5.3.1 Glaciation climate case

General description

The *glaciation climate case* assumes that the development towards colder climate conditions after 50 ka will result in ice-sheet development such that glacial conditions prevail at Forsmark within the assessment period. Potential doses to humans are typically several orders of magnitude higher during temperate periods – when vast land areas can be exploited for cultivation and agriculture – than during glacial periods when the area is covered by an ice sheet. Therefore, a potential glaciation at Forsmark resulting from the 54 ka AP insolation minimum is of particular interest as this enables radiological consequences to be evaluated during temperate conditions subsequent to deglaciation and submerged conditions at the site. Periods of temperate conditions subsequent to Forsmark glaciations and submerged periods that result from later insolation minima (around 77 ka AP and 96 ka AP, see Figure 3-29) would emerge after the 100-ka assessment period.

As argued in Section 4.4, ice-sheet development at Forsmark in response to the 54 ka AP insolation minimum is considered to be a less likely development than the continuation of temperate conditions throughout the assessment period or the development of periglacial conditions during the latter half of the assessment period.

Air temperature, precipitation and potential evapotranspiration

In the *glaciation climate case*, the air temperature, precipitation and potential evapotranspiration are assumed to be identical to the *present-day climate case* (Section 5.2.1) during temperate conditions and to the *cold climate case* (Section 5.2.3) during periglacial conditions.

During glacial conditions, the air temperature, precipitation and potential evapotranspiration to some extent controls the extent and duration of the glaciation (which is already explicitly described by the climate case, see subsection *Glacial conditions* below). Apart from this, air temperature, precipitation and potential evapotranspiration are not of relevance for the safety assessment during the glacial conditions.

Glacial conditions

The timing and duration of the glacial periods, including the thermal conditions (frozen/unfrozen) beneath the ice sheet, are adopted from the Weichselian glacial cycle climate case in the SR-PSU (SKB TR-13-05, Chapter 4). The same glacial conditions were also used in the reference glacial cycle climate case used in the safety assessments of the spent nuclear fuel repository, e.g. SR-Site (SKB TR-10-49). These climate cases represent a repetition into the future of conditions reconstructed for the last 120 ka (Section 3.2.3). Although changes in insolation over the next 100 ka are expected to be considerably different than during the past 120 ka, periods of glacial conditions in the climate cases coincide reasonably well with the timing of anticipated future periods of colder climate conditions and ice-sheet growth in the Northern Hemisphere (Sections 3.4.5 and 4.3).

In accordance with the SR-PSU Weichselian glacial cycle climate case, the 100-ka long assessment period encompasses two glacial periods at Forsmark. The first glacial period begins at 57.6 ka AP, a few thousand years after the summer insolation minimum at 54 ka AP, and the second glacial period begins at 90.8 ka AP. Further, frozen conditions beneath the ice sheet are considered to persist during the initial 4 300 years of the first glaciation. During the remaining time of the first glacial period (also 4 300 years), as well as the entire second glacial period, thawed conditions are considered at repository depth as well as at the surface.

Periglacial conditions

Permafrost and frozen ground develop during periglacial climate conditions, but may, or may not, also prevail beneath an ice sheet during glacial conditions (Section 1.4.3). For an ice sheet to advance over a region, below-freezing annual air temperatures are required for some time prior to the ice-sheet migration (Section 3.2.3). Thus, the landscape at Forsmark is considered to be dominated by periglacial conditions prior to the ice-sheet advance over the region.

The durations of the periglacial periods are derived from the same future climate projection (Lord et al. 2019) as in the *cold climate case* (Section 5.2.3). However, whilst periglacial conditions in the *cold climate variant* were defined to arise when the annual average surface air temperature at Forsmark drops below −1 °C, in this projection a lower threshold of −3 °C during ice-free conditions is used in the *glaciation calculation case*. The lower threshold is defined by the consideration that a rapid Northern Hemisphere ice-sheet expansion, as assumed in this climate case, typically requires more precipitation which produces a thicker average snow cover on the ground. Since snow has an insulating effect on permafrost, a lower threshold in the air temperature would be needed for permafrost to develop (e.g. Hartikainen et al. 2010). Further, using a lower threshold is arguably cautious as it results in shorter periods of periglacial conditions and, consequently, in a longer period of temperate conditions when doses to humans are higher.

Using the −3 °C threshold from Lord et al. (2019) results in 3 000 and 1 000 years of periglacial conditions prior to the first and second glaciation at the site, respectively. These periods are considerably shorter than the corresponding periods of periglacial conditions in the SR-PSU Weichselian glacial cycle climate case. In that climate case, periglacial conditions prevailed for 20 ka of the latter 50 ka of the assessment period as opposed to only 4 000 years in the *glaciation climate case*.

Relative sea level

The development of the relative sea level, up until the time of the first glaciation, is assumed to be the same in the *present-day climate case* (Section 5.2.1). As argued for the *cold climate case* (Section 5.2.3), this assumption is reasonable given that a development towards colder conditions during the last 50 ka of the assessment period likely requires that the effects of climate change, including sea-level rise, are strongly mitigated within the next few decades.

After the first glaciation, the Forsmark site is considered to be submerged beneath the sea for almost 10 ka. The duration of this period is adopted from the SR-PSU Weichselian glacial cycle climate case (SKB TR-13-05, Chapter 4), and thus follows from a repetition of the reconstructed conditions of the last glacial cycle (Section 3.2.3).

Evolution of climate domains

The evolution of climate domains is shown in Figure 5-6. In order not to underestimate the radiological consequences of a glaciation, the period of temperate and terrestrial conditions after the first glacial period is assigned a relatively long duration of 13.9 ka. Together with the preceding submerged period, this results in almost 24 ka of uninterrupted temperate conditions after the first glaciation in this climate case. Such an extended period of continuous temperate interstadial conditions, embedded within a glacial cycle, is considered to be pessimistic. For example, in the reconstruction of the Weichselian glacial cycle (Section 3.2.3), which is supported by geological records, the terrestrial period between the first and second glaciation is dominated by periglacial conditions rather than temperate conditions. This notion is also supported by the future climate projections by Lord et al. (2019). In the simulations assuming a reduced anthropogenic influence on climate, they found that a substantial cooling at Forsmark after the 54 ka AP insolation minimum is typically followed by about 10 ka of air temperatures above freezing, thus less than half of the almost 24 ka assumed here.

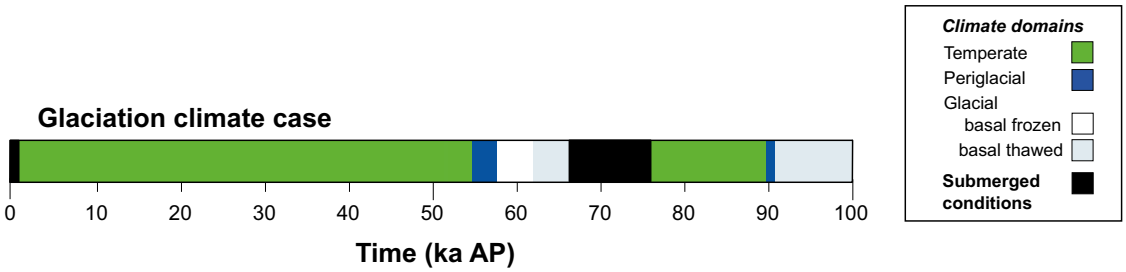

Figure 5-6. *Succession of climate domains, including periods of submerged conditions, in the glaciation climate case.*

5.4 Climate cases evaluated in residual scenarios

Climate cases evaluated in less probable scenarios represent developments associated with *very low* likelihood in Chapter 4 that serve to illustrate the significance of individual barriers and barrier functions. One climate case, the *hypothetical early permafrost climate case*, was identified based on these criteria.

5.4.1 Hypothetical early permafrost climate case

General description

This climate case considers a period of periglacial conditions before 50 ka AP. Thus, it is reminiscent of the early periglacial climate case which was included in the main scenario in the SR-PSU (SKB TR-14-01). However, owing to its very low likelihood of occurrence (Section 4.3) and its demonstrated low impact on annual dose in the SR-PSU (SKB TR-14-01, Brandefelt et al. 2016, Näslund et al. 2017a, b), an early period of permafrost development is analysed in a residual scenario in the present safety assessment rather than in the main scenario.

Air temperature, precipitation and potential evapotranspiration

During temperate conditions, the air temperature, precipitation and potential evapotranspiration are assumed to be identical to the *present-day climate case* (Section 5.2.1), whereas during periglacial conditions, the air temperature range as well as the net precipitation of the periglacial periods of the *cold climate case* are assumed (Section 5.2.3).

Note that in this climate case, it is also assumed that the cold conditions during periglacial periods may cause freezing of the repository concrete structures and result in the formation of an ice-lens around the silo bentonite. It is important to emphasise that these events are *not* considered to be realistic; even in the highly unlikely event of a periglacial period before 50 ka AP (Section 4.3), the combined climate and permafrost modelling presented in Section 2.1.4 show that freezing of the concrete structures before 50 ka AP can be excluded.

Relative sea level

See the *cold climate case* (Section 5.2.3).

Periglacial conditions and evolution of climate domains

The timing and duration of the early periglacial period are inferred from the SR-PSU supplementary study of Näslund et al. (2017a). Thus, the evolution of climate domains is identical to the *base case* with the exception of a hypothetical periglacial period between 10 and 15 ka AP. The evolution of climate domains is shown in Figure 5-7.

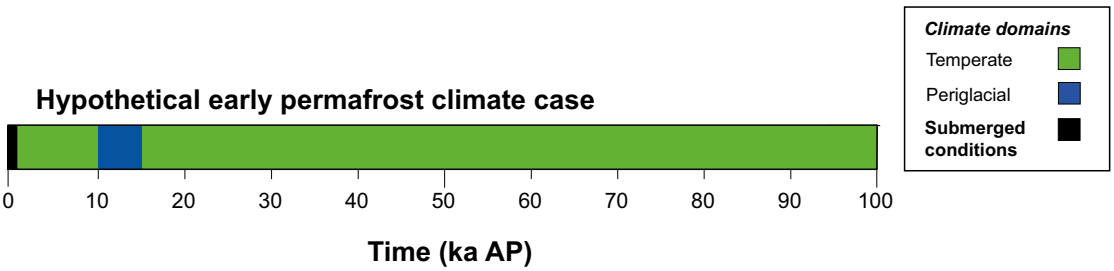

Figure 5-7. *Succession of climate domains, including periods of submerged conditions, in the hypothetical early permafrost climate case.*

5.5 Summary of climate cases

In summary, five climate cases are identified and selected for further analysis in the PSAR, summarised in Figure 5-8.

First, the *present-day climate case* was selected as a simplified development where present-day climate conditions are assumed for the complete assessment period and the initial shoreline displacement is assumed to be dominated by the isostatic rebound following the last glaciation. This climate case fulfils the regulatory requirement that the safety assessment should include a case where the biosphere conditions prevailing at the time of the application will not change (SSMFS 2008:37).

In addition, four climate cases representing time-varying conditions were selected. Similar to the SR-PSU, these climate cases in the PSAR were identified and selected based on the climate-related issues relevant for post-closure safety (Chapter 2) and the scientific knowledge on the past, present and future climate evolution (Chapter 3). Aiming at the selection of appropriate evolutions of external conditions for the main, less probable- and residual scenarios, the following knowledge and assessment of the future climate evolution were considered:

- The climate evolution of the next 100 ka will be determined primarily by changes in the insolation during the boreal summer, current levels of atmospheric CO_2 and the amount of anthropogenic greenhouse-gas emissions within this century (Sections 3.4.5 and 4.3). Future changes in insolation can be predicted with high accuracy, whereas future anthropogenically-induced net emissions are more uncertain.
- It is highly likely that either similar-to-present levels of anthropogenic greenhouse-gas emissions will continue for the next few decades, or that lower net emissions are achieved through successful climate-change mitigation within this time (Section 4.2).
- It is highly likely that the current interglacial, the Holocene, will be significantly longer than previous interglacials. The current interglacial will last at least for another 50 ka if anthropogenic greenhouse-gas emissions are substantially reduced within the coming decades, but likely for 100 ka or longer if current, or higher, levels of anthropogenic emissions prevail for the next few decades (Sections 3.4.5 and 4.3).

Taken these assessments of future climate evolution into account, the following time-varying climate cases were defined:

The *warm climate case* represents a future development where similar-to-present levels of anthropogenic greenhouse-gas emissions continue for the next few decades, after which they gradually decline to net-zero emissions at the beginning of the next century. This is in line with recent business-as-usual projections of future emissions (RCP4.5 and 6.0) which assume that current policies to mitigate climate change are implemented, but no new policies are adopted in the future (Section 4.2). This development results in 100 ka of temperate climate conditions and a continuation of the current submerged conditions for an extended period of time as compared to the *present-day climate case* (Figure 5-8).

The *cold climate case* represents a future development characterised by substantial reductions in anthropogenic greenhouse-gas emissions and/or removal of atmospheric CO_2 by technological measures. This development results in gradually colder conditions and two periods of periglacial climate conditions at Forsmark within the latter half of the assessment period (Figure 5-8).

The *glaciation climate case* represents an unlikely future development towards colder climate conditions that results in the succession of periglacial, glacial, submerged and temperate climate conditions at Forsmark within the latter half of the assessment period (Figure 5-8).

The *hypothetical early permafrost climate case* represents a highly unlikely future development characterised by the development of permafrost and periglacial conditions at Forsmark within the next 50 ka (Figure 5-8). This variant is included in the PSAR to facilitate illustration of the significance of individual barriers and barrier functions independently of probabilities, under hypothetical assumptions of early permafrost development.

The climate cases in the PSAR collectively describe a similar range of future climate evolutions as the climate cases in the SR-PSU.

The *present-day*, *warm* and *cold climate cases* are selected as reference external conditions in the present assessment, representing the range of probable evolution of the external conditions at Forsmark during the next 100 ka. Radiological consequences of these developments are consequently evaluated in the main scenario (**Post-closure safety report**, Chapter 7). Consequences of the *glaciation* and *hypothetical early permafrost climate cases* are evaluated in a less probable scenario and residual scenario, respectively (**Post-closure safety report**, Chapters 8–9).

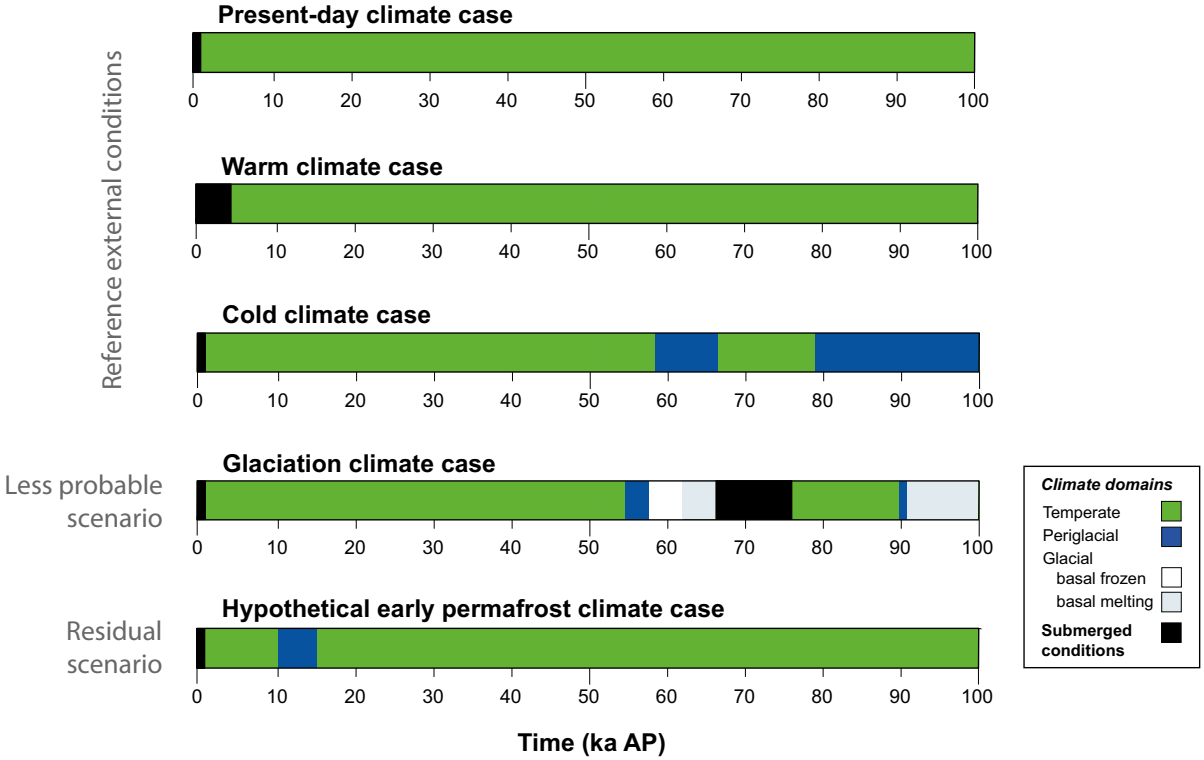

Figure 5-8. *Summary of the climate cases used in the PSAR.*

References

SKB's (Svensk Kärnbränslehantering AB) publications can be found at www.skb.com/publications. SKBdoc documents will be submitted upon request to document@skb.se.

References with abbreviated names

Post-closure safety report, 2023. Post-closure safety for SFR, the final repository for short-lived radioactive waste at Forsmark. Main report, PSAR version. SKB TR-23-01, Svensk Kärnbränslehantering AB.

Barrier process report, 2023. Post-closure safety for SFR, the final repository for short-lived radioactive waste at Forsmark. Engineered barrier process report, PSAR version. SKB TR-23-04, Svensk Kärnbränslehantering AB.

Biosphere synthesis report, 2023. Post-closure safety for SFR, the final repository for short-lived radioactive waste at Forsmark. Biosphere synthesis report, PSAR version. SKB TR-23-06, Svensk Kärnbränslehantering AB.

Data report, 2023. Post-closure safety for SFR, the final repository for short-lived radioactive waste at Forsmark. Data report, PSAR version. SKB TR-23-10, Svensk Kärnbränslehantering AB.

FEP report, 2014. FEP report for the safety assessment SR-PSU. SKB TR-14-07, Svensk Kärnbränslehantering AB.

FHA report, 2023. Post-closure safety for SFR, the final repository for short-lived radioactive waste at Forsmark. Handling of future human actions, PSAR version. SKB TR-23-08, Svensk Kärnbränslehantering AB.

Geosphere process report, 2014. Geosphere process report for the safety assessment SR-PSU. SKB TR-14-05, Svensk Kärnbränslehantering AB.

Initial state report, 2023. Post-closure safety for SFR, the final repository for short-lived radioactive waste at Forsmark. Initial state of the repository, PSAR version. SKB TR-23-02, Svensk Kärnbränslehantering AB.

Model tools report, 2023. Post-closure safety for SFR, the final repository for short-lived radioactive waste at Forsmark. Model tools summary report, PSAR version. SKB TR-23-11, Svensk Kärnbränslehantering AB.

Radionuclide transport report, 2023. Post-closure safety for SFR, the final repository for short-lived radioactive waste at Forsmark. Radionuclide transport and dose calculations, PSAR version. SKB TR-23-09, Svensk Kärnbränslehantering AB.

Waste process report, 2023. Post-closure safety for SFR, the final repository for short-lived radioactive waste at Forsmark. Waste form and packaging process report, PSAR version. SKB TR-23-03, Svensk Kärnbränslehantering AB.

Regular references

Abe-Ouchi A, Saito F, Kawamura K, Raymo M E, Okuno J, Takahashi K, Blatter H, 2013. Insolation-driven 100,000-year glacial cycles and hysteresis of ice-sheet volume. Nature 500, 190–193.

Ahonen L, 2001. Permafrost: occurrence and physicochemical processes. Posiva 2001-05, Posiva Oy, Finland.

Alexandersson H, 2003. Korrektion av nederbörd enligt enkel klimatologisk metodik. SMHI, Meteorologi, Nr 111. (In Swedish.)

Allen D, Michel F, Judge A, 1988. Paleoclimate and permafrost in the Mackenzie Delta. In Proceedings of the fifth international conference on permafrost. Trondheim, 2–5 August 1988. Vol 1. Trondheim: Tapir.

Allen M R, Dube O P, Solecki W, Aragón-Durand F, Cramer W, Humphreys S, Kainuma M, Kala J, Mahowald N, Mulugetta Y, Perez R, Wairiu M, Zickfeld K, 2018. Framing and context. In: Global warming of 1.5 °C. An IPCC special report on the impacts of global warming of 1.5 °C above pre-industrial levels and related global greenhouse gas emission pathways, in the context of strengthening the global response to the threat of climate change, sustainable development, and efforts to eradicate poverty. Available at: http://www.ipcc.ch

Allen R G, Smith M, Perrier A, Pereira L S, 1994. An update for the calculation of reference evapotranspiration. ICID Bulletin 43, 35–92.

Alley R B, 1992. Flow-law hypotheses for ice-sheet modeling. Journal of Glaciology 38, 245–256.

Andersen B G, Mangerud J, 1989. The last interglacial-glacial cycle in Fennoscandia. Quaternary International 3–4, 21–29.

Andrews J T, Barber D C, 2002. Dansgaard-Oeschger events: is there a signal off the Hudson Strait Ice Stream? Quaternary Science Reviews 21, 443–454.

Archer D, Ganopolski A, 2005. A movable trigger: Fossil fuel CO_2 and the onset of the next glaciation. Geochemistry, Geophysics, Geosystems 6, Q05003. doi:10.1029/2004GC000891

Archer D, Eby M, Brovkin V, Ridgwell A, Cao L, Mikolajewicz U, Caldeira K, Matsumoto K, Munhoven G, Montenegro A, Tokos K, 2009. Atmospheric lifetime of fossil fuel carbon dioxide. Annual Review of Earth and Planetary Sciences 37, 117–134.

Árnadóttir T, Lund B, Jiang W, Geirsson H, Björnsson H, Einarsson P, Sigurdsson T, 2009. Glacial rebound and plate spreading: results from the first countrywide GPS observations in Iceland. Geophysical Journal International 177, 691–716.

Artemieva I M, Mooney W D, 2001. Thermal thickness and evolution of Precambrian lithosphere: a global study. Journal of Geophysical Research 106, 16387–16414.

Bakker A M, Wong T E, Ruckert K L, Keller K, 2017. Sea-level projections representing the deeply uncertain contribution of the West Antarctic ice sheet. Scientific reports 7, 3880. doi:10.1038/s41598-017-04134-5

Balling N, 1984. Gravity and isostasy in the Baltic Shield. In Galson D A, Mueller S, Munch B (eds). Proceedings of the first workshop on the European Geotraverse Project (EGT): The northern segment. Strasbourg: European Science Foundation, 53–66.

Bamber J L, Riva R E M, 2010. The sea-level fingerprint of 21st century ice mass flux. The Cryosphere Discussions 4, 1593–1606.

Bamber J L, Riva R E M, Vermeersen B L A, LeBrocq A M, 2009. Reassessment of the potential sea-level rise from a collapse of the West Antarctic ice sheet. Science 324, 901–903.

Bard E, Hamelin B, Fairbanks R G, 1990. U-Th ages obtained by mass spectrometry in corals from Barbados: sea-level during the past 130,000 years. Nature 346, 456–458.

Bard E, Hamelin B, Arnold M, Montaggioni L, Cabioch G, Faure G, Rougerie F, 1996. Deglacial sea-level record from Tahiti corals and the timing of global meltwater discharge. Nature 382, 241–244.

Bassett S E, Milne G A, Mitrovica J X, Clark P U, 2005. Ice sheet and solid Earth influences on far-field sea-level histories. Science 309, 925–928.

Bauder A, Mickelson D M, Marshall S J, 2003. Modelling ice sheet permafrost interaction around the southern Laurentide ice sheet. EGS – AGU – EUG Joint Assembly. Abstracts from the meeting held in Nice, France, 6–11 April 2003, abstract 12348.

Bauer N, Hilaire J, Brecha R J, Edmonds J, Jiang K, Kriegler E, Rogner H-H, Sferra F, 2016. Assessing global fossil fuel availability in a scenario framework. Energy 111, 580–592.

Beardsmore G R, Cull J P, 2001. Crustal heat flow: a guide to measurement and modelling. Cambridge: Cambridge University Press.

Benn D I, Evans D J A, 1998. Glaciers & glaciation. London: Arnold.

Berger A, 1978. Long-term variations of daily insolation and Quaternary climatic changes. Journal of the Atmospheric Sciences 35, 2362–2367.

Berger A, Loutre M F, 1991. Insolation values for the climate of the last 10 million years. Quaternary Science Reviews 10, 297–317.

Berger A, Loutre M F, 2002. An exceptionally long interglacial ahead? Science 297, 1287–1288.

Berglund S, Lindborg T (eds), 2017. Monitoring Forsmark – evaluation and recommendations for programme update. SKB TR-15-01, Svensk Kärnbränslehantering AB.

BIOCLIM, 2003. Deliverable D7. Continuous climate evolution scenarios over western Europe (1000 km scale). Work package 2: Simulation of the future evolution of the biosphere system using the hierarchical strategy. Châtenay-Malabry: Andra.

Birch F, Roy R F, Decker E R, 1968. Heat flow and thermal history in New England and New York. In Zen E-an (ed). Studies of Appalachian geology: northern and maritime. New York: Interscience, 437–451.

Bittermann K, Rahmstorf S, Kopp R E, Kemp A C, 2017. Global mean sea-level rise in a world agreed upon in Paris. Environmental Research Letters 12, 124010.

Björck S, 1995. A review of the history of the Baltic Sea, 13.0–8.0 ka BP. Quaternary International 27, 19–40.

Booth B B, Harris G R, Murphy J M, House J I, Jones C D, Sexton D, Sitch S, 2017. Narrowing the range of future climate projections using historical observations of atmospheric CO_2. Journal of Climate 30, 3039–3053.

Bos J A A, Helmens K F, Bohncke S J P, Seppä H, Birks H J B, 2009. Flora, vegetation and climate at Sokli, northeastern Fennoscandia, during the Weichselian Middle Pleniglacial. Boreas 38, 335–348.

Bosson E, Gustafsson L-G, Sassner M, 2008. Numerical modelling of surface hydrology and near-surface hydrogeology at Forsmark. Site descriptive modelling, SDM-Site Forsmark. SKB R-08-09, Svensk Kärnbränslehantering AB.

Bosson E, Lindborg T, Berglund S, Gustafsson L-G, Selroos J-O, Laudon H, Claesson L L, Destouni G, 2013. Water balance and its intra-annual variability in a permafrost catchment: hydrological interactions between catchment, lake and talik. Hydrology and Earth System Sciences Discussions 10, 9271–9308.

Boulton G S, Clark C D, 1990. The Laurentide Ice Sheet through the last glacial cycle: the topology of drift lineations as a key to the dynamic behaviour of former ice sheets. Transactions of the Royal Society of Edinburgh: Earth Sciences 81, 327–347.

Boulton G S, Payne A, 1992. Simulation of the European ice sheet through the last glacial cycle and prediction of future glaciation. SKB TR 93-14, Svensk Kärnbränslehantering AB.

Boulton G S, Kautsky U, Morén L, Wallroth T, 2001. Impact of long-term climate change on a deep geological repository for spent nuclear fuel. SKB TR-99-05, Svensk Kärnbränslehantering AB.

BP, 2019. BP Statistical review of world energy. 68th ed. London: BP. Available at: https://www.bp.com/en/global/corporate/energy-economics/statistical-review-of-world-energy.html

Brandefelt J, Otto-Bliesner B L, 2009. Equilibrium and variability in a Last Glacial Maximum climate simulation with CCSM3. Geophysical Research Letters 36, L19712. doi:10.1029/2009GL040364

Brandefelt J, Kjellström E, Näslund J-O, Strandberg G, Voelker A H L, Wohlfarth B, 2011. A coupled climate model simulation of Marine Isotope Stage 3 stadial climate. Climate of the Past 7, 649–670.

Brandefelt J, Näslund J-O, Zhang Q, Hartikainen J, 2013. The potential for cold climate conditions and permafrost in Forsmark in the next 60,000 years. SKB TR-13-04, Svensk Kärnbränslehantering AB.

Brandefelt J, Näslund J-O, Andersson E, 2016. Kompletterande information om hantering av klimatscenarierna i ansökan om utbyggnad av SFR. SKBdoc 1541317 ver 1.0, Svensk Kärnbränslehantering AB. (In Swedish.)

Brydsten L, 2009. Sediment dynamics in the coastal areas of Forsmark and Laxemar during an interglacial. SKB TR-09-07, Svensk Kärnbränslehantering AB.

Brydsten L, Strömgren M, 2013. Landscape development in the Forsmark area from the past into the future (8500 BC – 40,000 AD). SKB R-13-27, Svensk Kärnbränslehantering AB.

Brydsten L, Engqvist A, Näslund J-O, Lindborg T, 2009. Expected extreme sea levels at Forsmark and Laxemar-Simpevarp up until year 2100. SKB TR-09-21, Svensk Kärnbränslehantering AB.

Capellán-Pérez I, Arto I, Polanco-Martínez J M, González-Eguino M, Neumann M B, 2016. Likelihood of climate change pathways under uncertainty on fossil fuel resource availability. Energy & Environmental Science 9, 2482–2496.

Čermák V, Balling N, Kukkonen I, Zui V I, 1993. Heat flow in the Baltic Shield – results of the lithospheric geothermal modelling. Precambrian Research 64, 53–65.

Chapman M R, Shackleton N J, 1999. Global ice-volume fluctuations, North Atlantic ice-rafting events, and deep-ocean circulation changes between 130 and 70 ka. Geology 27, 795–798.

Chappell J, Polach H, 1991. Post-glacial sea-level rise from a coral record at Huon Peninsula, Papua New Guinea. Nature 349, 147–149.

Chappell J, Omura A, Esat T, McCulloch M, Pandolfi J, Ota Y, Pillans B, 1996. Reconciliation of late Quaternary sea levels derived from coral terraces at Huon Peninsula with deep sea oxygen isotope records. Earth and Planetary Science Letters 141, 227–236.

Church J A, Clark P U, Cazenave A, Gregory J M, Jevrejeva S, Levermann A, Merrifield M A, Milne G A, Nerem R S, Nunn P D, Payne A J, Pfeffer W T, Stammer D, Unnikrishnan A S, 2013. Sea level change. In Stocker T F, Qin D, Plattner G-K, Tignor M, Allen S K, Boschung J, Nauels A, Xia Y, Bex V, Midgley P M (eds). Climate change 2013: the physical science basis: Working Group I Contribution to the Fifth Assessment Report of the Intergovernmental Panel on Climate Change. Cambridge: Cambridge University Press, 1137–1216. (The report has to be read in conjunction with the document entitled "Climate change 2013: the physical science basis. Working Group I Contribution to the IPCC 5th Assessment Report – Changes to the underlying scientific/technical assessment". Available at: http://www.ipcc.ch.)

Ciais P, Sabine C, Bala G, Bopp L, Brovkin V, Canadell J, Chhabra A, DeFries R, Galloway J, Heimann M, Jones C, Le Quéré C, Myneni R B, Piao S, Thornton P, 2013. Carbon and Other Biogeochemical Cycles. In Climate Change 2013: The Physical Science Basis. Contribution of Working Group I to the Fifth Assessment Report of the Intergovernmental Panel on Climate Change [Stocker, T.F., D. Qin, G.-K. Plattner, M. Tignor, S.K. Allen, J. Boschung, A. Nauels, Y. Xia, V. Bex and P.M. Midgley (eds.)]. Cambridge: Cambridge University Press.

Claesson Liljedahl L, Kontula A, Harper J, Näslund J-O, Selroos J-O, Pitkänen P, Puigdomenech I, Hobbs M, Follin S, Hirschorn S, Jansson P, Kennell L, Marcos N, Ruskeeniemi T, Tullborg E-L, Vidstrand P, 2016. Greenland Analogue Project: Final report. SKB TR-14-13, Svensk Kärnbränslehantering AB.

Clark J A, Farrell W E, Peltier W R, 1978. Global changes in postglacial sea level: a numerical calculation. Quaternary Research 9, 265–287.

Clark P U, Mix A C, 2002. Ice sheets and sea level of the Last Glacial Maximum. Quaternary Science Reviews 21, 1–7.

Clark P U, Alley R B, Keigwin L D, Licciardi J M, Johnsen S J, Wang H X, 1996. Origin of the first global meltwater pulse following the Last Glacial Maximum. Paleoceanography 11, 563–577.

Clark P U, Shakun J D, Marcott S A, Mix A C, Eby M, Kulp S, Levermann A, Milne G A, Pfister P L, Santer B D, Schrag D P, Solomon S, Stocker T F, Strauss B H, Weaver A J, Winkelmann R, Archer D, Bard E, Goldner A, Lambeck K, Pierrehumbert R T, Plattner G-K, 2016. Consequences of twenty-first-century policy for multi-millennial climate and sea-level change. Nature Climate Change 6, 360–369.

Clason C C, Applegate P J, Holmlund P, 2014. Modelling Late Weichselian evolution of the Eurasian ice sheets forced by surface meltwater-enhanced basal sliding. Journal of Glaciology 60, 29–40.

Clauser C, Huenges E, 1995. Thermal conductivity of rocks and minerals. In Ahrens T J (ed). Rock physics and phase relations: handbook of physical constants. Washington, DC: American Geophysical Union, 105–126.

Cochelin A-S B, Mysak L L, Wang Z, 2006. Simulation of long-term future climate changes with the green McGill paleoclimate model: the next glacial inception. Climatic Change 79, 381–401.

Colleoni F, Liakka J, 2020. Transient simulations of the Eurasian ice sheet during the Saalian glacial cycle. SKB TR-19-17, Svensk Kärnbränslehantering AB.

Collins M, Knutti R, Arblaster J M, Dufresne J-L, Fichefet T, Friedlingstein P, Gao X, Gutowski W J, Johns T, Krinner G, Shongwe M, Tebaldi C, Weaver A J, Wehner M, 2013. Long term climate change: projections, commitement and irreversibility. In Stocker T F, Qin D, Plattner G-K, Tignor M, Allen S K, Boschung J, Nauels A, Xia Y, Bex V, Midgley P M (eds). Climate change 2013: the physical science basis: Working Group I Contribution to the Fifth Assessment Report of the Intergovernmental Panel on Climate Change. Cambridge: Cambridge University Press, 1029–1136. (The report has to be read in conjunction with the document entitled "Climate change 2013: the physical science basis. Working Group I Contribution to the IPCC 5th Assessment Report – Changes to the underlying scientific/technical assessment". Available at: http://www.ipcc.ch.)

Collinson J, 2005a. Erosional sedimentary structures. In Selley R C, Cocks L R M, Plimer I R (eds). Encyclopedia of geology. Amsterdam: Elsevier Academic Press.

Collinson J, 2005b. Depositional sedimentary structures. In Selley R C, Cocks L R M, Plimer I R (eds). Encyclopedia of geology. Amsterdam: Elsevier Academic Press.

Cox P M, Pearson D, Booth B B, Friedlingstein P, Huntingford C, Jones C D, Luke C M, 2013. Sensitivity of tropical carbon to climate change constrained by carbon dioxide variability. Nature 494, 341–344.

Creutzig F, Agoston P, Goldschmidt J C, Luderer G, Nemet G, Pietzcker R C, 2017. The underestimated potential of solar energy to mitigate climate change. Nature Energy 2, 17140.

Danielson E W, Levin J, Abrams E, 2003. Meteorology. 2nd ed. New York: McGraw-Hill.

Dansgaard W, Johnsen S J, Clausen H B, Dahl-Jensen D, Gundestrup N S, Hammer C U, Hvidberg C S, Steffensen J P, Sveinbjörnsdottir A E, Jouzel J, Bond G, 1993. Evidence for general instability of past climate from a 250-kyr ice-core record. Nature 364, 218–220.

Davis J L, Mitrovica J X, 1996. Glacial isostatic adjustment and the anomalous tide gauge record of eastern North America. Nature 379, 331–333.

Davis J L, Mitrovica J X, Scherneck H G, Fan H, 1999. Investigations of Fennoscandian glacial isostatic adjustment using modern sea level records. Journal of Geophysical Research 104, 2733–2747.

DeConto R M, Pollard D, 2016. Contribution of Antarctica to past and future sea-level rise, Nature 531, 591–597.

Denton G H, Hughes T J (eds), 1981. The last great ice sheets. New York: John Wiley.

Drewry D, 1986. Glacial geologic processes. London: Arnold.

Dumitru O A, Austermann J, Polyak V J, Fornós J J, Asmerom Y, Ginés J, Ginés A, Onac B P, 2019. Constraints on global mean sea level during Pliocene warmth. Nature 574, 233–236.

Dutton A, Carlson A E, Long A J, Milne G A, Clark P U, DeConto R, Horton B P, Rahmstorf S, Raymo M E, 2015. Sea-level rise due to polar ice-sheet mass loss during past warm periods. Science 349, 6244. doi:10.1126/science.aaa4019

Duval P, Ashby M F, Anderman I, 1983. Rate-controlling processes in the creep of polycrystalline ice. Journal of Physical Chemistry 87, 4066–4074.

Dziewonski A M, Anderson D L, 1981. Preliminary reference earth model. Physics of the Earth and Planetary Interiors 25, 297–356.

Ebert K, 2009. Cenozoic landscape evolution in northern Sweden: geomorphological interpretation within a GIS-framework. PhD thesis. Department of Physical Geography and Quaternary Geology, Stockholm University.

Eby M, Zickfeld K, Montenegro A, Archer D, Meissner K J, Weaver A J, 2009. Lifetime of anthropogenic climate change: millennial time scales of potential CO_2 and surface temperature perturbations. Journal of Climate 22, 2501–2511.

Edwards T L, Brandon M A, Durand G, Edwards N R, Golledge N R, Holden P B, Nias I J, Payne A J, Ritz C, Wernecke A, 2019. Revisiting Antarctic ice loss due to marine ice-cliff instability. Nature 566, 58–73.

Ehlers J, Gibbard P L (eds), 2004. Quaternary glaciations: extent and chronology. Part I: Europe. Amsterdam: Elsevier. (Developments in Quaternary Science 2)

EIA, 2020. Monthly energy review. Report DOE/EIA-0035(2020/5), Energy Information Administration, U.S. Department of Energy.

Ekman M, 1991. A concise history of postglacial land uplift research (from its beginning to 1950). Terra Nova 3, 358–365.

Engelhardt H, Kamb B, 1998. Basal sliding of Ice Stream B, West Antarctica. Journal of Glaciology 44, 223–230.

Engelhardt H, Humphrey N, Kamb B, Fahnestock M, 1990. Physical conditions at the base of a fast moving Antarctic ice stream. Science 248, 57–59.

Engels S, Bohncke S J P, Bos J A A, Brooks S J, Heiri O, Helmens K F, 2008. Chironomid-based palaeotemperature estimates for northeast Finland during Oxygen Isotope Stage 3. Journal of Palaeolimnology 40, 49–61.

Engels S, Helmens K F, Väliranta M, Brooks S J, Birks H J B, 2010. Early Weichselian (MIS 5d and 5c) temperatures and environmental changes in northern Fennoscandia as recorded by chironomids and macroremains at Sokli, northeast Finland. Boreas 39, 689–704.

Engström J, Kukkonen I, Ruskeeniemi T, Claesson Liljedahl L, Lehtinen A, 2012. Temperature measurements providing evidence for permafrost thickness and talik occurrences in Kangerlussuaq, West Greensland. 30th Nordic Geological Winter Meeting, Reykjavik, Iceland, 9–12 January 2012. Abstract EC3-5.

Eronen M, Gluckert G, Hatakka L, van de Plassche O, van der Plicht J, Rantala P, 2001. Rates of Holocene isostatic uplift and relative sea-level lowering of the Baltic in SW Finland based on studies of isolation contacts. Boreas 30, 17–30.

Eyring V, Bony S, Meehl G A, Senior C A, Stevens B, Stouffer R J, Taylor K E, 2016. Overview of the Coupled Model Intercomparison Project Phase 6 (CMIP6) experimental design and organization. Geoscientific Model Development 9, 1937–1958.

Fairbanks R G, 1989. A 17,000-year glacio-eustatic sea level record: influence of glacial melting rates on the Younger Dryas event and deep-ocean circulation. Nature 342, 637–642.

Farrell W E, Clark J A, 1976. On postglacial sea level. Geophysical Journal of the Royal Astronomical Society 46, 647–667.

Fastook J L, 1990. A map-plane finite-element program for ice sheet reconstruction: a steady-state calibration with Antarctica and a reconstruction of the Laurentide ice sheet for 18,000 BP. In Brown H U (ed). Computer assisted analysis and modeling on the IBM 3090. White Plains, NY: IBM Scientific and Technical Computing Department.

Fastook J L, 1994. Modeling the ice age: the finite-element method in glaciology. Computational Science & Engineering 1, 55–67.

Fastook J L, Chapman J E, 1989. A map plane finite-element model: three modeling experiments. Journal of Glaciology 35, 48–52.

Fastook J L, Holmlund P, 1994. A glaciological model of the Younger Dryas event in Scandinavia. Journal of Glaciology 40, 125–131.

Fastook J L, Prentice M, 1994. A finite-element model of Antarctica: sensitivity test for meteorological mass-balance relationship. Journal of Glaciology 40, 167–175.

Fisher U H, 2009. Glacial erosion: a review of its modelling. Nagra Arbeitsbericht NAB 09-23, Nagra, Switzerland.

Fjeldskaar W, 1994. The amplitude and decay of the glacial forebulge in Fennoscandia. Norsk Geologisk Tidsskrift 74, 2–8.

Fleming K, Johnston P, Zwartz D, Yokoyama Y, Lambeck K, Chappell J, 1998. Refining the eustatic sea-level curve since the Last Glacial Maximum using far- and intermediate-field sites. Earth and Planetary Science Letters 163, 327–342.

Forsström P-L, Sallasmaa O, Greve R, Zwinger T, 2003. Simulation of fast-flow features of the Fennoscandian ice sheet during the Last Glacial Maximum. Annals of Glaciology 37, 383–389.

Fotiev S M, 1997. Permafrost groundwater Russian Literature Review. In Haldorsen S, Liebman M, Nelson G, van Everdingen R O, Boike J, 1997: State-of-the-art report on saturated water movement in permafrost areas. Report No 4/97 (lnr 54). Ås: Norges landbrukshøgskole.

Fredén C (ed), 2002. Sveriges nationalatlas. Berg och Jord. Stockholm: SNA publishing. (In Swedish.)

French H M, 2007. The periglacial environment. 3rd ed. Chichester: Wiley.

Friedlingstein P, Meinshausen M, Arora V K, Jones C D, Anav A, Liddicoat S K, Knutti R, 2014. Uncertainties in CMIP5 climate projections due to carbon cycle feedbacks. Journal of Climate 27, 511–526.

Friedlingstein P, Jones M W, O'Sullivan M, Andrew R M, Hauck J, Peters G P, Peters W, Pongratz J, Sitch S, Le Quéré C, Bakker D C, Canadell J G, Ciais P, Jackson R B, Anthoni P, Barbero L, Bastos A, Bastrikov V, Becker M, Bopp L, Buitenhuis E, Chandra N, Chevallier F, Chini L P, Currie K I, Feely R A, Gehlen M, Gilfillan D, Gkritzalis T, Goll D S, Gruber N, Gutekunst S, Harris I, Haverd V, Houghton R A, Hurtt G, Ilyina T, Jain A K, Joetzjer E, Kaplan J O, Kato E, Goldewijk K K, Korsbakken J I, Landschützer P, Lauvset S K, Lefèvre N, Lenton A, Lienert S, Lombardozzi D, Marland G, McGuire P C, Melton J R, Metzl N, Munro D R, Nabel J E M S, Nakaoka S-I, Neill C, Omar A M, Ono T, Peregon A, Pierrot D, Poulter B, Rehder G, Resplandy L, Robertson E, Rödenbeck C, Séférian R, Schwinger J, Smith N, Tans P P, Tian H, Tilbrook B, Tubiello F N, van der Werf G R, Wiltshire A J, Zaehle S, 2019. Global carbon budget 2019. Earth System Science Data 11, 1783–1838.

Frieler K, Betts R, Burke E, Ciais P, Denvil S, Deryng D, Ebi K, Eddy T, Emanuel K, Elliott J, Galbraith E, Gosling S N, Halladay K, Hattermann F, Hickler T, Hinkel J, Huber V, Jones C, Krysanova V, Lange S, Lotze H K, LotzeCampen H, Mengel M, Mouratiadou I, Müller Schmied H, Ostberg S, Piontek F, Popp A, Reyer C P O, Schewe J, Stevanovic M, Suzuki T, Thonicke K, Tian H, Tittensor D P, Vautard R, van Vliet M, Warszawski L, Zhao F, 2016. Assessing the impacts of 1.5 ◦C global warming – simulation protocol of the Inter-Sectoral Impact Model Intercomparison Project (ISIMIP2b), Geoscientific Model Development 10, 4321–4345.

Fronval T, Jansen E, 1996. Late Neogene paleoclimates and paleoceanography in the Iceland-Norwegian Sea: evidence from the Iceland and Vøring plateaus. In Thiede J, Myhre A M, Firth J V, Johnson G L, Ruddiman W F (eds). Proceedings of the Ocean Drilling Program, Scientific results 151, 455–468.

Frölicher T L, Winton M, Sarmiento J L, 2014. Continued global warming after CO_2 emissions stoppage. Nature Climate Change 4, 40–44.

Fujimori S, Hasegawa T, Masui T, Takahashi K, Herran D S, Dai H, Hijioka Y, Kainuma M, 2017. SSP3: AIM implementation of shared socioeconomic pathways. Global Environmental Change 42, 268–283.

Furlong K P, Chapman D S, 1987. Crustal heterogeneities and the thermal structure of the continental crust. Geophysical Research Letters 14, 314–317.

Fyke J, Matthews H, 2015. A probabilistic analysis of cumulative carbon emissions and long-term planetary warming. Environmental Research Letters 10, 115007. doi:10.1088/1748-9326/10/11/115007

Galbraith D, Levy P E, Sitch S, Huntingford C, Cox P, Williams M, Meir P, 2010. Multiple mechanisms of Amazonian forest biomass losses in three dynamic global vegetation models under climate change. New Phytologist 187, 647–665.

Ganopolski A, Calov R, Claussen M, 2010. Simulation of the last glacial cycle with a coupled climate ice-sheet model of intermediate complexity. Climate of the Past 6, 229–244.

Ganopolski A, Winkelmann R, Schellnhuber H J, 2016. Critical insolation–CO_2 relation for diagnosing past and future glacial inception. Nature 529, 200–203.

Garisto F, Avis J, Chshyolkova T, Gierszewski P, Gobien M, Kitson C, Melnyk T, Miller J, Walsh R, Wojciechowski L, 2010. Glaciation scenario: safety assessment for a deep geological repository for used fuel. NWMO TR-2010-10, Nuclear Waste Management Organization, Canada.

Gascoyne M, 2000. A review of published literature on the effects of permafrost on the hydrogeochemistry of bedrock. SKB R-01-56, Svensk Kärnbränslehantering AB.

Gillet N P, Arora V K, Zickfeld K, Marshal S J, Merryfield W J, 2011. Ongoing climate change following a complete cessation of carbon dioxide emissions. Nature Geoscience 4, 83–87.

Giovinetto M B, Zwally H J, 2000. Spatial distribution of net surface accumulation on the Antarctic ice sheet. Annals of Glaciology 31, 171–178.

Glen J W, 1955. The creep of polycrystalline ice. Proceedings of the Royal Society of London, Series A 228, 519–538.

Golledge N R, Kowalewski D E, Naish T R, Levy R H, Fogwill C J, Gasson E G, 2015. The multi-millennial Antarctic commitment to future sea level rise. Nature 526, 421–425.

Goodfellow B W, Stroeven A P, Martel S J, Heyman J, Rossi M, Caffee M W, 2019. Exploring alternative models for the formation of conspicuously flat basement surfaces in southern Sweden. SKB TR-19-22, Svensk Kärnbränslehantering AB.

Goodrich L E, 1978. Some results of a numerical study of ground thermal regimes. In Proceedings of the Third International Conference on Permafrost, Edmonton, Alberta, Canada, 10–13 July 1978. Ottawa: National Research Council of Canada, 30–34.

Goodwin P, Haigh I D, Rohling E J, Slangen A, 2017. A new approach to projecting 21st century sea-level changes and extremes. Earth's Future 5, 240–253.

Goodwin P, Brown S, Haigh I D, Nicholls R J, Matter J M, 2018. Adjusting mitigation pathways to stabilize climate at 1.5 °C and 2.0 °C rise in global temperatures to year 2300. Earth's Future 6, 601–615.

Gregory J M, Huybrechts P, 2006. Ice-sheet contributions to future sea-level change. Philosophical Transactions of the Royal Society A 364, 1709–1731.

Gregory J M, Huybrechts P, Raper S C B, 2004. Threatened loss of the Greenland ice sheet. Nature 428, 616.

Greve R, Hutter K, 1995. Polythermal three-dimensional modelling of the Greenland ice sheet with varied geothermal heat flux. Annals of Glaciology 21, 8–12.

Grigull S, Peterson G, Nyberg J, Öhrling C, 2019. Phanerozoic faulting of Precambrian basement in Uppland. SKB R-19-22, Svensk Kärnbränslehantering AB.

Grinsted A, Jevrejeva S, Riva R E, Dahl-Jensen D, 2015. Sea level rise projections for northern Europe under RCP8.5. Climate Research 64, 15–23.

Guimberteau M, Ducharne A, Ciais P, Boisier J, Peng S, De Weirdt M, Verbeeck H, 2014. Testing conceptual and physically based soil hydrology schemes against observations for the Amazon Basin. Geoscientific Model Development 7, 1115–1136.

Hall A, van Boeckel M, 2020. Origin of the Baltic Sea basin by Pleistocene glacial erosion. GFF 142, 237–252.

Hall A M, Ebert K, Goodfellow B W, Hättestrand C, Heyman J, Krabbendam M, Moon S, Stroeven A P, 2019a. Past and future impact of glacial erosion in Forsmark and Uppland. Final report. SKB TR-19-07, Svensk Kärnbränslehantering AB.

Hall A M, Krabbendam M, van Boeckel M, Hättestrand C, Ebert K, Heyman J, 2019b. The sub-Cambrian unconformity in Västergötland, Sweden: Reference surface for Pleistocene glacial erosion of basement. SKB TR-19-21, Svensk Kärnbränslehantering AB.

Hall A M, Krabbendam M, van Boeckel M, Goodfellow B W, Hättestrand C, Heyman J, Palamakumbara R N, Stroeven A P, Näslund J-O, 2020. Glacial ripping: geomorphological evidence from Sweden for a new process of glacial erosion. Geografiska Annaler, Series A 102, 333–353.

Hallet B, Hunter L, Bogen J, 1996. Rates of erosion and sediment evacuation by glaciers: a review of field data and their implications. Global and Planetary Change 12, 213–235.

Hambrey M J, Barrett P J, Ehrmann W U, Larsen B, 1992. Cainozoic sedimentary processes on the Antarctic continental margin and the record from deep drilling. Zeitschrift für Geomorphologie, Suppl. 86, 77–103.

Hanasaki N, Kanae S, Oki T, Masuda K, Motoya K, Shirakawa N, Shen Y, Tanaka K, 2008. An integrated model for the assessment of global water resources--Part 1: Model description and input meteorological forcing. Hydrology & Earth System Sciences 12, 1007–1025.

Hanasaki N, Yoshikawa S, Pokhrel Y, Kanae S, 2018. A global hydrological simulation to specify the sources of water used by humans. Hydrology and Earth System Sciences 22, 789–817.

Hanebuth T, Stattegger K, Grootes P M, 2000. Rapid flooding of the Sunda Shelf: a late-glacial sea-level record. Science 288, 1033–1035.

Haq B U, Hardenbol J, Vail P R, 1987. Chronology of fluctuating sea levels since the Triassic. Science 235, 1156–1165.

Hargreaves G L, Hargreaves G H, Riley J P, 1985. Agricultural benefits for Senegal river basin. Journal of Irrigation and Drainage Engineering 111, 113–124.

Harper J, Hubbard A, Ruskeeniemi T, Claesson Liljedahl L, Kontula A, Bougamont M, Brown J, Dirkson A, Dow C, Doyle S, Drake H, Engström J, Fitzpatrick A, Follin S, Frape S, Graly J, Hansson K, Harrington J, Henkemans E, Hirschorn S, Hobbs M, Humphrey N, Jansson P, Johnson J, Jones G, Kinnbom P, Kennell L, Klint K E S, Liimatainen J, Lindbäck K, Meierbachtol T, Pere T, Pettersson R, Tullborg E-L, van As D, 2016. The Greenland Analogue Project: Data and processes. SKB R-14-13, Svensk Kärnbränslehantering AB.

Harper J, Meierbachtol T, Humphrey N, 2019. Greenland ICE project. Final report. SKB R-18-06, Svensk Kärnbränslehantering AB

Harrison S P, Braconnot P, Joussaume S, Hewitt C, Stouffer R J, 2002. Comparison of palaeo-climate simulations enhances confidence in models. Eos 83, 447.

Hartikainen J, 2004. Permafrost modelling in DECOVALEX III for BMT3. In Eloranta E (ed). DECOVALEX III, 1999–2003. An international project for the modelling of coupled Thermo-Hydro-Mechanical processes for spent fuel disposal. Finnish national contributions. Helsinki: Radiation and Nuclear Safety Authority. (STUK-YTO-TR 209), Appendix IV.

Hartikainen J, 2013. Simulations of permafrost evolution at Olkiluoto. Posiva Working Report 2012-34, Posiva Oy, Finland.

Hartikainen J, 2018. Continuum thermodynamic modelling of porous medium with application to ground freezing. PhD thesis. Aalto University.

Hartikainen J, Kouhia R, Wallroth T, 2010. Permafrost simulations at Forsmark using a numerical 2D thermo-hydro-chemical model. SKB TR-09-17, Svensk Kärnbränslehantering AB.

Hays J D, Imbrie J, Shackleton N, 1976. Variations in the Earth's orbit: pacemaker of the ice ages. Science 194, 1121–1132.

Haywood A M, Hill D J, Dolan A M, Otto-Bliesner B L, Bragg F, Chan W-L, Chandler M A, Contoux C, Dowsett H J, Jost A, Kamae Y, Lohmann G, Lunt D J, Abe-Ouchi A, Pickering S J, Ramstein G, Rosenbloom N A, Salzmann U, Sohl L, Stepanek C, Ueda H, Yan Q, Zhang Z, 2013. Large-scale features of Pliocene climate: results from the Pliocene Model Intercomparison Project, Climate of the Past 9, 191–209.

Hedenström A, Risberg J, 2003. Shore displacement in northern Uppland during the last 6500 calender years. SKB TR-03-17, Svensk Kärnbränslehantering AB.

Heginbottom J A, Dubreuil M A, Harker P A, 1995. Canada – Permafrost. In National Atlas of Canada. 5th ed. Ottawa: National Atlas Information Service, Natural Resources Canada.

Heinrich H, 1988. Origin and consequences of cyclic ice rafting in the northeast Atlantic Ocean during the past 130,000 years. Quaternary Research 29, 142–152.

Helmens K, 2009. Climate, vegetation and lake development at Sokli (northern Finland) during early MIS 3 at ~ 50 kyr: Revising earlier concepts on climate, glacial and vegetation dynamics in Fennoscandia during the Weichselian. SKB TR-09-16, Svensk Kärnbränslehantering AB.

Helmens K, 2013. The last interglacial-glacial cycle (MIS 5-2) re-examined based on long proxy records from central and northern Europe. SKB TR-13-02, Svensk Kärnbränslehantering AB.

Helmens K F, 2019. The last 130 000 years in Fennoscandia reconstructed based on a long and fossil-rich sediment sequence preserved at Sokli, northern Finland: new evidence for highly dynamic environmental and climate conditions. SKB TR-18-04, Svensk Kärnbränslehantering AB.

Helmens K F, Engels S, 2010. Ice-free conditions in eastern Fennoscandia during early Marine Isotope Stage 3: lacustrine records. Boreas 39, 399–409.

Helmens K F, Bos J A A, Engels S, Van Meerbeeck C J, Bohncke S J P, Renssen H, Heiri O, Brooks S J, Seppä H, Birks H J B, Wohlfarth B, 2007. Present-day temperatures in northern Scandinavia during the last glaciation. Geology 35, 987–990.

Helmens K F, Risberg J, Jansson K N, Weckström J, Berntsson A, Kaislahti Tillman P, Johansson P W, Wastegård S, 2009. Early MIS 3 glacial lake evolution, ice-marginal retreat pattern and climate at Sokli (northeastern Fennoscandia). Quaternary Science Reviews 28, 1880–1894.

Helmens K F, Väliranta M, Engels S, Shala S, 2012. Large shifts in vegetation and climate during the Early Weichselian (MIS 5d-c) inferred from multi-proxy evidence at Sokli (northern Finland). Quaternary Science Reviews 41, 22–38.

Helmens K F, Katrantsiotis C, Salonen J S, Shala S, Bos J A A, Engels S, Kuosmanen N, Luoto T P, Väliranta M, Luoto M, Ojala A, Risberg J, Weckström J, 2018. Warm summers and rich biotic communities during N-Hemisphere deglaciation. Global and Planetary Change 167, 61–73.

Helmens K F, Katrantsiotis C, Kuosmanen N, Luoto T P, Salonen J S, Väliranta M, 2021. Prolonged interglacial warmth during the Last Glacial in northern Europe. Boreas 50, 331–350.

Henton J A, Craymer M R, Ferland R, Dragert H, Mazotti S, Forbes D L, 2006. Crustal motion and deformation monitoring of the Canadian landmass. Geomatica 60, 173–191.

Herrington T, Zickfeld K, 2014. Path independence of climate and carbon cycle response over a broad range of cumulative carbon emissions. Earth System Dynamics 5, 409–422.

Hindmarsh R C A, Boulton G S, Hutter K, 1989. Modes of operation of thermo-mechanically coupled ice sheets. Annals of Glaciology 12, 57–69.

Ho E, Budescu D V, Bosetti V, van Vuuren D P, Keller K, 2019. Not all carbon dioxide emission scenarios are equally likely: a subjective expert assessment. Climatic Change 155, 545–561.

Hoegh-Guldberg O, Jacob D, Taylor M, Bindi M, Brown S, Camilloni I, Diedhiou A, Djalante R, Ebi K, Engelbrecht F, Guiot J, Hijioka Y, Mehrotra S, Payne A, Seneviratne S I, Thomas A, Warren R, Zhou G, 2018. Impacts of 1.5ºC global warming on natural and human systems. In Global warming of 1.5 °C. An IPCC special report on the impacts of global warming of 1.5 °C above pre-industrial levels and related global greenhouse gas emission pathways, in the context of strengthening the global response to the threat of climate change, sustainable development, and efforts to eradicate poverty. Available at: https://www.ipcc.ch/sr15

Hohl V, 2005. Northern European long term climate archives. SKB TR-05-01, Svensk Kärnbränslehantering AB.

Hohmann M, 1997. Soil freezing – the concept of soil water potential. State of the art. Cold Regions Science and Technology 25, 101–110.

Holgate S J, Matthews A, Woodworth P L, Rickards L J, Tamisiea M E, Bradshaw E, Foden P R, Gordon K M, Jevrejeva S, Pugh J, 2013. New data systems and products at the Permanent Service for Mean Sea Level. Journal of Coastal Research 29, 493–504.

Holmlund P, Fastook J, 1993. Numerical modelling provides evidence of a Baltic ice stream during the Younger Dryas. Boreas 22, 77–86.

Holmlund P, Fastook J, 1995. A time dependent glaciological model of the Weichselian ice sheet. Quaternary International 27, 53–58.

Holmlund P, Jansson P, 2003. Glaciologi. Stockholm: Stockholm University and the Swedish Research Council. (In Swedish.)

Hooke R LeB, 1977. Basal temperatures in polar ice sheets: a qualitative review: Quaternary Research 7, 1–13.

Hooke R LeB, 1991. Positive feedbacks associated with erosion of glacial cirques and overdeepenings. Geological Society of America Bulletin 103, 1104–1108.

Hooke R LeB, 2004. Principles of glacier mechanics. 2nd ed. Cambridge: Cambridge University Press.

Hooke R LeB, Fastook J, 2007. Thermal conditions at the bed of the Laurentide ice sheet in Maine during deglaciation: implications for esker formation. Journal of Glaciology 53, 646–658.

Horton B P, Rahmstorf S, Engelhart S E, Kemp A C, 2014. Expert assessment of sea level rise by AD 2100 and AD 2300. Quaternary Science Reviews 84, 1–6.

Horton B P, Kopp R E, Garner A J, Carling C H, Khan N S, Roy K, Shaw T A, 2018. Mapping sea level change in time, space and probability. Annual Review of Environment and Resources 43, 481–521.

Houmark-Nielsen M, 2009. MIS 3 interstadial climate and rapid ice advances in the south-western Baltic. SKB P-09-10, Svensk Kärnbränslehantering AB.

Hubau W, Lewi, S L, Phillips O L, Affum-Baffoe K, Beeckman H, Cuní-Sanchez A, Daniels A K, Ewango C E N, Fauset S, Mukinzi J M, Sheil D, Sonké B, Sullivan M J P, Sunderland T C H, Taedoumg H, Thomas S C, White L J T, Abernethy K A, Adu-Bredu S, Amani C A, Baker T R, Banin L F, Baya F, Begne S K, Bennett A C, Benedet F, Bitariho R, Bocko Y E, Boeckx P, Boundja P, Brienen R J W, Brncic T, Chezeaux E, Chuyong G B, Clark C J, Collins M, Comiskey J A, Coomes D A, Dargie G C, de Haulleville T, Djuikouo Kamdem M N, Doucet J-L, Esquivel-Muelbert A, Feldpausch T R, Fofanah A, Foli E G, Gilpin M, Gloor E, Gonmadje C, Gourlet-Fleury S, Hall J S, Hamilton A C, Harris D J, Hart T B, Hockemba M B N, Hladik A, Ifo S A, Jeffery K J, Jucker T, Kasongo Yakusu E, Kearsley E, Kenfack D, Koch A, Leal M E, Levesley A, Lindsell J A, Lisingo J, Lopez-Gonzalez G, Lovett J C, Makana J-R, Malhi Y, Marshall A R, Martin J, Martin E H, Mbayu F M, Medjibe V P, Mihindou V, Mitchard E T A, Moore S, Munishi P K T, Bengone N N, Ojo L, Ondo F E, Peh K S-H, Pickavance G C, Dalberg Poulsen A, Poulsen J R, Qie L, Reitsma J, Rovero F, Swaine M D, Talbot J, Taplin J, Taylor D M, Thomas D W, Toirambe B, Mukendi J T, Tuagben D, Umunay P M, van der Heijden G M F, Verbeeck H, Vleminckx J, Willcock S, Wöll H, Woods J T, Zemagho L, 2020. Asynchronous carbon sink saturation in African and Amazonian tropical forests. Nature 579, 80–87.

Huybers P, 2011. Combined obliquity and precession pacing of late Pleistocene deglaciations. Nature 480, 229–232.

Huybers P, Wunsch C, 2005. Obliquity pacing of the late Pleistocene glacial terminations. Nature 434, 491–494.

Huybrechts P, 1986. A three dimensional time-dependent numerical model for polar ice sheets: some basic testing with a stable and efficient finite difference scheme. Report 86-1, Geografisch Instituut, Vrije Universiteit Brussel, Belgium.

Huybrechts P, 1990. A 3D model for the Antarctic ice sheet: a sensitivity study on the glacial-interglacial contrast. Climate Dynamics 5, 79–92.

Huybrechts P, 2006. Numerical modeling of ice sheets through time. In Knight P G (ed). Glacier science and environmental change. Malden: Blackwell Publishing, 406–412.

Huybrechts P, T'Siobbel S, 1995. Thermomechanical modelling of northern hemisphere ice sheets with a two-level mass-balance parameterization. Annals of Glaciology 21, 111–116.

Huybrechts P, Payne A J, EISMINT Intercomparison Group, 1996. The EISMINT benchmarks for testing ice-sheet models. Annals of Glaciology 23, 1–12.

IEA, 2019. World energy outlook 2019. Paris: IEA. Available at: https://www.iea.org/reports/world-energy-outlook-2019

Imbrie J, Boyle E A, Clemens S C, Duffy A, Howard W R, Kukla G, Kutzbach J, Martinson D G, McIntyre A, Mix A C, Molfino B, Morley J J, Peterson L C, Pisias N G, Imbrie J, Hays J D, Martinson D G, McIntyre A, Mix A C, Morley J J, Pisias N G, W L Prell, Shackleton N J, 1984. The orbital theory of Pleistocene climate: support from a revised chronology of the marine $\delta^{18}O$ record. In Berger A L, Imbrie J, Hays J D, Kukla G, Saltzman B (eds). Milankovitch and climate: understanding the response to astronomical forcing. Dordrecht: Reidel, 269–305.

Imbrie J Z, Imbrie-Moore A, Lisiecki L E, 2011. A phase-space model for Pleistocene ice volume. Earth and Planetary Science Letters 307, 94–102.

IPCC, 2001. Climate change 2001: the scientific basis. Contribution of Working Group I to the Third Assessment Report of the Intergovernmental Panel on Climate Change. New York: Cambridge University Press.

IPCC, 2007. Climate change 2007: the physical science basis. Contribution of Working Group I to the Fourth Assessment Report of the Intergovernmental Panel on Climate Change. Cambridge: Cambridge University Press.

IPCC, 2013a. Climate change 2013: the physical science basis: summary for policymakers. Contribution of Working Group I to the Fifth Assessment Report of the Intergovernmental Panel on Climate Change. Available at: http://www.ipcc.ch

IPCC, 2013b. Annex I: Atlas of Global and Regional Climate Projections. In Climate Change 2013: The Physical Science Basis. Contribution of Working Group I to the Fifth Assessment Report of the Intergovernmental Panel on Climate Change. Cambridge: Cambridge University Press.

IPCC, 2014. Climate change 2014: mitigation of climate change. Contribution of Working Group III to the Fifth Assessment Report of the Intergovernmental Panel on Climate Change [Edenhofer O, Pichs-Madruga R, Sokona Y, Farahani E, Kadner S, Seyboth K, Adler A, Baum I, Brunner S, Eickemeier P, Kriemann B, Savolainen J, Schlömer S, von Stechow C, Zwickel T, Minx J C (eds)]. Cambridge University Press.

IPCC, 2018. Global warming of 1.5°C. An IPCC Special Report on the impacts of global warming of 1.5 °C above pre-industrial levels and related global greenhouse gas emission pathways, in the context of strengthening the global response to the threat of climate change, sustainable development, and efforts to eradicate poverty [Masson-Delmotte V, Zhai P, Pörtner H-O, Roberts D, Skea J, Shukla P R, Pirani A, Moufouma-Okia W, Péan C, Pidcock R, Connors S, Matthews J B R, Chen Y, Zhou X, Gomis M I, Lonnoy E, Maycock T, Tignor M, Waterfield T (eds)]. Geneva: World Meteorological Organization.

IPCC, 2019. IPCC special report on the ocean and cryosphere in a changing climate. [Pörtner H-O, Roberts D C, Masson-Delmotte V, Zhai P, Tignor M, Poloczanska E, Mintenbeck K, Alegría A, Nicolai M, Okem A, Petzold J, Rama B, Weyer N M (eds)]. Cambridge University Press.

IPCC, 2021. Climate change 2021: the physical science basis. Contribution of Working Group I to the Sixth Assessment Report of the Intergovernmental Panel on Climate Change[Masson-Delmotte V, Zhai P, Pirani A, Connors S L, Péan C, Berger S, Caud N, Chen Y, Goldfarb L, Gomis M I, Huang M, Leitzell K, Lonnoy E, Matthews J B R, Maycock T K, Waterfield T, Yelekçi O, Yu R, Zhou B (eds)]. Cambridge University Press. In press. doi:10.1017/9781009157896

Isaksen K, Holmlund P, Sollid J L, Harris C, 2001. Three deep alpine-permafrost boreholes in Svalbard and Scandinavia. Permafrost and Periglacial Processes 12, 13–26.

Iverson N R, 1991. Potential effects of of subglacial water-pressure fluctuations on quarrying. Journal of Glaciology 37, 27–36.

Iverson N R, 1993. Regelation of ice through debris at glacier beds: implications for sediment transport. Geology 21, 559–562.

Iverson N R, 2000. Sediment entrainment by a soft-bedded glacier: a model based on regelation into the bed. Earth Surface Processes and Landforms 25, 881–893.

Iverson N R, Hanson B, Hooke R LeB, Jansson P, 1995. Flow mechanism of glaciers on soft beds. Science 267, 80–81.

Ivins E R, 2009. Ice sheet stability and sea-level. Science 324, 888–889.

Jackson L P, Jevrejeva S, 2016. A probabilistic approach to 21st century regional sea-level projections using RCP and high-end scenarios. Global and Planetary Change 146, 179–189.

Jackson L P, Grinsted A, Jevrejeva S, 2018. 21st century sea-level rise in line with the Paris accord. Earth's Future 6, 213–229.

Jansen E, Sjøholm J, 1991. Reconstruction of glaciation over the past 6 Myr from ice-borne deposits in the Norwegian Sea. Nature 349, 600–603.

Jansson P, Näslund J-O, 2009. Spatial and temporal variations in glacier hydrology on Storglaciären, Sweden. SKB TR-09-13, Svensk Kärnbränslehantering AB.

Jaquet O, Siegel P, 2006. Regional groundwater flow model for a glaciation scenario. Simpevarp subarea – version 1.2. SKB R-06-100, Svensk Kärnbränslehantering AB.

Jaquet O, Namar R, Jansson P, 2010. Groundwater flow modelling under ice sheet conditions: scoping calculations. SKB R-10-46, Svensk Kärnbränslehantering AB.

Jaquet O, Rabah N, Pascal S, Jansson P, 2012. Groundwater flow modelling under ice sheet conditions in Greenland (phase II). SKB R-12-14, Svensk Kärnbränslehantering AB

Jevrejeva S, Moore J C, Grinsted A, 2012. Sea level projections to AD 2500 with a new generation of climate change scenarios. Global Planetary Change 80, 14–20.

Jevrejeva S, Grinsted A, Moore J C, 2014. Upper limit for sea level projections by 2100. Environmental Research Letters 9, 104008. doi:10.1088/1748-9326/9/10/104008

Johansson E, Berglund S, Lindborg T, Petrone J, Van As D, Gustafsson L-G, Näslund J-O, Laudon H, 2015. Hydrological and meteorological investigations in a periglacial lake catchment near Kangerlussuaq, west Greenland – Presentation of a new multi-parameter data set. Earth System Science Data 7, 93–108.

Johansson J M, Davis J L, Scherneck H-G, Milne G A, Vermeer M, Mitrovica J X, Bennett R A, Jonsson B, Elgered G, Elósegui P, Koivula H, Poutanen M, Rönnäng B O, Shapiro I I, 2002. Continuous GPS measurements of postglacial adjustment in Fennoscandia. 1. Geodetic results. Journal of Geophysical Research 107, 400–428.

Johansson P-O, 2008. Description of surface hydrology and near-surface hydrogeology at Forsmark. Site descriptive modelling, SDM-Site Forsmark. SKB R-08-08, Svensk Kärnbränslehantering AB.

Johansson P-O, Öhman J, 2008. Presentation of meteorological, hydrological and hydrogeological monitoring data from Forsmark. Site descriptive modelling SDM-Site Forsmark. SKB R-08-10, Svensk Kärnbränslehantering AB.

Johnsen S J, Dahl-Jensen D, Dansgaard W, Gundestrup N, 1995. Greenland palaeotemperatures derived from GRIP bore hole temperature and ice core isotope profiles. Tellus 47B, 624–629.

Johnson J, 1994. A basal water model for ice sheets. PhD thesis. University of Minnesota.

Johnson J, 2004. Estimating basal melt rate in Antarctica. International Symposium on Ice and Water Interactions: processes across the phase boundary. Portland, Oregon, 26–30 July 2004.

Joughin I, Tulaczyk S, 2002. Positive mass balance for the Ross Ice Streams, West Antarctica. Science 295, 476–480.

Joughin I, Abdalati W, Fahnestock M, 2004. Large fluctuations in speed on Greenland's Jakobshavn Isbræ glacier. Nature 432, 608–610.

Joussaume S, Taylor K E, 2000. The paleoclimate modeling intercomparison project. In Braconnot P (ed). Proceedings of the third Paleoclimate Modelling Intercomparison Project (PMIP) workshop. La Huardière, Canada, 4–8 October 1999. (WCRP-111, WMO/TD-1007)

Jouzel J, Barkov N I, Barnola J M, Bender M, Chappellaz J, Genthon C, Kotlyakov V M, Lipenkov V, Lorius C, Petit J R, Raynaud D, Raisbeck G, Ritz C, Sowers T, Stievenvard M, Yiou F, Yiou P, 1993. Extending the Vostok ice-core record of paleoclimate to the penultimate glacial period. Nature 364, 407–412.

Jouzel J, Stiévenard M, Johnsen S J, Landais A, Masson-Delmotte V, Sveinbjornsdottir A, Vimeux F, von Grafenstein U, White J W C, 2007. The GRIP deuterium-excess record. Quaternary Science Reviews 26, 1–17.

Jupp T E, Cox P M, Rammig A, Thonicke K, Lucht W, Cramer W, 2010. Development of probability density functions for future South American rainfall. New Phytologist 187, 682–693.

Kageyama M, Laîné A, Abe-Ouchi A, Braconnot P, Cortijo E, Crucifix M, de Vernal A, Guiot J, Hewitt C D, Kitoh A, Kucera M, Marti O, Ohgaito R, Otto-Bliesner B, Peltier W R, Rosell-Melé A, Vettoretti G, Weber S L, Yu Y, MARGO project members, 2006. Last Glacial Maximum temperatures over the North Atlantic, Europe and western Siberia: a comparison between PMIP models, MARGO sea-surface temperatures and pollen-based reconstructions. Quaternary Science Reviews 25, 2082–2102.

Kamb B, 2001. Basal zone of the West-Antarctic ice streams and its role in their rapid motion. In Alley R B, Bindschadler R A (eds). The West Antarctic ice sheet: behavior and environment. Washington, DC: American Geophysical Union, 157–200.

Kaufmann G, Lambeck K, 2002. Glacial isostatic adjustment and the radial viscosity profile from inverse modeling. Journal of Geophysical Research 107, 2280. doi:10.1029/2001JB000941

Kim S-J, Crowley T J, Erickson D J, Govindasamy B, Duffy P B, Lee B Y, 2008. High-resolution climate simulation of the last glacial maximum. Climate Dynamics 31, 1–16.

King L, 1984. Permafrost in Skandinavien: Untersuchungsergebnisse aus Lappland, Jotunheimen und Dovre/Rondane. Heidelberg: Geographisches Institut der Univ. (Heidelberger geographische Arbeiten 76) (In German.)

Kjellström E, Strandberg G, Brandefelt J, Näslund J-O, Smith B, Wohlfarth B, 2009. Climate conditions in Sweden in a 100,000-year time perspective. SKB TR-09-04, Svensk Kärnbränslehantering AB.

Kjellström E, Nikulin G, Hansson U, Strandberg G, Ullerstig A, 2011. 21st century changes in the European climate: uncertainties derived from an ensemble of regional climate model simulations. Tellus A 63, 24–40.

Kleinen T, Brovkin V, 2018. Pathway-dependent fate of permafrost region carbon. Environmental Research Letters 13, 094001. doi:10.1088/1748- 9326/aad824

Kleman J, 1994. Preservation of landforms under ice sheets and ice caps. Geomorphology 9, 19–32.

Kleman J, Glasser N F, 2007. The subglacial thermal organisation (STO) of ice sheets. Quaternary Science Reviews 26, 585–597.

Kleman J, Hättestrand C, 1999. Frozen-based Fennoscandian and Laurentide ice sheets during the last glacial maximum. Nature 402, 63–66.

Kleman J, Stroeven A P, 1997. Preglacial surface remnants and Quaternary glacial regimes in northwestern Sweden. Geomorphology 19, 35–54.

Kleman J, Hättestrand C, Borgström I, Stroeven A, 1997. Fennoscandian palaeoglaciology reconstructed using a glacial geological inversion model. Journal of Glaciology 43, 283–299.

Kleman J, Stroeven A, Lundqvist J, 2008. Patterns of Quaternary ice sheet erosion and deposition in Fennoscandia and a theoretical framework for explanation. Geomorphology 97, 73–90.

Kleman J, Fastook J, Ebert K, Nilsson J, Caballero R, 2013. Pre-LGM Northern Hemisphere paleo-ice sheet topography. Climate of the Past Discussions 9, 2557–2587.

Knutti R, Sedláček J, 2013. Robustness and uncertainties in the new CMIP5 climate model projections. Nature Climate Change 3, 369–373.

Kopp R E, Horton R M, Little C M, Mitrovica J X, Oppenheimer M, Rasmussen D J, Strauss B H, Tebaldi C, 2014. Probabilistic 21st and 22nd century sea-level projections at a global network of tide-gauge sites. Earth's Future 2, 383–406.

Kopp R E, Kemp A C, Bittermann K, Horton B P, Donnelly J P, Gehrels W R, Hay C C, Mitrovica J X, Morrow E D, Rahmstorf S, 2016. Temperature-driven global sea-level variability in the Common Era. Proceedings of the National Academy of Sciences 113, E1434–E1441.

Kopp R E, DeConto R M, Bader D A, Horton R M, Hay C C, Kulp S, Oppenheimer M, Pollard D, Strauss B H, 2017. Implications of Antarctic ice-cliff collapse and ice-shelf hydrofracturing mechanisms for sea-level projections. Earth's Future 5, 1217–1233.

Koppes M N, Montgomery D R, 2009. The relative efficacy of fluvial and glacial erosion over modern to orogenic timescales. Nature Geoscience 2, 644–647.

Kriegler E, Bauer N, Popp A, Humpenöder F, Leimbach M, Strefler J, Baumstark L, Leon Bodirsky B, Hilaire J, Klein D, Mouratiadou J, Weindl I, Bertram C, Dietrich J-P, Luderer G, Pehl M, Pietzcker R, Piontek F, Lotze-Campen H, Biewald A, Bonsch M, Giannousakis A, Kreidenweis U, Müller C, Rolinski S, Schultes A, Schwanitz J, Stevanovic M, Calvin K, Emmerling J, Fujimori S, Mouratiadou I, 2017. Fossil-fueled development (SSP5): an energy and resource intensive scenario for the 21st century. Global Environmental Change 42, 297–315.

Krogh Andersen K, Svensson A, Rasmussen S O, Steffensen J P, Johnsen S, Bigler M, Röthlisberger R, Ruth U, Siggaard-Andersen M-L, Dahl-Jensen D, Vinther B M, Clausen H B, 2006. The Greenland ice core chronology 2005, 15–42 kyr. Part 1: constructing the time scale. Quaternary Science Reviews, 25, 3246–3257.

Kukkonen I, 1989. Terrestrial heat flow and radiogenic heat production in Finland, the central Baltic Shield. Tectonophysics 164, 219–230.

Kukkonen I T, Šafanda J, 2001. Numerical modelling of permafrost in bedrock in northern Fennoscandia during the Holocene. Global and Planetary Change 29, 259–274.

Kåberger T, 2018. Progress of renewable electricity replacing fossil fuels. Global Energy Interconnection 1, 48–52.

Lachenbruch A H, 1968. Preliminary geothermal model of the Sierra Nevada. Journal of Geophysical Research 73, 6977–6989.

Lagerbäck R, 1988a. The Veiki moraines in northern Sweden – widespread evidence of an Early Weichselian deglaciation. Boreas 17, 469–486.

Lagerbäck R, 1988b. Periglacial phenomena in the wooded areas of northern Sweden – relicts from the Tärendö Interstadial. Boreas 17, 487–499.

Lagerbäck R, Robertsson A-M, 1988. Kettle holes – stratigraphical archives for Weichselian geology and palaeoenvironment in northernmost Sweden. Boreas 17, 439–468.

Lambeck K, 1995. Late Devensian and Holocene shorelines of the British Isles and North Sea from models of glacio-hydroisostatic rebound. Journal of the Geological Society 152, 437–448.

Lambeck K, 1999. Shoreline displacements in southern-central Sweden and the evolution of the Baltic Sea since the last maximum glaciation. Journal of the Geological Society 156, 465–486.

Lambeck K, Chappell J, 2001. Sea level change through the last glacial cycle. Science 292, 679–686.

Lambeck K, Smither C, Johnston P, 1998. Sea-level change, glacial rebound and mantle viscosity for northern Europe. Geophysical Journal International 134, 102–144.

Lambert A, Courtier N, Sasagawa G S, Klopping F, Winester D, James T S, Liard J O, 2001. New constraints on Laurentide postglacial rebound from absolute gravity measurements. Geophysical Research Letters 28, 2109–2112.

Lambeck K, Yokoyama Y, Purcell T, 2002. Into and out of the Last Glacial Maximum: sea-level change during Oxygen Isotope Stages 3 and 2. Quaternary Science Reviews 21, 343–360.

Lambeck K, Purcell A, Zhao J, Svensson N-O, 2010. The Scandinavian Ice Sheet: from MIS 4 to the end of the Last Glacial Maximum. Boreas 39, 410–435.

Landström O, Larsson, S Å, Lind G, Malmqvist D, 1979. Geothermal investigations in the Bohus granite area in southwestern Sweden. Tectonophysics 64, 131–162.

Lang C, Leuenberger M, Schwander J, Johnsen S, 1999. 16°C rapid temperature variation in central Greenland 70,000 years ago. Science 286, 934–937.

Larson S A, Tullborg E-L, Cederbom C, Stiberg J P, 1999. Sveconorwegian and Caledonian foreland basins in the Baltic Shield revealed by fission-track thermochronology. Terra Nova-Oxford 11, 210–215.

Larsson-McCann S, Karlsson A, Nord M, Sjögren J, Johansson L, Ivarsson M, Kindell S, 2002. Meteorological, hydrological and oceanographical information and data for the site investigation program in the communities of Östhammar and Tierp in the northern part of Uppland. SKB TR-02-02, Svensk Kärnbränslehantering AB.

Laskar J, Robutel P, Joutel F, Gastineau M, Correia A C M, Levrard B, 2004. A long-term numerical solution for the insolation quantities of the Earth. Astronomy & Astrophysics 428, 261–285.

Latychev K, Mitrovica J X, Tamisiea M E, Tromp J, Moucha R, 2005. Influence of lithospheric thickness variations on 3-D crustal velocities due to glacial isostatic adjustment. Geophysical Research Letters 32, L01304. doi:10.1029/2004GL021454

Le Bars D, Drijfhout S, de Vries H, 2017. A high-end sea level rise probabilistic projection including rapid Antarctic ice sheet mass loss. Environmental Research Letters 12, 044013. doi:10.1088/1748-9326/aa6512

Le Quéré C, Andrew R M, Friedlingstein P, Sitch S, Hauck J, Pongratz J, Pickers P A, Korsbakken J I, Peters G P, Canadell J G, Arneth A, Arora V K, Barbero L, Bastos A, Bopp L, Chevallier F, Chini L P, Ciais P, Doney S C, Gkritzalis T, Goll D S, Harris I, Haverd V, Hoffman F M, Hoppema M, Houghton R A, Hurtt G, Ilyina T, Jain A K, Johannesen T, Jones C D, Kato E, Keeling R F, Klein Goldewijk K, Landschützer P, Lefèvre N, Lienert S, Liu Z, Lombardozzi D, Metzl N, Munro D R, Nabel J E M S, Nakaoka S, Neill C, Olsen A, Ono T, Patra P, Peregon A, Peters W, Peylin P, Pfeil B, Pierrot D, Poulter B, Rehder G, Resplandy L, Robertson E, Rocher M, Rödenbeck C, Schuster U, Schwinger J, Séférian R, Skjelvan I, Steinhoff T, Sutton A, Tans P P, Tian H, Tilbrook B, Tubiello F N, van der Laan-Luijkx I T, van der Werf G R, Viovy N, Walker A P, Wiltshire A J, Wright R, Zaehle S, Zheng B, 2018. Global carbon budget 2018. Earth System Science Data 10, 2141–2194.

Le Quéré C, Korsbakken J I, Wilson C, Tosun J, Andrew R, Andres R J, Canadell J G, Jordan A, Peters G P, van Vuuren D P, 2019. Drivers of declining CO_2 emissions in 18 developed economies. Nature Climate Change 9, 213–217.

Le Quéré C, Jackson R B, Jones M W, Smith A J, Abernethy S, Andrew R M, De-Gol A J, Willis D R, Shan Y, Canadell J G, Friedlingstein P, Creutzig F, Peters G P, 2020. Temporary reduction in daily global CO_2 emissions during the COVID-19 forced confinement. Nature Climate Change 10, 647–653.

Leduc M, Matthews H D, de Elía R, 2015. Quantifying the limits of a linear temperature response to cumulative CO_2 emissions. Journal of Climate 28, 9955–9968.

Lemieux J-M, Sudicky E A, Peltier W R, Tarasov L, 2008a. Dynamics and groundwater recharge and seepage over the Canadian landscape during the Wisconsinian glaciation. Journal of Geophysical Research 113, F01011. doi:10.1029/2007JF000838

Lemieux J-M, Sudicky E A, Peltier W R, Tarasov L, 2008b. Simulating the impact of glaciations on continental groundwater flow systems: 1. Relevant processes and model formulation. Journal of Geophysical Research 113, F03017. doi:10.1029/2007JF000928

Lemieux J-M, Sudicky E A, Peltier W R, Tarasov L, 2008c. Simulating the impact of glaciations on continental groundwater flow systems: 2. Model application to the Wisconsinian glaciation over the Canadian landscape. Journal of Geophysical Research 113, F03018. doi:10.1029/2007JF000929

Levermann A, Clark P U, Marzeion B, Milne G A, Pollard D, Radic V, Robinson A, 2013. The multimillennial sea-level commitment of global warming. Proceedings of the National Academy of Sciences 110, 13745–13750.

Li C, Battisti D S, 2008. Reduced Atlantic storminess during Last Glacial Maximum: Evidence from a coupled climate model. Journal of Climate 21, 3561–3579.

Liakka J, Lofverstrom M, 2018. Arctic warming induced by the Laurentide Ice Sheet topography. Climate of the Past 14, 887–900.

Liakka J, Nilsson J, 2010. The impact of topographically forced stationary waves on local ice-sheet climate. Journal of Glaciology 56, 534–544.

Liakka J, Löfverström M, Colleoni F, 2016. The impact of the North American glacial topography on the evolution of the Eurasian ice sheet over the last glacial cycle. Climate of the Past 12, 1225–1241.

Liakka J, Näslund J O, Brandefelt J, 2021. Timing of future glacial inception. In Haeberli W, Whiteman C (eds). Snow and ice-related hazards, risks and disasters. 2nd ed. Oxford: Elsevier, Chapter 11.2.

Lidmar-Bergström K, 1995. Relief and saprolites through time on the Baltic shield. Geomorphology 12, 45–61.

Lidmar-Bergström K, 1997. A long-term perspective on glacial erosion. Earth Surface Processes and Landforms 22, 297–306.

Lidmar-Bergström K, Näslund J-O, 2002. Landforms and uplift in Scandinavia. In Doré A G, Cartwright J A, Stoker M S, Turner J P, White N (eds). Exhumation of the North Atlantic margin: timing, mechanisms, and implications for petroleum exploration. London: Geological Society. (Special publication 196), 103–116.

Lidmar-Bergström K, Näslund J-O, 2005. Major landforms and bedrock. In Seppälä M (ed). The physical geography of Fennoscandia. Oxford: Oxford University Press.

Lidmar-Bergström K, Olsson S, Olvmo M, 1997. Palaeosurfaces and associated saprolites in southern Sweden. In Widdowson M (ed). Palaeosurfaces: recognition, reconstruction and palaeo-environmental interpretation. London: Geological Society. (Special publication 120), 95–124.

Lind P, Kjellström E, 2008. Temperature and precipitation changes in Sweden: a wide range of model-based projections for the 21st century. Norrköping: Sveriges meteorologiska och hydrologiska institut (Swedish Meteorological and Hydrological Institute). (SMHI reports. Meteorology and Climatology 113)

Lindborg T (ed), 2010. Landscape Forsmark – data, methodology and results for SR-Site. SKB TR-10-05, Svensk Kärnbränslehantering AB.

Lisiecki L E, 2010. Links between eccentricity forcing and the 100,000-year glacial cycle. Nature Geoscience 3, 349–352.

Lisiecki L E, Raymo M E, 2005. A Pliocene-Pleistocene stack of 57 globally distributed benthic $\delta^{18}O$ records. Paleoceanography 20. doi:10.1029/2004PA001071

Lisiecki L E, Raymo M E, 2007. Plio–Pleistocene climate evolution: trends and transitions in glacial cycle dynamics. Quaternary Science Reviews 26, 56–69.

Liu W, Xie S P, Liu Z, Zhu J, 2017. Overlooked possibility of a collapsed Atlantic Meridional Overturning Circulation in warming climate. Science Advances 3, e1601666. doi:10.1126/sciadv.1601666

Lokrantz H, Sohlenius G, 2006. Ice-marginal fluctuations during the Weichselian glaciation in Fennoscandia, a literature review. SKB TR-06-36, Svensk Kärnbränslehantering AB.

Lord N S, Ridgwell A, Thorne M C, Lunt D J, 2015. The 'long tail' of anthropogenic CO_2 decline in the atmosphere and its consequences for post-closure performance assessments for disposal of radioactive wastes. Mineralogical Magazine 79, 1613–1623.

Lord N S, Ridgwell A, Thorne M C, Lunt D J, 2016. An impulse response function for the "long tail" of excess atmospheric CO_2 in an Earth system model. Global Biogeochemical Cycles 30, 2–17.

Lord N S, Crucifix M, Lunt D J, Thorne M C, Bouncer N, Dowsett H, O'Brien C L, Ridgwell A, 2017. Emulation of long-term changes in global climate: application to the mid-Pliocene and future. Climate of the Past 13, 1539–1571.

Lord N S, Lunt D, Thorne M, 2019. Modelling changes in climate over the next 1 million years. SKB TR-19-09, Svensk Kärnbränslehantering AB.

Loutre M F, Berger A, 2000. Future climatic changes: are we entering an exceptionally long interglacial? Climatic Change 46, 61–90.

Lunardini V J, 1978. Theory of n-factors and correlation of data. In Proceedings of the 3rd International Conference on Permafrost. Edmonton, Alta, 10–13 July 1978. Ottawa: National Research Council of Canada, Vol 1, 40–46.

Lunardini V J, 1995. Permafrost formation time. CRREL Report 95-8, U.S. Army Cold Regions Research and Engineering Laboratory.

Lund B, Näslund J-O, 2009. Glacial isostatic adjustment: implications for glacially induced faulting and nuclear waste repositories. In Connor C B, Chapman N A, Connor L J (eds). Volcanic and tectonic hazard assessment for nuclear facilities. Cambridge: Cambridge University Press, 142–155.

Lund B, Schmidt P, Hieronymus C, 2009. Stress evolution and fault stability during the Weichselian glacial cycle. SKB TR-09-15, Svensk Kärnbränslehantering AB.

Lundqvist J, 1992. Glacial stratigraphy in Sweden. Geological Survey of Finland Special Paper 5, 43–59.

Lundqvist J, 2007. Surging ice and break-down of an ice dome – a deglaciation model for the Gulf of Bothnia. Geologiska Föreningens i Stockholm Förhandlingar 129, 329–336.

Lundqvist J, Wohlfarth B, 2000. Timing and east-west correlation of south Swedish ice-marginal lines during the Late Weichselian. Quaternary Science Reviews 20, 1127–1148.

Lundqvist J, Lundqvist T, Lindström M, Calner M, Sivhed U, 2011. Sveriges geologi från urtid till nutid. 3rd ed. Lund: Studentlitteratur. (In Swedish.)

Lüthi D, Le Floch M, Bereiter B, Blunier T, Barnola J-M, Siegenthaler U, Raynaud D, Jouzel J, Fischer H, Kawamura K, Stocker T F, 2008. High-resolution carbon dioxide concentration record 650,000–800,000 years before present. Nature 453, 379–382.

Löfverström M, Caballero R, Nilsson J, Kleman J, 2014. Evolution of the large-scale atmospheric circulation in response to changing ice sheets over the last glacial cycle. Climate of the Past 10, 1453–1471.

Lönnqvist M, Hökmark H, 2010. Assessment of potential for glacially induced hydraulic jacking at different depths. SKB R-09-35, Svensk Kärnbränslehantering AB.

Mackay J R, 1997. A full-scale field experiment (1978–1995) on the growth of permafrost by means of lake drainage, western Arctic coast: a discussion of the method and some results. Canadian Journal of Earth Sciences 34, 17–33.

Mai H, Thomsen T, 1993. Permafrost studies in Greenland. In Proceedings of the sixth international conference on permafrost. Beijing, 5–9 July 1993. Guangzhou: South China University of Technology, Vol 2.

Malmqvist D, Larson S Å, Landström O, Lind G, 1983. Heat flow and heat production from the Malingsbo granite, central Sweden. Bulletin of the Geological Institutions of the University of Uppsala 9, 137–152.

Mangerud J, Gyllencreutz R, Lohne O, Svendsen J I, 2011. Glacial history of Norway. In Ehlers J, Gibbard P L, Hughes P D (eds). Quaternary glaciations – extent and chronology: a closer look. Amsterdam: Elsevier. (Developments in Quaternary Sciences 15), 279–298.

Marchant D R, Denton G H, Sugden D E, Swisher C C, 1993. Miocene glacial stratigraphy and landscape evolution of the western Asgard Range, Antarctica. Geografiska Annaler 75A, 303–330.

Marshall S J, Clarke G K C, 1997. A continuum mixture model of ice stream thermodynamics in the Laurentide Ice Sheet. 1. Theory. Journal of Geophysical Research 102, 20599–20614.

Matthews H D, Gillett N P, Stott P A, Zickfeld K, 2009. The proportionality of global warming to cumulative carbon emissions. Nature 459, 829–832.

McConnell R K, 1968. Viscosity of the mantle from relaxation time spectra of isostatic adjustment. Journal of Geophysical Research 73, 7089–7105.

McGuire A D, Lawrence D M, Koven C, Clein J S, Burke E, Chen G, Jafarov E, MacDougall A H, Marchenko S, Nicolsky D, Peng S, Rinke A, Ciais P, Gouttevin I, Hayes D J, Ji D, Krinner G, Moore J C, Romanovsky V, Schädel C, Schaefer K, Schuur E A G, Zhuang Q, 2018. Dependence of the evolution of carbon dynamics in the northern permafrost region on the trajectory of climate change. Proceedings of the National Academy of Sciences 115, 3882–3887.

McIntyre K, Delaney M L, Ravelo A C, 2001. Millennial-scale climate change and oceanic processes in the late Pliocene and early Pleistocene. Paleoceanography 16, 535–543.

McKee Smith J, Sherlock A R, Resio D T, 2001. STWAVE: Steady-State Spectral Wave Model. User's manual for STWAVE, Version 3.0. Coastal and Hydraulics Laboratory U.S. Army Engineer Research and Development Center.

Meehl G A, Stocker T F, Collins W D, Friedlingstein P, Gaye A T, Gregory J M, Kitoh A, Knutti R, Murphy J M, Noda A, Raper S C B, Watterson I G, Weaver A J, Zhao Z-C, 2007. Global climate projections. In IPCC, 2007. Climate change 2007: the physical science basis. Contribution of Working Group I to the fourth assessment report of the Intergovernmental Panel on Climate Change. Cambridge: Cambridge University Press.

Meier H E M, 2006. Baltic Sea climate in the late twenty-first century: a dynamical downscaling approach using two global models and two emission scenarios. Climate Dynamics 27, 39–68.

Meinshausen M, Smith S J, Calvin K, Daniel J S, Kainuma M L T, Lamarque J-F, Matsumoto K, Montzka S A, Raper S C B, Riahi K, Thomson A, Velders G J M, van Vuuren D P P, 2011. The RCP greenhouse gas concentrations and their extensions from 1765 to 2300. Climatic Change 109, 213–241.

Mengel M, Levermann A, Frieler K, Robinson A, Marzeion B, Winkelmann R, 2016. Future sea level rise constrained by observations and long-term commitment. Proceedings of the National Academy of Sciences 113, 2597–2602.

Mikolajewicz U, Gröger M, Maier-Reimer E, Schurgers G, Vizcaíno M, Winguth A M E, 2007. Long-term effects of anthropogenic CO_2 emissions simulated with a complex earth system model. Climate Dynamics 28, 599–633.

Miller F P, Vandome A F, McBrewster J, 2008. Coefficient of determination. In Dodge Y. The concise encyclopedia of statistics. New York: Springer, 88–91.

Miller K G, Wright J D, Browning J V, Kulpecz A, Kominz M, Naish T R, Cramer B S, Rosenthal Y, Peltier W R, Sosdian S, 2012. High tide of the warm Pliocene: implications of global sea level for Antarctic deglaciation. Geology 40, 407–410.

Miller K G, Kopp R E, Horton B P, Browning J V, Kemp A C, 2013. A geological perspective on sea-level rise and impacts along the U.S. mid-Atlantic coast. Earth's Future 1, 3–18.

Milne G A, 1998. Refining models of the glacial isostatic adjustment process. PhD thesis. University of Toronto.

Milne G A, Mitrovica J X, 1998. Postglacial sea-level change on a rotating Earth. Geophysical Journal International 133, 1–19.

Milne G A, Mitrovica J X, Davis J L, 1999. Near-field hydro-isostasy: the implementation of a revised sea-level equation. Geophysical Journal International 139, 464–482.

Milne G A, Davis J L, Mitrovica J X, Scherneck H-G, Johansson J M, Vermeer M, Koivula H, 2001. Space-geodetic constraints on glacial isostatic adjustment in Fennoscandia. Science 291, 2381–2385.

Milne G A, Mitrovica J X, Schrag D P, 2002. Estimating past continental ice volume from sea-level data. Quaternary Science Reviews 21, 361–376.

Milne G A, Mitrovica J X, Scherneck H G, Davis J L, Johansson J M, Koivula H, Vermeer M, 2004. Continuous GPS measurements of postglacial adjustment in Fennoscandia: 2. Modeling results. Journal of Geophysical Research 109, B02412. doi:10.1029/2003JB002619

Milne G A, Gehrels W R, Hughes C W, Tamisiea M E, 2009. Identifying the causes of sea-level change. Nature Geoscience 2, 471–478.

Mitrovica J X, 2003. Recent controversies in predicting post-glacial sea-level change. Quaternary Science Reviews 22, 127–133.

Mitrovica J X, Forte A M, 1997. Radial profile of mantle viscosity: results from the joint inversion of convection and postglacial rebound observables. Journal of Geophysical Research 102, 2751–2769.

Mitrovica J X, Forte A M, 2004. A new inference of mantle viscosity based upon joint inversion of convection and glacial isostatic adjustment data. Earth and Planetary Science Letters 225, 177–189.

Mitrovica J X, Milne G A, 2002. On the origin of late Holocene sea-level highstands within equatorial ocean basins. Quaternary Science Reviews 21, 2179–2190.

Mitrovica J X, Milne G A, 2003. On post-glacial sea level: I. General theory. Geophysical Journal International 154, 253–267.

Mitrovica J X, Peltier W R, 1991. On post-glacial geoid subsidence over the equatorial oceans. Journal of Geophysical Research 96, 20053–20071.

Mitrovica J X, Davis J L, Shapiro I I, 1994. A spectral formalism for computing three-dimensional deformations due to surface loads. 2. Present-day glacial isostatic-adjustment. Journal of Geophysical Research 99, 7075–7101.

Mitrovica J X, Tamisiea M E, Davis J L, Milne G A, 2001. Recent mass balance of polar ice sheets inferred from patterns of global sea-level change. Nature 409, 1026–1029.

Moberg A, Sonechkin D M, Holmgren K, Datsenko N M, Karlén W, 2005. Highly variable Northern Hemisphere temperatures reconstructed from low- and high-resolution proxy data. Nature 433, 613–617.

Mitrovica J X, Gomez N, Clark P U, 2009. The sea-level fingerprint of West Antarctic Collapse. Science 323, 753.

Mohr S H, Wang J, Ellem G, Ward J, Giurco D, 2015. Projection of world fossil fuels by country. Fuel 141, 120–135.

Montagnat M, Duval P, 2000. Rate controlling processes in the creep of polar ice, influence of grain boundary migration associated with recrystallization. Earth and Planetary Science Letters 183, 179–186.

Moss R H, Edmonds J A, Hibbard K A, Manning M R, Rose S K, van Vuuren D P, Carter T R, Emori S, Kainuma M, Kram T, Meehl G A, Mitchell J F B, Nakicenovic N, Riahi K, Smith S J, Stouffer R J, Thomson A M, Weyant J P, Wilbanks T J, 2010. The next generation of scenarios for climate change research and assessment. Nature 463, 747–756.

Myhre G, Highwood E J, Shine K P, Stordal F, 1998. New estimates of radiative forcing due to well mixed greenhouse gases. Geophysical Research Letters 25, 2715–2718.

Myhre G, Shindell D, Bréon F-M, Collins W, Fuglestvedt J, Huang J, Koch D, Lamarque J-F, Lee D, Mendoza B, Nakajima T, Robock A, Stephens G, Takemura T, Zhang H, 2013. Anthropogenic and natural radiative forcing. In: Climate change 2013: the physical science basis. Contribution of Working Group I to the Fifth Assessment Report of the Intergovernmental Panel on Climate Change [Stocker, T.F., D. Qin, G.-K. Plattner, M. Tignor, S.K. Allen, J. Boschung, A. Nauels, Y. Xia, V. Bex and P.M. Midgley (eds.)]. Cambridge: Cambridge University Press.

Müller Schmied H, Adam L, Eisner S, Fink G, Flörke M, Kim H, Oki T, Portmann F T, Reinecke R, Riedel C, Song Q, Zhang J, Döll P, 2016. Variations of global and continental water balance components as impacted by climate forcing uncertainty and human water use. Hydrology and Earth System Sciences 20, 2877–2898.

Müller U C, Kukla G J, 2004. North Atlantic Current and European environments during the declining stage of the last interglacial. Geology 32, 1009–1012.

Myoung B, Nielsen-Gammon J W, 2010. Sensitivity of monthly convective precipitation to environmental conditions. Journal of Climate 23, 166–188.

Mysak L A, 2008. Glacial inceptions: past and future. Atmosphere-Ocean 46, 317–341.

Mäkinen J, Engfeldt A, Harsson B G, Routsalainen H, Strykowski G, Oja T, Wolf D, 2005. The Fennoscandian land uplift gravity lines 1966–2003. In Jekeli C, Bastos L, Fernades J (eds). Gravity, geoid and space missions. Berlin: Springer. (International Association of Geodesy symposia 129), 328–332.

Mörner N-A, 1977. Past and present uplift in Sweden: glacial isostasy, tectonism and bedrock influence. Geologiska föreningen i Stockholms förhandlingar 99, 48–54.

Mörner N-A, 1979. The Fennoscandian uplift and Late Cenozoic geodynamics: geological evidence. GeoJournal 3, 287–318.

Naish T R, Wilson G S, 2009. Constraints on the amplitude of Mid-Pliocene (3.6–2.4 Ma) eustatic sea-level fluctuations from the New Zealand shallowmarine sediment record. Philosophical Transactions of the Royal Society A 367, 169–187.

Nakićenović N, Swart R (eds), 2000. Special report on emissions scenarios. A Special Report of Working Group III of the Intergovernmental Panel on Climate Change. Cambridge: Cambridge University Press.

Nauels A, Meinshausen M, Mengel M, Lorbacher K, Wigley T M, 2017. Synthesizing long-term sea level rise projections – the MAGICC sea level model v2.0. Geoscientific Model Development 10, 2495–2524.

NEEM community members, 2013. Eemian interglacial reconstructed from a Greenland folded ice core. Nature 493, 489–494.

Nerem R S, Beckley B D, Fasullo J T, Hamlington B D, Masters D, Mitchum G T, 2018. Climate-change–driven accelerated sea-level rise detected in the altimeter era. Proceedings of the National Academy of Sciences 115, 2022–2025.

Nerheim S, Schöld S, Persson G, Sjöström Å, 2017. Framtida havsnivåer i Sverige. Norrköping: SMHI. (Klimatologi 48) (In Swedish.)

Nicholls R J, Brown S, Goodwin P, Wahl T, Lowe J, Solan M, Godbold J A, Haigh I D, Lincke D, Hinkel J, Wolff C, Merkens J-L, 2018. Stabilization of global temperature at 1.5 C and 2.0 C: implications for coastal areas. Philosophical Transactions of the Royal Society A: Mathematical, Physical and Engineering Sciences 376. doi:10.1098/rsta.2016.0448

North G R, Stevens M J, 2006. Energy-balance climate models. In Kiehl J T and Ramanathan V (eds). Frontiers of Climate Modeling. Cambridge: Cambridge University Press 52–72.

North G R, Cahalan R F, Coakley Jr. J A, 1981. Energy balance climate models. Reviews of Geophysics 19, 91– 121.

NorthGRIP community members, 2004. High-resolution record of the Northern Hemisphere climate extending into the last interglacial period. Nature 431, 147–151.

Näslund J-O, 1997. Subglacial preservation of valley morphology at Amundsenisen, western Dronning Maud Land, Antarctica. Earth Surface Processes and Landforms 22, 441–455.

Näslund J-O, 1998. Ice sheet, climate, and landscape interactions in Dronning Maud Land, Antarctica. PhD thesis. Department of Physical Geography, Stockholm University.

Näslund J-O, 2001. Landscape development in western and central Dronning Maud Land, East Antarctica. Antarctic Science 13, 302–311.

Näslund J–O, 2011. Data used in the SR-Site climate program. SKBdoc 1265613 ver 1.0, Svensk Kärnbränslehantering AB.

Näslund J-O, Fastook J L, Holmlund P, 2000. Numerical modelling of the ice sheet in western Dronning Maud Land, East Antarctica: impact of present, past, and future climates. Journal of Glaciology 46, 54–66.

Näslund J-O, Rodhe L, Fastook J L, Holmlund P, 2003. New ways of studying ice sheet flow directions and glacial erosion by computer modelling – examples from Fennoscandia. Quaternary Science Reviews 22, 245–258.

Näslund J-O, Jansson P, Fastook J L, Johnson J, Andersson L, 2005. Detailed spatially distributed geothermal heat-flow data for modeling of basal temperatures and meltwater production beneath the Fennoscandian ice sheet. Annals of Glaciology 40, 95–101.

Näslund J-O (ed), Wohlfarth B (ed), Alexanderson H, Helmens K, Hättestrand M, Jansson P, Kleman J, Lundqvist J, Brandefelt J, Houmark-Nielsen M, Kjellström E, Strandberg G, Knudsen K L, Krogh Larsen N, Ukkonen P, Mangerud J, 2008. Fennoscandian paleo-environment and ice sheet dynamics during Marine Isotope Stage (MIS) 3. Report of a workshop held September 20–21, 2007 in Stockholm, Sweden. SKB R-08-79, Svensk Kärnbränslehantering AB.

Näslund J-O, Brandefelt J, Claesson Liljedahl L, 2013. Climate considerations in long-term safety assessments for nuclear waste repositories. Ambio 42, 393–401.

Näslund J-O, Mårtensson P, Lindgren M, Åstrand P-G, 2017a. Information om klimat och effekter på SFR till följd av frysning av betong. SKBdoc 1572377 ver 1.0, Svensk Kärnbränslehantering AB. (In Swedish.)

Näslund J-O, Mårtensson P, Andersson E, 2017b. Svar till SSM på begäran om komplettering av ansökan om utökad verksamhet vid SFR – effekter av tidig permafrostpåverkan. SKBdoc 1564242 ver 1.0, Svensk Kärnbränslehantering AB. (In Swedish.)

O'Neill B C, Tebaldi C, van Vuuren D P, Eyring V, Friedlingstein P, Hurtt G, Knutti R, Kriegler E, Lamarque J F, Lowe J, Meehl G A, Moss R, Riahi K, Sanderson B M, 2016. The Scenario Model Intercomparison Project (ScenarioMIP) for CMIP6. Geoscientific Model Development 9, 461–482.

O'Neill K, Miller R D, 1985. Exploration of rigid ice model of frost heave. Water Resources Research 21, 281–296.

Olvmo M, 2010. Review of denudation processes and quantification of weathering and erosion rates at a 0.1 to 1 Ma time scale. SKB TR-09-18, Svensk Kärnbränslehantering AB.

Olvmo M, Johansson M, 2002. The significance of rock structure, lithology, and pre-glacial deep weathering for the shape of intermediate-scale glacial erosional landforms. Earth Surface Processes and Landforms 27, 251–268.

Olvmo M, Lidmar-Bergström K, Ericson K, Bonow J M, 2005. Saprolite remnant as indicators of pre-glacial landform genesis in southeast Sweden. Geografiska annaler 87A, 447–460.

Otto-Bliesner B L, Brady E C, Clauzet G, Thomas R, Levis S, Kothavala Z, 2006. Last glacial maximum and Holocene climate in CCSM3. Journal of Climate 19, 2526–2544.

Paananen M, Ruskeeniemi T, 2003. Permafrost at Lupin: Interpretation of SAMPO electromagnetic soundings at Lupin. Report YST-117, Geological Survey of Finland.

Padilla F, Villeneuve J-P, 1992. Modelling and experimental studies of frost heave including solute effects. Cold Regions Science and Technology 20, 183–194.

Paillard D, 1998. The timing of Pleistocene glaciations from a simple multiple-state climate model. Nature 391, 378–381.

Paterson W S B, 1994. The physics of glaciers. 3rd ed. Oxford: Pergamon.

Patton H, Hubbard A, Andreassen K, Winsborrow M, Stroeven A P, 2016. The build-up, configuration, and dynamical sensitivity of the Eurasian ice-sheet complex to Late Weichselian climatic and oceanic forcing. Quaternary Science Reviews 153, 97–121.

Pattyn F, 2003. A new three-dimensional higher-order thermomechanical ice sheet model: basic sensitivity, ice-stream development, and ice flow across subglacial lakes. Journal of Geophysical Research 108, 2382. doi:10.1029/2002JB002329

Pattyn F, Huybrechts P, Decleir H, 1989. Modelling glacier fluctuations in the Sør Rondane, Dronning Maud Land, Antarctica. Zeitschrift fur Gletscherkunde und Glazialgeologie 25, 33–47.

Payne A J, 1995. Limit cycles in the basal thermal regime of ice sheets. Journal of Geophysical Research 100, 4249–4263.

Payne A J, Baldwin D J, 1999. Thermomechanical modelling of the Scandinavian ice sheet: implications for ice-stream formation. Annals of Glaciology 28, 83–89.

Payne A J, Dongelmans P W, 1997. Self-organization in the thermomechanical flow of ice sheets. Journal of Geophysical Research 102, 12219–12234.

Payne A J, Huybrechts P, Abe-Ouchi A, Calov R, Fastook J L, Greve R, Marshall S J, Marsiat I, Ritz C, Tarasov L, Thomassen M P A, 2000. Results from the EISMINT model intercomparison: the effects of thermomechanical coupling. Journal of Glaciology 46, 227–238.

Pellikka H, Särkkä J, Johansson M, Pettersson H, 2020. Probability distributions for mean sea level and storm contribution up to 2100 AD at Forsmark, Sweden. SKB TR-19-23, Svensk Kärnbränslehantering AB.

Peltier W R, 1994. Ice age palaeotopography. Science 265, 195–201.

Peltier W R, 1998. Postglacial variations in the level of the sea: implications for climate dynamics and solid-earth geophysics. Reviews of Geophysics 36, 603–689.

Peltier W R, 2002. On eustatic sea level history: Last Glacial Maximum to Holocene. Quaternary Science Reviews 21, 377–396.

Peltier W R, 2004. Global glacial isostasy and the surface of the ice-age Earth: the ICE-5G (VM2) model and GRACE. Annual Review of Earth and Planetary Science 32, 111–149.

Peltier W R, 2005. On the hemispheric origins of meltwater pulse 1a. Quaternary Science Reviews 24, 1655–1671.

Peltier W R, Fairbanks R, 2006. Global glacial ice volume and Last Glacial Maximum duration from an extended Barbados sea-level record. Quaternary Science Reviews 25, 3322–3337.

Penman H L, 1948. Natural evaporation from open water, bare soil and grass. Proceedings of the Royal Society of London. Series A 193, 120–145.

Pereira A R, Pruitt W O, 2004. Adaptation of the Thornthwaite scheme for estimating daily reference evapotranspiration. Agricultural Water Management 66, 251–257.

Perrette M, Landerer F, Riva R, Frieler K, Meinshausen M, 2013. A scaling approach to project regional sea level rise and its uncertainties. Earth System Dynamics 4, 11–29.

Person M, McIntosh J, Bense V, Remenda V H, 2007. Pleistocene hydrology of North America: the role of ice sheets in reorganizing groundwater flow systems. Reviews of Geophysics 45, RG3007. doi:10.1029/2006RG000206

Persson G, Bärring L, Kjellström E, Strandberg G, Rummukainen M, 2007. Climate indices for vulnerability assessments. Norrköping: Sveriges meteorologiska och hydrologiska institut (Swedish Meteorological and Hydrological Institute). (SMHI reports. Meteorology and Climatology 111)

Petit J R, Jouzel J, Raynaud D, Barkov N I, Barnola J M, Basile I, Bender M, Chappellaz J, Davis M, Delaygue G, Delmotte M, Kotlyakov V M, Legrand M, Lipenkov V Y, Lorius C, Pepin L, Ritz C, Saltzman E, Stievenard M, 1999. Climate and atmospheric history of the past 420,000 years from the Vostok ice core, Antarctica. Nature 399, 429–436.

Pfeffer W T, Harper J T, O'Neel S, 2008. Kinematic constraints on glacier contributions to 21st-century sea-level rise. Science 321, 1340–1343.

Pimenoff N, Venäläinen A, Järvinen H, 2011. Climate scenarios for Olkiluoto on a time-scale of 120,000 years. Posiva 2011-04, Posiva Oy, Finland.

Pimenoff N, Venäläinen A, Järvinen H, 2012. Climate and sea level scenarios for Olkilouto for the next 10,000 years. Posiva 2012-26, Posiva Oy, Finland.

Placidi L, Greve R, Seddik H, Faria S H, 2010. Continuum-mechanical, Anisotropic Flow model for polar ice masses, based on an anisotropic Flow Enhancement factor. Continuum Mechanics and Thermodynamics 22, 221–237.

Pollack H N, Hurter S J, Johnson, J R, 1991. A new global heat flow compilation. Available at: http://www.wdcb.ru/sep/data/hdata/hf_global.dat

Pollack H N, Hurter S J, Johnson J R, 1993. Heat flow from the Earth's interior: analysis of the global data set. Reviews of Geophysics 31, 267–280.

Porter S C, 1989. Some geological implications of average Quaternary glacial conditions. Quaternary Research 32, 245–261.

Priestley C B H, Taylor R J, 1972. On the assessment of surface heat flux and evaporation using large scale parameters. Monthly Weather Review 100, 81–92.

PSMSL, 2018. Tide gauge data. Permanent Service for Mean Sea Level. Available at: http://www.psmsl.org/data/obtaining/

Påsse T, 2001. An empirical model of glacio-isostatic movements and shore-level displacement in Fennoscandia. SKB R-01-41, Svensk Kärnbränslehantering AB.

Påsse T, 2004. The amount of glacial erosion of the bedrock. SKB TR-04-25, Svensk Kärnbränslehantering AB.

Påsse T, Daniels J, 2015. Past shore-level and sea-level displacements. Uppsala: Geological Survey of Sweden. (Rapporter och meddelanden 137)

Radtke U, Grün R, Schwarcz H P, 1988. Electron spin resonance dating of the Pleistocene coral reef tracts of Barbados. Quaternary Research 29, 197–215.

Rammig A, Jupp T, Thonicke K, Tietjen B, Heinke J, Ostberg S, Lucht W, Cramer W, Cox P, 2010. Estimating the risk of Amazonian forest dieback. New Phytologist 187, 694–706.

Ramstein G, Kageyama M, Guiot J, Wu H, Hély C, Krinner G, Brewer S, 2007. How cold was Europe at the Last Glacial Maximum? A synthesis of the progress achieved since the first PMIP model-data comparison. Climate of the Past 3, 331–339.

Rasmussen D J, Bittermann K, Buchanan M K, Kulp S, Strauss B H, Kopp R E, Oppenheimer M, 2018. Extreme sea level implications of 1.5 C, 2.0 C, and 2.5 C temperature stabilization targets in the 21st and 22nd centuries. Environmental Research Letters 13, 034040.

Raymo M E, Ganley K, Carter S, Oppo D W, McManus J, 1998. Millennial-scale climate instability during the early Pleistocene epoch. Nature 392, 699–702.

Raymond C F, Harrison W D, 1975. Some observations on the behaviour of the liquid and gas phases in temperate glacier ice. Journal of Glaciology 14, 213–234.

Reiche P, 1950. Survey of weathering processes and products. (University of New Mexico Publications in Geology 3)

Remy F, Minster J F, 1993. Precise altimetric topography in ice-sheet flow studies. Annals of Glaciology 17, 195–200.

Riahi K, Rao S, Krey V, Cho C, Chirkov V, Fischer G, Kindermann G, Nakicenovic N, Rafaj P, 2011. RCP 8.5 – A scenario of comparatively high greenhouse gas emissions. Climatic change 109, 33. doi:10.1007/s10584-011-0149-y

Riahi K, van Vuuren D P, Kriegler E, Edmonds J, O'Neill B C, Fujimori S, Bauer N, Calvin K, Dellink R, Fricko O, Lutz W, Popp A, Cuaresma J C, KC S, Leimbach M, Jiang L, Kram T, Rao S, Emmerling J, Ebi K, Hasegawa T, Havlik P, Humpenöder F, Da Silva L A, Smith S, Stehfest E, Bosetti V, Eom J, Gernaat D, Masui T, Rogelj J, Strefler J, Drouet L, Krey V, Luderer G, Harmsen M, Takahashi K, Baumstark L, Doelman J C, Kainuma M, Klimont Z, Marangoni G, Lotze-Campen H, Obersteiner M, Tabeau A, Tavoni M, 2017. The Shared Socioeconomic Pathways and their energy, land use, and greenhouse gas emissions implications: an overview. Global Environmental Change 42, 153–168.

Richardson C, 2004. Spatial characteristics of snow accumulation in Dronning Maud Land, Antarctica. Global and Planetary Change 42, 31–43.

Riddihough R P, 1972. Regional magnetic anomalies and geology in Fennoscandia: a discussion. Canadian Journal of Earth Sciences 9, 219–232.

Rignot E, Bamber J L, van den Broeke M R, Davis C, Li Y, van de Berg W J, van Meijgaard E, 2008. Recent Antarctic ice mass loss from radar interferometry and regional climate modelling. Nature Geoscience 1, 106–110.

Riis F, 1996. Quantification of Cenozoic vertical movements of Scandinavia by correlation of morphological surfaces with offshore data. Global and Planetary Change 12, 331–357.

Riseborough D W, Shiklomanov N, Etzelmüller B, Gruber S, Marchenko S, 2008. Recent advances in permafrost modelling. Permafrost and Periglacial Processes 19, 137–156.

Ritchie J, Dowlatabadi H, 2017. Why do climate change scenarios return to coal? Energy 140, 1276–1291.

Ritz C, Fabre A, Letreguilly A, 1996. Sensitivity of a Greenland ice sheet model to ice flow and ablation parameters: Consequences for evolution through the last climatic cycle. Climate Dynamics 13, 11–24.

Robinson A, Calov R, Ganopolski A, 2012. Multistability and critical thresholds of the Greenland ice sheet. Nature Climate Change 2, 429–432.

Roderick M L, 1992. Methods for calculating solar position and day length including computer programs and subroutines. Report 137, Department of Agriculture and Food, Western Australia, Perth.

Rohling E J, Haigh I D, Foster G L, Roberts A P, Grant K M, 2013. A geological perspective on potential future sea-level rise. Scientific Reports 3, 3461. doi:10.1038/srep03461

Rohling E J, Foster G L, Grant K M, Marino G, Roberts A P, Tamisiea M E, Williams F, 2014. Sea-level and deep-sea-temperature variability over the past 5.3 million years. Nature 508, 477–482.

Rudberg S, 1954. Västerbottens berggrundsmorfologi: ett försök till rekonstruktion av preglaciala erosionsgenerationer i Sverige. PhD thesis. Uppsala University. (In Swedish.)

Rummukainen M, 2003. The Swedish regional climate modeling program, SWECLIM, 1996–2003. Final report. Norrköping: Sveriges meteorologiska och hydrologiska institut (Swedish Meteorological and Hydrological Institute). (SMHI Meteorologi 104)

Ruosteenoja K, Vihma T, Venäläinen A, 2019. Projected changes in European and North Atlantic seasonal wind climate derived from CMIP5 simulations. Journal of Climate 32, 6467–6490.

Ruskeeniemi T, Paananen M, Ahonen L, Kaija J, Kuivamäki A, Frape S, Moren L, Degnan P, 2002. Permafrost at Lupin: report of Phase I. Report YST-112, Geological Survey of Finland.

Ruskeeniemi T, Ahonen L, Paananen M, Frape S, Stotler R, Hobbs M, Kaija J, Degnan P, Blomqvist R, Jensen M, Lehto K, Moren L, Puigdomenech I, Snellman M, 2004. Permafrost at Lupin: report of Phase II. Report YST-119, Geological Survey of Finland.

Ruskeeniemi T, Engström J, Lehtimäki J, Vanhala H, Korhonen K, Kontula A, Claesson Liljedahl L, Näslund J-O, Pettersson R, 2018. Subglacial permafrost evidencing re-advance of the Greenland Ice Sheet over frozen ground. Quaternary Science Reviews 199, 174–187.

Sanberg J A M, Oerlemans J, 1983. Modelling of Pleistocene European ice sheets: the effect of upslope precipitation. Geologie en Mijnbouw 62, 267–273.

Sánchez Goñi M F, 2007. Introduction to climate and vegetation in Europe during MIS 5. In Sirocko F, Claussen M, Sánchez Goñi M F, Litt T (eds). The climate of past interglacials. Amsterdam: Elsevier. (Developments in Quaternary Sciences 7), 197–205.

Sanderson B M, Xu Y, Tebaldi C, Wehner M, O'Neill B C, Jahn A, Pendergrass, A G, Lehner F, Strand W G, Lin L, Knutti R, Lamarque J F, 2017. Community climate simulations to assess avoided impacts in 1.5 and 2 °C futures. Earth System Dynamics 8, 827–847.

Schaeffer M, Hare W, Rahmstorf S, Vermeer M, 2012. Long-term sea-level rise implied by 1.5 °C and 2 °C warming levels. Nature Climate Change 2, 867–870.

Schenk F, Wohlfarth B, 2019. The imprint of hemispheric-scale climate transitions on the European climate during the last deglaciation (15.5 ka to 9 ka BP). SKB TR-18-05, Svensk Kärnbränslehantering AB.

Schenk F, Väliranta M, Muschitiello F, Tarasov L, Heikkilä M, Björck S, Brandefelt J, Johansson A V, Näslund J-O, Wohlfarth B, 2018. Warm summers during the Younger Dryas cold reversal. Nature Communications 9, 1634. doi:10.1038/s41467-018-04071-5

Scherneck H-G, Johansson J M, Vermeer M, Davis J L, Milne G A, Mitrovica J X, 2001. BIFROST project: 3D crustal deformation rates derived from GPS confirm postglacial rebound in Fennoscandia. Earth Planets Space 53, 703–708.

Schiermeier Q, 2013. Greenland defied ancient warming. Nature 493, 459–460.

Schleussner C-F, Lissner T K, Fischer E M, Wohland J, Perrette M, Golly A, Rogelj J, Childers K, Schewe J, Frieler K, Mengel M, Schaeffer M, Hare W, 2016. Differential climate impacts for policy-relevant limits to global warming: the case of 1.5°C and 2°C. Earth System Dynamics 7, 327–351.

Seipold U, 1995. The variation of thermal transport properties in Earth's crust. Journal of Geodynamics 20, 145–154.

Selby M J, 1993. Hillslope materials and processes. 2nd ed. Oxford: Oxford University Press.

SFS 1984:3. Lag om kärnteknisk verksamhet (Nuclear Activities Act). Stockholm: Ministry of the Environment. (In Swedish.)

SFS 1998:808. Miljöbalk (Environmental Code). Stockholm: Ministry of the Environment. (In Swedish.)

Shackleton N J, Kennett J P, 1975. Paleotemperature history of the Cenozoic and the initiation of Antarctic glaciation: oxygen and carbon isotopic analyses in DSDP sites 277, 279, and 281. In Kennett J P, Houtz R (eds). Initial reports of the Deep Sea Drilling Project 29, 743–755.

Sharp R P, 1960. Glaciers. Eugene: University of Oregon Press. (Condon lectures 1960).

Shin S-I, Liu Z, Otto-Bliesner B, Brady E C, Kutzbach J E, Harrison S P, 2003. A simulation of the Last Glacial Maximum climate using the NCAR-CSM. Climate Dynamics 20, 127–151.

Siddall M, Rohling E J, Almogi-Labin A, Hemleben C, Meischner D, Schmelzer I, Smeed D A, 2003. Sea-level fluctuations during the last glacial cycle. Nature 423, 853–858.

Siegert M J, Dowdeswell J A, 1996. Spatial variations in heat at the base of the Antarctic ice sheet from analysis of the thermal regime above subglacial lakes. Journal of Glaciology 42, 501–509.

Simons M, Hager B H, 1997. Localization of the gravity field and the signature of glacial rebound. Nature 390, 500–504.

Sitch S, Smith B, Prentice I C, Arneth A, Bondeau A, Cramer W, Kaplan J O, Levis S, Lucht W, Sykes M T, Thonicke K, Venevsky S, 2003. Evaluation of ecosystem dynamics, plant geography and terrestrial carbon cycling in the LPJ dynamic global vegetation model. Global Change Biology 9, 161–185.

Sjökvist E, Asp M, Axén Mårtensson J, Berggreen-Clausen S, Berglöv G, Björck E, Johnell A, Nylén L, Ohlsson A, Persson H, 2015. Framtidsklimat i Uppsala län – enligt RCP-scenarier. SMHI Klimatologi Nr 20. Available at: https://www.smhi.se/polopoly_fs/1.165054!/Klimatologi_20%20Framtidsklimat%20i%20Uppsala%20l%C3%A4n%20-%20enligt%20RCP-scenarier.pdf (In Swedish.)

SKB R-05-18. SKB 2005. Preliminary site description. Forsmark area – version 1.2. Svensk Kärnbränslehantering AB.

SKB R-08-130. SKB 2008. Safety analysis SFR 1. Long-term safety. Svensk Kärnbränslehantering AB.

SKB R-10-59. SKB 2010. The Greenland Analogue Project. Yearly report 2009. Svensk Kärnbränslehantering AB.

SKB R-23-01. SKB 2023. Assessment activities and input data for the post-closure safety assessment in PSAR SFR. Svensk Kärnbränslehantering AB.

SKB TR-06-19. SKB 2006. Geosphere process report for the safety assessment SR-Can. Svensk Kärnbränslehantering AB.

SKB TR-06-23. SKB 2006. Climate and climate-related issues for the safety assessment SR-Can. Svensk Kärnbränslehantering AB.

SKB TR-10-48. SKB 2010. Geosphere process report for the safety assessment SR-Site. Svensk Kärnbränslehantering AB.

SKB TR-10-49. SKB 2010. Climate and climate-related issues for the safety assessment SR-Site. Svensk Kärnbränslehantering AB.

SKB TR-10-51. SKB 2010. Model summary report for the safety assessment SR-Site. Svensk Kärnbränslehantering AB.

SKB TR-13-05. SKB 2014. Climate and climate-related issues for the safety assessment SR-PSU. Svensk Kärnbränslehantering AB.

SKB TR-14-01. SKB 2015. Safety analysis for SFR. Long-term safety. Main report for the safety assessment SR-PSU. Revised edition. Svensk Kärnbränslehantering AB.

Slangen A B A, Carson M, Katsman C A, Van de Wal R S W, Köhl A, Vermeersen L L A, Stammer D, 2014. Projecting twenty-first century regional sea-level changes. Climatic Change 124, 317–332.

Slater A G, Lawrence D M, 2013. Diagnosing present and future permafrost from climate models. Journal of Climate 26, 5608–5623.

SMHI, 2020. Ekvationer för medelvattentillståndet i RH2000. Available at: https://www.smhi.se/hfa_coord/BOOS/dbkust/mwreg_MWekvationer_2020.pdf

Sohlenius G, Hedenström A, Rudmark L, 2004. Forsmark site investigation. Mapping of unconsolidated Quaternary deposits 2002–2003. Map description. SKB R-04-39, Svensk Kärnbränslehantering AB.

Solomon S, Plattner G-K, Knutti R, Friedlingstein P, 2009. Irreversible climate change due to carbon dioxide emissions. Proceedings of the National Academy of Sciences of the United States of America 106, 1704–1709.

Solomon S, Battisti D, Doney S, Hayhoe K, Held I M, Lettenmaier D P, Lobell D, Matthews H D, Pierrehubert R, Raphael M, Richels R, Root R L, Steffen K, Tebalidi C, Yohe G W, 2011. Climate stabilization targets: emissions, concentrations, and impacts over decades to millennia. Washington, DC: National Academies Press.

Sriver R L, Urban N M, Olson R, Keller K, 2012. Towards a physically plausible upper bound of sea-level rise projections. Climatic Change 115, 893–902.

SSM, 2019. Granskningsrapport – Utbyggnad och fortsatt drift av SFR. Rapport 2019:18, Swedish Radiation Safety Authority. (In Swedish.)

SSMFS 2008:21. Strålsäkerhetsmyndighetens föreskrifter och allmänna råd om säkerhet vid slutförvaring av kärnämne och kärnavfall (Regulations concerning safety in connection with the disposal of nuclear material and nuclear waste). Stockholm: Strålsäkerhetsmyndigheten (Swedish Radiation Safety Authority). (In Swedish.)

SSMFS 2008:37. Strålsäkerhetsmyndighetens föreskrifter och allmänna råd om skydd av människors hälsa och miljön vid slutligt omhänder-tagande av använt kärnbränsle och kärnavfall (Regulations on the protection of human health and the environment in connection with the final management of spent nuclear fuel and nuclear waste). Stockholm: Strålsäkerhetsmyndigheten (Swedish Radiation Safety Authority). (In Swedish.)

Staiger J K W, Gosse J C, Johnson J V, Fastook J, Gray J T, Stockli D F, Stockli L, Finkel R, 2005. Quaternary relief generation by polythermal glacier ice. Earth Surface Processes and Landforms 30, 1145–1159.

Stephens M B, 2010. Forsmark site investigation. Bedrock geology – overview and excursion guide. SKB R-10-04, Svensk Kärnbränslehantering AB.

Stone E J, Lunt D J, Rutt I C, Hanna E, 2010a. The effect of more realistic forcings and boundary conditions on the modelled geometry and sensitivity of the Greenland ice-sheet. The Cryosphere Discussion 4, 233–285.

Stone E J, Lunt D J, Rutt I C, Hanna E, 2010b. Investigating the sensitivity of numerical model simulations of the modern state of the Greenland ice sheet and its future response to climate change. The Cryosphere 4, 379–417.

Stroeven A P, Fabel D, Hättestrand C, Harbor J, 2002a. A relict landscape in the centre of Fennoscandian glaciation: cosmogenic radionuclide evidence of tors preserved through multiple glacial cycles. Geomorphology 44, 145–154.

Stroeven A P, Fabel D, Hättestrand C, Kleman J, 2002b. Quantifying the erosional impact of the Scandinavian ice sheet in the Torneträsk-Narvik corridor, northern Sweden, based on cosmogenic radionuclide data. Geografiska Annaler 84A, 275–287.

Stroeven A P, Hättestrand C, Kleman J, Heyman J, Fabel D, Fredin O, Goodfellow B W, Harbor J M, Jansen J D, Olsen L, Caffee M W, Fink D, Lundqvist J, Rosqvist G C, Strömberg B, Jansson K N, 2016. Deglaciation of Fennoscandia. Quaternary Science Reviews 147, 91–121.

Sugden D E, 1977. Reconstruction of the morphology, dynamics and thermal characteristics of the Laurentide ice sheet at its maximum. Arctic and Alpine Research 9, 27–47.

Sugden D E, 1978. Glacial erosion by the Laurentide ice sheet. Journal of Glaciology 20, 367–391.

Sugden D E, John B S, 1976. Glaciers and landscape: a geomorphological approach. London: Arnold.

Sundberg J, 1988. Thermal properties of soils and rocks. PhD thesis. Chalmers University of Technology.

Sundberg J, Back P-E, Ländell M, Sundberg A, 2009. Modelling of temperature in deep boreholes and evaluation of geothermal heat flow at Forsmark and Laxemar. SKB TR-09-14, Svensk Kärnbränslehantering AB.

Sundh M, Sohlenius G, Hedenström A, 2004. Forsmark site investigation. Stratigraphical investigation of till in machine cut trenches. SKB P-04-34, Svensk Kärnbränslehantering AB.

Sutter J, Gierz P, Grosfeld K, Thoma M, Lohmann G, 2016. Ocean temperature thresholds for Last Interglacial West Antarctic Ice Sheet collapse. Geophysical Research Letters 43, 2675–2682.

Svendsen J I, Mangerud J, 1987. Late Weichselian and Holocene sea-level history for a cross-section of western Norway. Journal of Quaternary Science 2, 113–132.

Svendsen J I, Alexanderson H, Astakhov V I, Demidov I, Dowdeswell J A, Funder S, Gataullin V, Henriksen M, Hjort C, Houmark-Nielsen M, Hubberten H W, Ingólfsson O, Jakobsson M, Kjær K H, Larsen E, Lokrantz H, Lunkka J P, Lyså A, Mangerud J, Matiouchkov A, Murray A, Moller P, Niessen F, Nikolskaya O, Polyak L, Saarnisto M, Siegert C, Siegert M J, Spielhagen R F, Stein R, 2004. Late Quaternary ice sheet history of northern Eurasia. Quaternary Science Reviews 23, 1229–1271.

Swantesson J O H, 1992. Recent micro-weathering phenomena in southern and central Sweden. Permafrost and Periglacial Processes 3, 275–292.

Sweet W V, Horton R, Kopp R E, LeGrande A N, Romanou A, 2017a. Sea level rise. In Climate Science Special Report (CSSR): Fourth National Climate Assessment, Volume I. Washington DC: U.S. Global Change Research Program, 333–363.

Sweet W V, Kopp R E, Weaver C P, Obeysekera J, Horton R M, Thieler E R, Zervas C, 2017b. Global and regional sea level rise scenarios for the United States. NOAA Technical Report NOS CO -OPS 083, Silver Spring, Maryland.

Tamisiea M E, Mitrovica J X, Milne G A, Davis J L, 2001. Global geoid and sea level changes due to present-day ice mass fluctuations. Journal of Geophysical Research 106, 30849–30863.

Tamisiea M E, Mitrovica J X, Davis J L, Milne G A, 2003. Long wavelength sea level and solid surface perturbations driven by polar ice mass variations: fingerprinting Greenland and Antarctic ice sheet flux. Space Science Reviews 108, 81–93.

Taylor K E, Stouffer R J, Meehl G A, 2012. An overview of CMIP5 and the experiment design. Bulletin of the American Meteorological Society 93, 485–498.

Texier D, Degnan P, Loutre M, Paillard D, Thorne M, 2003. Modelling sequential BIOsphere systems under CLIMate change for radioactive waste disposal. Project BIOCLIM. In Proceedings of the International High-Level Waste Management Conference, Las Vegas, 30 March–2 April 2003.

Thomas M F, 1994. Geomorphology in the tropics: a study of weathering and denudation in low latitudes. Chichester: Wiley.

Thornthwaite C W, 1948. An approach toward a rational classification of climate. Geographical Review 38, 55–94.

Tjernström M, Rummukainen M, Bergström S, Rodhe J, Persson G, 2003. Klimatmodellering och klimatscenarier ur SWECLIMS perspektiv. Norrköping: Sveriges meteorologiska och hydrologiska institut (Swedish Meteorological and Hydrological Institute). (SMHI reports. Meteorology and Climatology 102) (In Swedish.)

Toniazzo T, Gregory J M, Huybrechts P, 2004. Climatic impact of a Greenland deglaciation and its possible irreversibility. Journal of Climate 17, 21–33.

Tushingham A M, Peltier W R, 1991. ICE-3G: a new global model of Late Pleistocene deglaciation based upon geophysical predictions of post-glacial relative sea level change. Journal of Geophysical Research 96, 4497–4523.

Tzedakis P C, Raynaud D, McManus J F, Berger A, Brovkin V, Kiefer T, 2009. Interglacial diversity. Nature Geoscience 2, 751–755.

UNEP, 2019. Emissions Gap Report 2019. Nairobi: United Nations Environment Programme.

UNEP/GRID-Arendal, 2005. Permafrost distribution in the Arctic. UNEP/GRID-Arendal Maps and Graphics Library. Available at: https://www.grida.no/resources/7000 [22 June 2022].

UNFCCC, 2015. United Nations Framework Convention on Climate Change. Adoption of the Paris Agreement. Conference of the Parties, Twenty-first session, Paris, 30 November – 11 December 2015. Paris: United Nations.

Van Tatenhove F G M, Huybrechts P, 1996. Modelling of the thermal conditions at the Greenland ice sheet margin during Holocene deglaciation: boundary conditions from moraine formation. Geografiska Annaler 78A, 83–99.

van Vuuren D P, Edmonds J, Kainuma M L T, Riahi K, Thomson A, Hibbard K, Hurtt G C, Kram T, Krey V, Masui T, Lamarque J-F, Meinshausen M, Nakicenovic N, Smith S J, Rose S K, 2011. Representative concentration pathways: An overview. Climatic Change 109, 5. doi:10.1007/s10584-011-0148-z

Vermeer M, Rahmstorf S, 2009. Global sea level linked to global temperature. Proceedings of the National Academy of Sciences of the United States of America 106, 21527–21532.

Vestøl O, Ågren J, Steffen H, Kierulf H, Tarasov L, 2019. NKG2016LU: a new land uplift model for Fennoscandia and the Baltic Region. Journal of Geodesy 93, 1759–1779.

Vidstrand P, 2003. Surface and subsurface conditions in permafrost areas – a literature review. SKB TR-03-06, Svensk Kärnbränslehantering AB.

Vidstrand P, Follin S, Zugec N, 2010. Groundwater flow modelling of periods with periglacial and glacial conditions – SR-Site Forsmark. SKB R-09-21, Svensk Kärnbränslehantering AB.

Vidstrand P, Follin S, Selroos J-O, Näslund J-O, Rhén I, 2013. Modeling of groundwater flow at depth in crystalline rock beneath a moving ice-sheet margin, exemplified by the Fennoscandian Shield, Sweden. Hydrogeology Journal 21, 239−255.

Väliranta M, Birks H H, Helmens K F, Engels S, Piirainen M, 2009. Early-Weichselian interstadial (MIS 5c) summer temperatures were higher than today in northern Fennoscandia. Quaternary Science Reviews 28, 777–782.

Waddington E D, 1987. Geothermal heat flux beneath ice sheets. In Waddington E D, Walder J S (eds). The physical basis of ice sheet modelling. Wallingford, Oxfordshire: International Association of Hydrological Sciences. (IAHS Publication 170), 217–226.

Waelbroeck C, Labeyrie L, Michel E, Duplessy J C, McManus J F, Lambeck K, Balbon E, Labracherie M, 2002. Sea-level and deep water temperature changes derived from benthic foraminifera isotopic records. Quaternary Science Reviews 21, 295–305.

Washburn A L, 1979. Geocryology: a survey of periglacial processes and environments. 2nd ed. London: Arnold.

Watts A B, 2001. Isostasy and flexure of the lithosphere. Cambridge: Cambridge University Press.

WCRP Global Sea Level Budget Group, 2018. Global sea-level budget 1993 – present. Earth System Science 10, 1551–1590.

Werner K, Sassner M, Johansson E, 2013. Hydrology and near-surface hydrogeology at Forsmark – synthesis for the SR-PSU project. SR-PSU Biosphere. SKB R-13-19, Svensk Kärnbränslehantering AB.

Werner K, Norville J, Öhman J, 2014. Meteorological, hydrological and hydrogeological monitoring data from Forsmark – compilation and analysis for the SR-PSU project. SR-PSU Biosphere. SKB R-13-20, Svensk Kärnbränslehantering AB.

Whitehouse P, 2009. Glacial isostatic adjustment and sea-level change. State of the art report. SKB TR-09-11, Svensk Kärnbränslehantering AB.

Williams P J, Smith M W, 1989. The frozen earth: fundamentals of geocryology. Cambridge: Cambridge University Press.

Willmott C J, Rowe C M, Mintz Y, 1985. Climatology of the terrestrial seasonal water cycle. Journal of Climatology 5, 589–606.

Winkelmann R, Levermann A, Ridgwell A, Caldeira K, 2015. Combustion of available fossil-fuel resources sufficient to eliminate the Antarctic Ice Sheet. Science Advances 1, e1500589. doi:10.1126/sciadv.1500589

Winnick M J, Caves J K, 2015. Oxygen isotope mass-balance constraints on Pliocene sea level and East Antarctic Ice Sheet stability. Geology 43, 879–882.

Witt A, Schumann A Y, 2005. Holocene climate variability on millennial scales recorded in Greenland ice cores. Nonlinear Processes in Geophysics 12, 345–352.

Wohlfarth B, 2009. Ice-free conditions in Fennoscandia during Marine Oxygen Isotope Stage 3? SKB TR-09-12, Svensk Kärnbränslehantering AB.

Wohlfarth B, 2010. Ice free conditions in Sweden during Marine Oxygen Isotope Stage 3? Boreas 39, 377–398.

Wohlfarth B, 2013. A review of Early Weichselian climate (MIS 5d-a) in Europe. SKB TR-13-03, Svensk Kärnbränslehantering AB.

Wohlfarth B, Näslund J-O (eds), 2010. Fennoscandian ice sheet in MIS 3. Boreas 39, 325–456.

Wong T E, Bakker A M R, Keller K, 2017. Impacts of Antarctic fast dynamics on sea level projections and coastal flood defense. Climatic Change 144, 347–364.

Woodard D L, Davis S J, Randerson J T, 2019. Economic carbon cycle feedbacks may offset additional warming from natural feedbacks. Proceedings of the National Academy of Sciences 116, 759–764.

Wu H, Guiot J, Brewer S, Guo Z, 2007. Climatic changes in Eurasia and Africa at the last glacial maximum and mid-Holocene: reconstruction from pollen data using inverse vegetation modelling. Climate Dynamics 29, 211–229.

Wu P, Jackson L, Pardaens A, Schaller N, 2011. Extended warming of the northern high latitudes due to an overshoot of the Atlantic meridional overturning circulation. Geophysical Research Letters 38. doi:10.1029/2011GL049998

Yershov E D, 1998. General geocryology. Cambridge: Cambridge University Press.

Yokoyama Y, Lambeck K, De Deckker P, Johnston P, Fifield L K, 2000. Timing of the last glacial maximum from observed sea level minima. Nature 406, 713–716.

Zeebe R E, Ridgwell A, Zachos J C, 2016. Anthropogenic carbon release rate unprecedented during the past 66 million years. Nature Geoscience 9, 325–329.

Zickfeld K, Herrington T, 2015. The time lag between a carbon dioxide emission and maximum warming increases with the size of the emission. Environmental Research Letters 10, 031001.

Zickfeld K, Eby M, Matthews H D, Weaver A J, 2009. Setting cumulative emissions targets to reduce the risk of dangerous climate change. Proceedings of the National Academy of Sciences of the United States of America 106, 16129–16134.

Zickfeld K, Arora V K, Gillett N P, 2012. Is the climate response to CO_2 emissions path dependent? Geophysical Research Letters 39. doi:10.1029/2011GL050205

Zickfeld K, Eby M, Weaver A J, Alexander K, Crespin E, Edwards N R, Eliseev A V, Feulner G, Fichefet T, Forest C E, Friedlingstein P, Goosse H, Holden P B, Joos F, Kawamiya M, Kicklighter D, Kienert H, Matsumoto K, Mokhov I I, Monier E, Olsen S M, Pedersen J O P, Perrette M, Philippon-Berthier G, Ridgwell A, Schlosser A, Schneider Von Deimling T, Shaffer G, Sokolov A, Spahni R, Steinacher M, Tachiiri K, Tokos K S, Yoshimori M, Zeng N, Zhao F, 2013. Long-term climate change commitment and reversibility: An EMIC intercomparison. Journal of Climate 26, 5782–5809.

Zickfeld K, MacDougall A H, Matthews H D, 2016. On the proportionality between global temperature change and cumulative CO_2 emissions during periods of net negative CO_2 emissions. Environmental Research Letters 11, 055006.

Zweck C, Huybrechts P, 2003. Modeling the marine extent of northern hemisphere ice sheets during the last glacial cycle. Annals of Glaciology 37, 173–180.

Öhman J, Odén M, 2018. SR-PSU (PSAR) Bedrock hydrogeology. TD18 – Temperate climate conditions. SKB P-18-02, Svensk Kärnbränslehantering AB.

Appendix A

Terms and abbreviations

The present report contains terms and acronyms that either are rarely used outside SKB or can be regarded as specialised terminology within one or several of the scientific and modelling disciplines involved in the reported work. To facilitate the readability of the report, selected terms and acronyms are explained in Table A-1.

Table A-1. Terms and acronyms used is this report.

Terms/abbreviations	Description
1–2BMA	Vaults for intermediate-level waste in SFR.
1–2BTF	Vaults for concrete tanks in SFR1.
1–5BLA	Vaults for low-level waste in SFR.
1BRT	Vault for reactor pressure vessels in SFR3.
1D	One-dimensional.
2D	Two-dimensional.
3D	Three-dimensional.
A1B	Emission scenario used in the 4th assessment report of the IPCC.
A2	Emission scenario used in the 4th assessment report of the IPCC.
AD	Anno Domini.
AMOC	Atlantic meridional overturning circulation.
Annual dose	Assessment endpoint calculated as the annual effective dose to an adult, where the annual effective dose is defined as the effective dose from external exposure in a year, plus the committed effective dose from intakes of radionuclides in that year.
AOGCM	Atmosphere-ocean general circulation model.
AP	After Present.
AR4	Fourth assessment report of the IPCC.
AR5	Fifth assessment report of the IPCC.
AR6	Sixth assessment report of the IPCC.
B2	Emission scenario used in the 4th assessment report of the IPCC.
Barrier	In the safety assessment context, a barrier is a physical feature, engineered or natural, which in one or several ways contributes to the containment and retention or prevention of dispersion of radioactive substances, either directly or indirectly by protecting other barriers.
Bedrock	In the safety assessment context, the solid rock beneath the regolith also including the groundwater in the rock.
BIFROST	Baseline Inferences for Fennoscandian Rebound, Sea-level, and Tectonics, an international project using GPS to measure crustal deformation in Fennoscandia.
BIOCLIM	Modelling sequential BIOsphere systems under CLIMate change for radioactive waste disposal, a project funded by the EU.
BP	Before Present.
CMIP	Coupled Model Intercomparison Project, a collaborative framework designed to improve knowledge about climate change.
CRU	Climatic Research Unit (University of East Anglia).
DEM	Digital elevation model. Describes the topography and bathymetry of the modelled area.
DJF	December, January, February (winter).
ELA	Equilibrium-line altitude, marks the area or zone on a glacier where accumulation is balanced by ablation over a 1-year period.
EMIC	Earth system Model of Intermediate Complexity.
Emission scenario	Possible future pathways of anthropogenic greenhouse-gas and aerosol emissions.
ESM	Earth System Model.
Eustasy	Change in sea level due to, for example, changes in the volume and spatial distribution of sea water in the world's oceans.

Terms/abbreviations	Description
F-PSAR	First Preliminary Safety Analysis Report.
FEPs	Features, events and processes.
FHAs	Future human actions.
GAP	The Greenland Analogue Project, a multilateral research project on the west coast of Greenland.
GCM	General circulation model, a model capable of representing physical processes of the atmosphere and ocean often used to simulate the response of global climate to increasing greenhouse gas concentrations.
Geosphere	The bedrock, including groundwater, surrounding the repository, bounded above by the surface system.
GI	Greenland Interstadial.
GIA	Glacial isostatic adjustment.
GIS	Geographical information system.
GPS	Global Positioning System.
GRACE	Gravity Recovery and Climate Experiment, a joint mission of the National Aeronautics and Space Administration and the German Aerospace Center.
GRIP	European Greenland Ice Core Project.
GS	Greenland Stadial.
HadCM3	Hadley Centre Coupled Model, version 3, a coupled atmosphere-ocean general circulation model (AOGCM) developed at the Hadley Centre in the United Kingdom.
HFD	Heat flow density, or geothermal heat flow.
IAM	Integrated assessment model.
ICE-5G	A global ice sheet reconstruction.
IEA	International Energy Agency.
Initial state	The expected state of the repository and its environs at closure of the repository.
InSAR	Interferometric synthetic aperture radar.
Insolation	The amount of solar radiation received per unit area at the top of the Earth's atmosphere.
IPCC	Intergovernmental Panel on Climate Change.
Isostasy	Vertical movement of the Earth's crust, which in Forsmark is dominated by isostatic rebound following the latest glaciation.
JJA	June, July, August (summer).
KBS-3	Method developed by SKB for final disposal of spent nuclear fuel.
LGM	Last Glacial Maximum.
LLN 2-D NH	The Louvain-la-Neuve two-dimensional Northern Hemisphere climate model.
LOVECLIM	LOch–Vecode-Ecbilt-CLio-agIsm Model (Climate model of intermediate complexity).
LPJ-GUESS	A dynamic vegetation model.
MIS	Marine isotope stage.
MPWP	Mid-Piacenzian Warm Period (3.264 to 3.025 Ma BP).
NCAR	National Center for Atmospheric Research (USA).
NEEM	North Greenland Eemian Ice Drilling, an international ice core research project.
NGRIP	North Greenland Ice Core Project, a multinational research program.
NH	Northern Hemisphere.
NWMO	Nuclear Waste Management Organization (Canada).
Pessimistic	Indicates an expected overestimate of annual effective dose that follows from assumptions made, or models and parameter values selected, beyond the reasonably expected range of possibilities.
PET	Potential evapotranspiration.
PMIP	Paleoclimate Modelling Intercomparison Project.
PSAR	Preliminary Safety Analysis Report.
PSU	Programme SFR extension.
QA	Quality assurance.

Terms/abbreviations	Description
RCA3	Rossby Centre Regional Climate Model.
RCM	Regional climate model.
RCP2.6	Emission scenario from IPCC in which radiative forcing peaks at approximately 3 W m-2 before 2100 AD and then declines.
RCP4.5	Emission scenario from IPCC in which radiative forcing is stabilised at approximately 4.5 W m-2 at 2100 AD.
RCP6.0	Emission scenario from IPCC in which radiative forcing is stabilised at approximately 6.0 W m-2 at 2100 AD.
RCP8.5	Emission scenario from IPCC in which radiative forcing reaches approximately 8.5 W m-2 by 2100 AD and continues to rise for some time after that.
Relative sea level	The vertical position of the sea relative to land, as measured in the reference height system RH 2000. The relative sea level is determined by the net effect of eustasy and isostasy.
RNT	Radionuclide transport.
RSL	Relative sea level.
Safety analysis	In the context of the present safety assessment, the distinction is generally not viewed as important and therefore safety analysis and safety assessment are used interchangeably. However, if the distinction is important, safety analysis should be used as a documented process for the study of safety and safety assessment should be used as a documented process for the evaluation of safety.
Safety assessment	The safety assessment is the systematic process periodically carried out throughout the lifetime of the repository to ensure that all the relevant safety requirements are met and entails evaluating the performance of the repository system and quantifying its potential radiological impact on human health and the environment. The safety assessment corresponds to the term safety analysis in the Swedish Radiation Safety Authority's regulations.
SAR	Safety Analysis Report.
SAT	Surface air temperature.
Scenario	A description of a potential evolution of the repository and its environs, given an initial state and specified external conditions and their development and how the protective capability of the repository is affected.
SFR	Final repository for short-lived radioactive waste at Forsmark.
SFR1	The existing part of SFR.
SFR3	The extension part of SFR.
Shoreline displacement	The movement of the shoreline, that is the variation in time of the spatial location of the shoreline.
SKB	Swedish Nuclear Fuel and Waste Management Company.
SKBdoc	Internal document management system at SKB.
SMHI	Swedish Meteorological and Hydrological Institute.
SR-Can	Preliminary post-closure safety assessment for the planned spent nuclear fuel repository, published in 2006.
SR-PSU	Post-closure safety assessment that was a reference to the F-PSAR for the extended SFR, reported to the regulatory authority in 2014.
SRES	Special Report on Emission Scenarios, a report by the IPCC.
SROCC	Special Report on the Ocean and Cryosphere in a Changing Climate, a report by the IPCC.
SR-Site	Post-closure safety assessment for a spent nuclear fuel repository in Forsmark, reported to the regulatory authority in 2011.
SSM	Swedish Radiation Safety Authority.
SSMFS	Regulations of the Swedish Radiation Safety Authority.
SSP	Shared Socioeconomic Pathway.
SWECLIM	Swedish Regional Climate Modelling Programme.
THM	Thermo-Hydro-Mechanical.
UMISM	University of Maine Ice Sheet Model.
UNFCCC	United Nations Framework Convention on Climate Change.
WEO	World Energy Outlook, yearly IEA publication, providing a critical analysis and insights on trends in energy demand and supply, and what they mean for energy security, environmental protection and economic development.

Appendix B

The construction of surface air temperature and precipitation at Forsmark until 12 000 AD

B1 Surface air temperature change until 12 000 AD

B1.1 Background and theory

The construction of the annual mean surface air temperature until 12 000 AD at Forsmark, illustrated in Figure 3-27, was predominately derived from the present knowledge from contemporary studies of long-term climate change (Table 3-6). However, because the number of studies covering the topic of anthropogenic climate change over these long time-scales is very limited, it is also helpful to use conceptual modelling to gain a better understanding on the important mechanisms behind the long-term temperature change. Here a zero-order energy balance model (EBM) is used for that purpose (e.g. North et al. 1981, North and Stevens 2006):

$$C\frac{\partial T_s}{\partial t} = \frac{S}{4}(1-\alpha) - (A + BT_s), \qquad \text{Equation B-1}$$

where t is time, T_S the global annual mean surface air temperature, and C a numerical constant describing the heat capacity. Equation B-1 describes the evolution of the global mean surface air temperature as a result of the global mean net radiation at the top of the atmosphere, decomposed into the net incoming short-wave radiation ($S(1-\alpha)/4$) and the outgoing long-wave radiation ($A + BT_S$). The net short-wave radiation is estimated from the solar constant S and the planetary albedo α, and the long-wave radiation is here assumed to increase linearly with the surface air temperature. The numerical constant A describes a background state about which the long-wave radiation is linearised, and the numerical constant B is the inverse of the climate sensitivity, i.e. it represents how the outgoing long-wave radiation responds to changes in temperature. Note that the relationship between temperature and outgoing long-wave radiation is approximately linear only for a realistic range of "Earth-like" temperatures (e.g. North and Stevens 2006). In reality, the long-wave radiation depends on the fourth-power of the absolute temperature according to the Stefan-Boltzmann law.

To introduce the effect of anthropogenic greenhouse gases, the background long-wave radiation is first decomposed into a part describing the natural greenhouse gas effect (A_0) and another part describing the anthropogenic contribution (ΔA), such that $A = A_0 + \Delta A$. Similarly, the surface air temperature is decomposed as $T_S = T_{S0} + \Delta T_S$, where T_{S0} describes the global mean surface air temperature in the absence of anthropogenic greenhouse forcing and ΔT_S is the global mean temperature response to anthropogenic greenhouse gas forcing. Using the decompositions of A and T_S, it is possible to separate Equation B-1 into two new equations:

$$C\frac{\partial T_{s0}}{\partial t} + BT_{s0} = \frac{S}{4}(1-\alpha) - A_0, \qquad \text{Equation B-2}$$

and

$$C\frac{\partial \Delta T_s}{\partial t} + B\Delta T_s = -\Delta A. \qquad \text{Equation B-3}$$

Equation B-2 describes the evolution of the unperturbed global mean surface air temperature, and Equation B-3 yields the global mean temperature response to anthropogenic greenhouse gas forcing. To simplify the usage of the conceptual EBM, it is assumed that the combined effect of all anthropogenic greenhouse gases is represented only by the CO_2. The radiative forcing from CO_2 has been estimated to high accuracy from detailed radiative-transfer calculations (e.g. Myhre et al. 1998):

$$\Delta A = -5.35\ln(p/p_0), \qquad \text{Equation B-4}$$

where p_0 is the atmospheric CO_2 concentration in the absence of anthropogenic influence (~ 280 ppmv for pre-industrial conditions) and p describes the total CO_2 concentration including the anthropogenic contribution. Substituting Equation B-4 into Equation B-3 yields:

$$C\frac{\partial \Delta T_s}{\partial t} + B\Delta T_s = 5.35\ln(p/p_0). \qquad \text{Equation B-5}$$

Equation B-5 describes the temporal evolution of the global mean surface air temperature response to changes in the atmospheric CO_2 concentration. The magnitude and timing of the temperature response to a specific CO_2 pathway is largely controlled by the parameters B and C. The magnitude of the response can be estimated by assuming that the climate is in equilibrium ($\partial \Delta T_S / \partial t = 0$), resulting in $\Delta T_S = 5.35 \ln (p/p_0)$, whereas the typical timescale (relative to the CO_2 forcing) is determined by $\tau = C/B$. Here $B = 1.9$ W m^{-2} K^{-1} is used, which is within the typical range of values found by satellite measurement and in the literature (North and Stevens 2006). Over the long timescales considered here, the Earth's heat capacity is almost entirely controlled by the world's oceans. This means that the total heat capacity can be estimated as $C = c_{pw} \rho_w h_{ocean}$, where c_{pw} and ρ_w are the specific heat capacity and density of sea water, respectively, and h_{ocean} is taken to be the average depth of the oceans (3 700 m). In reality, only the thermal capacity of the upper layers of the oceans (first couple of hundred metres) is available on seasonal to centennial timescales, after which the heat in the upper ocean would be gradually transferred to the deep ocean by mixing processes. Hence, in a situation with a persistent atmospheric forcing over millennial timescales h_{ocean} (and therefore C) would effectively increase with time. However, because the time dependency of the EBM is only used for illustration in this appendix, a constant effective heat capacity reasonable for the long timescales considered here (10 ka) is chosen for simplicity. In summary the total heat capacity assumed here is $C = (4 \times 10^3)(1 \times 10^3)(3.7 \times 10^3) \approx 1.5 \times 10^{10}$ J m^{-2} K^{-1}, resulting in an adjustment timescale of $\tau \approx 250$ years. Although this value of τ should be interpreted carefully due to the simplistic treatment of C, it demonstrates that global warming may continue for several centuries after the emissions have ceased.

In order to illustrate the behaviour of the EBM (Equation B-5), the resulting atmospheric CO_2 concentrations from the high emission scenario (5 120 Pg C cumulative emissions) in Clark et al. (2016) are used (Figure B-1a). The amplitude of the associated global mean temperature response in the EBM is typically only 60–70 % of that in Clark et al. (2016) (Figure B-1b). This result is not surprising as many important climate feedbacks accounted for in Clark et al. (2016) are omitted in the EBM, e.g. increased melting of sea ice and land-based glaciers and ice sheets, which would result in a reduced planetary albedo. As discussed in Section 3.5.3, the strong melting of the ice sheets under the high emission scenario in Clark et al. (2016) is largely responsible for the relatively large projections of sea-level rise until 12 000 AD found in their study.

However, aside from the amplitude, typical features of the CO_2-induced global mean temperature response in more sophisticated models are also captured by the conceptual EBM. For example, in both the models used by Clark et al. (2016) and the EBM, the initial temperature increase culminates sometime after the maximum CO_2 concentration has been reached, after which the temperature slowly returns towards pre-industrial values. Furthermore, in both models the fractional reduction of the global mean temperature from its maximum to 12 000 AD is significantly smaller than the equivalent reduction of CO_2 (see also Eby et al. 2009). This shows that the effects of global warming are present for a relatively long time even after the atmospheric CO_2 has returned to pre-industrial levels.

Figure B-1b also shows the global mean temperature from the conceptual EBM assuming that the climate responds instantaneously to the CO_2 forcing (i.e. the equilibrium response; $\partial \Delta T_S / \partial t = 0$ in Equation B-5). This curve is included to identify times during which the adjustment timescale plays an important role for the ΔT_S response, and when it can be neglected. In general, the equilibrium temperature response in the EBM is similar to the "full" response from the time of the maximum temperature change at ~ 3000 AD until 12 000 AD (Figure B-1b). Hence, for this time period the surface air temperature is expected to be in quasi-equilibrium with the CO_2-forcing, implying that the amplitude of the temperature response within this time interval should be approximately proportional the amount of anthropogenic emissions remaining in the atmosphere.

In contrast to the latter part of the 10-ka period, for which the surface air temperature and CO_2 forcing are approximately in phase, the maximum temperature response reveals a significant time lag relative to the maximum CO_2 forcing. This is illustrated by the difference in timing of the maximum temperature responses between the thin and thick black curves in Figure B-1b. As discussed above, this difference is ultimately controlled by the adjustment timescale of the EBM, given by C/B. However, the time lag is also dependent on the amplitude of the forcing, hence the peak CO_2 concentration (see also Zickfeld and Herrington 2015). This is illustrated in Figure B-2, which shows the time lag of the maximum surface air temperature in the EBM following an instantaneous CO_2 pulse of different amplitudes. The timing of the peak temperature response is more sensitive at lower CO_2 concentrations than at higher ones.

For example, increasing the CO_2 concentration relative to pre-industrial from 2 to 3 (560 to 840 ppmv, respectively, assuming p_0 = 280 ppmv as the baseline concentration) results in a similar delay of the peak temperature response (~ 100 years) as in the case in which the fractional CO_2 increases from 4 to 9 (1 120 to 2 520 ppmv for p_0 = 280 ppmv, respectively).

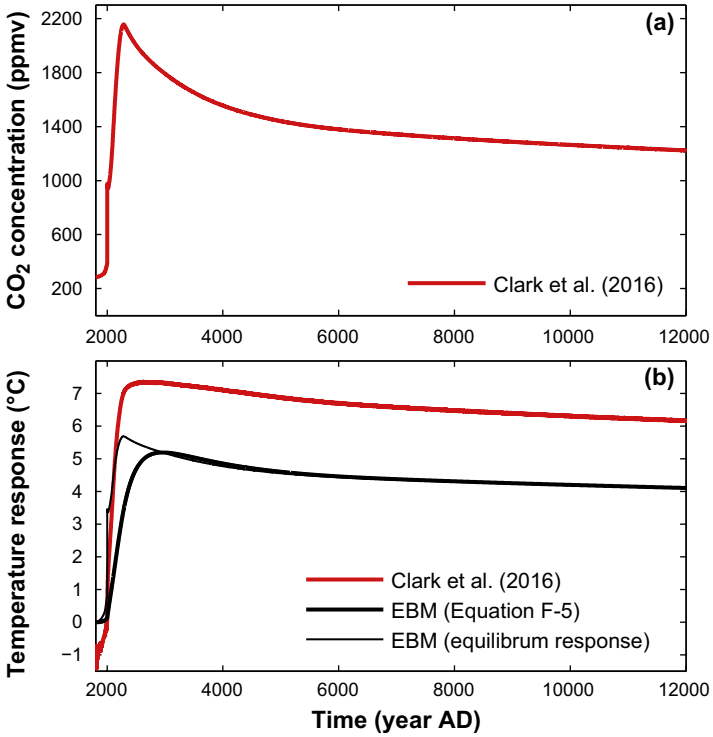

Figure B-1. *(a) Atmospheric CO_2 concentration resulting from the high emission scenario of 5 120 Pg C cumulative emissions in Clark et al. (2016), and (b) associated global mean surface air temperature responses as computed by Clark et al. (2016) (red curve), the conceptual EBM (Equation B-5; thick black curve) and the EBM, but assuming that the temperature is always in equilibrium with the CO_2 forcing ($\partial \Delta T_S / \partial t = 0$ in Equation B-5; thin black line). The atmospheric CO_2 concentration and temperature response from Clark et al. (2016) represent the ensemble mean across five versions of two different intermediate complexity Earth system models (ESMs). In all the simulations in Clark et al. (2016), anthropogenic CO_2 emissions were assumed to increase linearly between 2000 and 2100 AD, after which they drop linearly back to zero by 2300 AD.*

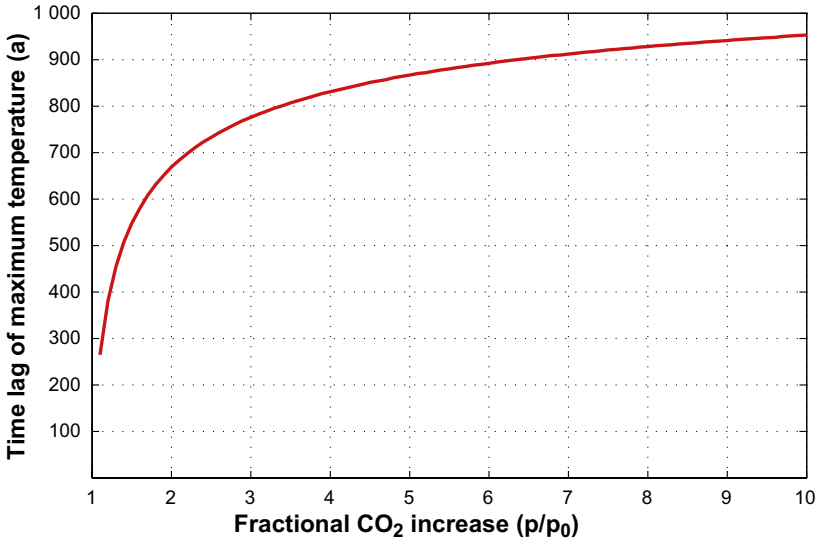

Figure B-2. *Time lag of the maximum global mean surface air temperature response following instantaneous CO_2 pulses of different amplitudes (given by the x-axis).*

B1.2 Global mean surface air temperature change

In this section, results from modelling studies on long-term climate change are combined with the theoretical understanding from the conceptual EBM (Equation B-5) to estimate the lower and upper bounds of the global annual mean surface air temperature evolution until 12 000 AD. The evaluation is performed for low emissions (comparable with RCP2.6), medium emissions (comparable with RCP4.5), and high emissions (comparable with RCP8.5).

The studies used to estimate the global mean surface air temperature until 12 000 AD are listed in Table B-1. The number of studies covering the temperature response over these timescales is very limited. Therefore, also shorter-range climate projections from the IPCC (Collins et al. 2013) are used in the evaluation, in particular for estimating the range of the projected temperature increase in the near future. The values used to construct the range of the global annual mean surface air temperature are summarised in Table B-2, and the resulting temperature curves are shown in Figure B-3. The motivations and assumptions behind the values in Table B-2, and hence the temperature curves in Figure B-3, are discussed for different time periods in the following subsections.

Table B-1. Summary of the projected global annual mean surface air temperature change (relative to present) until 12 000 AD as reported in the literature. The ranges in square brackets represent uncertainties associated with inter-model differences and/or internal variability. Only studies in which the models are integrated using historical emissions and realistic emission scenarios, comparable with RCP2.6, RCP4.5 and RCP8.5 (Section 3.4.1), are listed. In the following, cumulative emissions < 1 000 Pg C are comparable with RCP2.6, scenario B1 and cumulative emissions < 3 000 Pg C are comparable with RCP4.5, and scenario A2 and cumulative emissions > 5 000 Pg C are comparable with RCP8.5. Note that the modelling studies of Mikolajewicz et al. (2007), Eby et al. (2009) and Clark et al. (2016) include the global carbon cycle.

Reference	Emission scenario/ Total carbon emissions	Max. ΔT (°C)	Timing of max. T increase (AD)	ΔT 2100 AD (°C)	ΔT 12000 AD (°C)
Mikolajewicz et al. (2007)[1]	B1[2]	2	2500	1	
	A2[2]	5	3000	2	
Eby et al. (2009)[3]	160 PgC[4]	0.3	2250	0.2	0.2
	640 PgC[4]	1.4	5500	1.1	0.8
	960 PgC[4]	2.0	4000	1.7	1.0
	1280 PgC[5]	2.5	3800	0.8	1.5
	2560 PgC[5]	4.7	3000	1.7	3.1
	5120 PgC[5]	7.8	3200	3.0	5.9
Collins et al. (2013)	RCP2.6			1.0[6] [0.3–1.7]	
	RCP4.5			1.8[6] [1.1–2.6]	
	RCP8.5			3.7[6] [2.6–4.8]	
Clark et al. (2016)[7]	160 PgC[8]	0.4	2200	0.4	0.3
	640 PgC[8]	1.4	5500	1.2	0.7
	960 PgC[8]	1.9	3900	1.8	1.0
	1280 PgC[9]	2.0 [0.8–3.2]	2300	1.3 [0.4–2.2]	1.3 [0.5–2.2]
	2560 PgC[9]	4.1 [3.0–5.2]	2500	2.4 [1.2–3.6]	2.9 [2.4–3.5]
	5120 PgC[9]	7.4 [7.0–7.7]	2600	3.9 [2.2–5.6]	6.2 [5.5–6.8]

[1] Earth system model (ESM) simulations are integrated until 5000 AD. Temperature changes are shown relative to a control simulation with zero anthropogenic emissions.

[2] Emissions follow the SRES emission scenarios (used in the fourth assessment IPCC report, IPCC 2007) until 2100 AD, after which they are instantaneously reduced to zero.

[3] Temperature changes are relative to a 10-ka control simulation with zero anthropogenic emissions. Incoming solar radiation was held fixed at its present-day value in all the simulations.

[4] Emissions follow observations until 2000 AD. At the beginning of 2001 AD, a pulse of CO_2 was applied over one year.

[5] Emissions follow the A2 SRES emission scenario until 2100 AD, after which they decline linearly to zero by 2300 AD. The scenarios were then created by scaling the A2 emissions such that the cumulative emissions reached the values reported in this table by 2300 AD.

[6] Same as in Table 3-3.

[7] Temperature changes are relative to the 1980–2004 AD reference period.

[8] Same ESM and future emission pathways as in Eby et al. (2009) (see footnote 4), except for a varying future orbital forcing.

[9] Ensemble-mean surface air temperature response across eight versions of two different intermediate complexity ESMs. Emissions increased linearly between 2000 and 2100 AD, after which they decline linearly back to zero by 2300 AD.

Table B-2. Construction of the lower and upper bounds (values within the square brackets), and the average (values without brackets) of the global annual mean surface air temperature change until 12 000 AD (relative to present) for low, medium and high emissions (comparable with RCP2.6, RCP4.5 and RCP8.5, respectively; see Section 3.4.1). The average temperature change has been calculated using average values of the parameters that were used construct the lower and upper bounds. For a description on how these parameters and the resulting temperature bounds have been derived, see the text.

Part of ΔT curve	Low emissions (RCP2.6)	Medium emissions (RCP4.5)	High emissions (RCP8.5)	Based on
ΔT at 2100 AD (°C)	1.0 [0.3–1.7]	1.9 [1.1–2.6]	3.7 [2.6–4.8]	Collins et al. (2013)
Maximum ΔT (°C)	1.0 [0.3–1.9]	3.7 [1.7–6.5]	8.3 [4.9–12.5]	Eby et al. (2009), Clark et al. (2016)
Timing of maximum ΔT (year AD)	2075 [2050–2100]	2475 [2150–2800]	2875 [2550–3200]	Eby et al. (2009), Meinshausen et al. (2011), Clark et al. (2016), Lord et al. (2016).
ΔT at 12 000 AD (°C)	0.5 [0.1–1.1]	1.9 [0.5–4.6]	5.6 [2.5–10.6]	Archer et al. (2009), Eby et al. (2009), Clark et al. (2016), EBM (Equation B-5).

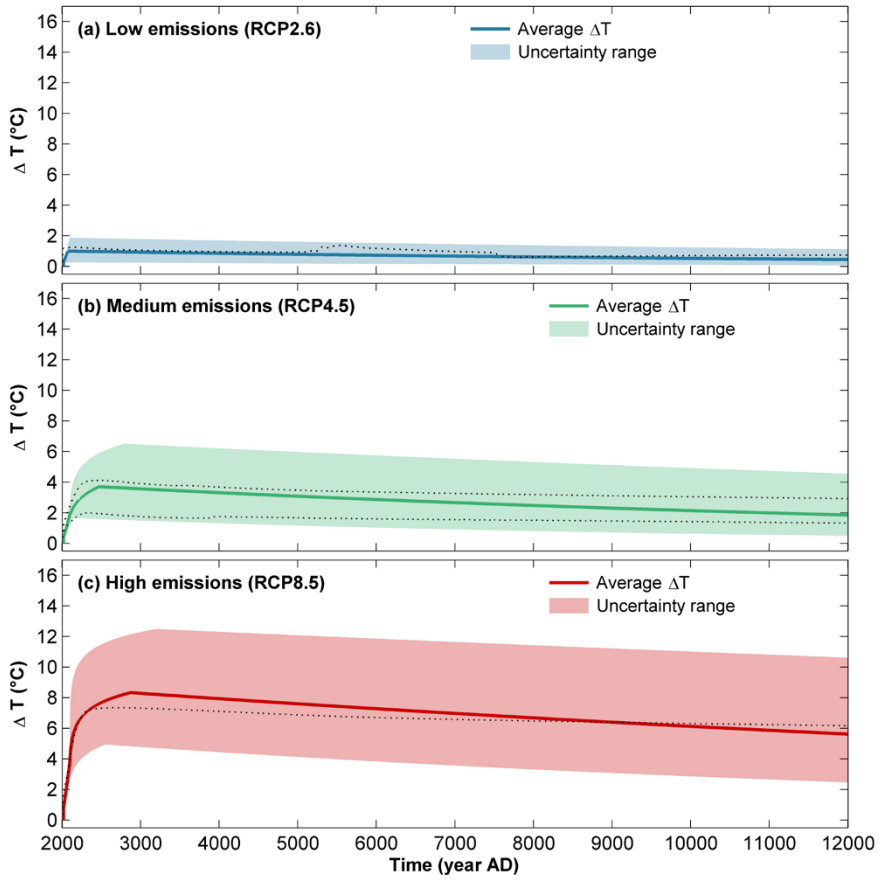

Figure B-3. *Constructed global annual mean surface air temperature change until 12 000 AD (relative to present) for (a) low, (b) medium and (c) high carbon emissions (comparable with RCP2.6, RCP4.5 and RCP8.5, respectively; see Section 3.4.1). The uncertainty range has been constructed using the values in Table B-2, and the average temperature change ("Average ΔT") has been calculated using average values of the parameters that were used construct the lower and upper bounds. To that end, average ΔT illustrates a typical mid-range temperature evolution for each emission scenario over the next 10 ka. The dotted lines in the figure shows the evolution of ensemble-mean temperature change from the Clark et al. (2016) projections with 640 Pg C cumulative emissions (comparable with RCP2.6; panel a), 1 280 and 2 560 Pg C cumulative emissions (comparable with RCP4.5; panel b), and 5 120 Pg C cumulative emissions (comparable with RCP8.5; panel c).*

B1.2.1 Temperature change until 2100 AD

The global annual mean surface air temperature change until 2100 AD is completely based on the RCP2.6, RCP4.5 and RCP8.5 scenarios from IPCC AR5 (Collins et al. 2013). The lower and upper bounds represent the 5th and 95th percentile of the distribution across all participating climate models (see also Table 3-3).

B1.2.2 Maximum surface air temperature change

For low emission scenarios, it is generally assumed that the emissions start declining within the first few decades from now as a result of strong climate change mitigation policies (IPCC 2013a, Allen et al. 2018). As a consequence, the maximum global annual mean surface air temperature change in the low emission scenario is comparable with the temperature change at 2100 AD (Collins et al. 2013). A similar relationship between 2100 AD temperatures and the maximum surface air temperature in low cumulative emission experiments by Eby et al. (2009) and Clark et al. (2016) (Table B-1) is also present.

For the medium and high emission scenarios, the maximum global annual mean surface air temperature change is first evaluated using the ratio of the peak temperature change to the temperature change at 2100 AD in Mikolajewicz et al. (2007), Eby et al. (2009) and Clark et al. (2016). These ratios are then multiplied by the 2100 AD temperature changes from Collins et al. (2013) (Table B-2) to obtain the range of peak temperatures for each scenario.

The lowest ratios (1.5 and 1.9), obtained from Clark et al. (2016), are multiplied by the lowest IPCC warming estimates for 2100 AD to yield the lower limit of the maximum temperature response. Similarly, the highest ratios (1.9 and 2.6; from Eby et al. 2009) are used in combination with the highest IPCC warming estimates to obtain the upper limit of the maximum temperature response.

B1.2.3 Timing of maximum surface air temperature change

The idealised experiments with the EBM (Equation B-5) suggest that the time of the peak temperature, following a specific CO_2 pathway, should increase as a result of higher emissions (Figure B-2). This is generally also the case in the studies of Eby et al. (2009) and Clark et al. (2016) (Table B-1). The only exception is found in some of the low emission experiments in those studies, which result in a rapid but delayed temperature increase between 3500 and 5500 AD due to "flushing events in the Southern Ocean" (Eby et al. 2009). However, since the existence of these events appears to be highly model-dependent, and non-existent in most Earth system models (ESMs) (Archer et al. 2009), they have been neglected in the present analysis. Instead, for low emissions, the timing of the maximum surface air temperature change is primarily based on IPCC (2013a) which suggests that the maximum temperature response under the RCP2.6 scenario occurs between 2050 and 2100 AD (Collins et al. 2013).

An interesting feature in Table B-1 is the overall difference in timing of the peak temperature between Eby et al. (2009) and Clark et al. (2016). Except for the low-emission scenarios, discussed above, the temperatures in Eby et al. (2009) typically reach their maximum values ~ 500 years later than in Clark et al. (2016), despite using comparable emission pathways. In other words, this means that the maximum temperature response lags the maximum CO_2 forcing by ~ 700–900 years in Eby et al. (2009) and ~ 50–300 years in Clark et al. (2016). For comparison, Lord et al. (2016) reported temperature lag times of ~ 60–700 years for a broad range of emission pulses between 1 000 and 20 000 Pg C. Hence, the results in Lord et al. (2016) broadly fall within the range of the lag times found in Eby et al. (2009) and Clark et al. (2016).

In addition to the time delay following the peak CO_2 forcing, the timing of the peak temperature response is naturally also dependent on the CO_2 pathway itself, in particular the time at which the CO_2 maximum is reached. The CO_2 pathways in both Eby et al. (2009) and Clark et al. (2016) assume peak emissions by year 2100 AD, resulting in a peak atmospheric CO_2 concentration by 2200–2250 AD for the lower emissions and 2250–2300 AD for the higher emissions. The timing of peak emissions in the IPCC RCP8.5 scenario is comparable to Eby et al. (2009) and Clark et al. (2016), whereas the RCP4.5 scenario assumes that emissions peak already by ~ 2050 AD, resulting in maximum concentrations by ~ 2100 AD (Meinshausen et al. 2011).

In summary, the timing of the peak temperature in the constructed global mean temperature anomaly (Table B-2 and Figure B-3) is primarily based on Clark et al. (2016) for the lower bound and Eby et al. (2009) for the upper bound. In addition to using Clark et al. (2016), the peak temperature of the lower bound under medium emissions has been shifted further toward the present-day by 100 years to account for the relatively early peak emissions from the RCP4.5 scenario (Meinshausen et al. 2011).

B1.2.4 Temperature change beyond the maximum until 12 000 AD

The temperature change at 12 000 AD is first evaluated by how much of the maximum temperature anomaly in Eby et al. (2009) and Clark et al. (2016) is remaining by 12 000 AD. In Eby et al. (2009), the temperature by 12 000 AD has declined to about 50–60 % of its maximum value for the lower and intermediate emission scenarios and to about 75 % for the higher emissions. In Clark et al. (2016) the corresponding values are similar for the lower emission scenarios (< 1 000 Pg C), but slightly higher for the intermediate and high emissions scenarios (> 1 000 Pg C), being approximately 65 and 85 %, respectively.

As illustrated by the zero-order EBM in Section B1.1, the temperature anomaly beyond the peak response should be roughly proportional to the remaining CO_2 concentration in the atmosphere (Figure B-1). This suggests that the slower temperature decline in Clark et al. (2016) relative to Eby et al. (2009), for cumulative emission > 1 000 Pg C, can be explained by a slower decline in the atmospheric CO_2 forcing. The emissions remaining by 12 000 AD in Clark et al. (2016) are indeed consistently 5–10 % higher than in Eby et al. (2009) in the intermediate and high emission scenarios, suggesting that the prediction from the EBM is (at the very least) qualitatively accurate.

It is important to note that although the ESM in Eby et al. (2009) predicts a faster decline of the CO_2 (and hence the temperature anomaly) compared with the multi-model ensembles in Clark et al. (2016), it nevertheless predicts a significantly slower decline than most other comparable models (Archer et al. 2009). This means that the studies of Eby et al. (2009) and Clark et al. (2016) do not cover the full range of literature values regarding the rate of temperature decline until 12 000 AD. However, there is unfortunately not much information on the long-term global mean temperature change until 12 000 AD from other ESMs. Therefore, the proportional relationship between CO_2 forcing and temperature response found in the EBM is employed to extrapolate the temperature anomalies from Eby et al. (2009) into a regime of lower CO_2 concentrations. The result from this exercise is summarised in Table B-3.

As a first step, the global mean temperature anomaly at 12 000 AD from Eby et al. (2009) is reproduced with the EBM. The reported climate sensitivity (global mean surface air temperature increase resulting from doubling of the atmospheric CO_2 concentration) in the model of Eby et al. (2009) is 3.5 °C. Assuming that the temperature is in equilibrium ($\partial \Delta T_s / \partial t = 0$ in Equation B-5), the global mean temperature change can be predicted by:

$$\Delta T_{s,ebm} = \frac{3.5}{\ln(2)} \ln(p/p_0) \qquad \text{Equation B-6}$$

Applying Equation B-6 to the six emission scenarios from Eby et al. (2009) results in very similar temperature responses at 12 000 AD to the ones obtained in Eby et al. (2009) (Table B-3). This result enables the use of Equation B-6 for predicting the temperature response to other CO_2 concentrations.

According to Archer et al. (2009) the models with the fastest CO_2 decline over the next 10 000 years have about ~ 50 % less emissions remaining at 12 000 AD than in the model of Eby et al. (2009). Assuming 50 % lower CO_2 concentrations than in Eby et al. (2009), Equation B-6 yields a reduction of the temperature anomaly by ~ 45 % for lower emissions and ~ 35 % for the highest emission scenario. In other words, the reduced CO_2 forcing at 12 000 AD means that only ~ 30–50 % of the maximum temperature anomaly persists at 12 000 AD as opposed to ~ 60–75 % in Eby et al. (2009).

The fractional temperature decline at 12 000 AD relative to the peak temperature, as predicted by the EBM with 50 % less remaining emissions, is used to construct the lower bounds of the global mean surface air temperature curves (Table B-2 and Figure B-3). The upper bound of the 12 000 AD temperature response is constructed using the fractional temperature decline from Clark et al. (2016), amounting to 60 %, 70 % and 85 % of the peak temperature in the low, medium and high emission scenarios, respectively.

Table B-3. Atmospheric CO_2 concentration (p) and associated global annual mean surface air temperature anomalies at 12 000 AD as predicted by the ESM in Eby et al. (2009) ($\Delta T_{s,eby}$) and by Equation B-6 ($\Delta T_{s,ebm}$). The baseline CO_2 concentration is p_0 = 320 ppm (from Eby et al. 2009). The right-most column shows the projected temperature anomaly (using Equation B-6) with the assumption that 50 % less of the emissions are remaining in the atmosphere by 12 000 AD compared with Eby et al. (2009), thus roughly corresponding to lower-end estimates in ESMs (Archer et al. 2009), see also the text. The %-values within square-brackets show how much of the maximum temperature increase is remaining by 12 000 AD.

Scenario	p (ppmv)	$\Delta T_{s,eby}$ (°C)	$\Delta T_{s,ebm}$ (°C)	$\Delta T_{s,ebm}$ with 50 % less emissions remaining (°C)
160 Pg C	330	0.2 [67 %]	0.2	0.1 [33 %]
640 Pg C	370	0.8 [57 %]	0.7	0.4 [29 %]
960 Pg C	390	1.0 [50 %]	1.0	0.5 [25 %]
1 280 Pg C	430	1.5 [60 %]	1.5	0.8 [32 %]
2 560 Pg C	600	3.1 [66 %]	3.2	1.8 [38 %]
5 120 Pg C	1 050	5.9 [76 %]	6.0	3.8 [49 %]

B1.3 Surface air temperature change at Forsmark

To construct the annual mean surface air temperature change at Forsmark until 12 000 AD two major modifications are made to the global annual mean curve (Table B-4). First, it is assumed that the temperature increase at Forsmark will be higher than the global average due to the Arctic temperature amplification (Section B1.3.1). Second, the potential impact of a collapse (defined here as a slowdown to an "off" state) of the Atlantic Meridional Overturning Circulation (AMOC) on the Forsmark temperature is considered (Section B1.3.2). The resulting estimated changes of the annual mean surface air temperature until 12 000 AD at Forsmark are shown in Figure B-4. The specific modifications of these curves in relation to the global mean curves in Figure B-3 are summarised in Table B-4 and justified in the next two subsections.

Table B-4. Modifications of the constructed global annual mean surface air temperature change (Table B-2, Figure B-3), utilised to construct the annual mean surface air temperature change at Forsmark until 12 000 AD (Figure B-4). The specific values in the table are discussed and justified in the text.

Modification	Low emissions (RCP2.6)	Medium emissions (RCP4.5)	High emissions (RCP8.5)	Based on
Arctic temperature amplification factor (1 = global average)	1.35 [1.2–1.5]	1.35 [1.2–1.5]	1.35 [1.2–1.5]	Eby et al. (2009), Pimenoff et al. (2012), Collins et al. (2013)
∆T due to AMOC collapse (°C)	-	−2.5 °C	−2.5 °C	Mikolajewicz et al. (2007), Pimenoff et al. (2012), Liu et al. (2017)
Duration of AMOC collapse (years)	-	300	300	Liu et al. (2017)
Start of AMOC collapse (year AD)	-	2150 AD	2150 AD	Mikolajewicz et al. (2007), Pimenoff et al. (2012)

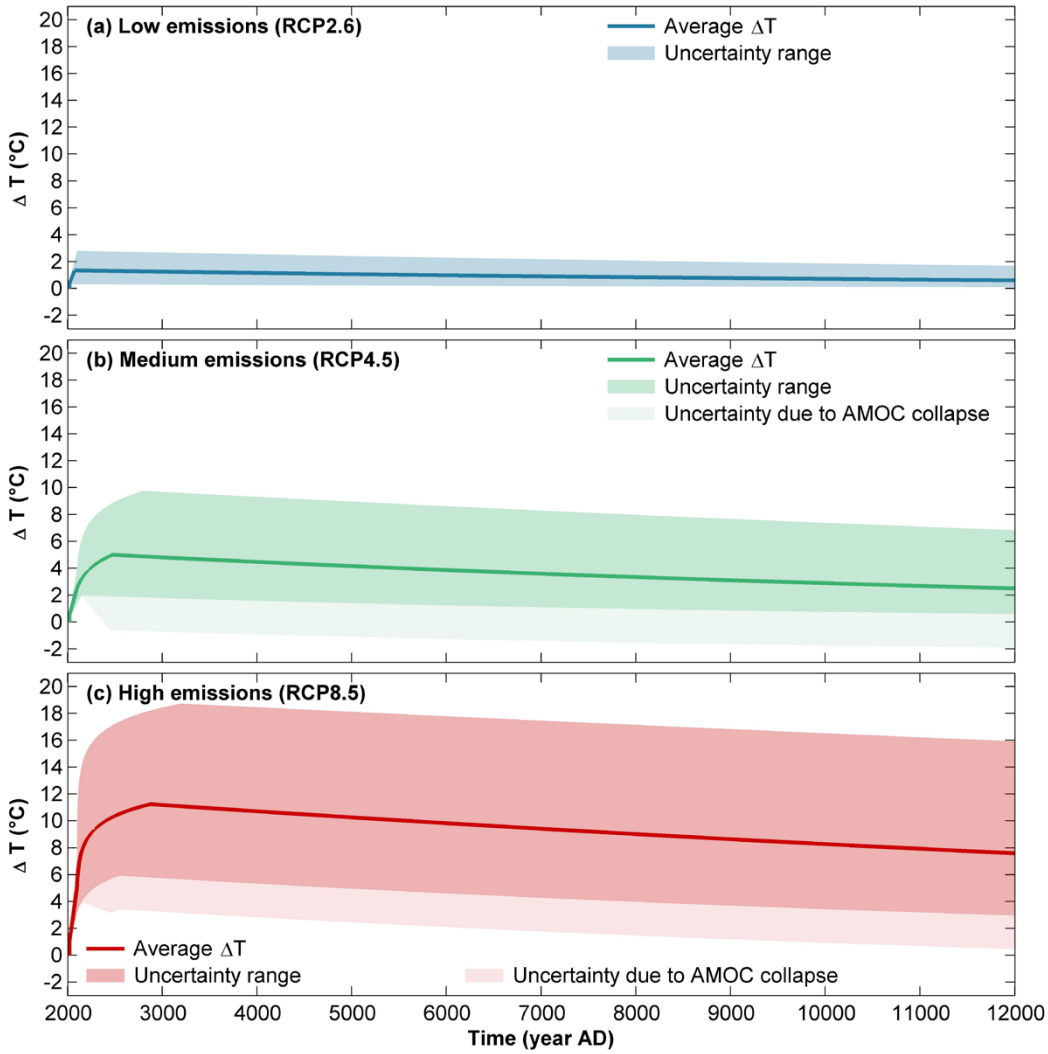

Figure B-4. *Constructed annual mean surface air temperature change until 12 000 AD at Forsmark (relative to present) for (a) low, (b) medium and (c) high carbon emissions (comparable to RCP2.6, RCP4.5 and RCP8.5, respectively; see Section 3.4.1). The uncertainty ranges are constructed using the global annual mean surface air temperature change (Figure B-3) and the values in Table B-4. The average temperature change ("Average ΔT") has been calculated using average values of the parameters used to construct the lower and upper bounds. To that end, average ΔT illustrates a typical mid-range temperature evolution for each emission scenario over the next 10 ka. The uncertainty range associated with a collapse of the AMOC in the medium and high emission scenarios is illustrated with another colour to highlight the low confidence in the assessment of this uncertainty range.*

B1.3.1 Arctic temperature amplification

A well-known feature of anthropogenic global warming is that the northern high latitudes typically warm at a faster rate than the global average. State-of-the-art climate models demonstrate that the mean Arctic (67.5°N to 90°N) warming is between 2.2 and 2.4 times the global average warming by 2100 AD depending on the emission scenario (Collins et al. 2013). The same set of models project that the warming in the Forsmark region is between 1.25 and 1.5 times the global average by the end of the 21st century across all emission scenarios (Figure 12.10 in Collins et al. 2013). The reduced temperature amplification at Forsmark compared with the Arctic average is partly explained by the relatively southern location of Forsmark (at 60°N), but also by a weakened AMOC in the future climate projections (Section B1.3.2).

The Forsmark temperature amplification on longer timescales can be estimated from the study of Pimenoff et al. (2012), which shows the projected annual mean surface air temperature evolution until 12 000 AD at the grid point closest to Olkiluoto in Finland from the model simulation in Eby et al. (2009). Since the distance between Forsmark and Olkiluoto is only ~ 200 km, the projected polar temperature amplification for Olkiluoto is likely also a good estimate for Forsmark. In summary, the model in Eby et al. (2009) predicts that the warming in Olkiluoto over the next 10 ka is approximately between 1.2 and 1.35 times the global average, thus slightly lower than the estimated temperature amplification in Collins et al. (2013).

In the following, the Forsmark temperature amplification based on low-end estimate from Pimenoff et al. (2012) is used to construct the lower bound of Figure B-4, and the high-end estimate from Collins et al. (2013) is used for the upper bound (Table B-4).

B1.3.2 Ocean circulation and AMOC instability

Until 2100 AD

Virtually all climate model projections show that the enhanced 21st century surface air temperature increase at high latitudes is also associated with increased precipitation (Collins et al. 2013). Both of these effects tend to make the high-latitude surface waters less dense and hence increase their stability. All the models included in IPCC AR5 show a weakening of the AMOC over the course of the 21st century (IPCC 2013a), but none of the models shows a collapse over this time period. Most models even show a recovery of the AMOC once the greenhouse-gas forcing has stabilised. The recovery may include a significant overshoot if the anthropogenic radiative forcing is eliminated (Wu et al. 2011). The AMOC overshoot could give an extended period of anomalously strong northward heat transport, maintaining warmer northern high latitudes for decades after the atmospheric CO_2 concentration returns to preindustrial values.

Based on the assessment of climate model projections and of understanding from observations and physical mechanisms, IPCC conclude that it is very likely that the AMOC will weaken over the 21st century (Collins et al. 2013). It is however very unlikely that the AMOC will undergo an abrupt transition or collapse in the 21st century (Collins et al. 2013). This was concluded taking both the high latitude temperature and precipitation increase and a possible rapid melting of the Greenland ice sheet into account.

The weakening of the AMOC in the 21st century contributes to reducing the warming in northern Europe, resulting in a slightly weakened temperature amplification in the area (Section B1.3.1, Collins et al. 2013). To roughly estimate the effect of the weakened AMOC by 2100 AD on the annual mean surface air temperature in the Forsmark region, the projected temperature increase in that region is compared with the projected warming further east at comparable latitudes, i.e. in central Russia. The rationale for this comparison is that central Russia is significantly less influenced by the North Atlantic sector, and hence also the dynamics of AMOC, than the Scandinavian region. In general, the projected annual mean warming in the Forsmark area is ~ 1 °C smaller under RCP4.5 and ~ 1–2 °C under RCP8.5 than the projected warming in central Russia (Figure 12.11 in Collins et al. 2013). It should be emphasised that this methodology to evaluate the AMOC influence on the temperature is highly uncertain and should therefore only be regarded as a broad first-order estimate. In reality, there are also other features that likely contribute to the different warming rates between Scandinavia and central Russia, e.g. differences due to changes in the atmospheric circulation and/or snow cover.

Beyond 2100 AD

For the centuries and millennia beyond 2100 AD the fate of the AMOC is more uncertain. In an EMIC intercomparison study, all models predicted an almost complete recovery of AMOC by 3000 AD under the low and intermediate RCPs (Zickfeld et al. 2013). However, under RCP8.5 the AMOC response was highly variable among the models; while some models simulate an almost complete recovery, others suggest a more persistent weakening. One of the 12 models even projected a collapse of AMOC under this scenario. A collapsed AMOC beyond 2100 AD was also projected under the high emission scenario (SRES A2, approximately equivalent to RCP8.5) in Mikolajewicz et al. (2007). Pimenoff et al. (2012) reported that the annual mean surface air temperature at the Olkiluoto region in Finland decreases by a total of ~ 3 °C between ~ 2150 and 2300 AD as a result of this AMOC collapse.

More recently, Liu et al. (2017) argued that the relatively moderate changes of AMOC in current state-of-the-art climate model projections may be attributed to a common model bias that favours a stable AMOC. In an attempt to adjust for this bias, Liu et al. (2017) reported that the AMOC may collapse also for moderate emission levels (doubling of the atmospheric CO_2 concentration relative to preindustrial). The duration of the AMOC collapse in Liu et al. (2017) is ~ 300 years and the resulting AMOC-induced temperature reduction is ~ 3.5 °C in the Forsmark region.

Here the results from Mikolajewicz et al. (2007), Pimenoff et al. (2012) and Liu et al. (2017) are used to construct a second uncertainty range that brackets the lower end of the surface air temperature evolution under the scenario of an AMOC collapse (Figure B-4). Because of the great uncertainties involved regarding the potential existence of an AMOC collapse beyond 2100 AD, and its effect on the Forsmark temperature, the uncertainty range is highlighted with a different colour in Figure B-4. The total annual mean surface air temperature reduction in the Forsmark region as a result of the AMOC collapse is assumed to be 3.5 °C in both the medium and high emission scenarios. However, because the warming signal at Forsmark is expected to be attenuated by a weakened AMOC by 2100 AD, the effects of a modest AMOC weakening is already included in the main uncertainty range in Figure B-4. As discussed above, it is broadly estimated that the weakening until 2100 AD contributes to reduce the Forsmark temperature by ~ 1 °C, implying that the "remaining" temperature reduction resulting from a collapse is estimated to be 2.5 °C (Table B-4). The duration of the AMOC collapse is assumed to be 300 years and the collapse is assumed to begin at 2150 AD for both emission scenarios.

The possibility of an AMOC collapse under low future carbon emissions is considered very unlikely and has therefore been omitted in the present analysis.

B1.3.3 Seasonal distribution of temperature

A set of future climate projections for Sweden until 2100 AD, performed with a regional climate model, is utilised to estimate the seasonal distribution of the surface air temperature increase at Forsmark. The results are available as seasonal averages for different regions in Sweden. The projected future changes presented for Uppsala County (Sjökvist et al. 2015) are here chosen to represent the projected seasonal change at Forsmark. The results presented by Sjökvist et al. (2015) were obtained using boundary conditions from nine different global climate models under the RCP4.5 and RCP8.5 scenarios, and three different models under the RCP2.6 scenario. The projected seasonal temperature change is calculated for the period 2070–2099 AD from the ensemble mean across all global climate models for each RCP.

The seasonal distribution of the warming at Forsmark is similar under all the emission scenarios considered here (Tables B-5, B-6 and B-7): the largest warming occurs during the boreal winter season (December-February), estimated to be 1.2–1.25 times the annual average, and smallest warming occurs during summer (June-August) amounting to 0.8–0.9 times the annual average. During the spring (March-May) and autumn (September-November) the projected warming is generally similar to the annual average. The constructed seasonal surface air temperature evolution until 12 000 AD is shown in Figure B-5.

Table B-5. Summary of annual and seasonal averages of the constructed surface air temperature change at Forsmark in the low emission scenario (comparable to RCP2.6). The values within square-brackets represent lower and upper bounds of the temperature change whereas the other values represent the average temperature change. The seasonal ratios to the annual mean temperature change are derived from Sjökvist et al. (2015); see the text.

Season	Low emissions (RCP2.6)			
	Ratio to annual mean ΔT	ΔT 2100 AD (°C)	Max. ΔT (°C)	ΔT 12 000 AD (°C)
Annual mean	1.0	1.4 [0.3–2.6]	1.4 [0.3–2.8]	0.6 [0.1–1.7]
December – February	1.2	1.6 [0.4–3.1]	1.6 [0.4–3.4]	0.7 [0.1–2.0]
March – May	1.0	1.4 [0.3–2.6]	1.4 [0.3–2.8]	0.6 [0.1–1.7]
June – August	0.9	1.2 [0.3–2.3]	1.2 [0.3–2.5]	0.5 [0.1–1.5]
September – November	0.9	1.2 [0.3–2.3]	1.2 [0.3–2.5]	0.5 [0.1–1.5]

Table B-6. Summary of annual and seasonal averages of the constructed surface air temperature change at Forsmark in the medium emission scenario (comparable to RCP4.5). The values within square-brackets represent lower and upper bounds of the temperature change whereas the other values represent the average temperature change. The lower bound associated with the potential AMOC collapse (Figure B-4) has been omitted. The seasonal ratios to the annual mean temperature change are derived from Sjökvist et al. (2015); see the text.

Season	Medium emissions (RCP4.5)			
	Ratio to annual mean ΔT	ΔT 2100 AD (°C)	Max. ΔT (°C)	ΔT 12 000 AD (°C)
Annual mean	1.0	2.5 [1.3–3.9]	5.0 [2.0–9.8]	2.5 [0.6–6.8]
December – February	1.25	3.1 [1.7–4.9]	6.2 [2.5–12.2]	3.1 [0.7–8.5]
March – May	1.05	2.6 [1.4–4.1]	5.2 [2.1–10.2]	2.6 [0.6–7.2]
June – August	0.8	2.0 [1.1–3.1]	4.0 [1.6–7.8]	2.0 [0.5–5.5]
September – November	0.9	2.2 [1.2–3.5]	4.5 [1.8–8.8]	2.2 [0.5– 6.1]

Table B-7. Summary of annual and seasonal averages of the constructed surface air temperature change at Forsmark in the high emission scenario (comparable to RCP8.5). The values within square-brackets represent lower and upper bounds of the temperature change whereas the other values represent the average temperature change. The lower bound associated with the potential AMOC collapse (Figure B-4) has been omitted. The seasonal ratios to the annual mean temperature change are derived from Sjökvist et al. (2015); see the text.

Season	High emissions (RCP8.5)			
	Ratio to annual mean ΔT	ΔT 2100 AD (°C)	Max. ΔT (°C)	ΔT 12 000 AD (°C)
Annual mean	1.0	5.0 [3.1–7.2]	11.2 [5.9–18.7]	7.6 [3.0–15.9]
December – February	1.2	6.0 [3.7–8.6]	13.5 [7.1–22.5]	9.1 [3.6–19.1]
March – May	1.0	5.0 [3.1–7.2]	11.2 [5.9–18.7]	7.6 [3.0–15.9]
June – August	0.85	4.2 [2.7–6.1]	9.6 [5.0–15.9]	6.4 [2.5–13.5]
September – November	0.95	4.7 [3.0–6.8]	10.7 [5.6–17.8]	7.2 [2.8–15.1]

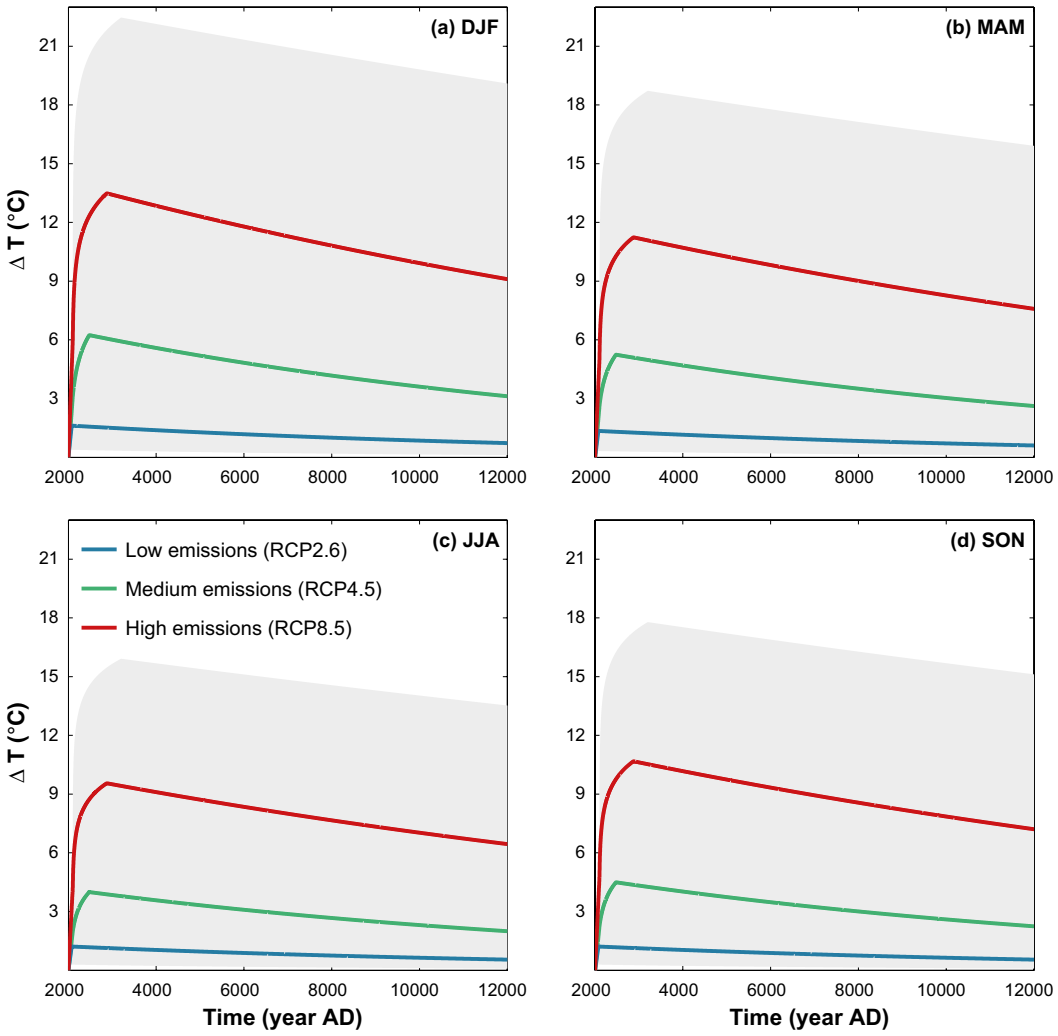

Figure B-5. *Constructed seasonal averages of the surface air temperature change until 12 000 AD at Forsmark (relative to present) for low (blue curve), medium (green curve) and high (red curve) carbon emissions (comparable to RCP2.6, RCP4.5 and RCP8.5, respectively). The grey shading indicates the total uncertainty range across all emission scenarios. The solid lines illustrate typical mid-range temperature evolutions for each emission scenario over the next 10 ka. Abbreviations in the panel titles are DJF = December-January-February, MAM = March-April-May, JJA=June-July-August and SON=September-October-November.*

B2 Precipitation change at Forsmark until 12 000 AD

Most global climate projections demonstrate a positive correlation between mid-to-high latitude changes in annual precipitation and increases of the annual-mean surface air temperature (e.g. Collins et al. 2013). Hence, any increase in the annual-mean temperature in the Forsmark region is expected to be accompanied by a higher annual precipitation. Using the global ESM simulations from Mikolajewicz et al. (2007), Pimenoff et al. (2012) demonstrated that the annual precipitation at Olkiluoto increases almost linearly with the annual-mean surface air temperature change at a rate of ~ 3 % $°C^{-1}$. An approximately linear relationship between annual changes in precipitation and temperature is also found in the regional climate model projections for Uppsala County (Sjökvist et al. 2015), but with a slightly higher rate of change (~ 5.1 % $°C^{-1}$) (Figure B-6a).

In contrast to the projected changes in annual precipitation, models indicate that the seasonal precipitation response may be more complex. This is particularly true for the summer season. In the projections of Sjökvist et al. (2015), for example, it is found that precipitation increases as a result of global warming for both the winter and summer seasons (Figure B-6b,c). However, whilst the projected changes in winter precipitation correlate strongly with the temperature change, manifested by a high value of the linear correlation coefficient (r^2 = ~ 0.94), the summer precipitation response is more scattered, resulting in a weaker correlation with the temperature change (r^2 = ~ 0.66).

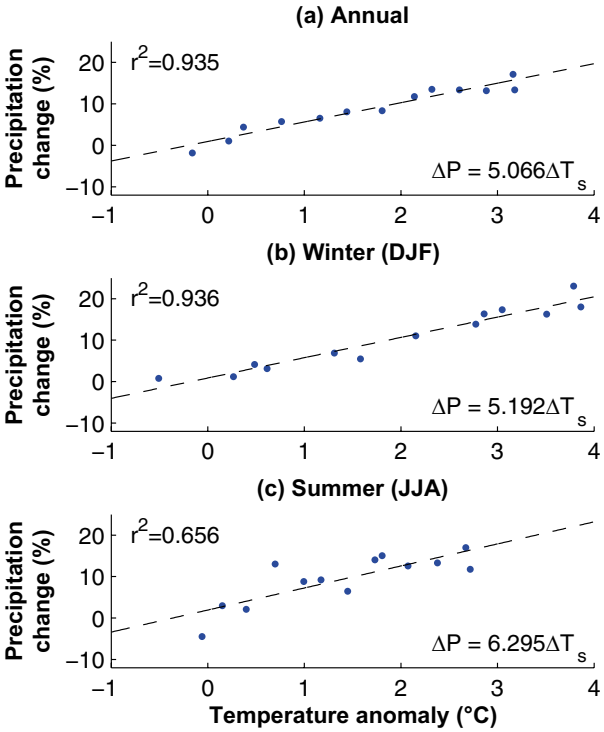

Figure B-6. *Correlation between (a) annual, (b) winter (December-February) and (c) Summer (June-August) precipitation change (in %) and surface air temperature change (in °C) derived from the regional climate modelling data between 1970 and 2099 AD for Uppsala County (Sjökvist et al. 2015). All dots represent the average precipitation and temperature change. Each dot represents a different decadal average of the precipitation and temperature change, calculated from the average change across all 21 ensemble simulations (comprised of nine different global climate models for RCP4.5 and RCP8.5, and three models for RCP2.6). The dashed lines represent a linear regression of the data, described by the equation in the bottom-right corner of each panel. The linear correlation coefficients (r^2) are displayed in upper-left corner of each panel. Note that the correlation is constrained to zero.*

The variability in the summer precipitation response is partly explained by the fact that winter precipitation mostly comes from large-scale synoptic weather systems that are comparatively well resolved in climate models, whereas summer precipitation to a larger degree originates from less predictable local convective systems. Furthermore, it has been demonstrated that a warmer climate may imply significant changes to the general circulation of the atmosphere (e.g. Collins et al. 2013). In Europe during the summer season, these changes are primarily manifested by a general northward expansion of the dry climate conditions presently found in the Mediterranean region (Collins et al. 2013, IPCC 2013b). The latitudinal extent affected by the future expansion of this region is however highly uncertain. Whilst some of the CMIP5 projections suggest that the region of drier summer conditions may not expand further north than to central Europe, other projections suggest that it may even influence large parts of Fennoscandia under the RCP4.5 and RCP8.5 emissions scenarios (IPCC 2013b). This uncertainty therefore results in a large spread across the models of the projected summer precipitation response in the Forsmark region. This is also clearly evident in Figure B-7, which shows the projected change in seasonal precipitation at Forsmark from seven CMIP5 models (Table B-8) under the RCP8.5 emissions scenario. For the winter, spring and autumn seasons, all the CMIP5 models considered here suggest a general precipitation increase as a result of global warming (Figure B-7a,b,d). For the summer season, however, the precipitation response is much more divergent across the models. Whilst three out of the seven CMIP5 models project a significant increase of the summer precipitation, the remaining four models suggest either a significant summer precipitation decrease or a limited precipitation change relative to present day (Figure B-7).

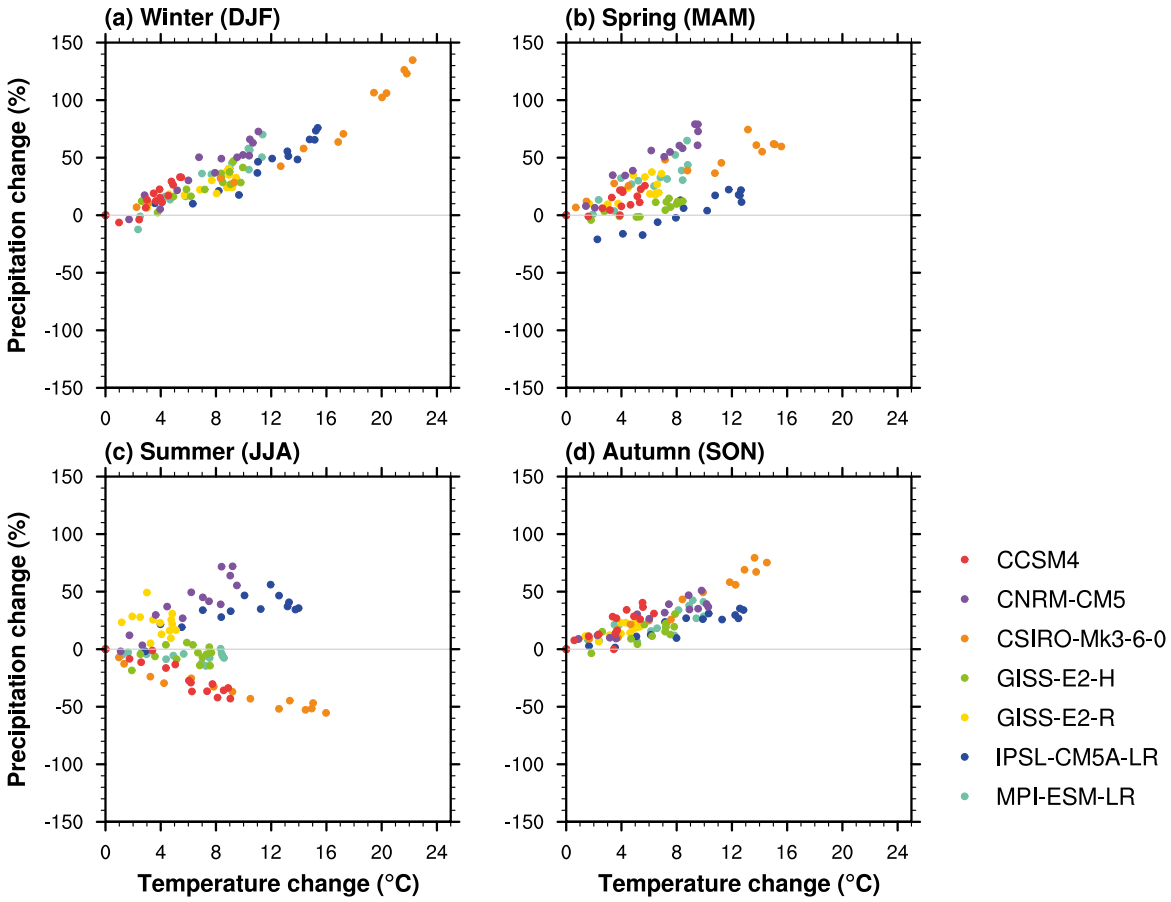

Figure B-7. *Projected seasonal precipitation change (relative to 1986–2005 AD) as a function of surface air temperature change from the grid cell covering the Forsmark region in seven CMIP5 models (indicated by different colours, see the legend and Table B-8) that were integrated until 2300 AD under the RCP8.5 scenario. Each dot represents 20-year averages of precipitation and temperature change ranging from 2021–2040 AD to 2281–2300 AD.*

Table B-8. List of the CMIP5 models used in Figure B-7.

Model	Organisation
CCSM4	NCAR, University Corporation for Atmospheric Research, United States
CNRM-CM5	Centre National de Recherches Météorologiques and Centre Européen de Recherche et Formation Avancées en Calcul Scientifique, France
CSIRO-MK3.6.0	Commonwealth Scientific and Industrial Research Organisation, Australia
GISS-E2-R	NASA Goddard Institute for Space Studies, United States
GISS-E2-H	NASA Goddard Institute for Space Studies, United States
IPSL-CM5A-LR	Laboratoire de Météorologie Dynamique and L'Institut Pierre-Simon Laplace, France
MIROC-ESM	Atmosphere and Ocean Research Institute, National Institute for Environmental Studies, and Japan Agency for Marine-Earth Science and Technology, Japan
MPI-ESM-LR	Max Planck Institute for Meteorology (MPI-M), Germany

The large uncertainty related to the summer precipitation response at Forsmark is taken into account when constructing the lower and upper bounds of the seasonal and annual precipitation response until 12 000 AD, summarised in Table B-9. For all the seasons in the case of low emissions, as well as for the winter, spring and autumn seasons in the case of medium and high emissions, it is assumed that precipitation at Forsmark increases linearly with the surface air temperature change according to the range of coefficients listed in Table B-9. This assumption is based on a combined assessment of the estimated relationships between precipitation and temperature changes from Pimenoff et al. (2012), Sjökvist et al. (2015), IPCC (2013b) and the investigated CMIP5 models in Figure B-7. For

medium and high emissions, it is assessed that summer precipitation may either increase or *decrease* as a result of global warming (Table B-9), based on the CMIP5 results (Figure B-7). The resulting ranges of the annual precipitation change at Forsmark for low, medium and high carbon emissions are shown in Figure B-8.

Table B-9. Linear regression coefficients representing the ratio of precipitation change to temperature change (% °C^{-1}). The coefficients are used to construct the total range of seasonal precipitation change at Forsmark until 12 000 AD (relative to present). For each season and emissions scenario, the coefficients are presented as a range, given by the minimum and maximum values below, accounting for the uncertainty in scientific literature. To obtain the total precipitation change for each season the coefficients are multiplied with the seasonal temperature change at Forsmark, see Figure B-5. Note that for medium and high emissions, it is assumed that summer (June–August) precipitation can either increase or decrease as a result of global warming.

	Precipitation to temperature coefficient (% °C^{-1})						
Season	**Low emissions (RCP2.6)**		**Medium emissions (RCP4.5)**		**High emissions (RCP8.5)**		**Based on**
	Min.	**Max.**	**Min.**	**Max.**	**Min.**	**Max.**	
December – February	3.0	5.0	3.0	5.0	3.0	5.0	Pimenoff et al. (2012), IPCC (2013b), Sjökvist et al. (2015), CMIP5 (Figure B-7)
March – May	3.0	5.0	3.0	5.0	3.0	5.0	Pimenoff et al. (2012), IPCC (2013b), Sjökvist et al. (2015), CMIP5 (Figure B-7)
June – August (increased summer precipitation due to warming)	3.0	5.0	3.0	5.0	3.0	5.0	Pimenoff et al. (2012), IPCC (2013b), Sjökvist et al. (2015), CMIP5 (Figure B-7)
June – August (decreased summer precipitation due to warming)	-	-	−3.0	−3.0	−3.0	−3.0	CMIP5 (Figure B-7)
September – November	3.0	5.0	3.0	5.0	3.0	5.0	Pimenoff et al. (2012), IPCC (2013b), Sjökvist et al. (2015), CMIP5 (Figure B-7)

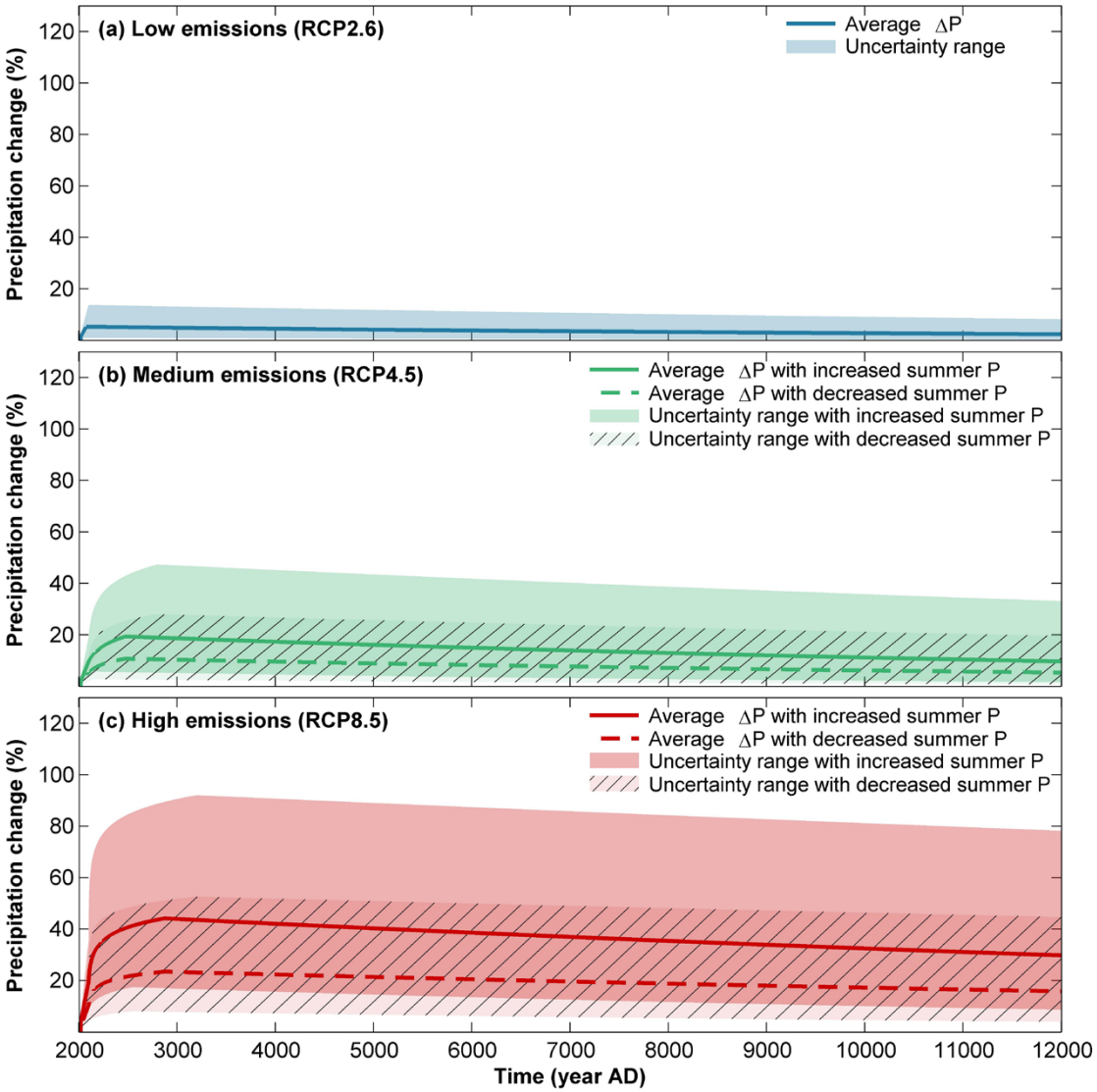

Figure B-8. *Constructed annual precipitation change until 12 000 AD at Forsmark (relative to present) for (a) low, (b) medium and (c) high carbon emissions (comparable to RCP2.6, RCP4.5 and RCP8.5, respectively; see Section 3.4.1). The uncertainty ranges are constructed from the seasonal average surface air temperature change (Figure B-5) and the coefficients in Table B-9. For medium and high emissions (b and c), two uncertainty ranges were constructed (see Table B-9): one with increased summer precipitation and the other one with decreased summer precipitation. Note that there is a considerable overlap between the uncertainty ranges (highlighted by the hatched areas and darker shades). The red solid line represents the average annual precipitation change in case of increased summer precipitation, and the red dashed line shows the average precipitation change in case of decreased summer precipitation. As with the average temperature change (Figure B-4), the average precipitation changes have been calculated using average values of the parameters used to construct the lower and upper bounds.*

Appendix C

Estimating Forsmark surface air temperature and precipitation for the IPCC reference period 1986–2005 AD

To estimate future evolution of surface air temperature (SAT) and precipitation, the anticipated changes of the climate under different emission scenarios, as described in Section 3.4, must be added to some baseline climatology, representative for present-day conditions at Forsmark. The current baseline climatology used by SMHI represents average climate conditions between 1961 and 1990 AD. This period typically has also been used as representative for present-day climate at Forsmark in previous safety assessments (see e.g. SKB TR-10-49, SKB TR-13-05). In SKB (TR-13-05), for example, present-day annual-mean SAT at Forsmark was defined to be 5.5 °C based on SMHI data between 1961 and 1990 AD from the Örskär station (Larsson-McCann et al. 2002), and annual precipitation during this period was estimated to be 568 mm based on data from nearby SMHI stations (Johansson 2008).

Using the 1961–1990 AD reference period to define present-day climatology at Forsmark inevitably introduces some inconsistencies with other climate or climate-related features used in the safety assessment, as these may be based on other baseline periods. For example, hydrological modelling at SKB typically relies on using the "normal year", defined as the period between October 2003 and September 2004, to define present-day conditions in their simulations (e.g. Werner et al. 2013). Even if this period is too short to be defined as a typical climatology, it is clearly also defined for a full year after the 1961–1990 AD period.

Furthermore, the projected future SAT and precipitation changes over the next millennia (Section 3.4.4) are chiefly based on results from the fifth IPCC assessment report (IPCC 2013a), which uses 1986–2005 AD as reference period. Therefore, using 1961–1990 AD as baseline climatology could potentially introduce a bias in assessments of the future evolution of the Forsmark climate, as the climate during this period may be slightly different compared with the IPCC baseline. This is particularly evident at higher latitudes where the current rate of warming is significantly faster than the global mean (Appendix B, Section B1.3.1). The rate of the current warming can be exemplified by comparing the SAT from Uppsala County during 1961–1990 AD to more recent SAT measurements from the area. At the Örskär station, for instance, the annual average SAT between 1986 and 2014 AD amounts to ~ 6.6 °C[11], i.e. approximately 1 °C warmer than the SAT recorded for the 1961–1990 AD baseline period (Larsson-McCann et al. 2002). This further highlights the need for an updated baseline climatology for Forsmark. Therefore, in this appendix, monthly climatologies of SAT and precipitation at Forsmark are calculated for the IPCC baseline period 1986–2005 AD.

C1 Methodology

Local meteorological measurements at Forsmark started in May 2003 and are still ongoing (Berglund and Lindborg 2017). Hence, the initial 2.5 years of Forsmark measurements overlap with the latter part of the IPCC reference period. Therefore, local measurements of SAT and precipitation from the full years 2004 and 2005 AD are here used to describe the last two years of the Forsmark climatology between 1986 and 2005 AD. For the remaining part of this period, i.e. between 1986 and 2003 AD, Forsmark climatology is estimated using multiple linear regression analysis of data from nearby SMHI stations in Uppsala County. The regression analysis is done in two steps. First, regression coefficients are estimated using Forsmark (Högmasten) and SMHI data between the full years 2004 and 2014 AD. Second, once the regression coefficients have been estimated, they are used together with SMHI data between 1986 and 2003 AD to predict the Forsmark climatology for the same period. The regression analysis uses daily-averaged data for SAT and monthly data for precipitation (see below). For simplicity, missing days and months have been omitted in the analysis. However, these missing data account for less than 1 % of the total SAT dataset and less than 2 % of the precipitation dataset, and thus are not critical for the results presented here. SMHI data were downloaded from their website (https://www.smhi.se/data).

[11] Using official SAT measurements from SMHI (https://smhi.se/data).

C2 Surface air temperature

Two nearby SMHI stations provide SAT data between 1986 and 2014: Films Kyrkby[12] and Örskär. The correlation coefficient (r^2) between each of those stations and the Högmasten station for daily-averaged SAT data between 2004 and 2014 AD is 0.98 for Films Kyrkby and 0.97 for Örskär. The very high correlation with Högmasten data of each SMHI station is partly explained by the relatively flat terrain in Uppsala County, implying that local SAT variations due to variations in surface elevation are negligible in the region. Moreover, excluding seasonal effects, the SAT in the region is primarily determined by the atmospheric circulation which operates on much larger spatial scales than that of Uppsala County. Therefore, any change in the prevailing temperature of the air mass, which is controlled by the large-scale atmospheric circulation, will affect the entire region in a similar manner.

According to the regression analysis, daily averaged SAT at Forsmark for the 1986–2003 AD period can be predicted by the SAT at Örskär and Films Kyrkby as: $SAT_{Forsmark} = 0.2687 + 0.4660 \times SAT_{Örskär} + 0.5340 \times SAT_{Films\ kyrkby}$. Combined, these two stations capture 99 % of the observed SAT variability at Forsmark, as estimated by the coefficient of determination (often referred to as R^2, see Miller et al. 2008).

The resulting monthly Forsmark SAT climatology for the 1986–2005 AD reference period is summarised in Table C-1 and Figure C-1. The annual average SAT is 6.1 °C, i.e. 0.6 °C warmer than during 1961–1990 AD, but 0.7 °C colder than during 2004–2014 AD. The predicted annual average SAT between 1986 and 2005 AD hence is consistent with the overall warming trend in the region.

Table C-1. Estimated monthly average SAT (°C) at Forsmark between 1961 and 1990 AD, 1986 and 2005 AD, and 2004 and 2014 AD. The rightmost column ("Ann") shows the annual average SAT for each period. Forsmark SAT for the 1961–1990 AD period was estimated based on data from the Örskär station (Larsson-McCann et al. 2002). These data were used to define present-day SAT at Forsmark in the SR-PSU (SKB TR-13-05). The SAT data for the 2004–2014 AD period represent local measurements from the Högmasten station, whereas data for the 1986–2005 AD period were computed using the methodology outlined in this section.

	Jan	Feb	Mar	Apr	May	Jun	Jul	Aug	Sep	Oct	Nov	Dec	Ann
1961–1990	−3.0	−4.0	−1.4	2.3	7.5	13.1	15.7	15.1	11.4	7.2	2.6	−0.8	5.5
1986–2005	−2.0	−2.5	0.0	4.1	9.5	13.9	16.3	15.9	11.4	6.6	2.3	−0.9	6.1
2004–2014	−2.0	−2.4	0.0	5.3	9.9	14.2	17.7	16.4	12.3	7.0	3.1	−0.4	6.8

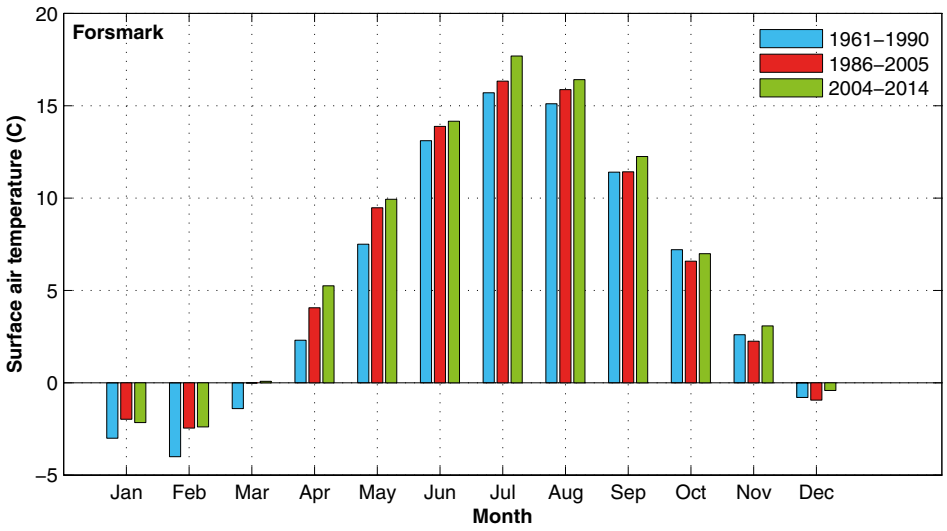

Figure C-1. *Monthly average SAT (°C) at Forsmark between 1961 and 1990 AD (blue), 1986 and 2005 AD (red), and 2004 and 2014 AD (green).*

[12] Note that different stations have been in operation by SMHI at Films Kyrkby in recent years: Films Kyrkby D (1982–2014 AD) and Film A (2001 AD–). In the present work, data from Films Kyrkby D are used for the 1986–2001 AD period, whereas data from Film A are used for 2001–2014 AD.

C3 Precipitation

Four nearby SMHI stations provide precipitation data between 1986 and 2014: Örskär, Risinge, Lövsta and Films Kyrkby. The spatial scales associated with precipitation are typically much smaller than for SAT. This is particularly true for the summer season when most precipitation comes from local convective showers rather than large-scale synoptic weather systems (e.g. Figure 1 of Myoung and Nielsen-Gammon 2010). Depending on the local meteorological conditions on a certain day, abundant precipitation may thus fall over certain areas in the Uppsala County whereas other locations receive very little to no precipitation. However, when considering precipitation on longer timescales some of these spatial differences in daily precipitation are likely to be averaged out. Therefore, in contrast to SAT, for which daily averaged data were used to calculate correlations with nearby SMHI stations, data at monthly resolution are used for precipitation. The regression analysis is based on data of "uncorrected" precipitation. This means that measurement losses, mainly due to the prevailing wind conditions, have not been accounted for. Therefore, following Johansson (2008), a correction of the monthly precipitation, using the methodology described in Alexandersson (2003), is conducted subsequent to the regression analysis to yield an estimate of the "true" precipitation at the site.

On a monthly basis, the correlation coefficient (r^2) between each of the SMHI stations and the Högmasten station for the years between 2004 and 2014 AD is 0.79 for Örskär, 0.79 for Risinge, 0.83 for Lövsta and 0.75 for Films Kyrkby. According to the regression analysis, monthly precipitation at Forsmark for the 1986–2003 AD period can be predicted from these stations as:

$$P_{Forsmark} = 0.3942 \times P_{Örskär} + 0.1737 \times P_{Risinge} + 0.2925 \times P_{Lövsta} + 0.1159 \times P_{Films\ kyrkby}.$$

Combined, these four stations capture ~ 89 % of the observed monthly precipitation variability at Forsmark, as estimated by the coefficient of determination.

The resulting Forsmark precipitation climatology for the 1986–2005 AD reference period is summarised in Table C-2 and Figure C-2. Annual precipitation is 607 mm, i.e. approximately 40 mm higher than during 1961–1990 AD but similar to the measured average annual precipitation at Högmasten between 2004 and 2014 AD. The lack of an increasing trend in annual precipitation over the last 30 years is supported by data from the SMHI stations. Only one SMHI station (Films Kyrkby) shows higher annual precipitation between 2004 and 2014 AD as compared with 1986–2003 AD, whereas the other three stations demonstrate a slight decrease in annual precipitation for this period.

Table C-2. Estimated monthly average precipitation (mm) at Forsmark between 1961 and 1990 AD, 1986 and 2005 AD, and 2004 and 2014 AD. The rightmost column ("Ann") shows the average annual precipitation for each period. Forsmark precipitation for the 1961–1990 AD period was estimated by Johansson (2008). These data were used to define present-day precipitation at Forsmark in the SR-PSU (SKB TR-13-05). The precipitation data for the 2004–2014 AD period represent local measurements from the Högmasten station, whereas the data for the 1986–2005 AD period were computed using the methodology outlined in this section.

	Jan	Feb	Mar	Apr	May	Jun	Jul	Aug	Sep	Oct	Nov	Dec	Ann
1961–1990	44	33	29	35	27	39	71	66	61	53	61	50	568
1986–2005	45	36	35	41	36	59	71	73	54	53	57	51	612
2004–2014	45	34	32	28	39	66	47	89	52	62	61	52	606

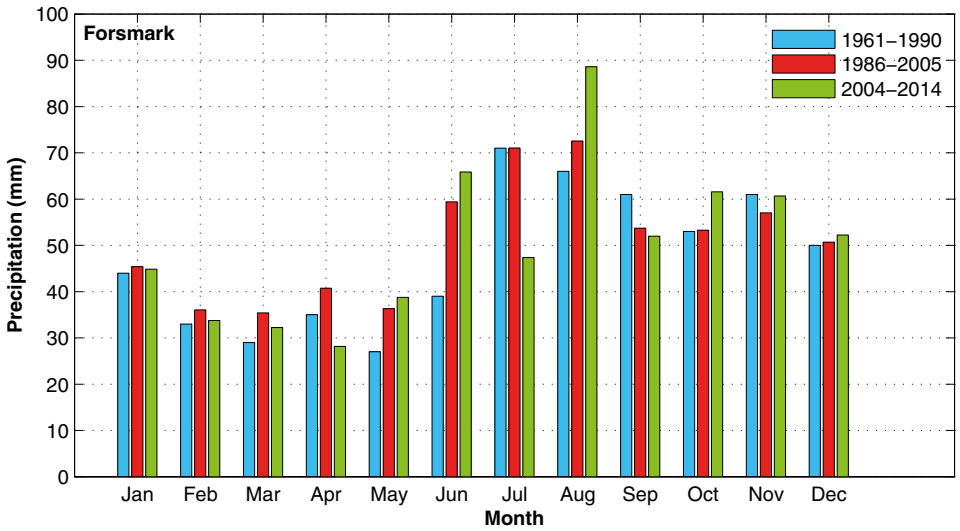

Figure C-2. *Monthly average precipitation (mm) at Forsmark between 1961 and 1990 AD (blue), 1986 and 2005 AD (red), and 2004 and 2014 AD (green).*

Appendix D

Simplified methodology for estimating potential evapotranspiration in a warmer climate

D1 Introduction

Potential evapotranspiration (PET) is defined as the evaporation that would occur if a sufficient water source were available. It is often used as input in hydrological models, such as Mike-SHE (e.g. Bosson et al. 2008), and thus is considered an important variable when modelling hydrological conditions at Forsmark.

There is no specific set of equations that can be applied to calculate PET *exactly* for a certain time and location. Thus, the calculation of PET needs to be approximated. Methods to approximate PET range from relatively complex formulas that take several different meteorological variables as input (e.g. Penman and Penman-Monteith; see Penman 1948 and Allen et al. 1994), through radiation-based formulations (e.g. Pristley-Taylor; see Priestley and Taylor 1972), to more simplified approximations where PET is primarily estimated from the surface air temperature (e.g. Thornthwaite 1948, Hargreaves et al. 1985, Willmott et al. 1985).

Previously at SKB, PET has typically been calculated using the relatively comprehensive Penman formula (e.g. Bosson et al. 2008, Johansson and Öhman 2008, Werner et al. 2014). This formula takes abundant meteorological information as input, such as the water vapour deficit, net (solar and terrestrial) radiation at the surface and near-surface wind speed. However, whilst the required input data in the present climate typically can be acquired at high resolution from meteorological measurements, estimating future changes of these data is often much more challenging. In contrast to changes in the surface air temperature (SAT), which is considered to be relatively well-constrained for a given emission scenario (Section 3.4.1), variables that demonstrate larger spatial and temporal variability are often more difficult to accurately predict. This includes, for example, future changes in net surface radiation and near-surface wind properties. The radiation at the surface is largely controlled by the cloudiness, which is known to be among the major uncertainties in state-of-the-art climate models (e.g. IPCC 2013a). Future climate-model projections of the near-surface wind field are also ambiguous, particularly for the Scandinavian region (e.g. Ruosteenoja et al. 2019).

In light of these uncertainties, a need to develop a more simplified PET formulation has been identified in this safety assessment, where future changes in PET can be estimated from the amount of warming envisaged in the climate cases. A brief description of the adopted PET formulation is provided below, along with a comparison to other, more complex, PET methods.

D2 Methodology

The chosen methodology for estimating PET changes in a warmer climate is adopted from Pereira and Pruitt (2004) (hereafter referred to as PP2004). It combines the Thornthwaite equation (Thornthwaite 1948) with the Willmott equation (Willmott et al. 1985) to calculate the daily PET using SAT and day-length as input. Day length is defined as the time between sunrise and sunset, and thus varies considerably at Forsmark during a year. In addition to those sub-annual variations, however, day length also changes slowly over timescales associated with Earth's orbital variants which can be predicted with high accuracy for the next 100 ka and beyond (e.g. Berger 1978)[13]. These long-term changes typically can be neglected when considering climate warming on shorter timescales, i.e. the next decades to centuries, but they are relevant over the long timescales covered by the present safety assessment.

[13] Specifically, day-length at a certain latitude is computed from the solar declination angle, see e.g. Roderick (1992).

D3 Comparison with other methods

In order to examine the performance of the PET formulation in PP2004, it is compared to the PET estimated from global hydrological models participating in phase 2b of the Inter-Sectoral Impact Model Intercomparison Project (ISIMIP; https://www.isimip.org/, see also Frieler et al. 2016). The models use identical forcing of climate (SAT and precipitation) and atmospheric CO_2. They are run with historical forcing until 2005 AD, and with forcing derived from the RCP2.6, RCP6.0 and RCP8.5 emission scenarios from 2006 to 2099 AD. In this analysis, only the future simulations under the RCP8.5 scenario are considered, as these allow for evaluation of PET over a larger SAT interval than the other RCPs. Four ISIMIP models provide simulated data of PET both from the historical and future projections (Table D-1). Two of these models (LPJmL and WaterGAP2) use the radiation-based formula of Priestley and Taylor (1972) to calculate PET, albeit with some minor adjustments (Table D-1), whereas the other two models use more comprehensive methods. Each ISIMIP model was forced by simulated climate from four different CMIP5 models (Section 3.4.1). In the present analysis, the PET from each hydrological model is calculated as the average across the four sets of climate forcing.

Table D-1. List of ISIMIP models and their PET formulations analysed in this section.

Model	Reference	Potential evapotranspiration
H08	Hanasaki et al. (2018)	Surface energy balance with bulk methodology (see Hanasaki et al. 2008)
LPJmL	Sitch et al. (2003)	Priestley-Taylor (modified for transpiration)
WaterGAP2	Müller Schmied et al. (2016)	Priestley-Taylor (using two different “alpha” factors depending on the aridity of the grid cell
ORCHIDEE	Guimberteau et al. 2014	Penman-Monteith with correction for soil moisture stress

Figure D-1 shows the relative change of PET as a function of warming as computed by each of the four ISIMIP models. Changes are calculated relative to the 1986–2005 AD average for each year from 2006 to 2099 AD, and only the results from the grid point closest to Forsmark are shown. The hydrological models predict that PET increases approximately linearly with SAT, with correlation coefficients (r^2) ranging from 0.83 in the H08 model to 0.90 in WaterGAP2. The sensitivity of PET to changes in SAT is on average 5.5 % $°C^{-1}$ across the models, ranging from 3.9 % $°C^{-1}$ in LPJmL to 7.1 % $°C^{-1}$ in ORCHIDEE. Interestingly, the models that exhibit the lowest PET sensitivity (LPJmL and WaterGAP2) both use the radiation-based Priestley-Taylor formula, whereas the models that yield higher sensitivities (H08 and ORCHIDEE) use more comprehensive methods.

The black dots in Figure D-1 illustrate the corresponding PET changes calculated with the formula in PP2004 using an identical SAT forcing to that in the ISIMIP models. As in the ISIMIP models, PET according to PP2004 increases almost linearly with SAT (r^2=0.99). The PET sensitivity amounts to 5.3 % $°C^{-1}$, and is thus in general agreement with average PET sensitivity across the ISIMIP models.

In summary, the simplified temperature-based PET formulation in PP2004 behaves reasonably similarly in response to warming as more comprehensive methods. To that end, it is assessed that the PP2004 methodology is appropriate to use for estimating PET in warmer climate using e.g. the future SAT changes in Figure 3-27 as input.

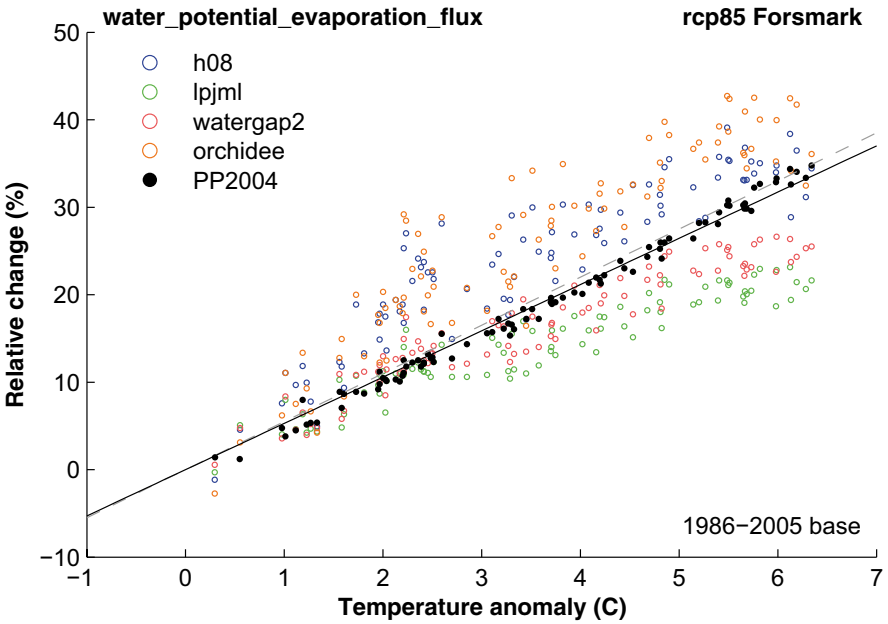

Regression equations

Average hydro models	y=5.5x
h08	y=6.5x
lpjml	y=3.9x
watergap2	y=4.5x
orchidee	y=7.1x
Pereira and Pruitt (2004)	y=5.3x

Figure D-1. *Relative change of PET (%) at Forsmark as a function of warming (°C) as computed by the ISIMIP models (coloured circles) and the simplified PET formulation from PP2004 (black dots). Also shown are linear regressions of PET changes as calculated from PP2004 (solid line) and the across all the ISIMIP models (dashed line). Note that the regressions have been constrained to zero.*

Appendix E

Ice-sheet profiles

E1 Background

In various PSAR studies, e.g. on groundwater flow and THM processes, ice-sheet profiles are useful as input for investigating how these processes are affected by glacial conditions. This appendix gives background and data for selection of two ice-surface profiles used in the safety assessment. Two different types of ice-sheet profiles are discussed; ice profiles derived mainly from theoretical considerations, and ice profiles derived from more complex numerical ice-sheet modelling.

The steepness of an ice-sheet surface is determined by the combination and interplay of several factors such as basal shear stresses, englacial ice temperatures, temperatures at the ice-sheet bed, the basal hydrological conditions and the presence or absence of deformable sediments at the bed. As a rule, a retreating ice sheet has a less steep profile than an advancing ice sheet, and so does an ice sheet ending in the sea compared with a terrestrial ice sheet. Warm basal conditions, with presence of basal water, and presence of deformable bed sediments also results in less steep ice than cold-based conditions. The steepness of the ice-sheet surface is important for the ice flow and for the water routing and water flow at the base of the ice. In addition, it is also of high importance for e.g. the flow of groundwater in the bedrock and for the stress situation in the Earth's crust.

E2 Theoretical ice-sheet profiles

The easiest way of describing an ice-sheet profile is by assuming that ice is a perfectly plastic material. One can further assume that this ice sheet is circular and situated on a flat and horizontal bed, and that the ice-sheet is in steady-state, i.e. that no change in ice configuration occurs over time. In this case the ice-sheet surface profile constitutes a simple parabola e.g. Paterson (1994), and is calculated by:

$$h^2 = \frac{2\tau_0}{\rho g}(L - x) \qquad \text{Equation E-1}$$

where h is the ice thickness at distance x from the centre, L is the radius of the ice-sheet, τ_0 is the basal shear stress, ρ is the ice density and g is the acceleration due to gravity. With L = 400 km, ρ = 0.9 kg dm^{-3}, g = 9.81 m s^{-2} and τ_0 set to 50 and 100 kPa, the resulting parabolas are as shown in Figure E-1. A basal shear stress of 100 kPa is more appropriate for small valley glaciers whereas 50 kPa (with large variation) is more representative for ice-sheet conditions.

To have a more realistic description, Equation E-2 introduces a flow of the ice (Paterson 1994). The same assumptions are made as above, except for a removal of the perfect-plasticity assumption, and the introduction of an assumption of basal frozen conditions.

$$(h/H)^{2+2/n} + (x/L)^{1+1/n} = 1 \qquad \text{Equation E-2}$$

Here H is the ice thickness at the centre of the ice-sheet and n is a flow parameter (the strain-rate exponent) in Glen's flow law of ice, often set to 3, e.g. Paterson (1994). The resulting profile when L is set to 400 km and 900 km, H = 3 000 m and n=3 is shown also in Figure E-1.

Equation E-2 results in a steeper profile (for the corresponding profile length) than the parabolas described by Figure E-1, and presumably it is more in line with real ice-sheet profiles (Paterson 1994). For the further use of theoretical ice profiles, the steeper theoretical profiles of Equation E-2 are chosen. Furthermore, steeper profiles also give larger impacts in studies of groundwater flow and crustal stresses under glacial conditions, and thus represent a more pessimistic choice from the safety assessment point of view.

The theoretical profiles (Equations E-1 and E-2) are compared with an ice-sheet profile from the western part of the Greenland ice-sheet in Figure E-2, see also Jaquet et al. (2010). Note that in this figure the ice-sheet surface topography for the theoretical profiles is reflecting the full relief of the bed topography, which is not the case in the real world. The less steep theoretical profile is similar to the Greenland profile, whereas the steeper theoretical profile is steeper than the Greenland ice-sheet profile.

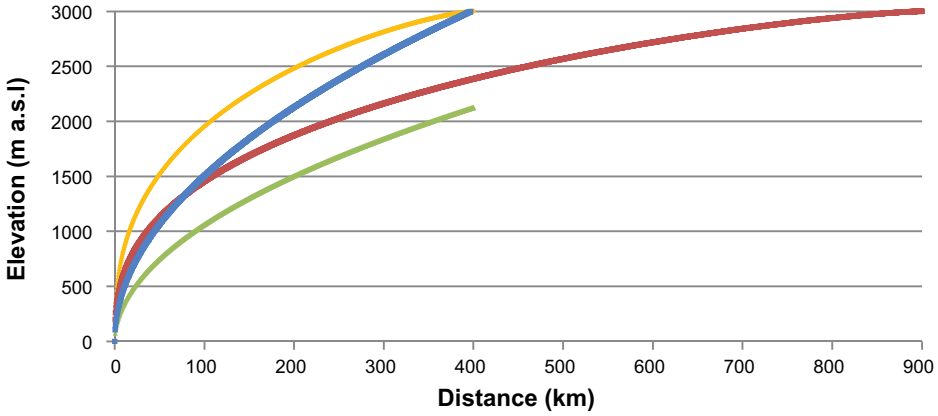

Figure E-1. *Theoretical steady-state ice-sheet profiles according to Paterson (1994). Parabolas produced by Equation E-1 are shown in green (400 km long profile with a basal shear stress of 50 kPa) and blue (400 km long profile with a basal shear stress of 100 kPa). The steeper profiles produced by Equation E-2 are shown in yellow (400 km long profile) and red (900 km long profile). The latter two profiles are considered to be more realistic representations of steady-state ice-sheet profiles (Paterson 1994).*

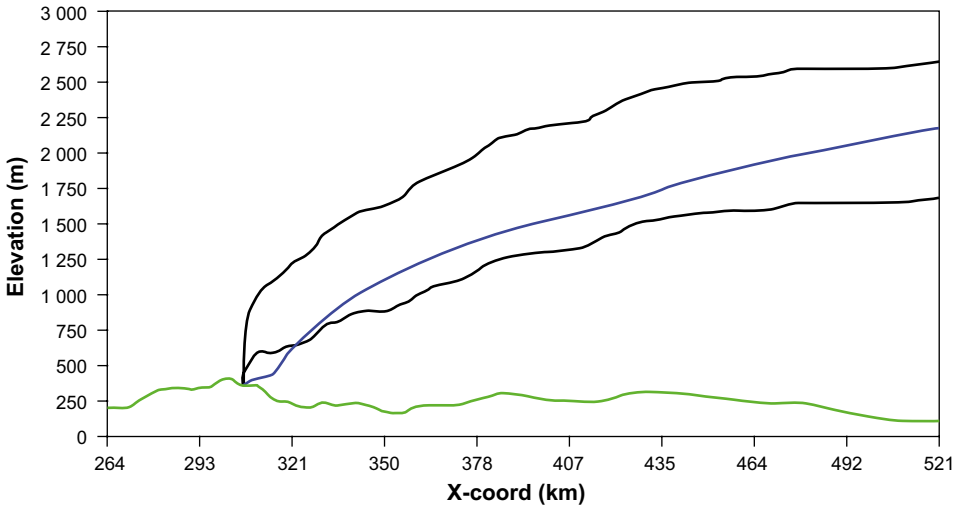

Figure E-2. *Comparison between the theoretical ice profiles (Equation E-1 with τ0 set to 50 kPa upper black line and Equation E-2 lower black line) with an ice-sheet profile from the Greenland ice sheet (blue). The bed is shown in green. The theoretical profiles are, unrealistically, displayed as reflecting the full relief of the bed topography, which has resulted in too much relief in the ice surface. From Jaquet et al. (2010).*

E3 Ice profiles from numerical ice-sheet simulations

Ice profiles were extracted from the time-transient reconstruction of the Weichselian ice-sheet simulated by the University of Maine Ice-sheet Model (UMISM), see Section 2.3.4. In the following text, this model simulation is denoted the *Weichselian ice-sheet simulation*. The location of the transect from which the profiles were extracted is shown in Figure E-3. Several ice-sheet profiles from the last stadial of the reconstructed Weichselian ice-sheet (e.g. from MIS 2 that included the Last Glacial Maximum, see Section 3.2), are shown in Figure E-4. Figure E-4a shows profiles from the advancing phase and Figure E-4b from the retreating phase of the simulated MIS 2 ice-sheet.

In the Weichselian ice-sheet simulation, the ice-sheet advances over the Forsmark region from NW-NNW whereas during the deglaciation it generally retreats in a more northerly direction. All profiles in Figure E-4 were extracted along transect 1 (Figure E-3). The orientation of transect 1 was selected to capture the steepest surface gradients during ice advance (i.e. generally oriented along the flow lines of the advancing ice, perpendicular to the advancing ice margin). Consequently, profiles extracted along the same transect but for the retreat phase, which occurred in a somewhat other direction, are somewhat underestimating the steepness of the ice-sheet surface.

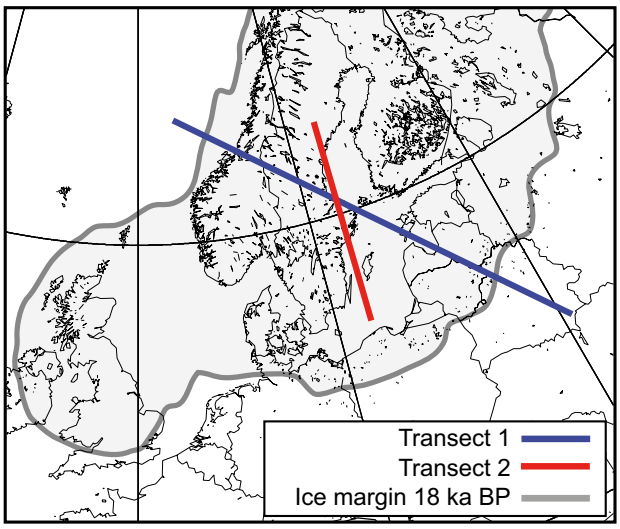

Figure E-3. *Locations of ice-sheet profiles. Transect 1: transect for all profiles shown in Figure E-4a and b. Transect 2: location of retreat profile extracted for 14.3 ka BP shown in Figure E-7.*

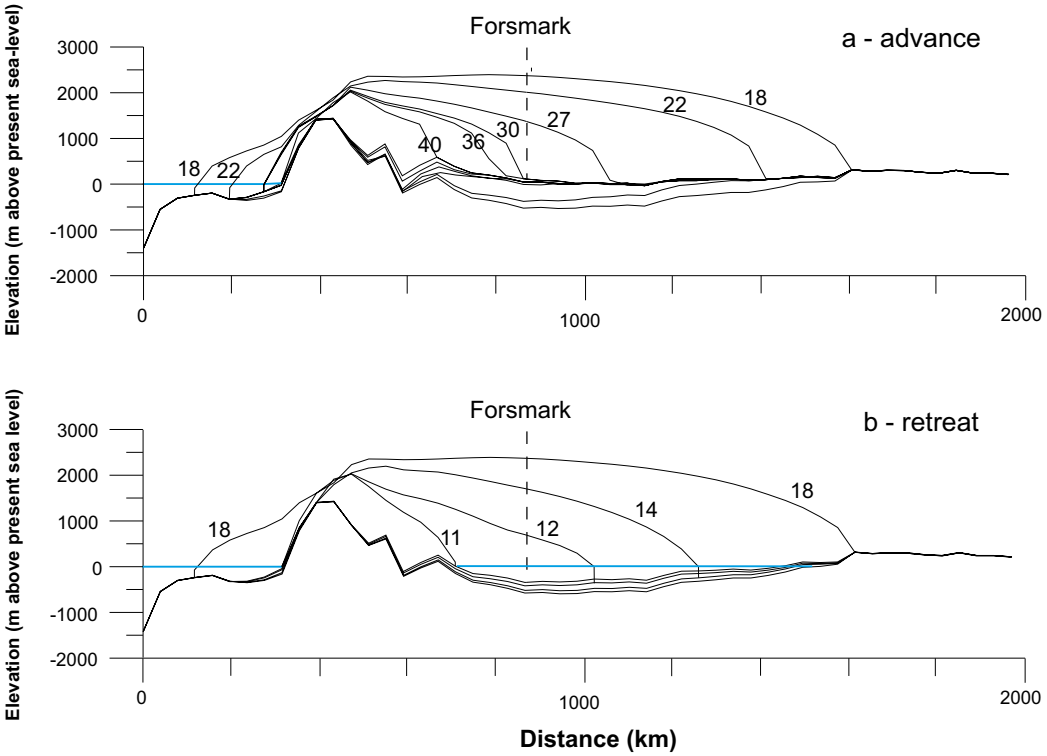

Figure E-4. *Examples of ice-sheet profiles from the Weichselian ice-sheet simulation during the MIS 2 advance and retreat. Profiles are extracted from transect 1 (Figure E-3). Numbers indicate time (ka BP). It should be noted that the y-scale has a vertical exaggeration of 100x and that sea-level change associated with ice-sheet growth is not shown. In the frontal-most part of the profile, the 10 km spatial resolution of the ice-sheet model can be seen as a sharp knick in the ice surface. Present-day sea level is shown in blue. The LGM ice-sheet configuration, along this specific profile, occurs at around 18 ka BP.*

In addition to the profiles selected along transect 1 (Figure E-3), a c. 900 km long retreat profile was selected along transect 2. This profile was extracted for the time 14 300 ka BP. All profiles selected from the ice-sheet advance phase are discussed in Section E4.1, whereas all profiles from the retreat phase are discussed in Section E4.3.

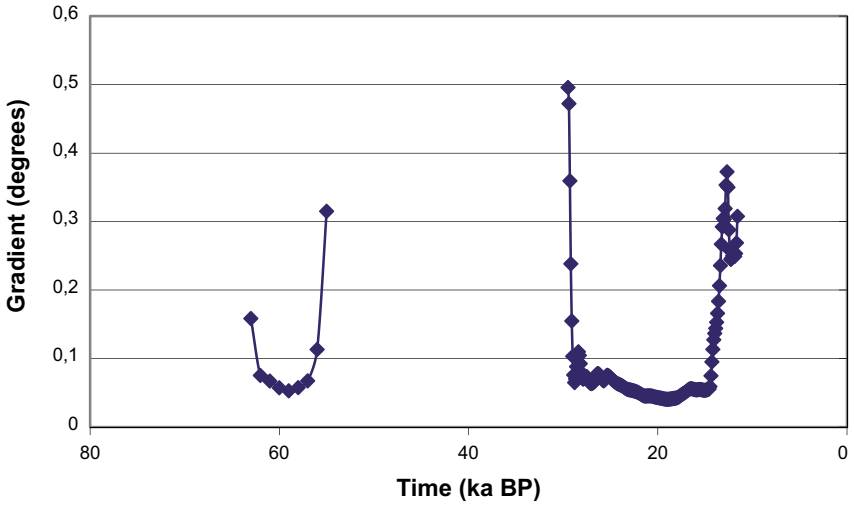

Figure E-5. *Modelled ice-surface gradients above the Forsmark site for the Weichselian glacial cycle. Note that the steepest part of the ice sheet is not included in the figure and is estimated to have an inclination of 0.8° (0.014 m m^{-1}). Steep gradients occur when the ice front passes the site, whereas low gradients prevail when the ice margin is situated far from the site.*

E3.1 Ice surface gradients

Figure E-5 shows the ice surface gradients that occur above the Forsmark site in the Weichselian ice-sheet simulation. There are two phases of ice-sheet coverage in this model simulation, during MIS 4 and MIS 2, and hence two periods with gradients in Figure E-5. Steep gradients occur during the short periods when the ice front passes that area, whereas low gradients prevail during the long periods of time when the ice front is located far from the repository. For the second and main ice-covered period, the mean value of low gradients is around 0.06 degrees (or 0.98 m km^{-1}), corresponding to about one third of the present-day regional topographic gradient at Forsmark (3 m km^{-1}) (Vidstrand et al. 2010). The resulting steepest hydraulic gradient in the reconstructed conditions of the last glacial cycle (Section 3.2.3) is about 0.8 degrees (0.014 m m^{-1}) over the first 10 km of the modelled ice-sheet profile.

E4 Comparison of ice profiles from numerical simulations with the theoretical profile

In all comparisons below, it should be remembered that, at a given time, the ice configuration of a realistically modelled ice-sheet, such as the one used here, is quite complex; the ice surface is irregular on both small and large spatial scales, and thus far from being a circular and regularly shaped dome as in the theoretical examples. This is due to variations in the dynamics and flux of the ice as a response to e.g. varying mass balance at the surface and variations in bed topography. Such complex ice configurations are seen also on the present-day Greenland and Antarctic ice sheets. Consequently, at a given time, ice-surface profiles derived from one part of the simulated ice sheet may differ from profiles extracted from another part. When selecting profiles from the Weichselian ice-sheet simulation, the aim has been to select profiles both relevant for a broad understanding of how the ice sheet looks and behaves and profiles specifically relevant for the Forsmark site.

E4.1 Simulated advancing profiles compared with the theoretical steady-state profile

In the Weichselian ice-sheet simulation, the main phase of ice-sheet coverage at Forsmark takes place during the MIS 2 stadial (Section 3.2.3), with the ice-sheet margin reaching Forsmark at around 30 ka BP (Section 3.2.3 and Figure E-4a).

In Figure E-6, all extracted profiles from the ice-sheet *advance* phase (Figure E-4a) are stacked and compared with the theoretical profiles of Equation E-2 (Figure E-1). It is seen that none of the simulated advancing profiles is steeper than the two theoretical steady-state profiles.

It is also seen that the steepest advancing profile, at 30 ka BP, is close to being as steep as one of the theoretical profiles described by Equation E-2. The simulated 30 ka BP profile is the ice-sheet profile when the ice margin is located in the Forsmark area (Figure E-6).

Having the seeming contradiction that the steady-state profiles are not steeper than the advancing profiles, is in this case not surprising. Such differences are expected since the profiles are produced in completely different ways. All profiles derived from the numerical ice-sheet model incorporate several parameters with considerably more realistic representations than how they are treated in the theoretical profile calculation. The ice-sheet model includes, for instance, realistic bed topography instead of a flat horizontal bed, a description of ice-sheet thermodynamics, where ice flow and ice temperatures are allowed to interact, and also a better representation of basal conditions (Section 2.3.4). Even though the ice-sheet model is far from being a full and complete representation of the natural system, it is significantly better than the theoretical equations. Consequently, the simulated less-steep profiles are here considered more realistic for the advancing phases than the steeper theoretical profiles.

There are no large variations in the steepness of the advancing profiles extracted from the ice-sheet simulation (Figure E-6). The steepest simulated advancing profile (from 30 ka BP) is close to being as steep as the least steep theoretical profile. Although the simulated profiles are here considered more realistic than the theoretical profiles, the above results show that if one uses the theoretical profiles of Equation E-2, the ice-sheet steepness is not underestimated if compared with the simulated advancing profiles. Therefore, the theoretical profiles of Equation E-2 may be used as a good and pessimistic (from a safety assessment point of view) mathematical representation of an *advancing* ice-sheet over Forsmark (Figure E-6).

In line with this, the theoretical profiles of Equation E-2 are used in several other, but not all, safety assessment studies where the effect of a simple mathematical ice profile advancing over Forsmark is studied, for instance in groundwater flow studies (Vidstrand et al. 2010) and THM studies of hydraulic jacking (Lönnqvist and Hökmark 2010).

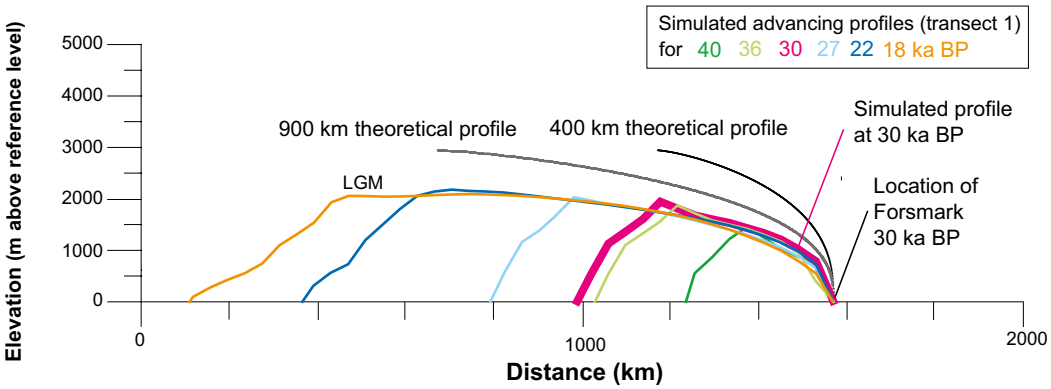

Figure E-6. *Comparison of ice surface topography from simulated advancing Weichselian ice profiles (from Figure E-4a) and two theoretical steady-state profiles of Equation E-2 (from Figure E-1) (Paterson 1994). To make the comparison meaningful, the fronts of all simulated profiles have been normalized to start at the same position and elevation (0 m) as the theoretical profile. Note that the simulated profiles would be somewhat "steeper" if they were to show ice thickness instead of surface elevation (since the bedrock in the ice-sheet simulation gets depressed, Figure E-4), i.e. if they were normalized also to have a flat bed, such as that of the theoretical profiles. However, for e.g. groundwater flow simulations, it is the gradient of the upper ice surface that is of interest for the water flux, and accordingly that is what is shown also for the simulated profiles. However, this results in differences between the theoretical and simulated profiles appearing larger. The frontal parts of all simulated advancing profiles are less steep than the theoretical steady-state profiles.*

E4.2 Simulated LGM profile compared with the steady-state profile

The LGM profile at 18 ka BP represents the profile closest to steady-state in the Weichselian ice-sheet simulation. In Figure E-6 it is seen that both theoretical steady-state profiles are steeper than the simulated LGM profile. Given the expected differences due to the different approaches taken to produce the profiles, see above, there is also one additional reason why the simulated LGM profile is less steep than the theoretical steady-state profile. It is likely that the modelled Weichselian ice-sheet never reached steady-state conditions during the LGM. This was most probably the case also for the real Weichselian ice sheet. In nature, ice sheets are constantly trying to adapt to the ever-changing climate conditions, and the ice sheet probably did not have time to build a maximum-thick, steep ice at the LGM.

E4.3 Simulated retreating profiles compared with theoretical steady-state profile

In Figure E-7, the extracted profiles from the *retreat* phase of ice-sheet model simulation (from Figure E-4b), together with the retreat profile extracted from year 14.3 ka BP (Figure E-3), are stacked and compared with the theoretical profiles of Equation E-2.

The profile extracted along transect 2 for 14.3 ka BP has an ice margin that ends in the Baltic Sea, and so do the 14 and 12 ka BP profiles along transect 1. When comparing the profiles in Figure E-7, only the grounded parts of all profiles are shown and compared, i.e. the parts of the profiles that are located upstream of the grounding-line.

In line with theory, it can be seen when comparing Figure E-6 and Figure E-7 that the simulated profiles generally are steeper during the ice-sheet advance than for the retreat. In Figure E-7 it is also seen that the retreating profiles are, as expected, considerably less steep than the theoretical steady-state profiles. The steepest of the retreat profiles is from 11 ka BP. At this time the ice has a relatively steep profile caused by the steep bed topography in the mountainous region from where the profile is located (see Figure E-4b). These topographic conditions of the ice-sheet bed are not at all representative for the Forsmark area, and this profile is therefore not discussed further.

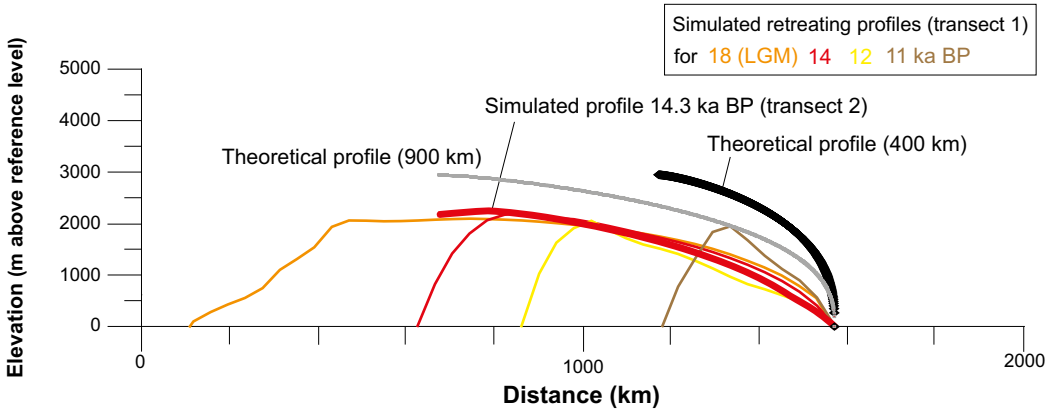

Figure E-7. *Comparison of ice-surface topography between simulated retreating Weichselian glacial cycle ice profiles (from Figure E-6b and the profile extracted from transect 2 for 14.3 ka BP) and the theoretical steady-state profiles of Equation E-2 (from Figure E-1). To make the comparison meaningful, the fronts of all simulated profiles have been normalized to start at the same position and elevation (0 m) as the theoretical profiles. Note that the simulated profiles would be somewhat "steeper" if they were to show ice thickness instead of surface topography (since the bedrock in the ice-sheet simulation gets depressed, Figure E-4), i.e. if they were normalized also to have a flat bed, as with the theoretical profiles. However, for e.g. groundwater flow simulations, it is the gradient of the upper ice surface that is of interest for the water flux, and accordingly that is what is shown also for the simulated profiles. However, this results in the differences between the theoretical and simulated profiles appearing larger. The frontal parts of all retreating profiles are considerably less steep than the theoretical steady-state profiles. Profiles selected for other safety assessment studies are shown as bold lines.*

Comparing the steepness of the frontal parts of the profiles along transect 1, it can be seen that the steepest profile is the 18 ka BP (LGM) profile, followed by the 14, and 12 ka BP profiles (Figure E-7), i.e. the ice-sheet is getting less and less steep during the deglaciation over the lowland. It can also be noted that the 14.3 ka BP profile from transect 2 has a steepness that is very similar to the profile for 14 ka of transect 1 (Figure E-7), even though the profiles have different orientations. It is clearly seen that, for the Weichselian ice-sheet simulation, profiles describing the retreat phase should be considerably less steep than the theoretical profiles.

Average hydraulic gradients from the selected theoretical ice-sheet profile for various distances from the ice-sheet margin are given in Table E-1. The maximum hydraulic gradient associated with the steep frontal part of the theoretical profile is up to c. 1.5 m m^{-1}.

Table E-1. Hydraulic gradients (m m^{-1}) from the selected theoretical ice-sheet profile (Equation E-2) averaged over various distances from the ice-sheet margin.

Distance from ice margin (m)	Hydraulic gradient (m m^{-1})	Hydraulic gradient (degrees)
100	1.49	56
200	0.96	44
400	0.62	32
1 000	0.35	19
2 000	0.23	13
4 000	0.15	8.5

E4.4 Selection of profiles

Since the theoretical profiles of Equation E-2 are considered to be more realistic than profiles from Equation E-1, and because it is steeper than the steepest of the simulated advancing ice profiles (Figure E-6), the steepest theoretical profile is selected to represent an advancing ice-sheet over Forsmark.

The frontal near parts of the profile extracted for 14.3 ka BP (transect 2) is the least steep retreat profile from the Weichselian ice-sheet simulation (Figure E-7). This profile is selected to represent a retreating ice sheet over Forsmark.

The two selected profiles are shown by the bold lines in Figure E-7. These two profiles constitute, in their frontal parts, the steepest and the least steep profiles of all profiles analysed, and they are considered to cover a broad enough span of possible profiles to be employed in other studies, such as modelling of groundwater flow under glacial conditions (Vidstrand et al. 2010) and THM studies (Lönnqvist and Hökmark 2010).

E5 Conclusions

1. The steepest theoretical profile (Equation E-2, Figure E-7) (Paterson 1994) is selected to represent an advancing ice-sheet over Forsmark in the *glaciation climate case.*
2. The least steep simulated profile from 14.3 ka BP (Figure E-7) is selected to represent a retreating ice-sheet over Forsmark in the *glaciation climate case.*

Appendix F

Transitions between climate domains

The climate cases represent a succession of climate domains (Section 1.4.3) at Forsmark. Depending on what spatial scale is considered, the transitions between climate domains may look different. If considering a repository site only, or even a repository footprint area, the transitions between climate domains (temperate-, periglacial-, glacial domains and submerged conditions) may be described as more or less instantaneous in time. This is in line with the way the succession of climate domains is depicted in Chapter 5. The ice-sheet and GIA modelling used in support of the climate cases were done on a coarser spatial scale. Nevertheless, the results from the larger model grid cells in these simulations are taken to represent the ice sheet- and isostatic development at the SFR repository location.

However, if looking at Forsmark on a site-scale, i.e. several hundreds of square km, the transition between climate domains is of a gradual nature, both spatially and temporally. Examples of the duration of the main transitions within the reconstructed last glacial cycle (Section 3.2.3) which occur when the site goes from i) temperate climate domain to periglacial climate domain, ii) periglacial climate domain to glacial climate domain, iii) glacial domain to submerged conditions and finally iv) from submerged conditions back to temperate climate domain are given in the following paragraphs.

The transient nature of the change from a temperate climate domain to a periglacial climate domain is illustrated in Figure 3-21, which shows permafrost evolution of the last glacial cycle. Sporadic permafrost starts to grow more or less simultaneously over the site. Subsequently, if climate allows, the permafrost may develop to discontinuous- and then continuous spatial coverage. The duration of such a full transition in the reconstruction of the last glacial cycle, i.e. the development from a landscape without permafrost to a landscape with permafrost coverage of 90 % or more at the Forsmark site, is approximately between 2 and 5 ka (Figure 3-21).

The transition from a periglacial to a glacial climate domain manifests itself as an ice-sheet margin that advances over the site. A spatially transient change takes place in one specific direction over the Forsmark site, by which the periglacial climate domain is replaced by the glacial climate domain following the advance of the ice-sheet front. In the reconstruction of the last glacial cycle, the ice-sheet margin advances over the site at a speed of ~ 50 m a^{-1}. The duration of this transition, i.e. the time it takes for the ice sheet to advance over the Forsmark site, is around 250 years. Note that permafrost may still exist under the ice sheet for some of the time that the site is assigned to the glacial climate domain.

The transition from glacial to submerged conditions constitutes the deglaciation phase of the site when ice-sheet conditions are replaced by submerged conditions. The retreat rate of the ice sheet margin during deglaciation of the Forsmark site is ~ 300 m a^{-1} in the reconstructed last glacial cycle. The duration of this transition, i.e. the time during which one deglaciation occurs over the Forsmark site in the reconstruction of the last glacial cycle, is around 50 years. It should be noted, as previously described, that during both advancing and retreating phases, there is a possibility of having the ice sheet margin oscillating over the site due to climate variability. However, such a case should be regarded as an exception from the more common situation of having a continuously advancing or retreating margin.

According to the model reconstruction of the last phase of ice-sheet coverage in the Forsmark area (Section 2.3.4), the ice-flow direction during the MIS 2 ice-sheet advance was approximately from the north, whereas the ice-flow direction during the deglaciation was from the north-west. This is in line with the interpretation of glacial striae, with a northerly direction recorded both in the oldest glacial striae and the oldest documented directional transport of the till material as recorded in clast fabric analysis (Sundh et al. 2004), and with an overall dominating younger striae system showing transport and deposition from the north-west (Sohlenius et al. 2004). This demonstrates that the transition to and from the glacial climate domain may be spatially different during phases of ice-sheet growth and decay.

The transition from submerged conditions to the temperate climate domain is manifested by the relative sea-level change caused by the isostatic rebound that follows deglaciation. The duration of this transition in the reconstructed last glacial cycle, i.e. the time it takes from the very first

appearance of land at the site (SKB TR-10-49, Figure 4-37) until the last remnants of sea have disappeared from the site is around 12 ka (Lindborg 2010). This is the transition that is occurring at the Forsmark site at present, manifested by the slow movement of the shoreline across the site and indeed across the SFR repository. The transient nature of the relative sea-level change over the site is further described in Lindborg (2010).

The durations of the four transitions above are summarised in Table F-1.

Given the climate evolution of the reconstructed last glacial cycle, the assumptions made in all modelling exercises (Chapter 2), and the physiographical characteristics of the site, the glacial processes result in the fastest transition between climate domains (Table F-1). The transition from glacial climate domain to submerged conditions for the Forsmark site is around 50 years. The transition from periglacial to glacial climate domain is about five times slower. These two fastest transitions relate to the glacial climate domain, i.e. to the relatively fast processes of ice-sheet advance and decay. The transition from a temperate- to a periglacial climate domain with continuous permafrost is 40 to 100 times slower than the transition from a glacial climate domain to submerged conditions (Table F-1). The slowest transition is the one from submerged conditions back to a temperate climate domain, which, in the reconstructed last glacial cycle, is around 240 times slower than the transition from glacial climate domain to submerged conditions. This is due to very slow glacial isostatic adjustment of the Earth's crust to the unloading associated with deglaciation (Section 2.2).

Note that for any given time during these transitions, the Forsmark site contains more than one type of climate domain. For instance, parts of the site may be subject to the periglacial climate domain, having permafrost conditions without an ice sheet, at the same time as another part of the site may be overridden by an ice sheet and thus be subject to the glacial climate domain. Also note that the transition from one climate domain to another over the site does not need to be a full transition (as in the above examples). For instance, discontinuous permafrost may start to form within the site due to lower air temperatures, transforming the affected areas to periglacial climate domain. Thereafter, the climate may become warmer, such that permafrost (and the periglacial climate domain) diminishes and disappears.

Table F-1. Approximate durations of full transitions between climate domains over the Forsmark site for the reconstructed last glacial cycle (Section 3.2.3). To compare the duration of the transitions from and to various climate domains, the relative durations of the transitions are expressed as numbers compared with the duration of deglaciation of the site.

Transition	Approximate duration in the reconstructed last glacial cycle	Relative duration of transition
Temperate- to periglacial climate domain with continuous permafrost coverage	~ 2 000 to ~ 5 000 years	40 to 100
Periglacial- to glacial climate domain	~ 250 years	5
Glacial climate domain to submerged conditions (deglaciation)	~ 50 years	1
Submerged conditions to temperate climate domain	~ 12 000 years	240

Appendix G

Construction of a Holocene relative sea-level curve for the Forsmark site

To describe the long-term development of the landscape in general and biosphere objects in particular, the landscape development needs to be modelled continuously based on the change in relative sea level covering the appropriate period. SKB has done an extensive amount of work on relative sea level and shoreline displacement at the Forsmark site and has also made many additional studies based on other types of analyses of these data, such as landscape development and groundwater flow modelling. To this end, the reconstructed relative sea level of the Holocene, together with results from the GIA modelling (Section 2.2.4), constitute the basis for the future assessments of long-term relative sea-level changes at Forsmark and their implications.

G1 Background and previous work

In previous safety assessment reports, e.g. the SR-PSU (SKB TR-13-05, SKB TR-14-01), the relative sea-level change at Forsmark was described using a combination of empirically-based modelling of the Holocene relative sea level (Påsse 2001) and GIA modelling (Section 2.2.4, Whitehouse 2009).

In the empirical model by Påsse (2001), the Holocene relative sea level is calculated as the sum of two equations, representing the temporal evolution of global sea-level changes (eustasy) and the glacio-isostatic uplift after unloading of ice (isostasy). The eustasy is assumed to be spatially independent, and the equation for isostasy contains five site-specific parameters that are constrained by observational data, e.g. geological relative sea-level reconstructions and lake-tilting information.

Påsse (2001) calculated the empirical parameters for numerous sites across Scandinavia, but unfortunately not for Forsmark. Instead, the Forsmark-specific parameter values were estimated in Brydsten (2009) by interpolating the parameter values from nearby sites in east-central Sweden and the Baltic Sea. In addition, Brydsten (2009) constrained these parameters by using the historic relative sea-level data from Hedenström and Risberg (2003) (hereafter referred to as HR2003; red dots in Figure G-1), who evaluated the relative sea-level change of the last 3.2 ka based on radiocarbon dating of terrestrial macrofossils from four lakes in the Forsmark area. They also included isolation ages from six additional lake basins located further away from Forsmark to extend their relative sea-level curve back to 6.3 ka BP.

The Holocene relative sea-level curve used in the SR-PSU (from Brydsten 2009) is displayed in Figure G-1 (blue line) together with observational data from HR2003 (red dots). The error bars in the HR2003 data represent the 95 % confidence interval (1.96 times the standard error) based on radiocarbon dating uncertainties. The standard error typically ranges from ~ 100–150 years for the youngest data points to ~ 200–300 years for older ones (see HR2003 for more details). As expected, because Brydsten (2009) used the HR2003 data to determine the Forsmark-specific parameters, the resulting relative sea-level curve agrees well with HR2003 (Figure G-1). For the early Holocene (prior to ~ 6 ka BP), the Forsmark relative sea level from Brydsten (2009) is not constrained by any observational data but represents a “best guess” estimate based on the historic relative sea-level data from nearby sites, such as Stockholm and Gästrikland (Påsse 2001, Brydsten 2009).

Since Påsse (2001), a more recent empirical model of the Holocene relative sea-level change in Scandinavia has been developed by Påsse and Daniels (2015) (hereafter referred to as PD2015). Although the general methodology in PD2015 is similar to that of Påsse (2001), there are also some notable differences:

- The governing equations in PD2015 have been simplified and contain three unknown site-specific parameters instead of the five used in Påsse (2001).
- PD2015 also used data from tide gauges and geological records of highest coastline levels to constrain the site-specific parameters. These datasets were not included in Påsse (2001).
- In contrast to Påsse (2001), the relative sea-level parameters were specifically estimated and presented for the Forsmark site in PD2015.
- The relative sea-level curve was updated to the new national height reference system RH2000 in PD2015 as opposed to the outdated RH70 height reference system used in Påsse (2001).

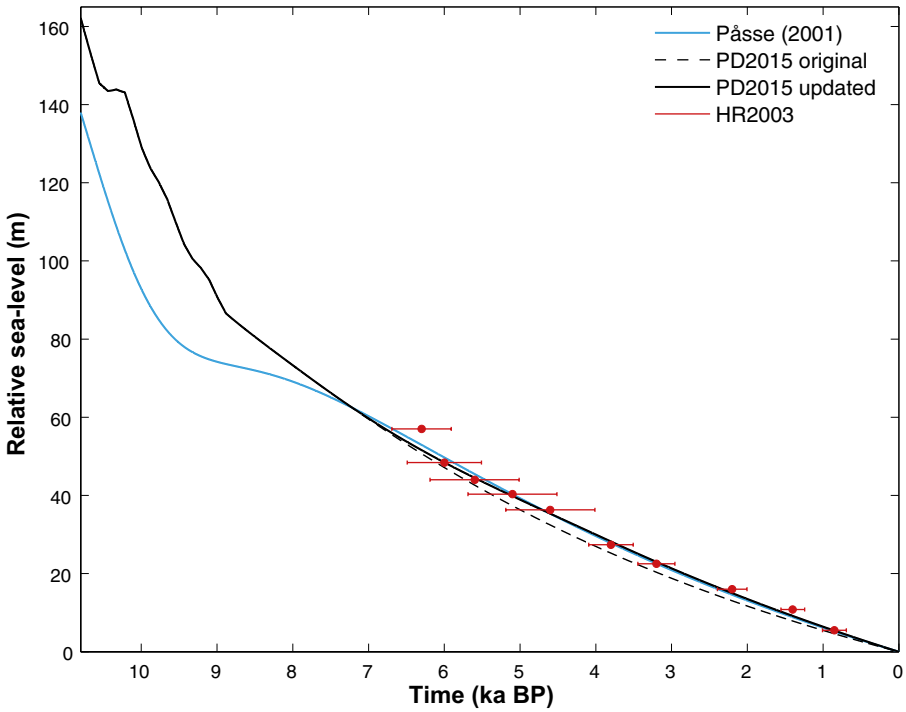

Figure G-1. *Holocene relative sea-level change (relative to present-day) at Forsmark based on Påsse (2001) (parameters were derived in Brydsten 2009; blue line), PD2015 with original parameter values (black dashed line), and PD2015 with updated parameter values (black solid line). The red points and associated horizontal lines, respectively, represent the relative sea-level data and the 95 % confidence intervals from HR2003.*

PD2015 is also the accepted official model for the Holocene relative sea-level change used by the Geological Survey of Sweden (SGU). Because of the improvements presented above, the Holocene relative sea level for Forsmark is updated in this appendix using the methodology outlined in PD2015. The results from the GIA modelling presented in this report are identical to those used in the SR-PSU (SKB TR-13-05). In the following subsections, the construction of the updated Holocene relative sea-level curve based on PD2015 is outlined in detail.

G2 Updated Holocene relative sea level

G2.1 The PD2015 model

Following Påsse (2001), the model presented in PD2015 is fully empirical. This means that the Holocene relative sea-level evolution in Scandinavia is modelled using relatively straight-forward mathematical equations, for which the unknown parameters are constrained by observational data. The main advantage of the empirical modelling approach over physically based modelling is that it is primed to give a good fit with observational data. One of the main disadvantages with empirical modelling is that the temporal coverage of the model is more or less limited by that of the observational data, implying that it cannot be used to predict the relative sea-level development into the future with high accuracy. Therefore, it is crucial to resort to physically based modelling, such as GIA modelling (Whitehouse 2009), for that purpose. As already discussed, PD2015 used data from geological relative sea-level curves, lake-tilting investigations and tide gauges as well as recorded levels of highest coastline to constrain the site-specific parameters.

The equation for the isostatic uplift (U) in PD2015 takes the following form

$$U = \frac{2}{\pi} A \left[\arctan\left(\frac{T}{B_e}\right) - \arctan\left(\frac{T-t}{B_e}\right) + \arctan\left(\frac{T}{B_v}\right) - \arctan\left(\frac{T-t}{B_v}\right)\right], \quad \text{Equation G-1}$$

where t is time in calendar years BP (0 BP corresponds to 2000 AD), and

$B_v = 19A + 5\,000$.

Hence, the time-dependent isostatic uplift at a certain site is completely determined by three parameters (A, B_e and T), representing the download factor from the retreating ice-sheet (A), relaxation factor for the elastic uplift (B_e) and the time for the maximum uplift rate (T). The temporal eustatic evolution is defined as

$$E = -\frac{2}{\pi}\left[29\left(\arctan\left(\frac{9200}{1300}\right) - \arctan\left(\frac{9200-t}{1300}\right)\right) + 36\left(\arctan\left(\frac{13700}{1350}\right) - \arctan\left(\frac{13700-t}{1350}\right)\right)\right] \quad \text{Equation G-2}$$

The reconstructed eustasy in PD2015 generally results in higher values compared with Påsse (2001), particularly in the early Holocene (see Figure G-2). In fact, the relatively large difference in the early Holocene relative sea level between PD2015 and Påsse (2001) can be almost entirely explained by the difference in eustasy (Figure G-1 and Figure G-2). However, the higher eustatic values in PD2015 are in better agreement with other independent data from the early Holocene, e.g. eustatic migration data derived from corals (Peltier and Fairbanks 2006; see Figure 17 in PD2015) and is, therefore, considered to be an improvement with respect to Påsse (2001). Note that the present-day eustatic contribution in PD2015 does not account for any changes related to anthropogenic global warming, such as thermal expansion of the oceans and melting of the Greenland and Antarctic ice sheets. The eustasy is therefore significantly underestimated for this period (see also Section 3.5).

The Baltic was also subject to two lake phases during the Holocene: the Baltic Ice Lake (~ 15–11.5 ka BP) and the Ancylus Lake (~ 10.5–9 ka BP). During those lake stages, the Baltic Sea was isolated from the Atlantic and hence not influenced by global eustatic changes. The influence of those lakes on the local relative sea level is not taken into account in the equations above, so they need to be modelled separately for the times when Forsmark was free of ice. Because Forsmark became deglaciated ~ 10.8 ka BP (Section 3.2), it was still covered by the ice-sheet during the phase of the Baltic Ice Lake, whereas it was mostly ice-free during the Ancylus Lake stage. Hence, the relative sea-level change of the Baltic Ice Lake is omitted here, whereas the effect of the Ancylus Lake is parameterised.

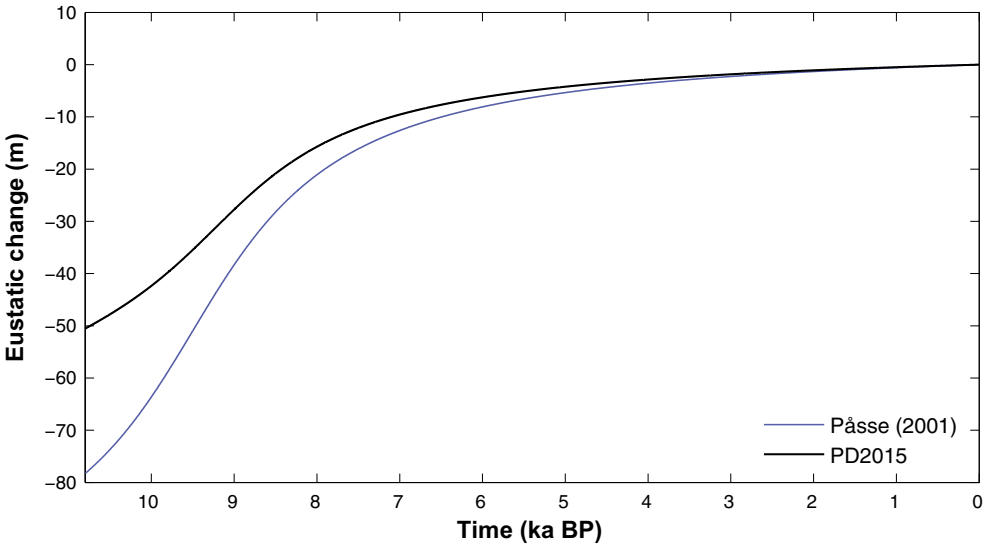

Figure G-2. *Holocene eustatic change (relative to present-day) based on equations from Påsse (2001) (blue line) and PD2015 (black line).*

The parameterised relative sea-level change resulting from the Ancylus Lake is shown in Figure G-3 (see also Figure 3 in PD2015). Its effect is also clearly visible by the bumpy part of the black lines at around 10 ka BP in Figure G-1. During the phase of rising water levels, i.e. the transgression phase, the outlet of the Ancylus Lake was located near Degerfors in west-central Sweden. This phase is characterized by rising water levels, culminating at ~ 17 m above the prevailing sea level at ~ 10.2 ka BP. The outlet in Degerfors was eventually disconnected as a result of the rapid isostatic uplift in central Scandinavia during this time, which created a new outlet at the Darss Sill south of Denmark. Meanwhile, the Ancylus Lake entered its regression phase as a result of increasing eustatic levels. The relative sea-level change resulting from the Ancylus Lake (L) can thus be roughly estimated by the recorded relative sea levels at Degerfors and Darss Sill from this time period (Table G-1); see also Påsse 2001 and PD2015), and takes the following form

$$L = \begin{cases} 0, & t \leq 8990\ yrs\ BP, \\ \min(L_D, L_S), & 8990\ yrs\ BP < t \leq 10\,440\ yrs\ BP, \\ 0, & t > 10\,440\ yrs\ BP, \end{cases} \qquad \text{Equation G-3}$$

where L_D and L_S are the Ancylus Lake level displacement recorded at Degerfors and the Darss Sill (Table G-1), respectively. It is important to note that the parameterization of the Ancylus Lake is highly uncertain as it is based on only a few data points outside the Forsmark area.

In summary, the Holocene relative sea-level change (S) is given by the sum of Equations G-1, G-2 and G-3:

$$S = U + E + L. \qquad \text{Equation G-4}$$

In the following subsection, the choice of parameters values for computing the isostatic uplift (U) in Forsmark is discussed.

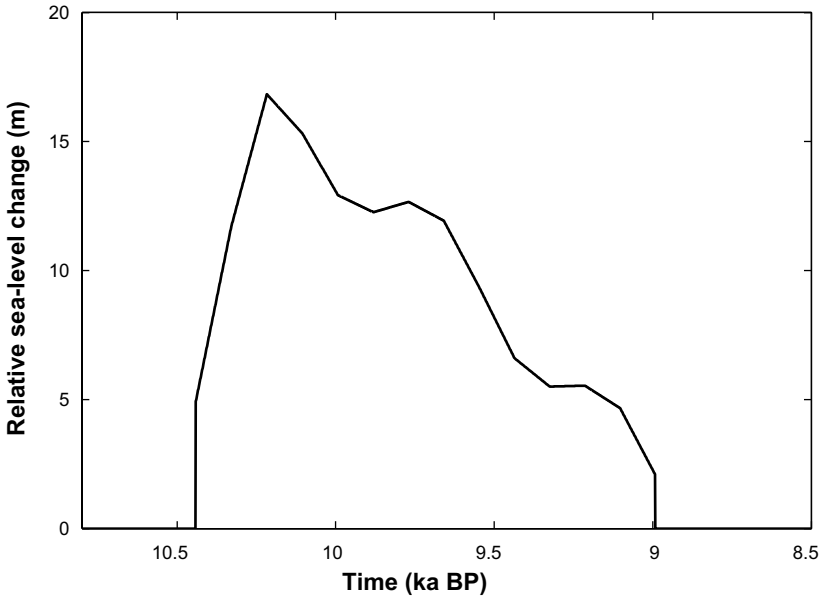

Figure G-3. *Estimated Forsmark relative sea-level change resulting from the transgression and regression of the Ancylus Lake, based on data from the outlets in Degerfors and Darss Sill (Table G-1).*

Table G-1. The level of damming (in m) in the Baltic during the Ancylus Lake stage as recorded in outlet the areas of Degerfors and the Darss Sill. Data are from the Swedish Geological Survey (based on Påsse 2001, PD2015).

Time (ka BP)	Degerfors (m)	Darss Sill (m)
10.4	4.9	17.1
10.3	11.7	17.9
10.2	16.8	17.6
10.1	20.5	15.3
10.0	28.4	12.9
9.9	31.1	12.3
9.8	33.4	12.7
9.7	35.3	11.9
9.6	36.8	9.3
9.4	37.9	6.6
9.3	38.8	5.5
9.2	39.5	5.5
9.1		4.7
9.0		2.1

G2.2 Parameter values and the resulting Holocene relative sea-level curve for Forsmark

As discussed in the previous subsection, three parameters (*A, B_e* and *T*) need to be determined to construct a Holocene relative sea-level curve for a specific location using the PD2015 equations. The original parameter values for Forsmark, presented in PD2015, were set to *A=165, B_e=1 200* and *T=11 250*. These parameters were determined by combining historic relative sea-level data from nearby sites with tide gauge data from PSMSL (Permanent Service for Mean Sea Level; PD2015). However, although HR2003 contains the most recent and comprehensive analysis of the historic relative sea-level change in the Forsmark area, their data were *not* included to further constrain the parameters in PD2015. As a result, there is a clear mismatch between the original Forsmark curve from PD2015 and the HR2003 data (dashed black line and red dots in Figure G-1). For comparison, the Holocene relative sea-level curve from Brydsten (2009), which was used in the SR-PSU (SKB TR-13-05), shows a significantly better agreement with the HR2003 data than the original curve described in PD2015 (blue and dashed lines in Figure G-1).

To correct for this mismatch, an updated PD2015 curve was constructed using the data from HR2003. To determine the parameter values for this curve, a wide range of parameter combinations were explored and evaluated using the least squares method. The best fit with the HR2003 data, using this methodology, was obtained with the following parameter values: *A=253*, *B_e=1 400* and *T=14 000*. Since those values are only constrained by the HR2003 data, the resulting relative sea-level curve is only applicable for the period covered by those data, i.e. from 0 to 6.3 ka BP. For the early Holocene, there are unfortunately no equivalent data that could be used to constrain the relative sea-level parameters in the Forsmark area; thus, the original relative sea-level curve from PD2015 is primarily used for this period.

The details on how the original and updated PD2015 curves are combined to construct an updated relative sea-level curve through the Holocene are summarised in Table G-2. In general, a time-dependent cubic weight function, based on the Hermite basis functions, was applied to determine the relative importance of each curve. This technique is bound to give a smooth transition between the relative sea-level curves as the Hermite functions ensure that the values as well as their derivatives are continuous through the entire interpolation domain. Hence, the weight function (f_w) is defined as:

$$f_w = \begin{cases} 0, & r \le 0, \\ -2r^3 + 3r^2, & 0 < r \le 1, \\ 1, & r > 1, \end{cases}$$ Equation G-5

where

$$r = \frac{\mathrm{t} - t_1}{t_2 - t_1},$$ Equation G-6

and t_1 and t_2 represent the start and end times (in calendar years BP) of the interpolation, respectively. The resulting relative sea level was subsequently calculated as:

$$S = f_w S_m + (1 - f_w) S_o, \qquad \text{Equation G-7}$$

where S_m and S_o are the calculated relative sea level using the original parameter values (from PD2015) and the updated parameter values based on the HR2003 data, respectively. Here we used t_1=*3.8* ka BP and t_2=*8.0* ka BP as interpolation limits. Hence, for the early Holocene (t > 8.0 ka BP), the Forsmark relative sea level is represented by the PD2015 curve with original parameter values, and for the late Holocene (t < 3.8 ka BP) by the curve with modified parameters based on the HR2003 data. Between those time limits, the two curves were interpolated according to the cubic weight function (Table G-2).

Table G-2. Data used for the construction of the Holocene relative sea-level curve for Forsmark. The site-specific parameters A, B_e and T are used in the PD2015 equations.

Time period (ka AP)	Data used	Comments
−10.8 to −8	PD2015 with A=165, Be=1 400 and T=11 250	Forsmark parameter values from Table 1 in PD2015.
−8 to −3.8	Interpolation	Using cubic Hermite interpolation
−3.8 to 0	PD2015 with A=253, Be=1 400 and T=14 000	Parameters derived from the relative sea-level data in HR2003.

The chosen interpolation domain ensures that the five youngest data points in HR2003 are fully weighted ($t < 3.8$ ka BP => f_w=*1*) whereas the five oldest data points receive less weight. It is thus assumed that the older data from HR2003 are less important for describing the Holocene relative sea-level development in Forsmark than the younger data. The rationale for this choice is that the older sites are located further away from Forsmark (see Figure 1-1 in HR2003), and collectively have significantly larger uncertainties due to the radiocarbon dating than the younger sites (Figure G-1). The larger uncertainty interval of these older radiocarbon dates mainly relates to them constituting bulk samples instead of dating of individual macrofossils which was the case for the younger sites.

The updated Holocene relative sea-level curve for Forsmark is depicted by the black solid line in Figure G-1. This curve agrees significantly better with the HR2003 data than the original PD2015 curve. For the late Holocene, the updated relative sea-level curve is similar to that of Brydsten (2009) who used data from HR2003 to constrain the parameters in Påsse (2001) (Figure G-1). During the middle Holocene, the updated relative sea-level curve slowly starts evolving towards the original PD2015 curve, eventually resulting in a complete merging of the two curves at 8 ka BP.

G2.3 Comparison with tide gauges and GPS data

In contrast to PD2015, relative sea-level data from tide gauges were not used to constrain the parameters in the updated relative sea-level curve constructed here. This choice is motivated by the relatively short temporal coverage of tide gauge data (1976–2017 AD), which provides very limited information on how the relative sea level changed through the Holocene. It should be noted that the model from PD2015 was primarily developed to cover the Holocene, i.e. a significantly longer timescale than those covered by the tide gauge and GPS data. Therefore, the primary aim of the Holocene relative sea level presented here is to capture the overall relative sea-level migration through the Holocene. However, because the relative sea-level evolution within the next 10 ka is highly relevant for certain aspects related to the safety assessment, e.g. emergence of new biosphere objects (see the **Biosphere synthesis report**), it is important to ensure that the modelled Holocene relative sea level also captures the first-order behaviour of the observed present-day relative sea-level changes.

The annual relative sea level in Forsmark based on the tide gauge data from PSMSL (Holgate et al. 2013, PSMSL 2018) is shown in Figure G-4 (red curve). These data reveal a significant annual variability, but also a clear overall negative trend over the period covered by the data. This indicates that the post-glacial isostatic uplift is still highly active in the area and exceeds the anthropogenic sea-level rise. The negative trend is also found in the Holocene relative sea-level curve used in the SR-PSU (Påsse 2001, Brydsten 2009) and in the updated relative sea-level curve.

A linear regression of the tide gauge data reveals that the current rate of relative sea-level change in Forsmark[14] is −4.1 mm a^{-1}. The relative sea-level rise in the updated curve presented here is −6.1 mm a^{-1}, which is comparable to the relative sea-level curve based on Påsse (2001) (−5.8 mm a^{-1}). Thus, both curves overestimate the negative relative sea-level rate in Forsmark by ~ 50 % with respect the tide gauge data.

Using Equations G-1 and G-2, it is possible to decompose the present-day relative sea-level change, predicted by the updated relative sea-level curve, into its eustatic and isostatic components. The eustatic contribution to the present-day relative sea-level change in the updated curve is only 0.4 mm a^{-1}, whereas the isostatic contribution amounts to −6.5 mm a^{-1}. The modelled isostatic contribution is thus comparable to the observed isostasy for Forsmark from GPS data which amounts to −6.7 mm a^{-1} (Vestøl et al. 2019, see also Sections 2.2.4 and 3.5.1).

It is possible to estimate the present-day eustatic contribution (sea-level rise) in Forsmark by taking the difference between the tide gauge data, which represents the total relative sea-level change, and the measurement of the isostatic component by the GPS. This calculation results in a present-day eustatic sea-level rise of 2.6 mm a^{-1}, thus about 2 mm a^{-1} greater than in the PD2015 model. However, it is important to note that the eustatic signal recorded in the tide gauge data is primarily a result of the current global warming, which has *not* been accounted for in the PD2015 model. All in all, it is reasonable to believe that the large difference in the eustasy between tide gauges and the PD2015 model is primarily explained by anthropogenic global warming.

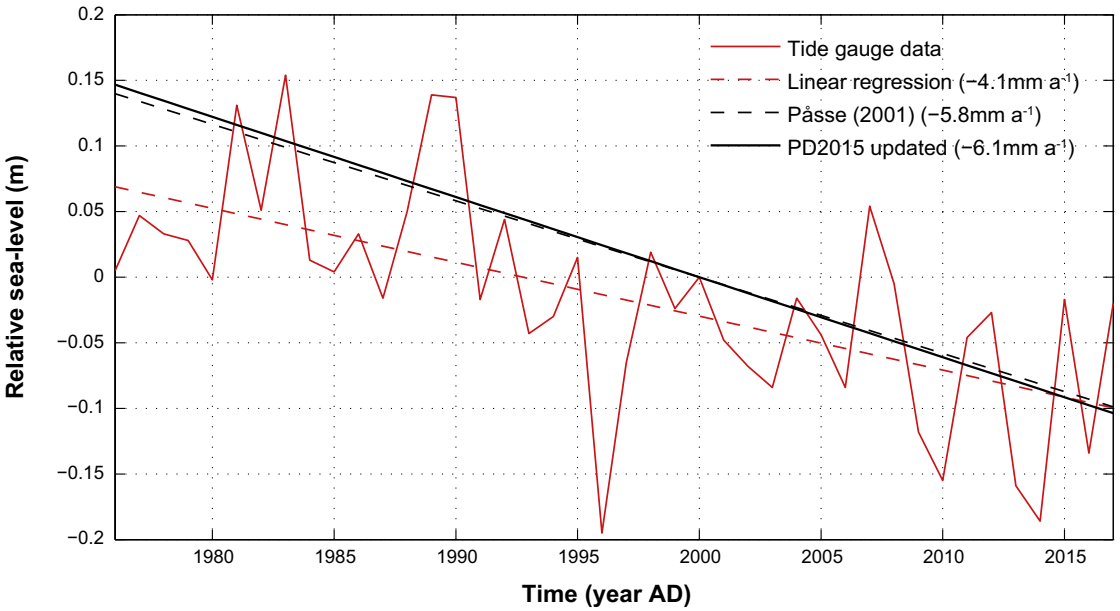

Figure G-4. *Annual relative sea-level change at Forsmark from tide gauge data (Holgate et al. 2013, PSMSL 2018) (red solid curve), its linear regression (red dashed line), and modelled relative sea level using the model from Påsse (2001) (parameter values from Brydsten 2009) and the PD2015 equations with updated parameters (black solid line). The legend also shows the average present-day Forsmark relative sea-level change, given by the slope of each curve.*

[14] The linear regression, which is used to calculate this value, is statistically significant at the 0.01 level ($p < 0.01$).

The estimated value of the eustasy from tide gauge and GPS provided here is comparable to other studies. For instance, Johansson et al. (2002) evaluated the eustatic contribution to be 1.9 mm a^{-1} in Fennoscandia. The global-mean sea-level rise was estimated by IPCC (2013a) to be about 2 mm a^{-1} towards the end of the last century mainly due to the thermal expansion of the oceans and the melting of glaciers (except Greenland and Antarctica). In a more recent study, Nerem et al. (2018) used a 25-year time series (1993–2017 AD) of precision satellite altimeter data and estimated the global mean sea-level rise to be 3 ± 0.4 mm a^{-1} for this period. It is hence likely that the difference between the present-day relative sea-level changes resulting from the PD2015 curve and the tide gauge data (2 mm a^{-1}; see Figure G-4) can be primarily explained by the underestimated present-day eustasy in the PD2015 model.

G2.4 Confidence intervals

The empirical modelling approach of the Holocene relative sea level entails that the uncertainties in the observational data can be used to estimate confidence intervals. The study of HR2003 presents two major sources of quantifiable errors associated with (i) the estimated threshold height for the investigated lake, and (ii) the radiocarbon dating. The errors associated with the radiocarbon dating represent uncertainties in the age of the measured material and are depicted as horizontal bars in Figure G-1. In general, the radiocarbon-based errors are significantly larger (several orders of magnitude) than those of the threshold height measurements (HR2003). Therefore, in the following analysis, only the reported errors from radiocarbon dating in HR2003 are used to construct confidence intervals to the main relative sea-level curve.

As already discussed, the reported radiocarbon-induced error in HR2003 is significantly larger for the older data points than for the younger ones (Figure G-1). Because of this difference, the uncertainty ranges for the five youngest data points were computed separately from the older data. This implies that the data is effectively separated into two bins with different error characteristics. To construct the uncertainty ranges for each bin, the part of the relative sea-level curve covered by that bin was shifted along the x-axis until a best-fit agreement (using the least square method) with the radiocarbon-based confidence intervals from HR2003 was obtained. This approach hence resulted in four confidence interval curves, separated into the two bins on both sides of the main relative sea-level curve. The confidence intervals on each side of the main relative sea-level curve were ultimately connected using linear interpolation.

The resulting confidence intervals for the Forsmark relative sea level are shown in Figure G-5. There is a clear transition of the uncertainty range between 3.8 ka BP and 4.6 ka BP as a result of the larger errors associated with the older data. This means that the 95 % confidence range of the Forsmark relative sea level, based on uncertainties in the radiocarbon dating in HR2003, increases from approximately 3 m to 10 m from the late to the middle Holocene.

G3 Conclusions

In this appendix an updated Holocene relative sea-level curve for Forsmark, ranging from 10.8 to 0 ka BP, has been described, based on a relatively recent and comprehensive empirical model (the PD2015 model). This model is considered to be an improved version of the model presented in Påsse (2001), which was used in previous safety assessments.

The difference in the Holocene relative sea-level representation between the updated curve and the curve used in the previous safety assessment is shown in Figure G-6. The updated relative sea-level curve results in only minor changes for the late and middle Holocene with respect to the SR-PSU. However, in the early Holocene, the difference becomes progressively larger, culminating at ~ 40 m around 10 ka ago. The small difference between the relative sea-level curves in the late and middle Holocene stems from using the same observational dataset (HR2003) to constrain the curves for those periods, whereas the relatively large difference in the early Holocene primarily results from an improved representation of the eustatic development in PD2015 compared with Påsse (2001). In conclusion, the analysis in this appendix supports the continued use of the historical relative sea-level curve developed for the SR-PSU.

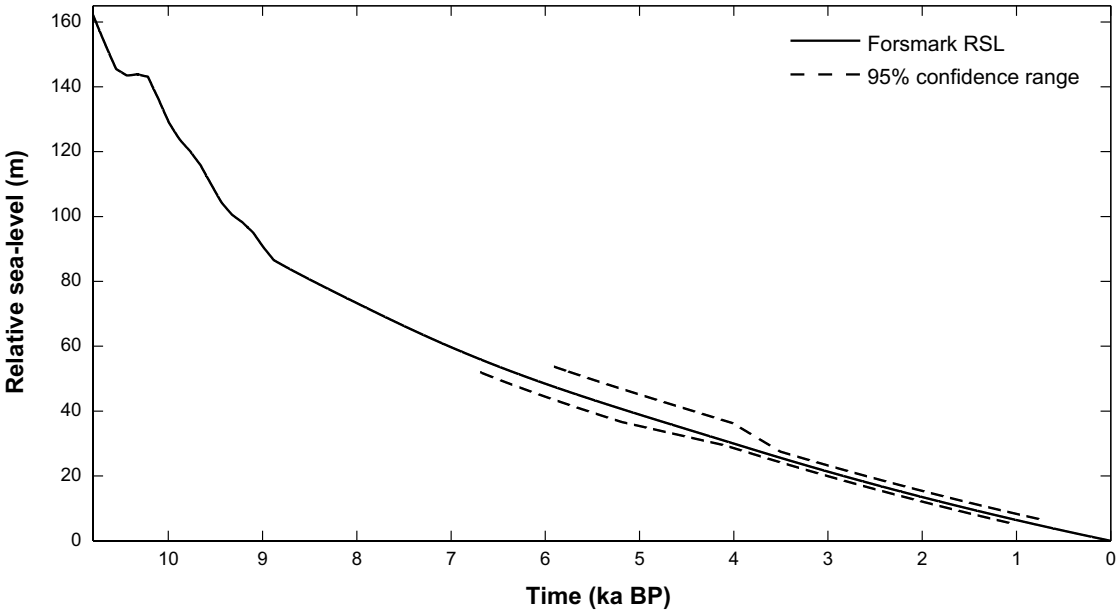

Figure G-5. *The updated Holocene relative sea-level curve for Forsmark, constructed using the methodology summarised in Table G-2 (black solid line). The black dotted lines represent the lower and upper confidence intervals (at 95 % level) based on uncertainties in the radiocarbon dating (HR2003). The details on how the confidence intervals have been computed are provided in Section G2.4.*

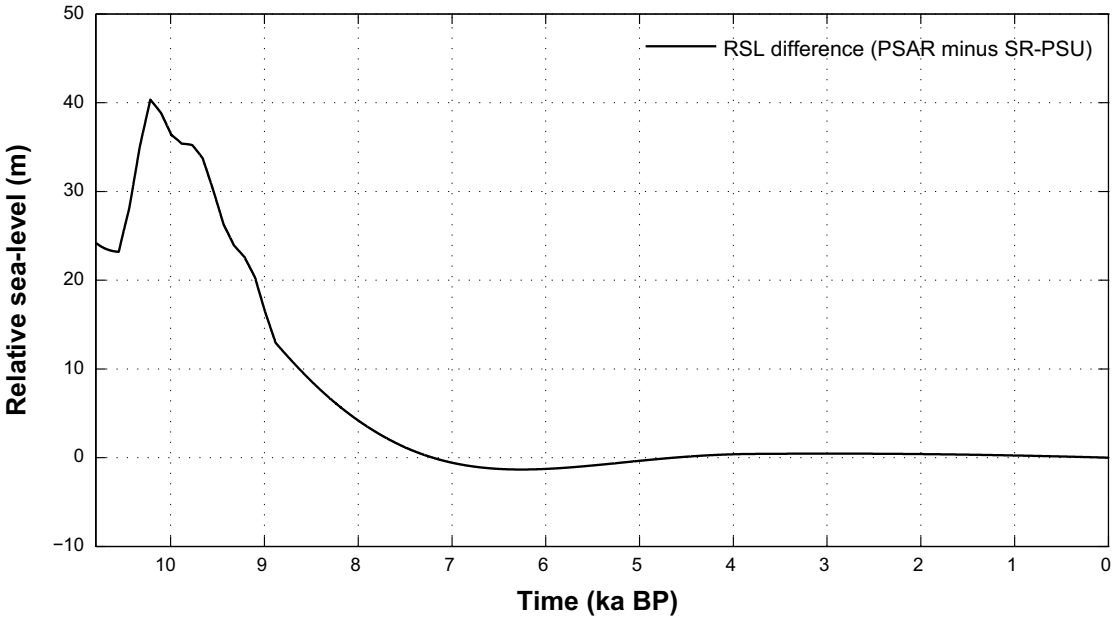

Figure G-6. *Difference in the Holocene relative sea-level development for Forsmark used in this report and in the SR-PSU (SKB TR-13-05). Note that the difference is small for the late and middle Holocene but becomes progressively larger for the early Holocene.*

Arkitektkopia AB, Bromma, 2023

SKB is responsible for managing spent nuclear fuel and radioactive waste produced by the Swedish nuclear power plants such that man and the environment are protected in the near and distant future.

skb.se